Tampere University

MEHMET YAMAC

Advances in Sparse Representation

Efficient modeling and applications

Tampere University Dissertations 985

Tampere University Dissertations 985

MEHMET YAMAC

Advances in Sparse Representation
Efficient modeling and applications

ACADEMIC DISSERTATION
To be presented, with permission of
the Faculty of Information Technology and Communication Sciences
of Tampere University,
for public discussion in TB109
of Tietotalo Building, Korkeakoulunkatu 1, Tampere,
on 19 March 2024, at 12 o'clock.

ACADEMIC DISSERTATION
Tampere University, Faculty of Information Technology and Communication Sciences, Finland

Responsible supervisor and Custos	Professor Moncef Gabbouj Tampere University Finland	
Supervisor	Professor Serkan Kiranyaz Qatar University Qatar	
Pre-examiners	Professor Ljubiša Stanković University of Montenegro Montenegro	Assistant Professor Jian Zhang Peking University China
Opponent	Professor Gonzalo R. Arce University of Delaware USA	

The originality of this thesis has been checked using the Turnitin OriginalityCheck service.

Cover design: Roihu Inc.

ISBN 978-952-03-3356-0 (print)
ISBN 978-952-03-3357-7 (pdf)
ISSN 2489-9860 (print)
ISSN 2490-0028 (pdf)
http://urn.fi/URN:ISBN:978-952-03-3357-7

Carbon dioxide emissions from printing Tampere University dissertations have been compensated.

PunaMusta Oy – Yliopistopaino
Joensuu 2024

Dedicated to my wife, Aytuna, and my daughter, Peri.

PREFACE

In his declaration following successfully receiving the radio echo from the moon for the first time, John H. DeWitt Jr. stated, "If one allows the imagination free rein, many future possibilities appear." I tried approaching the research directions presented in this dissertation with this spirit of discovery and innovation. I hope that the humble efforts I will present in this dissertation may not only provide new directions for sparse representation and compressed sensing theory but also lead to new directions in machine learning and signal processing in general.

This dissertation is a compilation of my selected research papers in the field of sparse representation and compressed sensing theories. The dissertation includes studies carried out from 2017 to 2024 within the Signal Analysis and Machine Intelligence (SAMI) group at Tampere University, focusing on the core contents of innovative ideas and research directions I initiated. It excludes the studies that are less relevant or the works that can be considered as continuations of the findings in this dissertation and studies I contributed to before 2017.

For their invaluable guidance, constant support, and mentorship throughout my doctoral journey at Tampere University, I would like to express my deepest gratitude to my supervisor and my second supervisor, Prof. Moncef Gabbouj and Prof. Serkan Kiranyaz, respectively. It is also my pleasure to thank the pre-examiners of my dissertation, Prof. LJubisa Stankovic (University of Montenegro) and Assist. Prof. Jian Zhang (Peking University), for their valuable contributions. My gratitude extends to Prof. Gonzalo R. Arce (University of Delaware) for agreeing to serve as the opponent in my dissertation defense.

Throughout my academic journey and professional development, Prof. Gabbouj's profound expertise and valuable feedback have always served as a guide for me. Not only as a supervisor but also as a mentor and source of inspiration, he has never hesitated to offer his help and experience in helping me to make important decisions regarding my career and advancing in my field of expertise. As a concrete example of

this continuous support, when I was hospitalized before a conference, Prof. Gabbouj's concern for my well-being throughout the night and his handling of my conference and travel-related paperwork clearly demonstrated his supportive and kind nature. This and many similar events are only a small indication of Gabbouj's outstanding qualities not only as an academic guide but also as a respected supervisor who provides encouragement, help, and understanding in difficult times.

Prof. Kiranyaz's technical expertise and never-ending passion for research and science have always motivated me, even while working full-time at another workplace, continuing my Ph.D. studies outside working hours, and also taking care of my newborn daughter. During this process, his kind acceptance to hold meetings about my dissertation outside working hours, even at midnight, is the clearest indication of his endless excitement and dedication. This generous attitude shows how valuable and understanding Prof. Kiranyaz is not only as an academician but also as a human being. This flexibility and understanding not only improved the quality of my dissertation work but also gave me inspiration and strength to tackle challenges in my personal and professional life.

I owe a special debt of gratitude to Bulent Sankur, who supervised my research at Bogazici University before I started my Ph.D. at Tampere University. He played a significant role in developing my academic discipline, and even after I began my new career at Tampere University, he continued to support me and contribute to some of my dissertation publications as a co-author. Professor Sankur's selfless commitment to science and progress is reflected in this approach, which always puts students' needs first. He has been recognized as one of the leading scientists in Turkey in the field of signal processing for his contributions to the training of the next generation of scientists in this discipline. Prof. Sankur's support and guidance throughout my academic journey have been and will be indispensable for me both in my academic development and in my professional career.

I would like to express my special thanks to my friends Mete Ahishali, Aysen Degerli, Ugur Akpinar, Mert Duman, Dr. Erdem Sahin, Dr. Sinem Aslan, who shared the same excitement and made valuable contributions to my work during this period. Each of them enriched my work by sharing their knowledge and experiences with me during my Ph.D. journey. In addition to directly contributing to some studies of this dissertation, Mete Ahishali deserves special recognition for continuing the follow-up studies on the methods we developed in the publications presented in this dissertation.

I am also grateful to Fahad Sohrab, all my other friends in the SAMI group and former group members for their support throughout this journey. The discussions we had in the group over the years were incredibly enlightening and pushed me to think more critically and deeply about my dissertation.

I would like to express my deepest gratitude to my wife, Aytuna Yamaç, my life partner and greatest friend, who has been with me at every stage of this dissertation study, my biggest supporter, my source of motivation, and my companion. Without her presence, it would not have been possible for me to complete this dissertation successfully. Throughout this academic journey, Aytuna never hesitated to support me both mentally and physically; she stayed awake with me as I worked late into the night and even into the morning to meet deadlines. While I was working full time at another workplace and continuing my Ph.D. studies outside working hours, even while she was taking care of our newborn daughter, she was not only understanding about the long hours my studies required, in the evenings and on weekends but also did not forget to provide motivation and moral support. Aytuna's dedication played a vital role in completing my dissertation, and her love, patience, and understanding have inspired me at every step of this journey.

Finally, I would like to express my sincere gratitude to my father, my mother, who believed in me at every step of my academic journey since childhood; and my brother, who helped me understand advanced radar signal processing topics better and significantly increased my interest in the subject.

Tampere, February 2024

Mehmet YAMAC

ABSTRACT

This dissertation investigates the analysis of linear systems of equations, particularly focusing on underdetermined systems where the solution vector is sparse or approximately sparse. With its roots in Compressive Sensing (CS), this dissertation identifies several critical challenges in the literature of Sparse Representation theory and introduces a number of novel methodologies. The methods proposed in this dissertation are applicable to a wide range of application areas.

In this dissertation, a considerable portion of the research focuses on the task of sparse support estimation, exploring methods to estimate the locations of the non-zero elements of the sparse vector without the need to fully recover it. This dissertation demonstrates that learning such a direct mapping from the measurement vector to the location indices of sparse signals, which is also called as support set, is indeed possible via a compact neural network even if only a small or moderate-size training dataset is available. A new classifier is presented as a key application, which integrates dictionary-based and neural network approaches into an efficient hybrid method. The classifier proved its effectiveness in data-scarce scenarios, particularly in COVID-19 detection from chest X-RAY images task, which was developed in the early stage of the pandemic when large training sets were unavailable. Despite such training data scarcity, the CSEN-based classification approach achieved remarkably good performance in COVID-19 detection from X-ray images, achieving over 98% sensitivity and over 95% specificity on the QaTa-Cov19 dataset.

Specifically focused on the challenge of handling large-scale and multi-dimensional signals, the dissertation introduces a novel factorization method, the Generalized Tensorial Sum (GTS-T), to represent the CS matrix with far fewer parameters than the conventional CS system, formulated by matrix-vector multiplication. This method enables the training of neural networks for efficient optimization of the CS matrix, which is especially advantageous for large-scale and multi-dimensional signals. The proposed GTS-T factorization remarkably reduces the complexity of optimizing such

large-scale CS matrices by using separable multi-linear learning and showed significant performance enhancement in signal recovery, especially at low measurement rates compared to commonly used factorization approaches such as block-wise learning.

This dissertation also investigates methods that perform signal processing directly on the measurement vector rather than first requiring the recovery of the sparse vector. It first investigates two different methods of direct classification of CS measurements, one of which is for multi-linear compressive learning where CS matrix is learned in the form of GTS-1, and the other is for more vectorized compressive learning where CS system is in conventional matrix-vector multiplication form. Second, by reforming the direct data hiding over CS measurement technology, the dissertation provides both single-level and multi-level CS-based encryption for compressive and secure sensing based monitoring. The proposed methodology is specifically important for privacy-preserving surveillance systems, with its effectiveness in applying increased security to the sensitive part of the signals at a low cost. The experimental validations showed the effectiveness of the proposed approach in robustly hiding sensitive data during joint compression and encryption at a very low cost in the sensory part while maintaining high-quality signal recovery in the receiver. This scheme successfully balanced privacy protection with image fidelity, demonstrating its potential for use in real-world surveillance scenarios with face anonymization on top of compressive encryption.

The dissertation further presents a method for domain transition strategy based on sparse representation and personalized dictionary learning. The method is demonstrated for a specific case study of zero-shot ECG anomaly detection, providing evidence of its effectiveness in efficiently transferring samples representing both normal and abnormal beats from the source to the target directly in the signal domain. The proposed zero-shot classification approach achieved a remarkable accuracy of 98.2% and an F1-Score of 92.8% on the MIT-BIH ECG dataset, significantly outperforming the existing approaches and demonstrating its usefulness for personalized, energy-efficient ECG monitoring.

CONTENTS

List of Tables

ABBREVIATIONS

ADMM	Alternating Direction Method of Multipliers
AES	Advanced Encryption Standard
AMP	Approximate Message Passing
AMP-Net	Approximate Message Passing Network
BoW	Bag of Words
BP	Basis Pursuit
BPDN	Basis Pursuit Denoising
CNN	Convolutional Neural Network
COAST	COntrollable Arbitrary-Sampling NeTwork
CS	Compressive Sensing
CSENs	Convolutional Sparse Support Estimator Networks
CSMs	Compressively Sensed Measurements
DCT	Discrete Cosine Transform
DPA-Net	Dual-Path Attention Network for Compressed Sensing
DSP	Digital Signal Processing
ECG	Electrocardiogram
FFT	Fast Fourier Transform
FISTA	Fast Iterative Shrinkage Thresholding Algorithm
FLOP	Floating Point Operation
GAN	Generative Adversarial Network
GDPR	General Data Protection Regulation

GPR	Ground Penetrating Radar
GPSR	Gradient Projection for Sparse Reconstruction
GTSNet	Generalized Tensor Summation Compressive Sensing Network
HOSVD	Higher-Order Singular Value Decomposition
HR	High-Resolution
IDCT	Inverse Discrete Cosine Transform
IFFT	Inverse Fast Fourier Transform
IoT	Internet of Things
ISTA	Iterative Shrinkage Thresholding Algorithm
JL	Johnson-Lindenstrauss
JPEG	Joint Photographic Experts Group
KNN	K-Nearest Neighbors
LAMP	Learned Approximate Message Passing
LASSO	Least Absolute Shrinkage and Selection Operator
LISTA	Learned Iterative Shrinkage Thresholding Algorithm
LR	Low-Resolution
MAC-Net	Memory Augmented Cascading Network
MCL	Multilayer Compressive Learning
ML	Machine Learning
MPEG	Moving Picture Experts Group
MR	Measurement Rate
NN	Neural Network
NPE	Null Space Projection Error
NSP	Null Space Property
OMP	Orthogonal Matching Pursuit
OPINE-Net	OPtimization-INspired Explicable deep Network
PCA	Principal Component Analysis

PSNR	Peak Signal-to-Noise Ratio
RDN	Residual Dense Network
RIC	Restricted Isometry Constant
RIP	Restricted Isometry Property
RSA	Rivest–Shamir–Adleman
SAE	Sparse Approximation Error
SCOP	Second Order Cone Program
SDN	Stacked Denoising Autoencoder
SFS	Stepped-Frequency Systems
SNR	Signal-to-Noise Ratio
SVM	Support Vector Machine
TV	Total Variation
TWRI	Through-the-Wall Radar Imaging
VCL	Vectorized Compressive Learning

ORIGINAL PUBLICATIONS

Publication I M. Yamaç, M. Ahishali, S. Kiranyaz, and M. Gabbouj, "Convolutional Sparse Support Estimator Network (CSEN): From Energy-Efficient Support Estimation to Learning-Aided Compressive Sensing," *IEEE Transactions on Neural Networks and Learning Systems*, vol. 34, no. 1, pp. 290–304, 2023. DOI: 10.1109/TNNLS.2021.3093818.

Publication II M. Yamaç, M. Ahishali, A. Degerli, S. Kiranyaz, M. E. H. Chowdhury, and M. Gabbouj, "Convolutional Sparse Support Estimator-Based COVID-19 Recognition From X-Ray Images," *IEEE Transactions on Neural Networks and Learning Systems*, vol. 32, no. 5, pp. 1810–1820, 2021. DOI: 10.1109/TNNLS.2021.3070467.

Publication III M. Yamaç, M. Orhan, B. Sankur, A. S. Turk, and M. Gabbouj, "Through the Wall Target Detection/Monitoring from Compressively Sensed Signals via Structural sparsity," in *5th International Workshop on Compressed Sensing applied to Radar, Multimodal Sensing, and Imaging*, 2018.

Publication IV M. Yamaç, M. Ahishali, N. Passalis, J. Raitoharju, B. Sankur, and M. Gabbouj, "Multi-Level Reversible Data Anonymization via Compressive Sensing and Data Hiding," *IEEE Transactions on Information Forensics and Security*, vol. 16, pp. 1014–1028, 2021. DOI: 10.1109/TIFS.2020.3026467.

Publication V M. Yamaç, B. Sankur, and M. Gabbouj, "Robust Data Hiding Scheme for Compressively Sensed Signals," in *2018 26th European Signal Processing Conference (EUSIPCO)*, 2018, pp. 1760–1764. DOI: 10.23919/EUSIPCO.2018.8553522.

Publication VI A. Değerli, S. Aslan, M. Yamac, B. Sankur, and M. Gabbouj, "Compressively Sensed Image Recognition," in *2018 7th European Workshop on Visual Information Processing (EUVIP)*, 2018, pp. 1–6. DOI: 10.1109/EUVIP.2018.8611657.

Publication VII D. T. Tran, M. Yamaç, A. Degerli, M. Gabbouj, and A. Iosifidis, "Multilinear Compressive Learning," *IEEE Transactions on Neural Networks and Learning Systems*, vol. 32, no. 4, pp. 1512–1524, 2021. DOI: 10.1109/TNNLS.2020.2984831.

Publication VIII M. Yamaç, U. Akpinar, E. Sahin, S. Kiranyaz, and M. Gabbouj, "Generalized Tensor Summation Compressive Sensing Network (GTSNET): An Easy to Learn Compressive Sensing Operation," *IEEE Transactions on Image Processing*, vol. 32, pp. 5637–5651, 2023. DOI: 10.1109/TIP.2023.3318946.

Publication IX M. Yamaç, M. Duman, İ. Adalıoğlu, S. Kiranyaz, and M. Gabbouj, "A Personalized Zero-shot Ecg Arrhythmia Monitoring System: From Sparse Representation Based Domain Adaption to Energy Efficient Abnormal Beat Detection for Practical Ecg Surveillance," *IEEE Transactions on Neural Networks and Learning Systems*, 2022, Under review. Pre-print version available on arXiv. ArXiv ID: 2207.07089v1.

Author's contribution

Publication I — The candidate introduced the concept of learning-based support estimation for sparse signals to the compressive sensing and sparse representation literature. This publication presents Convolutional Support Estimator Networks (CSENs), a family of neural architectures with compact configurations, as a proof-of-concept design. The proposed CSEN has a wide range of applications, including improvements in dictionary-based classifiers and recovery performances in sparse signal recovery algorithms. The candidate developed the idea, wrote the paper, designed the experiment, and contributed significantly to implementation and experimental validation. Mete Ahishali contributed to the implementation and experimental validation, while the remaining co-authors supervised the work and reviewed the publication.

Publication II — Building on the support estimation strategy in Publication I, this publication introduces an approach to overcome the data scarcity problem in developing deep learning-based COVID-19 detection by demonstrating the effectiveness of CSEN-C. The candidate developed the idea, wrote the paper, and contributed to the experimental designs. Mete Ahishali contributed to experimental validation, while the remaining co-authors supervised the work and reviewed the publication.

Publication III — This publication discusses the case of insufficient training data in specialized tasks such as compressive sensing-based through-the-wall radar imaging, where producing realistic synthetic data is challenging. The publication proposes a structural sparse model as a solution to the support estimation problem for this specific task. The proposed model enhances the recovery of non-zero locations of structural sparse signals, proving especially effective in CS radar imaging for accurate target localization. The candidate implemented the solution, conducted the experimental work, and wrote the paper, while the co-authors supervised the work and

reviewed the publication.

Publication IV — This publication introduces a Compressive Sensing (CS) based data encryption method, designed especially for surveillance systems. This method effectively obfuscates and encrypts both sensitive and non-sensitive parts of the data while providing multi-level security for these sensitive portions. The candidate developed the idea, Mete Ahishali contributed to the implementation, wrote the paper, while the co-authors supervised the work and reviewed the publication.

Publication V — This publication enhances the concept of direct data hiding over CS measurements by introducing an improved encoding and decoding scheme for linear data hiding in compressively sensed measurements (CSMs). The key contribution in this publication is to have two different data fidelity terms in the design of the optimization problem, which is developed for joint estimation of the sparse signal and watermark. The candidate developed the idea, implemented it, and wrote the paper, while the co-authors supervised the work and reviewed the publication.

Publication VI — This publication proposes a strategy for classifying compressively sensed signals without the need to recover them first. The publication also proposes a method for utilizing features that are extracted in both the signal space and a sparsifying domain over proxy signals. In that way, significant performance increases can be obtained in recovery-free classification over CSMs tasks. The candidate developed the idea, wrote most of the paper, and contributed to the experiments. Both Aysen Degerli and Sinem Arslan contributed to the experimental validation of the study, with Sinem Arslan assisting with some stages of manuscript preparation. The remaining co-authors supervised the work and reviewed the publication.

Publication VII — This publication contributes to direct classification of Compressive Sensing measurements (CSMs). The study introduces an approach to the reconstruction-free classification of CSMs. Unlike

previous works, including Publication VI, which utilized vectorial compressive learning with matrix-vector CS operations, this study factorizes the CS matrix using Kronecker multiplication. In that way, the proposed factorization can be seen as a special case of the factorization proposed in Publication VIII. The publication proposes a joint learning framework for the CS operation and a task-specific module for inference via proxy. The candidate contributed to the development of the concept and the experimental setup by designing the experimental procedure. Dat Thanh Tran conducted the experiments and wrote the paper. The remaining co-authors supervised the work and reviewed the publication.

Publication VIII — This publication introduces a factorization method, Generalized Tensorial Sum (GTS-T), to the compressive sensing (CS) literature. This method parametrizes the CS matrix as the sum of matrices derived from Kronecker multiplications. This approach enables learnable CS matrices, especially for large-scale and multi-dimensional signals. The candidate's GTS-T factorization notably simplifies and enhances the process of jointly learning the CS matrix and the neural network-based recovery algorithm. The candidate developed the concept and was responsible for the implementation and experimental validation of the concept. He also wrote the paper. Ugur Akpinar contribute the implementation. The remaining co-authors supervised the work and reviewed the publication.

Publication IX — This publication presents a domain transition strategy based on sparse representation and personalized dictionary learning. The application of this strategy in the context of zero-shot ECG anomaly detection illustrates the method's potential for transferring normal as well as abnormal samples directly from a known source to a new target. The candidate developed the concept, contributed significantly to the implementation, and wrote most of the paper. The co-authors supervised the work and reviewed the publication.

1 INTRODUCTION

Over the past few decades, Sparse Representation and Compressive Sensing have received significant attention from the signal processing and machine learning communities. Despite significant progress in recent years, there remain a number of unexplored areas and unresolved challenges that require further research. This dissertation addresses some of these complicated challenges in a manner that contributes to the field by introducing innovative methods and potentially practical applications. This dissertation takes a closer look into linear system of equations

$$\mathbf{y} = \mathbf{D}\mathbf{x}, \tag{1.1}$$

where $\mathbf{y} \in \mathbb{R}^m$ is the measurement vector, and $\mathbf{D}$ is an $m \times n$ matrix. We focus specifically on cases where $\mathbf{x}$ is a sparse or approximately sparse vector.

Throughout this dissertation, our primary interest lies in scenarios where the system in Eq. (1.1) is an underdetermined linear system, i.e., $m < n$, except in Chapter 6, where we explore the case $m > n$. The Fundamental Theorem of Linear Algebra [1] tells us that perfect recovery of $\mathbf{x}$ from $\mathbf{y}$ is generally not achievable, especially for the case where $m < n$. The recent approaches in compressive sensing and sparse representation theory, however, prove to us that by using the prior knowledge of $\mathbf{x}$ being sparse, such recovery is feasible and indeed guaranteed for special cases regarding $\mathbf{D}$.

In the literature on compressive sensing and sparse representation, there are primarily two research directions. The first involves designing the matrix $\mathbf{D}$ to ensure a stable embedding of $\mathbf{x}$ in $\mathbf{y}$ in order to maximize information preservation. The second direction focuses on developing algorithms to recover $\mathbf{x}$ given a fixed $\mathbf{D}$. Traditional CS theory literature has extensively explored the recovery guarantees and algorithms under the assumption that $\mathbf{x}$ is sparse. In subsequent advances, additional prior information about the sparse coefficients, such as structural sparsity, was incorporated to improve the performance of the recovery process. The advent of neural network technology has further enhanced the performance of these algorithms.

However, the sparse recovery methods from $\mathbf{y}$ in Eq. (1.1) are typically iterative and computationally expensive. In a typical CS monitoring system, an edge device (transmitter) performs computationally inexpensive linear sampling while the receiver handles the more demanding recovery process. This leads to several challenges that are partly addressed by literature or still unexplored:

(i) Can signal processing tasks be performed directly on $\mathbf{y}$, without first needing to recover $\mathbf{x}$?

This question can be related to any signal processing task over compressively sensed signals, tasks that were traditionally performed on signals obtained via traditional acquisition methods, such as quantization, watermarking, and recognition. Even though recent attention has been paid to this direction [2], it remains a less focused area compared to well-studied sparse signal recovery methods. Particularly, we are interested in methods of direct data hiding and privacy preservation applied directly to $\mathbf{y}$, without first needing to recover $\mathbf{x}$, which are less explored in CS literature. One of the main focuses of this dissertation is to fill this gap in the literature by introducing a type of efficient embedding technique that can jointly provide encryption, privacy-preservation, compression, and data hiding while compressively sensing the signal. In addition, this dissertation enhances the field of compressive learning (direct inference on measurements without first needing to recovery $\mathbf{x}$), a branch of direct signal processing over CS measurement literature. We propose two novel learning methodologies for classifying the signal $\mathbf{x}$ directly from its compressive sensing representation $\mathbf{y}$, thus avoiding first needing to recover sparse signals.

When considering sparse recovery, we refer to identifying the non-zero elements of $\mathbf{x}$ with their locations, magnitudes, and signs. However, many applications require only partial information about $\mathbf{x}$. Specifically, estimating the locations of the non-zero elements, known as the sparse support set, is sufficient in many practical scenarios. Traditional approaches estimate support set by first recovering $\mathbf{x}$ and then applying ordinary thresholding. This leads to the next question:

(ii) How can we coarsely estimate the sparse signal support set without recovering $\mathbf{x}$, and how can this estimation be beneficial in various applications?

Another challenge this dissertation addresses is the feasibility of handling large-scale signals, especially regarding the matrix $\mathbf{D}$. While the Kronecker CS technique offers a factorization approach for conventional CS matrices, this often compromises the quality of recovery compared to the one achieved with non-factorized matrices for

a fixed measurement rate. Therefore:

(iii) How can we factorize $\mathbf{D}$ to represent it with fewer parameters without significantly sacrificing performance in signal recovery and other signal processing tasks?

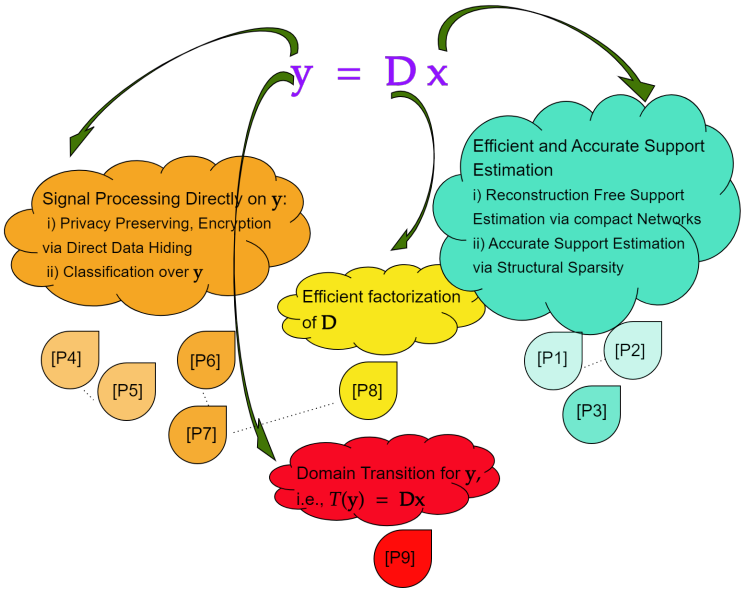

Figure 1.1 Diagrammatic representation of the interconnections among the works presented in the dissertation.

Literature findings within compressive sensing theory about sparse recovery from linear systems, as represented in Eq. (1.1), are highly useful for a variety of tasks. These include representing the signal $\mathbf{y}$ as a linear combination of a subset of vectors from $\mathbf{D}$. It can be used for a variety of purposes, including representation-based classification, anomaly detection, and more. Additionally, the literature discusses optimizing $\mathbf{D}$ for specific tasks by enforcing sparse representation of the target signal in $\mathbf{D}$, a process known as dictionary learning. Once a dictionary is learned and established, it is generally assumed that the new test samples can be sparsely represented in $\mathbf{D}$. However, in some cases, especially when the training set is highly specific to a particular measurement device or the measured item, this assumption may not hold. A notable example is the ECG signal morphology, which is unique to each individual. We can conceptualize personalized dictionary learning as the process of learning the subspaces in which a specific data type lives for any sensory system or dataset using its own samples. In such scenarios, signals from new devices may not be adequately

represented by the dictionary $\mathbf{D}$, even if they are of the same type. In the case of ECG anomaly detection, for example, if we learn a dictionary from the healthy signals of user p, it may not accurately represent the signals of a new user who recently registered with the monitoring system, regardless of whether the new user's test signals are healthy. Mathematically, this situation results in the system in Eq. (1.1) to be highly inconsistent, potentially making the analysis of $\mathbf{x}$ unreliable. This leads to the challenge:

(iv) Can we design a transformation, $T(\cdot)$, for the measurement $\mathbf{y}$, that enables stable analysis of $\mathbf{x}$ from $T(\mathbf{y}) = \mathbf{D}\mathbf{x}$, even when direct analysis based on $\mathbf{y} = \mathbf{D}\mathbf{x}$ is not robust?

1.1 Motivation and Objectives

This dissertation addresses these questions and provides practical application scenarios. For instance, [P9] is about addressing the challenge (iv), where we explore zero-shot ECG anomaly detection. In this system, the assumption is that only a limited number of healthy samples for new users are available, while the abnormal (arrhythmic) ECG signals are unknown. We estimate a transformation $T(\cdot)$ acting as a domain transition [3] between users, which can transform existing users' healthy signal into the healthy signal subspace of the new user. Upon learning this transformation, it can be applied to both healthy and abnormal beat signals of the existing users in order to make them appear as if they originated from the new user. The majority of studies in transfer learning and domain adaptation focus on transforming high-level features rather than input signals, regardless of whether they are based on sparse representation or not [4]. A noticeable exception to this trend is the use of methods based on Generative Adversarial Networks (GANs), such as the signal-to-signal translation process [5]. An example of this can be found in a study using Cycle-GAN, where the direct translation of input signals from one domain to another is referred to as 'domain transition' [3]. As stated above, in this dissertation, we have developed a technique for domain transition using sparse representation, specifically designed for zero-shot ECG anomaly detection.

Regarding the challenge (iii), in [P8], we introduce a new factorization method, Generalized Tensorial Sum (GTS-T), which parametrizes $\mathbf{D}$ as the sum of matrices resulting from Kronecker multiplication. This approach allows for efficient optimiza-

tion of the CS matrix together with the neural network-based recovery algorithm, both of which are jointly learned. For a special case, T=1, we demonstrate that direct inference from $\mathbf{y}$ can be optimized through a neural network, addressing (i) as well in [P7]. Regarding challenge (i), another significant contribution of this dissertation, presented in [P6], is the concept of utilizing extracted features from both the spatial and sparse domains. This approach significantly enhances classification performance for the task of direct recognition of compressively sensed signals.

Regarding challenge (i), in addition to the above-mentioned studies on direct inference over compressively sensed signals, compressive and secure sensing strategies are also investigated in [P4] and [P5]. In [P4], we discuss our proposed method for multi-level CS-based encryption, which incorporates direct data hiding within the CS measurements. This approach enables multi-level encryption, providing enhanced privacy protection. Specifically, we employ double cryptography for highly sensitive parts of the signal, while using single-level encryption for less sensitive portions, both are CS-based. Furthermore, in [P5], we propose an advanced recovery technique for this direct data-hiding approach. This technique is not only applicable to the system outlined in [P4] but also improves the accuracy and robustness of the signal recovery for any other applications that also require reconstruction-free direct data hiding over CS measurements.

To tackle challenge (ii), we develop a non-iterative neural network-based framework for sparse support estimation in [P1] and [P2]. This framework has broad applications, including dictionary-based classification and anomaly detection. In addition, the method can enhance the performance of the conventional CS algorithms when coarse support estimation is used as a priori information for the sparse signal recovery. Furthermore, in scenarios where data collection poses significant challenges, such as in radar monitoring applications, the integration of certain handcrafted prior assumptions can still significantly improve recovery performance. When combined with the idea of focusing on support estimation rather than full recovery, prior assumptions about sparse signal support can be particularly effective for localization problems in radar monitoring. This approach, which we categorize as a structural sparsity assumption for support recovery, is also discussed in [P3].

As a result, we can re-arrange the more generic research questions mentioned above into more specific objectives and corresponding key research questions (RQs) that are targeted in this dissertation in the following manner:

RQ-1: How can we extract information about $\mathbf{x}$, particularly the locations of its non-zero elements, without fully recovering $\mathbf{x}$? How can this coarse estimation of the support set be utilized in practical applications?

a) For the case where we have access to enough training data, can we learn compact NNs for direct mapping from $\mathbf{y}$ to the support set of $\mathbf{x}$?

b) In the case where we do not have access to enough data, how can we use our prior assumptions to have structural sparsity models, and how can we improve the support estimation performance of optimization-based approaches?

RQ-2: How can we design a factorization $\mathbf{D}$ to make CS feasible for large-scale signals, including efficient recovery of $\mathbf{x}$?

RQ-3: How can we perform resource-efficient signal processing directly on the measurement vector $\mathbf{y}$ without the need to recover $\mathbf{x}$?

a) How can we ensure privacy-preserving observations of $\mathbf{y}$?

b) How can we more efficiently classify $\mathbf{x}$ without recovering it, directly from $\mathbf{y}$?

RQ-4: How can we design a transform $T(\cdot)$ for $\mathbf{y}$ to enable stable analysis of $\mathbf{x}$ from $T(\mathbf{y}) = \mathbf{D}\mathbf{x}$, even when direct analysis from $\mathbf{y} = \mathbf{D}\mathbf{x}$ is infeasible?

1.2 Main Contributions

In this dissertation, we investigated, for the first time in the literature, whether sparse support estimation can be achieved using neural networks. As a result of our research, we have observed that learning such a mapping with compact neural networks is feasible, and this approach can have numerous applications. Dictionary-based classification methods, for example, use features extracted from the training set as atoms in the dictionary matrix. Consequently, when estimating the contributions of each column as a representation vector (ideally sparse) in the representation of the test signal on the pre-organized dictionary, this information is very beneficial in determining the class of the test signal. Although this method is commonly used, finding the corresponding representation vector becomes more difficult as the training set grows. Our method, in contrast, offers a more effective classifier by using only a part of the training data

in the dictionary and the rest in the training of a compact support estimator network rather than expanding the dictionary size by using the whole training dataset in it. As the location of the non-zeros is the most critical information to determine the class among such dictionary-based techniques, the proposed technique leads to a very effective compact classifier. Such a classifier not only yields more accurate results but also reduces computational load compared to competing methods in many classification problems. We also discovered that using this support estimator network's outputs as prior information injected into the classical sparse signal recovery methods significantly enhances both convergence speed and recovery accuracy.

We also worked on optimization-based methods for support estimation and experienced that collecting training data remains a challenging task in certain scenarios. A typical example is the task of acquiring images through walls using radar technology. In such instances, we demonstrated that defining and addressing the optimization problem as a structural sparsity model is notably more effective by using some intuitive priori assumptions rather than solving the conventional optimization problem based on an ordinary sparse model.

A challenge not yet fully addressed in the literature is that the CS system, which is traditionally defined in the classical vector-matrix multiplication form, is not very easy to implement, especially for large-scale signals such as high-resolution images. Specifically, optimizing the CS matrix via a neural network module as a part of a deep network that jointly optimizes the CS matrix and the mapping responsible for the reconstruction of the signal from its measurements would be highly costly. The prevalent recent solution for this challenge is to divide images into smaller blocks and apply the CS matrix to each block independently. As an alternative, we propose a factorization method based on multiple uses of Tucker Decomposition to factorize a CS matrix. By using this factorization technique, neural networks were able to learn even large-scale CS matrices effectively.

We demonstrated that learning the compressive sensing matrix via the proposed factorization based on Tucker Decomposition is effective for both signal recovery and direct classification of measurements. We also showed that there is still room for improvement in the reconstruction-free classification of compressively sensed signals, even for CS systems using either conventional or learned CS matrices in their traditional, unfactorized form. For conventional ordinary CS systems, we introduce an alternative feature extraction and classification scheme to the literature works.

Experimentally, we have shown a good improvement in classification performance using the proposed method.

As another example of direct signal processing on CS measurements, we studied the method of data hiding over CS measurements. By reforming this concept, we introduced a multi-level CS-based encryption technique. Our experimental results have demonstrated the effectiveness of this method in helping to address the challenges of privacy preservation in CS monitoring systems.

Finally, we introduce a novel domain transition technique via sparse representation and personalized dictionary learning. This method involves estimating such domain transitions from one subspace to another that are represented by corresponding personalized dictionaries for independent identities. As an example of this method, we present a zero-shot ECG anomaly detection case study that illustrates its ability to transform both healthy as well as anomalous samples from the source (ECG signal subspace belonging to an existing user that has healthy and abnormal ECG signals, already labeled) to the target domain (ECG signal subspace of a new user with only a limited number of healthy samples and no anomalies) directly at the input level without the need for any feature extraction first. Such a domain transition enables us to train neural networks directly in the target domain by transforming abundant healthy and abnormal ECG signals in order to make them appear as if they originated from the target domain.

1.3 Dissertation Structure

The dissertation is organized into seven chapters as follows: Chapter 2 provides preliminaries on Sparse Representation Theory, including a detailed discussion of key topics from literature, such as commonly used recovery algorithms and conventional compressive sensing theoretical guarantees on sparse signal recovery. The concepts, explained in more detail, form the basis for our theoretical and experimental results in subsequent chapters. Chapter 3 addresses RQ-1, focusing on sparse support estimation from the measurement vector $\mathbf{y}$. It investigates two main directions: a non-iterative neural network-based approach and a method that exploits a specific structural sparsity model and an optimization theory-based algorithm to achieve enhanced accuracy compared to the conventional sparsity model and its corresponding recovery algorithm. Chapter 4, addressing RQ-2, introduces a novel factorization method, the Generalized

Tensorial Sum (GTS-T). This method factorizes $\mathbf{D}$ as a sum of matrices derived from Kronecker multiplication, thus allowing efficient neural network-based optimization of the CS matrix. Chapter 5, considering RQ-3, presents our proposed methodologies for direct inference from the measurement vector $\mathbf{y}$. This includes, first, an idea of utilizing features from both spatial and sparse domains to enhance signal classification. Secondly, a technique that optimizes neural network-based inference using tensorial factorization of CS matrix, i.e., GTS-1, which is jointly learned with the deep module responsible for feature extraction and classification. Additionally, the chapter investigates compressive and secure sensing strategies via direct data hiding over CS measurements. Chapter 6, addresses RQ-4 and explores zero-shot ECG anomaly detection. The chapter assumes the availability of only a limited number of healthy signal samples from new users, with no abnormal ECG signals. It focuses on estimating a transformation $T(\cdot)$ that acts as a domain adaptation between users. Finally, Chapter 7 concludes the dissertation, summarizes the key findings and contributions of the research, and suggests topics for future research.

2 SPARSE REPRESENTATION

In this chapter, we will briefly explore the theories of sparse representation and compressive sensing (CS). Initially, we will introduce the general concepts of sparse representation and its specialized subfield, the CS theory. Following this, we will discuss the essential characteristics that CS matrices and dictionary matrices should possess, taking a closer look at the relevant classical theories. Among these, the concepts of the Restricted Isometry Property (RIP) and the coherence will be examined in greater detail. This is because, based on the classical RIP-based guarantee conditions, we aim to derive the guarantee conditions for the reversible multi-level CS-based encryption method in Chapter 5.1. Additionally, the coherence index will serve as a crucial tool for the experimental design that motivates us to develop the proposed GTS factorization of CS matrices in Chapter 4.

Following the properties of CS matrices, we will provide a summary of the most commonly used optimization-based recovery algorithms under the topic of proximal algorithms. These classical CS recovery methods will be used throughout the dissertation in many places, either in their original form or in an improved version, particularly as competing methods to those we have proposed in this dissertation. Afterward, we will summarize the latest neural network-based methods. In subsequent chapters, these methods will be directly compared with those developed in this dissertation.

2.1 Preliminaries

The ℓ_p-norm of a vector $\mathbf{x} \in \mathbb{R}^n$ is defined throughout this dissertation as $\|\mathbf{x}\|_p = \left(\sum_{j=1}^{n} |x_j|^p\right)^{1/p}$ for $p \geq 1$. In addition, the number of the non-zero coefficients is denoted by the ℓ_0-norm, i.e., $\|\mathbf{x}\|_0 = \lim_{p\to 0} \sum_{i=1}^{n} |x_i|^p = \#\{j : x_j \neq 0\}$.

In a proper basis (or dictionary), $\mathbf{\Phi} \in \mathbb{R}^{d\times n}$, if a signal of interest, $\mathbf{s} \in \mathbb{R}^d$, can be represented by at most k number of non-zero coefficients, then this signal or its

representation vector, $\mathbf{x} \in \mathbb{R}^n$, is called to be *strictly k-sparse*, i.e.,

$$\|\mathbf{x}\|_0 \leq k, \tag{2.1}$$

where $\mathbf{s} = \mathbf{\Phi x}$. On the other hand, the majority of the signals we find in real-world applications exhibit a power-law decay in $\mathbf{\Phi}$ when the coefficients of $\mathbf{x}$ are sorted by magnitude i.e., $\left|\mathbf{x}^1\right| \geq \left|\mathbf{x}^2\right| \geq ... \geq \left|\mathbf{x}^{n-1}\right| \geq |\mathbf{x}^n|$, where $\mathbf{x}^j$ is the j^{th} largest coefficient of $\mathbf{x}$ in magnitude. In this point, let us define the *support set*, $\Lambda \subset \{1, 2, 3, ..., n\}$, of a sparse signal as the set of indices of the location of the non-zero coefficients in the signal $\Lambda := \{i : x_i \neq 0\}$. Let also $\Lambda\,(k)$ be the set of indices of k largest coefficients in magnitude, then $\mathbf{x}$ is called to be *approximately k-sparse* or *compressible* in $\mathbf{\Phi}$, if

$$\left\|\mathbf{s} - \mathbf{\Phi x}_{\Lambda(k)}\right\|_2 \leq \varrho, \tag{2.2}$$

where ϱ is a small constant.

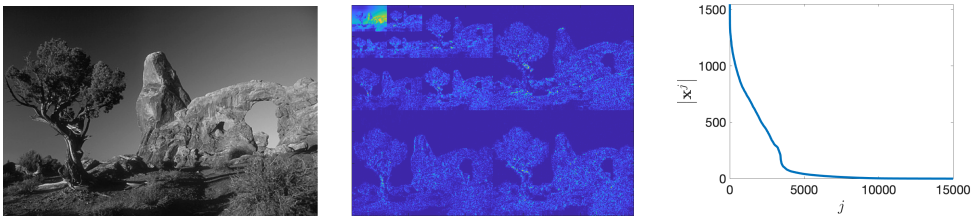

(a) **(b)** **(c)**

Figure 2.1 A well-known example of compressible signals is the wavelet domain representation of an image. (a) The original image. (b) The wavelet coefficients of the image. Pixels with small coefficients are in blue color. c) When sorted in descending order, the magnitudes of the coefficients exhibit a rapid decay.

Given a dictionary $\mathbf{\Phi} \in \mathbb{R}^{d \times n}$ of collection of the discrete-time waveforms of length n which are commonly called as atoms, we assume that the signal of interest $\mathbf{s}$ can be represented as the linear combination of these atoms,

$$\mathbf{s} = \mathbf{\Phi x}, \tag{2.3}$$

where $\mathbf{x} \in \mathbb{R}^n$ is the vector of representation coefficients of $\mathbf{s}$ in $\mathbf{\Phi}$.

For example, in the classical case where $d = n$, it is possible to have a matrix $\mathbf{\Phi}$ that

consists of n linearly independent atoms, where $\mathbf{\Phi}$ is called *complete dictionary* (or *basis*) such as Fourier [6] and DCT [7]. As a consequence of linear independence of columns and rows of the dictionary $\mathbf{\Phi}$, each signal representation in $\mathbf{\Phi}$ will be unique, i.e., $\mathbf{x} = \mathbf{\Phi}^{-1}\mathbf{s}$. It is possible, however, that one can enrich the representation by adding more atoms, in which case we will have $\mathbf{\Phi} \in \mathbb{R}^{d \times n}$ with $n > d$, which is called *over-complete dictionary* (or *frame*). Therefore, representation in Eq. (2.3) cannot be unique in this case. We need to make one more assumption to satisfy the uniqueness requirement. Traditionally, this assumption could be searching for a solution having the minimum energy (which is defined by ℓ_2-norm) among all solutions satisfying Eq. (2.3) i.e.,

$$\min_{\mathbf{x}} \ \|\mathbf{x}\|_2^2 \ \text{subject to } \mathbf{\Phi}\mathbf{x} = \mathbf{s}. \tag{2.4}$$

The solution of the optimization problem defined in Eq. (2.4) will be unique, and also known as *minimum norm solution* (the method also called as *method of frames*),

$$\hat{\mathbf{x}} = \mathbf{\Phi}^{+}\mathbf{y} = \mathbf{\Phi}^{T}\left(\mathbf{\Phi}\mathbf{\Phi}^{T}\right)^{-1}\mathbf{y}, \tag{2.5}$$

where $\mathbf{\Phi}^{+} = \mathbf{\Phi}^{T}\left(\mathbf{\Phi}\mathbf{\Phi}^{T}\right)^{-1}$ is known as *Moore-Penrose pseudo-inverse* or *canonical dual frame*. Alternatively, one may desire a more efficient representation in which a signal is represented by only a linear combination of a relatively small number of atoms,

$$\min_{\mathbf{x}} \ \|\mathbf{x}\|_0 \ \text{subject to } \mathbf{\Phi}\mathbf{x} = \mathbf{s}, \tag{2.6}$$

which is called *sparse signal representation* of $\mathbf{s}$ [8]. The concept of sparse representation is encountered in a wide range of disciplines. An overview of a specific application area, compressive sensing, is provided in the sequel. Compressive sensing relies heavily on sparse representation. With the efforts done in this field, the mathematical framework of sparse representation defined in Eq. (2.6) is now mature. For clarity, as of now, we have only given the definition of sparse representation, which is Eq. (2.6). The question of whether the representation is unique or not was not discussed. For example, how can we estimate the sparse representation vector as close to that of the ground truth as possible within a feasible time and budget? Despite the fact that the following section describes uniqueness, stability, and recovery methods in compressive sensing theory, the conclusions apply to general cases in which we can represent data in the form of Eq. (2.6).

2.2 Compressive Sensing

Data or signal representation in compressive sensing can be regarded as a special case of the sparse representation in Eq. (2.3). Since its inception in 2006, [9]–[11], compressive sensing theory has had a significant impact on signal processing. According to CS theory, a sparse signal can be recovered using fewer measurements than is required by traditional Shannon-Nyquist data acquisition methods. In conventional CS theory, the measurements are taken linearly in the discrete form via inner products (Interested readers can also see recent literature [12] for the extension of the theory to the infinite-dimensional CS schemes i.e., Hilbert space formulation). Mathematically speaking, let a CS scheme acquire m number of measurements of finite-dimensional signal ($\mathbf{s} \in \mathbb{R}^d$ a vector living in Euclidean space),

$$\mathbf{y} = \mathbf{A}\mathbf{s}, \tag{2.7}$$

where $\mathbf{A} \in \mathbb{R}^{m \times d}$ is called the measurement matrix with $m << d$, which represents such linear signal acquisition system.

There are two groups of effort in designing such a linear measurement system: (i) Developing a measurement matrix, $\mathbf{A}$, that preserves the information of $\mathbf{s}$ while transforming it into a lower dimensional space, as in (2.7). (ii) Development of an algorithm that recovers $\mathbf{s}$ from $\mathbf{y}$ within a reasonable amount of time while minimizing reconstruction errors. The sequel will provide a brief overview of CS literature, emphasizing existing measurement designs to maximize information preservation. CS reconstruction algorithms will be then discussed in terms of computational cost, minimum measurements needed to guarantee recovery, stability, and advantages and disadvantages.

Based on elementary linear algebra, it can be stated that Eq. (2.7) is an underdetermined linear system of equations whose solution set has infinitely many elements for given $\mathbf{A}$ and $\mathbf{y}$. The only way to reach a unique solution is to make at least one more assumption. Following the same approach we used in the previous section, we can start by selecting the solution with the minimum energy from this set of solutions,

$$\min_{\mathbf{s}} \|\mathbf{s}\|_2^2 \text{ subject to } \mathbf{A}\mathbf{s} = \mathbf{y}. \tag{2.8}$$

From Eq. (2.5), assuming $\mathbf{A}$ is full row rank, then the solution of Eq. (2.8) is unique,

i.e., $\hat{\mathbf{s}} = \mathbf{A}^T \left(\mathbf{A}\mathbf{A}^T\right)^{-1} \mathbf{y}$. The minimum energy of the reconstruction error that can be achieved with this technique is defined as $\|\mathbf{s} - \hat{\mathbf{s}}\|_2 = \mathbf{s}^T \left(\mathbf{I} - \mathbf{A}^T \left(\mathbf{A}\mathbf{A}^T\right)^{-1} \mathbf{A}\right) \mathbf{s}$. As we know $\mathbf{I} \neq \mathbf{A}^T \left(\mathbf{A}\mathbf{A}^T\right)^{-1} \mathbf{A}$ since $m < d$, we can conclude that the exact recovery of $\mathbf{s}$ is not possible.

In CS theory, the solution is sought in the subspace defined by a dictionary $\mathbf{\Phi} \in \mathbb{R}^{d \times n}$, where $\mathbf{s}$ has sparse representation $\mathbf{x}$. Mathematically speaking, Eq. (2.7) can be re-formulated,

$$\mathbf{y} = \mathbf{A}\mathbf{s} = \mathbf{A}\mathbf{\Phi}\mathbf{x} = \mathbf{D}\mathbf{x} \tag{2.9}$$

where $\mathbf{D} = \mathbf{A}\mathbf{\Phi} \in \mathbb{R}^{m \times n}$ is equivalent dictionary.

Let $\mathbf{x}$ be the strictly k-sparse signal representation of $\mathbf{s}$. The question then becomes, "Can $\mathbf{x}$ be exactly recovered from $\mathbf{y}$?" The answer is yes; perfect recovery is possible if the equivalent dictionary satisfies certain conditions. If the representation in Eq. (2.9) is unique, provided that $\mathbf{x}$ is k-sparse, then this unique solution can be recovered exactly via

$$\min_{\mathbf{x}} \|\mathbf{x}\|_0 \text{ subject to } \mathbf{D}\mathbf{x} = \mathbf{y}. \tag{2.10}$$

In other words, $\mathbf{x}$ can be found using ℓ_0-minimization if it is the only k-sparse solution of Eq. (2.9). *To put it another way, whereas exact signal recovery was not possible in the original domain (except the signals that are sparse in canonical base) where the signal is dense (nonsparse), it is possible to do it in a sparsifying domain.* Having the sparse recovery $\hat{\mathbf{x}}$, one can easily turn back to original domain, i.e., $\hat{\mathbf{s}} = \mathbf{D}\hat{\mathbf{x}}$.

As a result, the only remaining question is which conditions must be met by $\mathbf{D}$ so that Eq. (2.9) becomes the unique representation of any k-sparse $\mathbf{x}$. In order to satisfy the uniqueness, $\mathbf{D}$ should not map any two distinct k-sparse signals $\mathbf{x}'$ and $\mathbf{x}''$ to the exact same point, i.e., $\mathbf{D}\mathbf{x}' \neq \mathbf{D}\mathbf{x}''$. This statement implies that the null space of $\mathbf{D}$ should not include any $2k$-sparse signal $\mathbf{x}'''$, i.e., $\mathbf{x}''' \notin \text{Null}(\mathbf{D})$. Put in other words, if $\mathbf{D}\mathbf{x}' = \mathbf{D}\mathbf{x}''$, which means $\mathbf{D}(\mathbf{x}' - \mathbf{x}'') = 0$, then no method can distinguish $\mathbf{x}'$ and $\mathbf{x}''$. And, by definition $\mathbf{x}''' = \mathbf{x}' - \mathbf{x}''$ becomes $2k$-sparse signal.

This condition first appeared in [13] with a concept called the spark of a matrix, $\text{Spark}(\mathbf{D})$, which is defined as the minimum number of linearly dependent atoms that the matrix $\mathbf{D}$ can have. The requirement $\mathbf{x}''' \notin \text{Null}(\mathbf{D})$ implies that $\mathbf{D}$ should satisfies $\text{Spark}(\mathbf{D}) > 2k$. Therefore, the minimum number of measurements to take can also be determined as $m \geq 2k$ because $\text{Spark}(\mathbf{D}) \in [2, m+1]$.

Summary 1

Uniqueness of the k-sparse solution of ℓ_0-minimization problem defined in Eq. (2.10) is guaranteed given equivalent dictionary $\mathbf{D}$ has $m > 2k$ number of linearly independent rows. In plain English, no algorithm can guarantee the exact recovery of any k-sparse signal from the measurement vector $\mathbf{y}$ if the number of measurements does not exceed $2k$.

Nevertheless, the problem in Eq. (2.10) is not convex and is known to be NP-hard. The most common approach involves relaxing the ℓ_0-norm to the closest convex norm, the ℓ_1-norm. Specifically, the sparse signal can be recovered by solving the following minimization problem:

$$\min_{\mathbf{x}} \|\mathbf{x}\|_1 \text{ subject to } \mathbf{D}\mathbf{x} = \mathbf{y}. \tag{2.11}$$

Without further ado, let us address the question of why the ℓ_1-minimization solution is sparse. Afterwards, we can consider the conditions that must exist for this solution to be exactly equal to the solution of ℓ_0-minimization. Sparsity is indeed promoted by any ℓ_p-norm minimization for $p \leq 1$ (However, the ℓ_p-norms for $p < 1$ are quasinorms, and therefore the corresponding optimization problems become non-convex. There exist studies considering such sparse data representations, i.e., ℓ_p-norm minimization solvers for $0 < p < 1$ [14].). Let us examine a simple example of a linear system equation that can be graphically solved. The measurement in this toy example is $\mathbf{y} = \mathbf{D}\mathbf{x} = x_1 + 2x_2 = 10$. The system plot is shown in Figure 2.2, and the intersection of the ℓ_p-ball and the solution set's line represents the graph's solution. We can see that the ℓ_2-ball supports a nonsparse (dense) solution in Figure 2.2a, with the intersection occurring at point $(2, 4)$. As seen in Figures 2.2b and 2.2c, the ℓ_1-norm and $\ell_{0.5}$-norm on the other hand, encourage a sparse solution where the intersection emerges at point $(5, 0)$. Note that this visualization just demonstrates how ℓ_1-norm promotes sparsity and says nothing about whether $\mathbf{y} = \mathbf{D}\mathbf{x}$ is met by an exact solution for every $k = 1$-sparse $\mathbf{x}$ with $\mathbf{D} = \begin{bmatrix} 1 & 2 \end{bmatrix}$ (in fact, it does not, as we will see next).

Until now, our first conclusion was that any k-sparse signal can be uniquely represented by a sparse representation, so these signals can be recovered perfectly with a ℓ_0-norm minimization procedure, however, this solution cannot be achieved in a polynomial time. Afterward, we relax the problem to the ℓ_1-norm minimization opti-

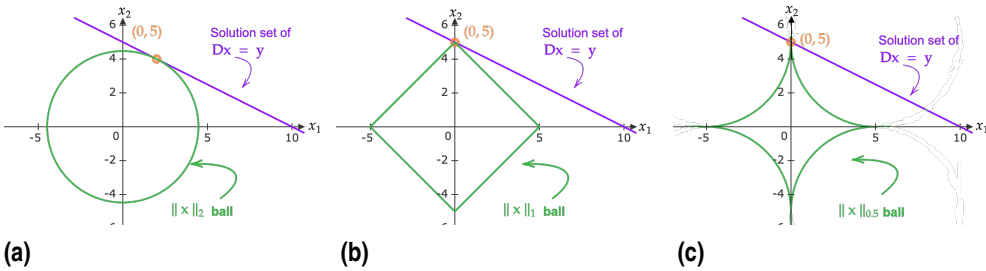

(a) (b) (c)

Figure 2.2 Illustration of the graphing solution of a linear system of equations (a) The solution of ℓ_2-minimization is nonsparse. (b) ℓ_1-norm minimization tends to produce sparse solution. c) $\ell_{0.5}$-norm also promotes sparsity.

mization problem, also known as Basis Pursuit (BP) [15]. In addition, we discussed that ℓ_1-norm minimization tends to result in sparse solutions as well. It is now time to explore whether the sparse solution given by ℓ_0-norm minimization can also be achieved by BP (therefore, ℓ_1-norm minimization solution becomes exact as well). In order to ensure the equivalence of the solutions of ℓ_0-norm and ℓ_1-norm minimization problems, a notation called Null Space Property (NSP) [16], [17] can be used:

Definition 2.1 (Null Space Property [17]) *A matrix* $\mathbf{D} \in \mathbb{R}^{m \times n}$ *fulfils the Null Space Property (NSP) of order* k *is, if*

$$\|\mathbf{v}_\Lambda\|_1 \leq \|\mathbf{v}_{\Lambda^c}\|_1 \tag{2.12}$$

is met for all $\mathbf{v} \in$ *Null* $(\mathbf{D})$*, where* Λ *is the set of* k *indices.*

If a matrix $\mathbf{D} \in \mathbb{R}^{m \times n}$ satisfies the NSP of order k, then any k-sparse vector can be exactly recovered from Eq. (2.9) by solving Eq. (2.11). This theorem and its formal proof can be found in [17]. On the other hand, we can give the following worst-case scenario to give an intuition behind the theorem. Let us select two possible solution of $\mathbf{Da} = \mathbf{y}$; one is our desired k-sparse vector $\mathbf{x}$ and the other is any vector $\mathbf{z}$. Therefore, we will have $\mathbf{Dz} = \mathbf{Dx}$. We desire any ℓ_1-norm minimization solver to choose $\mathbf{x}$ instead of $\mathbf{z}$, which is only possible if $\|\mathbf{x}\|_1 < \|\mathbf{z}\|_1$ for any $\mathbf{z}$ satisfying $\mathbf{D}(\mathbf{x}-\mathbf{z}) = 0$. Consider, we are in worst case scenario where $\mathbf{z}_\Lambda = \mathbf{0}$, Λ is set of non-zero indices of $\mathbf{x}$ and $\mathbf{0}$ is zero vector of length-k. In that case, we need $\|\mathbf{x}\|_1 = \|\mathbf{x}_\Lambda\|_1 < \|\mathbf{z}_{\Lambda^c}\|_1 = \|-\mathbf{z}_{\Lambda^c}\|_1$. This implies $\|\mathbf{h}_\Lambda\|_1 < \|\mathbf{h}_{\Lambda^c}\|_1$ because $\mathbf{h}_\Lambda = \mathbf{x}_\Lambda$, $\mathbf{h}_{\Lambda^c} = -\mathbf{z}_{\Lambda^c}$ for this special case where $\mathbf{h} = \mathbf{x} - \mathbf{z} \in$ Null $(\mathbf{D})$ from the starting assumption (i.e., $\mathbf{D}(\mathbf{x} - \mathbf{z}) = 0$).

To put the overall discussion simply, we stated that Null ($\mathbf{D}$) should not possess any $2k$-sparse sparse vector in order to satisfies the uniqueness of the solution of ℓ_0-norm minimization problem. Now, the Null Space Property further dictates that Null ($\mathbf{D}$) should not contain overly compressible vectors [18] to guarantee to have uniqueness of the solution of ℓ_1-norm minimization problem (which also implies the exact solution or the equivalence of ℓ_0-norm and ℓ_1-norm minimization problems).

NSP not only guarantees the equivalence of ℓ_0-norm and ℓ_1-norm minimization problems, but also serves as a convenient tool for assessing the recovery performance when $\mathbf{x}$ is not strictly k-sparse but rather compressible [16]. However, when we deal with approximately sparse signals and the measurements vector that are also impacted by additive noise, then a stronger property, Restricted Isometry Property (RIP) [19], [20] is used (There are studies that attempt to give a stability condition based on a concept called robust null space property, which first appeared in [21]. Nevertheless, this property does not purely depend on the null space of $\mathbf{D}$ [22].).

Definition 2.2 (Restricted Isometry Property) *The restricted isometry property of order k is fulfilled by a matrix $\mathbf{D} \in \mathbb{R}^{m\times n}$ if*

$$(1 - \delta_k(\mathbf{D}))\, \|\mathbf{x}\|_2^2 \leq \|\mathbf{D}\mathbf{x}\|_2^2 \leq (1 + \delta_k(\mathbf{D}))\, \|\mathbf{x}\|_2^2 \tag{2.13}$$

for all k-sparse signal, $\mathbf{x}$ with the smallest possible scalar $\delta_k(\mathbf{D})$, which is called Restricted Isometry Constant (RIC).

It is important to emphasize that the RIP is a stronger property than the NSP, in a way that any matrix that satisfies the RIP is guaranteed to satisfy the NSP as well [18]. As we will discuss in more detail, giving theoretical guarantees for some specific types of measurement matrices to have RIP is much easier than showing NSP guarantees. Furthermore, RIP may be used to show guarantee conditions in more general circumstances, where the measurement may be corrupted by additive noise, i.e., $\mathbf{y} = \mathbf{D}\mathbf{x} + \mathbf{e}$, where $\mathbf{e}$ is additive noise; and the sparse signal, $\mathbf{x}$, may not be strictly sparse, but rather compressible. In order to handle such a situation, the following relaxation on optimization problem (2.11) (BP) can be done,

$$\min_{\mathbf{x}} \|\mathbf{x}\|_1 \ \text{ subject to } \ \|\mathbf{y} - \mathbf{D}\mathbf{x}\|_2 \leq \varepsilon, \tag{2.14}$$

where ε is small constant. The optimization problem defined in (2.14) is also known

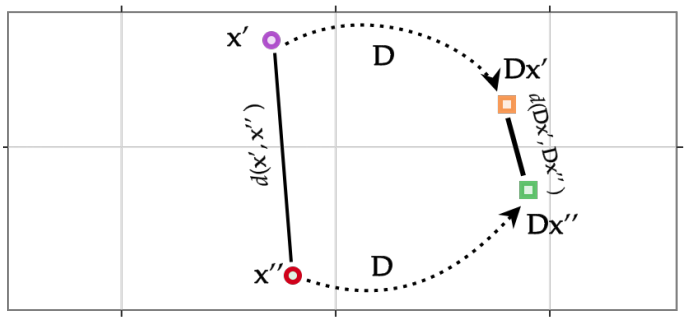

Figure 2.3 The principle behind the RIP property is that the distance $d(.,.)$ (e.g., $d(\mathbf{a},\mathbf{b}) = \|\mathbf{a}-\mathbf{b}\|_2^2$) between any arbitrary k-sparse signal pairs should be preserved after dimension reduction with $\mathbf{D}$, in order to ensure robust recovery. This graph is intended to illustrate the intuition only, and not to serve as a formal definition.

as Basis Pursuit Denoising (BPDN) [8]. Considering this, it is important to point out that another important contribution of the traditional CS literature is its effort to provide stability conditions for sparse recovery algorithms like BPDN in erroneous measurement cases. From a mathematical standpoint, a stable solution $\widehat{\mathbf{x}}$ should obey $\|\mathbf{x}-\widehat{\mathbf{x}}\|_p \leq \kappa \|e\|_p$ with a smaller as possible constant κ, the ℓ_p-norm is most commonly selected as the ℓ_2-norm, and $\mathbf{e}$ represents additive perturbations.

Studies in the CS field have carefully analyzed guarantee conditions for the equivalence of ℓ_0-norm and ℓ_1-norm minimization problems (in noise-free case for BP) and the stability conditions of BPDN in relation to RIC of the measurement matrix. The authors of [19] demonstrate that the ℓ_0-ℓ_1 equivalence is achieved when $\delta_{2k}(\mathbf{D}) \leq \sqrt{2}-1$. According to study [20], for any perturbed measurement, $\mathbf{y} = \mathbf{D}\mathbf{x} + \mathbf{e}$ with bounded energy noise, $\|\mathbf{e}\|_2 \leq \varepsilon$, the solution of (2.14) obeys

$$\|\mathbf{x}-\widehat{\mathbf{x}}\|_2 \leq C\varepsilon, \tag{2.15}$$

where the constant C varies with the RIC $\delta_{2k}(\mathbf{D}) < \sqrt{2}-1$. When considering the recovery guarantee of a k-sparse signal, it has been observed that $2k$-order RIC, $\delta_{2k}(\mathbf{D})$, is necessary instead of $\delta_k(\mathbf{D})$. In order to explain this concept intuitively, we should note that the null space analysis enforces $\text{Spark}(\mathbf{D}) > 2k$. This ensures that two different k-sparse signal $\mathbf{x}'$ and $\mathbf{x}''$ will not be mapped to the same location. Now, RIP provides a stronger assurance that the distance between $\mathbf{x}'$ and $\mathbf{x}''$ after mapping with a $\mathbf{D}$ should be maintained as follows: $(1-\delta_{2k}(\mathbf{D}))\,\|\mathbf{x}'-\mathbf{x}''\|_2^2 \leq \|\mathbf{D}\mathbf{x}'-\mathbf{D}\mathbf{x}''\|_2^2$.

Figure 2.3 visualizes this concept: The distance between any arbitrary k-sparse pairs should be preserved after mapping by $\mathbf{D}$. To put it another way, we want to ensure that any submatrix consisting of a set of any arbitrary selection of k columns of the matrix $\mathbf{D}$ has a high condition number (i.e., as close as possible to 1).

The following theorem, which first appeared in [23], gives a sense of how many measurements are required for a matrix to have RIP of order 2k:

Theorem 2.3 ([18, Ch. 1]) *For an $m \times n$ matrix $\mathbf{D}$ that satisfies the RIP of order $2k$ with $0 < \delta_{2k}(\mathbf{D}) \leq 0.5$, the following inequality should hold*

$$m \geq O\left(k.\log\left(n/k\right)\right). \tag{2.16}$$

Summary 2

As summarized in Summary 2.2, the exact recovery of any k-sparse signal could be achieved with $m > 2k$ measurements if the ℓ_0-minimization problem, defined in Eq. (2.10), was solvable. However, since this is an NP-hard problem, we relax it to an ℓ_1-minimization problem. The Restricted Isometry Property provides the conditions for the exact recovery of k-sparse signal by solving the ℓ_1-minimization problem. Theorem 2.3 states that a sufficient number of measurements, $m \geq \mathrm{O}\left(k\log\left(\frac{n}{k}\right)\right)$, is required to guarantee exact recovery. To put it another way, the increase in the required number of measurements when we moved from ℓ_0-minimization to ℓ_1-minimization is the trade-off for a tractable solution.

2.2.1 Measurement Matrices that satisfy RIP

The measurement matrices $\mathbf{A}$, which preserve information after dimensional reduction in the sparsity domain $\mathbf{\Phi}$, can be regarded as good measurement matrices. In other words, we need to check if the equivalent dictionary $\mathbf{D} = \mathbf{A}\mathbf{\Phi}$ satisfies the RIP rather than $\mathbf{A}$.

While there are deterministic measurement matrix designs that satisfy RIP, these matrices generally require a large number of measurements to satisfy RIP [24]. Meanwhile, random matrices are well known to fulfill the RIP with high probability with almost an optimal number of measurements, $m \geq \mathrm{O}\left(k.\log\left(n/k\right)\right)$. An example would be a Gaussian random matrix whose elements, $\mathbf{D}_{i,j}$ are i.i.d. (independent identically

distributed) and drawn from $\mathcal{N}\left(0, \frac{1}{m}\right)$. It is therefore reasonable to assume that if the measurement matrix $\mathbf{A}$ is Gaussian with elements $\mathbf{A}_{i,j} \sim \mathcal{N}\left(0, \frac{1}{m}\right)$ then the equivalent dictionary will be Gaussian with elements $\mathbf{D}_{i,j} \sim \mathcal{N}\left(0, \frac{1}{m}\right)$ (assuming that sparsifying matrix, $\mathbf{\Phi}$, is an orthonormal basis). This property is known to be *universality* of the random matrices. In fact, all *sub-Gaussian matrices* (A matrix $\mathbf{M}$ is called sub-Gaussian if there exists a constant c that fulfills $\mathbb{E}\left(e^{M_{i,j}t}\right) \leq e^{c^2t^2/2}, \forall t \in \mathbb{R}$.) possess these properties as the following lemma and theorem demonstrate:

Lemma 2.4 ([25]) *For any fixed vector $\mathbf{x} \in \mathbb{R}^n$, it is possible to select a probability distribution $\mathfrak{D}$ which would enable the construction of an $m \times N$ matrix $\mathbf{D}$ with entries obtained from $\mathfrak{D}$ that holds*

$$\mathbb{E}\left(\|\mathbf{D}\mathbf{x}\|_2^2\right) = \|\mathbf{x}\|_2^2 \tag{2.17}$$

and

$$Pr\left((1-\gamma)\|\mathbf{x}\|_2^2 \leq \|\mathbf{D}\mathbf{x}\|_2^2 \leq (1+\gamma)\|\mathbf{x}\|_2^2\right) \leq 1 - 2e^{(-mC(\gamma))}, \tag{2.18}$$

where $C(\gamma)$ is a positive constant that depends on $\mathfrak{D}$ and γ.

The inequality defined in Lemma 2.4 is also known as *concentration of measure inequality for random matrices*. It says, after dimensional reduction, the energy (in squared norm) is concentrated around its expected value, while the deviation from it exponentially decays with respect to m and $C(\gamma)$. As a result, a small $C(\gamma)$ is a good indicator of how well a matrix will preserve information after dimension reduction (i.e., we want to retain the distance between any two distinct points after dimensional reduction). As an example, aforementioned Gaussian matrix with elements with elements

$$\mathbf{D}_{i,j} \sim \mathcal{N}\left(0, \frac{1}{m}\right), \tag{2.19}$$

yields $C(\gamma) = \frac{\gamma^2}{4} - \frac{\gamma^3}{4}$. In literature [26]–[28], considerable efforts have been expended to determine $C(\gamma)$ for different distributions; for instance the authors of [26] has demonstrated that the same result, $C(\gamma) = \frac{\gamma^2}{4} - \frac{\gamma^3}{4}$ holds true for the following distributions as well:

$$\mathbf{D}_{i,j} = \begin{cases} \frac{+1}{\sqrt{m}} & \text{with probability } 1/2, \\ \frac{-1}{\sqrt{m}} & \text{with probability } 1/2, \end{cases} \tag{2.20}$$

$$\mathbf{D}_{i,j} = \sqrt{3} \times \begin{cases} \frac{+1}{\sqrt{m}} & \text{with probability } 1/6, \\ 0 & \text{with probability } 2/3, \\ \frac{-1}{\sqrt{m}} & \text{with probability } 1/6. \end{cases} \tag{2.21}$$

One can note that the concentration of measure inequality is not only valid for sparse signals, but it is also valid for any fixed n-length signal. On the other hand, we want to select dimensional reduction matrices that guarantee to preserve the information after compression for all signals that live in a space of interest. Fortunately, such a guarantee can be given if our space of interest is reduced from $\mathbb{R}^n$ to the set of all k-sparse signals in $\mathbb{R}^n$:

Theorem 2.5 ([25]) *Provided that the measurement matrix* $\mathbf{D} \in \mathbb{R}^{m \times n}$ *fulfills the inequality expressed in Eq.* (2.17) *and* (2.18) *with* $\gamma = \frac{\delta_k(\mathbf{D})}{4}$ *and if*

$$m \geq O\left(k . \log\left(n/k\right)\right), \tag{2.22}$$

then $\mathbf{D}$ *possess the Restricted Isometry Property of order k with a probability of at least* $1 - 2e^{-O(m)}$.

2.2.1.1 Strategy of proving RIP via Johnson-Lindenstrauss Lemma

The proof of the Theorem 2.5 can be accomplished using the same strategies used in the modern proofs of the Johnson-Lindestrauss Lemma [29]. This Lemma states a dimensional reduction mapping from $\mathbb{R}^n$ to $\mathbb{R}^m$ can be found, which preserves the distance between arbitrary any two points selected from a set $\mathcal{S} \subset \mathbb{R}^n$. Johnson–Lindenstrauss is a valuable formulation that aids in providing a low-dimensional representation of the data. Compression is significant in various applications such as machine learning, manifold learning, and compressive sensing. Reducing the dimensionality can notably increase the speed of most algorithms employed in machine learning.

In the sequel, we will briefly summarize the general strategy to prove the Theorem 2.5 rather than complete proof which can be found in [25]. The strategy can be listed as follows:

1. The heart of the proof is the concentration of measure inequality for random

matrices provided in Lemma 2.4. For a fixed point pair, $\mathbf{x}', \mathbf{x}''$ selected from set of interest $\mathcal{S}$;

(a) it can be demonstrated that after the dimensional reduction, the energy of the distance vector $\mathbf{x}' - \mathbf{x}''$ tends to concentrate in the vicinity of its expected value, i.e., if the elements of the matrix $\mathbf{D}$ are i.i.d. with var $\left(\mathbf{D}_{i,j}\right) = \frac{1}{m}$,

(b) the strategy of using Chernoff Bound for the upper and lower tail can be applied in order to find a bound for the probability of failure, i.e., $\Pr\left(\|\mathbf{Dx}\|_2^2 \leq (1-\gamma)\|\mathbf{x}\|_2^2\right) + \Pr\left(\|\mathbf{Dx}\|_2^2 \geq (1+\gamma)\|\mathbf{x}\|_2^2\right) \leq \mathrm{P}_e$, where P_e is the probability of error bound (e.g. $\mathrm{P}_e = 2e^{(-mC(\gamma))}$ for sub-Gaussian matrices).

2. Having the bound of the probability of deviation from the center, P_e, the probability of success bound can be defined using the union bound,

$$\Pr\left((1-\gamma)\|\mathbf{x}\|_2^2 \leq \|\mathbf{Dx}\|_2^2 \leq (1+\gamma)\|\mathbf{x}\|_2^2\right) \leq 1 - |\mathcal{S}|\,\mathrm{P}_e, \tag{2.23}$$

where $|\mathcal{S}|$ is the cardinality of the set of interest. Because the concentration inequality was for a fixed vector (e.g., the distance vector), we desire to have a guarantee condition of information-preserving embedding for all points in our set of interest. As mentioned earlier if we restrict our interest to the set of all n dimensional k-sparse signals, then such an embedding can be guaranteed with high probability. In order to find a bound for the number of points in the set, $|\mathcal{S}|$, the following two steps can be applied:

(a) Fix support set Λ_k and discretize the subset of k-sparse signal's space, $\mathcal{S}_{\Lambda_k}$ whose number of non-zero elements are indexed by Λ_k. The following definition and lemma describe covering number theory, a commonly used tool for such discretization.

Definition 2.6 (Covering numbers, Nets [30, Ch. 4]) *For a metric space $\mathcal{M}$ equipped with a distance metric $d(.)$, a subset $N_\varepsilon \subseteq \mathcal{M}$ is called an ε-net of $\mathcal{M}$ if every point $\mathbf{x} \in \mathcal{M}$ can be approximated by a point $\mathbf{v} \in N_\varepsilon$ [1], i.e.,*

$$\forall \mathbf{x} \in \mathcal{M} \;\; \exists \mathbf{v} \in N_e \;\; d(\mathbf{x}, \mathbf{v}) \leq \varepsilon. \tag{2.24}$$

[1] In plain English, $\mathbf{v} \in N_e$ is the center of ball with radii of ε and the set $\mathcal{M}$ is covered by these balls.

The smallest possible cardinality of N_e is called as covering number and denoted by $N(\mathcal{M}, d, \varepsilon)$.

In mathematical analyses, we are mostly interested in bounded sets, i.e., $N(\mathcal{M}, d, \varepsilon)$. In our analysis, we need to use the Euclidean norm as the distance metric, i.e., $d(.) = \|.\|_2$. In addition, without loss of generality, we can restrict our metric space to a unit Euclidean sphere, i.e., $\mathcal{M} = S^{n-1}$:

Lemma 2.7 ([30, Ch. 4]) *The covering number of unit Euclidean sphere S^{n-1} equipped with $d(.) = \|.\|_2$ will be*

$$N(S^{n-1}, \|.\|_2, \varepsilon) \leq \left(\frac{3}{\varepsilon}\right)^n, \tag{2.25}$$

for $0 < \varepsilon < 1$.

For a specific chosen of radii as $\varepsilon = \frac{\sqrt{\delta_k(\mathbf{D})}}{4}$ during the discretization of $\mathcal{S}_{\Lambda_k}$ we need concentration inequality (2.18) to hold with $\gamma = \frac{\delta_k(\mathbf{D})}{4}$ [2] in order for inequality (2.13) to fulfill for all $\mathbf{x} \in \mathcal{S}_{\Lambda_k}$ [25].

Using the covering number theory with $\varepsilon = \frac{\sqrt{\delta_k(\mathbf{D})}}{4}$, the minimum cardinality of such a subset can be given as

$$\left|\mathcal{S}_{\Lambda_k}\right| \leq \left(\frac{12}{\sqrt{\delta_k(\mathbf{D})}}\right)^k \tag{2.26}$$

(b) For now, we determine a bound for the number of points only for k-sparse signals with a fixed support set Λ_k. However, for all k-sparse signals in $\mathbb{R}^n$, there are $\binom{n}{k}$ such combinations of different support sets. Therefore, using the Sterling's approximation $\binom{n}{k} \leq \frac{n^k}{k!} \leq \left(\frac{\exp(n)}{k}\right)^k$, we obtain

$$|\mathcal{S}| \leq \left(\frac{\exp(n)}{k}\right)^k \left(\frac{12}{\sqrt{\delta_k(\mathbf{D})}}\right)^k \tag{2.27}$$

3. Having the cardinality of the set of interest, we can apply union bound as stated in Eq. (2.23). Then can find the probability of $\mathbf{D}$ satisfying the RIP of order k

[2] The increase in distortion factor from $\gamma = \frac{\delta_k(\mathbf{D})}{4}$ to $\delta_k(\mathbf{D})$ (RIC) is the cost we pay due to the discretization with the ball of radii $\varepsilon = \frac{\sqrt{\delta_k(\mathbf{D})}}{4}$.

with probability.

$$\geq 1 - 2\left(\frac{\exp(n)}{k}\right)^k \left(\frac{12}{\sqrt{\delta_k(\mathbf{D})}}\right)^k e^{-C\left(\frac{\delta_k(\mathbf{D})}{4}\right)m} \tag{2.28}$$

$$= 1 - 2\exp\left\{\left(-C\left(\frac{\delta_k(\mathbf{D})}{4}\right)m + k\left(\log\left(\frac{n}{k}\right) + \log\left(\frac{12}{\sqrt{\delta_k(\mathbf{D})}}\right) + 1\right)\right)\right\}, \tag{2.29}$$

where $C(\gamma)$ is a constant depending on $\mathbf{D}$ e.g., $C(\gamma) = \frac{\gamma^2}{4} - \frac{\gamma^3}{4}$ for $\mathbf{D}$ with $\mathbf{D}_{i,j} \sim \mathcal{N}\left(0, \frac{1}{m}\right)$ and the matrices defined in Eq. (2.20) and (2.21). In order for the error probability (i.e., $\mathrm{P}_e = 2\exp\left\{\left(-C\left(\frac{\delta_k(\mathbf{D})}{4}\right)m + k\left(\log\left(\frac{n}{k}\right) + \log\left(\frac{12}{\sqrt{\delta_k(\mathbf{D})}}\right) + 1\right)\right)\right\}$) to decay exponentially, we need to have $m \geq \mathrm{O}\left(k.\log\left(n/k\right)\right)$, which completes the proof.

Summary 3

Sub-Gaussian measurement matrices, $\mathbf{D} \in \mathbb{R}^{m\times n}$, which are discussed in Theorem 2.5, satisfy the Restricted Isometry Property (RIP) of order k provided that $m \geq \mathrm{O}\left(k\log\left(\frac{n}{k}\right)\right)$. In this context, random matrices can be considered optimal up to a certain extent in terms of the required number of measurements. This is because the lower bound of the necessary measurements for exact recovery, which requires checking the RIP of order $2k$ and given in Theorem 2.3, can be achieved with an order.

It is important to note that despite the fact that we only consider whether the equivalent dictionary $\mathbf{D}$ holds RIP or not, the analysis remains valid when the measurement matrix $\mathbf{A}$ is a sub-Gaussian basis and the sparsifying dictionary $\mathbf{\Phi}$ is any orthonormal basis. If we choose our net of points in the k-dimensional subspace spanned by sets of k columns of $\mathbf{\Phi}$, we can make the same analysis as we did above and reach the same conclusion [25]. As a result, *universality holds for all sub-Gaussian measurement matrices*, not just Gaussian ones.

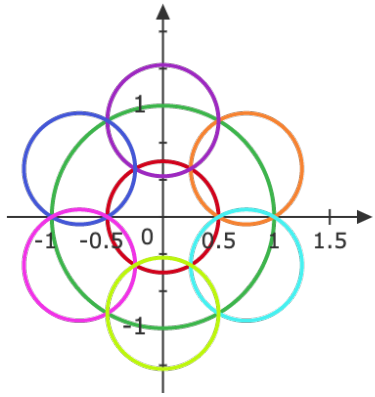

Figure 2.4 Covering of unit Euclidean sphere. For $n = 2$ and $\varepsilon = 0.5$, the sphere can be covered by minimum 7 balls.

Summary 4

Sub-Gaussian measurement matrices are universal in the sense that when the sparsifying dictionary $\mathbf{\Phi}$ is an orthonormal basis, guarantee conditions established for $\mathbf{A}$ are valid for the entire CS system represented by the equivalent dictionary $\mathbf{D} = \mathbf{A}\mathbf{\Phi}$.

2.2.1.2 Stability of ℓ_1-minimization under Gaussian Noise

The following lemma will be used in several places throughout this dissertation in order to provide stability conditions for BPDN when the measurement matrix is a Gaussian random matrix (so that the equivalent dictionary is also Gaussian), and when the measurements are perturbed with additive white Gaussian noise (AWGN) during various experiments and in the theoretical analysis of the encryption scheme presented in Chapter 5.1.

Lemma 2.8 *(Refined from [18, p. 32].) For the measurement system, where* $\mathbf{D} \in \mathbb{R}^{m \times N}$ *fulfills the RIP of order* $2k$ *with* $\delta_{2k}(\mathbf{D})$ *and measurements are obtained under i.i.d. Gaussian noise with elements drawn from* $\mathcal{N}\left(0, \frac{1}{\sigma^2}\right)$*, the solution of BPDN with*

$\varepsilon = (1+\gamma)\sqrt{m}\sigma$ *obeys*

$$\|\mathbf{x} - \hat{\mathbf{x}}\|_2 \leq 4\frac{\sqrt{1+\delta_{2k}(\mathbf{D})}}{1-(1+\sqrt{2})\delta_{2k}(\mathbf{D})}(1+\gamma)\sqrt{m}\sigma \tag{2.30}$$

with probability greater than $1 - \exp\left(-\frac{3m}{4}\gamma^2\right)$ *where* $0 < \gamma < 1$.

2.2.2 Different variants of ℓ_1-norm minimization

Until now, we have discussed the ℓ_1-norm minimization problems given by Eq. (2.11) and Eq. (2.14). They can be represented in the form:

$$\min_{\mathbf{x}} \|\mathbf{x}\|_1 \text{ subject to } \mathbf{x} \in \mho(\mathbf{y}) \tag{2.31}$$

where

$$\mho(\mathbf{y}) = \begin{cases} \{\mathbf{x} : \mathbf{D}\mathbf{x} = \mathbf{y}\} & \text{for BP as in Eq. (2.11)} \\ \{\mathbf{x} : \|\mathbf{D}\mathbf{x} - \mathbf{y}\|_2 \leq \epsilon\} & \text{for BPDN as in Eq. (2.14)} \end{cases}$$

Other forms of the data fidelity term $\mho(.)$ are also possible: For instance, the problem in Eq. (2.31) is called Dantzig Selector [31] if

$$\mho(\mathbf{y}) = \left\{\mathbf{x} : \left\|\mathbf{D}^T(\mathbf{y} - \mathbf{D}\mathbf{x})\right\|_\infty \leq \lambda\right\}. \tag{2.32}$$

The stable recovery of the Dantzig Selector has also been well studied in the literature [18], [32]. Another related formulation is:

$$\min_{\mathbf{x}} \left(\frac{1}{2}\|\mathbf{D}\mathbf{x} - \mathbf{y}\|_2^2 + \lambda\|\mathbf{x}\|_1\right), \tag{2.33}$$

known as the Lasso [33] formulation. Lasso is well known for producing stable solutions in noisy scenarios and exact solutions when noise-free and strictly sparse case [34].

2.2.3 Coherence

While Spark, NSP, and RIP are essential tools for a CS measurement system to ensure accurate and robust recovery of k-sparse signals, verifying that a measurement matrix possesses these properties is an *NP-hard* problem. This verification necessitates the

examination of all $\binom{n}{k}$ submatrices.

The coherence index, a measure that represents the maximum normalized inner product between any pair of normalized columns in the measurement matrix, is frequently used as a metric to evaluate the quality of the measurement matrix. Mathematically speaking, the coherence of a matrix $\mathbf{D}$ is defined as

$$\mu(\mathbf{D}) = \max_{1 \le i \le j \le N} \left(\frac{\left| < \mathbf{d_i}, \mathbf{d_j} > \right|}{\|\mathbf{d_i}\| \left\|\mathbf{d_j}\right\|} \right), \tag{2.34}$$

where $\mathbf{d_i}$ and $\mathbf{d_j}$ are the columns of $\mathbf{D}$ and $\langle \mathbf{d_i}, \mathbf{d_j} \rangle$ denotes the inner product between columns.

The exact and robust recovery condition guarantees have been well-studied by the literature. For example, it was shown in [35] that for exact recovery of k-sparse signals (in noise-free case) the condition $(2k-1)\mu(\mathbf{D}) < 1$ should hold. Then, in [36], it was proved that this condition also satisfies the robust recovery in noisy cases. The efforts still continue to give a more optimistic bound based on the coherence index [37], [38].

Corollary 2.9 ([39]) *The coherence of the $m \times n$ Gaussian matrix with elements with elements $\mathbf{D}_{i,j} \sim \mathcal{N}\left(0, \frac{1}{m}\right)$ can be given as follows*

$$\mu(\mathbf{D}) \approx 2\sqrt{\frac{\log N}{m}}. \tag{2.35}$$

In the following sections, we will provide a succinct overview of the primary approach used to demonstrate the proof of Corollary 2.9. For a more comprehensive proof for a range of Sub-Gaussian measurement matrices, readers are directed to [39]. The strategy is outlined as follows:

1. ***For each element, $M_{i,j}$ of the matrix, $\mathbf{M} = \mathbf{D}^T\mathbf{D}$, derive the Bernstein-type tail inequality:***

   The moment generating function of a Gaussian random variable $x \sim \mathcal{N}(0, \sigma^2)$ is given by $\mathbb{E}\left(e^{\lambda x}\right) = e^{\frac{\lambda^2\sigma^2}{2}}$. Drawing upon the discussions in [18, Ch. 5] and [30, P. 33], the moment generating function (MGF) for the sub-exponential variable $z = x_i x_j$, where $x_i, x_j \sim \mathcal{N}(0, \sigma^2)$, can be upper-bounded as $\mathbb{E}\left(e^{\lambda x}\right) \le e^{\frac{C\lambda^2\sigma^4}{2}}$. Here, C is a positive constant, and this bound holds provided $|\lambda| \le \kappa$, with κ being a small positive constant. Given the random variable $S_m = \sum_{i=1}^{m} z_i$ where each $z_i = x_i x_j$ and $x_i, x_j \sim \mathcal{N}(0, \sigma^2)$, we can derive a tail bound using the

exponential Markov inequality and the properties of the MGF that is defined above. Since the z_i are independent, the MGF of their sum is the product of their individual MGFs, $\mathbb{E}\left(e^{\lambda S_m}\right) = \prod_{i=1}^{m} \mathbb{E}\left(e^{\lambda z_i}\right) \leq \left(e^{\frac{C\lambda^2\sigma^4}{2}}\right)^m = e^{\frac{C\lambda^2\sigma^4 m}{2}}$. Now, we can use exponential Markov inequality,

$$P(S_m \geq t) = P(e^{\lambda S_m} \geq e^{\lambda t}) \leq \frac{\mathbb{E}\left(e^{\lambda S_m}\right)}{e^{\lambda t}} \leq \frac{e^{\frac{C\lambda^2\sigma^2 m}{2}}}{e^{\lambda t}}$$

By optimizing $f(\lambda) = \frac{1}{2}C\lambda^2\sigma^4 m - \lambda t$ under the constraint $0 < |\lambda| \leq \kappa$, we obtain $\lambda = \min\left(\frac{t}{C\sigma^4 m}, \kappa\right)$. Using this optimal value of λ, one can derive:

$$P(S_m \geq t) \leq \exp\left(-\min\left(\frac{t^2}{2C\sigma^4 m}, \frac{\kappa t}{2}\right)\right) \tag{2.36}$$

2. ***Apply the Union Bound in order to ensure that the tail bound given in Eq.*** (2.36) ***holds for every element in the matrix*** $\mathbf{M} = \mathbf{D}^T\mathbf{D}$***:***

   If we apply the Union Bound to every non-diagonal element in $\mathbf{M} = \mathbf{D}^T\mathbf{D}$ (which consists of approximately N^2 elements) for a specific measurement matrix $\mathbf{D}$ with elements $D_{i,j} \sim \mathcal{N}(0, \frac{1}{m})$, and for a given α, we obtain:

$$\begin{aligned} P(|S_m| \geq \alpha) &\leq 2 * N^2 * \exp\left(-\min\left(\frac{\alpha^2}{2C\frac{1}{m^2}m}, \frac{\kappa t}{2}\right)\right) \\ &= 2\exp\left(2\log(N) - \min\left(\frac{\alpha^2 m}{2C}, \frac{\kappa t}{2}\right)\right). \end{aligned} \tag{2.37}$$

   Following a similar analysis as in [40], one can deduce that for the probability of exceeding α to converge to zero as m becomes large, the condition $\frac{\alpha^2 m}{2C} > 2\log(N)$ must be satisfied. This implies that for $\alpha > 2\sqrt{\frac{\log N}{m}}$, the probability converges to zero with increasing values of m and N.

2.2.4 Structural Sparsity

We intend to provide a short overview of the CS literature in the review section of this dissertation by discussing the theoretical foundations of classical CS. Thus far, this scheme has assumed that the only prior knowledge is the sparsity of the signals. Classical sparsity only considers the level of sparsity without any specific

knowledge about the statistics of the non-zero elements. However, any additional information about the sparse signal can be used to develop advanced sparse signal recovery schemes, which fall outside the scope of this brief review. In structural sparsity models [41]–[43], additional assumptions regarding the non-zero coefficients, x, of the signal s can be made. A common assumption centers on the group structure inherent in the coefficients. This structure suggests that the non-zero elements are often closely located to each other and can be represented using the mixed norm minimization problems [44], [45]. For instance, the indices of the location of non-zero wavelet coefficients in an image typically display this group sparsity effect [46]. Moreover, these coefficients exhibit multiscale characteristics and tree-like configurations [47]. For those interested in structural sparsity preserving regularizers, we recommend relevant surveys [48].

2.3 Recovery Algorithms

In order to reconstruct sparse signals based on available measurements, several prevalent methods have been developed. Some of these include: (i) Convex Relaxation methods, often referred to as the aforementioned ℓ_1 minimization techniques such as BP defined in Eq. (2.11) and BPDN as defined in Eq. (2.14) (ii) Greedy Approaches like Matching Pursuit (MP) [49], Orthogonal Matching Pursuit (OMP) [50], and Compressive Sampling Matched Pursuit (CoSaMP) [51]. (iii) Bayesian Framework [52]. (iv) Non-convex optimization methods [14].

As we mentioned in our discussion of convex relation techniques, for exact sparse and noise-free cases, one can use the BP formulation defined in Eq. (2.11). If this is the case, BP can be solved using interior-point methods by recasting it as a linear program (LP) [8]. If the sparse signal is noisy or not exactly sparse, then the BPDN optimization problem can be solved by formulating it as a second-order cone program (SCOP) [53]. However, both LP and SCOP are computationally expensive and are not feasible for large signals. Therefore, we will mostly use proximal algorithms, which will be discussed in more detail in the sequel. Aside from these traditional iterative techniques, the latest approaches include neural network-based machine learning solutions. Many of the literature works will also be discussed after the section on proximal algorithms.

2.3.1 Proximal Theory

The objective of a generic optimization problem can be mathematically stated as follows:

$$\min_{\mathbf{x}\in\mathcal{S}} \mathcal{F}(\mathbf{x})$$

This formulation aims to minimize the objective function $\mathcal{F}(\mathbf{x})$ by searching for the optimal value of $\mathbf{x}$ within the set $\mathcal{S}$.

The classical gradient descent algorithm is a common method of solving optimization problems. This algorithm is particularly effective when the objective function is both convex and differentiable (smooth). In such cases, the algorithm can be used to seek the optimal solution $\mathbf{x}^*$ by iteratively approaching it to satisfy the condition $\nabla\mathcal{F}(\mathbf{x}^*) = 0$. Iterations of the classical gradient descent algorithm can be expressed as follows:

$$\mathbf{x}^{j+1} = \mathbf{x}^j - \gamma^j \nabla\mathcal{F}(\mathbf{x}^j) \tag{2.38}$$

where $\mathbf{x}^j$ is the current estimation of the optimal solution and γ^j is the step-size. A key feature of the classical gradient descent algorithm is that it is designed specifically for differentiable functions since calculating gradients is crucial to the optimization steps. There are, however, many optimization problems encountered in this dissertation that involve minimizing convex but non-differentiable functions. Hence, our interest lies in proximal theory, which provides approximations for the gradient step in Equation (2.38). Known as proximal maps, these approximations enable us to handle a wide variety of non-differentiable functions effectively. Following is a summary of proximal algorithms to serve as a basis for deriving our proximal algorithms presented in Section 3.2 and in Section 5.1.2, especially for the ADMM part of [P3] and [P5]. ADMM-based weighted L1 minimization is also used in P[1]. Additionally, proximal algorithms ISTA, AMP and ADMM will appear in various forms as competing algorithms in [P1], [P2], [P3], [P8], [P9]. It should be noted that many other manuscripts also discuss the following proximal algorithms preliminaries, including but not limited to [54]–[58].

Convex Set: A set $S \in \mathbb{E}$, where $\mathbb{E}$ is a finite-dimensional Euclidean space equipped with an inner product $\langle ., . \rangle$ and Euclidean norm $\|.\|_2$, is considered convex if $\forall \mathbf{x}, \mathbf{y} \in S$ and any $\gamma \in [0, 1]$, where $[\mathbf{x}, \mathbf{y}] = \{\alpha\mathbf{x} + (1-\alpha)\mathbf{y} \,|\, 0 \leq \alpha \leq 1\}$ is the line segment

between the points $\mathbf{x}$ and $\mathbf{y}$, the following condition holds:

$$\gamma\mathbf{x} + (1-\gamma)\mathbf{y} \in S.$$

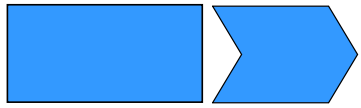

Figure 2.5 (a) A convex set. (b) A non-convex set.

Convex Functions: An extended real function $f(\mathbf{x})$ (An extended real function f, denoted as $f : \mathbb{E} \to \mathbb{R} \cup \{+\infty\}$,) is called convex if it satisfies the following conditions:

1. The domain of the function, denoted as $dom\, f$, is a convex set.
2. For all $\mathbf{x}, \mathbf{y} \in \mathbb{E}$ and any $\gamma \in [0, 1]$, it satisfies the inequality:

$$f(\gamma\mathbf{x} + (1-\gamma)\mathbf{y}) \leq \gamma f(\mathbf{x}) + (1-\gamma) f(\mathbf{y}).$$

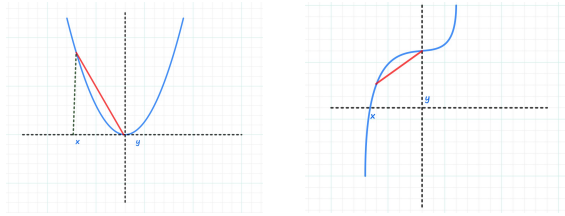

Figure 2.6 (a) A convex function. (b) A non-convex function.

First Order Condition An extended real function $f(\mathbf{x})$ is called convex if it satisfies the following conditions:

1. The domain of the function, denoted as $dom\, f$ (Domain of f, $dom\, f = \{\mathbf{x} \in \mathbb{E} : f(\mathbf{x}) < +\infty\}$.), is a convex set.
2. For all $\mathbf{x}, \mathbf{y} \in \mathbb{E}$, it satisfies the inequality:

$$f(\mathbf{y}) \geq f(\mathbf{x}) + \nabla f(\mathbf{x})^T (\mathbf{y} - \mathbf{x}) \tag{2.39}$$

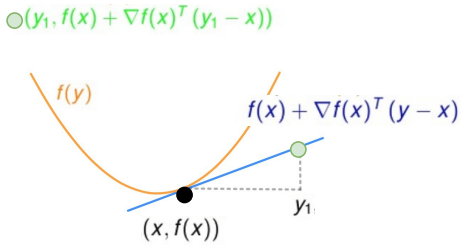

Figure 2.7 Illustrative representation on the interpretation of first order condition: $f(\mathbf{x})+\nabla f(\mathbf{x})^T(\mathbf{y}-\mathbf{x})$ is always the global underestimator of f.

As it is illustrated in Figure 2.7, the expression $f(\mathbf{x}) + \nabla f(\mathbf{x})^T(\mathbf{y} - \mathbf{x})$ has several important interpretations:

- It acts as the first-order Taylor approximation of f near the point $\mathbf{x}$.
- It reflects a global underestimator of f.
- It represents an affine function defined by the slope $\nabla f(\mathbf{x})^T$.

Subgradient A subgradient of a real proper (a function $f(.)$ is considered proper if $dom\ f \neq \emptyset$) convex function f at a point $\mathbf{x}$ is the vector $\mathbf{g} \in \mathbb{E}$ which satisfies:

$$f(\mathbf{y}) \geq f(\mathbf{x}) + \mathbf{g}^T(\mathbf{y} - \mathbf{x}), \quad \forall \mathbf{y} \in \mathbb{E}. \tag{2.40}$$

Note that when we compare Eq. (2.40) and Eq. (2.39), then we can define the gradient as a special case of subgradient: If the proper convex function f is differentiable at the point $\mathbf{x} \in \mathbb{E}$, then $\mathbf{g}$ is unique, and it is the gradient of f, denoted as $\mathbf{g} = \nabla f(\mathbf{x})$.

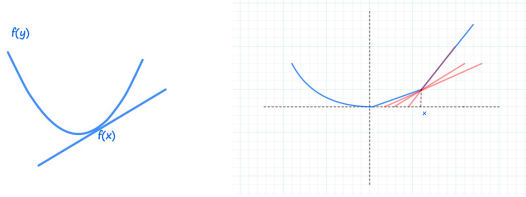

Figure 2.8 (a) Gradient. (b) Sub-gradient. Each slope of red line goes through $\mathbf{x}$, $f(\mathbf{x})$. is a sub-gradient

Subdifferential At the point $\mathbf{x} \in \mathbb{E}$, the subdifferential of the proper convex function f can be defined as

$$\partial f(\mathbf{x}) = \{\mathbf{g} \in \mathbb{E} : f(\mathbf{y}) - f(\mathbf{x}) \geq \langle \mathbf{g}, \mathbf{y} - \mathbf{x} \rangle, \quad \forall \mathbf{y} \in \mathbb{E}\}$$

At a point $\mathbf{x}$, a subdifferential $\partial f(\mathbf{x})$ of a function f is either empty or a closed convex set. An important property of the subdifferential, which we will use throughout the dissertation, is Fermat Rule [54, Theorem 16.2]: A point $\mathbf{x}^*$ is a minimizer of the function f iff $0 \in \partial f(\mathbf{x}^*)$ at $\mathbf{x}^*$. Proof: If $\mathbf{g} = 0$ at point $\mathbf{x}^*$, then

$$f(\mathbf{y}) \geq f(\mathbf{x}^*), \quad \forall \mathbf{y} \in \mathbb{E}.$$

.

Example 1: Subdifferential of the ℓ_1-norm Let $f(\mathbf{x}) = |\mathbf{x}|$, then the subdifferential $\partial f(\mathbf{x})$ is defined as:

$$\partial f(\mathbf{x}) = \begin{cases} -1 & \text{if } \mathbf{x} < 0 \\ [-1, 1] & \text{if } \mathbf{x} = 0 \\ 1 & \text{if } \mathbf{x} > 0 \end{cases} \tag{2.41}$$

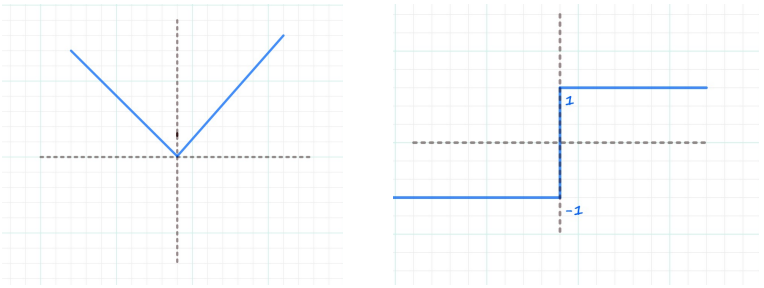

Figure 2.9 (a) $f(\mathbf{x}) = |\mathbf{x}|$. (b) Visualization of set $\partial f(\mathbf{x})$. Note that in this case, the set $\partial f(\mathbf{x})$ has infinitely many points as it includes the line segment $[-1, 1]$ of infinitely many points.

Example 2: Subdifferential of the ℓ_2-norm Let $f : \mathbb{R}^n \to \mathbb{R}$, $f(\mathbf{x}) = \|\mathbf{x}\|_2$, then

$$\partial f(\mathbf{x}) = \begin{cases} \frac{\mathbf{x}}{\|\mathbf{x}\|_2} & \text{if } \mathbf{x} \neq 0 \\ \{\mathbf{z} : \|\mathbf{z}\|_2 \leq 1\} & \text{if } \mathbf{x} = 0 \end{cases}$$

Proximal Operators As mentioned at the beginning of this section, proximal maps constitute the core of proximal algorithms, which are widely used to solve a variety of optimization problems that include non-differentiable functions such as ℓ_1-minimization problems. Having the preliminaries stated above, we are now ready to define the proximal operator (proximal mapping) and derive some well-known proximal-based sparse recovery techniques.

Proximity Operator of a function f at a point $\mathbf{z}$ with a parameter $\gamma > 0$ can be defined as

$$\text{prox}_{\gamma f}(\mathbf{z}) = \arg\min_{\mathbf{x}} \left\{ f(\mathbf{x}) + \frac{1}{2\gamma} \|\mathbf{x} - \mathbf{z}\|^2 \right\}. \tag{2.42}$$

The algorithm that involves the proximal operations (proximal mappings) is quite handy since it works for non-smooth (non-differentiable) functions.

Proximity Operator of ℓ_1-norm Let the absolute value function be defined as $f : \mathbb{R} \to \mathbb{R}$ where $f(x) = |x|$. The proximity operator that solves the problem is:

$$\text{prox}_{\gamma f}(\mathbf{z}) = \arg\min_{\mathbf{x}} \left\{ \gamma|\mathbf{x}| + \frac{1}{2}\|\mathbf{x} - \mathbf{z}\|^2 \right\} \tag{2.43}$$

and is given by:

$$\text{prox}_{\gamma|.|}(\mathbf{z}) = \text{sign}(\mathbf{z})\,(|\mathbf{z}| - \gamma)^+ = \begin{cases} \mathbf{z} + \gamma & \text{if } \mathbf{z} \leq -\gamma \\ 0 & \text{if } -\gamma \leq \mathbf{z} \leq \gamma \\ \mathbf{z} - \gamma & \text{if } \mathbf{z} \geq \gamma \end{cases} \tag{2.44}$$

In order to prove Eq. (2.44), we need to solve Eq. (2.43) via subdifferential calculus: Let $F(\mathbf{x}) = \gamma\,|\mathbf{x}| + \frac{1}{2}\|\mathbf{x} - \mathbf{z}\|_2^2$, from the above-mentioned Fermat rule, we know that $\mathbf{x}^*$ is a minimizer of $F(\mathbf{x})$ if $0 \in \partial F(\mathbf{x}^*)$ i.e.,

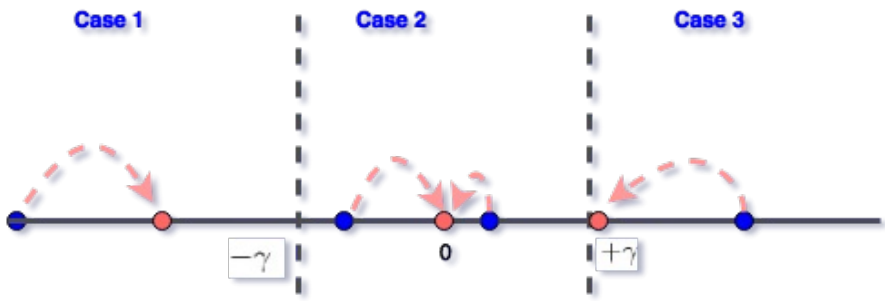

Figure 2.10 Visual illustration of soft-thresholding

$$0 \in \mathbf{x}^* - \mathbf{z} + \gamma \partial f(\mathbf{x}^*), \tag{2.45}$$

where $f(\mathbf{x}) = |\mathbf{x}|$. Let us consider the three specific scenarios to comprehend the behavior of the proximity operator: Consider the first case where $\mathbf{x}^* < 0$, from Eq. (2.41) we know that $\partial f(\mathbf{x}^*) = -1$ which is nothing but a singleton therefore Eq. (2.45) becomes

$$0 = \mathbf{x}^* - \mathbf{z} - \gamma.$$

This implies

$$\mathbf{x}^* = \mathbf{z} + \gamma \text{ for } \mathbf{x}^* < 0.$$

Therefore we get,

$$\text{prox}_{\gamma f}(\mathbf{z}) = \mathbf{z} + \gamma \text{ if } \mathbf{z} < -\gamma.$$

For the case where $\mathbf{x}^* < 0$ we have from Eq. (2.41) we have $\partial f(\mathbf{x}^*) = -1$. Similar derivation will result in

$$\text{prox}_{\gamma f}(\mathbf{z}) = \mathbf{z} - \gamma \text{ if } \mathbf{z} > +\gamma. \tag{2.46}$$

And for the last case where $\mathbf{x}^* = 0$, now the subdifferential is not a singleton but a set, i.e., $\partial f(\mathbf{x}^*) = [-1, 1]$. By inserting this into Eq. (2.45), we get

$$0 \in -\mathbf{z} + \gamma[-1, 1],$$

which implies $\mathbf{z} \in [-\gamma, \gamma]$ for $\mathbf{x}^* = 0$. Therefore,

$$\text{prox}_{\gamma f}(\mathbf{z}) = 0 \text{ if } -\gamma \leq \mathbf{z} \leq \gamma,$$

which completes the proof of Eq. (2.44).

Proximal Gradient Methods (Forward-Backward Type Algorithms) Let us consider the case where we have the following generic optimization problem:

$$\min \{f_1(\mathbf{x}) + f_2(\mathbf{x}) : \mathbf{x} \in \mathbb{E}\}, \tag{2.47}$$

where $f_1 : \mathbb{E} \to (-\infty, +\infty)$ is a continuously differentiable function. On the other hand, $f_2 : \mathbb{E} \to [-\infty, +\infty]$ is a proper, closed, convex function that is subdifferentiable over its domain. Such problems frequently arise in the sparsity-promoting optimization problems discussed throughout the chapter. For example, the Lasso formulation, as defined in Eq. (2.33), is a widely-used ℓ_1-minimization approach. A deeper examination of the possible solutions for this optimization problem will be conducted later, focusing on iterative shrinkage thresholding algorithms and related ones. But before we proceed, let us briefly discuss the derivation of the generic proximal gradient algorithm for the optimization problem given in Eq. (2.47):

Consider the optimization problem as defined in Eq. (2.47). If $\mathbf{x}^*$ serves as a local minimum for this problem, then it also serves as a stationary point for the same optimization problem. Applying aforementioned Fermat's rule, we obtain:

$$\mathbf{0} \in \nabla f_1(\mathbf{x}^*) + \partial f_2(\mathbf{x}^*). \tag{2.48}$$

Given a fixed $\gamma > 0$, we can derive the following equivalent expressions:

$$\mathbf{0} \in \gamma \nabla f_1(\mathbf{x}^*) + \gamma \partial f_2(\mathbf{x}^*). \tag{2.49}$$

Now, if we add the vector $\mathbf{x}^*$ to both left and right sets using Minkowski sum we obtain

$$\mathbf{x}^* \in \gamma \nabla f_1(\mathbf{x}^*) + \mathbf{x}^* + \gamma \partial f_2(\mathbf{x}^*). \tag{2.50}$$

Similarly, if we subtract $\gamma \nabla f_1(\mathbf{x}^*)$ vector from both sets via Minkowski difference, we

obtain

$$(I - \gamma \nabla f_1)(\mathbf{x}^*) \in (I + \gamma \partial f_2)(\mathbf{x}^*). \tag{2.51}$$

Then, using the uniqueness [3] of the minimizer $\mathbf{x}^*$, we conclude

$$\mathbf{x}^* = (I + \gamma \partial f_2)^{-1} (I - \gamma \nabla f_1)(\mathbf{x}^*). \tag{2.52}$$

Indeed, the resolvent [4] of the subdifferential is proximal operation by definition, i.e.,

$$\mathbf{x}^* = (I + \gamma \partial f_2)^{-1} (I - \gamma \nabla f_1)(\mathbf{x}^*) = prox_{\gamma f_2} (I - \gamma \nabla f_1)(\mathbf{x}^*). \tag{2.53}$$

In order to prove that the resolvent of the subdifferential is the proximal operation, assume

$$\mathbf{x} \in (I + \gamma \partial f)^{-1}(\mathbf{z}),$$

which implies

$$\mathbf{z} \in (I + \gamma \partial f)(\mathbf{x}),$$

[3]

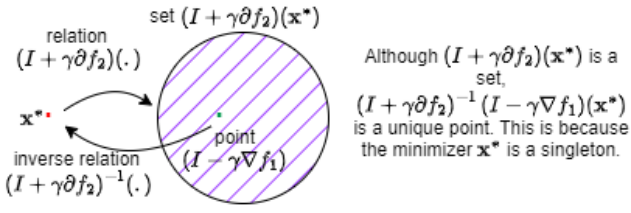

[4]A relation, denoted as $R()$, is often referred to as a "point-to-set map". It is also known as a "set-valued map" or "multifunction". This concept is essentially a generalization of operators. While standard operators, such as linear transformations, map a vector to another vector from its domain to codomain, a set-valued map (or relation) maps a vector in its domain to a set of vectors in its codomain. A resolvent of a relation $R(.)$ operation can be defined as the inverse mapping of the relation $(I+\gamma R)(.)$, where $I(.)$ is identity relation $I = \{(\mathbf{x}, \mathbf{x}) \mid \mathbf{x} \in \mathbb{R}^n\}$ [59].

and can be expressed as

$$0 \in \frac{1}{\gamma}(\mathbf{x} - \mathbf{z}) + \partial f(\mathbf{x}),$$

leading to

$$0 \in \partial_{\mathbf{x}} \left(f(\mathbf{x}) + \frac{1}{2\gamma} \|\mathbf{z} - \mathbf{x}\|_2^2 \right). \tag{2.54}$$

The solution set of Eq. (2.54) is the minimizer set of $F(\mathbf{x}) = f(\mathbf{x}) + \frac{1}{2\gamma} \|\mathbf{z} - \mathbf{x}\|_2^2$. As $F(\mathbf{x})$ is strictly convex, it has a unique minimizer.

Forward-Backward Algorithm Let $\mathbf{x}^*$ be a minimizer of $f(\mathbf{x}) = f_1(\mathbf{x}) + f_2(\mathbf{x})$, where f_1 is smooth and $f_2(\mathbf{x})$ is a non-smooth convex function. We have shown that

$$\mathbf{x}^* = (I + \gamma \partial f_2)^{-1} (I - \gamma \nabla f_1)(\mathbf{x}^*),$$

where $\gamma > 0$. This gives us the possibility of an iterative method, i.e.,

$$\mathbf{x}^{j+1} = \text{prox}_{\gamma^j f_2} \left(\mathbf{x}^j - \gamma^j \nabla f_1(\mathbf{x}^j) \right), \tag{2.55}$$

where $\mathbf{x}^j$ is the estimation of $\mathbf{x}$ at j^{th} iteration.

Iterative Shrinkage Thresholding (ISTA) ISTA [60] is a well-known solver for the ℓ_1-minimization problem, particularly in the form of the Lasso as given in Eq. (2.33). The algorithm can be described by the following iterative steps:

$$\mathbf{r}^j = \mathbf{y} - \mathbf{D}\widehat{\mathbf{x}}^j, \tag{2.56}$$

$$\widehat{\mathbf{x}}^{j+1} = \text{prox}_{\lambda \|.\|_1}(\widehat{\mathbf{x}}^j + \beta \mathbf{D}^T \mathbf{r}^j). \tag{2.57}$$

where $\beta \in \frac{1}{\|\mathbf{D}\|_2^2}$ is the stepsize. The function $\text{prox}_{\lambda \|.\|_1}(z_i)$ represents the soft thresholding operation, which is defined as $\text{prox}_{\lambda |.|}(z_i)$ in Eq. (2.44). The update equations is nothing but the Forward-Backward step defined in Eq. (2.55) for Lasso formulation Eq. (2.33) with a specific step size where the quadratic term $\frac{1}{2} \|\mathbf{Dx} - \mathbf{y}\|_2^2$ is differentiable with gradient $\nabla f_1(\mathbf{x}) = -\mathbf{D}^\mathbf{T}(\mathbf{y} - \mathbf{Dx})$.

Fast ISTA (FISTA) Numerous variants of the original ISTA algorithm have been proposed in the literature. The Fast Iterative Soft Thresholding Algorithm (FISTA) is one of the best-known algorithms among these: The step update in FISTA is performed by

$$\mathbf{r}^j = \mathbf{y} - \mathbf{D}\widehat{\mathbf{x}}^j, \tag{2.58}$$

$$\widehat{\mathbf{x}}^{j+1} = \text{prox}_{\lambda\|.\|_1}(\widehat{\mathbf{x}}^j + \beta\mathbf{D}^T\mathbf{r}^j + \frac{j-2}{j+1}(\widehat{\mathbf{x}}^j - \widehat{\mathbf{x}}^{j-1})), \tag{2.59}$$

where $\beta \in \frac{1}{\|\mathbf{D}\|_2^2}$.

Approximate Message Passing (AMP) For the special case where $\mathbf{D}$ is Gaussian matrix, the more recently proposed modification called approximate message passing (AMP) [61] algorithm can provide better reconstruction accuracy or/and faster convergence with the following modification in step update:

$$\mathbf{r}^j = \mathbf{y} - \mathbf{D}\widehat{\mathbf{x}}^j + \alpha^j\mathbf{r}^{j-1}, \tag{2.60}$$

$$\widehat{\mathbf{x}}^{j+1} = \text{prox}_{\lambda^j\|.\|_1}(\widehat{\mathbf{x}}^j + \beta\mathbf{D}^T\mathbf{r}^j), \tag{2.61}$$

where $\alpha^j = \frac{1}{m}\left\|\widehat{\mathbf{x}}^j\right\|_0$ and $\lambda^j = \frac{\nu}{\sqrt{m}}\left\|\mathbf{r}^j\right\|_2$ with a tuning parameter ν. In the AMP algorithm, the Onsager correction term $\alpha^j\mathbf{r}^{j-1}$ guarantees that the input of the soft-thresholding has Gaussian error compared to the original signal with a variance of $\frac{1}{m}\left\|\mathbf{r}^j\right\|_2^2$.

Alternating Direction Method of Multipliers (ADMM) The Alternating Direction Method of Multipliers (ADMM) is a method used to solve optimization problems of the form:

$$\min\{f_1(\mathbf{x}) + f_2(\mathbf{x}) : \mathbf{x} \in \mathbb{E}\}, \tag{2.62}$$

where both functions, f_1 and f_2, can be non-smooth.

The ADMM algorithm can be described by the following iterative updates:

$$\mathbf{x}^{j+1} \leftarrow prox_{\gamma f_1}\left(\mathbf{z}^j + \mathbf{u}^j\right), \tag{2.63}$$

$$\mathbf{z}^{j+1} \leftarrow prox_{\gamma f_2}\left(\mathbf{x}^{j+1} - \mathbf{u}^j\right), \tag{2.64}$$

$$\mathbf{u}^{j+1} = \mathbf{u}^j + \mathbf{z}^{j+1} - \mathbf{x}^{j+1}. \tag{2.65}$$

From Dual Ascent to Methods of Multipliers The consensus form of the optimization problem can be represented as:

$$\begin{aligned} \min \quad & f_1(\mathbf{x}) + f_2(\mathbf{z}) \\ & \text{subject to} \quad \mathbf{z} = \mathbf{x}. \end{aligned} \tag{2.66}$$

A simple and early approach to solve Problem (2.66) is to add a quadratic penalty function which is known as the quadratic penalty method [62], [63] whose first appearance [64] dates back to 1943 i.e.,

$$\min f_1(\mathbf{x}) + f_2(\mathbf{z}) + \frac{\mu}{2} \|\mathbf{z} - \mathbf{x}\|_2^2 \tag{2.67}$$

In this method, the variables $(\mathbf{z}, \mathbf{x})$ can be solved in an alternating manner and the penalty parameter μ is increased to make the solutions of sub-optimization problems closer to the one of original optimization problem (2.66). Despite the success stories in convex [65] and even in non-convex cases [66] when μ's become very larger, such sub-optimization problems tend to be more ill-conditioned and it is reported that such iterative algorithms may cause numerical solutions to stop before converging the feasible solution [62].

An alternative formulation to the problem could be the Lagrangian form of the original problem:

$$L(\mathbf{x}, \mathbf{z}, \alpha) = f_1(\mathbf{x}) + f_2(\mathbf{z}) + \alpha \left(\mathbf{z} - \mathbf{x}\right). \tag{2.68}$$

where α is the Lagrange multiplier or dual variable. The dual function is defined as:

$$g(\alpha) = \inf_{(\mathbf{x},\mathbf{z})} L(\mathbf{x}, \mathbf{z}, \alpha) = -f_1^*(\alpha) - f_2^*(-\alpha), \tag{2.69}$$

where $f^*(.)$ is the convex conjugate of $f(.)$. The dual problem aims to maximize $g(\alpha)$. To recover the primal optimal $\mathbf{x}^*$ and $\mathbf{z}^*$, one can use:

$$(\mathbf{x}^*, \mathbf{z}^*) = \arg\min_{(\mathbf{x},\mathbf{z})} L(\mathbf{x}, \mathbf{z}, \alpha^*). \tag{2.70}$$

where, α^* is the dual optimal point. The dual ascent method involves the following

updates:

$$\text{Primal update: } (\mathbf{x}^{j+1}, \mathbf{z}^{j+1}) = \arg\min_{(\mathbf{x},\mathbf{z})} L(\mathbf{x}, \mathbf{z}, \alpha^j), \tag{2.71}$$

$$\text{Dual Update: } \alpha^{j+1} = \alpha^j + \rho^j \nabla_\alpha g(\alpha) = \alpha^j + \rho^j \left(\mathbf{z}^{j+1} - \mathbf{x}^{j+1}\right). \tag{2.72}$$

Here, the dual variable updates come from the specific choice of gradient step as μ in gradient ascent steps, because $\nabla_\beta g(.) = (\mathbf{z}^{j+1} - \mathbf{x}^{j+1})$ under the assumption of fixed and unique minimizers $(\mathbf{z}^{j+1}, \mathbf{x}^{j+1})$ of the primal update problem. This could be only possible if f_1 and f_2 are strictly convex. On the other hand, if we bring the quadratic penalty term back and use it together with the Lagrangian term, we can guarantee the uniqueness of the output of the gradient ascent step [67]. The augmented Lagrangian in its scaled form is:

$$L_\mu(\mathbf{x}, \mathbf{z}, \alpha) = f_1(\mathbf{x}) + f_2(\mathbf{z}) + \alpha\,(\mathbf{z} - \mathbf{x}) + \frac{\mu}{2} \|\mathbf{x} - \mathbf{z}\|_2^2 . \tag{2.73}$$

In the method of multiplier method (MM) [68], dual and primal optimum points for Eq. (2.73) are found in an iterative manner i.e.,

$$(\mathbf{x}, \mathbf{z})^{j+1} \leftarrow \arg\min_{(\mathbf{x},\mathbf{z})} L(\alpha_1^j, ..., \alpha_{P-2}^j, \mathbf{x}, ..., \mathbf{z}_{P-1}) \tag{2.74}$$

$$\alpha^{j+1} \leftarrow \alpha^j + \mu(\mathbf{z}^{j+1} - \mathbf{x}^{j+1}). \tag{2.75}$$

Alternating Direction Method of Multipliers MM does not require to make the μ to be increased to very large values to guarantee convergence. However, the primal optimal variable update steps require joint optimization of primal variables, which is not trivial. Alternatively, the alternating direction method of multiplier (ADMM) [67], [69] is a Gauss-Seidel type method that can deal with the primal update step separately with respect to primal variables and can still guarantee convergence. The update steps in ADMM are performed as follows:

$$\mathbf{x}^{j+1} \leftarrow \arg\min_{\mathbf{x}} L(\alpha^j, \mathbf{x}, \mathbf{z}^j), \tag{2.76}$$

$$\mathbf{z}^{j+1} \leftarrow \arg\min_{\mathbf{z}} L(\alpha^j, \mathbf{x}^{j+1}, \mathbf{z}), \tag{2.77}$$

$$\alpha^{j+1} \leftarrow \alpha^j + \mu(\mathbf{z}^{j+1} - \mathbf{x}^{j+1}). \tag{2.78}$$

Eq. (2.73) can be recast as:

$$L_{\mu}(\mathbf{x},\mathbf{z},\alpha) = f_1(\mathbf{x}) + f_2(\mathbf{z}) + \frac{\mu}{2}\left\|\mathbf{z} - \left(\mathbf{x} - \frac{\alpha}{\mu}\right)\right\|_2^2. \tag{2.79}$$

The method of multipliers involves the following updates:

$$\mathbf{x}^{j+1} \leftarrow \arg\min_{\mathbf{x}} \left\{ f_1(\mathbf{x}) + \frac{\mu}{2}\left\|\mathbf{x} - \left(\mathbf{z}^j + \frac{\alpha^j}{\mu}\right)\right\|_2^2 \right\}, \tag{2.80}$$

$$\mathbf{z}^{j+1} \leftarrow \arg\min_{\mathbf{z}} \left\{ f_2(\mathbf{z}) + \frac{\mu}{2}\left\|\mathbf{z} - \left(\mathbf{x}^{j+1} - \frac{\alpha^j}{\mu}\right)\right\|_2^2 \right\}, \tag{2.81}$$

$$\alpha^{j+1} = \alpha^j + \rho^j\left(\mathbf{z}^{j+1} - \mathbf{x}^{j+1}\right). \tag{2.82}$$

2.3.2 Neural Network Based Solutions

It is important to note that, in addition to the aforementioned traditional approaches, neural network (NN) based solutions have recently become very popular in this domain as well. This first category of algorithms can be categorized as sparse recovery NN algorithms, i.e., $\hat{\mathbf{x}} \leftarrow \mathcal{P}(\mathbf{y})$, where $\mathcal{P}$ is a learned NN-based mapping from compressed domain signal to sparse coefficient vector. The purpose of these techniques is to further enhance the effectiveness of existing convex relaxations by reducing the number of iterations and enhancing reconstruction accuracy. In these types of algorithms, which are also called unrolled deep models, the denoiser matrices such as $\mathbf{D}^T$, or $\left(\mathbf{D}^T\mathbf{D} + \lambda\mathbf{I}\right)^{-1}\mathbf{D}^T$ are learned as well as hyperparameters such as λ. For instance, Learned-ISTA (LISTA) [70], and Learned AMP (LAMP) [71], which is the deep version of AMP are deep unrolling versions of ISTA and AMP, respectively.

The second category of NN-based compressed sensing (CS) solutions makes the signal recovery in the spatial domain rather than the sparsifying domain, i.e., $\hat{\mathbf{s}} \leftarrow \mathcal{P}(\mathbf{y})$. Among them, a group of algorithms keep traditional sensing matrices, e.g., random Gaussian matrices, and only learn the recovery part [72]–[74]. One of the best-known examples of this type of work is the stacked denoising autoencoder (SDA) [72], the non-iterative reconstruction of compressively sensed images using CNN (ReconNet) [73], as well as the learned version of the iterative shrinkage thresholding algorithm for CS imaging (ISTA-Net) [74]. SDA networks use fully connected layers while others use convolutional layers.

Another group of algorithms within this category focuses on jointly optimizing the CS matrix and the recovery part. Convolutional compressive sensing networks (CSNET) [75] and scalable convolutional compressive sensing networks (SCSNET) [76] are recent examples of state-of-the-art networks in this category. In these algorithms, compressive sensing is applied to blocks of the image independently while convolutional layers are applied to the entire image in the recovery part.

3 SPARSE SUPPORT ESTIMATION AND ITS APPLICATIONS

Regarding sparse signal recovery, the focus is typically on identifying the nonzero components of $\mathbf{x}$, including their positions, magnitudes, and signs. However, it is essential to note that many applications only need a part of this information about $\mathbf{x}$. For instance, in many application scenarios, simply determining the positions of these nonzero elements is sufficient. This is a process known as sparse support set estimation or support estimation (SE) for short. To give an example, in a classifier method based on sparse representation, the atoms that constitute the dictionary are placed in such a way that the features of samples belonging to the same class become adjacent to one another [77], [78]. In such a design, when a new test sample has arrived, its representation within this dictionary is estimated. If we ensure that the signal is represented with the least amount of atoms while finding this representation, the most critical factor in determining the class is to find out which atoms contribute to the representation. As another example, in a CS-based radar imaging process [79], the primary purpose is to determine the location of the target rather than determining the actual signal magnitudes when the reflected signal is represented by sparse approximation.

Suppose that we obtain a measurement, $\mathbf{y}$, from a corrupted measurement system, $\mathbf{y} = \mathbf{D}\mathbf{x} + \mathbf{z}$, where $\mathbf{z}$ is the noise vector representing the additive perturbation, and the equivalent dictionary $\mathbf{D}$ is given. We can mathematically define a support estimator, $\mathcal{E}(.)$, as follows

$$\widehat{\Lambda} = \mathcal{E}\left(\mathbf{y}, \mathbf{D}\right) \tag{3.1}$$

where $\widehat{\Lambda}$ is the estimated set of indices corresponding to the non-zero elements' locations. Consider an ideal scenario where we have zero noise in the system, and $\mathbf{x}$ is an exact k-sparse signal. The exact sparse signal recovery and exact sparse support estimation problems are equivalent in this particular case. If we recall the discussion after Eq. (2.10) in Chapter 2, we can easily observe this. Furthermore, although exact

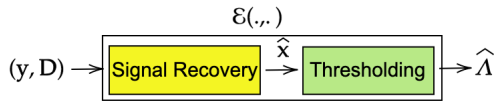

Figure 3.1 The Conventional Strategy for a Practical Support Estimator [P1].

sparse signal recovery is not possible when noise appears, exact support estimation can still be performed [80]. In this regard, the support estimation problem may seem more manageable than the signal recovery problem.

The traditional SE strategies consist of reconstructing $\mathbf{x}$ first and then estimating the support set based on standard thresholding techniques. Such an approach is illustrated in Figure 3.1 . Nevertheless, if the final goal is to estimate the support set, the process of recovering the sparse signal with its magnitude and sign may be unnecessary and costly. This is why we investigated the possibility of direct mapping from the measurement, $\mathbf{y}$, to support set, Λ. In the first part of the chapter, we will discuss whether it is possible to train a neural network that maps directly from y to the support set. The Convolutional Support Estimator Networks (CSENs), which are proposed in [P1] and [P2], serve as supervised support estimators, providing low-cost but accurate support estimation with their compact architectures. Such a direct mapping technique has a variety of applications, such as a new type of dictionary-based classifier (i.e., hybrid usage of a pre-defined dictionary and a compact SE network) or improved sparse signal recovery algorithms equipped with priori information provided by NN-based support estimators.

The second part of the chapter discusses a particular scenario where learning such a mapping is very challenging due to a lack of sufficient training data for these highly specialized tasks. These situations may occur, especially in CS systems where specialized CS matrices are required due to their hardware constraints, such as CS-based radar imaging [P3]. In such cases where data collection is difficult, producing synthetic data and training an NN on it could be considered. However, for Ground Penetrating Radar (GPR) applications where high target-surface interaction occurs, such as through-the-wall radar imaging, producing realistic synthetic data is challenging due to difficulties in electromagnetic modeling, and current simulation tools suffer from very long simulation times [81]. In these specific scenarios, one possible solution for the support estimation problem is to use the conventional way, in which the sparse signal recovery is performed, as depicted in Figure 3.1 . However, for the above

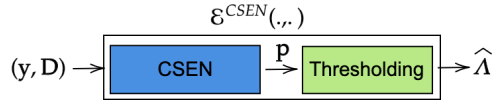

Figure 3.2 Proposed NN-based Design for Highly Efficient Support Estimator [P1].

reasons, SE performance of the algorithms that use this conventional strategy may remain short, especially in challenging situations where using a low measurement rate is very beneficial. As an example, in a rescue operation, it is crucial to sample and process GPR data rapidly in order to detect structures close to the surface, such as buried survivors or utilities under rubble. Instead of using the ordinary sparse signal model, where we do not have any other assumption other than $\mathbf{x}$ being sparse, we will propose a structural sparse model, introduced in [P3], for a particular task regarding CS-radar imaging. This model sacrifices signal magnitude and sign estimation accuracy for increased support estimation accuracy. For this reason, even though the sparse signal is recovered by solving this special optimization problem, the estimated sparse signal, $\widehat{\mathbf{x}}$, serves as an estimation of the support and, therefore, can be considered a special form of Eq. (3.1). It will be shown that such a structural sparsity model and its corresponding recovery algorithm provide more accurate target localization in through-the-wall CS radar imaging problems.

3.1 Convolutional Sparse Support Estimator Networks (CSENs)

Given a pre-defined dictionary, $\mathbf{D}$, when a new query measurement, $\mathbf{y}$, arrives, we have proposed to use an NN-based support estimator in [P1] instead of the traditional SE algorithms mentioned in Figure 3.1 . Such a machine learning algorithm aims to estimate the support set directly from the measurement vector. The proposed strategy is illustrated in Figure 3.2 .

An ideal support estimator should produce the following binary mask, $\mathbf{b} \in \{0, 1\}^n$, when it receives a new query measurement, $\mathbf{y}$, as input:

$$b_i = 1 \text{ if } i \in \Lambda \tag{3.2}$$

which marks the ground-truth signal support i.e., $\Lambda = \{i \in \{1, 2, .., n\} : b_i = 1\}$.

The proposed NN-based support estimators, CSENs, serve as a mapping, $\mathcal{P}(\mathbf{y}, \mathbf{D})$, attempting to approximate such ideal binary mask by producing a probability-like

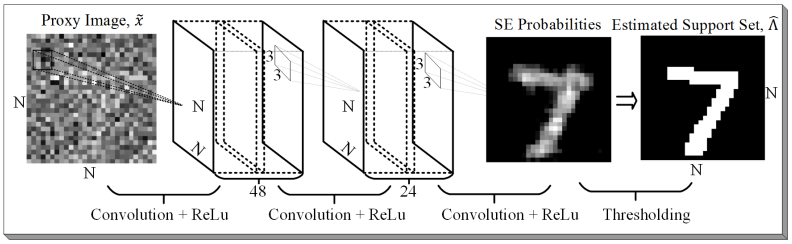

Figure 3.3 Convolutional Support Estimator Network-1 (CSEN1) [P1].

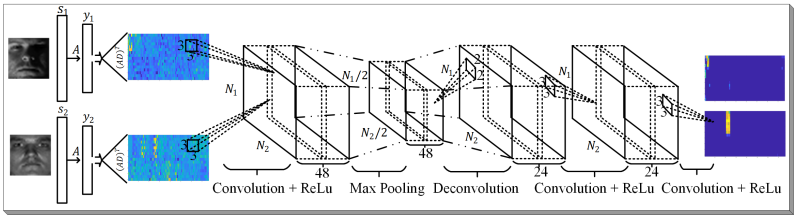

Figure 3.4 Convolutional Support Estimator Network-2 (CSEN2) [P1].

measure as the output vector, $\mathbf{p}$. In other words, each element, $p_i \in [0, 1]$, of this vector is considered a measure of how probable this index is in the support set. Having such a probability-like vector, simple thresholding could be applied in order to obtain the final estimator of the support set if needed, i.e., $\widehat{\Lambda} = \{i \in \{1, 2, .., n\} : p_i > \tau\}$, where τ is a predefined threshold.

Two different architectures are proposed, each being a fully convolutional type of neural network. Therefore, instead of using $\mathbf{y}$ as input, they take a proxy sparse signal, $\tilde{\mathbf{x}} = \mathbf{B}\mathbf{y}$ (where $\mathbf{B} = \mathbf{D}^T$ or $\mathbf{B} = \left(\mathbf{D}^T\mathbf{D} + \lambda\mathbf{I}\right)^{-1}\mathbf{D}^T$) as input and produce the probability-like measure vector $\mathbf{p}$ from $\tilde{\mathbf{x}}$. The architectures of the proposed networks, CSEN1 and CSEN2, are visualized in Figure 3.3 and Figure 3.4, respectively. In the proposed CSENs, 2-D convolution layers are used, as depicted in the figures. To this end, the proxy signal $\tilde{\mathbf{x}}$ is reshaped to have a 2D representation before being used as an input signal to CSENs.

The first architecture, CSEN1, consists of three convolution layers with 48 and 24 hidden neurons. The second one, CSEN2, is obtained by slightly modifying CSEN1. In CSEN2, compared to CSEN2, a downsampling and an upsampling layers are placed between the 48-neuron convolutional layer and the 24-neuron one. Max-pooling is used for downsampling, and a 24-neuron transpose convolution layer is used for upsampling. In both CSEN configurations, the kernel size for each layer is set to 3×3.

Proof-of-the concept: An Experiment on Support Estimation From CS Measurements This proof-of-concept experiment will consider a general problem of sparse support estimation from compressively sensed signals. For this purpose, the handwritten digits dataset, MNIST, whose each sample is an image of 28×28 pixels, was used. In each image, the pixel intensity of the handwritten character is close to 1, while the black background pixel values are 0. Therefore, each vectorized image, $\mathbf{x}_i \in \mathbb{R}^{n=784}$, can be considered as a k_i-sparse signal in the canonical domain, i.e., $\mathbf{\Phi} = \mathbf{I}$. A sensing system, where each of these signals is compressively sampled with Gaussian CS matrix, $\mathbf{A} \in \mathbb{R}^{m \times n}$, is simulated via

$$\mathbf{y_i} = \mathbf{A}\mathbf{x_i} + \mathbf{z}_i = \mathbf{D}\mathbf{x_i} + \mathbf{z}_i, \tag{3.3}$$

where $\mathbf{D} = \mathbf{A}$ and $\mathbf{z}_i \in \mathbb{R}^m$ is an additive white Gaussian noise. Briefly, we define the problem as estimating the support set directly from the measurement vector, $\mathbf{y_i}$ defined in Eq. (3.3), via a support estimator network, $\mathcal{P}_{\text{SE}}$, i.e., $\widehat{\mathbf{\Lambda}} \leftarrow \mathcal{P}_{\text{SE}}(\mathbf{y})$, where $\mathcal{P}_{\text{SE}}$ is a learned NN-based mapping from compressed domain signal to sparse support set.

Since the proposed CSENs are the first of their kind as support estimator networks in the literature, it is not possible to compare them directly with a competing algorithm. For this reason, the SOTA NN-based sparse signal recovery algorithms (i.e., $\hat{\mathbf{x}} \leftarrow \mathcal{P}(\mathbf{y})$, where $\mathcal{P}$ is a learned NN-based mapping from CS signal, $\mathbf{y}$ to sparse coefficient vector, $\mathbf{x}$.) described in Section 2.3.2, LISTA, and LAMP were trained under the same conditions as proposed CSEN networks to be support estimators.

Table 3.1 Comparative Analysis of Algorithmic Performance in Support Recovery from Noise-Free Measurements.

MR	**0.25**	**0.1**	**0.05**	**0.25**	**0.1**	**0.05**	**0.25**	**0.1**	**0.05**	**0.25**	**0.1**	**0.05**
	F1 Measure			**Precision**			**Recall**			**CE**		
CSEN	0.91	0.85	0.80	0.90	0.84	0.77	0.92	0.87	0.84	0.03	0.06	0.08
CSEN2	**0.94**	0.89	**0.84**	0.93	0.88	**0.82**	**0.94**	**0.90**	**0.87**	**0.02**	**0.04**	**0.06**
ReconNet	0.90	0.85	0.79	0.89	0.82	0.76	0.90	0.87	0.83	0.05	0.06	0.09
LAMP (2)	0.92	0.89	0.82	0.94	0.90	**0.82**	0.89	0.87	0.83	0.05	0.05	0.08
LAMP (3)	0.93	0.89	0.82	0.95	0.90	**0.82**	0.91	0.88	0.82	0.03	0.05	0.08
LAMP (4)	0.93	**0.90**	0.83	0.95	**0.92**	**0.82**	0.92	0.89	0.83	0.03	**0.04**	0.08
LISTA (2)	0.93	0.89	0.82	**0.96**	0.90	**0.82**	0.90	0.87	0.82	0.03	0.05	0.07
LISTA (3)	0.93	0.89	0.82	0.95	0.90	**0.82**	0.90	0.87	0.82	0.03	0.05	0.07
LISTA (4)	0.93	0.89	0.82	0.95	0.90	**0.82**	0.90	0.87	0.83	0.03	0.05	0.07

Furthermore, as also discussed in Section 2.3.2, even if it was not proposed as

Table 3.2 Comparative Evaluation of Algorithmic Efficacy in Support Recovery with 10 dB Measurement Noise.

MR	0.25	0.1	0.05	0.25	0.1	0.05	0.25	0.1	0.05	0.25	0.1	0.05
	F1 Measure			Precision			Recall			CE		
CSEN	0.89	0.82	0.77	0.89	0.82	0.75	0.89	0.82	0.79	0.04	0.07	0.09
CSEN2	**0.92**	**0.86**	**0.80**	**0.92**	0.86	**0.80**	0.92	0.86	**0.82**	**0.03**	**0.06**	**0.08**
ReconNet	0.89	0.83	0.78	0.89	0.81	0.74	0.89	0.85	0.81	0.04	0.07	0.09
LAMP (2)	0.87	0.85	0.79	0.90	0.86	0.78	0.84	0.83	0.80	0.08	0.08	0.10
LAMP (3)	0.87	0.84	0.77	0.91	**0.87**	0.78	0.84	0.81	0.77	0.06	0.08	0.12
LAMP (4)	0.86	0.85	0.77	0.87	**0.87**	0.78	0.85	0.82	0.77	0.08	0.07	0.12
LISTA (2)	0.72	0.82	0.79	0.58	0.77	0.76	0.93	**0.88**	**0.82**	0.18	0.08	0.10
LISTA (3)	0.68	0.83	0.79	0.54	0.78	0.76	**0.94**	0.87	**0.82**	0.22	0.08	0.10
LISTA (4)	0.68	0.82	0.78	0.53	0.77	0.75	**0.94**	**0.88**	**0.82**	0.22	0.08	0.10

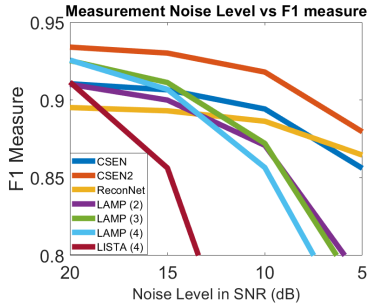

Figure 3.5 F1 Measure graphs of the performance of competing algorithms at various noise levels at MR = 0.25 [P1].

a sparse signal recovery algorithm, rather the CS signal recovery algorithm in the input domain directly ($i.e., \hat{\mathbf{s}} \leftarrow \mathcal{P}(\mathbf{y})$), ReconNet, was also trained to be a support estimator. This network is also fully convolution type like the proposed CSENs. We repeated the experiment under different noise levels and with different Measurement Rates (MRs). Performance comparisons of the competing algorithms are given in Table 3.1, Table 3.2, and Figure 3.5. When we examined Table 3.1, it was observed that there was no performance increase when we increased the block numbers of both LISTA and LAMP from 2 to 4. For this reason, deeper models were not trained anymore. As can be seen from the tables and Figure 3.5, for many different MR and under different noise conditions, the proposed CSENS, either achieved the highest SE performance or achieved the performance level comparable to their closest competitor. MSE is used as the loss function in that particular experiment; more details about the experiments can be found in [P1].

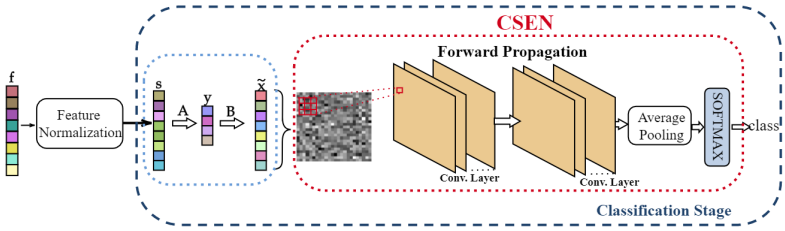

Figure 6 CSEN-C is trained end-to-end

3.1.1 Convolutional Sparse Support Estimator Network Based Classification (CSEN-C)

There is no doubt that one of the most successful applications of sparse representation theory is that of dictionary-based classification, also known as representation-based classification technologies. Among these methods, the first of its kind, sparse-representation-based classification (SRC) [77], [78] and collaborative representation-based classification (CRC) [82] are the most widely used ones. Among these, SRC has been specially adapted to many applications including but not limited to face recognition [77], [78], human action recognition [83], and hyperspectral image segmentation [84]. The method, SRC, can be summarized as follows: (i) Normalize each atom in $\mathbf{D}$ and the query vector $\mathbf{y}$ to have a unit ℓ_2-norm. (ii) Find the coefficient vector $\hat{\mathbf{x}}$ via a sparse recovery algorithm such as the ℓ_1-norm minimization: $\hat{\mathbf{x}} = \arg\min_{\mathbf{x}} \|\mathbf{x}\|_1 \text{ s.t } \|\mathbf{y} - \mathbf{D}\mathbf{x}\|_2$. (iii) For each class i, compute the residual $\mathbf{e_i} = \|\mathbf{y} - \mathbf{D_i}\hat{\mathbf{x}}_\mathbf{i}\|_2$, where $\hat{\mathbf{x}}_\mathbf{i}$ is the vector consists of coefficients of $\hat{\mathbf{x}}$ corresponding class i. (iv) Determine the class of $\mathbf{y}$ by finding the minimum of the residuals $\mathbf{e_i}$. However, despite its success in a wide range of applications, in step (ii), SRC requires a sparse recovery method such as solving ℓ_1-minimization problem, which is an iterative and relatively costly operation, as it is discussed many times in the dissertation. The following CRC method introduced a simplification in this step by attempting to find the coefficient vector via ordinary regularized least squares, i.e., $\hat{\mathbf{x}} = \left(\mathbf{D}^T\mathbf{D} + \lambda\mathbf{I}_{n\times n}\right)^{-1}\mathbf{D}^T\mathbf{y}$.

Machine learning literature has witnessed an enormous increase in the number of classes, samples, and sample sizes handled by machine learning algorithms in recent years. As a result, despite significant simplification with CRC, even the least square solution may become very costly (even direct usage of the methodology unmanageable

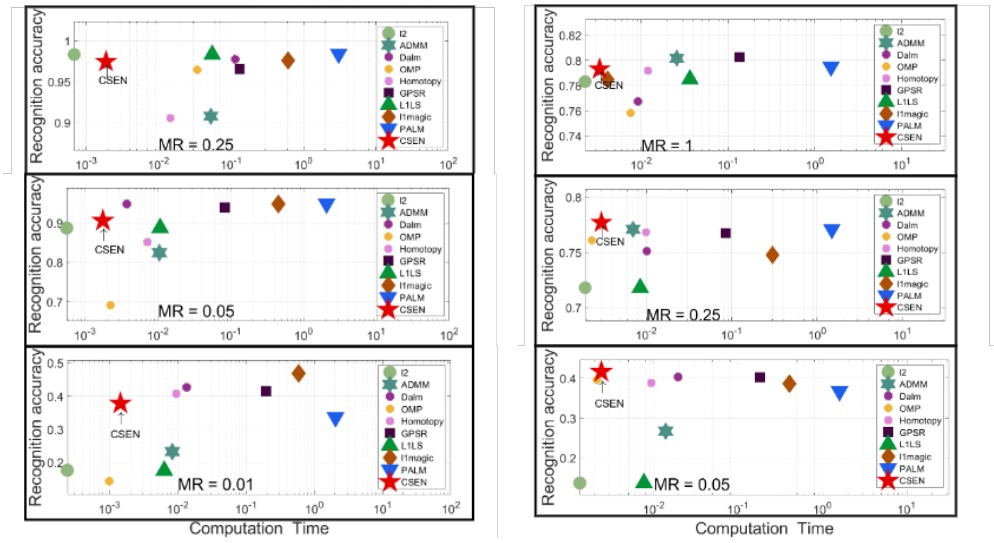

(a) Yale-B **(b)** CelebA

Figure 3.7 Performance comparison of competing face recognition algorithms in two databases. [P1]

in practice). This is why, in this dissertation, we proposed a new type of representation-based classifier family, CSEN-C. To develop CSEN-C, instead of using entire training samples in the dictionary, a random sub-set is selected to construct the dictionary, and the rest of the training dataset is used to train the above-mentioned NN-based support estimator-supported classifier. Then, we adopt and train the CSEN-C in the following manner:

End-to-end training of CSEN-C: As a vanilla approach, the aforementioned support estimator, CSEN, could be trained first with a proper lost function such as ℓ_1 or a more structural version of it such as a loss that encourages group sparsity [P1]. Then, more layers could be added to the network and fine-tuned to have the final class. Instead, we modified CSEN to have a more compact network: An average pooling layer is added at the end of the CSEN network, and then we finish the architecture with a softmax to have class probabilities. The cross-entropy loss function is used. The overall CSEN-C architecture is visualized in Figure 6. In the figure, we particularly place measurement matrix, $\mathbf{A}$, because a feature extraction matrix could be applied to the query samples, such as PCA.

Now, we summarized the performance of the proposed technique in two different

Table 3.3 Comparative Classification Performance of CSEN and Other Methods for COVID-19 Detection.

Metric	Category	k-NN	SVM	MLP	CRC	ReconNet	CSEN1	CSEN2
Accuracy	**Bacterial**	0.777	0.780	0.763	0.820	0.765	0.793	0.794
	Viral	0.801	0.787	0.765	0.827	0.785	0.805	0.803
	Normal	0.903	0.934	0.933	0.928	0.918	0.926	0.927
	COVID-19	0.950	0.945	0.949	0.955	0.936	0.955	**0.959**
TN	**Bacterial**	3166	3219	3114	3063	3180	3177	3173
	Viral	4123	3965	3923	4385	4005	4109	4091
	Normal	4253	4444	4442	4380	4364	4388	4396
	COVID-19	5525	5489	5522	5554	5435	5548	**5572**
TP	**Bacterial**	1720	1687	1680	2091	1629	1810	1818
	Viral	909	979	884	816	928	954	959
	Normal	1420	1427	1421	1456	1407	1431	1428
	COVID-19	446	452	444	447	448	**455**	**455**
FP	**Bacterial**	360	307	412	463	346	349	353
	Viral	678	836	878	416	796	692	710
	Normal	454	263	265	327	343	319	311
	COVID-19	299	335	302	270	389	276	**252**
FN	**Bacterial**	1040	1073	1080	669	1131	950	942
	Viral	576	506	601	669	557	531	526
	Normal	159	152	158	123	172	148	151
	COVID-19	16	10	18	15	14	**7**	**7**
Sensitivity	**Bacterial**	0.623	0.611	0.609	0.758	0.590	0.656	0.659
	Viral	0.612	0.660	0.595	0.550	0.625	0.642	0.646
	Normal	0.899	0.904	0.900	0.922	0.891	0.906	0.904
	COVID-19	0.965	0.978	0.961	0.968	0.970	**0.985**	**0.985**
Specificity	**Bacterial**	0.898	0.913	0.883	0.869	0.902	0.901	0.900
	Viral	0.859	0.826	0.817	0.913	0.834	0.856	0.852
	Normal	0.904	0.944	0.944	0.931	0.927	0.932	0.934
	COVID-19	0.949	0.943	0.948	0.954	0.933	0.953	**0.957**
F1-score	**Bacterial**	0.711	0.710	0.693	0.787	0.688	0.736	0.737
	Viral	0.592	0.593	0.545	0.601	0.578	0.609	0.608
	Normal	0.823	0.873	0.870	0.866	0.845	0.860	0.861
	COVID-19	0.740	0.724	0.735	0.758	0.690	0.763	**0.778**

multi-class classification problems, face recognition and chest X-ray image classification (with an emphasis on COVID-19 detection). Both of them are particularly good examples of data scarcity problems in their own way. Considering the face recognition problem, one major challenge in the practical usage of such a system is to recognize the identities that have a limited number of face samples. The majority of works focus on achieving a generalizable neural network in order to produce discriminative features. And, having the pre-trained deep networks, they use less complicated conventional classifiers such as KNN to recognize the identity from the features that pre-trained networks produce. The literature representation-based classifiers SRC and CRC, which are equipped with either row images or high-level features from the deep models, are also very popular methods. The proposed CSEN-C presents a new alternative to the representation-based classifiers with its compact configuration.

In Figure 3.7, we summarized the performance comparison of competing algo-

rithms for two different datasets, Yale-B [85] and CelebA [86]. The competing algorithms are listed as conventional classifiers, KNN, MLP, SVM, and representation-based classifiers, SRC and CRC. Furthermore, we tried most of the SOTA sparse signal recovery algorithms to have different versions of SRC. These are also listed as, ADMM [67], Dalm [87], OMP [87], Homotopy [88], GPSR [89], L1LS [90], ℓ_1-magic [91], and Palm [87]. All the algorithms use exactly the same features, which are extracted from pre-trained deep network library [92], then passed through the PCA matrix, $\mathbf{A}$. For the sake of brevity, we skip all the details about the experimental setup and hyper-parameters, which can be found in [P1]. An important observation from the results is that the proposed algorithm gives high or very comparable performance scores in all settings. When we particularly compare with the SRC technique, we can say that the performance of SRC highly depends on the algorithm chosen and set-up.

When it comes to chest X-ray classification, the data imbalance and scarcity problem were the major difficulties to be handled, especially in the beginning of the pandemic. In [P2], we give a very detailed analysis of how to handle data scarcity problems with the proposed CSEN-C. Particularly, we developed a CSEN-C algorithm that classifies X-Ray images into 4 categories: (i) Viral, (ii) Bacterial, (iii) Covid-19 based pneumonia or control group, (iv) normal. The performance comparison of the competing algorithms is given in Table 3.3. As can be seen in the Table, the proposed algorithm surpasses the competing ones in Covid-19 recognition. The details of the experimental setup are given in [P2]. In [P2], we also address the analysis of computational complexity vs performance of representation-based classifiers, CRC, SRC, and CSEN-C. Particularly when using a subset of the training set or the entire training set in the dictionary.

3.1.2 Convolutional Sparse Support Estimator Network Based Compressively Sensed Signal Reconstruction

In literature [93], [94], side information about the support set is used to improve the sparse recovery performance of compressive sensing systems via weighted ℓ_1-minimization,

$$\min_{\mathbf{x}} \left\{ \|\mathbf{D}\mathbf{x} - \mathbf{y}\|_2^2 + \lambda \|\mathbf{w} \odot \mathbf{x}\|_1 \right\} \tag{3.4}$$

where $\odot$ the element-wise multiplication (Hadamard Product), $\mathbf{w}$ is the cost function with elements $w_i = \frac{1}{p_i + \epsilon}$ and p is the measure defining the probability of each

coefficient's being non-zero. However, most of the works [94] either do not specify how to have such information or design hand-crafted functions to estimate such priors for specific application scenarios [93]. One of the major application areas of the NN-based support estimator proposed in this dissertation is that the output of the estimation networks can serve as prior information, p. Such a p can be produced by a CSEN, on the fly and particular to the given input sample, $\mathbf{y}$. The idea is visualized in Figure 3.8a. Such an algorithm not only improves the recovery accuracy but also reduces the number of iterations for conventional sparse recovery algorithms to converge. We compared the conventional sparse recovery algorithm with the proposed CSEN-aided sparse recovery in Figure 3.8b. For comparison, we use phase transition graphs. We can see the border of the exact sparse recovery region for each algorithm by looking at such graphs (or vice versa, where the algorithm starts failing). We followed the exact procedure and definition of phase transition given in [95]. In [P1], a more detailed analysis of the experiment is given. In [P1] also, CSEN-aided sparse recovery is applied on natural images in the gradient domain (i.e., using Total Variation minimization)

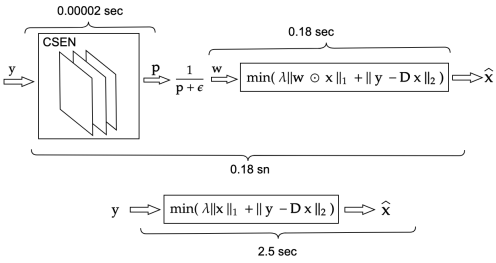

(a) Proposed CSEN-aided Sparse Signal Recovery

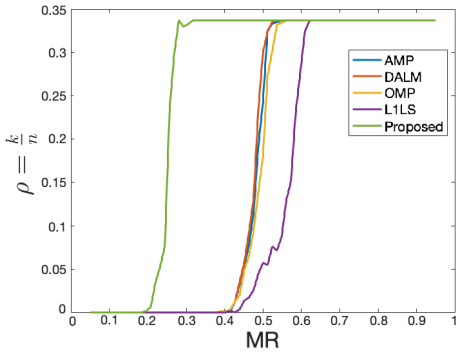

(b) Comparison of competing algorithms with phase transition graphs in MNIST dataset

Figure 3.8 Proposed CS-Aided Sparse Signal Recovery. [P1]

3.2 Structural Sparse Support Estimation via Proximal Operation Based Algorithms

The aforementioned support estimation methods based on neural networks are useful in many situations, provided that there is access to a small, moderate, or large training

database. In the sequel, we will develop a structural sparsity model and corresponding optimization problem for a specific application called the "through-the-wall radar imaging (TWRI)" system. The proposed sparsity model imposes more accurate SE by sacrificing the actual magnitude of the signal, which is not critical information for localization and detection.

Through the wall Target Detection/Monitoring from Compressively Sensed Signals via Structural Sparsity Stepped-frequency systems (SFS) [96] apply stepped-frequency steps to transmit short electromagnetic waveforms, and then measure the magnitude and phase difference between the reflected signal and the transmitted signal. We can define this method as frequency domain sampling over a wide bandwidth. As a result of its reduced noise exposure at discrete stepped frequencies, it offers benefits such as ultra-bandwidth illumination, lower transmission power, and higher SNR. Nevertheless, such sampling is costly and time-consuming, since only one frequency bin at a time is sampled, and many frequency bins must be sampled at a location. Studies have explored simultaneous transmissions of multiple frequencies, but the most common method involves transmitting a subset of stepped frequencies and reconstructing the signal using CS theory [97].

In recent literature, random frequency radar imaging has received significant attention with various studies [79], [97]–[99] exploring different assumptions about the sparsity of the scene that is being imaged. According to some of these studies, the targets in a discretized scene allocate fewer grids than the total number of grids, which is a simple unstructured sparsity assumption in the canonical domain. It has been assumed in some studies that vectorized radar images are sparse in a proper dictionary, such as one derived from GPR images. Nevertheless, these methods may not be suitable for some scenes that show structural sparsity patterns, such as block-sparse models. In contrast to previous works, this study proposes estimating the target locations by assuming the group structure and the continuity of non-zero support sets across consecutive scans.

Proposed Compressive GPR System Building on the above-mentioned stepped-frequency radar technology, we will develop a TWRI system via CS and structural sparsity. Using this system, stationary objects can be detected within close proximity even when they are obscured by walls. A system of this type is illustrated in Figure 3.9, from which it is clear that possible application areas include emergencies such as

[1]It is an AI-generated representative image generated with DALLE-3 [100].

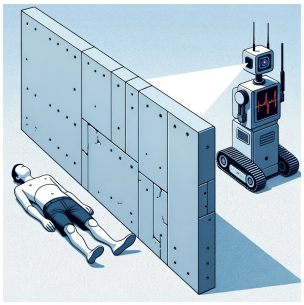

Figure 3.9 Illustration of the proposed through-the-wall target detection and localization[1].

earthquakes and fires where timing is extremely critical.

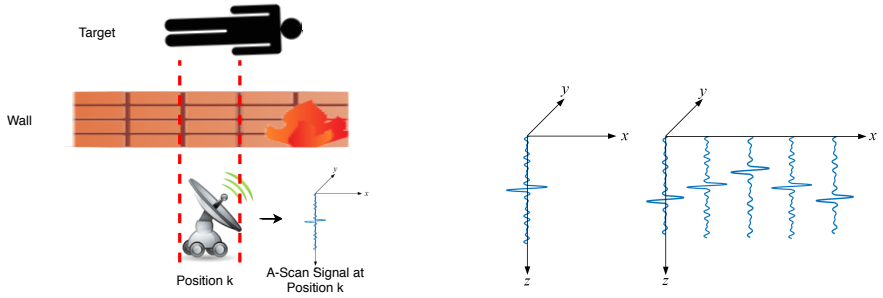

(a) **(b)**

Figure 3.10 Pictorial illustration of TWRI data acquisition: (a) A-scan data is acquired in a constant spatial displacement along the x-axis. (b) The B-scan is created from the collection of A-scans.

When a signal $s(t)$ is modulated using a series of carrier frequencies defined as $f_n = f_0 + n\Delta f$, where $n = 0, ..., N-1$ the reflected signal (demodulated), can be approximated as

$$r(n,t) \approx \kappa.s\left(\frac{t-2R/c}{T_d}\right)e^{\left(-j\frac{4\pi(f_0+n\Delta f)R}{c}\right)}, \tag{3.5}$$

where Δ_f represents the frequency interval, κ is a constant for the attenuation effect, c is the speed of light, $s(t)$ denotes the base modulated signal that is transmitted, R signifies the range, and T_d is the pulse duration. Taking the inverse fast Fourier transform (IFFT) of the discretized $r(:,t)$ with respect to n should result in an impulse-like response [99]. This impulse-like response can be considered as a sparse signal in the depth domain, which in turn provides us with the range profile. It is called an

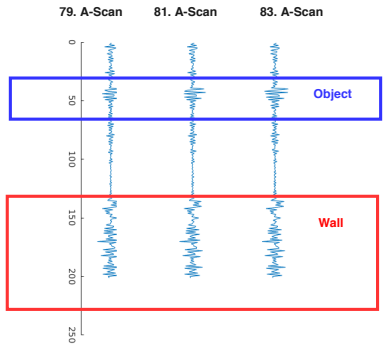

Figure 3.11 A-Scan signals are obtained by taking IFFT of $n = 201$ uniformly sampled frequencies between 0.1 GHz-15 GHz at positions 79, 81 and 83 [P3].

A-Scan when referring to a range profile for a fixed location. A pictorial representation explaining an A-Scan is given in Figure 3.10a. A series of one-dimensional signals along the x-axis, A-Scans, is gathered to create a two-dimensional image, called a *B-Scan*, which displays the scene's visual characteristics. The aforementioned A-Scan and B-Scan are illustrated in Figure 3.10b.

For the stepped frequency TWRI scenario, a reasonable choice for the measurement matrix involves randomly selecting rows of Fourier basis. Let $\mathbf{F}_\Omega$ be the CS matrix of m number of randomly selected rows from the Fourier matrix indexed by set Ω. This essentially means measuring m random frequency responses at a specific location l yielding the measurement $\mathbf{y}_l = \mathbf{F}_{\Omega_l}\mathbf{x}_l$, where $\mathbf{x} \in \mathbb{R}^n$ and $\mathbf{y} \in \mathbb{R}^m$. This corresponds to one A-Scan. For the B-Scan, the TWRI device is slid from position l to $l+1$ to obtain the subsequent m measurements, given by $\mathbf{y}_{l+1} = \mathbf{F}_{\Omega_{l+1}}\mathbf{x}_{l+1}$, and this process continues along the x-axis trajectory. In this configuration, each 1-D vector, $\mathbf{x}_l$, which represents depth information, is assumed to be sparse. In this setup, CS speeds up the measurement acquisition time because $m << n$. In an ideal scenario where $\mathbf{x}_l$ is exactly sparse, it could be exactly reconstructed as discussed in Chapter 2. However, real-world time domain A-Scans, as shown in Figure 3.11 (obtained from n measurements), exhibit noisy yet sparse peaks at object positions. Despite not being strictly sparse, small coefficients can be zeroed out to make the object positions visible.

Structural sparsity with mixed norms We define the $\ell_{p,q}$-norm of a matrix $\mathbf{Z} \in \mathbb{R}^{n\times T}$ as

$$\|\mathbf{Z}\|_{p,q} = \left(\sum_{i=1}^{n}\left(\sum_{t=1}^{T}|Z_{i,t}|^p\right)^{\frac{q}{p}}\right)^{\frac{1}{q}}, \tag{3.6}$$

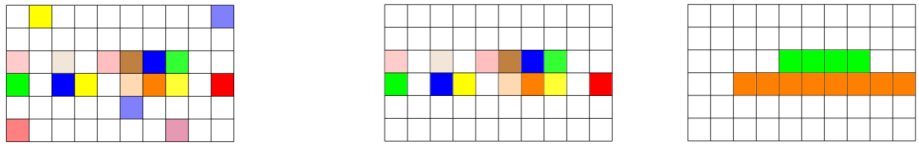

(a) (b) (c)

Figure 3.12 (a) Sparse Approximation of $\mathbf{X}$: $\min \lambda_1 \sum_{d=1}^{T} \|\mathbf{y_d} - \mathbf{F_d}\mathbf{x_d}\|_2^2 + \lambda_2 \|\mathbf{X}\|_0$, (b) Group Sparse Approximation of $\mathbf{X}$, (c) Group Sparsity + Smoothness Approximation of $\mathbf{X}$: $\min \lambda_1 \sum_{d=1}^{T} \|\mathbf{y_d} - \mathbf{F_d}\mathbf{x_d}\|_2^2 + \lambda_2 \|\mathbf{X}\|_{2,0} + \lambda_3 \sum_{i=1}^{n-1} \sum_{k=1}^{m} |X_{k,i+1} - X_{k,i}|$

where $p, q \geq 1$. For $p = 2$ and $q = 1$, this norm represents the sum of ℓ_2-norms (energy) of the columns: $\|\mathbf{Z}\|_{2,1} = \sum_{i=1}^{T} \left\|\mathbf{z}_j\right\|_2$. Conversely, for $p = 1$ and $q = 2$, it denotes the sum of ℓ_2-norms (energy) of the rows: $\|\mathbf{Z}\|_{1,2} = \sum_{i=1}^{n} \left\|\mathbf{z}_j^r\right\|_2$, where $\mathbf{z}_j^r$ denotes the j-th row of $\mathbf{Z}$. This norm often serves as a convex approximation to $\|\mathbf{Z}\|_{0,2}$, which counts the number of non-zero rows. Specifically, $\|\mathbf{Z}\|_{0,2} = \sum_k I\left(\left\|\mathbf{Z}_{k,:}\right\|_2\right)$ counts the non-zero rows. Similarly, $\|\mathbf{Z}\|_{2,0}$ returns the number of non-zero columns.

The Proposed Support Set Recovery When we check the real measurements that compose the B-Scan in Figure 3.11, a key observation can be made that consecutive A-Scan signals are quite similar to each other. Notably, they have the same sparse support sets as expected. In addition, the strength or magnitude of these non-zero elements changes gradually and smoothly with time. In the proposed radar imaging, we aim to find an approximation of a matrix $\mathbf{X}$, which holds a series of consecutive A-Scan signals within a specific sliding window, i.e., T number of A-Scans. We recover the sparse matrix, by imposing some required characteristics via an optimization approach:

$$\widehat{\mathbf{X}} = \arg\min_{X} \sum_{d=1}^{T} \|\mathbf{y_d} - \mathbf{F_d}\mathbf{x_d}\|_2^2 + \Gamma\left(\mathbf{X}\right), \tag{3.7}$$

where $\Gamma(.)$ is used to incorporate specific characteristics into the model. As mentioned above, these characteristics include having a shared location of non-zero elements (i.e., support sets) across the A-Scans and ensuring that the signal, which indicates the object's position along the x-axis, remains relatively constant as the object should have a length if it is close enough to the radar system. How to characterize this structural sparsity of the matrix $\mathbf{X}$ is explained step-by-step by a visualization shown in Figure 3.12. First, the concept of group sparsity is introduced to improve the representation of the matrix $\mathbf{X}$. This matrix contains representative images under both sparsity and group

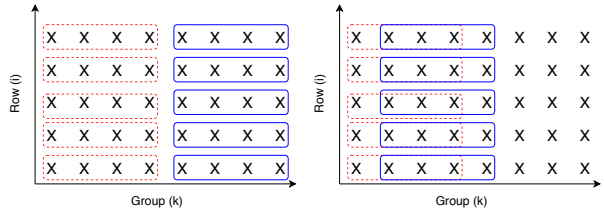

Figure 3.13 Grouping of each row in current sliding window ($L = 4, T = 8$). (a) Overlapping grouping. (b) Non-overlapping grouping

sparsity assumptions. In these images, colored squares indicate non-zero elements. The difference between sparse approximation, $\min \lambda_1 \sum_{d=1}^{T} \|\mathbf{y_d} - \mathbf{F_d}\mathbf{x_d}\|_2^2 + \lambda_2 \|\mathbf{X}\|_0$, and group sparse approximation, $\mathbf{X}$: $\min \lambda_1 \sum_{d=1}^{T} \|\mathbf{y_d} - \mathbf{F_d}\mathbf{x_d}\|_2^2 + \lambda_2 \|\mathbf{X}\|_{2,0}$, is clear when comparing Figure 3.12-(a), Figure 3.12-(b).

Furthermore, the rows of the state matrix $\mathbf{X}$ are assumed to be piece-wise constant, which means that there is an inherent smoothness in the group sparsity approximation. The expected improvement is visualized in Figure 3.12-(c). This smoothness is also imposed to ensure that the approximation is more accurate and representative enough to see the shape of the object (sparse support set for $\mathbf{X}$). This can be guaranteed by the optimization problem

$$\min \lambda_1 \sum_{d=1}^{T} \|\mathbf{y_d} - \mathbf{F_d}\mathbf{x_d}\|_2^2 + \lambda_2 \|\mathbf{X}\|_{2,0} + \lambda_3 \sum_{i=1}^{n-1} \sum_{k=1}^{m} \left| X_{k,i+1} - X_{k,i} \right|. \tag{3.8}$$

The optimization problem in Eq. (3.9) is obviously not convex, but can be easily relaxed:

$$\min \lambda_1 \sum_{d=1}^{T} \|\mathbf{y_d} - \mathbf{F_d}\mathbf{x_d}\|_2^2 + \lambda_2 \|\mathbf{X}\|_{2,1} + \lambda_3 \sum_{i=1}^{N-1} \sum_{k=1}^{m} \left| X_{k,i+1} - X_{k,i} \right|. \tag{3.9}$$

Nevertheless, sparsifying entire rows requires zeroing out many rows while keeping some entirely intact. This may cause undesired artifacts throughout the non-zero rows especially when $T >> D$, where D is possible object length along the x-axis. This is why, we applied group row sparsity (or social sparsity [45]) that imposes adjacent L-length A-Scans compose groups along the x-axis where $L << T$. This division can be done in two ways: (i) When each group is distinct and does not share any columns with its neighboring groups, then the adjacent groups are non-overlapping, i.e., $\overline{\mathbf{X}}^{i,k} = \mathbf{X}^{i}_{1+(k-1)L:kL}$, where $\overline{\mathbf{X}}^{i,k}$ denotes the k^{th} group of the i^{th} row. (ii)

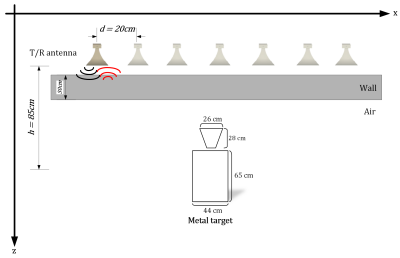

Figure 3.14 The design of real-world measurement system [P3]

Likewise, if the adjacent groups are overlapping then the group will be formulated as $\overline{\mathbf{X}}^{i,k} = \mathbf{X}^{i}_{k:(L+k)}$. Consider the two illustrations in Figure 3.13, the first illustrates overlapping grouping, and the second depicts non-overlapping grouping. In this manner, the optimization problem in Eq. (3.9) can be updated as

$$\widehat{\mathbf{X}} = \arg\min_{\mathbf{X}} \left(\frac{\lambda_1}{2} \sum_{d=1}^{T} \|\mathbf{y}_d - \mathbf{F}_d \mathbf{x}_d\|_2^2 + \lambda_2 \|\mathbf{X}\|_{2,0;L} + \lambda_3 \|\mathbf{X}\|_{\mathrm{Tv},1} \right), \tag{3.10}$$

where $\|\mathbf{X}\|_{2,0;L} = \sum_{i=1}^{n} \sum_{k} I\left(\left\| \overline{\mathbf{X}}^{i,k} \right\|_2 \right)$ counts the number of non-zero groups in rows, and $\|\mathbf{X}\|_{Tv,1} = \sum_{i=1}^{N-1} \sum_{k=1}^{m} \left| \mathbf{X}_{k,i+1} - \mathbf{X}_{k,i} \right|$ refers to total variation along row vectors. Now, we can relax the optimization problem,

$$\widehat{\mathbf{X}} = \arg\min_{\mathbf{X}} \left(\frac{\lambda_1}{2} \sum_{d=1}^{T} \|\mathbf{y}_d - \mathbf{F}_d \mathbf{x}_d\|_2^2 + \lambda_2 \|\mathbf{X}\|_{2,1;L} + \lambda_3 \|\mathbf{X}\|_{\mathrm{Tv},1} \right). \tag{3.11}$$

In [P3], we derived an ADMM-based algorithm via using the technique that was explained in Section 2.3.1 in order to solve Eq. 3.11.

Experimental Setup Figure 3.14 illustrates the specific arrangement and conditions under which the measurement was conducted. The Anritsu Network Analyzer was used for this experiment. Broadband frequencies in the range of 100 MHz to 15 GHz were sampled uniformly in 201 steps (each corresponding 2 cm). A metal object with a width of 44 cm (i.e., 22 steps along the x-axis) was used as the target.

Our experimental analysis compared three distinct techniques for reconstructing B-Scan images. A full uniform scan was initially used as a reference image, where the Inverse Fast Fourier Transform (IFFT) was applied to $n = 201$ uniformly sampled frequencies in the 0.1 GHz to 15 GHz signal band. Then a standard random subsampling method is applied, which is then followed by IFFT that was applied to a randomly

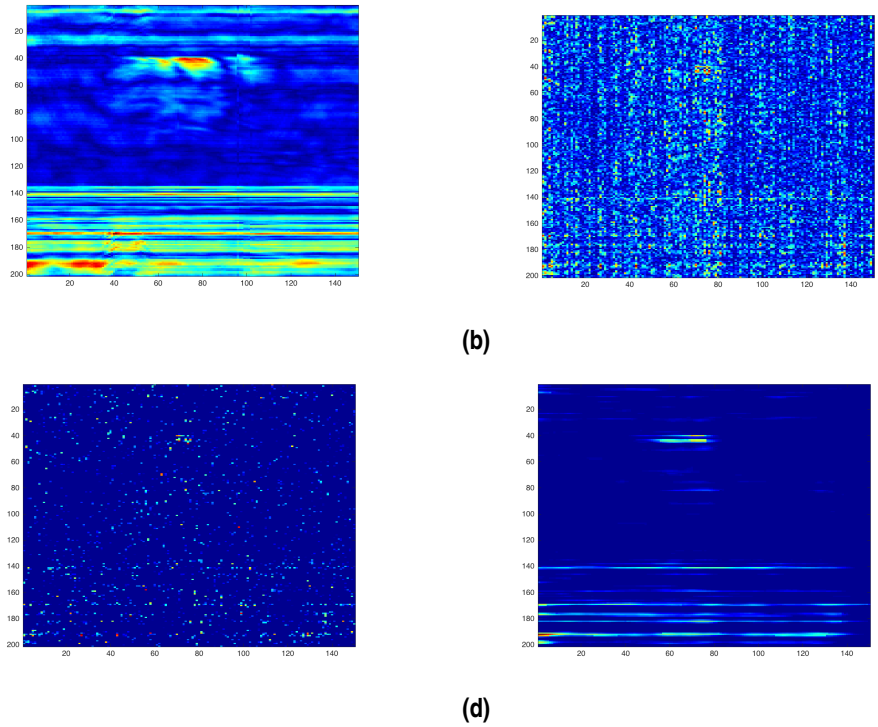

Figure 3.15 Comparison of B-Scan image reconstruction techniques: (a) Non-CS B-scan with IFFT applied to uniformly sampled frequencies. (b) B-scan estimation with IFFT applied to a randomly chosen subset of frequencies. (c) B-scan estimation with ℓ_1 minimization. (d) B-scan estimation using the proposed reconstruction method [P3].

chosen subset, $m = 0.2 \times n$, by zero-filling to non-sampled FFT coefficients. This corresponds to the traditional ℓ_2-norm minimization (i.e., the Least Squares solution). Then, conventional ℓ_1 minimization is applied which is compared to the proposed solution. As can be seen in Figure 3.15, our proposed method provides superior image quality. As can be seen in the figure, the recovered image shape appears to be in roughly the correct location, and its length appears to align with the expected 22 steps along the x-axis.

4 LEARNED COMPRESSIVE SENSING MATRICES AND DEEP LEARNING FOR SIGNAL RECOVERY

In Chapter 2, we outlined the broad range of NN-based compressed sensing (CS) solutions, classifying them based on their approach to signal acquisition and recovery. In particular, we emphasized two primary categories: those that recover signals for the traditional compressive sampling system i.e., sub-Gaussian sampling, such as the stacked denoising autoencoder (SDA), ReconNet, and ISTA-Net, and those that jointly optimize both the CS matrix and the recovery process, such as CSNET and SCSNET. While the former group retains traditional sensing matrices and focuses on learning the recovery part only, the latter emphasizes a unified approach, optimizing both the sensing and recovery components. In the sequel, we present the proposed approach that uses a neural network for learning compressive sensing and recovering.

4.1 An easy to learn compressive sensing operation

The previous chapter discussed the traditional compressed sensing (CS) framework and its foundational principles. Even though this conventional approach is mathematically elegant and robust, it may not be feasible for large-scale and multi-dimensional signal acquisition, particularly in imaging systems, when vector-matrix multiplication is used as a CS system. Consider a scenario in which the desired signal is a grayscale image of 512×512, denoted as $\mathbf{S}$. For example, if we are designing a sub-Gaussian CS system for $\frac{m}{N} = 0.36$, the CS scheme that samples the vectorized image would have dimensions 94372×262144 and the measurement matrix would be 94372×262144.

Storing such large matrices alone requires over 80GB of memory space, which is not feasible. The above-mentioned unified neural network solutions, such as CSNet and SCSNET, attempt to apply the CS matrix to image blocks rather than the entire image. However, this method can lead to the introduction of blocking artifacts. Instead, inspired by the Kronecker CS scheme we will introduce our Generalized Tensor Summation CS operation, in which CS matrices are factorized as the sum of

Kronecker CS matrices. As a result, the proposed approach makes the learning of the CS matrix possible without resorting to a block-by-block sensing strategy.

4.1.1 Separable Compressive Sensing (Kronecker CS)

Consider an input image $\mathbf{S} \in \mathbb{R}^{\sqrt{n}\times\sqrt{n}}$ that we aim to sense using CS theory. In a traditional CS setup, this image can be vectorized to form $\mathbf{s} \in \mathbb{R}^{n\times 1}$, which is then sampled using the CS matrix $\mathbf{A} \in \mathbb{R}^{m\times n}$. If the CS matrix can be separated into left and right matrices (similar to how a 2-D DCT matrix can be separated into two 1-D DCT matrices), then the separable CS imaging method can be applied. This method allows the CS sampling operator to be separable along both axes, i.e.,

$$\mathbf{Y} = \mathbf{A_1 S A_2'}, \tag{4.1}$$

where $\mathbf{A_1} \in \mathbb{R}^{\sqrt{m}\times\sqrt{n}}$ and $\mathbf{A_2} \in \mathbb{R}^{\sqrt{m}\times\sqrt{n}}$ are the left and right measurement matrices, respectively. Indeed, the separable CS formulation in Eq. (4.1) can also be turned into traditional matrix-vector multiplication form, i.e., $\mathbf{y} = \text{vec}(\mathbf{Y}) = (\mathbf{A_1} \otimes \mathbf{A_2})\ \text{vec}(\mathbf{S}) = \mathbf{As}$, where $\otimes$ denotes the Kronecker product. With the separable CS system, the number of required parameters to represent the CS matrix, $\mathbf{A}$ can be reduced to $2 \times \sqrt{m} \times \sqrt{n}$ from $m \times n$. In addition, when we compare the number of required flops to perform such a CS operation, the number of flops can be reduced from $2 \times m \times n$ to $4 \times \sqrt{m} \times n$.

We have discussed above the separable CS for 2-D signals. When it comes to multi-dimensional and separable compressed sensing (CS), consider a J-dimensional signal $\mathcal{S} \in \mathbb{R}^{n_1\times n_2\times\ldots\times n_J}$, where $n = \prod_{j=1}^{J} n_j$. The acquisition of $\mathcal{S}$ can be done via separable sensing, i.e.,

$$\mathcal{Y} = \mathcal{S} \times_1 \mathbf{A_1} \times_2 \mathbf{A_2} \ldots \times_J \mathbf{A_J}, \tag{4.2}$$

where $\mathcal{S} \times_i \mathbf{A_i}$ denotes the i-mode product of the tensor $\mathcal{S}$ and the matrix $\mathbf{A_i} \in \mathbb{R}^{m_i\times n_i}$, and $\mathcal{Y} \in \mathbb{R}^{m_1\times m_2\times\ldots\times m_J}$ is the CS tensor, with total $m = \prod_{j=1}^{J} m_j$ coefficients. If the sparsifying basis is also separable, the equation can be re-formulated as follows:

$$\mathcal{Y} = \mathcal{X} \times_1 \mathbf{D_1} \times_2 \mathbf{D_2} \ldots \times_J \mathbf{D_J}, \tag{4.3}$$

with $\mathbf{D_i}$ defined as $\mathbf{A_i \Phi_i}$, and $\mathcal{X} \in \mathbb{R}^{n_1\times n_2\times\ldots\times n_J}$ representing the sparse coefficient tensor. As we discussed previously, the separable CS operation can be written in the

form of matrix-vector multiplication as in conventional CS:

$$\mathbf{y} = (\mathbf{D_1} \otimes \mathbf{D_2} \otimes \ldots \otimes \mathbf{D_J})\, \mathbf{x}, \tag{4.4}$$

where $\mathbf{y}$ is the vectorized form of $\mathcal{Y}$ and $\mathbf{x}$ is the vectorized form of $\mathcal{X}$.

4.1.2 Factorizing CS matrix as sum of Kronecker CS matrices

Even if it is possible to reduce the memory and computation requirements, the separable CS system may require a larger minimum number of measurements to achieve similar recovery performance compared to the conventional CS system where the CS matrix is unstructured. In Chapter 2, we discussed several properties that a proper CS matrix should have. Such as RIP provides strong guarantee conditions for a CS matrix. We conclude that random matrices satisfy RIP with high probabilities. Nevertheless, for a given measurement matrix, estimating the restricted isometry constants is an NP-hard problem. In Section 2.2.3, we discussed a measurable metric, the coherence of a matrix, which can easily calculate in a feasible time.

In the sequel, we will use the coherence metric to measure the goodness of the CS matrices. We experimentally show that when we factorize a new CS matrix which is the summation of the CS matrices that are factorized by the Kronecker product of left and right CS matrices ("Kronecker CS matrices" by short), the goodness of the CS matrices can be improved. As a result of this, the sparse recovery performance is improved. Before going further ado, let us give the mathematical definition of tensorial sum factorization:

$$\mathcal{Y} = \sum_{t=1}^{T} \mathcal{S} \times_1 \mathbf{A}_{\mathbf{1}}^{(\mathbf{t})} \times_2 \mathbf{A}_{\mathbf{2}}^{(\mathbf{t})} \ldots \times_{J-1} \mathbf{A}_{\mathbf{J-1}}^{(\mathbf{t})} \times_J \mathbf{A}_{\mathbf{J}}^{(\mathbf{t})}, \tag{4.5}$$

where, T is the number of different separable CS tensors $\mathbf{A}_{\mathbf{i}}^{(\mathbf{t})}$ represents the i^{th} dimension CS matrix for the t^{th} operation. Therefore, we can define a factorized CS matrix, $\mathbf{P}$ as follows

$$\mathbf{P} = \sum_{t=1}^{T} \left(\mathbf{A}_{\mathbf{1}}^{(\mathbf{t})} \otimes \mathbf{A}_{\mathbf{2}}^{(\mathbf{t})} \otimes \ldots \otimes \mathbf{A}_{\mathbf{J}}^{(\mathbf{t})} \right), \tag{4.6}$$

when we write the vectorized version of measurements, i.e., $\mathbf{y} = \mathbf{P}\mathbf{s}$. Figure 4.1 shows the comparison between the goodness of a non-separable Gaussian matrix, $\mathbf{A} \in \mathbb{R}^{m \times n}$, with elements drawn from $\mathcal{N}(0, \frac{1}{m})$, with a separable CS matrix $\mathbf{P}$ with left

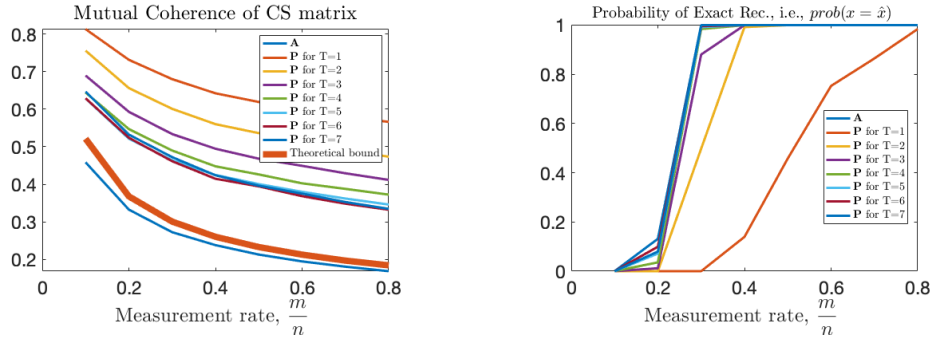

(a) (b)

Figure 4.1 Using 250 repetitions, we evaluated the average mutual coherence of the compressive sensing matrix across various measurement rates and determined the probability of exact signal reconstruction. For these tests, a perfectly sparse signal was artificially generated with a dimensionality of $N = 1024$ and a sparsity level of $k = 80$.

and right CS matrices, $\mathbf{A}_1^{(t)} \in \mathbb{R}^{\sqrt{m}\times\sqrt{n}}$ and $\mathbf{A}_2^{(t)} \in \mathbb{R}^{\sqrt{m}\times\sqrt{n}}$ whose elements are drawn from $\mathcal{N}(0, \frac{1}{\sqrt{m}})$. For the sake of simplicity, we assume the signal is sparse in canonical basis, i.e., $\mathbf{x} = \mathbf{s}$ (As discussed in detail in Section 2.2.1 and summarized in Summary 2.2.1.1, the analysis does not change if the signal is sparse in a proper basis, Φ). As T increases, the mutual coherence of the matrix $\mathbf{P}$ decreases until a lower boundary is reached. This figure also presents the probability of exact signal reconstruction from measurements $\mathbf{y} = \mathbf{P}\mathbf{x}$ for different values of T, in comparison to reconstructions from $\mathbf{y} = \mathbf{A}\mathbf{x}$. The sparse signal length is set to 1024, and the Orthogonal Matching Pursuit (OMP) algorithm [50], is used for sparse signal recovery from CSMs. It is still possible to obtain similar recovery performance after a certain number of summations, T, even though the lower boundary of mutual coherence of the factorized CS matrix $\mathbf{P}$ cannot reach the mutual coherence of the non-factorized full Gaussian CS matrix $\mathbf{A}$. Over 250 independent simulations, the probability of exact recovery is achieved, and mutual coherence metrics are averaged. As a side note is that the theoretical bound of mutual coherence of $\mathbf{A}$ in the figure is calculated by the Corollary 2.9 is a loose upper bound [101], and in practice lower coherence is achievable as seen in the figure.

4.2 Generalized Tensor Summation CS Network (GTSNET)

In the literature, a popular approach is having a structured CS matrix, as in [102] where the CS matrix is formed as a multiplication of a random permutation matrix, an

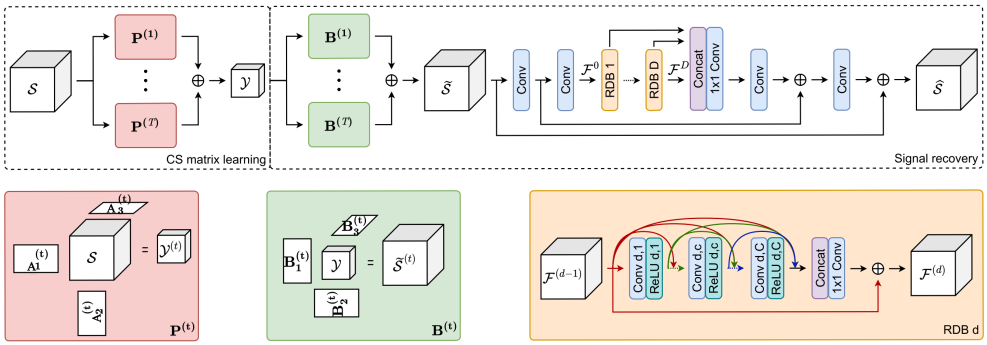

Figure 4.2 The proposed GTSNet [P8].

orthonormal basis, and a subsequent subsampling matrix in order to have a more manageable CS matrix compared to conventional sub-Gaussian matrices. Furthermore, in some CS-based encryption techniques [103], [104], the CS matrix is obtained by multiplying the sparsifying basis by the conventional sub-Gaussian matrix, i.e., $\mathbf{A} = \mathbf{A}^*\mathbf{\Phi}'$, where $\mathbf{\Phi}'$ is the transpose of the aforementioned proper sparsifying domain matrix, and $\mathbf{A}^*$ is the conventional sub-Gaussian matrix. In this way, direct comparison in the sparsifying domain can be achieved. For separable sparse bases, such as DCT, this system can be incorporated into the tensorial and sum-of-tensorial CS schemes we propose, where $\mathbf{A}_i^{(t)} = \mathbf{A}_i^{(t)*}\mathbf{\Phi}_i^{(t)'}$, and $\mathbf{\Phi}_i^{(t)'}$ is the i^{th}-coordinate matrix of the separable transformation basis.

We propose NN based approach, GTSNet, in [P8] that jointly optimizes the CS matrix and corresponding recovery part. During training, only $\mathbf{A}_i^{(t)*}$ matrices are optimized and $\mathbf{\Phi}_i^{(t)'}$ are fixed to DCT transformation. In this system, compared to the non-factorized CS matrix, the number of trainable parameters is reduced from $\prod_{j=1}^{J} m_j n_j$ to $T\sum_{j=1}^{J} m_j n_j$.

The iterative signal recovery algorithms, which are explained in Section 2.3.1, for compressively sensed signals include taking either the transpose (if the CS matrix is real) or the conjugate transpose (in the case of a Hilbert Space). The adjoint of the CS matrix could provide an initial step, or coarse estimation, in general. Indeed, most recent deep learning-based recovery works also used this idea and coarse estimation of the signal is obtained by adjoint operators. We also propose a coarse estimator block where the proxy signal $\widetilde{\mathbf{s}}$ is reconstructed from measurements $\mathbf{y}$ using a learnable operation $\mathbf{B}$. This operator is also learnable instead of using $\mathbf{P}'$. The adjoint operation can be applied directly to the tensorized measurements, thereby avoiding the need for

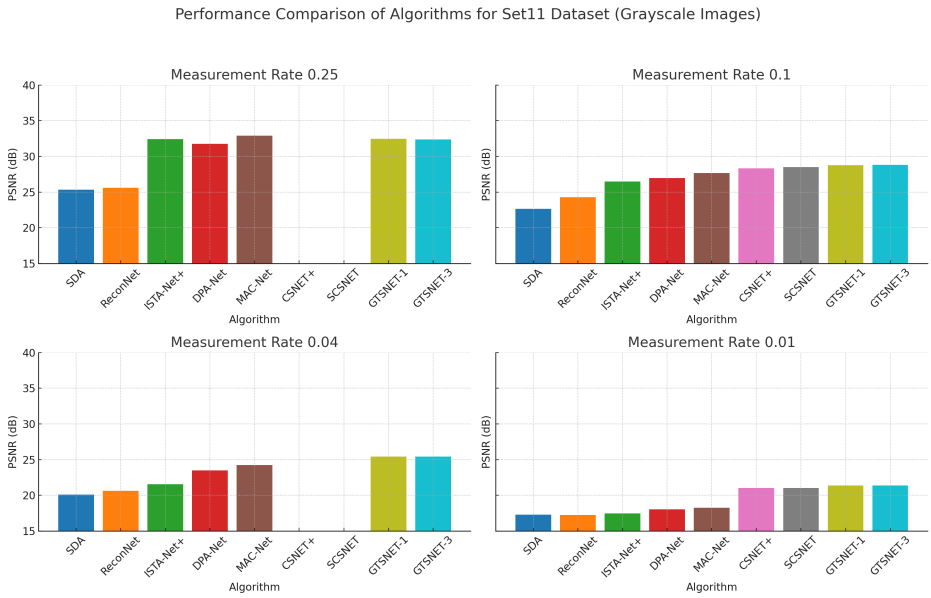

Figure 4.3 The performance comparison of competing networks for gray-scale image dataset, Set11

a vector-matrix multiplication:

$$\widetilde{\mathcal{S}} = \sum_{t=1}^{T} \mathcal{Y} \times_1 \left(\mathbf{\Phi}_1^{(t)} \mathbf{B}_1^{(t)^*} \right) \times_2 \ldots \times_J \left(\mathbf{\Phi}_J^{(t)} \mathbf{B}_J^{(t)^*} \right), \tag{4.7}$$

where $\mathbf{B}_i^{(t)^*}$ denotes the learnable adjoint matrix for the i^{th} dimension of the t^{th} term, and $\mathbf{\Phi}_i^{(t)}$ is the fixed inverse transformation operation. The tensor factorization approach allows the adjoint operation to be trainable, eliminating the need to directly learn a non-factorized matrix $\mathbf{B}$.

The final refinement block consisting of CNN layers takes the proxy signal, $\widetilde{\mathbf{S}}$ as input and produces the final estimation of the signal, $\widehat{\mathbf{S}}$. We modified the Residual Dense Network (RDN) [105] as the refinement block. The overall network structure is illustrated in Figure 4.2.

4.2.1 Results

As competing algorithms, the following neural network-based solutions, mostly developed for grayscale images, are listed: SDA, ReconNet, ISTA-Net, CSNET, SCSNET, Memory Augmented Cascading Network (MAC-Net) [106], Dual-Path Attention Net-

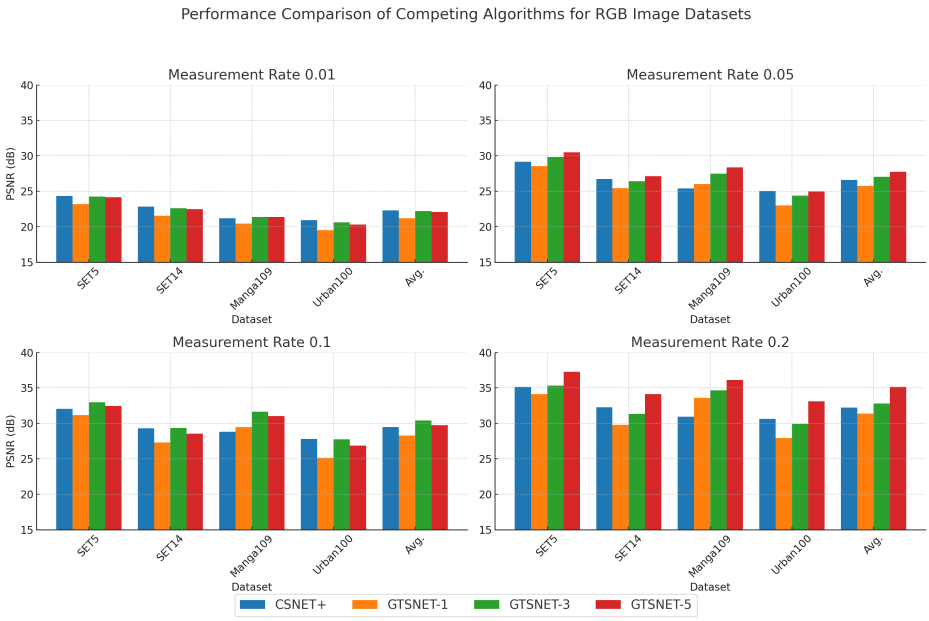

Figure 4.4 The performance comparison of competing networks for RGB datasets

work for Compressed Sensing (DPA-Net) [107], OPINE-NET [108], AMP-Net+ [109], and COAST [110]. The performance comparison in PSNR for Set11 dataset [73] can be seen in Figure 4.3. As it can be seen from Figure 4.3 that the proposed GTSNets demonstrate superior performance over existing SoTa NN-based solutions at low measurement rates (MR < 0.1), while maintaining comparable performance at higher measurement rates, thus demonstrating its robustness and suitability across a wide range of MR values.

Among the listed algorithms, only CSNet+ provides both grayscale and RGB image CS schemes. Therefore, when evaluating performance on RGB datasets, our analysis particularly focuses on the comparison between GTSNET and the RGB variant of CSNet+. Indeed, the block-by-block compressive sensing scheme, implemented through stride convolution in order to learn the CS matrix and recovery block jointly, was initially introduced in the CSNet framework. Until our proposed GTSNet, this learned sampling strategy has been a fundamental component of most subsequent neural network architectures listed above.

Using benchmark RGB image datasets such as Set5 [111], Set11, Manga109 [112], and Urban100 [113], the performance scores are reported in PSNR for different MRs.

Figure 4.5 Example visual comparison of competing algorithms in RGB datasets [P8].

The results, presented in Figure 4.4, show a notable improvement in performance when moving from GTSNET-1 to GTSNET-T ($T > 1$): GTSNET-1 displays performance comparable to CSNET+, but the more complex configurations of GTSNET significantly outperform CSNET+. Clearly, this increase in quality can be observed in the visual comparison of the recovered images, as illustrated in Figure 4.5. It is apparent that images reconstructed by CSNET+ may exhibit blocking artifacts, which are completely eliminated in images sampled and recovered by GTSNET-T networks.

As part of this dissertation summary section, we have briefly summarized the concepts of GTSNets and presented key findings. For a more comprehensive understanding, including detailed visual and quantitative results, extensive ablation studies, in-depth discussions on GTSNet hyper-parameters, training strategies, and a comparative analysis with model-based sparse reconstruction methods, we encourage interested readers to see [P8].

5 SIGNAL PROCESSING OVER COMPRESSIVELY SENSED MEASUREMENTS

With the advent of technology such as the Internet of Things (IoT), the amount of data produced by sensing systems has grown exponentially. In light of this rapid growth, the requirements associated with capturing signals at increasing sampling rates, storing these large datasets efficiently, and processing them have become more challenging. Applications such as video surveillance, the gathering of information from unmanned vehicles, or the monitoring of patients in real-time further aggravate the challenges associated with these applications. There is a clear need for solutions that can reduce communication overheads and facilitate the implementation of these applications in real-time, given the potential resource constraints.

When it comes to conventional signal processing pipelines, particularly when it comes to performing specific inference tasks, several steps often introduce redundancy in the process. First of all, sensor devices usually acquire data according to the Nyquist/Shannon sampling theory. This means that a band-limited analog signal is sampled at a rate at least twice its bandwidth. Second, once the signal has been acquired, it is compressed, usually using transform-based techniques such as JPEG or MPEG, especially if the signal exhibits sparsity or can be compressed in a specific domain. It is crucial to compress data before storing or transmitting it. Redundancy, however, becomes apparent at the receiver, where the compressed signal is first decompressed before being subjected to further signal processing operations tailored for specific tasks, such as classification or detection in computer vision. Furthermore, as the volume and dimensionality of digital samples continue to increase as a result of technological advancements, dimensionality reduction techniques are becoming increasingly important before inference. Methods such as PCA [114] or random projection [26] are employed even before any meaningful inference is drawn from the decompressed data [115]. One can question whether this multi-step process, which involves sampling at high rates, compressing, decompressing, and then compressing

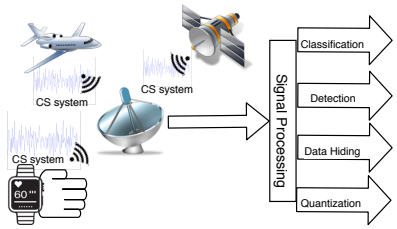

Figure 5.1 CS Monitoring System: Compressively sensed measurements are directly transmitted from sensors to a receiver, instead of performing CS recovery at the sensory device (edge device)

again before inference, is necessary if the ultimate goal is to perform inference tasks already on compressed signals.

This scenario leads us to compressive sensing (CS) as a possible solution. CS theory integrates sensing and compression into a single step, as opposed to the traditional approach of sampling followed by compression. In standard Nyquist/Shannon data acquisition systems, signal reconstruction is achieved using sinc interpolation, a straightforward linear process that can be computed efficiently. CS further simplifies data acquisition by jointly sampling and compressing data, also via linear projection. However, the recovery of signals from Compressively Sensed Measurements (CSMs) requires the use of more sophisticated optimization-driven iterative algorithms. These algorithms can be more resource-intensive compared to the traditional linear signal reconstruction. This situation may lead us to transfer the reconstruction load from the transmitter side to the receiver side in a possible CS transmitter (sensor)/receiver system such as a CS-based wide-band monitoring system [2], [116].

In such a CS-based monitoring scheme, as depicted in Figure 5.1, there may be a preference for performing direct inference on compressively sensed measurements, such as classification or detection, without reconstructing the original signal first. This preference derives from the above-mentioned practical considerations. Additionally, certain signal processing tasks can become mandatory over measurements, such as quantization or data hiding. Both topics are well investigated for Nyquist-based sensing systems. Among them there is also considerable recent literature work on the quantization of CSMs [117], [118]. On the other hand, data hiding directly over CSMs has been relatively less studied [119].

Furthermore, data privacy has become a critical concern in recent years. This is why, in the following section of the dissertation, we will present our CS-based

privacy-preserving scheme where joint encryption, multi-level privacy preservation, and compression are done via low-cost linear operation in the sensor part. The technique relies on the concept of "direct data hiding over CSMs" mentioned above. Secondly, a more robust data hiding over CSMs method will be proposed. Lastly, we will present two methods for direct signal classification over CSMs.

5.1 Data Hiding Over Compressively Sensed Measurements

5.1.1 Multi-level reversible data anonymization via compressive sensing and data hiding

As 5G and IoT technologies advance, smart surveillance applications are expected to transform continuous data monitoring and collection [120]. From intelligent building systems [121] to health monitoring systems [122], these applications raise major privacy concerns, particularly given the large amount of personal data they handle. This privacy concern has already been highlighted in the European General Data Protection Regulation (GDPR) [123].

It is important to note that privacy preservation can vary depending on the application scenario, even the very definition of privacy can be different depending on the context [124]. Typically, documents (signals) and datasets contain sensitive (private) and non-sensitive (public) components. It is necessary to encrypt sensitive parts without affecting the quality of non-sensitive parts. While strong cryptographic methods such as AES [125] and RSA [126] offer high security, they can be computationally expensive and are not always necessary for applications such as video [127], image and health monitoring [128].

Throughout the dissertation, compressive sensing theory was discussed as an efficient alternative to traditional methods for acquiring data. Additionally, we discussed in Chapter 2 that the theoretically optimal sensing matrices are chosen as random matrices or pseudo-random matrices. This randomness provides CS systems with the ability to provide privacy and cryptographic protection over measurements to some extent.

In the following section, we will utilize the cryptographic property of compressive sensing to encrypt the entire signal while jointly obscuring the sensitive parts. Therefore, we can propose a multi-level encryption system, in which unauthorized

users cannot recover anything but can only observe noise-like measurements, semi-authorized users can recover non-sensitive parts, and fully authorized users can recover the entire signal. Using the recently proposed direct data hiding over CSM technology [119], [129], we can implement this encryption at a low cost by linear compression and linear embedding. Among the primary advantages of this method are its cost-effectiveness and reversible anonymization for selected users. The experimental part will focus on image data; however, the approach is flexible and can be applied to other types of data, such as videos or bio-signals. A more detailed analysis of the proposed system can be found in [P4].

Proposed Two-tiered Encryption This method combines compressive sensing, CS-based encryption, and direct data hiding over CSMs techniques. Let the CS-encryption system be $\mathbf{y} = \mathbf{A}\mathbf{s}$, where $\mathbf{A}$ $m \times n$ is random or pseudorandom CS measurement matrix and $\mathbf{s} \in \mathbb{R}^n$ is the signal of interested to be encrypted. In addition to providing cryptographic security while compressing/sensing, such an approach provides an exact or stable recovery of the compressed signals thanks to the mathematical framework discussed in Section 2.2. This system, however, encrypts the entire signal with only one key, which is the measurement matrix A, and does not satisfy a second level of encryption. Furthermore, although Shannon perfect security [130] can be achieved in one-time usage with some constraints [131], the system is resilient against some types of attacks in multi-usage cases [P4]. Recently, a method [132] was proposed for obscuring sensitive portions of the signal by partially corrupting some columns of the measurement matrix. However, it is not trivial to convey the information about such partial corruption in each case. We will be discussing a more complete multi-level linear encryption scheme in the sequel, in which CS encryption matrix columns can be subjected to different partial degradation in each usage to obfuscate the more sensitive part, and the information about such partial degradation can then be encrypted and hidden through simple linear embedding.

Embedding Operator, $\mathcal{E}(.)$

1. **Obfuscation of the Sensitive Part within CS-Encryption**:

   Let Λ_p be the set of indices of the elements belonging to the sensitive portion of the signal of interest. The sensitive part of the signal, denoted as $\mathbf{s}_{\mathbf{\Lambda}_\mathrm{p}}$, is obfuscated using a masking pattern $\mathbf{\Delta}_{\mathbf{\Lambda}_\mathrm{p}}$, i.e., $\Delta_{\Lambda_p}\mathbf{s}_{\mathbf{\Lambda}_\mathrm{p}}$, where $\mathbf{\Delta}_{\mathbf{\Lambda}_\mathrm{p}}$ is a multiplicative obfuscation operator, which is a diagonal matrix consisting of random numbers.

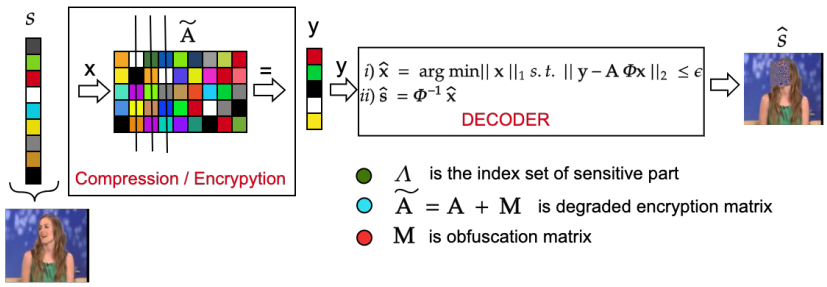

Figure 5.2 *Obfuscation during CS:* When CS is applied using the system in Eq. (5.2), the decoder path, with knowledge of the measurement matrix $\mathbf{A}$ but without knowledge of the masking operator $\mathbf{M}$, cannot recover the sensitive part. However, it can recover the rest using classical CS recovery methods.

The entire signal, which includes the non-sensitive part, $\mathbf{s}_{\Lambda_p^c}$ and the masked sensitive part, is then compressively sampled. The resulting intermediate code $\mathbf{y_d}$ is represented as:

$$\mathbf{y_d} = \mathbf{A}_{\Lambda_p^c}\mathbf{s}_{\Lambda_p^c} + \mathbf{A}_{\Lambda_p}\mathbf{\Delta}_{\Lambda_p}\mathbf{s}_{\Lambda_p}. \tag{5.1}$$

In fact, such intermediate codes are possible directly during compressive sampling, since instead of obfuscating the sensitive part of the signal, the measurement matrix column is degraded. The new degraded measurement matrix can then be applied to the signal of interest in the CS scheme,

$$\mathbf{y_d} = (\mathbf{A} + \mathbf{M})\mathbf{s}, \tag{5.2}$$

where the matrix $\mathbf{M}$ serves as the masking matrix. It is primarily composed of zeros, except for its columns represented by Λ_p. Specifically, $\mathbf{M}$ can be defined as:

$$\mathbf{M} = \begin{cases} \mathbf{A}_{\Lambda_p}\mathbf{\Delta}_{\Lambda_p} - \mathbf{A}_{\Lambda_p} & \text{for columns in } \Lambda_p \\ 0 & \text{otherwise} \end{cases}$$

This operator masks the sensitive part of the signal during compressive sensing. Figure 5.2 illustrates such joint obfuscating and compressive sampling.

2. **Data Hiding with Reversibility**:

The obfuscation matrix $\mathbf{\Delta}_{\Lambda_p}$ and its location information are converted to a

binary code, which is then secretly embedded on top of the compressively sensed (encrypted) signal $\mathbf{y_d}$. This embedding ensures reversibility, allowing for the exact recovery of the watermark sequence. The watermark is represented as $\beta\left(\mathbf{\Delta}_{\mathbf{\Lambda_p}}\right) \rightarrow \mathbf{w}' \in \{-a, +a\}^{T'}$, where $\beta\left(\mathbf{\Delta}_{\mathbf{\Lambda_p}}\right)$ is the fully reversible bit converter. Since T' can change in every usage, as the sensitive portion of the watermark varies from usage to usage, we can fix a maximum embedding bit capacity, and then extend the watermark code by filling in the $T - T'$ zeros at its end,

$$\beta\left(\mathbf{\Delta}_{\mathbf{\Lambda_p}}\right) \rightarrow \mathbf{w} \in \{-a, +a, 0\}^{T}. \tag{5.3}$$

The watermark is then linearly embedded into the CS-encrypted signal, resulting in the cipher-text:

$$\mathbf{y_w} = \mathbf{y_d} + \mathbf{Bw} = (\mathbf{A} + \mathbf{M})\mathbf{s} + \mathbf{Bw} \tag{5.4}$$

where $\mathbf{B} \in \mathbb{R}^{m \times T}$ is the watermark embedding matrix and an embedding power constraint $\|\mathbf{Bw}\| \leq P_E$ is imposed to limit the degradation of the recovered non-sensitive part of the image for semi-authorized users.

Described below are the embedding techniques that are used in the proposed two-tiered encryption method. This method ensures that only fully authorized users can recover the entire signal, while semi-authorized users can only retrieve the non-sensitive portions. The overall method is illustrated in Figure 5.3. Without going further ado, assuming $\mathbf{s}$ to be sparse in a proper basis $\mathbf{\Phi}$, then Eq. (5.4) can be re-formulated as follows

$$\mathbf{y_w} = \mathbf{y_d} + \mathbf{Bw} = (\mathbf{A} + \mathbf{M})\mathbf{s} + \mathbf{Bw} = \mathbf{Dx} + \mathbf{Bw} + \mathbf{n}, \tag{5.5}$$

where $\mathbf{As} = \mathbf{A\Phi x} = \mathbf{Dx}$, and the jointly masked and spread portion of the signal is expressed as additive perturbation term, i.e., $\mathbf{n} = \mathbf{Ms} = \mathbf{M}_{\mathbf{\Lambda_p}}\mathbf{s}_{\mathbf{\Lambda_p}} = \left(\mathbf{A}_{\mathbf{\Lambda_p}}\mathbf{\Delta}_{\mathbf{\Lambda_p}} - \mathbf{A}_{\mathbf{\Lambda_p}}\right)\mathbf{s}_{\mathbf{\Lambda_p}}$.

Decoders

1. **Decoder for semi-authorized user,** $\mathcal{D}_1(.)$ A partially authorized individual (referred to as User A) possessing only the key $\mathbf{A}$ can utilize the ℓ_1-decoding method described in Algorithm 1 to recover the signal with obfuscation of

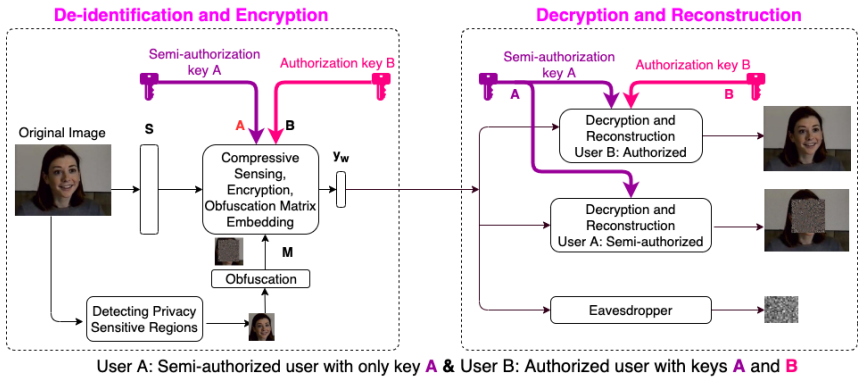

Figure 5.3 CS monitoring with multi-level reversible data anonymization [P4].

sensitive part as illustrated in Figure 5.2.

Algorithm 1 Type A Decoding Algorithm [P4], $\mathcal{D}_1(.)$

Input: $\mathbf{y_w}$, $\mathbf{A}$, $\mathbf{\Phi}$
Hyper-parameters: ϵ
1. Estimate $\widehat{\mathbf{x}}$:
$\widetilde{\mathbf{x}} = \arg\min_{\mathbf{x}} \|\mathbf{x}\|_1$ subject to $\|\mathbf{y_w} - \mathbf{D}\mathbf{x}\|_2 \leq \varepsilon$
2. $\hat{\mathbf{s}} = \mathbf{\Phi}\hat{\mathbf{x}}$
Return: $\hat{\mathbf{s}}$

---

2. **Decoder for full-authorized user,** $\mathcal{D}_2(.)$

   A fully authorized User B, called a Type-B receiver, is equipped with both the CS-encryption key $\mathbf{A}$ and the watermark encryption key $\mathbf{B}$. The purpose of the Type-B decoder is to accurately reconstruct the entire signal, including both sensitive and non-sensitive components. A three-stage recovery strategy is introduced, inspired by the method presented in [119]:

   (a) An initial approximation of the sparse signal is obtained by first eliminating the watermark by a left annihilator matrix $\mathbf{F}$, i.e., $\widetilde{\mathbf{y}} = \mathbf{F}(\mathbf{D}\mathbf{x} + \mathbf{B}\mathbf{w} + \mathbf{n}) = \mathbf{F}\mathbf{D}\mathbf{x} + \mathbf{n}'$ and then using ℓ_1-minimization given in Eq. (2.14).

   (b) With a preliminary estimate of $\mathbf{x}$, $\widetilde{\mathbf{x}}$, the least squares estimation can be performed for the watermark from the over-determined system of linear equations $\mathbf{y}_w - \mathbf{D}\mathbf{x} = \mathbf{B}\mathbf{w}$. Then, thresholding is applied to obtain the final estimate of the watermark.

(c) In the concluding phase, the masking matrix $\mathbf{M}$ is derived using the deciphered watermark. A refined estimate is then acquired using the combined $\mathbf{A}+\mathbf{M}$ as the CS-encryption matrix via ℓ_1-minimization.

The overall algorithm is presented in Algorithm 2.

Algorithm 2 Type B Decoding Algorithm [P4] , $\mathcal{D}_2(.)$

Input: $\mathbf{y_w}$, $\mathbf{A}$, $\mathbf{B}$, $\mathbf{\Phi}$
Hyper-parameters: ϵ, a, η (thresholding parameter)
1. Apply $\mathbf{F}$ to $\mathbf{y_w}$: $\widetilde{\mathbf{y}} = \mathbf{F}\mathbf{y_w}$
2. Estimate $\widetilde{\mathbf{x}}$: $\widetilde{\mathbf{x}} = \arg\min_{\mathbf{x}} \|\mathbf{x}\|_1$ s.t. $\|\widetilde{\mathbf{y}} - \mathbf{F}\mathbf{D}\mathbf{x}\|_2 \leq \varepsilon$
3. Estimate $\mathbf{w}''$: $\mathbf{w}'' = (\mathbf{B}^{\mathrm{T}}\mathbf{B})^{-1}\mathbf{B}^{\mathrm{T}}(\mathbf{y_w} - \mathbf{D}\widetilde{\mathbf{x}})$
4a. Thresholding $\mathbf{w}''$: $\widetilde{\mathbf{w}} = \mathbf{w}'' \odot \mathbf{1}_{|w_i''|>\eta}$
4b. Forming $\widehat{\mathbf{w}}$, where $\widehat{w}_i = a \times \mathrm{sgn}(\widetilde{w}_i)$
5. Obtain $\widehat{\mathbf{M}}$ from $\widehat{\mathbf{w}}$:
  (a) $\widehat{\mathbf{w}} \overset{\beta^{-1}}{\longrightarrow} \widehat{\mathbf{\Delta}}_{\mathbf{\Lambda_p}}$
  (b) $\widehat{\mathbf{M}} = \left(\mathbf{A}_{\mathbf{\Lambda_p}}\widehat{\mathbf{\Delta}}_{\mathbf{\Lambda_p}} - \mathbf{A}_{\mathbf{\Lambda_p}}\right)$
6. $\widehat{\mathbf{x}} = \arg\min_{\mathbf{x}} \|\mathbf{x}\|_1$ s.t. $\left\|(\mathbf{y_w} - \mathbf{B}\widehat{\mathbf{w}}) - (\mathbf{A}+\widehat{\mathbf{M}})\mathbf{\Phi}\mathbf{x}\right\|_2 \leq \varepsilon$
7. $\widehat{\mathbf{s}} = \mathbf{\Phi}\widehat{\mathbf{x}}$
Return: $\widehat{\mathbf{s}}$

The following theorem provides a worst-case analysis of Algorithm 2 watermark recovery probability:

Theorem 5.1 ([P4]) *Given the Gaussian CS-encryption matrix as described in Eq.* (2.19)*, and assuming the watermark-encoding matrix* $\mathbf{B}$ *possesses orthonormal columns, the conditions* $\delta_{2k}(\mathbf{H}) < \sqrt{2}-1$ *and* $\delta_{2k}(\mathbf{FH}) < \sqrt{2}-1$ *hold. Additionally, let the annihilator matrix* $\mathbf{F}$ *be such that its rows are orthogonal and the magnitude of the* i^{th} *row, denoted by* $\left\|F_{i,:}\right\|_2^2 = \frac{m}{p}$ [1]*. For a specific marked ciphertext,* $\mathbf{y_w}$*, and a chosen value of* $\varepsilon = (1+\gamma)\sqrt{m}\sigma_n$*, the watermark bits,* w_i*, can be accurately retrieved in Algorithm 2. The probability of correct recovery,* $\Pr(w_i = \hat{w}_i)$*, is at least*

$$\left(1 - 2\exp\left(\frac{-a'^2 m}{8\left\{C^2(1+\gamma)^2\right\}\left\|\mathbf{s_p}\right\|^2}\right)\right) \times \left(1 - \exp\left(-\frac{3p}{4}\gamma^2\right)\right), \tag{5.6}$$

[1] $\left\|F_{i,:}\right\|_2 = \frac{m}{p}$ should be $\|Fi,:\|_2^2 = \frac{m}{p}$ in [P4]

with $C = 4\frac{\sqrt{1+\delta_{2k}(\mathbf{FH})}}{1-(1+\sqrt{2})\,\delta_{2k}(\mathbf{FH})}$ *and* $a' = a - \eta$. *Here,* a, ε, *and* η *are hyper-parameters utilized in Algorithm 2.*

A summary of the proof can be found in [P4], while the detailed proof follows.

Proof

The proof of the theorem can be divided into eight main steps:

1. **Proof for Lemma 1 in [P4]: if** $\mathbf{s}_p \in \mathbb{R}^{|\Lambda_p|}$ **denotes the perturbation in the sensitive segment of the signal, expressed as** $\mathbf{s_p} = \Delta_{\Lambda_p}\mathbf{s}_{\Lambda_p} - \mathbf{s}_{\Lambda_p}$**, and if A is an** $m \times N$ **CS-encryption matrix with elements** $A_{i,j}$ **that are i.i.d. following the distribution** $\mathcal{N}(0, \frac{1}{m})$**, then the elements of the noise vector** $\mathbf{n}$ **defined in Eq.** (5.5) **will also be Gaussian and i.i.d., characterized by** $n_i \sim \mathcal{N}\left(0, \frac{\|\mathbf{s_p}\|_2^2}{m}\right)$**.**

   Let $\widetilde{\mathbf{s}}_\mathbf{p} \in \mathbb{R}^{N\times 1}$ be the augmented version of the perturbation vector $\mathbf{s}_p \in \mathbb{R}^{|\Lambda_p|\times 1}$ with all zeros except for the perturbed part indexed by Λ_p i.e., $\widetilde{\mathbf{s}}_{p_{\Lambda_p}} = \mathbf{s}_p$. Therefore, it is easy to see that $\mathbf{A}_{\mathbf{\Lambda_p}}\mathbf{s}_p = \mathbf{A}\widetilde{\mathbf{s}}_\mathbf{p}$ and $\left\|\mathbf{s_p}\right\|_2^2 = \left\|\widetilde{\mathbf{s}}_\mathbf{p}\right\|_2^2$.

   The problem of embedding an arbitrary signal in a lower-dimensional space is a well-studied problem in the literature, especially concerning the identification of optimal linear embedding matrices. These matrices' properties are often determined using the Johnson-Lindenstrauss [29] formulation in the data mining literature and the design of the compressive sensing matrix that satisfies the Restricted Isometry Property [19] in the signal processing literature as we already discussed these strategies in Section 2.2.1.1. As mentioned in Section 2.2.1.1 the Gaussian matrix $\mathbf{A} \in \mathbb{R}^{m\times n}(n \gg m)$, with elements $A_{i,j}$ drawn from an i.i.d according to $\mathcal{N}(0, \frac{1}{m})$, is a well-studied example of random linear embedding matrices due to the 2-stability of the Gaussian Distribution. Let A_i be the i^{th} row of $\mathbf{A}$. Following the discussions in [26], even if $\mathbf{A}$ does not have orthogonal rows, the elements of vector $\mathbf{A}\tilde{\mathbf{s}}_\mathbf{p}$, denoted as $\mathbf{n}_i = \langle A_i, \tilde{\mathbf{s}}_\mathbf{p}\rangle$, will be independent Gaussian random variables for any arbitrary vector $\tilde{\mathbf{s}}_\mathbf{p}$. Achlioptas [26] used observations on the property of i.i.d Gaussian random projection, as given in [27], [28], to reach this conclusion. this is due to the fact that as the signal dimension n increases, the rows of $\mathbf{A}$ rapidly approach orthogonality. Thus, the primary task is to determine this Gaussian distribution's sufficient statistics, namely the mean, μ_{n_i}, and variance, $\sigma_{n_i}^2$.

   The variance $\sigma_{n_i}^2$ of $\mathbf{n}_i$ can be computed as:

$$\mathbb{E}\left(n_i^2\right) = \mathbb{E}\left(\left\langle A_{i,\Lambda_p}, \mathbf{s_p}\right\rangle^2\right) = \mathbb{E}\left(\left\langle A_{i,:}, \widetilde{\mathbf{s}}_\mathbf{p}\right\rangle^2\right) \tag{5.7}$$

$$= \mathbb{E}\left(\sum_{j=1}^{n} A_{i,j}^2 \widetilde{s}_{p_j}^2\right) + \mathbb{E}\left(\sum_{k=1}^{n}\sum_{l=1,l\neq k}^{n} 2\widetilde{s}_{p_k}\widetilde{s}_{p_l} A_{i,k}A_{i,l}\right) = \sum_{j=1}^{n} \widetilde{s}_{p_j}^2 \mathbb{E}\left(A_{i,j}^2\right) \tag{5.8}$$

$$= \sum_{j\in\Lambda_p} s_{p_j}^2 \mathbb{E}\left(A_{i,j}^2\right) = \frac{1}{m}\sum_{j\in\Lambda_p} s_{p_j}^2 = \frac{\left\|\mathbf{s_p}\right\|_2^2}{m}, \tag{5.9}$$

where the term $\mathbb{E}\left(\sum_{k=1}^{n}\sum_{l=1,l\neq k}^{n} \widetilde{s}_{p_k}\widetilde{s}_{p_l} A_{i,k}A_{i,l}\right) = 0$ arises from that the elements $A_{i,j}$ are independent. Following these calculations, it is straightforward to see that $\mathbf{n}$ has zero mean.

2. **Effective Noise on Dimensionally Reduced Measurement, $\mathbf{F}\mathbf{y}_\mathbf{w}$:**

   Considering Eq. (23) in [P4],

$$\widetilde{\mathbf{y}} = \mathbf{F}\mathbf{y}_\mathbf{w} = \mathbf{F}\left(\mathbf{D}\mathbf{x} + \mathbf{B}\mathbf{w} + \mathbf{n}\right) = \mathbf{F}\mathbf{D}\mathbf{x} + \mathbf{n}', \tag{5.10}$$

   where $\mathbf{n}' = \mathbf{F}\mathbf{n}$, it becomes obvious that this is another CS-setup. Thus, the estimation of $\mathbf{x}$ can be achieved using a sparse reconstruction algorithm such as ℓ_1-minimization, as presented in (2.14). The theoretical reconstruction performance is determined by the restricted isometry constant of matrix $\mathbf{FD}$ and the noise term $\mathbf{n}'$. Given that the left annihilator matrix $\mathbf{F}$ is constructed with orthogonal rows with $\left\|F_{i,:}\right\|_2^2 = \frac{m}{p}$, and the vector $\mathbf{n}$ (from Lemma 1) consists of i.i.d. Gaussian elements, the noise on the measurement defined in (5.10), $\mathbf{Fn}$, also has i.i.d. Gaussian elements. A similar calculation to (5.9) provides

$$\mathbf{n}'_i \sim \mathcal{N}(0, \frac{m}{p}\sigma_n^2), \tag{5.11}$$

   where σ_n^2 is determined by (5.9).

3. **Restricted Isometry Property of FD:** To ensure that ℓ_1-minimization-based methods successfully reconstruct the k-sparse signal $\mathbf{x}$, $\mathbf{FD}$ must satisfy the RIP such that $\delta_{2k}(\mathbf{FD}) < \sqrt{2}-1$. It is worth noting that $\mathbf{D}_{i,j} \sim \mathcal{N}(0, \frac{1}{m})$. According to Theorem 2.5, such a Gaussian random matrix adheres to the RIP of order k

with a probability of at least $1 - 2\exp(-O(m))$ provided $m \geq O\left(k \log\left(\frac{n}{k}\right)\right)$.

By employing arguments analogous to those in the previous section, matrix $\mathbf{FD}$ has i.i.d. Gaussian elements, with $\mathbf{FD}_{i,j} \sim \mathcal{N}(0, \frac{1}{p})$ (as referenced in Lemma 3 of [119]). Thus, $\mathbf{FD}$ also satisfies the RIP of order k with a probability of at least $1 - 2\exp(-O(p))$ when $p \geq O\left(k \log\left(\frac{n}{k}\right)\right)$.

Observation: Assuming sufficiently large values for p and m, the dimensional reduction from $\mathbf{y}$ to $\mathbf{Fy}$ does not lead to a significant loss in terms of the reconstruction error. However, as anticipated, there is a slight increase in the power of the effective noise. As the watermark embedding capacity grows, and consequently the value of $\frac{m}{p}\sigma_n^2$ increases, we expect a rise in the effective noise power.

4. **Worst-Case Analysis on Pre-Estimation $\widetilde{\mathbf{x}}$ (Applying an Existing Theorem from CS Literature for Bounded Noise Case):**

   Assume that we have $\mathbf{Fy_w} = \mathbf{FDx} + \mathbf{n}'$, where $\mathbf{x}$ is a k-sparse vector and $\mathbf{n}'$ is a noise pattern satisfying $\|\mathbf{n}'\|_2 \leq \epsilon$. According to Theorem [19], the solution $\widetilde{\mathbf{x}}$ to the optimization problem

   $$\widetilde{\mathbf{x}} = \arg\min \|\mathbf{x}\|_1 \text{ subject to } \|\widetilde{\mathbf{y}} - \mathbf{FDx}\|_2 \leq \varepsilon, \tag{5.12}$$

   ensures that

   $$\|\mathbf{x} - \widetilde{\mathbf{x}}\|_2 \leq 4\frac{\sqrt{1 + \delta_{2k}(\mathbf{FD})}}{1 - (1 + \sqrt{2})\delta_{2k}(\mathbf{FD})}\epsilon, \tag{5.13}$$

   provided $\delta_{2k}(\mathbf{FD}) \leq \sqrt{2} - 1$.

5. **Chernoff Bound on Effective Gaussian Noise:** Since the noise vector, $\mathbf{n}'$, is not energy-bounded but is an i.i.d. Gaussian random vector, we can determine an ϵ using the Chernoff inequality.

   Using Lemma 1 in [119], it is obvious that the energy of a Gaussian vector satisfies

   $$\Pr\left(\|\mathbf{n}'\|_2 \geq (1 + \gamma)\sqrt{p}\sigma_{\mathbf{n}'}\right) \leq e^{-\frac{3p}{4}\gamma^2}, \tag{5.14}$$

   for any $0 \leq \gamma \leq 1$. In our case, we found in Eq. (5.11) that $\sigma_{\mathbf{n}'} = \frac{\sqrt{m}}{\sqrt{p}}\sigma_n$. Substituting this in Eq. (5.14), we get

   $$\Pr\left(\|\mathbf{n}'\|_2 \geq (1 + \gamma)\sqrt{p}\frac{\sqrt{m}}{\sqrt{p}}\sigma_n\right) \leq e^{-\frac{3p}{4}\gamma^2}. \tag{5.15}$$

6. **Worst-Case Analysis on Pre-Estimation $\widetilde{\mathbf{x}}$ (for Effective i.i.d. Gaussian):** By selecting a specific $\varepsilon = (1+\gamma)$ (for the ℓ_1-minimization problem defined in Eq. (2.14)), the solution $\tilde{\mathbf{x}}$ to optimization problem,

$$\widetilde{\mathbf{x}} = \arg\min_{\mathbf{x}} \|\mathbf{x}\|_1 \text{ s.t. } \|\widetilde{\mathbf{y}} - \mathbf{FDx}\|_2 \leq \varepsilon,$$

ensures

$$\|\mathbf{x} - \widetilde{\mathbf{x}}\|_2 \leq C\varepsilon, \tag{5.16}$$

with a probability greater than or equal to $1 - \exp\left(-\frac{3p}{4}\gamma^2\right)$, where

$$C = 4\frac{\sqrt{1+\delta_{2k}(\mathbf{FD})}}{1-(1+\sqrt{2})\delta_{2k}(\mathbf{FD})}. \tag{5.17}$$

7. **Effective Noise on the Estimation of w:** Now, let us define the error uncertainty, $\mathbf{z}$, for the over-determined system given by $\mathbf{y_w} - \mathbf{D}\widetilde{\mathbf{x}} = \mathbf{Bw} + \mathbf{z}$. By substituting $\widetilde{\mathbf{x}}$ from Eq. (5.5), we get

$$\mathbf{y_w} = \mathbf{Bw} + \mathbf{D}(\mathbf{x} - \widetilde{\mathbf{x}}) + \mathbf{D}\widetilde{\mathbf{x}} + \mathbf{n}, \tag{5.18}$$

which can be rearranged as

$$\mathbf{y_w} - \mathbf{D}\widetilde{\mathbf{x}} = \mathbf{Bw} + \mathbf{D}(\mathbf{x} - \widetilde{\mathbf{x}}) + \mathbf{n} = \mathbf{Bw} + \mathbf{z}', \tag{5.19}$$

where $\mathbf{z}' = \mathbf{D}(\mathbf{x} - \widetilde{\mathbf{x}}) + \mathbf{n}$. Given that $\|\mathbf{x} - \widetilde{\mathbf{x}}\|_2 \leq C\varepsilon$ and $\mathbf{D}_{i,j} \sim \mathcal{N}(0, \frac{1}{m})$, it follows that $\mathbf{D}(\mathbf{x} - \widetilde{\mathbf{x}})$ is a Gaussian random vector, with each element having a variance $\sigma^2 \leq \frac{C^2\varepsilon^2}{m} = C^2(1+\gamma)^2\sigma_n^2$. However, the independence between $\mathbf{D}(\mathbf{x} - \widetilde{\mathbf{x}})$ and $\mathbf{n}$ cannot be guaranteed. Therefore, the elements of $\mathbf{z}'$ are also zero-mean Gaussian vectors with a variance given by

$$\sigma_{z'}^2 \leq \max\left\{4C^2(1+\gamma)^2\sigma_n^2, 4\sigma_n^2\right\}. \tag{5.20}$$

Assuming $C^2(1+\gamma)^2 \geq 1$, we can conclude that $\sigma_{z'}^2 \leq 4C^2(1+\gamma)^2\sigma_n^2$.

8. **Recovery Probability of the Watermark Bit w_i:** Given that the matrix $\mathbf{B}$ consists of orthonormal vectors, the pre-estimation $\mathbf{w}''$ using $\mathbf{w}'' = (\mathbf{B}^{\mathrm{T}}\mathbf{B})^{-1}\mathbf{B}^{\mathrm{T}}(\mathbf{y_w} -$

$\mathbf{D}\widetilde{\mathbf{x}}$) satisfies

$$\mathbf{w} - \mathbf{w}'' = \mathbf{B}^T \mathbf{z}' = \mathbf{z}'', \tag{5.21}$$

where $z_i'' \sim \mathcal{N}(0, \sigma_{z'}^2)$. Finally, using Eq. (2.17) in [133, Chapter 2], the error probability for each watermark bit can be expressed as

$$\begin{aligned} \Pr(w_i \neq \hat{w}_i | \{\|\mathbf{x} - \tilde{\mathbf{x}}\|_2 \leq C\epsilon\}) &= \Pr\left(|z_i'| \geq a'\right) \\ &\leq 2\exp\left(\frac{-a'^2 m}{8C^2(1+\gamma)^2 \left\|\mathbf{s}_p\right\|^2}\right), \end{aligned} \tag{5.22}$$

where $a' = a - \eta$ with a and η being user-defined parameters used in Algorithm 2.

Figure 5.4 Example frames recovered for semi-authorized (User A) and fully authorized (User B) users at measurement rates of 0.6 and 0.7 [P4].

Experimental Results We present a summary of the experimental analysis of the effectiveness of the proposed CS-monitoring scheme in this section. In [P4], the detailed analysis is presented.

The study tested the proposed method using the YouTube Faces Database [134], with a selection of 5,000 frames from 100 identities. For the evaluation of recovery performances of decoders $\mathcal{D}_1(.)$ and $\mathcal{D}_2(.)$, 3,000 frames were utilized, while

a distinct set of 2,000 frames served as the training set for evaluating the privacy preservation performance. The method employed a subset of the noiselet basis as measurement matrix and we utilized the "Coiflet 2" wavelet as the sparsifying matrix, with WaveLab850 [135] as the wavelet toolbox. The encoding matrix $\mathbf{B}$'s columns were derived from a random subset of the $m \times m$ DCT basis and subsequently shuffled. Consequently, the rows of the annihilator matrix, $\mathbf{F}$ were selected from the remaining columns and then shuffled. We adopted Gradient Projection for Sparse Reconstruction (GPSR) [89] as ℓ_1-minimization solver. In this experimental part, although more complex masking strategies can be found in [P4], we only report binary masking here for simplicity: The target sensitive area (for instance, a facial region) that needs to be covered is identified by Λ_p. In the obscuring matrix, all elements are zeros, except for the diagonals, which are sampled from a Bernoulli distribution with probability p_1:

$$\Pr\left(\left(\mathbf{\Delta}_{\mathbf{\Lambda_p}}\right)_{i,i} = \pm 1\right) = p_1 \tag{5.23}$$

In Table 5.1, the recovery performances are presented for different compression rates and for an embedding value of $\frac{\|\mathbf{Bw}\|}{\|\mathbf{y_d}\|} = 0.085$. Visually, from Figure 5.4, and quantitatively, from the PSNR values, it can be observed that User A's reconstructions make faces unrecognizable, while other less sensitive regions exhibit good quality. In contrast, User B achieves satisfactory reconstructions for the whole signal.

As a next step, we would like to test the effectiveness of second-level data encryption. In the proposed CS monitoring scheme, one possibility is that an adversary may have the stolen key $\mathbf{A}$ and also have access to the training dataset. In that scenario, the malicious user can try to train a machine learning model to decode some information from a masked sensitive region of the signal. To evaluate de-identification resilience against such attacks, we created a database of 2000 original frames (20 per identity). Following this, we conduct face recognition on regions reconstructed using User A's key $\mathbf{A}$ and User B keys e.g., both keys. Table 5.2 reports the face recognition accuracies. User A's performance is nearly 1%, which is close to random guessing, while User B's accuracies are satisfactory, reaching approximately 75% for high MRs, comparable to recognition rates on original uncompressed images.

Table 5.1 Reconstruction accuracy in PSNR over sensitive and non-sensitive regions for $\frac{\|\mathbf{Bw}\|}{\|\mathbf{y_d}\|} = 0.085$.

	Sensitive Region		Non-sensitive Region		Whole Frame	
MR	**User A**	**User B**	**User A**	**User B**	**User A**	**User B**
0.3	11.90	16.61	26.37	27.31	21.67	24.24
0.4	11.65	20.23	28.61	30.91	22.20	27.36
0.5	11.48	24.63	30.51	34.59	22.50	30.92
0.6	11.36	29.79	32.06	38.17	22.66	34.92
0.7	11.28	35.0	33.29	41.30	22.75	38.83
0.8	11.22	39.37	34.25	43.69	22.80	42.02

Table 5.2 Face recognition rates at $\frac{\|\mathbf{Bw}\|}{\|\mathbf{y_d}\|} = 0.085$. Using the original frames, 77.37% recognition accuracy is achieved.

MR	0.3	0.4	0.5	0.6	0.7	0.8
User A	0.0167	0.0183	0.0197	0.019	0.0187	0.0183
User B	0.0813	0.2353	0.4347	0.6107	0.7037	0.7353

5.1.2 Robust data hiding scheme for compressively sensed signals

In the previous section, we used linear embedding to hide extra information either directly within CSMs or during compressive sampling operation, i.e., $\mathbf{y} = \mathbf{Ax} + \mathbf{Bw}$. In the decoding part, Algorithm 2 modifies the Algorithm 1 in [119]. This algorithm sequentially recovers the sparse signal $\mathbf{x}$ and the T-bit binary hidden message $\mathbf{w}$. The purpose of this section is to present a method for estimating sparse signals and embedded data jointly. This method summarizes the methodology described in [P5].

Our approach involves jointly estimating the embedded data and resolving the sparse signal using the following optimization problem formulation:

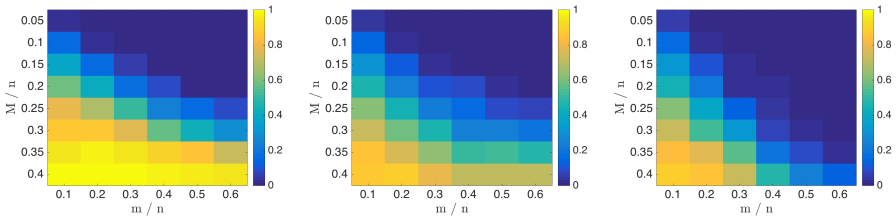

Figure 5.5 Heat-maps of Prob($\mathbf{w} \neq \hat{\mathbf{w}}$) over $\frac{m}{N}$ and $\frac{M}{m}$. (a) Algorithm in [119]. (b) The proposed method excluding the term $\|\mathbf{Fy} - \mathbf{FAx}\|_2^2$. (c) Proposed method [P5].

$$(\mathbf{x}^*, \mathbf{w}^*) = \arg\min_{(\mathbf{x},\mathbf{w})} \left\{ \frac{\lambda_1}{2} \|\mathbf{y} - (\mathbf{Ax} + \mathbf{Bw})\|_2^2 + \lambda_3 \|\mathbf{x}\|_1 + \frac{\lambda_2}{2} \|\mathbf{Fy} - \mathbf{FAx}\|_2^2 + i_{\{-a,+a\}^T}(\mathbf{w}) \right\}, \quad (5.24)$$

where the *indicator function* $i_S : \mathbb{E} \rightarrow \{0, \infty\}$ of a set S is defined as

$$i_S(\mathbf{x}) = \begin{cases} 0 & \text{if } \mathbf{x} \in S \\ \infty & \text{if } \mathbf{x} \notin S \end{cases}$$

In Eq. (5.24), we introduce a secondary fidelity term, $\|\mathbf{Fy} - \mathbf{FAx}\|_2^2$, in order to strengthen the stability of the solution in addition to the fidelity term $\|\mathbf{y} - (\mathbf{Ax} + \mathbf{Bw})\|_2^2$. The optimization problem Eq. (5.24) is non-convex one due to the last term $i_{\{-a,+a\}^T}(\mathbf{w})$ which is responsible from projecting the estimation of $\mathbf{w}$ onto set $\{-a, +a\}^T$. Despite the non-convexity, the ADMM-based solution can solve the problem stably. Using the arguments in Section 2.3.1, we derived the ADMM-based algorithm in [P5]. For the sake of brevity, we refer to [P5] for detailed derivations.

Experimental Results The CS matrix and left annihilating matrix were generated as defined in Theorem 5.1. The length of the synthetically generated sparse signal and the number of non-zero coefficients are set, $N = 512$ and $k = \frac{m}{5}$ respectively. The embedded-data-to-document ratio is fixed to -6 dB, i.e., $\|\mathbf{w}\|_2 = \frac{\|\mathbf{Ax}\|_2}{4}$. The results of each experiment are averaged over 250 repetitions. We compare the performance of the proposed algorithm with the SoTa one proposed in [119]. Additionally, we conducted an ablation study to compare the performance with and without the data fidelity term

$\|\mathbf{Fy} - \mathbf{FAx}\|_2^2$. Figures 5.5 shows that the proposed algorithm outperforms the existing solution in [119], and joint optimization with the newly data fidelity term $\|\mathbf{Fy} - \mathbf{FAx}\|_2^2$ gives the highest performance. Measurements are subjected to Gaussian noise with 24 dB SNR. More results at different noise levels are available in [P5].

5.2 Reconstruction Free Signal Recognition over Compressively Sensed Measurements

As mentioned in the introductory part of this section, two types of signal monitoring techniques equipped with distinct sampling strategies are already well-studied in the literature: traditional sensing, and compressive sensing (CS) with signal recovery done in the receiver part. In addition to these direct inferences on CS measurements, is a less studied research area. During this dissertation, we proposed two different techniques of direct inference on CSMs, which are reported in [P6] and [P7]. In traditional sensing, signals are uniformly sampled according to the Nyquist/Shannon theory and then compressed, transmitted, and stored. In the receiver, the signal is decompressed, reconstructed, and then used to make inferences such as classification or detection. With the second method, a CS-based monitoring scheme, sensing, and compression are combined in the initial stages, but the receiver must perform a complex, nonlinear, and iterative signal recovery procedure before any inference can be made. Alternatively, a third less studied method is performing direct inference on compressively sensed and possibly transmitted measurements, either at the transmitter or receiver. Alternatively, the third and less studied method involves performing direct inference on compressively sensed and possibly transmitted measurements, either at the transmitter or the receiver. In this method, the resource-intensive signal recovery step is completely bypassed, allowing the compressed measurements to be utilized directly for tasks such as classification and detection. In systems where rapid or real-time inference is critical, this approach promises greater efficiency and faster processing by eliminating the need for signal reconstruction. Figure 5.6 illustrates these three signal monitoring strategies.

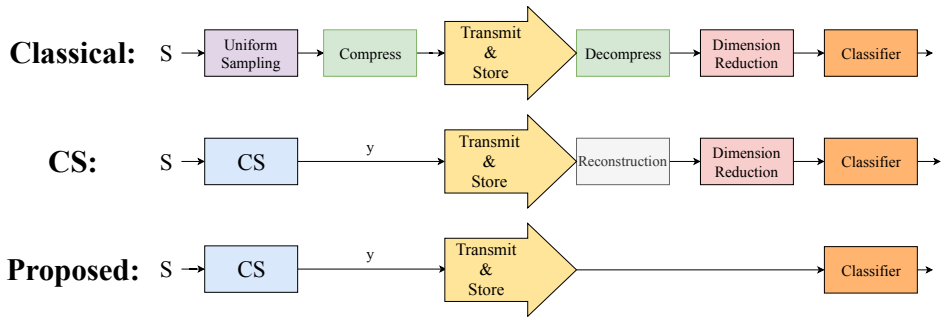

Figure 5.6 From sampling to recognition, representative pipeline of a signal's journey in three different monitoring schemes

5.2.1 Compressively sensed image recognition

The problem of direct inference on compressively sensed measurements was discussed for the first time in [2]. It was then shown, in [136], that with sparse random projections, the accuracy of the SVM classifier is maintained. Additionally, works such as [137], [138] have provided theoretical guarantees for the achievable accuracy of different compressive sensing measurement setups, including sparse and non-sparse cases. As a result of the theory that the inner product of two signals is relatively preserved for compressively sampled signals when the sampling matrix contains random values picked from some specific probability distributions [29], the authors of [139] presented the concept of the smashed filters. Later, the smashed filter concept was applied to the surveillance systems based on compressive imaging, including compressive face recognition [140], and action recognition based on compressed video [141]. In the smashed filter technique [141], compressed (smashed) filters are implemented: A set of correlation filters is generated from the original (uncompressed) images in the training set. Then, during the testing phase, the technique involves correlating the compressively sensed test images with the projected versions of these filters, which have been previously projected to the compressed domain using the CS matrix.

All the above works consider compressive sensing measurement vectors as direct inputs to their algorithms for inference problems. On the other vein, the alternative approach is to increase the size of the measurement vector to that of the original image using a simple linear projection by bypassing the costly nonlinear reconstruction process. With this simple back-projection, proximal signals are generated, and this coarse signal estimation is then used as the input of the inference algorithms directly.

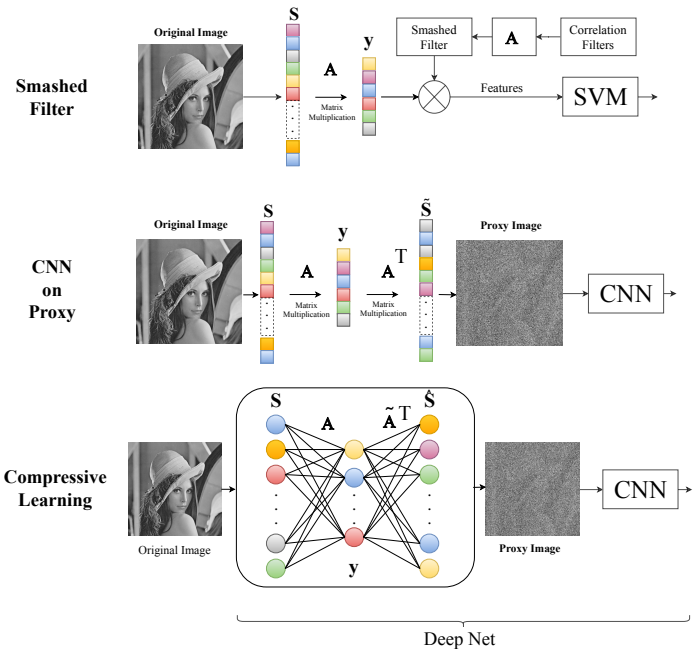

Figure 5.7 Previous solutions to the Compressive Learning problem

The mentioned proxy signal can be simply obtained by multiplying the measurement vector with the transpose of the measurement matrix, i.e., $\widetilde{\mathbf{s}} = \mathbf{A}^{\mathbf{T}}\mathbf{y}$. In a first-of-its-kind study [142], the authors used the Gaussian matrix as the measurement operation and then applied its transposition to obtain a proxy vector. This proxy vector is then reshaped to the 2-D domain to produce a proxy image that will be used as input to a CNN classifier, $\widetilde{\mathbf{S}} = reshape(\widetilde{\mathbf{s}})$.

In later work [143], the measurement matrix, the back-projection matrix, and the subsequent CNN layers are all learned by a deeper neural network in an end-to-end manner. Figure 5.7 summarizes these three alternative literature solutions: The upper graph illustrates the aforementioned smashed filter approach followed by an SVM classifier. In the middle one, the proxy image from the measurement, $\mathbf{y}$, is obtained via $\mathbf{A}$. Then, a CNN-based classifier is applied to the proxy image. In this case, $\mathbf{A}$ is the aforementioned sub-Gaussian CS matrix. In the last graph, both the CS matrix, $\mathbf{A}$, and its backprojection matrix, $\widetilde{\mathbf{A}}^{\mathbf{T}}$, are learned via a neural network. In that case, the CNN-based classifier block is applied on top of these two dense layers, enabling end-to-end learning during training.

Proposed Approach Let $\mathcal{P}_{\text{method}} : \mathbb{R}^{m\times 1} \rightarrow C$ be a mapping from the compressively sensed signal space of size $m \times 1$ to a class in the set of classes C, where $C = \{1, 2, \ldots, C\}$ and the method is an element of the set $\{\text{smashed}, \text{CNN}, \text{CL}\}$, representing the method used for the mapping. The above-mentioned methods are smashed filter-based classifier [139], CNN-based classifier [142] which works over the proxy signal, and compressive learning [143] where the proxy signal is also generated by learned CS matrix and its learned adjoint. For the smashed filter case, classification is performed directly on the compressed domain, i.e., $\mathcal{P}_{\text{smashed}}(\mathbf{y}) \rightarrow c_{\mathbf{y}} \in C$, where $c_{\mathbf{y}} \in C$ is a categorical variable, i.e., class of $\mathbf{y}$. When it comes to classification through the proxy signals, the mapping will be

$$\mathcal{P}_{\text{CNN,or CL}}(\widetilde{\mathbf{S}}) = \mathcal{D}(\widetilde{\mathbf{S}}) \circ \mathcal{F}$$

where $\widetilde{\mathbf{S}}$ is the proxy signal, either a random matrix product or learned matrices product having the same dimensionality as the original signal, $\mathcal{D}$ is feature processing block, and $\mathcal{F}$ is the final classifier mapping from feature space to class variable. In both algorithms, $\mathcal{D}$ and $\mathcal{F}$ are a block of CNN layers and a block of dense layers, respectively.

Unlike the methods mentioned in the literature that classify directly in the compressed domain or through proxy signals in the signal domain, we propose a classifier that utilizes features extracted in the signal space and in a sparsifying domain., i.e., through $\widetilde{\mathbf{S}}$, and a sparse coefficient matrix $\widetilde{\mathbf{X}}$ of $\widetilde{\mathbf{S}}$ ($\widetilde{\mathbf{X}}$ does not necessarily have the same dimensionality as $\mathbf{S}$):

$$\mathcal{P}_{\text{Proposed}} = \text{Fusion}(\mathcal{D}_1(\widetilde{\mathbf{S}}), \mathcal{D}_2(\widetilde{\mathbf{X}})) \circ \mathcal{F}$$

where $\mathcal{D}_1(.)$ is the feature extraction block for generating and processing features in the signal domain, $\mathcal{D}_2(.)$ extracts features from sparse coefficients, Fusion(.) fuses these features, and $\mathcal{F}$ is the final classifier mapping.

In this study, we employed Multiscale Binary-DCT (MB-DCT) features, as described in [144], which are extracted from the proxy signal. In this framework, $\widetilde{\mathbf{X}}$ can be conceptualized as the concatenation of block-wise DCT transformations of $\widetilde{\mathbf{S}}$. The operations performed by $\mathcal{D}_2(.)$ can be summarized as follows: (i) Mean quantization is performed within each block. (ii) The conventional Bag of Words (BoW) procedure is then applied to generate a representative vector for the image.

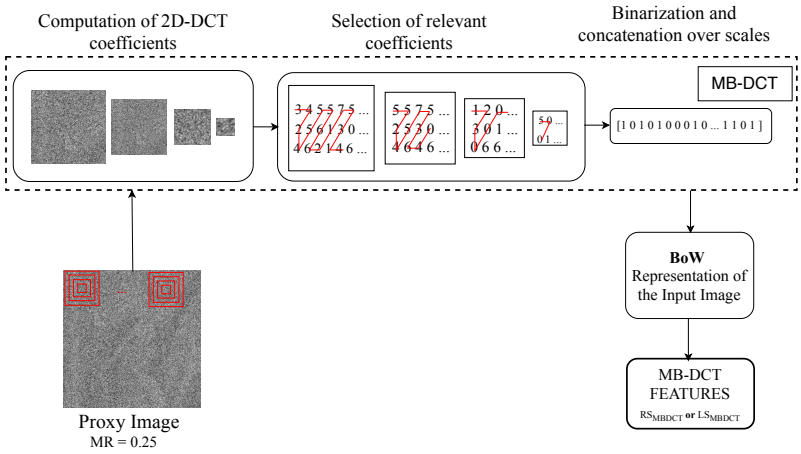

Figure 5.8 Proposed classifier over the proxy signal [P6].

In our proposed pipeline, as $\mathcal{D}_1(.)$, the CNN-based feature extractor used in both [142] and [143] was adopted. Fusion(.) operation is standard vector concatenation combining flattened (vectorized) CNN features and BoW features. We selected two different classifiers for the $\mathcal{F}$ operation: KNN and 1-D CNN classifier. The results of both classifiers are reported. The overall classification pipeline is illustrated in Figure 5.8.

Results We first need to clarify the terminology used in this study before proceeding to the comparative analysis. When it comes to sensing strategies, RS and LS are the abbreviations for the aforementioned sensing strategies, random and learned sampling, respectively. RS involves the use of random matrices for signal acquisition and its transpose to obtain the proxy signal. On the other hand, LS stands for learned, which refers to the application of learned matrices for the same purpose. Therefore, we reported the comparison results for these two alternative cases.

MNIST dataset was used for performance reporting. In this study, as competing SoTa algorithms, Smashed Filter [141], RS_CNN [142], and LS_CNN [143] were used. Among them, we revisited and re-implemented the most relevant ones, RS_CNN and LS_CNN. Our implementations of RS_CNN and LS_CNN produced results that were very similar to those reported in the original articles. The performance comparison is reported in Table 5.3 and Table 5.4. In particular, our binary descriptor approach, RS_MB-DCT, even when it is used alone without fusing it with CNN features as described above, demonstrated superior performance over the Smashed

Filter method, especially when it comes to images sensed by random sampling. On the other hand, the proposed scheme with two variants, RS_(CNN|MB-DCT) and LS_(CNN|MB-DCT), outperform the literature SoTa algorithms in both scenarios, random sensing and learned sensing, respectively. For the sake of simplicity, we only report the performance of the proposed algorithm equipped with a KNN classifier. The performance of the version with 1-D CNN classifier, all the necessary hyperparameters in the experimental setup, and more ablation study can be found in [P6].

Table 5.3 (a) KNN Classifier Test Errors with Random Sensing (RS) methods. RS denotes Random Sensing. The symbol [†] indicates our re-implementation of [142], while [*] represents our proposed classifier with corresponding features.

MR	*Smashed Filter*[141]	$RS_{\text{CNN}[142]}$	$RS^{\dagger}_{\text{CNN}}$	RS^{*}_{MBDCT}	$RS^{*}_{(\text{CNN}\|\text{MBDCT})}$
0.25	27.42%	**1.63%**	1.73%	7.26%	2.17%
0.10	43.55%	**2.99%**	2.98%	9.46%	3.02%
0.05	53.21%	5.18%	4.78%	14.28%	**4.44%**
0.01	63.03%	41.06%	45.8%	41.33%	**24.78%**

Table 5.4 (b) KNN Classifier Test Errors with Learned Sensing (LS) methods. LS denotes Learned Sensing. The symbol [†] indicates our re-implementation of [143], while [*] represents our proposed classifier with corresponding features.

MR	$LS_{\text{CNN}[143]}$	$LS^{\dagger}_{\text{CNN}}$	LS^{*}_{MBDCT}	$LS^{*}_{(\text{CNN}\|\text{MBDCT})}$
0.25	**1.56**%	1.95%	5.84%	1.58%
0.10	1.91%	1.88%	5.90%	**1.58**%
0.05	2.86%	2.12%	5.80%	**1.59**%
0.01	6.46%	5.52%	19.88%	**3.87**%

5.2.2 Multilinear compressive learning

In the previous section, we discussed how the use of a learned compressive sensing (CS) matrix and its corresponding adjoint matrix significantly enhances the performance of the direct classification of compressively sensed measurements task. For simplicity, let us refer to this joint CS-adjoint matrix learning approach as Vectorized Compressive Learning (VCL). In VCL, both the CS operation and back-propagation are essentially matrix-vector multiplications. However, as highlighted in Chapter 4, learning such

large CS matrices and their adjoints can be challenging, particularly for large-scale signals. This section will demonstrate how the factorization technique proposed in Chapter 4 can be adapted to facilitate the joint learning of CS and its adjoint matrices.

In [P8], we specifically aimed to make the sub-matrices in the separable CS setup learnable. Instead of reconstruction from the proxy, the CNN-based direct inference block was replaced and jointly optimized together with CS and adjoint sub-matrices to maximize the classification performance. In this work, we applied CNN-based feature extraction and classification block to the proxy in the signal domain, $\widetilde{\mathbf{S}}$. Mathematically, we adopt the compressive sensing operation and back-projection operations as they are in GTSNet with $T = 1$ and $\mathbf{\Phi} = \mathbf{I}$, which are expressed as follows:

$$\mathcal{Y} = \mathcal{S} \times_1 \mathbf{A_1} \times_2 \mathbf{A_2} \ldots \times_J \mathbf{A_J}, \tag{5.25}$$

and where $\mathbf{A_i}$ is the i^{th}-learnable CS sub-matrix and learnable adjoint operator is defined as:

$$\widetilde{\mathcal{S}} = \mathcal{Y} \times_1 \mathbf{B_1} \times_2 \ldots \times_J \mathbf{B_J}, \tag{5.26}$$

where $\mathbf{B_i}$ denotes the i^{th}-learnable adjoint sub-matrix. Learning of CS matrix and back-projection (adjoint matrix) constitutes the first two blocks of the network, then a classifier network blocks, $\mathcal{P}_{\text{MCL}}(.)$, takes the proxy as input and produces the final class estimation as,

$$\mathcal{P}_{\text{MCL}}(\widetilde{\mathbf{S}}) = \mathcal{D}(\widetilde{\mathbf{S}}) \circ \mathcal{F}$$

where $\mathcal{D}(.)$ and $\mathcal{F}(.)$ are feature processing and final classifier blocks. The representation illustration of the proposed MCL factorization is shown in Figure 5.9.

Results In our experiments, we used the CIFAR-10, CIFAR-100, and CelebA-32 datasets. Among them, CIFAR-10 and CIFAR-100 are 10 and 1000 classes 32×32 rgb images from CIFAR dataset [145] and the CelebA-32 dataset was specifically created by resizing the facial images from the CelebA dataset [86] to $32 \times 32 \times 3$. For initializing the parameters of the CS sub-matrices and their adjoint counterparts, we applied the Higher-Order Singular Value Decomposition (HOSVD) method [146]. Specifically, the i^{th} CS sub-matrix, $\mathbf{A}_i$, was initialized with the left singular vectors corresponding to the m_i largest singular values for mode i. Similarly, the i^{th} adjoint sub-matrix, $\mathbf{B}_i$, was initialized with the right singular vectors in a similar manner.

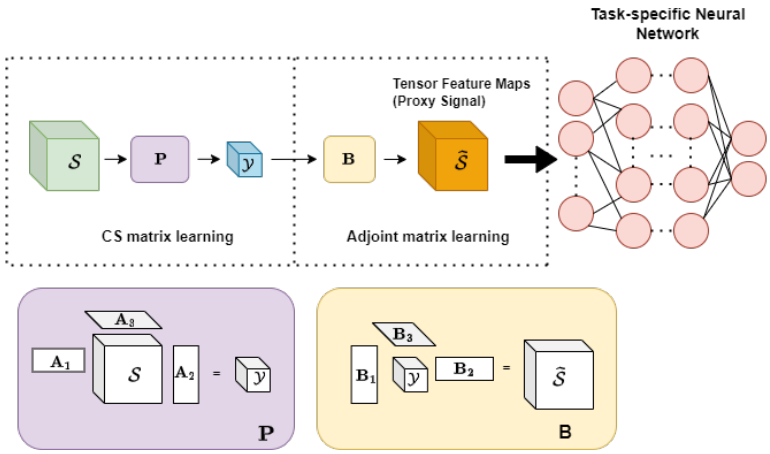

Figure 5.9 Illustrative representation of the proposed multi-linear compressive learning

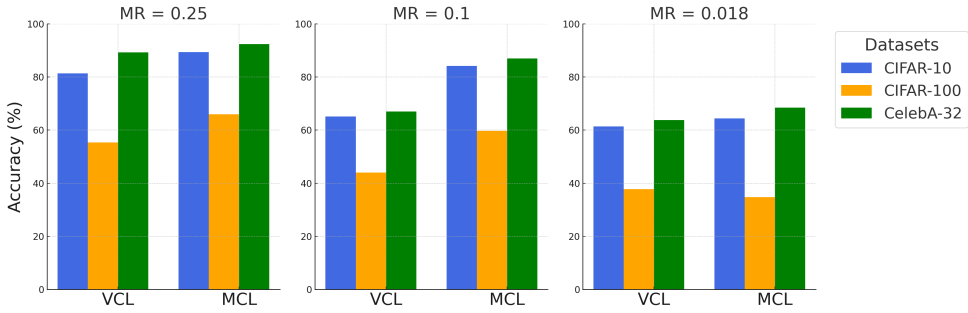

Figure 5.10 Performance comparison of competing algorithms across different measurement rates (MRs).

The proposed Multilayer Compression Learning (MCL) approach, was compared with aforementioned VCL method, $LS^{\dagger}_{\text{CNN}}$ [142] in the literature. For a fair comparison, VCL and MCL were trained over same datasets with an identical training setup. Figure 5.10 displays the test accuracy results of these competing algorithms across various measurement rates and datasets. Notably, despite the reduced computational complexity and fewer number of learnable parameters of MCL, it provides significant improvements in classification performance compared to VCL. For the CNN classifier component, we utilized the network architecture described in [147]. A more comprehensive analysis, including experimental results and ablation studies (such as the impact of different CNN classifiers, random versus HOSVD initialization, etc.), is available in [P8].

6 DOMAIN TRANSITION THROUGH PERSONALIZED DICTIONARY LEARNING

As we have discussed throughout this dissertation, the field of compressive sensing and sparse representation has made substantial progress in understanding how to recover sparse signals from linear systems, as illustrated by equation $\mathbf{y} = \mathbf{D}\mathbf{x}$. There has been a wide variety of applications that have been enabled by this theoretical framework. A good example of its application is representation-based classification or/and anomaly detection tasks, as discussed in Chapter 4.

Representation-based classification methods can benefit from the theory of compressive sensing and sparse representation. The efficiency of these methods has been demonstrated even with small size training datasets, in contrast to the extensive data requirements often associated with deep learning approaches. In representation-based classification methods, the first step is constructing a dictionary by using the entire training set in the following manner: Feature vectors or input signals themselves are placed as columns of the dictionary matrix, where the samples of the same class are placed together in the same location.

The effectiveness of representation-based classification depends on the creation of a well-constructed dictionary. When a new test sample, denoted as $\mathbf{y}$, is introduced, its representation is found within the dictionary, ideally fulfilling equation $\mathbf{y} = \mathbf{D}\mathbf{x}$ with minimal representation error. A significant aspect of this approach is the optimization of matrix $\mathbf{D}$ for specific applications, a technique known as dictionary learning. This involves learning $\mathbf{D}$ during training in order to enable new test samples to be (e.g., sparsely) represented within it. However, a challenge arises when the training dataset $\mathbf{D}$ is highly specific to a particular measurement device or data type. In such scenarios, the assumption that new samples can be effectively represented by the pre-learned dictionary may not always be valid. Such a domain gap problem can be mathematically summarized as follows: Let $\mathbf{y}_1$ and $\mathbf{y}_2$ originate from different datasets or sensory systems, system-I and system-II, respectively. Let the dictionary, $\mathbf{D}$, be learned by

using the dataset from only system-I. In the real world, we rarely end up with an ideal dictionary matrix that could represent any test signal perfectly. However, a well-constructed dictionary should enable the representation of any test signal in the target class with minimal possible error. Mathematically, even if we cannot find a representation coefficient, $\mathbf{x}_1$, which satisfies $\mathbf{y}_1 = \mathbf{D}\mathbf{x}_1$, we should be able to find a $\mathbf{x}_1$ that satisfies,

$$\mathbf{y}_1 \approx \mathbf{D}\mathbf{x}_1. \tag{6.1}$$

On the other hand, despite $\mathbf{y}_1$ and $\mathbf{y}_2$ belonging to the same class, since the signals are from different systems, the representation of $\mathbf{y}_2$ using $\mathbf{D}$ may be highly inconsistent, i.e.,

$$\mathbf{y}_2 \not\approx \mathbf{D}\mathbf{x}_2. \tag{6.2}$$

This inconsistency can cause inaccuracies in deduction tasks such as classification, detection, or analysis, emphasizing the importance of domain adaption or transfer learning for dictionary-based inference schemes.

6.1 Domain Transition for Sparse Representation

In real-world scenarios, domain differences between training data and actual real-world signals can lead to a significant performance degradation of machine learning algorithm performance [5], [148]. This problem can often occur because the training data is highly dependent on the specific signal acquisition device and the measurement conditions. The domain gap problem becomes even more challenging in healthcare applications, where the characteristics of biomedical signals can vary significantly from person to person. ECG (electrocardiogram) morphology is a good example of this phenomenon since every individual's cardiovascular system is unique [149].

In general, we aim to investigate whether a transformation $T(\cdot)$ is possible such that y_2 can be represented well enough in the dictionary $\mathbf{D}$, after that transformation, i.e.,

$$T(\mathbf{y}_2) \approx \mathbf{D}\mathbf{x}_2, \tag{6.3}$$

where $\mathbf{x}_2$ is the representation vector, ideally sparse. This transformation aims to approximate y_2 after transformation in the dictionary, even if when a direct representation in the dictionary was in the form of Eq. (6.2).

Most domain adaptation and transfer learning studies focus on the transformation of

higher-level features rather than the actual input signals, regardless of their approach based on sparse representation or another type of domain adaptation and transfer learning method [4]. The use of GAN-based methods based, such as signal-to-signal translations [5] is an exception to this trend. The concept of '*domain transition*' as a sub-topic of domain adaptation is introduced in a recent study employing Cycle-GAN, which discusses the direct transformation of input signals across different domains [3] instead of transforming high-level features. In this way, network training can be performed directly in the target domain using transformed signals from source domains. In this chapter, we introduce a novel approach for domain transition, an alternative to the aforementioned GAN-based works, based on sparse representation, which is designed specifically to address the challenges of zero-shot ECG anomaly detection.

Over the past few years, domain-adaptive dictionary learning [150], [151] and other types of sparsity-based transfer learning [152] techniques have gained increasing popularity. However, as discussed above, most earlier studies focus on transforming or modifying high-level features from the target domain to the source domain rather than on domain transition. While some studies employ sparse representation for image transition, including coupled dictionary learning strategies [153], these studies usually require signal pairs labeled in both the source and target domains to learn coupled dictionaries. An example of this is the recent super-resolution problem, which involves learning coupled dictionaries from low-resolution to high-resolution image pairs [153].

6.2 Case study: A Personalized Zero-Shot ECG Arrhythmia Monitoring System

Consider the scenario in which a healthy individual would like to enroll in a biomedical monitoring system that continuously monitors his/her health. In order to configure the device and algorithms, for the sake of convenience of the user, we may only be able to collect a limited number of samples from this new user, all of which are normal (healthy) ECG samples. A vanilla solution to such a problem is to train machine learning algorithms using datasets that have already been collected from registered users who have both normal and abnormal ECG signals. Due to the previously mentioned domain gap problem, however, the effectiveness of these algorithms is

often limited.

While this domain gap issue is a common problem with all machine learning algorithms, representation-based classification can provide an elegant way to track such a problem geometrically by interpreting it as follows: Let user p be the new user with only normal ECG beats recorded. We can still learn a dictionary that represents the normal signal subspace of that user, which is as compact as possible, by

$$\min_{\mathbf{X}^p,\ \mathbf{D}^p} \|\mathbf{S}^p - \mathbf{D}^p\mathbf{X}^p\|_2^2 + \lambda \|\mathbf{X}^p\|_1 , \tag{6.4}$$

where $\mathbf{S}^p$ (As the measurement of the signal is considered in the spatial domain itself, we will use $\mathbf{s}^p$ instead of $\mathbf{y}^p$ for the rest of the chapter.) is an $m \times T$ matrix of a collection of T number of normal ECG beats of the user p, $\mathbf{D}^p \in \mathbb{R}^{m\times n}$ is the dictionary to be learned, and $\mathbf{X}^p \in \mathbb{R}^{n\times T}$ are the sparse coefficients responsible for representing the ECG beats onto $\mathbf{D}^p$, and also for the compactness of $\mathbf{D}^p$. By compactness, we mean that $\mathbf{D}^p$ has the minimum dimensionality but is still able to represent normal signals in the training dataset on that dimension with the smallest possible error.

We observe that a relatively small number of atoms (e.g., $n = 20$) in comparison to the size of the heart beat signal (such as $m = 128$) is sufficient to represent the normal signal (beat) space effectively. Such an observation is also done in akin study [154]. In such scenarios, where we have ($m > n$), the left null space of $\mathbf{D^p} \in \mathbb{R}^{m\times n}$ emerges. Let us find the left annihilator matrix, $\mathbf{F^p} \in \mathbb{R}^{m-n\times m}$, of $\mathbf{D^p}$. Any test signal, $\mathbf{s}^p$, can be decomposed into two components, representing projections onto the column space and the left null space of a matrix $\mathbf{D^p}$. This decomposition can be expressed by

$$\mathbf{s^p} = \mathbf{D^p x} + \mathbf{F^p}^T\mathbf{F^p s^p}, \tag{6.5}$$

when the rows of $\mathbf{F^p}$ are orthonormalized. By analyzing the energies of the projected signals $\mathbf{D^p x}$ and $\mathbf{F^p}^T\mathbf{F^p s^p}$, onto the column space and left null space of $\mathbf{D^p}$ respectively, we can have a reasonable estimation of whether the signal is anomalous. In [P9], we propose a computationally efficient classifier that makes this decision by only evaluating the energy of the following null space projection, which we call it **Null Space Projection Error (NPE)**,

$$\widetilde{\mathbf{e}} = \mathbf{F^p s^p} = \mathbf{F^p}\left(\mathbf{D^p x^p} + \mathbf{e}\right) = \mathbf{F^p e}. \tag{6.6}$$

The result of this approach is a compact classifier based on threshold evaluation of the NPE. Computing the NPE is nothing but a matrix-vector multiplication, and the computational requirement of such an operation can be calculated as $2 \cdot n \cdot (n - m)$ in FLOPs. In related literature work [154], the first step involving to estimate $\mathbf{x}$ using a sparse recovery algorithm, and then substituting the estimation $\widehat{\mathbf{x}}$ to obtain the representation error, $\mathbf{e} = \mathbf{s}^p - \mathbf{D}^p\widehat{\mathbf{x}}$. Then, thresholding is applied to this error, which is termed **Sparse Approximation Error (SAE)**. However, finding the sparse coefficient $\mathbf{x}$ is computationally much more demanding, i.e., it requires $\approx 2 \cdot n \cdot k \cdot (k + 1.5) + 2 \cdot k \cdot m \cdot (n + 1) + (2 \cdot m + 1) \cdot n$ FLOPs, and in [P9], we demonstrate that thresholding based on NPE and SAE can result in similar anomaly detection performance.

Different from [154], our goal in this chapter is to train a personalized deep neural network for a newly registered user, denoted as p, by utilizing the labeled samples from previously registered users. This strategy aims to develop an advanced classifier that surpasses the accuracy of the cost-effective classifiers mentioned above. As an example, consider the labeled data of an existing user, l. Assume that this user has a significant number of normal and abnormal ECG beats. However, even if we take normal ECG samples and attempt to represent them in $\mathbf{D}^p$, they will appear anomalous in terms of their representation in $\mathbf{D}^p$ due to the domain gap problem. Mathematically speaking, the representation of a normal sample $\mathbf{s}^l$ within $\mathbf{D}^p$ will be severely inconsistent, i.e., $\mathbf{s}^l \not\approx \mathbf{D}^p\mathbf{x}$ with any possible $\mathbf{x}$. In the sequel, we will be looking for the possibility of learning a suitable transform, $T()$, which is to be called domain transition from user l to user p, to make normal signals of the user l to be represented within $\mathbf{D}^p$, i.e.,

$$T\left(\mathbf{s}^l\right) \approx \mathbf{D}^p\mathbf{x}. \tag{6.7}$$

Having such domain transition, it can be applied to both normal and abnormal samples belonging to the user l to employ them in the synthetic training set for user p. Such a scenario is illustrated in Figure 6.1. In Figure 6.1a, the magenta dots represent the newly collected samples from user p, which are not many, and all of them are labeled as normal ECG beats . Meanwhile, Figure 6.1b illustrates the dataset of user l, which contains abundant normal signals and enough abnormal samples as yellow dots. When a proper transformation, $T(.)$ is estimated which could map the normal signals of user l to the close enough vicinity of the subspace defined by column space of $\mathbf{D}^p$, such domain transition can be applied to the entire labeled dataset belonging to user l, which is graphically visualized in Figure 6.1c. Then, Figure 6.1d demonstrates how

one can combine both transformed data and the user p's own data to train a machine learning algorithm directly on the target domain which is determined by the column space and the left null space of $\mathbf{D}^p$.

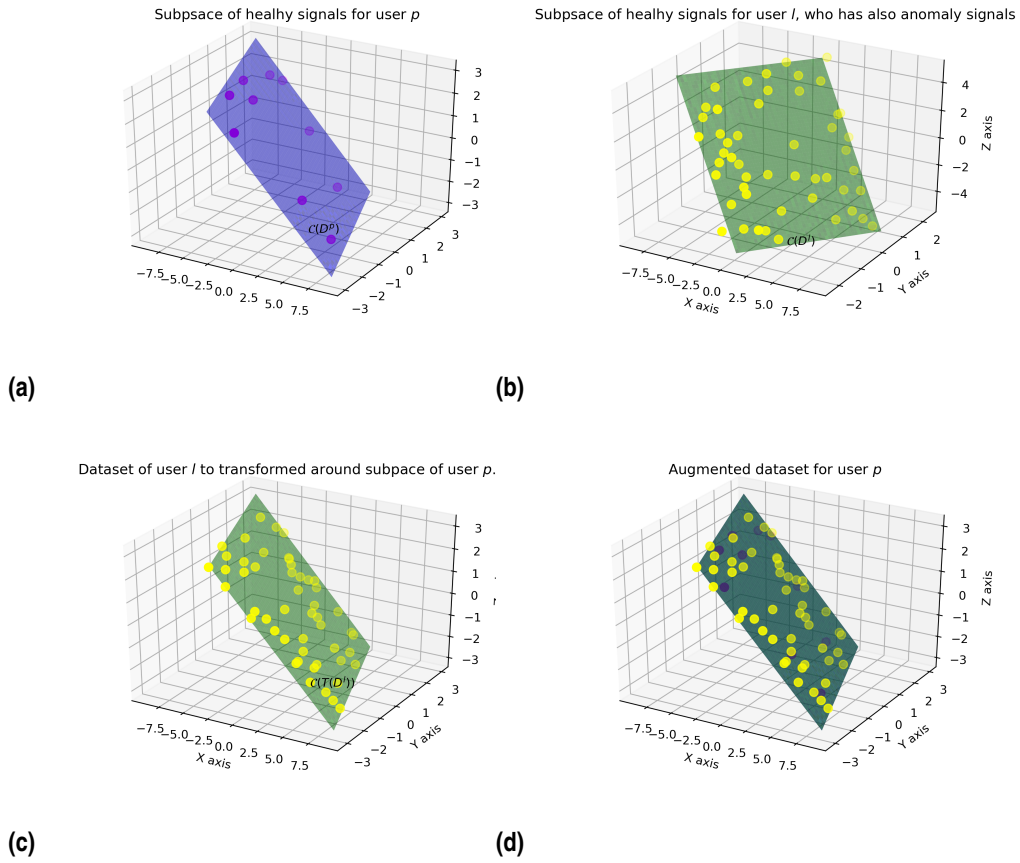

Figure 6.1 Illustration of the proposed domain transition: (a) New user p with limited normal samples and without any anomaly. (b) Existing user l with more abundant normal and abnormal data; however, ECG morphology is distinct from that of user p. (c) Transformation of user l's data to align with user p's healthy signal subspace. (d) Combined dataset of user p and transformed data from user l for personalized model training for user p.

6.2.1 Related Works on Zero-Shot ECG classification

For personalized and zero-shot ECG anomaly detection problems, the authors of [155] proposed a method that focuses on transforming normal heartbeats into potential abnormal heartbeat signals through a learned linear transformation. The proposed

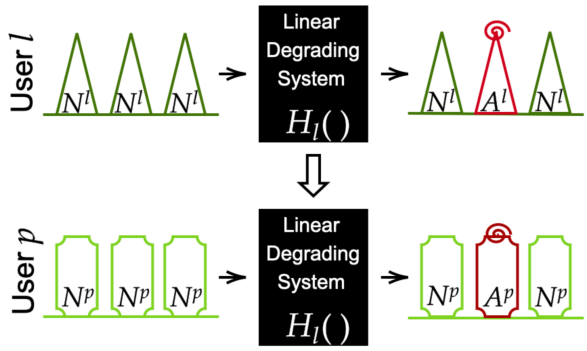

Figure 6.2 The concept of ABS system proposed in [155]: applying a linear degradation model estimated from the existing user l, to the average of normal ECG beats of a newly registered user p enables the generation of synthesized abnormal beats for user p [P9].

technique involves collecting normal ECG beats of a new user and then artificially creating abnormal signals by applying a set of linear time-invariant (LTI) degradation systems to the signal obtained by averaging the collected normal signals. This system attempts to approximately model how heart diseases morphologically impair normal ECG beats. Mathematically, an abnormal signal $\mathbf{s}_{\mathbf{A}}^{\mathbf{l}}$ is considered as a linearly corrupted version of a latent normal ECG signal $\mathbf{s}_{\mathbf{N}}^{\mathbf{l}}$, i.e., $\mathbf{s}_{\mathbf{N}}^{\mathbf{l}} \circledast \mathbf{h}^{\mathbf{l}} = \mathbf{s}_{\mathbf{A}}^{\mathbf{l}}$, where $\mathbf{h}^{\mathbf{l}} \in \mathbb{R}^M$ is the M-length filter representing the LTI system of a possible distortion and $\circledast$ is the standard convolution operation. The authors create a filter bank by averaging normal beats of the users and coupling them to the observed abnormal beats. Then, by using the Least-Squares filtering, possible filters are estimated and collected in the filter bank. A personalized training set is created for a new user p by generating synthetic abnormal beats using these filters. The proposed Abnormal Beat Synthesis (ABS) system is illustrated in Figure 6.2. While this approach is innovative in synthesizing possible abnormal ECG data for zero-shot classification tasks, it differs from our methodology, which aims to domain transition from one user to another.

6.2.2 Proposed Domain transition based Network Training in Target Subspace for Personalized Zero-Shot Anomaly Detection

As discussed above, the authors of [155] proposed a linear transformation that produces abnormal signals from normal signals of the same user. The assumption of linearity in that study seems to have been met in practice because experimental results show that

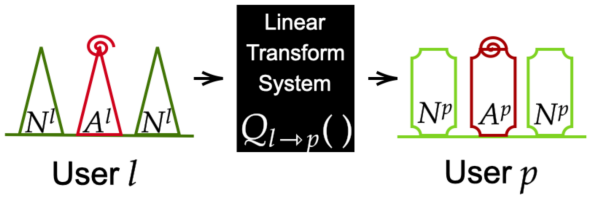

Figure 6.3 The proposed domain transition modelled as a linear transformation from user l's ECG heartbeat domain to that of the user p [P9]

the network trained with such generated anomalies provides high accuracy in zero-shot ECG classification problems. Considering these findings, we investigated whether the transformation we suggested for domain transition in Eq. (6.7), $T(.)$, can also be modeled with a linear transformation. However, unlike ABS, we did not impose a constraint on $T(.)$ to be an LTI system. In that way, whether the ECG heartbeat signal $\mathbf{s_i^l}$ of user l is abnormal or not, its linear transformation, represented as $\widehat{\mathbf{s}}_\mathbf{i}^\mathbf{l} = \mathbf{Q_{l\to p}}\mathbf{s_i^l}$, aims to align the transformed beat $\widehat{\mathbf{s}}_\mathbf{i}^\mathbf{l}$ morphologically with the real ECG beats of user p. It is critical to note that this linear transform defined with the Morphology Transformation Matrix (MTM), $\mathbf{Q_{l\to p}} \in \mathbb{R}^{m\times m}$, is designed for the specific transition from user l's ECG heartbeat domain to that of user p. The transformation process is depicted in Figure 6.3.

To learn the MTM, $\mathbf{Q_{l\to p}}$, for the source-target pair, user l and user p respectively, we propose to solve the following optimization problem,

$$\widehat{\mathbf{Q}}_\mathbf{l\to p}, \hat{\mathbf{X}}^\mathbf{l} = \underset{\mathbf{Q_{l\to p}},\, \mathbf{X^l}}{\arg\min} \|\mathbf{Q_{l\to p}}\mathbf{S^l} - \mathbf{D^p}\mathbf{X^l}\|_2^2 + \lambda\|\mathbf{X^l}\|_1 + \gamma\|\mathbf{S^l} - \mathbf{Q_{l\to p}}\mathbf{S^l}\|_2^2 \tag{6.8}$$

where λ and γ are trade-off parameters, $\mathbf{S^l}$ is the matrix of collection of healthy signals belonging to user l. The last term $\gamma\|\mathbf{S^l} - \mathbf{Q_{l\to p}}\mathbf{S^l}\|_2^2$, is responsible for preventing trivial solutions, and overfitting over the column space of $\mathbf{D}^p$.

The optimization problem in Eq. (6.8) is solved iteratively by fixing either $\widehat{\mathbf{Q}}_\mathbf{l\to p}$ or $\mathbf{X^l}$. In each iteration, the ECG signals belonging to user l, which are normalized and collected in matrix $\mathbf{S^l}$ are transformed with the current solution of $\widehat{\mathbf{Q}}_\mathbf{l\to p}$ resulting

$\widehat{\mathbf{S}}^{\mathbf{l}} \leftarrow \mathbf{Q}_{\mathbf{l}\rightarrow\mathbf{p}}\mathbf{S}^{\mathbf{l}}$. Then, the sparse coefficient matrix, $\mathbf{X}^{\mathbf{l}}$ is estimated via,

$$\widehat{\mathbf{X}}^{\mathbf{l}} \leftarrow \underset{\mathbf{X}^{\mathbf{l}}}{\arg\min} \left\| \widehat{\mathbf{S}}^{\mathbf{l}} - \mathbf{D}^{\mathbf{p}}\mathbf{X}^{\mathbf{l}} \right\|_2^2 + \lambda \left\| \mathbf{X}^{\mathbf{l}} \right\|_1 . \tag{6.9}$$

The ℓ_1-minimization problem defined in Eq. (6.9) is solved using ADMM algorithm explained in Section 2.3.1. Having the current estimate of $\mathbf{X}^{\mathbf{l}}$, we can update the MTM matrix via,

$$\widehat{\mathbf{Q}}_{\mathbf{l}\rightarrow\mathbf{p}} = \underset{\mathbf{Q}_{\mathbf{l}\rightarrow\mathbf{p}}}{\arg\min} \|\mathbf{Q}_{\mathbf{l}\rightarrow\mathbf{p}}\mathbf{S}^{\mathbf{l}} - \mathbf{D}^{\mathbf{p}}\mathbf{X}^{\mathbf{l}}\|_2^2 + \gamma\|\mathbf{S}^{\mathbf{l}} - \mathbf{Q}_{\mathbf{l}\rightarrow\mathbf{p}}\mathbf{S}^{\mathbf{l}}\|_2^2. \tag{6.10}$$

Although the optimization problem defined in Eq. (6.10) has closed form solution, we update $\widehat{\mathbf{Q}}_{\mathbf{l}\rightarrow\mathbf{p}}$ using gradient steps to encourage smoothness in the solution. The overall steps are given in Algorithm 3.

Algorithm 3 Proposed MTM Finding Algorithm [P9]

procedure DOMAIN_TRANSITION($\mathbf{D}^{\mathbf{p}}, \mathbf{S}^{\mathbf{l}}, \gamma, \eta$, epochs)
  $\mathbf{Q}_{\mathbf{l}\rightarrow\mathbf{p}} \leftarrow \mathbf{I}_{N\times N}$
  for $i \leftarrow 1$ to epochs **do**
    $\widehat{\mathbf{S}}^{\mathbf{l}} \leftarrow \mathbf{Q}_{\mathbf{l}\rightarrow\mathbf{p}}\mathbf{S}^{\mathbf{l}}$ ▷ Domain Transition
    $\widehat{\mathbf{s}}_{\mathbf{i}}^{\mathbf{l}} \leftarrow \dfrac{\widehat{\mathbf{s}}_{\mathbf{i}}^{\mathbf{l}}}{\left\|\widehat{\mathbf{s}}_{\mathbf{i}}^{\mathbf{l}}\right\|_2}$ ▷ Normalization
    $\mathbf{X}^{\mathbf{l}} \leftarrow \underset{\mathbf{X}^{\mathbf{l}}}{\arg\min} \left\| \widehat{\mathbf{S}}^{\mathbf{l}} - \mathbf{D}^{\mathbf{p}}\mathbf{X}^{\mathbf{l}} \right\|_2^2 + \lambda \left\| \mathbf{X}^{\mathbf{l}} \right\|_1$
    $\nabla\mathbf{Q}_{\mathbf{l}\rightarrow\mathbf{p}} \leftarrow \left((1+\gamma)\,\mathbf{Q}_{\mathbf{l}\rightarrow\mathbf{p}} - \gamma\mathbf{I}_{N\times N}\right)\mathbf{S}^{\mathbf{l}}\mathbf{S}^{\mathbf{l}T} - \mathbf{D}^{\mathbf{p}}\mathbf{X}^{\mathbf{l}}\mathbf{S}^{\mathbf{l}T}$
    $\mathbf{Q}_{\mathbf{l}\rightarrow\mathbf{p}} \leftarrow \mathbf{Q}_{\mathbf{l}\rightarrow\mathbf{p}} - \eta\nabla\mathbf{Q}_{\mathbf{l}\rightarrow\mathbf{p}}$
  end for
  return $\mathbf{Q}_{\mathbf{l}\rightarrow\mathbf{p}}$
end procedure

6.2.3 Experimental Results

Experimental Setup In our study, we used the MIT-BIH arrhythmia database, which consists of two-channel ECG records from 48 patients, each approximately half an hour long with annotated heartbeats [156], [157]. Focusing on two common beat representations which are *single beat* and *beat-trio*, both centered around the R-peak, we resized each beat to 128 samples, i.e., $m = 128$.

Following the guidelines of the Association for the Advancement of Medical Instrumentation (AAMI) [158], as also used in competing algorithms such as [155], heartbeats were classified as either normal (N) or abnormal (V, S, F, Q). From the original 48 patient records, we selected 34, excluding those with pacemakers or significant beat variations. In order to train the classifier, only normal heartbeats were included from each user's first five minutes, whereas abnormal beats of the same duration and the remaining of each recording were used for testing.

Training 1-D Classifier with Synthetically Generated Data As a first step toward training a personalized neural network (NN) for a specific user p, we rely on only the normal beats from the first five minutes of the user's recording to estimate $\mathbf{D}^p$. In the following steps, 33 different MTMs are estimated based on the healthy labelled beats in recordings of other users. Using the corresponding MTM, each user's normal and abnormal signals are transformed. Thus, the user's own normal heartbeats from the first five minutes of the recording are combined with the transformed signals from the other 33 users to produce the user's personalized training dataset.

As a result of this augmented training dataset, a neural network is trained separately and independently for each user p. For each user, this process is repeated, resulting in 34 unique personalized networks. A fixed 1-D CNN structure is used for each network, as shown in Figure 6.4. To ensure a fair comparison with the most closely related work detailed in Section 6.2.2, the same network architecture which is used in [155], was utilized then they were trained with three different data augmentation methods: (i) Our proposed domain transition method (Domain transition), (ii) ABS-based data synthesis for each user (ABS), and (iii) a combination of all existing users' datasets with corresponding one of user p's, first five minutes of healthy samples, without any modifications (Baseline Method).

Network Configuration and Training Parameters There are five layers in the network. The first three layers are 1-D CNNs, while the last two layers are dense layers. The kernel size of the convolution layer is set to 7, the number of layers is 32, 16, 16, 32, and the final output layer has two neurons. Following each convolution layer, max-pooling is used with a stride of 3 and a hyperbolic tangent activation function is applied. A ReLU activation function is used for the dense layer. Log-softmax is used for the output layer.

For the sake of brevity, we refer to [P9] for the details on training setups.

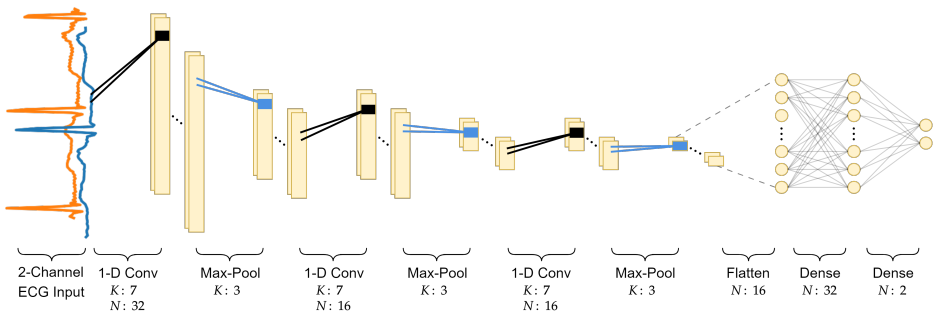

Figure 6.4 An illustration of the 1-D CNN that was used throughout the experiment. Here, K and N are filter size and number of neurons, respectively, in each layer [P9].

Ensemble Classification A method that combines the previously described NPE-based cost-efficient classifier with the trained CNN can be used to further increase performance.

To begin with, the personalized augmented training set described above can be used to determine the threshold for the NPE-based classifier. The NPE values for both healthy and anomalous signals are calculated in this synthetic dataset, and the threshold is determined using the Maximum Likelihood Estimation (MLE) method. The assumed probability distributions used in MLE are selected as exponential, and Gaussian, for NPE values calculated from healthy and abnormal beats, respectively.

In the output layer of the trained CNN, log-softmax was removed and softmax was substituted. In the testing phase, the value of the one with a value greater than 2 neurons was used to determine the confidence value of the network. Whenever the confidence value was less than a certain threshold C, the decision of the NPE-based classifier was accepted as the final decision rather than that of the CNN. In the validation set, we select C as the confidence level that maximizes F1-Score.

Competing Algorithms and Results In Table 6.1, a detailed comparison of various competing algorithms are given, by emphasizing the performance of personalized zero-shot methods, marked with $\diamond*$. These include ABS [155], SAE [154], GAN-based ECG generation [162], and our proposed variants. Additionally, the table features SOTA CNN-based [159]–[161] and GAN-based [163] algorithms. CNN-based methods are trained either person-specifically or globally, while the GAN-based method addresses data imbalance issues. We mean by global training is that the works do not put any constraint on the usage of the dataset for both training and testing.

Table 6.1 Comparison of competing ECG classification methods, including the SOTA globally trained algorithms, which do not restrict the use of an individual's own abnormal data, the personalized training-based classifiers, and zero-shot classifiers.
⋄ Personalized classifiers.
∗ Zero-shot classifiers.

Method	Accuracy	Specificity	Precision	Recall	F1-Score
CNN					
Kiranyaz *et al.* [159] ⋄	0.959	0.971	0.842	0.888	0.864
Zhai *et al.* [160] ⋄	0.968	0.976	0.879	0.920	0.899
Li *et al.* [161]	0.920	0.918	0.628	0.933	0.751
GAN					
Zhou *et al.* [162] ⋄ ∗	0.979	0.989	0.908	0.897	0.902
Shaker *et al.* Two-stage [163]	0.986	0.988	0.886	0.964	0.924
Shaker *et al.* End-to-end [163]	0.987	0.990	0.901	0.959	0.929
SR-based ⋄ ∗					
SAE-based	0.947	0.968	0.779	0.794	0.786
NPE-based (ours)	0.947	0.968	0.779	0.794	0.786
CNN ⋄ ∗					
ABS [155]	0.977	**0.995**	**0.956**	0.825	0.886
Baseline (ours)	0.965	0.987	0.899	0.809	0.852
Domain transition (ours)	0.978	0.987	0.911	0.907	0.909
Ensemble (ours)	**0.982**	0.988	0.919	**0.937**	**0.928**

In other words, they assume that we have access to abnormal signals belonging to everyone.

A baseline method is one that utilizes the global dataset while removing the abnormal data of the person of interest in order to train a person-specific network in a personalized manner. In other words, the same network is trained with the same training dataset used in our experiments, but this time without the proposed domain transition. As it is expected, due to the variation in heartbeat morphology across users, such a vanilla approach has limited performance, as can be seen in Table 6.1. On the other hand, our proposed domain transition significantly improves the performance of the network. For fair comparison, the same CNN network is trained using different data augmentation methods for zero-shot learning, such as ABS [155], and the proposed domain transition method.

Finally, as shown in Table 6.1, our ensemble classifier significantly outperforms other techniques, achieving the highest accuracy, recall, and F1-Score. It improves recall by over 11% and F1-Score by over 4% compared to akin data generator ABS [155].

In [P9], there is a more detailed discussion of hyperparameters, ablation studies, and a practical idea related to energy-efficient ECG monitoring that results from the proposed innovations in this chapter.

7 CONCLUSION AND FUTURE WORKS

The field of compressive sensing and sparse representation has seen significant progress, but there are several unexplored territories and unresolved complexities to be addressed. The purpose of this dissertation is to address some of these complicated challenges in a way that contributes to the field with innovative methods and practical applications. Most of the effort is made to bring a different perspective to the complexities of efficiently managing large-scale signals in CS and other sparse representation-based applications, optimizing the processing efficiency and applicability in real-world scenarios.

In Chapter 3, we investigated the novel methods of obtaining some information, possibly sufficient enough for the corresponding application, about $\mathbf{x}$ from $\mathbf{y}$ without the need to fully recover it. In particular, efficient estimation of the locations of its non-zero coefficients and its practical applications. In the first section of this chapter, for the first time in the literature, we investigate the possibility of direct mapping from the measurement to the signal's support set by learning compact neural networks. For this purpose, convolutional sparse support estimator networks, CSENs, are developed in [P1] and [P2]. The work provides a generic tool that could be applied to compressive sensing and any other applications based on sparse representation. The first major application area is any system that utilizes current representation-based classification technologies, such as sparse representation-based classifiers and collaborative representation-based classifiers. Although the representation-based classifier is still an active research area for the reasons mentioned above, as the number of classes or samples in the training set increases, the dictionary size becomes unmanageable. Our proposed support estimator network introduces to the literature a strategy of using a sub-set of the overall training set in the dictionary, and the remaining is for the training of the proposed support estimator network. In that way, we target both decreasing the computational and memory burden and increasing the performance at the same time.

In proof of concept work [P1], the proposed idea was evaluated for various classi-

fication tasks, including face recognition, and proved to be a very stable and energy-efficient solution, providing the best or comparable classification performance under all different scenarios. Then, in [P2], the proposed algorithm is tested in a real-life challenge, COVID-19 recognition from X-Ray images, under data scarcity constraints. In such a sudden pandemic, developing a machine learning solution, especially a deep learning-based solution, is a very challenging process. We have already witnessed some of the challenges during the COVID-19 breakout. Firstly, a very limited amount of data could be collected, especially in the early stages of the pandemic. Second, since these datasets were collected from many different devices and environments, there was a large domain gap within the training data samples. The proposed CSEN-based classifier was applied and compared to competing SOTA representation-based classifiers. The proposed solution was less costly and provided the best classification and detection performance among competing algorithms. The second central application area for sparse support estimator networks is to utilize the output of these networks as prior information about the sparse signal rather than using them as support estimation obtained by thresholding such outputs. Such prior knowledge can significantly improve the performance of conventional sparse signal recovery algorithms. In the article [P1], we showed that this can be done for two types of signals, the first of which is structurally sparse in the spatial domain, and the second one is natural images that are sparse in the gradient domain.

The second part of Chapter 3 discussed scenarios where using the previously mentioned NN-based support estimation is not feasible due to data access challenges in applications requiring specific hardware. We aimed to answer how support estimation performance can be achieved through prior assumptions and their integration into an optimization-based solution. In [P3], focusing on a specific case study, detection and localization of near-surface objects in CS-based through-the-wall radar imaging, we demonstrated that some prior information via structural sparsity modeling, which sacrifices accurate recovery of sparse coefficient magnitudes (which is not critical information for the application) for more accurate support estimation, significantly enhances performance.

In Chapter 4, we investigated the innovative ways of factorizing $\mathbf{D}$ to make CS more feasible for large-scale signals. We presented the NN-based solution GTSNet [P8], which jointly optimizes the CS matrix and the corresponding signal recovery module. In order to overcome the difficulties of handling large-scale signals, a new

factorization method, GTS-T, is presented that factorizes $\mathbf{D}$ as the sum of matrices, each produced by a Kronecker multiplication. Thanks to the separability of tensors, this factorization reduces the complexity and number of parameters significantly. Tensor learning improves performance and eases blocking artifacts when compared to the dominant strategy, block-wise CS, for NN-based CS imaging optimization.

Chapter 5 is devoted to investigating innovative ideas for resource-efficient signal processing applications that are performed directly on the measurement vector $\mathbf{y}$ without the need to recover $\mathbf{x}$. The first part of the chapter examines data hiding, privacy-preserving, and encryption while compressive sensing on sensory systems that are source-limited (e.g., edge devices). We introduced a multilevel encryption system, proposed in [P4], that uses cryptographic aspects of compression sensing to enable signal encryption that more comprehensively hides sensitive parts. This tiered approach ensures that unauthorized users cannot decrypt the signal and see only noise-like data, semi-authorized users access non-sensitive content, and fully authorized users decrypt the entire signal. Leveraging recent innovations in direct data hiding over CSMs technology [119], [129], our method offers an economical yet efficient solution via linear compression and embedding to achieve this goal. In the second part of the chapter, a more robust recovery for the direct data hiding over CSMs task is also discussed. This work, introduced in [P5], can be categorized in the current version as single-level CS-based encryption equipped with data hiding and brings improvement to current SOTA counterparts [119], [129].

The second part of Chapter 5 presents our novel solutions for more efficient and accurate classifying of $\mathbf{x}$ without recovering it directly from $\mathbf{y}$. We first introduced, in [P6], an ensemble-based classifier that surpasses the existing SOTA algorithms. The work proposed the idea of using the features from the proxy images, both in the sparsifying and spatial domain, to achieve better performance. Then, in [P7], a multilinear compressive learning strategy is introduced. The proposed network jointly optimizes the CS matrix and corresponding inference block. The proposed factorization of the CS matrix and its adjoint matrix are both in the form of a Tucker decomposition, which could be seen as a GTS factorization proposed in Chapter 4 with $T = 1$. This multilinear compressive learning scheme outperforms the SOTA compressive learning designs, including our previous work [P6], in which both CS and adjoint operations are in the form of matrix-vector multiplication.

Chapter 6 introduces a technique for domain transition using sparse representation

and personalized dictionary learning, as detailed in [P9]. The method is specifically designed for zero-shot ECG anomaly detection tasks. The proposed strategy surpassed the existing approaches with a significant gap in the zero-shot ECG classification task.

In summary, first of all, in our work, we pioneered two different subjects that provide generic solutions to be applied in a variety of applications: (i) neural network-based sparse support estimation and (ii) an efficient factorization of the dictionary (or measurement) matrix. These generic solutions serve the simultaneous objectives of computational efficiency and performance. However, they also have some limitations.

A GTS-T factorization of the measurement matrix is used in the proposed GTSNet to facilitate training, and it has been shown to provide highly improved recovery performance after learning both the CS matrix and recovery part jointly. GTSNet is suitable for a wide variety of computer science systems, including those that we use (e.g., sub-Gaussian [164], separable [165]), and structural CS matrices which are constructed by factorization via multiple matrix multiplications including the sparsifying bases [103], [104], [131]. However, certain CS systems require specialized CS matrixes due to their hardware constraints (CS MRI [166], [167], CS Radar [79], [P4]).). For example, CS MRI [168] is one of the most promising practical applications of compressive sensing theory.

In [P1], it is proposed that the output of the support estimator networks, CSENs, can be used as prior information about $\mathbf{x}$ in sparse signal recovery. Although it is experimentally shown in [P1] that the performance of conventional sparse signal recovery algorithms, in our experimental designs, we utilized sub-Gaussian and random sub-sampling matrices as CS matrices in this proof-of-concept work. Future work includes using such a support estimator-aided CS system in more challenging and practical CS designs. Indeed, our newest results [169] also show that the proposed support estimator network-based learned CS technology significantly increases recovery performance in such a CS MR imaging system. The future work also includes investigating the adaptation of CSEN-based classification to other applications. Our latest results even show that such support estimator-based inference can be extended from classification to regression tasks such as depth estimation [170].

As GTS-T factorization is a very generic solution for dictionary or CS matrix learning, it also deserves further investigation in future works in different applications, including multi-dimensional dictionary learning and even using it for any machine learning tasks that require a linear operation. In [P7], both sub-CS matrices and

their corresponding adjoints matrices are initialized with HOSVD decomposition. Given this context, the GTS-1 factorization is a suitable choice for this initialization. However, we aim to extend this for future work to GTS-T factorization with $T > 1$, which may necessitate a more sophisticated factorization approach than HOSVD.

In future works, we also plan to extend the domain transition idea proposed in [P9] for multi-class classification tasks where we want to generate specific anomaly types. Furthermore, we will search for possible adaptations for different types of applications where domain transition is needed.

REFERENCES

[1] G. Strang, "The Fundamental Theorem of Linear Algebra," *The American Mathematical Monthly*, vol. 100, no. 9, pp. 848–855, 1993. DOI: 10.2307/2324660.

[2] M. A. Davenport, P. T. Boufounos, M. B. Wakin, and R. G. Baraniuk, "Signal Processing with Compressive Measurements," *IEEE Journal of Selected Topics in Signal Processing*, vol. 4, no. 2, pp. 445–460, 2010. DOI: 10.1109/JSTSP.2009.2039178.

[3] S. Kiranyaz, O. C. Devecioglu, A. Alhams, S. Sassi, T. Ince, O. Abdeljaber, O. Avci, and M. Gabbouj, "Zero-Shot Motor Health Monitoring By Blind Domain Transition," *Mechanical Systems and Signal Processing*, vol. 210, p. 111 147, 2024, ISSN: 0888-3270. DOI: 10.1016/j.ymssp.2024.111147.

[4] L. Zhang and X. Gao, "Transfer Adaptation Learning: A Decade Survey," *IEEE Transactions on Neural Networks and Learning Systems*, vol. 35, no. 1, pp. 23–44, 2024. DOI: 10.1109/TNNLS.2022.3183326.

[5] Y. Yuan, S. Liu, J. Zhang, Y. Zhang, C. Dong, and L. Lin, "Unsupervised Image Super-Resolution Using Cycle-in-Cycle Generative Adversarial Networks," in *2018 IEEE/CVF Conference on Computer Vision and Pattern Recognition Workshops (CVPRW)*, 2018, pp. 701–710. DOI: 10.1109/CVPRW.2018.00113.

[6] J. Fourier, "Mémoire Sur La Propagation De La Chaleur Dans Les Corps Solides," *Nouveau Bulletin des Sciences par la Société Philomathique de Paris*, vol. 6, pp. 112–116, 1808.

[7] N. Ahmed, T. Natarajan, and K. Rao, "Discrete Cosine Transform," *IEEE Transactions on Computers*, vol. C-23, no. 1, pp. 90–93, 1974. DOI: 10.1109/T-C.1974.223784.

[8] S. S. Chen, D. L. Donoho, and Saunders, Michael A, "Atomic Decomposition By Basis Pursuit," in *SIAM Review*, vol. 43, 2001, pp. 129–159. DOI: 10.1137/S003614450037906X.

[9] E. Candes and T. Tao, "Decoding By Linear Programming," *IEEE Transactions on Information Theory*, vol. 51, no. 12, pp. 4203–4215, 2005. DOI: 10.1109/TIT.2005.858979.

[10] E. J. Candès *et al.*, "Compressive Sampling," in *Proceedings of the International Congress of Mathematicians*, vol. 3, 2006, pp. 1433–1452. DOI: 10.4171/022-3/69.

[11] D. L. Donoho *et al.*, "Compressed Sensing," *IEEE Transactions on Information Theory*, vol. 52, no. 4, pp. 1289–1306, 2006. DOI: 10.1109/TIT.2006.871582.

[12] B. Adcock, V. Antun, and A. C. Hansen, "Uniform Recovery in Infinite-Dimensional Compressed Sensing and Applications to Structured Binary Sampling," *Applied and Computational Harmonic Analysis*, vol. 55, pp. 1–40, 2021. DOI: 10.1016/j.acha.2021.04.001.

[13] D. L. Donoho and M. Elad, "Optimally Sparse Representation in General (Nonorthogonal) Dictionaries Via ℓ_1 Minimization," *Proceedings of the National Academy of Sciences*, vol. 100, no. 5, pp. 2197–2202, 2003. DOI: 10.1073/pnas.0437847100.

[14] R. Saab, R. Chartrand, and O. Yilmaz, "Stable Sparse Approximations Via Nonconvex Optimization," in *2008 IEEE International Conference on Acoustics, Speech and Signal Processing*, IEEE, 2008, pp. 3885–3888. DOI: 10.1109/ICASSP.2008.4518502.

[15] S. Chen and D. Donoho, "Basis Pursuit," in *Proceedings of the 1994 28th Asilomar Conference on Signals, Systems and Computers*, vol. 1, 1994, pp. 41–44. DOI: 10.1109/ACSSC.1994.471413.

[16] A. Cohen, W. Dahmen, and R. DeVore, "Compressed Sensing and Best K-Term Approximation," in *Journal of the American Mathematical Society*, vol. 22, 2009, pp. 211–231. DOI: 10.1090/S0894-0347-08-00610-3.

[17] H. Rauhut, "Compressive Sensing and Structured Random Matrices," *Theoretical Foundations and Numerical Methods for Sparse Recovery*, vol. 9, pp. 1–92, 2010. DOI: 10.1515/9783110226157.1.

[18] M. A. Davenport, M. F. Duarte, Y. C. Eldar, and G. Kutyniok, "Introduction to Compressed Sensing," in *Compressed Sensing: Theory and Applications*. Cambridge University Press, 2012. DOI: 10.1017/CBO9780511794308.002.

[19] E. J. Candès, "The Restricted Isometry Property and Its Implications for Compressed Sensing," *Comptes Rendus Mathématique*, vol. 346, no. 9, pp. 589–592, 2008, ISSN: 1631-073X. DOI: https://doi.org/10.1016/j.crma.2008.03.014. [Online]. Available: http://www.sciencedirect.com/science/article/pii/S1631073X08000964.

[20] E. J. Candes, J. K. Romberg, and T. Tao, "Stable Signal Recovery from Incomplete and Inaccurate Measurements," *Communications on Pure and Applied Mathematics: A Journal Issued by the Courant Institute of Mathematical Sciences*, vol. 59, no. 8, pp. 1207–1223, 2006. DOI: 10.1002/cpa.20124.

[21] S. Foucart, "Stability and Robustness of ℓ_1-minimizations with Weibull Matrices and Redundant Dictionaries," *Linear Algebra and its Applications*, vol. 441, pp. 4–21, 2014. DOI: https://doi.org/10.1016/j.laa.2012.10.003.

[22] J. Cahill, X. Chen, and R. Wang, "The Gap Between the Null Space Property and the Restricted Isometry Property," *Linear Algebra and its Applications*, vol. 501, pp. 363–375, 2016. DOI: https://doi.org/10.1016/j.laa.2016.03.022.

[23] M. A. Davenport, *Random Observations on Random Observations: Sparse Signal Acquisition and Processing*. Rice University, 2010.

[24] R. A. DeVore, "Deterministic Constructions of Compressed Sensing Matrices," *Journal of complexity*, vol. 23, no. 4-6, pp. 918–925, 2007. DOI: https://doi.org/10.1016/j.jco.2007.04.002.

[25] R. Baraniuk, M. Davenport, R. DeVore, and M. Wakin, "A Simple Proof of the Restricted Isometry Property for Random Matrices," *Constructive Approximation*, vol. 28, no. 3, pp. 253–263, 2008. DOI: 10.1007/s00365-007-9003-x.

[26] D. Achlioptas, "Database-friendly Random Projections: Johnson-lindenstrauss with Binary Coins," *Journal of computer and System Sciences*, vol. 66, no. 4, pp. 671–687, 2003. DOI: https://doi.org/10.1016/S0022-0000(03)00025-4.

[27] S. Dasgupta and A. Gupta, "An Elementary Proof of a Theorem of Johnson and Lindenstrauss," *Random Structures & Algorithms*, vol. 22, no. 1, pp. 60–65, 2003. DOI: 10.1002/rsa.10073.

[28] P. Indyk and R. Motwani, "Approximate Nearest Neighbors: Towards Removing the Curse of Dimensionality," in *Proceedings of the Thirtieth Annual ACM*

Symposium on Theory of Computing, 1998, pp. 604–613. DOI: https://doi.org/10.1145/276698.276876.

[29] W. B. Johnson and J. Lindenstrauss, "Extensions of Lipschitz Mappings Into a Hilbert Space," *Contemporary mathematics*, vol. 26, no. 189-206, p. 1, 1984.

[30] R. Vershynin, *High-dimensional Probability: An Introduction with Applications in Data Science*. Cambridge university press, 2018, vol. 47.

[31] E. Candes, T. Tao, *et al.*, "The Dantzig Selector: Statistical Estimation When p is much Larger Than n," *The annals of Statistics*, vol. 35, no. 6, pp. 2313–2351, 2007. DOI: 10.1214/009053606000001523.

[32] M. S. Asif and J. Romberg, "On the Lasso and Dantzig Selector Equivalence," in *2010 44th Annual Conference on Information Sciences and Systems (CISS)*, IEEE, 2010, pp. 1–6.

[33] R. Tibshirani, "Regression Shrinkage and Selection Via the Lasso," *Journal of the Royal Statistical Society: Series B (Methodological)*, vol. 58, no. 1, pp. 267–288, 1996. DOI: 10.1111/j.2517-6161.1996.tb02080.x.

[34] E. J. Candes and Y. Plan, "A Probabilistic and Ripless Theory of Compressed Sensing," *IEEE transactions on information theory*, vol. 57, no. 11, pp. 7235–7254, 2011. DOI: 10.1109/TIT.2011.2161794.

[35] J.-J. Fuchs, "On Sparse Representations in Arbitrary Redundant Bases," *IEEE transactions on Information theory*, vol. 50, no. 6, pp. 1341–1344, 2004. DOI: 10.1109/TIT.2004.828141.

[36] T. T. Cai, L. Wang, and G. Xu, "Stable Recovery of Sparse Signals and an Oracle Inequality," *IEEE Transactions on Information Theory*, vol. 56, no. 7, pp. 3516–3522, 2010. DOI: 10.1109/TIT.2010.2048506.

[37] L. Stanković, M. Brajović, D. Mandic, I. Stanković, and M. Daković, "Improved Coherence Index-based Bound in Compressive Sensing," *IEEE Signal Processing Letters*, vol. 28, pp. 1110–1114, 2021. DOI: 10.1109/LSP.2021.3084559.

[38] L. Stanković, "On the Sparsity Bound for the Existence of a Unique Solution in Compressive Sensing By the Gershgorin Theorem," *Signal Processing*, vol. 190, p. 108 316, 2022. DOI: 10.1016/j.sigpro.2021.108316.

[39] T. T. Cai and T. Jiang, "Limiting Laws of Coherence of Random Matrices with Applications to Testing Covariance Structure and Construction of Compressed Sensing Matrices," 2011. DOI: 10.1214/11-AOS879.

[40] D. L. Donoho, X. Huo, *et al.*, "Uncertainty Principles and Ideal Atomic Decomposition," *IEEE transactions on information theory*, vol. 47, no. 7, pp. 2845–2862, 2001. DOI: 10.1109/18.959265.

[41] G. Yu, G. Sapiro, and S. Mallat, "Solving Inverse Problems with Piecewise Linear Estimators: From Gaussian Mixture Models to Structured Sparsity," *IEEE Transactions on Image Processing*, vol. 21, no. 5, pp. 2481–2499, 2012. DOI: 10.1109/TIP.2011.2176743.

[42] R. G. Baraniuk, V. Cevher, M. F. Duarte, and C. Hegde, "Model-based Compressive Sensing," *IEEE Transactions on Information Theory*, vol. 56, no. 4, pp. 1982–2001, 2010. DOI: 10.1109/TIT.2010.2040894.

[43] F. Bach, R. Jenatton, J. Mairal, and G. Obozinski, "Structured Sparsity Through Convex Optimization," *Statistical Science*, pp. 450–468, 2012. DOI: 10.1214/12-STS394.

[44] M. Kowalski and B. Torrésani, "Structured Sparsity: From Mixed Norms to Structured Shrinkage," in *SPARS'09-Signal Processing with Adaptive Sparse Structured Representations*, 2009.

[45] M. Kowalski, K. Siedenburg, and M. Dörfler, "Social Sparsity! Neighborhood Systems Enrich Structured Shrinkage Operators," *IEEE transactions on signal processing*, vol. 61, no. 10, pp. 2498–2511, 2013. DOI: 10.1109/TSP.2013.2250967.

[46] D. Donoho and G. Kutyniok, "Microlocal Analysis of the Geometric Separation Problem," *Communications on Pure and Applied Mathematics*, vol. 66, no. 1, pp. 1–47, 2013. DOI: https://doi.org/10.1002/cpa.21418.

[47] R. Jenatton, J. Mairal, G. Obozinski, and F. Bach, "Proximal Methods for Hierarchical Sparse Coding," *Journal of Machine Learning Research*, vol. 12, no. Jul, pp. 2297–2334, 2011. DOI: 10.1145/1953048.2078194.

[48] M. Benning and M. Burger, "Modern Regularization Methods for Inverse Problems," *Acta Numerica*, vol. 27, pp. 1–111, 2018. DOI: doi:10.1017/S0962492918000016.

[49] S. G. Mallat and Z. Zhang, "Matching Pursuits with Time-frequency Dictionaries," *IEEE Transactions on signal processing*, vol. 41, no. 12, pp. 3397–3415, 1993. DOI: 10.1109/78.258082.

[50] J. A. Tropp and A. C. Gilbert, "Signal Recovery from Random Measurements Via Orthogonal Matching Pursuit," *IEEE Transactions on information theory*, vol. 53, no. 12, pp. 4655–4666, 2007. DOI: 10.1109/TIT.2007.909108.

[51] D. Needell and J. A. Tropp, "Cosamp: Iterative Signal Recovery from Incomplete and Inaccurate Samples," *Applied and computational harmonic analysis*, vol. 26, no. 3, pp. 301–321, 2009. DOI: 10.1016/j.acha.2008.07.002.

[52] S. Ji, Y. Xue, L. Carin, *et al.*, "Bayesian Compressive Sensing," *IEEE Transactions on signal processing*, vol. 56, no. 6, p. 2346, 2008. DOI: 10.1109/TSP.2007.914345.

[53] M. Grant and S. Boyd, *CVX: Matlab software for disciplined convex programming, version 2.1*, http://cvxr.com/cvx, Mar. 2014.

[54] H. Bauschke and P. Combettes, "Convex Analysis and Monotone Operator Theory in Hilbert Spaces, 2011," *CMS books in mathematics)*, vol. 10, pp. 978–1, DOI: https://doi.org/10.1007/978-1-4419-9467-7.

[55] N. G. Polson, J. G. Scott, and B. T. Willard, "Proximal Algorithms in Statistics and Machine Learning," *Statistical Science*, vol. 30, no. 4, pp. 559–581, 2015, ISSN: 08834237, 21688745. DOI: 10.1214/15-STS530. [Online]. Available: http://www.jstor.org/stable/24780820.

[56] N. Parikh and S. Boyd, "Proximal Algorithms," *Foundations and Trends® in Optimization*, vol. 1, no. 3, pp. 127–239, 2014, ISSN: 2167-3888. DOI: 10.1561/2400000003. [Online]. Available: http://dx.doi.org/10.1561/2400000003.

[57] P. L. Combettes and J.-C. Pesquet, "A Proximal Decomposition Method for Solving Convex Variational Inverse Problems," *Inverse Problems*, vol. 24, no. 6, p. 065 014, 2008. DOI: 10.1088/0266-5611/24/6/065014.

[58] P. L. Combettes and J.-C. Pesquet, "Proximal Splitting Methods in Signal Processing," *Fixed-Point Algorithms for Inverse Problems in Science and Engineering*, pp. 185–212, 2011. DOI: https://doi.org/10.1007/978-1-4419-9569-8_10.

[59] R. T. Rockafellar and R. J.-B. Wets, *Variational Analysis*. Springer Science & Business Media, 2009, vol. 317. DOI: 10.1007/978-3-642-02431-3.

[60] A. Chambolle, R. A. De Vore, N.-Y. Lee, and B. J. Lucier, "Nonlinear Wavelet Image Processing: Variational Problems, Compression, and Noise Removal Through Wavelet Shrinkage," *IEEE Transactions on image processing*, vol. 7, no. 3, pp. 319–335, 1998. DOI: 10.1109/83.661182.

[61] D. L. Donoho, A. Maleki, and A. Montanari, "Message-passing Algorithms for Compressed Sensing," *Proceedings of the National Academy of Sciences*, vol. 106, no. 45, pp. 18 914–18 919, 2009. DOI: 10.1073/pnas.0909892106.

[62] J. Nocedal and S. J. Wright, *Numerical Optimization*. Springer, 1999, ISBN: 978-0-387-98793-4. DOI: 10.1007/B98874. [Online]. Available: https://doi.org/10.1007/b98874.

[63] M. V. Afonso, J. M. Bioucas-Dias, and M. A. Figueiredo, "Fast Image Recovery Using Variable Splitting and Constrained Optimization," *IEEE transactions on image processing*, vol. 19, no. 9, pp. 2345–2356, 2010. DOI: 10.1109/TIP.2010.2047910.

[64] R. Courant, "Variational Methods for the Solution of Problems of Equilibrium and Vibrations," *Bulletin of the American Mathematical Society*, vol. 49, no. 1, pp. 1–23, 1943.

[65] Y. Wang, J. Yang, W. Yin, and Y. Zhang, "A New Alternating Minimization Algorithm for Total Variation Image Reconstruction," *SIAM Journal on Imaging Sciences*, vol. 1, no. 3, pp. 248–272, 2008. DOI: 10.1137/080724265.

[66] L. Xu, C. Lu, Y. Xu, and J. Jia, "Image Smoothing Via L 0 Gradient Minimization," in *Proceedings of the 2011 SIGGRAPH Asia Conference*, 2011, pp. 1–12. DOI: 10.1145/2070781.2024208.

[67] S. Boyd, N. Parikh, E. Chu, B. Peleato, J. Eckstein, *et al.*, "Distributed Optimization and Statistical Learning Via the Alternating Direction Method of Multipliers," *Foundations and Trends® in Machine learning*, vol. 3, no. 1, pp. 1–122, 2011. DOI: 10.1561/2200000016.

[68] M. R. Hestenes, "Multiplier and Gradient Methods," *Journal of optimization theory and applications*, vol. 4, no. 5, pp. 303–320, 1969. DOI: https://doi.org/10.1007/BF00927673.

[69] D. Gabay and B. Mercier, "A Dual Algorithm for the Solution of Nonlinear Variational Problems Via Finite Element Approximation," *Computers & mathematics with applications*, vol. 2, no. 1, pp. 17–40, 1976. DOI: https://doi.org/10.1016/0898-1221(76)90003-1.

[70] K. Gregor and Y. LeCun, "Learning Fast Approximations of Sparse Coding," in *Proceedings of the 27th International Conference on International Conference on Machine Learning*, Omnipress, 2010, pp. 399–406.

[71] M. Borgerding, P. Schniter, and S. Rangan, "Amp-inspired Deep Networks for Sparse Linear Inverse Problems," *IEEE Transactions on Signal Processing*, vol. 65, no. 16, pp. 4293–4308, 2017. DOI: 10.1109/TSP.2017.2708040.

[72] A. Mousavi, A. B. Patel, and R. G. Baraniuk, "A Deep Learning Approach to Structured Signal Recovery," in *2015 53rd Annual Allerton Conference on Communication, Control, and Computing (Allerton)*, IEEE, 2015, pp. 1336–1343. DOI: 10.1109/ALLERTON.2015.7447163.

[73] K. Kulkarni, S. Lohit, P. Turaga, R. Kerviche, and A. Ashok, "Reconnet: Non-iterative Reconstruction of Images from Compressively Sensed Measurements," in *Proceedings of the IEEE Conference on Computer Vision and Pattern Recognition*, 2016, pp. 449–458. DOI: 10.1109/CVPR.2016.55.

[74] J. Zhang and B. Ghanem, "Ista-net: Interpretable Optimization-inspired Deep Network for Image Compressive Sensing," in *Proceedings of the IEEE Conference on Computer Vision and Pattern Recognition*, 2018, pp. 1828–1837. DOI: 10.1109/CVPR.2018.00196.

[75] W. Shi, F. Jiang, S. Liu, and D. Zhao, "Image Compressed Sensing Using Convolutional Neural Network," *IEEE Transactions on Image Processing*, vol. 29, pp. 375–388, 2019. DOI: 10.1109/TIP.2019.2928136.

[76] W. Shi, F. Jiang, S. Liu, and D. Zhao, "Scalable Convolutional Neural Network for Image Compressed Sensing," in *Proceedings of the IEEE/CVF Conference on Computer Vision and Pattern Recognition*, 2019, pp. 12 290–12 299. DOI: 10.1109/CVPR.2019.01257.

[77] J. Wright, A. Y. Yang, A. Ganesh, S. S. Sastry, and Y. Ma, "Robust Face Recognition Via Sparse Representation," *IEEE transactions on pattern analysis and machine intelligence*, vol. 31, no. 2, pp. 210–227, 2008. DOI: DOI:10.1109/TPAMI.2008.79.

[78] J. Wright, Y. Ma, J. Mairal, G. Sapiro, T. S. Huang, and S. Yan, "Sparse Representation for Computer Vision and Pattern Recognition," *Proceedings of the IEEE*, vol. 98, no. 6, pp. 1031–1044, 2010. DOI: 10.1109/JPROC.2010.2044470.

[79] A. C. Gurbuz, J. H. McClellan, and W. R. Scott, "A Compressive Sensing Data Acquisition and Imaging Method for Stepped Frequency GPRs," *IEEE Transactions on Signal Processing*, vol. 57, no. 7, pp. 2640–2650, 2009. DOI: 10.1109/TSP.2009.2016270.

[80] E. J. Candès, Y. Plan, *et al.*, "Near-ideal Model Selection By ℓ_1 Minimization," *The Annals of Statistics*, vol. 37, no. 5A, pp. 2145–2177, 2009. DOI: DOI: 10.1214/08-AOS653.

[81] Y. E. Yamac and A. Kizilay, "Efie Analyses of 3-d Scattering from an Object Above Arbitrarily Rough Periodic Surfaces By Current Decomposition Method," *Journal of Electromagnetic Waves and Applications*, vol. 36, no. 13, pp. 1882–1898, 2022. DOI: doi.org/10.1080/09205071.2022.2046507.

[82] L. Zhang, M. Yang, and X. Feng, "Sparse Representation or Collaborative Representation: Which Helps Face Recognition?" In *2011 International Conference on Computer Vision*, IEEE, 2011, pp. 471–478. DOI: 10.1109/ICCV.2011.6126277.

[83] T. Guha and R. K. Ward, "Learning Sparse Representations for Human Action Recognition," *IEEE Transactions on Pattern Analysis and Machine Intelligence*, vol. 34, no. 8, pp. 1576–1588, 2011. DOI: 10.1109/TPAMI.2011.253.

[84] W. Li and Q. Du, "A Survey on Representation-based Classification and Detection in Hyperspectral Remote Sensing Imagery," *Pattern Recognition Letters*, vol. 83, pp. 115–123, 2016. DOI: https://doi.org/10.1016/j.patrec.2015.09.010.

[85] A. S. Georghiades, P. N. Belhumeur, and D. J. Kriegman, "From Few to Many: Illumination Cone Models for Face Recognition Under Variable Lighting and Pose," *IEEE Transactions on Pattern Analysis & Machine Intelligence*, no. 6, pp. 643–660, 2001. DOI: 10.1109/34.927464.

[86] Z. Liu, P. Luo, X. Wang, and X. Tang, "Deep Learning Face Attributes in the Wild," in *Proceedings of International Conference on Computer Vision (ICCV)*, Dec. 2015. DOI: 10.1109/ICCV.2015.425.

[87] A. Y. Yang, Z. Zhou, A. G. Balasubramanian, S. S. Sastry, and Y. Ma, "Fast ℓ_1-Minimization Algorithms for Robust Face Recognition," *IEEE Transactions on Image Processing*, vol. 22, no. 8, pp. 3234–3246, 2013. DOI: 10.1109/TIP.2013.2262292.

[88] D. M. Malioutov, M. Cetin, and A. S. Willsky, "Homotopy Continuation for Sparse Signal Representation," in *Proceedings.(ICASSP'05). IEEE International Conference on Acoustics, Speech, and Signal Processing, 2005.*, IEEE, vol. 5, 2005, pp. v–733. DOI: 10.1109/ICASSP.2005.1416408.

[89] M. A. Figueiredo, R. D. Nowak, and S. J. Wright, "Gradient Projection for Sparse Reconstruction: Application to Compressed Sensing and Other Inverse Problems," *IEEE Journal of selected topics in signal processing*, vol. 1, no. 4, pp. 586–597, 2007. DOI: 10.1109/JSTSP.2007.910281.

[90] K. Koh, S.-J. Kim, and S. Boyd, "An Interior-point Method for Large-scale L1-regularized Logistic Regression," *Journal of Machine learning research*, vol. 8, no. Jul, pp. 1519–1555, 2007.

[91] E. Candes and J. Romberg, "L1-magic: Recovery of Sparse Signals Via Convex Programming," *URL: www. acm. caltech. edu/l1magic/downloads/l1magic. pdf*, vol. 4, p. 14, 2005.

[92] D. E. King, "DLIB-ML: A Machine Learning Toolkit," *Journal of Machine Learning Research*, vol. 10, no. Jul, pp. 1755–1758, 2009.

[93] N. Vaswani and W. Lu, "Modified-cs: Modifying Compressive Sensing for Problems with Partially Known Support," *IEEE Transactions on Signal Processing*, vol. 58, no. 9, pp. 4595–4607, 2010. DOI: 10.1109/TSP.2010.2051150.

[94] O. D. Escoda, L. Granai, and P. Vandergheynst, "On the Use of a Priori Information for Sparse Signal Approximations," *IEEE transactions on signal processing*, vol. 54, no. 9, pp. 3468–3482, 2006.

[95] D. Donoho and J. Tanner, "Observed Universality of Phase Transitions in High-dimensional Geometry, with Implications for Modern Data Analysis and Signal Processing," *Philosophical Transactions of the Royal Society A: Mathematical, Physical and Engineering Sciences*, vol. 367, no. 1906, pp. 4273–4293, 2009. DOI: 10.1098/rsta.2009.0152.

[96] D. A. Noon, "Stepped-frequency Radar Design and Signal Processing Enhances Ground Penetrating Radar Performance," PhD Thesis, School of Computer Science and Electrical Engineering, The University of Queensland, 1996. DOI: https://doi.org/10.14264/uql.2016.1170.

[97] A. B. Suksmono, E. Bharata, A. A. Lestari, A. G. Yarovoy, and L. P. Ligthart, "Compressive Stepped-frequency Continuous-wave Ground-penetrating Radar," *IEEE geoscience and remote sensing letters*, vol. 7, no. 4, pp. 665–669, 2010. DOI: 10.1109/LGRS.2010.2045340.

[98] Y.-S. Yoon and M. G. Amin, "Imaging of Behind the Wall Targets Using Wideband Beamforming with Compressive Sensing," in *2009 IEEE/SP 15th Workshop on Statistical Signal Processing*, IEEE, 2009, pp. 93–96. DOI: 10.1109/SSP.2009.5278632.

[99] J. Yang, J. Thompson, X. Huang, T. Jin, and Z. Zhou, "Random-frequency Sar Imaging Based on Compressed Sensing," *IEEE transactions on geoscience and remote sensing*, vol. 51, no. 2, pp. 983–994, 2012. DOI: 10.1109/TGRS.2012.2204891.

[100] J. Betker, G. Goh, L. Jing, *et al.*, "Improving Image Generation with Better Captions," *openai*, 2023. [Online]. Available: https://cdn.openai.com/papers/dall-e-3.pdf.

[101] M. Elad, "Optimized Projections for Compressed Sensing," *IEEE Transactions on Signal Processing*, vol. 55, no. 12, pp. 5695–5702, 2007. DOI: 10.1109/TSP.2007.900760.

[102] T. T. Do, L. Gan, N. H. Nguyen, and T. D. Tran, "Fast and Efficient Compressive Sensing Using Structurally Random Matrices," *IEEE Transactions on Signal processing*, vol. 60, no. 1, pp. 139–154, 2011. DOI: 10.1109/TSP.2011.2170977.

[103] M. Impiö, M. Yamaç, and J. Raitoharju, "Multi-level Reversible Encryption for Ecg Signals Using Compressive Sensing," in *ICASSP 2021-2021 IEEE International Conference on Acoustics, Speech and Signal Processing (ICASSP)*, IEEE, 2021, pp. 1005–1009. DOI: 10.1109/ICASSP39728.2021.9414983.

[104] L. Y. Zhang, K.-W. Wong, Y. Zhang, and J. Zhou, "Bi-level Protected Compressive Sampling," *IEEE Transactions on Multimedia*, vol. 18, no. 9, pp. 1720–1732, 2016. DOI: 10.1109/TMM.2016.2581593.

[105] Y. Zhang, Y. Tian, Y. Kong, B. Zhong, and Y. Fu, "Residual Dense Network for Image Super-resolution," in *Proceedings of the IEEE Conference on Computer Vision and Pattern Recognition*, pp. 2472–2481. DOI: 10.1109/CVPR.2018.00262.

[106] J. Chen, Y. Sun, Q. Liu, and R. Huang, "Learning Memory Augmented Cascading Network for Compressed Sensing of Images.," in *ECCV (22)*, 2020, pp. 513–529. DOI: 10.1007/978-3-030-58542-6_31.

[107] Y. Sun, J. Chen, Q. Liu, B. Liu, and Q. Guo, "Dual-path Attention Network for Compressed Sensing Image Reconstruction," *IEEE Transactions on Image Processing*, vol. 29, pp. 9482–9495, 2020. DOI: 10.1109/TIP.2020.3023629.

[108] J. Zhang, C. Zhao, and W. Gao, "Optimization-inspired Compact Deep Compressive Sensing," *IEEE Journal of Selected Topics in Signal Processing*, vol. 14, no. 4, pp. 765–774, 2020. DOI: 10.1109/JSTSP.2020.2977507.

[109] Z. Zhang, Y. Liu, J. Liu, F. Wen, and C. Zhu, "Amp-net: Denoising-based Deep Unfolding for Compressive Image Sensing," *IEEE Transactions on Image Processing*, vol. 30, pp. 1487–1500, 2020. DOI: 10.1109/TIP.2020.3044472.

[110] D. You, J. Zhang, J. Xie, B. Chen, and S. Ma, "Coast: Controllable Arbitrary-sampling Network for Compressive Sensing," *IEEE Transactions on Image Processing*, vol. 30, pp. 6066–6080, 2021. DOI: 10.1109/TIP.2021.3091834.

[111] M. Bevilacqua, A. Roumy, C. Guillemot, and M. Alberi-Morel, "Low-Complexity Single-Image Super-Resolution based on Nonnegative Neighbor Embedding," in *British Machine Vision Conference, BMVC 2012, Surrey, UK, September 3-7, 2012*, R. Bowden, J. P. Collomosse, and K. Mikolajczyk, Eds., BMVA Press, 2012, pp. 1–10. DOI: 10.5244/C.26.135. [Online]. Available: https://doi.org/10.5244/C.26.135.

[112] A. Fujimoto, T. Ogawa, K. Yamamoto, Y. Matsui, T. Yamasaki, and K. Aizawa, "Manga109 Dataset and Creation of Metadata," in *Proceedings of the 1st International Workshop on Comics Analysis, Processing and Understanding*, 2016, pp. 1–5. DOI: 10.1145/3011549.3011551.

[113] J.-B. Huang, A. Singh, and N. Ahuja, "Single Image Super-resolution from Transformed Self-exemplars," in *Proceedings of the IEEE Conference on Computer Vision and Pattern Recognition*, 2015, pp. 5197–5206. DOI: 10.1109/CVPR.2015.7299156.

[114] H. Hotelling, "Analysis of a Complex of Statistical Variables Into Principal Components," *Journal of Educational Psychology*, vol. 24, no. 6, p. 417, 1933. DOI: 10.1037/h0071325.

[115] R. G. Baraniuk, "More Is Less: Signal Processing and the Data Deluge," *Science*, vol. 331, no. 6018, pp. 717–719, 2011. DOI: 10.1126/science.1197448.

[116] J. Treichler, M. Davenport, and R. Baraniuk, "Application of Compressive Sensing to the Design of Wideband Signal Acquisition Receivers," *US/Australia Joint Work. Defense Apps. of Signal Processing (DASP), Lihue, Hawaii*, vol. 5, 2009.

[117] S. Dirksen, "Quantized Compressed Sensing: A Survey," in *Compressed Sensing and Its Applications: Third International MATHEON Conference 2017*, Springer, 2019, pp. 67–95.

[118] R. Saab, R. Wang, and Ö. Yılmaz, "Quantization of Compressive Samples with Stable and Robust Recovery," *Applied and Computational Harmonic Analysis*, vol. 44, no. 1, pp. 123–143, 2018. DOI: 10.1016/j.acha.2016.04.005.

[119] M. Yamac, Ç. Dikici, and B. Sankur, "Hiding Data in Compressive Sensed Measurements: A Conditionally Reversible Data Hiding Scheme for Compressively Sensed Measurements," *Digital Signal Processing*, vol. 48, pp. 188–200, 2016. DOI: https://doi.org/10.1016/j.dsp.2015.09.017.

[120] M. R. Palattella, M. Dohler, A. Grieco, G. Rizzo, J. Torsner, T. Engel, and L. Ladid, "Internet of Things in the 5g Era: Enablers, Architecture, and Business Models," *IEEE Journal on Selected Areas in Communications*, vol. 34, no. 3, pp. 510–527, 2016. DOI: 10.1109/JSAC.2016.2525418.

[121] T. A. Nguyen and M. Aiello, "Energy Intelligent Buildings Based on User Activity: A Survey," *Energy and Buildings*, vol. 56, pp. 244–257, 2013. DOI: 10.1016/j.enbuild.2012.09.005.

[122] S. R. Islam, D. Kwak, M. H. Kabir, M. Hossain, and K.-S. Kwak, "The Internet of Things for Health Care: A Comprehensive Survey," *IEEE Access*, vol. 3, pp. 678–708, 2015. DOI: 10.1109/ACCESS.2015.2437951.

[123] P. Voigt and A. Von dem Bussche, "The EU General Data Protection Regulation (GDPR)," *A Practical Guide, 1st Ed., Cham: Springer International Publishing*, 2017. DOI: 10.1007/978-3-319-57959-7.

[124] I. Wagner and D. Eckhoff, "Technical Privacy Metrics: A Systematic Survey," *ACM Computing Surveys (CSUR)*, vol. 51, no. 3, p. 57, 2018. DOI: 10.1145/3168389.

[125] S. Heron, "Advanced Encryption Standard (AES)," *Network Security*, vol. 2009, no. 12, pp. 8–12, 2009, ISSN: 1353-4858. DOI: https://doi.org/10.1016/S1353-4858(10)70006-4. [Online]. Available: http://www.sciencedirect.com/science/article/pii/S1353485810700064.

[126] R. L. Rivest, A. Shamir, and L. Adleman, "A Method for Obtaining Digital Signatures and Public-Key Cryptosystems," *Communications of the ACM*, vol. 21, no. 2, pp. 120–126, 1978.

[127] F. Nilsson *et al.*, *Intelligent Network Video: Understanding Modern Video Surveillance Systems*. CRC Press, 2016. DOI: 10.1201/9781420061574.

[128] H. Mamaghanian, N. Khaled, D. Atienza, and P. Vandergheynst, "Compressed Sensing for Real-Time Energy-Efficient ECG Compression on Wireless Body Sensor Nodes," *IEEE Transactions on Biomedical Engineering*, vol. 58, no. 9, pp. 2456–2466, 2011. DOI: 10.1109/TBME.2011.2156795.

[129] M. Yamaç, Ç. Dikici, and B. Sankur, "Robust Watermarking of Compressive Sensed Measurements Under Impulsive and Gaussian Attacks," in *Proceedings of the European Signal Processing Conference*, 2013, pp. 1–5. DOI: 10.5281/zenodo.43699.

[130] C. E. Shannon, "Communication Theory of Secrecy Systems," *Bell System Technical Journal*, vol. 28, no. 4, pp. 656–715, 1949. DOI: 10.1002/j.1538-7305.1949.tb00928.x.

[131] Y. Zhang, Y. Xiang, L. Y. Zhang, Y. Rong, and S. Guo, "Secure Wireless Communications Based on Compressive Sensing: A Survey," *IEEE Communications Surveys Tutorials*, vol. 21, no. 2, pp. 1093–1111, 2019. DOI: 10.1109/COMST.2018.2878943.

[132] V. Cambareri, M. Mangia, F. Pareschi, R. Rovatti, and G. Setti, "Low-Complexity Multiclass Encryption By Compressed Sensing," *IEEE Transactions on Signal Processing*, vol. 63, no. 9, pp. 2183–2195, 2015. DOI: 10.1109/TSP.2015.2407315.

[133] M. J. Wainwright, *High-Dimensional Statistics: A Non-Asymptotic Viewpoint*. Cambridge University Press, 2019, vol. 48. DOI: 10.1090/bull/1692.

[134] L. Wolf, T. Hassner, and I. Maoz, "Face Recognition in Unconstrained Videos with Matched Background Similarity," in *CVPR 2011*, 2011, pp. 529–534. DOI: 10.1109/CVPR.2011.5995566.

[135] D. Donoho, A. Maleki, and M. Shahram, "Wavelab 850," *Software toolkit for time-frequency analysis*, 2006.

[136] R. Calderbank, S. Jafarpour, and R. Schapire, "Compressed Learning: Universal Sparse Dimensionality Reduction and Learning in the Measurement Domain," *preprint*, 2009.

[137] A. Kabán, "New Bounds on Compressive Linear Least Squares Regression," in *Artificial Intelligence and Statistics*, 2014, pp. 448–456.

[138] R. J. Durrant and A. Kabán, "Compressed Fisher Linear Discriminant Analysis: Classification of Randomly Projected Data," in *Proceedings of the 16th ACM SIGKDD International Conference on Knowledge Discovery and Data Mining*, ACM, 2010, pp. 1119–1128. DOI: 10.1145/1835804.1835945.

[139] M. A. Davenport, M. F. Duarte, M. B. Wakin, J. N. Laska, D. Takhar, K. F. Kelly, and R. G. Baraniuk, "The Smashed Filter for Compressive Classification and Target Recognition," in *Computational Imaging V*, International Society for Optics and Photonics, vol. 6498, 2007, 64980H. DOI: 10.1117/12.714460.

[140] K. Kulkarni and P. Turaga, "Reconstruction-free Action Inference from Compressive Imagers," *IEEE transactions on pattern analysis and machine intelligence*, vol. 38, no. 4, pp. 772–784, 2016. DOI: 10.1109/TPAMI.2015.2469288.

[141] S. Lohit, K. Kulkarni, P. Turaga, J. Wang, and A. C. Sankaranarayanan, "Reconstruction-free Inference on Compressive Measurements," in *Proceedings of the IEEE Conference on Computer Vision and Pattern Recognition Workshops*, 2015, pp. 16–24. DOI: 10.1109/CVPRW.2015.7301371.

[142] S. Lohit, K. Kulkarni, and P. Turaga, "Direct Inference on Compressive Measurements Using Convolutional Neural Networks," in *Image Processing (ICIP), 2016 IEEE International Conference On*, IEEE, 2016, pp. 1913–1917. DOI: 10.1109/ICIP.2016.7532691.

[143] A. Adler, M. Elad, and M. Zibulevsky, "Compressed Learning: A Deep Neural Network Approach," *arXiv preprint arXiv:1610.09615*, 2016. DOI: 10.48550/arXiv.1610.09615.

[144] S. Aslan, M. Yamaç, and B. Sankur, "A Dct-based Multiscale Binary Descriptor Robust to Complex Brightness Changes," in *2016 24th European Signal Processing Conference (EUSIPCO)*, 2016, pp. 1573–1577. DOI: 10.1109/EUSIPCO.2016.7760513.

[145] A. Krizhevsky, "Learning Multiple Layers of Features from Tiny Images," pp. 32–33, 2009. [Online]. Available: https://www.cs.toronto.edu/~kriz/learning-features-2009-TR.pdf.

[146] L. De Lathauwer, B. De Moor, and J. Vandewalle, "A Multilinear Singular Value Decomposition," *SIAM journal on Matrix Analysis and Applications*, vol. 21, no. 4, pp. 1253–1278, 2000. DOI: 10.1137/S0895479896305696.

[147] J. T. Springenberg, A. Dosovitskiy, T. Brox, and M. A. Riedmiller, "Striving for Simplicity: The All Convolutional Net," in *3rd International Conference on Learning Representations, ICLR 2015, San Diego, CA, USA, May 7-9, 2015, Workshop Track Proceedings*, Y. Bengio and Y. LeCun, Eds., 2015. [Online]. Available: http://arxiv.org/abs/1412.6806.

[148] M. Yamac, B. Ataman, and A. Nawaz, "Kernelnet: A Blind Super-resolution Kernel Estimation Network," in *Proceedings of the IEEE/CVF Conference on Computer Vision and Pattern Recognition*, 2021, pp. 453–462. DOI: 10.1109/CVPRW53098.2021.00056.

[149] R. Hoekema, G. J. Uijen, and A. Van Oosterom, "Geometrical Aspects of the Interindividual Variability of Multilead Ecg Recordings," *IEEE Transactions on Biomedical Engineering*, vol. 48, no. 5, pp. 551–559, 2001. DOI: 10.1109/10.918594.

[150] S. Shekhar, V. M. Patel, H. V. Nguyen, and R. Chellappa, "Generalized Domain-adaptive Dictionaries," in *Proceedings of the IEEE Conference on Computer Vision and Pattern Recognition*, 2013, pp. 361–368. DOI: 10.1109/CVPR.2013.53.

[151] H. Xu, J. Zheng, and R. Chellappa, "Bridging the Domain Shift By Domain Adaptive Dictionary Learning.," in *BMVC*, 2015, pp. 96–1. DOI: 10.5244/C.29.96.

[152] K. Kumar, A. Majumdar, A. A. Kumar, and M. G. Chandra, "Transform Based Subspace Interpolation for Unsupervised Domain Adaptation Applied to Machine Inspection," in *2023 31st European Signal Processing Conference (EUSIPCO)*, IEEE, 2023, pp. 1708–1712. DOI: 10.23919/EUSIPCO58844.2023.10289755.

[153] J. Yang, Z. Wang, Z. Lin, S. Cohen, and T. Huang, "Coupled Dictionary Training for Image Super-resolution," *IEEE transactions on image processing*, vol. 21, no. 8, pp. 3467–3478, 2012. DOI: 10.1109/TIP.2012.2192127.

[154] D. Carrera, B. Rossi, D. Zambon, P. Fragneto, and G. Boracchi, "Ecg Monitoring in Wearable Devices By Sparse Models," in *Joint European Conference on Machine Learning and Knowledge Discovery in Databases*, Springer, 2016, pp. 145–160. DOI: https://doi.org/10.1007/978-3-319-46131-1_21.

[155] S. Kiranyaz, T. Ince, and M. Gabbouj, "Personalized Monitoring and Advance Warning System for Cardiac Arrhythmias," *Scientific Reports*, vol. 7, no. 1, p. 9270, 2017. DOI: https://doi.org/10.1038/s41598-017-09544-z.

[156] G. B. Moody and R. G. Mark, "The Impact of the Mit-bih Arrhythmia Database," *IEEE Engineering in Medicine and Biology Magazine*, vol. 20, no. 3, pp. 45–50, 2001. DOI: 10.1109/51.932724.

[157] A. L. Goldberger, L. A. Amaral, L. Glass, J. M. Hausdorff, P. C. Ivanov, R. G. Mark, J. E. Mietus, G. B. Moody, C.-K. Peng, and H. E. Stanley, "Physiobank, Physiotoolkit, and Physionet: Components of a New Research Resource for Complex Physiologic Signals," *Circulation*, vol. 101, no. 23, e215–e220, 2000. DOI: 10.1161/01.cir.101.23.e215.

[158] A. for the Advancement of Medical Instrumentation, "Recommended Practice for Testing and Reporting Performance Results of Ventricular Arrhythmia Detection Algorithms.," *Arlington, VA*, 1987.

[159] S. Kiranyaz, T. Ince, and M. Gabbouj, "Real-time Patient-specific Ecg Classification By 1-d Convolutional Neural Networks," *IEEE Transactions on Biomedical Engineering*, vol. 63, no. 3, pp. 664–675, 2016. DOI: 10.1109/TBME.2015.2468589.

[160] X. Zhai and C. Tin, "Automated Ecg Classification Using Dual Heartbeat Coupling Based on Convolutional Neural Network," *IEEE Access*, vol. 6, pp. 27 465–27 472, 2018. DOI: 10.1109/ACCESS.2018.2833841.

[161] F. Li, Y. Xu, Z. Chen, and Z. Liu, "Automated Heartbeat Classification Using 3-d Inputs Based on Convolutional Neural Network with Multi-fields of View," *IEEE Access*, vol. 7, pp. 76 295–76 304, 2019. DOI: 10.1109/ACCESS.2019.2921991.

[162] Z. Zhou, X. Zhai, and C. Tin, "Fully Automatic Electrocardiogram Classification System Based on Generative Adversarial Network with Auxiliary Classifier," *Expert Systems with Applications*, vol. 174, p. 114 809, 2021. DOI: 10.1016/j.eswa.2021.114809.

[163] A. M. Shaker, M. Tantawi, H. A. Shedeed, and M. F. Tolba, "Generalization of Convolutional Neural Networks for Ecg Classification Using Generative Adversarial Networks," *IEEE Access*, vol. 8, pp. 35 592–35 605, 2020. DOI: 10.1109/ACCESS.2020.2974712.

[164] Y. C. Eldar and G. Kutyniok, *Compressed Sensing: Theory and Applications*. Cambridge University Press, 2012. DOI: 10.1017/CBO9780511794308.

[165] Y. Rivenson and A. Stern, "Compressed Imaging with a Separable Sensing Operator," *IEEE Signal Processing Letters*, vol. 16, no. 6, pp. 449–452, 2009. DOI: 10.1109/LSP.2009.2017817.

[166] M. Lustig, D. L. Donoho, J. M. Santos, and J. M. Pauly, "Compressed Sensing Mri," *IEEE signal processing magazine*, vol. 25, no. 2, pp. 72–82, 2008. DOI: 10.1186/s42490-019-0006-z.

[167] B. Adcock, A. C. Hansen, C. Poon, and B. Roman, "Breaking the Coherence Barrier: A New Theory for Compressed Sensing," in *Forum of Mathematics, Sigma*, Cambridge University Press, vol. 5, 2017. DOI: 10.1017/fms.2016.32.

[168] J. C. Ye, "Compressed Sensing Mri: A Review from Signal Processing Perspective," *BMC Biomedical Engineering*, vol. 1, no. 1, pp. 1–17, 2019. DOI: 10.1186/s42490-019-0006-z.

[169] M. Ahishali, M. Yamac, S. Kiranyaz, and M. Gabbouj, "Operational Support Estimator Networks," *arXiv preprint arXiv:2307.06065*, 2023. DOI: 10.48550/arXiv.2307.06065.

[170] M. Ahishali, M. Yamac, S. Kiranyaz, and M. Gabbouj, "Representation Based Regression for Object Distance Estimation," *Neural Networks*, vol. 158, pp. 15–29, 2023. DOI: 10.1016/j.neunet.2022.11.011.

PUBLICATIONS

PUBLICATION
I

Convolutional Sparse Support Estimator Network (CSEN): From Energy-Efficient Support Estimation to Learning-Aided Compressive Sensing

M. Yamaç, M. Ahishali, S. Kiranyaz, and M. Gabbouj

IEEE Transactions on Neural Networks and Learning Systems, vol. 34, no. 1, pp. 290–304
DOI: 10.1109/TNNLS.2021.3093818

Convolutional Sparse Support Estimator Network (CSEN): From Energy-Efficient Support Estimation to Learning-Aided Compressive Sensing

Mehmet Yamaç, Mete Ahishali, Serkan Kiranyaz, *Senior Member, IEEE*, and Moncef Gabbouj, *Fellow, IEEE*

***Abstract*— Support estimation (SE) of a sparse signal refers to finding the location indices of the nonzero elements in a sparse representation. Most of the traditional approaches dealing with SE problems are iterative algorithms based on greedy methods or optimization techniques. Indeed, a vast majority of them use sparse signal recovery (SR) techniques to obtain support sets instead of directly mapping the nonzero locations from denser measurements (e.g., compressively sensed measurements). This study proposes a novel approach for learning such a mapping from a training set. To accomplish this objective, the convolutional sparse support estimator networks (CSENs), each with a compact configuration, are designed. The proposed CSEN can be a crucial tool for the following scenarios: 1) real-time and low-cost SE can be applied in any mobile and low-power edge device for anomaly localization, simultaneous face recognition, and so on and 2) CSEN's output can directly be used as "prior information," which improves the performance of sparse SR algorithms. The results over the benchmark datasets show that state-of-the-art performance levels can be achieved by the proposed approach with a significantly reduced computational complexity.**

***Index Terms*— Learned compressive sensing (CS), sparse signal representation, support recovery.**

I. Introduction

SPARSE representation or sparse coding (SC) denotes representing a signal as a linear combination of only a small subset of a predefined set of waveforms. Compressive sensing (CS) [1], [2] can be seen as a special form of SC, while a signal, $\mathbf{s} \in \mathbb{R}^d$ that has a sparse representation, $\mathbf{x} \in \mathbb{R}^n$ in a dictionary or basis $\mathbf{\Phi} \in \mathbb{R}^{d \times n}$, can be acquired in a compressed manner using a linear dimensional reductional matrix, $\mathbf{A} \in \mathbb{R}^{m \times d}$. Therefore, this signal can also be represented in a sparse manner in the dictionary, $\mathbf{D} \in \mathbb{R}^{m \times n}$ (which can be called equivalent dictionary [3], where $m \ll n$, and typically assumed to be full-row rank), which is the matrix multiplication of the measurement matrix, $\mathbf{A}$, and predefined dictionary, $\mathbf{\Phi}$, i.e., $\mathbf{D} = \mathbf{A}\mathbf{\Phi}$. In the SC literature, *signal synthesis* refers to producing a signal, $\mathbf{y} = \mathbf{D}\mathbf{x} \in \mathbb{R}^m$, using a sparse code, $\mathbf{x} \in \mathbb{R}^n$ and a prespecified dictionary, $\mathbf{D}$. On the other hand, the *signal analysis* deals with finding the sparse codes, $\mathbf{x}$ from the given measurements, $\mathbf{y}$, with respect to the dictionary $\mathbf{D}$ [4]. Sparse support estimation (SE) [5]–[7] refers to finding the location indices of nonzero elements in SCs. In other words, it is the localization of the smallest subset of the atoms, which are the basis waveforms in the dictionary, whose linear combination represents the given signal well enough. On the other hand, *sparse signal recovery* (SR) refers to finding the values of these nonzero elements of SCs. SE and SR are intimately linked in such a way that the SE of a sparse signal is first performed; then, an SR will be trivial using the ordinary least-squares optimization. In fact, this is the main principle of most greedy algorithms [8], [9]

The literature that purely targets SE is relatively short compared to extensive studies on sparse SR [10]. Many existing works, first, apply a coarse SR using existing SR methods, and then, SE can be easily performed if SE is the main objective. Indeed, there are many applications where computing the support set is more important than computing the magnitudes of SCs. For instance, in an SR-based classification (SRC) [11], such as face recognition [12], the training samples are stacked in the dictionary in such a way that a subset of the columns consists of the samples of a specific class. As another example, in cognitive radio systems, only a small ratio of all spectrum is occupied for a given time interval. Therefore, finding the occupied spectrum (i.e., the support set) is the primary concern [13], [14]. Similarly, in a ground-penetrating radar imaging system, finding the location of the target is more important than predicting the actual signal magnitudes [15].

In this study, a novel convolutional sparse support estimator networks (CSENs) is proposed with two primary objectives, as shown in Fig. 1. First, this approach enables learning-based noniterative SE with minimal computational complexity. To accomplish this, we use two compact convolutional neural

Manuscript received 2 April 2020; revised 23 October 2020 and 16 April 2021; accepted 25 June 2021. Date of publication 14 July 2021; date of current version 5 January 2023. This work was supported in part by the NSF CVDI Program under Project AMALIA funded by the Business Finland and Mad@Work and Stroke-Data projects funded by Haltian and Business Finland. *(Corresponding author: Mehmet Yamaç.)*

Mehmet Yamaç, Mete Ahishali, and Moncef Gabbouj are with the Faculty of Information Technology and Communication Sciences, Tampere University, 33720 Tampere, Finland (e-mail: mehmet.yamac@tuni.fi).

Serkan Kiranyaz is with the Department of Electrical Engineering, Qatar University, Doha, Qatar.

This article has supplementary material provided by the authors and color versions of one or more figures available at https://doi.org/10.1109/TNNLS.2021.3093818.

Digital Object Identifier 10.1109/TNNLS.2021.3093818

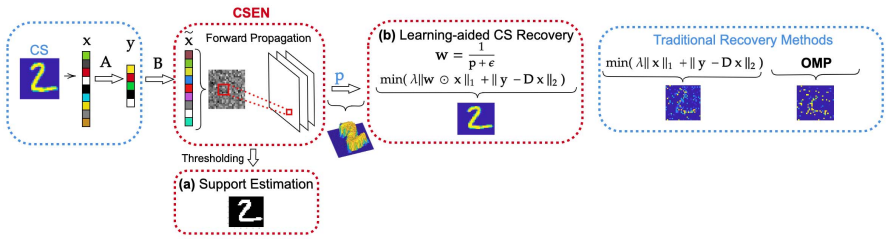

Fig. 1. Proposed CSEN with two potential applications. (a) (bottom-left) sparse SE. (b) (top-middle) Learned-aided CS-sparse signal reconstruction with CSEN versus (top-right) traditional recovery methods. 1) OMP [8] and 2) ℓ_1-minimization.

network (CNN) configurations, both of which are designed without the dense layers [16]. The proposed CSENs are trained to optimize the SEs. To the best of our knowledge, this is the first study that proposes a learning-based approach for noniterative SE. Hence, in order to perform comparative evaluations, we train the following state-of-the-art CS signal reconstruction deep neural networks as the support estimators: 1) ReconNet [17] that originally works on the spatial domain; 2) the learned AMP (LAMP) [18] that is the deep version of AMP [19], which is the state-of-the-art optimization scheme working on the sparse domain; and 3) learned ISTA (LISTA) [20] is the deep learning version of well-known SR algorithm, iterative soft-thresholding algorithm (ISTA) [21], which is the first attempt to unfold an optimization-based SR algorithm in a neural network manner. An extensive set of experiments over four benchmark datasets has demonstrated that the proposed CSEN approach outperforms deep counterparts, especially dealing with a structural sparse signal. In the first experimental setup, we simulate a CS system making data acquisition from the MNIST dataset in different measurement rates (MRs). Moreover, the proposed SE system is shown to improve the SE performance compared to its deep counterparts, especially in low MRs and imperfect sparsity (in the case of CS of approximate sparse signal or noisy environment). Furthermore, CSEN is tested on a well-known support recovery problem, where face recognition is performed based on sparse codes [11]. We use two benchmark datasets, Yale-B [22] and CelebA [23], in our experiments. Comparative evaluations performed against the two state-of-the-art dictionary-based (representation-based) face recognition methods in the literature, SR-based face recognition [11], and collaborative learning [24] have demonstrated that the proposed CSEN approach outperformed both methods. Furthermore, we develop a CSEN-based Coronavirus disease (COVID-19) recognition system from X-Ray images [25]. In this problem, CSEN shows its superiority over other representation-based classifiers and traditional approaches on classification tasks when the training size is small/moderate.

As for the second objective, we focus on an alternative usage of CSENs. Instead of using them as support estimators, which naturally requires the hard-thresholding of the network outputs, these outputs can be directly used as prior information about the sparse signals. It is a well-known fact that having prior information about the nonzero locations, such as the probability map, $p(x)$ (or simply $\mathbf{p}$), on the support set, could improve the conventional SR algorithms [26]. However, in many cases, it is not clear how to obtain such prior information in advance. The most common usage of such a system appears in dynamical sparse recovery [27], where previous SEs can be used as priors for the next estimation. In this study, we have demonstrated that CSEN outputs can be a better alternative for the prior information of the nonzero locations. Therefore, CSEN is now used as a *learning-aided CS reconstruction* scheme, where the prior information comes directly from the CSEN outputs. A wide range of experiments shows that this approach has great potential to improve the SR performance of traditional approaches for sparse SR problems. As mentioned above, we used CS imaging simulation, but this time signal reconstruction error is compared with state-of-the-art conventional SR approaches. Fig. 1 illustrates a representative graph of two different applications of CSENs: 1) performing SE from CS measurement vector, $\mathbf{y}$ and 2) the output of CSEN is used as the side information, $\mathbf{p}$, which gives the estimated probability of being nonzero for each index. In this simple illustration, we assume that the hand-writing signal "2" is sparse in the spatial domain such that $\mathbf{\Phi} = \mathbf{I}$; therefore, $\mathbf{D} = \mathbf{AI} = \mathbf{A}$, and $\mathbf{B}$ is a denoiser matrix such as $\mathbf{D}^T$, or $(\mathbf{D}^T\mathbf{D} + \lambda\mathbf{I})^{-1}\mathbf{D}^T$, where λ is the regularization parameter. Moreover, we also show the possibility of using the learning-aided CS reconstruction scheme when the signal is not sparse in the spatial domain but in a proper domain. In this respect, the sparsity of natural images in the gradient domain is used to have a CSEN-aided total variation minimization system.

The rest of this article is organized as follows. In Section II, we start by giving mathematical notation that is used in this article. A brief overview of sparse representation and CS theory, with an emphasis on state-of-the-art sparse SR and SE techniques, will be given in Section III. In the same section, we also introduce case studies of SE that are chosen for this work. Then, we discuss the limitations of existing support estimator techniques. In Section IV, we will present the proposed learned-based SE scheme and the two compact CSEN models. Experimental evaluations of the study will also be given at the end of this section, which we can divide into five main categories according to the case studies: 1) basic SE performance evaluation on the MNIST dataset that is performed to compare CSENs with the aforementioned state-of-art deep networks; 2) SE-based face recognition performance evolution

of proposed SE with an emphasis on how CSEN-based SE has the ability to improve the classical representation-based approaches; 3) a CSEN-based COVID-19 recognition system; 4) performance comparison of classical compressing sensing reconstruction techniques and proposed learned-aided SR in terms of both speed and reconstruction accuracy in the MNIST dataset; and 5) CSEN-aided total variation system for recovery of compressively sensed natural images. Having theoretical and experimental analysis, in Section VI, we will present a more detailed discussion on how the proposed scheme differs from the state-of-the-art SR and SE techniques, pros and cons, and possible usage scenarios with an emphasis on the flexibility of proposed CSEN in different scenarios. Finally, the conclusions are drawn in Section VII.

II. Notations

In this work, we define the ℓ_p-norm of any vector $\mathbf{x} \in \mathbb{R}^n$ as $\|\mathbf{x}\|_{\ell_p^n} = (\sum_{i=1}^n |x_i|^p)^{1/p}$ for $p \geq 1$. The ℓ_0-norm of the vector $\mathbf{x} \in \mathbb{R}^n$ is given as $\|\mathbf{x}\|_{\ell_0^n} = \lim_{p\to 0} \sum_{i=1}^n |x_i|^p = \#\{j : x_j \neq 0\}$, and the ℓ_∞ is defined as $\|\mathbf{x}\|_{\ell_\infty^n} = \max_{i=1,\ldots,n}(|x_i|)$. A signal $\mathbf{s}$ can be defined as a strictly k-sparse signal if it can be represented with less than $k+1$ nonzero coefficients in a proper basis $\mathbf{\Phi}$, i.e., $\|\mathbf{x}\|_0 \leq k$, where $\mathbf{s} = \mathbf{\Phi}\,\mathbf{x}$. We also define a sparse support set or simply support set, $\Lambda \subset \{1, 2, 3, \ldots, n\}$, as the set of indices that represent the nonzero coefficients, i.e., $\Lambda := \{i : x_i \neq 0\}$. The complement of support set, Λ, with respect to $\{1, 2, 3, \ldots, n\}$ is given as $\Lambda^c = \{1, 2, 3, \ldots, n\} \backslash \Lambda$. In this manner, $\mathbf{x}_\Lambda \in \mathbb{R}^{|\Lambda|}$ is a vector consisting of nonzero elements of $\mathbf{x} \in \mathbb{R}^n$, where $|\Lambda|$ refers to the number of the nonzero coefficients. Similarly, $\mathbf{M}_\Lambda \in \mathbb{R}^{m\times|\Lambda|}$ denotes a matrix that consists of the columns of a matrix $\mathbf{M} \in \mathbb{R}^{m\times n}$ indexed by support Λ.

III. Related Work

The CS theory claims that a signal $\mathbf{s}$ can be sensed using far fewer linear measurements m than Nyquist-/Shannon-based traditional methods' use, d, i.e.,

$$\mathbf{y} = \mathbf{A}\mathbf{s} = \mathbf{A}\mathbf{\Phi}\mathbf{x} = \mathbf{D}\mathbf{x} \tag{1}$$

where $\mathbf{A} \in \mathbb{R}^{m\times d}$ is the measurement matrix and $\mathbf{D} \in \mathbb{R}^{m\times n}$ is called the equivalent dictionary. It can be demonstrated that sparse representation

$$\min_{\mathbf{x}} \|\mathbf{x}\|_0 \quad \text{s.t. } \mathbf{D}\mathbf{x} = \mathbf{y} \tag{2}$$

is unique if $m \geq 2k$ [28] and $\|\mathbf{x}\|_0 \leq k$. In brief, the uniqueness of the sparse representation in (2) shows that any k-sparse signal pair can still be distinguished in the equivalent dictionary, $\mathbf{D}$. However, the problem in (2) is that this is a nonconvex problem and known to be NP-hard. The most common approach is the relaxation of the ℓ_0-norm to the closest convex norm, which is ℓ_1-norm

$$\min_{\mathbf{x}} \|\mathbf{x}\|_1 \quad \text{s.t. } \mathbf{x} \in \mho(\mathbf{y}) \tag{3}$$

where $\mho(\mathbf{y}) = \{\mathbf{x} : \mathbf{D}\mathbf{x} = \mathbf{y}\}$, which is known as basis pursuit [29]. The surprising result of the CS theory is that, even if the exact recovery of the signal, $\mathbf{s}$, was not possible by using the minimum norm solution, a tractable solution is possible using (3), when $\mathbf{D}$ satisfies some properties, such as restricted isometry property [30] and $m > k(\log(n/k))$.

However, the signal of interest, $\mathbf{x}$, is not perfectly k-sparse but approximately sparse in most of the cases. In addition, CS measurements, most probably, are corrupted by an additive noise during data acquisition, quantization, and so on. As a result, we handle $\mathbf{y} = \mathbf{D}\mathbf{x} + \mathbf{z}$, where $\mathbf{z}$ is the additive noise. In this case, the constraint can be relaxed by setting $\mho(\mathbf{y}) = \{\mathbf{x} : \|\mathbf{D}\mathbf{x}-\mathbf{y}\|_2 \leq \epsilon\}$, which is known as basis pursuit denoising (BPDN) [29] or the Dantzig selector [31], if we set $\mho(\mathbf{y}) = \{\mathbf{x} : \|\mathbf{D}^T(\mathbf{y}-\mathbf{D}\mathbf{x})\|_\infty \leq \lambda\}$. In the noisy case, even exact recovery of sparse signal is not possible, stable recovery is well studied in the literature for BPDN [32] and the Dantzig selector [33], [34]. We mean by stable recovery is that a stable solution $\hat{\mathbf{x}}$ obeys $\|\mathbf{x} - \hat{\mathbf{x}}\| \leq \kappa\|\mathbf{z}\|$, where the κ is small constant. Another related formulation is

$$\min_{\mathbf{x}} \left\{\|\mathbf{D}\mathbf{x} - \mathbf{y}\|_2^2 + \lambda\|\mathbf{x}\|_1\right\} \tag{4}$$

which is known as Lasso [35] formulation, which is also known to produce stable solution in noisy case and exact solution in noise free case [36].

A. Generic Sparse Support Estimation

In many application scenarios, detecting the indices of the nonzero coefficients' location, Λ, is more important than computing these coefficients. To list a few, in a sparse anomaly (either from CS [37] or uniform sampled measurements) detection problem [38], where a group of users initiates a flooding attack to a communication network (specifically for a VoIP network), detecting the malicious user group (a subset of all users) is more critical. Among others, CS-based active user detection in the downlink of a CDMA system [39] and for the uplink of an NOMA [40], [41] system can be counted. Such systems are believed to play an important role in 5G communication technology. As discussed in Section I, other examples may be listed as sparse representation-based classifications [11], [12] and radar imaging [15], [42].

Mathematically speaking, for the linear measurement model given in (1) and with additive noise, $\mathbf{y} = \mathbf{D}\mathbf{x} + \mathbf{z}$, we define the following support estimator $\mathcal{E}(.,.)$:

$$\hat{\Lambda} = \mathcal{E}(\mathbf{y}, \mathbf{D}) \tag{5}$$

where $\hat{\Lambda}$ is the estimated support. For the noise-free case, $\mathbf{x}$ is exactly k-sparse, and the exact Λ recovery performance of an algorithm coincides with the sparse SR performance. This an expected outcome since the unique representation is satisfied when $m > 2k$. In the noisy case, even if the exact SR is not possible, it is still possible to recover the support set exactly. In the literature, several studies have proposed to provide information-theoretical (i.e., the optimal decoder, $\mathcal{E}$'s performance) guarantee conditions for exact [5], [10], [43], [44] and partial SE [7], [10], [45]. However, in most of the practical applications, a tractable SR method is applied first to find an estimation $\hat{\mathbf{x}}$ of the sparse signal $\mathbf{x}$; then, a componentwise thresholding is applied to $\hat{\mathbf{x}}$ to compute the estimated support, as illustrated in Fig. 2.

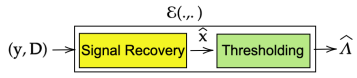

Fig. 2. Most common model for a practical support estimator.

A common approach is to follow an iterative sparse SR method from the CS literature. For instance, it is proven in [46] that, if $\min_{i\in\Lambda}|x_i| > 8\sigma(2*\log(n))^{1/2}$, then one can recover the support set exactly using Lasso with $\lambda = 2(2*\log(n))^{1/2}$, where σ^2 is variance of the measurement noise. This theorem is valid in the case that the equivalent dictionary satisfies the mutual coherence property defined in [46]. One may clearly deduce from their results that accurate SE is possible via Lasso if the nonzero coefficients' magnitudes are above a certain level determined by the noise. Similarly, the conditions of exact support recovery under noise using OMP are given in [47], and partial support recovery performance bounds of AMP are in [48]. Along with these SR algorithms in the CS literature, which are iterative methods, traditional linear decoders, such as maximum correlation (MC) [49], $\hat{\mathbf{x}}^{MC} = \mathbf{D}^T\mathbf{y}$, and LMSEE [48], $\hat{\mathbf{x}}^{\text{LMMSE}} = (\mathbf{D}^T\mathbf{D}+\sigma_z^2\mathbf{I}_{n\times n})^{-1}\mathbf{D}^T\mathbf{y}$, are also used in many applications. The theoretical performance bounds of these methods are also given in [48].

B. Case Study of SE: Representation-Based Classification

Consider an image from a particular class is queried. It can be expected from the estimated SCs, $\hat{\mathbf{x}}$, to have significant (nonzero) entries that are located in a specific location so that the corresponding columns in the dictionary matrix, $\mathbf{D}$, are the samples from the actual class of the image. This problem is also known as the representation-based classification, which is a typical example where the support set location is the main information that we are seeking.

In [11], ℓ_1-minimization is used to obtain such a sparse code to determine the identity of face images. However, in reality, such an ideal decomposition is not accomplished in general because face images show a high correlation among different classes. This is why, instead of using the estimated sparse codes, $\hat{\mathbf{x}}$ obtained by an SR technique, such as (4), the authors propose a four steps solution.

1) *Normalization:* Normalize all the atoms in $\mathbf{D}$ and $\mathbf{y}$ to have unit ℓ_2-norm.
2) *SR:* $\hat{\mathbf{x}} = \arg\min_{\mathbf{x}} \|\mathbf{x}\|_1$ s.t. $\|\mathbf{y} - \mathbf{D}\mathbf{x}\|_2$.
3) *Residual Finding:* $\mathbf{e_i} = \|\mathbf{y} - \mathbf{D_i}\hat{\mathbf{x}}_\mathbf{i}\|_2$, where $\hat{\mathbf{x}}_\mathbf{i}$ is the estimated coefficients corresponding the class i.
4) *Class Determination:* $\text{Class}(\mathbf{y}) = \arg\min(\mathbf{e_i})$.

This technique and its similar variants have been reported to perform well not only in face recognition but many other classification problems [50], [51]. Later, Zhang *et al.* [24] propose to change the second step, from ℓ_1-minimization to the classical ℓ_2-minimization; $\hat{\mathbf{x}} = \arg\min_{\mathbf{x}}\{\|\mathbf{y} - \mathbf{D}\mathbf{x}\|_2^2 + \lambda\|\mathbf{x}\|_2^2\}$, which has a closed-form solution, $\hat{\mathbf{x}} = (\mathbf{D}^T\mathbf{D} + \lambda\mathbf{I}_{n\times n})^{-1}\mathbf{D}^T\mathbf{y}$. This collaborative representation-based classification (CRC) was reported to achieve a comparable classification performance for different classification problems. For face recognition problems, in particular, the authors reported that high classification accuracies were obtained especially for high MRs.

C. Sparse Signal Reconstruction With Side Information of Support Set

Consider the case where SE is not the main concern but SR is. In case side information is available about the support set, an improvement to ℓ_1-minimization can be achieved in sparse SR as follows:

$$\min_{\mathbf{x}} \left\{\|\mathbf{D}\mathbf{x} - \mathbf{y}\|_2^2 + \lambda\|\mathbf{w}\odot\mathbf{x}\|_1\right\} \tag{6}$$

where $\odot$ is elementwise multiplication operator and $\mathbf{w}$ is the predefined cost that imposes the prior information about each element's values. In the concept of modified CS [52] and CS with prior information literature, the cost function, $\mathbf{w}$, generally appears in the form of $w_i = (1/(p_i + \epsilon))$, where $\epsilon > 0$ is a predefined constant and p_i is the ith element of the vector $\mathbf{p}$, which is a type of a measure, such as prior likelihood [26] of the support set, which could represent the probability of the (i)th element being nonzero.

D. Limitations of Existing Support Estimators

Both SE and SR algorithms guarantee to perform well if the equivalent dictionary $\mathbf{D}$ satisfies certain properties, such as mutual incoherence [53]. However, in many practical scenarios, $\mathbf{D}$ fails to satisfy these properties, e.g., in the face recognition problem, the atoms of $\mathbf{D}$, vectorized faces, are highly correlated. The second limitation of traditional sparse recovery algorithms is that they are iterative methods and computationally costly. Therefore, the support estimators relying on these sparse recovery algorithms may not be feasible, especially in real-time applications. The third limitation of state-of-the-art SR techniques, such as ℓ_1-minimization, is that there is a lower limit for MR (see phase transition [54]); below this limit, the SR algorithms start to fail completely. This limit generally depends on the wellness of $\mathbf{D}$ (defined by properties such as mutual incoherence [53]). Therefore, SE techniques that build upon an SR algorithm tend to fail if $\mathbf{D}$ does not satisfy the required properties, e.g., if the atoms of $\mathbf{D}$ are highly correlated.

On the other hand, when it comes to SR techniques leveraging SE as prior information, despite the fact that a good improvement can be achieved using such prior information, most of the works assume that the information is available in advance; however, they do not mention how to obtain such a $\mathbf{p}$.

IV. Convolutional Sparse Support Estimator Network

Recent advance in deep neural networks [18], [20] enables a noniterative solution for the sparse SR. It is often reported that they produce a solution $\hat{\mathbf{x}}$, which is closer to $\mathbf{x}$ than the ones obtained by an iterative approach. They can still work under those MRs where classical CS recovery algorithms fail. Nevertheless, their complex configuration with millions of parameters causes certain computational complexity issues, such as speed and memory problems, especially when they are used in edge devices with limited power, speed, and memory.

If one may wish to find only support Λ instead of the sign and amplitude of $\mathbf{x}$, a traditional machine learning approach would be sufficient. In this study, we propose a support estimator, $\mathcal{E}(.)$, which can be performed by a compact

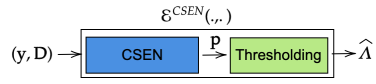

Fig. 3. Proposed model for an efficient support estimator.

CSEN network. Another crucial objective is to have the ability to learn from a minimal training set with a limited number of labeled data. A typical application where this approach can benefit from is face recognition via sparse representations, where only a few samples of each identity are available.

Let us define a binary mask $\boldsymbol{\alpha} \in \{0, 1\}^n$, as follows:

$$\alpha_i = \begin{cases} 1 & \text{if } i \in \Lambda \quad (7a) \\ 0 & \text{else.} \quad (7b) \end{cases}$$

Consequently, the problem of finding an estimation $\hat{\boldsymbol{\alpha}}$ of this binary mask will be equivalent to producing an SE $\hat{\Lambda}$, i.e., $\hat{\Lambda} = \{i \in \{1, 2, \ldots, n\} : \hat{\alpha}_i = 1\}$.

To accomplish this objective, first, the CSEN network with input and output, $\mathcal{P}(\mathbf{y}, \mathbf{D}) : \mathbb{R}^n \mapsto [0, 1]^n$, produces a vector $\mathbf{p}$ that gives the information about the probability of each index to be in support set such that $p_i \in [0, 1]$. Then, the final support estimator, $\mathcal{E}(\mathbf{y}, \mathbf{D})$, will produce an SE such that $\hat{\Lambda} = \{i \in \{1, 2, \ldots, n\} : p_i > \tau\}$, by thresholding $\mathbf{p}$ with τ, where τ is a fixed threshold.

As shown in Fig. 3, the proposed SE approach is different from the conventional SR-based methods, which directly thresholds $\hat{\mathbf{x}}$ for SE. Moreover, the input–output pair is different. The proposed CSEN learns over $(y^{\text{train}}, v^{\text{train}})$ to compute $\mathbf{p}$, while the conventional SR methods work with $(y^{\text{train}}, x^{\text{train}})$ to first make the sparse signal estimation and then compute SE by thresholding it. As evident in Fig. 1, the application of direct SR may cause noisy estimation of the support codes, while the proposed CSEN has the advantage of learning the pattern of the support codes and, therefore, can predict their most-likely location with proper training.

In this study, the proposed CSEN models consist of only convolutional layers in the type of fully convolutional networks [16] that are trained by optimizing the SEs. Since the SE problem involves one-to-one mapping, other network types, such as multilayer perceptrons (MLPs), can also be used as in [18]. However, this brings two limitations compared to CSENs: high computational complexity and overfitting due to the limited training data and number of parameters in the network. In Section V, it will be shown that such an approach yields a poor generalization and is not robust to noise.

When a CSEN is trained, it learns the following transformation: $\hat{\boldsymbol{\alpha}} \leftarrow \mathcal{P}(\tilde{\mathbf{x}})$, where $\hat{\boldsymbol{\alpha}}$ is the estimation of binary mask representing the estimated support for the signal $\mathbf{x}$, and the proxy $\tilde{\mathbf{x}} = \mathbf{B}\mathbf{y}$ with $\mathbf{B} = \mathbf{D}^{\mathbf{T}}$, or $(\mathbf{D}^T\mathbf{D} + \lambda\mathbf{I})^{-1}\mathbf{D}^T$, i.e., the MC and LMMSE formula in [48]; hence, $\mathbf{x}, \tilde{\mathbf{x}} \in \mathbb{R}^N$. First, the proxy $\tilde{\mathbf{x}}$ is reshaped to 2-D plane (e.g., the original size of the image or predefined search grid). Correspondingly, the proxy $\widetilde{\mathbf{X}}$ (the matrix version of $\tilde{\mathbf{x}}$) is convolved with $\mathbf{w_1}$, the set of weight kernels connecting the input layer to the next layer with N_1 filters to form the input of the next layer with the summation of weight biases $\mathbf{b_1}$ as follows:

$$\mathbf{f_1} = \left\{ S_1\left(\text{ReLu}\left(b_1^i + \mathbf{w}_1^i * \widetilde{\mathbf{X}}\right)\right)\right\}_{i=1}^{N} \quad (8)$$

where $S_1(.)$ is the down-sampling or identity operator, $\mathbf{w_1^i}$ is the ith kernel weight, and b_1^i is its corresponding bias term and $\text{ReLu}(x) = \max(0, x)$. In more general form, the kth feature map of layer l can be expressed as

$$\mathbf{f_l^k} = S_l\left(ReLu\left(b_l^k + \sum_i^{N_{l-1}} \mathbf{w_l^{ik}} * \mathbf{f_{l-1}^i}\right)\right) \quad (9)$$

where $\mathbf{w_1^i}$ is the ith kernel weight of the lth layer, b_l^i is its corresponding bias term, N_l is the number of filter in this layer, and $S_l(.)$ is either the down- or up-sampling or identity operator depending on the CSEN structure. The trainable parameters of the network would be

$$\boldsymbol{\Theta}_{\mathbf{CSEN}} = \left\{\left\{\mathbf{w}_1^i, b_1^i\right\}_{i=1}^{N_1}, \left\{\mathbf{w}_2^i, b_2^i\right\}_{i=1}^{N_2}, \ldots, \left\{\mathbf{w}_L^i, b_L^i\right\}_{i=1}^{N_L}\right\}$$

for a L layer CSEN.

In the proposed approach, the mean square error (mse) is computed between its binary mask, $\boldsymbol{\alpha}$, and CSEN's actual output, $\mathcal{P}_\Theta(\mathbf{x})_p$, as follows:

$$E(\mathbf{x}) = \sum_p \left(\mathcal{P}_\Theta(\mathbf{x})_p - \alpha_p\right)^2 \quad (10)$$

where v_p is the pth pixel of $\boldsymbol{\alpha}$. The CSEN network is trained using samples in the train data, $D_{train} = \{(\tilde{\mathbf{x}}^{(1)}, \boldsymbol{\alpha}^{(1)}), (\tilde{\mathbf{x}}^{(2)}, \boldsymbol{\alpha}^{(2)}), \ldots, (\tilde{\mathbf{x}}^{(s)}, \boldsymbol{\alpha}^{(s)})\}$. Please note that, even if we use mse as the loss function in the original CSEN design, depending on the application, any other regularization function (e.g., ℓ_1-norm and mixed norm) can be added to this cost function. As an example, we present a strategy to approximate the loss function, which is group ℓ_1-norm in addition to mse.

V. Results

In order to evaluate the effect of different network configurations, in this study, we use two different CSEN configurations and perform a comprehensive analysis of each of them. Generally, each convolutional layer has a dimension reduction capability with pooling functions. However, the first proposed network architecture consists of only convolutional layers with ReLu activation functions to preserve the sparse signal (e.g., image) dimensions at the output layer. In this configuration (CSEN1), we propose to use three convolutional layers with 48 and 24 hidden neurons and 3×3 filter size, as given in Fig. 4. CSEN2 is a slight modification of CSEN1 configuration, as shown in Fig. 5, by using up- and down-sampling layers. Although this modification increases the number of parameters, in return, it yields substantial performance improvement over MNIST. While the SE performance analysis over MNIST has done using CSEN1 and CSEN2, only CSEN1 results are reported since CSEN2 produces similar recognition rates ($\sim$0.001 difference) for face recognition. In any case, both network configurations are compact compared to the deep CNNs that have been proposed recently. For example, the study in [17] proposes ReconNet for SR, which consists of six convolutional layers with 32 neurons or more in each layer.

Since there is no competing method for SE that is similar to the proposed method, we use the ReconNet [17] in this study on the SE problem by directly giving $\tilde{\mathbf{x}}$ as the input

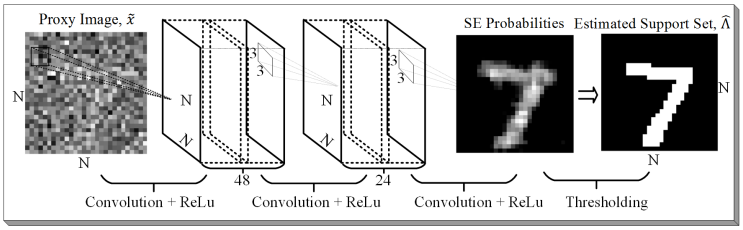

Fig. 4. Type-I CSEN (CSEN1).

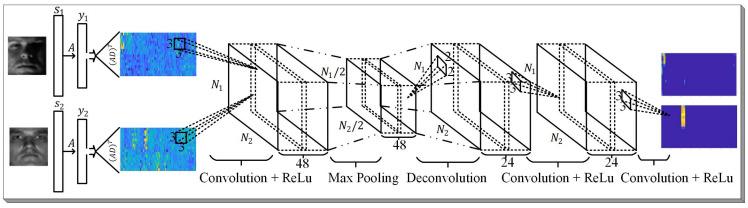

Fig. 5. Type-II CSEN (CSEN2).

and removing the denoiser block at the end for comparative evaluations. Finally, we apply thresholding over the output of ReconNet to generate SE i.e., $\hat{\Lambda}_{\mathrm{R}} = \{i \in \{1, 2, \ldots, n\} : \mathcal{P}_{\mathrm{R}}(\tilde{\mathbf{x}}) > \tau\}$, where $\mathcal{P}_{\mathrm{R}}(.)$ is ReconNet with fully convolutional layers. ReconNet is originally a CS recovery algorithm working directly on spatial domain, i.e., $\hat{\mathbf{s}} \leftarrow \mathcal{P}(\mathbf{y})$ instead of solving them in the sparsifying dictionary, i.e., $\hat{\mathbf{s}} = \mathbf{\Phi}\hat{\mathbf{x}}$ where $\hat{\mathbf{x}} \leftarrow \mathcal{P}(\mathbf{y})$. Therefore, ReconNet serves as a deep CSEN approach against which the performance of the two compact CSENs will be compared. Moreover, we also train the state-of-the-art deep SR solution, LAMP, and, first of its kind, LISTA networks, in order to use them over the SE problem. For the LAMP method, it is possible to predefine the number of layers in advance. For a fair comparison, we have tested the unfolded networks, LISTA and LAMP, for three different setups: two-, three-, and four-layer designs using their provided implementation. Next, in the experiments of face recognition based on SR, we consider both speed and recognition accuracy of the algorithms as it is performed only for the ℓ_1-minimization toolbox in [55]. Thus, in order to perform comparative evaluations, the proposed CSEN approach is evaluated against most of the conventional state-of-the-art SR techniques along with ReconNet. Finally, CSEN2 is applied as a preprocessing step for the CS-recovery to obtain $\mathbf{w}$ in the cost function, as illustrated in Fig. 1.

The experiments in this study have been carried out on a workstation that has four Nvidia TITAN-X GPU cards and Intel Xeon CPU E5-2637 v4 at 3.50 GHz with 128-GB memory. Tensorflow library [56] is used with Python. ADAM optimizer [57] is utilized during the training with the proposed default values of the learning parameters: learning rate: $lr = 0.001$ and moment updates: $\beta_1 = 0.9$ and $\beta_2 = 0.999$ with only 100 and 30 backpropagation iterations for MNIST and face recognition experiments, respectively.

A. Experiment I: Support Estimation From CS Measurements

The following metrics are used to report the performance of the proposed and competing methods:

$$\text{F1 Measure (F1-Score)} = 2 \times \frac{\text{Precision} \times \text{Recall}}{\text{Precision} + \text{Recall}} \tag{11}$$

$$\text{Specificity} = \frac{\text{TN}}{\text{TN} + \text{FP}} \tag{12}$$

$$\text{Sensitivity} = \frac{\text{TP}}{\text{TP} + \text{FN}} \tag{13}$$

where true negatives (TNs), false negative (FN), true positive (TP), and false positive (FP) are calculated between the predicted binary mask $\hat{\alpha}$ and its corresponding ground truth $\boldsymbol{\alpha}$ for each sample in test set. Then, the final reported performance metrics are the averaged ones using the macroaverage method.

For the experiments in this section, the MNIST dataset is used. This dataset contains 70 000 samples (50k/10k/10k as the sizes of the train/validation/test sets) of the handwritten digits (0–9). Each image in the dataset is a 28×28 pixel resolution with intensity values ranging from 0 (black, background) to 1 (white, foreground). Since the background covers more area than the foreground, each image can be considered as a sparse signal. Mathematically speaking, we may assume that the ith vectorized sample, $\mathbf{x}_i \in \mathbb{R}^{n=784}$, can be considered as the k_i-sparse signal. The sparsity rates of each sample are calculated as $\rho_i = (k_i/n)$, and its histogram is given in Fig. 6. We have designed an experimental setup where these sparse signals (sparse in canonical basis) $\mathbf{x}_i$'s are compressively sensed

$$\mathbf{y_i} = \mathbf{A}\mathbf{x_i} = \mathbf{D}\mathbf{x_i} \tag{14}$$

where $\mathbf{D} = \mathbf{A} \in \mathbb{R}^{m \times n}$ since $\mathbf{\Phi} = \mathbf{I}$. We calculate the MR as $\mathbf{MR} = (m/n)$. Therefore, the problem is SE from each CS measurement, i.e., finding $\hat{\Lambda}_i$ from each $\mathbf{y_i}$ in the test dataset.

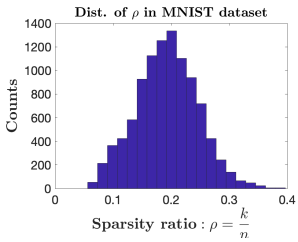

Fig. 6. Histogram of ρ_i's obtained from the 10k samples (test set). The vectorized gray-scale images, $\mathbf{x}_i$, in the MNIST dataset are already sparse in the spatial domain (in canonical basis, i.e., $\Phi = I$) with $\|\mathbf{x}_i\| \leq k_i$.

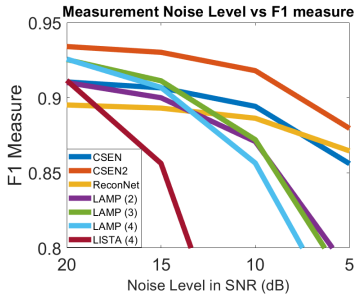

Fig. 7. F1 measure graph of CSEN and LAMP configurations in different noise levels at MR = 0.25.

For this dataset, the **MR** is varied from 0.05 to 0.25 in order to investigate the effect of MR on the SE performance. The measurement matrix is then chosen as the "Gaussian," and the elements $A_{i,j}$ of the matrix are i.i.d. drawn from $\mathcal{N}(0, (1/m))$. It is worth mentioning that the approximate message passing (AMP) algorithm is a well-optimized method for the Gaussian measurement matrix, and LAMP is a learned version of this algorithm. Therefore, they are reported to be state of the art if the measurement matrix is Gaussian, but they do not even guarantee the converge for other types of measurement matrices. On the other hand, the comparative performance evaluations against LAMP, LISTA, and deep CS-SR methods are presented in Tables I and II, and the results clearly indicate that the proposed method achieves the best SE performance in terms of F1 measure for MR = 0.25 and 0.05 and comparable for MR = 0.1. The results presented in Table I indicate that, despite its deep and complex configuration, compact CSENs achieve superior performance levels compared to ReconNet. For both LISTA and LAMP, both increasing the layer size from 2 to 4 does not improve their SE performances as it can be observed in Table I. Hence, their numbers of layers are not further increased.

Furthermore, comparative evaluations are performed when the measurements are exposed to noise in the test set, i.e., $\mathbf{y}_i = \mathbf{D}\mathbf{x}_i + \mathbf{z}_i$, where $\mathbf{z}_i$ is an additive white Gaussian noise. The results presented in Fig. 7 show that SE performances of the LAMP and LISTA method are adversely affected by increased measurement noise. Their performance gets even worse when the number of layers is increased [i.e., see results for LAMP (2) to LAMP (4) or LISTA (2) to LISTA (4)]. CSEN2, on the other hand, achieves the highest F1 measure for all noise levels.

TABLE I

SUPPORT RECOVERY PERFORMANCE OF ALGORITHMS FROM THE NOISE-FREE MEASUREMENTS

MR	0.25	0.1	0.05	0.25	0.1	0.05	0.25	0.1	0.05	0.25	0.1	0.05
	F1 Measure			Precision			Recall			CE		
CSEN	0.91	0.85	0.80	0.90	0.84	0.77	0.92	0.87	0.84	0.03	0.06	0.08
CSEN2	**0.94**	0.89	**0.84**	0.93	0.88	**0.82**	**0.94**	**0.90**	**0.87**	**0.02**	**0.04**	**0.06**
ReconNet	0.90	0.85	0.79	0.89	0.82	0.76	0.90	0.87	0.83	0.05	0.06	0.09
LAMP (2)	0.92	0.89	0.82	0.94	0.90	**0.82**	0.89	0.87	0.83	0.05	0.05	0.08
LAMP (3)	0.93	0.89	0.82	0.95	0.90	**0.82**	0.91	0.88	0.82	0.03	0.05	0.08
LAMP (4)	0.93	**0.90**	0.83	0.95	**0.92**	**0.82**	0.92	0.89	0.83	0.03	**0.04**	0.08
LISTA (2)	0.93	0.89	0.82	**0.96**	0.90	**0.82**	0.90	0.87	0.82	0.03	0.05	0.07
LISTA (3)	0.93	0.89	0.82	0.95	0.90	**0.82**	0.90	0.87	0.82	0.03	0.05	0.07
LISTA (4)	0.93	0.89	0.82	0.95	0.90	**0.82**	0.90	0.87	0.83	0.03	0.05	0.07

TABLE II

SUPPORT RECOVERY PERFORMANCE OF ALGORITHMS UNDER 10-dB MEASUREMENT NOISE

MR	0.25	0.1	0.05	0.25	0.1	0.05	0.25	0.1	0.05	0.25	0.1	0.05
	F1 Measure			Precision			Recall			CE		
CSEN	0.89	0.82	0.77	0.89	0.82	0.75	0.89	0.82	0.79	0.04	0.07	0.09
CSEN2	**0.92**	**0.86**	**0.80**	**0.92**	0.86	**0.80**	0.92	0.86	**0.82**	**0.03**	**0.06**	**0.08**
ReconNet	0.89	0.83	0.78	0.89	0.81	0.74	0.89	0.85	0.81	0.04	0.07	0.09
LAMP (2)	0.87	0.85	0.79	0.90	0.86	0.78	0.84	0.83	0.80	0.08	0.08	0.10
LAMP (3)	0.87	0.84	0.77	0.91	**0.87**	0.78	0.84	0.81	0.77	0.06	0.08	0.12
LAMP (4)	0.86	0.85	0.77	0.87	**0.87**	0.78	0.85	0.82	0.77	0.08	0.07	0.12
LISTA (2)	0.72	0.82	0.79	0.58	0.77	0.76	0.93	**0.88**	**0.82**	0.18	0.08	0.10
LISTA (3)	0.68	0.83	0.79	0.54	0.78	0.76	**0.94**	0.87	**0.82**	0.22	0.08	0.10
LISTA (4)	0.68	0.82	0.78	0.53	0.77	0.75	**0.94**	**0.88**	**0.82**	0.22	0.08	0.10

B. Convolutional Support Estimation-Based Classification (CSEN-C)

As explained in Section III-B, the dictionary-based (representation-based) classification could be seen as an SE problem. Therefore, CSEN presents an alternative and better approach to both CRC and SRC solutions. In this manner, the proposed CSEN approach is evaluated against both CRC and the state-of-the-art SRC techniques recently proposed. The algorithms are chosen by considering both their speed and performance on the SR problem since the speed-accuracy performance of SRC directly depends on the performance of the sparse SR algorithm [55], and there is no unique winner to achieve the top performance level for all databases. The proposed method is, of course, not limited to face recognition but can be applied in any other representation-based classification problem. In Section V-C, we will also consider a new and challenging classification task, Coronavirus disease (COVID-19) recognition from X-Ray Images.

End-to-End Learning of CSEN-Based Classifiers: In dictionary-based classification designs, the samples of a specific class are stacked in the dictionary as atoms with predefined indices, e.g., the atoms belonging to a particular class can be located in a concatenated manner. Consequently, in sparse representation-based classification, instead of using ℓ_1-minimization in (4), group ℓ_1-minimization can be introduced as follows:

$$\min_{\mathbf{x}} \left\{ \|\mathbf{D}\mathbf{x} - \mathbf{y}\|_2^2 + \lambda \sum_{i=1}^{c} \|\mathbf{x}_{\mathbf{Gi}}\|_2 \right\} \tag{15}$$

where $\mathbf{x_{Gi}}$ is the group of coefficients corresponds to class i. Hence, the mse cost function in (10) can be modified accordingly

$$E(\mathbf{x}) = \sum_{p} (\mathcal{P}_\Theta(\mathbf{x})_p - \alpha_p)^2 + \lambda \sum_{i=1}^{c} \|\mathcal{P}_\Theta(\mathbf{x})_{Gi}\|_2. \quad (16)$$

This modified cost function can be used to achieve a better estimation of the support set. Having this improved estimation, the query class can be obtained. However, having such an intermediate step is also redundant for a classification problem. In this study, we slightly modify the network to make it an end-to-end learning system: to approximate the new cost function defined in (16), a simple average pooling can be applied after the last layer of CSEN, which is then followed by the SoftMax function to produce class probabilities. Therefore, the modified cost function with the cross-entropy loss at the output would be $E(\mathbf{x}) = -\sum_i^C t_i log(\mathcal{P}_\Theta(\mathbf{x}))$, where t_i and $\mathcal{P}_\Theta(\mathbf{x})$ are the real and predicted values by CSEN, respectively, for class $i \in C$. In this way, the modified network can directly yield the predicted class labels as the output. The pipeline of the proposed end-to-end learning is drawn in Fig. S1 in the Supplementary Material. One may question whether the proposed compact network designs (CSEN1 and CSEN2) are the optimal ones. We also replaced CSEN compact networks with the deeper fully convolutional one, ReconNet, as an alternative network design and report also its performance as a competing method.

1) Multiclass Classification Problem: Face Recognition via CSEN-C (Experiment II): In the face recognition experiments, we have used Yale-B [22] and CelebA [23] databases. In the Yale-B dataset, there are 2414 face images with 38 identities; and a subset of CelebA is chosen with 5600 images and 200 identities. The face recognition experiments are repeated five times with samples randomly selected to build the dictionary, train, and test sets with 32, 16, and 16 and 8, 12, and 8 samples each for Yale-B and CelebA, respectively, for CSEN schemes, and 25% of training data is separated as validation. To have a fair comparison, for CRC and SRC methods, the training set is also included in the dictionary, which are 48 and 20 samples per identity for Yale-B and CelebA, respectively. The selected subset of the CelebA dataset is also different between each repeated run. For the Yale-B database, we use vectorized images in the dictionary. Earlier studies reported that both SRC and CRC techniques achieve a high recognition accuracy of 97%–98%, especially for high MR rate scenarios ($m/d > 0.25$ for $\mathbf{A} \in \mathbb{R}^{m \times d}$). On the other hand, for the CelebA dataset, both CRC and SRC solutions tend to fail when we use raw atoms in the dictionary without extracting descriptive features. This is why, in this study, we propose to use a more representative dictionary. Instead of using raw images, the atoms consist of more descriptive features extracted by a neural network-based face feature extractor in the library [58]. The proposed method is compared against CRC and SRC techniques with the following seven state-of-the-art SR solver: ADMM [59], Dalm [55], OMP [55], Homotopy [60], GPSR [61], L1LS [62], ℓ_1-magic [63], and Palm [55].

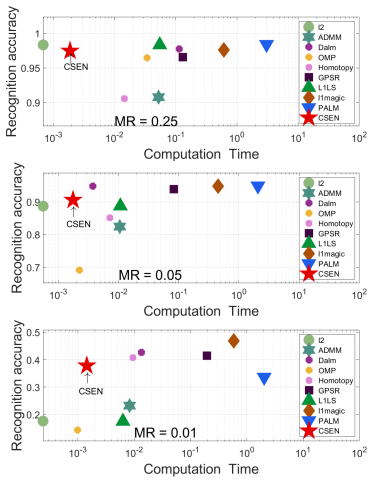

Fig. 8. Recognition accuracy versus process time comparison of algorithms in the Yale-B database.

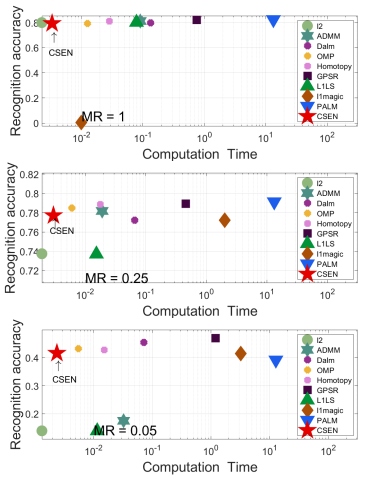

Fig. 9. Recognition accuracy versus process time comparison of algorithms in the CelebA database.

Overall, when we perform experiments in two facial image databases, Yale-B and CelebA for different MRs, the CSEN-based classification proves to be very stable; and in all MRs, it gives the highest or comparable recognition accuracy to the highest ones for all experiments, as presented in Figs. 8 and 9. Furthermore, it is significantly superior in terms of computational speed compared with SRC solutions.

To be able to use the same CSEN designs introduced in Section IV, we reorder the positions of the atoms, i.e., in the representative sparse codes corresponding nonzero coefficients remain next to each other in the 2-D plane. A simplified illustration of the comparison of conventional dictionary design and the proposed design for sparse representation-based

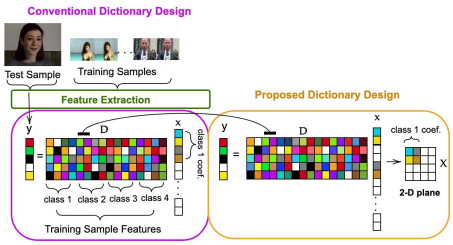

Fig. 10. Graphical representation of proposed dictionary design versus conventional design for face recognition problem.

TABLE III

FOR CSEN-BASED RECOGNITION, THE UTILIZED FACE RECOGNITION BENCHMARK DATASETS ARE GIVEN WITH THEIR CORRESPONDING MASK SIZE AND NUMBER OF SAMPLES IN DICTIONARY, TRAINING, AND TESTING PER CLASS

Dataset	Dictionary Samples	Train Samples	Test Samples	SC Size in 2D-Plane
Yale-B	32	16	16	16 x 76
CelebA	8	12	8	8 x 200

classification is shown in Fig. 10. Defined sparse code sizes and their representations in the 2-D grid for Yale-B and CelebA datasets are also given in Table III.

C. Binary Classification Problem: COVID-19 Recognition From X-Ray Images via CSEN-C (Experiment III)

The recent fast spread pandemic caused by Coronavirus disease (COVID-19) has affected millions worldwide. X-ray imaging is an easily affordable and accessible tool, which provides faster results, compared to other tests that are used in COVID-19 detection. It is well known that deep neural network models achieve state-of-the-art performance results in recognition and detection tasks. However, they require a large number of training samples to achieve a good generalization capability. On the other hand, representation-based classifiers are known to obtain reasonable classification performances with scarce data. In our previous work [25], we showed that CSEN-based classification is effective in recognizing COVID-19 among other classes when the classification problem is multiclass, i.e., COVID-19, bacterial pneumonia, viral pneumonia, and normal (healthy) classes. In the sequel, we will investigate the performance of CSEN-based classification in a binary classification task, that is, COVID-19 differentiation from other classes (control group). In such a sudden outbreak, such as COVID-19, preventing the spread should be a major concern. For this reason, we focus on minimizing FNs (while keeping the FPs as low as possible.

We used a benchmark dataset, Qata-Cov19 [25], of Chest X-Ray images from COVID-19 patients containing 462 samples. The control group (non-COVID class, a Kaggle dataset [64]) consists of 5824 X-Ray images that are 2760, 1485, and 1579 samples from Bacterial pneumonia, viral pneumonia, and normal class, respectively. We used fivefold cross-validation for evaluation, that is, for each fold, a different (20%) portion of the dataset was used as the test set, while the remaining (%80) of the data was used for training. In this way, all classifiers were evaluated over the entire dataset. Specifically, over 6286 total samples, for each fold, 5029 of them are selected for training, and 1257 (1164 samples from the control group and 63 samples from the COVID-19 class) are used as the test set. Data balancing was applied only to the training set, while the test set remained the same. The training set is augmented to have 9320 samples (4660 samples from the control group and 4660 samples from the COVID-19 class) via data balancing. The average performance over the fivefold was reported as the overall performance of each algorithm. The same experiment, with the same partitions, was conducted for all competing algorithms for a fair comparison.

TABLE IV

COVID-19 RECOGNITION PERFORMANCES OF THE ALGORITHMS

	k-NN	SVM	MLP	CRC	SRC	ReconNet	CSEN1	CSEN2
Accuracy	0.9446	**0.9701**	0.9613	0.9623	0.7887	0.9629	0.9618	0.9644
TN	5491	**5682**	5609	5602	4658	5604	5596	5610
TP	447	416	434	447	300	449	450	**452**
FP	333	**142**	215	222	1166	220	228	214
FN	15	46	28	15	162	13	12	**10**
Sensitivity	0.9675	0.9004	0.9394	0.9675	0.6494	0.9719	0.9740	**0.9784**
Specificity	0.9428	**0.9756**	0.9631	0.9619	0.7998	0.9622	0.9609	0.9633
F1-Score	0.7198	**0.8157**	0.7813	0.7905	0.3112	0.7940	0.7895	0.8014
F2-Score	0.8505	0.8645	0.8690	0.8880	0.4526	0.8919	0.8907	**0.8990**

In order to extract discriminative features from raw chest X-ray images, a pretrained model CheXNet [65], which was trained for other types of pneumonia detection from X-Ray images, is used. Using the pretrained CheXNet model, we extracted 1024-long vectors right after the last average pooling layer. After data normalization (zero mean and unit variance), we obtained a feature vector $\mathbf{s} \in \mathbb{R}^{d=1024}$. Then, the PCA matrix $\mathbf{A}$ is applied to the features, i.e., $\mathbf{y} = \mathbf{As}$. As competing algorithms to CSEN-based designs, CSEN1, CSEN2, and ReconNet, we selected the traditional classifiers KNN, MLP, and SVM, as well as the representation-based classifiers CRC and SRC. For SRC, we only reported the best-performed sparse recovery technique for this classification task, which is DALM. For the competing representation-based classifiers, CRC and SRC, the whole training data are used in the dictionary. On the other hand, for CSEN-based classifiers and ReconNet one, out of total training samples, 3200 samples (1600 samples for each class) are used in the dictionary, and the rest were used to train CSENs. For this smaller dictionary, the sparse code size in the 2-D plane is set as 80×40.

As it can be observed from Table IV, SRC performance drastically drops for the binary classification task. It is an expected result because the ideal representation coefficient, $\mathbf{x}$, is not sparse enough (e.g., the sparsity ratio $(k/n) = 0.5$). Although the CSEN-based classifier is also sparsity-driven and favors sparser representation (e.g., multiclass) problems, it still shows superior performance over other representation-based classifiers, which are CRC and SRC. When we compare with other traditional classifiers, the proposed scheme outperforms the second-best performing one, SVM, with respect to the missclassification rate of COVID-19, sensitivity, and F2-Score. These performance metrics can be considered major indicators because we want to achieve the highest sensitivity possible for the minimization of the FNs with a tolerable false

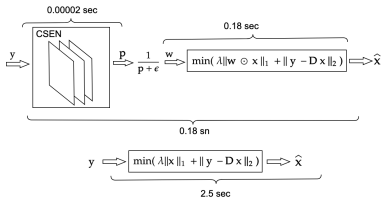

Fig. 11. Top: proposed CS reconstruction. Bottom: traditional ℓ_1-minimization-based CS-recovery.

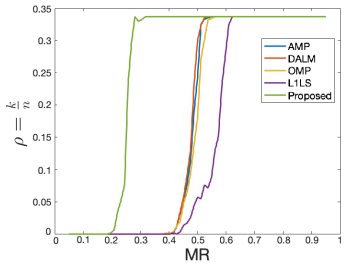

Fig. 12. Phase transition of the algorithms.

alarm rate. On the other hand, if one wants to compare the performance in terms of F1-Score instead of F2-Score, CSEN-based classification still achieves a comparable performance with SVM. F-2 Score is calculated as follows: F2-Score $= 5\times$ (Precision $\times$ Recall)/(4 $\times$ Precision + Recall). One may question whether or not the compact CSEN configuration is the optimal one. When we replace the proposed compact network configurations with a deeper well-known network, ReconNet, in the CSEN-based design, no significant performance improvement is observed. In fact, the results are even worse compared to CSEN2 configurations.

D. Learning-Aided Compressive Sensing

1) Experiment IV: Sparse in Spatial Domain: As the experimental setup, we randomly choose sparse signals, $\mathbf{x}$, in the MNIST database and use the Gaussian measurement matrix, $\mathbf{A}$, to simulate the CS, i.e., $\mathbf{y} = \mathbf{A}\mathbf{x}$. Then, we recover the sparse signal from $\mathbf{y}$ by using the aforementioned state-of-the-art SR tools and the proposed weighted ℓ_1-minimization [see (6)], where the weights $\mathbf{w}$ are obtained using CSEN output such that $\mathbf{w} = (1/(\mathbf{p}+\epsilon))$. Fig. 11 shows an illustration of how the proposed CS reconstruction scheme differs from the traditional CS recovery setup. Using the output of CSEN as prior information not only provides more accurate SR but also faster convergence of iterative sparse SR such as ℓ_1-minimization.

Furthermore, we draw the estimated phase transition of the algorithms in Fig. 12 using an experimental setup whose procedure is explained in [19]. Briefly summarizing the procedure, a grid of (MR, ρ) is generated for each algorithm, with 20 independent realizations of the problem: according to their sparsity ratios, ρ, randomly chosen sparse signals $\mathbf{x}$, among 10000 MNIST test images, are compressively sensed with the independent realization of measurement matrices. Then, they are recovered using the competing algorithms, and each realization is considered a success for the specific algorithm if $((\|\mathbf{x}-\hat{\mathbf{x}}\|_2)/\|\mathbf{x}\|) \leq$ tol, where tol is a predefined parameter; we choose tol $= 10^{-1}$ in our experiments. For a specific algorithm, we draw the phase transition in the border where a 50% success rate is achieved. The procedure is similar to [19], with the exception that they repeated the experiment only once, while we repeat it 100 times for each method, except L1LS due to its infeasibly high computational cost (it took almost two weeks with an ordinary computer). With an accurate SR algorithm, we expect the transition border to be close to the left-top corner in the phase transition graph because it is a good indicator that the algorithm performs well in low MRs and with a high sparsity ratio, ρ. From Fig. 12, one can easily deduce that the proposed CS-reconstruction approach clearly outperforms all competing state-of-the-art SR reconstruction methods. Moreover, the two examples where signals are compressively sensed with $MR = 0.25$ and their estimated versions by different SR methods are shown in Fig. 13. It is clear that the proposed approach recovers the sparse signal with the best quality, while the other state-of-the-art SR techniques perform poorly.

2) Experiment V: Sparse in a Proper Domain (Total Variation for Natural Images): In Section V-D1, we assumed that MNIST handwriting signals are sparse in the spatial domain, i.e., $\mathbf{\Phi} = \mathbf{I}$. Nevertheless, it is not the case for most of the real-world signals. For instance, natural images are not sparse in canonical basis but sparse in a convenient sparsifying basis, such as DCT and wavelet. In this section, we will use the gradient domain as sparsifying basis, i.e., $\mathbf{\Phi} = \mathbf{\nabla}$. Mathematically speaking, let we have an image $\mathbf{S} \in \mathbb{R}^{n_1 \times n_2}$ to be compressively sensed with the measurement matrix $\mathbf{A} \in \mathbb{R}^{m \times n}$ via $\mathbf{y} = \mathbf{A}\mathbf{s} \in \mathbb{R}^m$, where $\mathbf{s} \in \mathbb{R}^n$ is vectorized image, and $n = n_1 \times n_2$. The image can be sparsely represented in $\mathbf{\nabla}$ with sparse code pair $(\mathbf{X_h}, \mathbf{X_v})$, which are nothing but gradients on the horizontal axis (x-axis) and the vertical axis (y-axis), respectively, i.e., $\mathbf{\nabla_h S} = \mathbf{X_h}$ and $\mathbf{\nabla_v S} = \mathbf{X_v}$. Therefore, one can recover the image from $\mathbf{y}$ by solving the following total variation minimization problem:

$$\min_{\mathbf{S}} \lambda \|\mathbf{\nabla S}\|_{\mathrm{TV}} + \|\mathbf{y} - \mathbf{A}\mathrm{vec}(\mathbf{S})\|_2^2 \tag{17}$$

where we use the following anisotropic total variation definition:

$$\|\mathbf{\nabla S}\|_{\mathrm{TV}} = \|\nabla_h \mathbf{S}\|_1 + \|\nabla_v \mathbf{S}\|_1 \tag{18}$$

$$= \sum_{i,j} \left|S_{i+1,j} - S_{i,j}\right| + \sum_{i,j} \left|S_{i,j+1} - S_{i,j}\right|. \tag{19}$$

TV minimization-based solutions are mostly used in CS reconstruction problems and other inverse imaging systems to better preserve the edges and the boundaries compared to other sparsifying domains, such as DCT. In order to solve the optimization problem in (17), we use one of the state-of-the-art TV minimization solver, TV Minimization by Augmented Lagrangian and Alternating Direction Algorithms (TVAL3) [66]. Similar to Section V-D1, a CSEN can take the proxy of sparse code as input and produces a probability like measure that give a likelihood about the support of the sparse signal. In this TV-based problem, CSEN

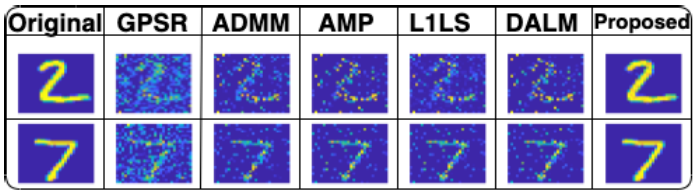

Fig. 13. Examples from MNIST that is compressively sensed and then reconstructed at MR = 0.25.

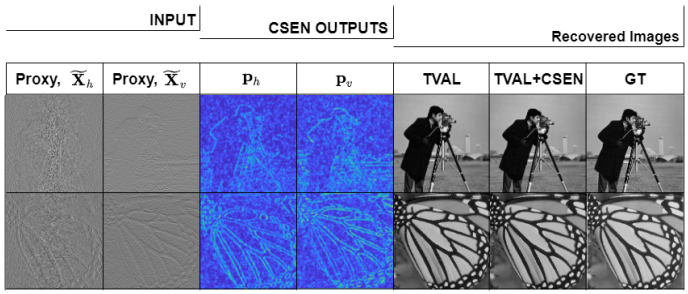

Fig. 14. Examples of the tested natural images. CSEN learns the **p** maps from the proxy images in both axes. Then, the **p** maps are used in solving the weighted total minimization problem. Traditional TVAL3 solutions have performance of 35.06 (dB) and 22.75 (dB) in PSNR, while CSEN-aided one achieves 36.97 (dB) and 23.68 (dB) in PSNR for butterfly and cameraman images, respectively.

takes two-channel input ($\widetilde{\mathbf{X_h}} = \widetilde{\nabla_{\mathbf{h}}\mathbf{S}}, \widetilde{\mathbf{X_v}} = \widetilde{\nabla_{\mathbf{v}}\mathbf{S}}$) and produces a two-channel **p**-map, ($\mathbf{p_h}, \mathbf{p_v}$). Example proxy images and CSEN outputs can be seen in Fig. 14. The proxies are obtained by having $\mathbf{A}^T\mathbf{y}$ first and then applying ∇ in both axes after reshaping $\mathbf{A}^T\mathbf{y}$ to the original image dimension, $n_1 \times n_2$. Hereafter, similar to Section V-D1, learning-aided CS recovery can be fulfilled by solving the following weighted TV minimization problem:

$$\min_{\mathbf{S}} \lambda \|\mathbf{W} \odot \nabla \mathbf{S}\|_{\mathrm{TV}} + \|\mathbf{y} - \mathbf{A}\mathrm{vec}(\mathbf{S})\|_2^2 \tag{20}$$

where

$$\|\mathbf{W} \odot \nabla \mathbf{S}\|_{\mathrm{TV}} = \|\mathbf{W_h} \odot \nabla_{\mathbf{h}}\mathbf{S}\|_1 + \|\mathbf{W_v} \odot \nabla_{\mathbf{v}}\mathbf{S}\|_1 \tag{21}$$

and $\mathbf{W_h}$ and $\mathbf{W_v}$ are calculated by using the outputs of CSENs $\mathbf{p_h}$ and $\mathbf{p_v}$, respectively i.e., $\mathbf{W_h} = (1/(\mathbf{p_h} + \boldsymbol{\epsilon}))$ and $\mathbf{W_v} = (1/(\mathbf{p_v} + \boldsymbol{\epsilon}))$.

In order to solve (20), the same solver can be utilized with the one that is used to solve (17) by only changing the soft-thresholding to the weighted soft-thresholding in the algorithm. In this manner, we use TVAL3 for both problems with the following parameter setup: $\mu = 2^{13}, \beta = 2^6$, $\mu_0 = 2^2, 2^{-2}$, tol $= 10^{-6}$, and maxit $= 300$.

In order to estimate p-maps, CSEN1 network was trained. The training dataset is prepared in the following manner: 89272 image patches of size 256 × 256 were randomly cropped from the DIV2K image dataset [67]. During data generation, data augmentation was applied to original DIV2K images with eight different rotations and three different scaling factors. The generated image patches are normalized to have values in [0, 1]-scale. We applied gradient operation to each patch; then, ground-truth support sets were obtained by defining a small threshold to the gradients, i.e., $\Lambda_{GT} = \{i, j \in \{1, 2, \ldots, n_1\} \times \{1, 2, \ldots, n_2\} : |\nabla S_{i,j}| > \tau_1\}$. We set $\tau_1 = 0.04$ and $n_1 = n_2 = 256$. Input images were first applied to CS, $\mathbf{y} = \mathbf{A}vec(\mathbf{S})$; then, proxies are obtained from CS images. Finally, the absolutes of the proxies are given as input and CSEN1 were trained to learn mapping to binary mask **v** [defined in (7a) and (7b)]. During training, the batch size was chosen as 8, and CSEN was trained with 100 epoch. The learning rate was set to be 0.001 for the first 50 epochs, and then, it was scheduled to be 0.0001 and 0.00001 for the following 30 and 20 epochs, respectively. To calculate the cost matrices, $\mathbf{W}$, ϵ is set to be 0.2.

Since applying the Gaussian random measurement matrix, **A**, to large-scale signals of size $n = \times 256$ is computationally infeasible, we applied structural measurement matrix. The rows of the measurement matrix can be chosen from a subset of the randomly permuted rows of a basis for which a computationally fast implementation is feasible. We used the Walsh Hadamard transform whose fast implementation is available in the TVAL3 toolbox. By using such a structural **A**, the computational complexity of matrix multiplications, e.g., **As** and $\mathbf{A}^T\mathbf{y}$, can be reduced to $O(n \log n)$ from $O(m \times n)$ compared to using fully random matrices.

In the experimental setup, we tested the possibility to have an improvement in CR recovery with such a learned-aided weighted total variation minimization. The test is conducted on the Set5 [68] image dataset and Barbara and Cameraman images. All the images were resized to be 256 × 256 size. Along with the PSNR performance metric, the relative error performance metric that was used in the TVAL3 study was also used during the test. The performance metric relative error is calculated as Relative Error $= (\|\mathbf{S} - \hat{\mathbf{S}}\|_F / \|\mathbf{S}\|_F)$, where $\hat{\mathbf{S}}$ is the estimated image and $\|.\|_F$ is the Frobenius norm. Table V shows the performance comparison of traditional TV minimization and CSEN-aided one. On average, the learning-aided

TABLE V
CS RECOVERY PERFORMANCE OF TV-BASED ALGORITHMS (MR = 0.6)

	TVAL		TVAL + CSEN			
			Epoch 50		Epoch 100	
	PSNR	Relative Error	PSNR	Relative Error	PSNR	Relative Error
Cameraman	35.06	0.034	38.20	0.023	36.97	0.027
Barbara	22.84	0.142	22.56	0.1467	23.33	0.134
Set 5	33.08	0.060	33.73	0.053	33.84	0.0523

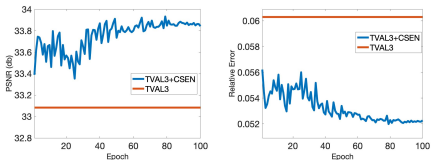

Fig. 15. Performance metrics on the SET 5 image dataset for conventional total variations minimization versus CSEN-aided one. Both techniques use a TVAL3 solver to solve the problem. The results also show when the CSEN trained with 50 epochs and 100 epochs and MR = 0.6.

scheme increases the recovery performance in the Set5 dataset compared to the conventional one and for Barbara and Cameraman Images. To further investigate whether this performance improvement is gained due to arbitrary changes in the threshold values caused by the usage of weighted soft thresholding instead of using soft thresholding, we repeated the same CS recovery tests by using the CSEN1 weights learned with the different number of epochs from 1 to 100. Fig. 15 shows the behavior of the recovery performance of the CSEN-aided solver and the conventional one. The results illustrate that, when CSEN is trained more, the recovery performance of the algorithm increases until convergences. This behavior proves that CSEN output, $(\mathbf{p_h}, \mathbf{p_v})$, carries information (more activation on nonzero values, e.g., edges and boundaries) to be used in model-based recovery algorithm, TV minimization in that specific case, and the quality of this output determines the image recovery quality.

All in all, this proof-of-the-concept study illustrates that the proposed learned-aided CS recovery scheme has the potential to help model-based solutions for CS imaging systems and worth further investigation.

VI. DISCUSSION

A. Sparse Modeling Versus Structural Sparse Modeling

The first generation CS-recovery or sparse representation methods only use the information that the signal, which we encounter in real life, is sparse in a proper domain or dictionary. These models do not utilize any further assumptions about the sparse signal, $\mathbf{x}$, in SR or SE. Therefore, they only impose sparsity to the signal to have support set with elements in arbitrary location, i.e., $\min \|\mathbf{x}\|_0$ s.t. $\mathbf{Dx} = \mathbf{y}$. However, most sparse signals that we face in practical applications exhibit a kind of structure. In second-generation sparse representation models, researchers realized that, in addition to arbitrary sparsity, any prior information about the sparse code can be used in modeling more advanced recovery schemes [69], [70]. For instance, the indices of the nonzero wavelet coefficients of an image mostly exhibit grouping effect [71]. This kind of group sparsity pattern can be imposed by designing the optimization problem involving mixed norm minimization problems [72] instead of simple ℓ_1-norm. On the other hand, more complex sparsity structures require a more complex model design.

This work proposes an alternative solution to the hand-crafted model-based sparse SR approaches, to be able to learn the pattern inside sparse code (or structural sparse signals), $\mathbf{x}$ by a machine learning technique. This proof of the concept work in which the performance is tested over three real datasets, MNIST, Yale, and CelebA, validates the possibility of such learning and deserves further investigation in different sparse representation problems.

B. Unrolling Deep Models Versus CSEN

The most common approaches to reconstruct sparse signals, $\mathbf{x}$, from the given measurements, $\mathbf{y}$, with a fixed dictionary $\mathbf{D}$ can be listed as follows.

1) *Convex Relaxation (or ℓ_1 Minimization) Such as Basis Pursuit [29]:* $\min_{\mathbf{x}} \|\mathbf{x}\|$ s.t. $\mathbf{y} = \mathbf{Dx}$ or BPDN [29]: $\min_{\mathbf{x}} \|\mathbf{x}\|$ s.t. $\|\mathbf{y} - \mathbf{Dx}\| \leq \epsilon$, where ϵ is a small constant.
2) Greedy algorithms such as matching pursuit (MP) [73], orthogonal MP (OMP) [8], and compressive sampling matched pursuit (CoSaMP) [9].
3) Bayesian framework [74].

These conventional algorithms dealing with sparse inverse problems work in an iterative manner; for instance, most convex relaxation techniques, such as BPDN, minimize the data fidelity term (e.g., ℓ_2-norm) and sparsifying term (e.g., ℓ_1-norm) in an alternating manner in each iteration. Therefore, these schemes suffer from computational complexity and not suitable for real-time applications.

Along with the traditional approaches listed above, deep learning methods used in this domain have recently become very popular: $\hat{\mathbf{x}} \leftarrow \mathcal{P}(\mathbf{y})$, where $\mathcal{P}$ is a learned mapping from m-dimensional compressed domain to n-dimensional sparse domain. These techniques are built on the idea that the performance of existing convex relaxation can further be improved by reducing the number of iterations and enhancing the reconstruction accuracy. The key idea is that both the possible denoiser matrices, $\mathbf{B}$ (responsible for dealing with data fidelity term), such as $\mathbf{D}^T$, or $(\mathbf{D}^T\mathbf{D} + \lambda\mathbf{I})^{-1}\mathbf{D}^T$, where λ is the regularization parameter, and the thresholding values (responsible from sparsifying) can be learned from the training data using a deep network generally with dense layers. For instance, the first example of this type is LISTA [20], which is built upon ISTA [21]. These categories of methods, also called unrolled deep models, design networks in an iterative manner, which are powerful tools for sparse SR.

However, in many practical applications, we may either no need to estimate the sparse signal itself or not have a large amount of training data for deep unrolling networks. In that manner, CSEN provides a third approach, by directly estimating the support set via a compact design, which requires less computational power, memory, and training set. It exhibits very good performance, especially in the problems that include sparse representation with sparse codes having

TABLE VI
1-D VERSUS 2-D CSENS IN THE CELEBA DATASET

MR=0.25 (CelebA)	1-D CSEN1	1-D CSEN2	2-D CSEN1	2-D CSEN2
Accuracy	0.776	0.776	0.777	0.777

structural patterns. The other advantage of the compact design with convolutional layers is that it is more stable against noise compared to unrolled deep models that include dense layers.

C. Proxy Signal Versus Measurement Vector as Input to CSEN

The proposed SE scheme utilizes proxy $\tilde{\mathbf{x}} = \mathbf{By}$ as input to convolutional layers. Making inference directly on proxy using the ML approach has been recently reported by several studies. For example, the study in [75] and [76] proposed to perform reconstruction-free image classification on the proxy, and the study in [77] performed signal reconstruction using proxy as an input to a deep fully convolutional network. Furthermore, proxy $\tilde{\mathbf{x}}$ can be learned by fully connected dense layers as presented in [75]. However, this brings additional complexity, and training the network may cause overfitting with a limited number of training data. As in [75], they had to adapt by first training the fully connected layers or try to freeze the other layers during the training.

On the other hand, choosing the denoiser matrix, $\mathbf{B}$, is another design problem. For example, Değerli *et al.* [75] and Lohit *et al.* [76] use $\mathbf{B} = \mathbf{D^T}$ as denoiser to obtain proxy. We reported the results in this article for denoiser matrix, $\mathbf{B} = (\mathbf{D}^T\mathbf{D} + \lambda\mathbf{I})^{-1}\mathbf{D}^T$, because it gives slightly more stable performance over $\mathbf{B}$.

D. 1-D Versus 2-D Representation of the Proxy Signal

In order to use the same CSEN networks, we reshaped the 1-D sparse codes into 2-D for representation-based classification tasks. Nevertheless, a 1-D CNN network structure can also be used. To test this claim, we created 1-D CNN versions of CSEN 1 and CSEN2 networks (the same number of hidden layers, nodes, and kernel sizes). In the CelebA dataset, they were tested, and as it can be seen in Table VI, 1-D versions can also achieve very similar classification performance.

E. Equal Size Dictionary Versus Equal Size Training Samples

In a representation-based classification scheme when dictionary size getting bigger (when the number of training samples is increased), the computational complexity of the method drastically increases. For instance, for the COVID-19 dataset, dictionary size reaches 512×9320; in that case, even CRC computational time drastically increases. Fortunately, the computational time of CSEN does not increase that much because only a subset of the training set is used in the dictionary i.e., 512×3200 and the rest to train CSEN. This phenomenon can be seen in Table VII. On the other hand, the recognition performance does not necessarily improve with increased dictionary size; on the contrary, it may even start deteriorating when the dictionary size reaches an impracticable level. SRC is computationally heavier when the dictionary size increases, the computational complexity becomes cumbersome, and the recognition performance does not necessarily increase. Furthermore, SRC can completely fail when the representation is not sparse enough, e.g., binary classification (see Table IV). On the other hand, the proposed SE-based classifiers perform very stable for both multiclass or binary classification problems and varying sizes of training datasets.

TABLE VII
COMPUTATION TIMES (S) OF EACH METHOD OVER 1257 TEST IMAGES IN THE COVID-19 DATASET

	CRC (light)	CRC	CSEN1	CSEN2	ReconNet	MLP
Computation Time (in sec.)	14.9806	40.3234	0.2439	0.2681	0.3393	0.2848

In the representation-based classification experimental results, the dictionary sizes are always higher than the dictionary size in the CSEN-based scheme, as mentioned above. The other fair comparison is using the same dictionaries for all competing methods. For COVID-19 recognition experiments, as computational times are reported in Table VII, the number of parameters of the networks is given in Table S4 in the Supplementary Material. The CRC algorithm's performance when the dictionary is the same as the one used in the CSEN-C approach is reported in Table S5 in the Supplementary Material. For face recognition, task performance versus computational time is reported in Figs. S2 and S3 in the Supplementary Material. CSEN-C has clear advantages compared to other dictionary-based classifiers by reducing computation complexity and increasing classification accuracy.

VII. CONCLUSION

Sparse support estimators that work based on traditional sparse SR techniques suffer from computational complexity and noise. Moreover, they tend to fail at low MRs completely. The proposed CSENs can be considered as reconstruction-free and noniterative support estimators. Of course, despite their high computational complexity, recent state-of-the-art deep signal reconstruction algorithms may be a cure to sparse recovery methods. However, they are still redundant if SR is not the main concern. In addition, such deep networks often require a large amount of training data that are not available in many practical applications. To address these drawbacks and limitations, in this study, we introduce novel learning-based support estimators that have compact network designs. The highlights of the proposed system are as follows: 1) signal reconstruction-free SE where sparse estimation can be done in a feed-forward manner, noniteratively at a low cost; 2) compact network designs enabling efficient learning even from a small-size training set; and 3) the proposed solution is generic; it could be used in any SE task, such as SE-based classification.

REFERENCES

[1] D. L. Donoho, "Compressed sensing," *IEEE Trans. Inf. Theory*, vol. 52, no. 4, pp. 1289–1306, Apr. 2006.
[2] E. J. Candès *et al.*, "Compressive sampling," in *Proc. Int. Congr. Mathematicians*, vol. 3, 2006, pp. 1433–1452.
[3] G. Li, Z. Zhu, D. Yang, L. Chang, and H. Bai, "On projection matrix optimization for compressive sensing systems," *IEEE Trans. Signal Process.*, vol. 61, no. 11, pp. 2887–2898, Jun. 2013.
[4] M. Elad, *Sparse and Redundant Representations: From Theory to Applications in Signal and Image Processing*. New York, NY, USA: Springer, 2010.

[5] W. Wang, M. J. Wainwright, and K. Ramchandran, "Information-theoretic limits on sparse support recovery: Dense versus sparse measurements," in *Proc. IEEE Int. Symp. Inf. Theory*, Jul. 2008, pp. 2197–2201.

[6] J. Haupt and R. Baraniuk, "Robust support recovery using sparse compressive sensing matrices," in *Proc. 45th Annu. Conf. Inf. Sci. Syst.*, Mar. 2011, pp. 1–6.

[7] G. Reeves and M. Gastpar, "Sampling bounds for sparse support recovery in the presence of noise," in *Proc. IEEE Int. Symp. Inf. Theory*, Jul. 2008, pp. 2187–2191.

[8] J. A. Tropp and A. C. Gilbert, "Signal recovery from random measurements via orthogonal matching pursuit," *IEEE Trans. Inf. Theory*, vol. 53, no. 12, pp. 4655–4666, Dec. 2007.

[9] D. Needell and J. A. Tropp, "CoSaMP: Iterative signal recovery from incomplete and inaccurate samples," *Appl. Comput. Harmon. Anal.*, vol. 26, no. 3, pp. 301–321, May 2009.

[10] J. Scarlett and V. Cevher, "Limits on support recovery with probabilistic models: An information-theoretic framework," *IEEE Trans. Inf. Theory*, vol. 63, no. 1, pp. 593–620, Jan. 2017.

[11] J. Wright, Y. Ma, J. Mairal, G. Sapiro, T. S. Huang, and S. Yan, "Sparse representation for computer vision and pattern recognition," *Proc. IEEE*, vol. 98, no. 6, pp. 1031–1044, Jun. 2010.

[12] J. Wright, A. Y. Yang, A. Ganesh, S. S. Sastry, and Y. Ma, "Robust face recognition via sparse representation," *IEEE Trans. Pattern Anal. Mach. Intell.*, vol. 31, no. 2, pp. 210–227, Feb. 2009.

[13] B. Khalfi, B. Hamdaoui, M. Guizani, and N. Zorba, "Efficient spectrum availability information recovery for wideband DSA networks: A weighted compressive sampling approach," *IEEE Trans. Wireless Commun.*, vol. 17, no. 4, pp. 2162–2172, Apr. 2018.

[14] B. Hamdaoui, B. Khalfi, and M. Guizani, "Compressed wideband spectrum sensing: Concept, challenges, and enablers," *IEEE Commun. Mag.*, vol. 56, no. 4, pp. 136–141, Apr. 2018.

[15] A. C. Gurbuz, J. H. McClellan, and W. R. Scott, "A compressive sensing data acquisition and imaging method for stepped frequency GPRs," *IEEE Trans. Signal Process.*, vol. 57, no. 7, pp. 2640–2650, Jul. 2009.

[16] J. Long, E. Shelhamer, and T. Darrell, "Fully convolutional networks for semantic segmentation," in *Proc. IEEE Conf. Comput. Vis. Pattern Recognit. (CVPR)*, Jun. 2015, pp. 3431–3440.

[17] K. Kulkarni, S. Lohit, P. Turaga, R. Kerviche, and A. Ashok, "ReconNet: Non-iterative reconstruction of images from compressively sensed measurements," in *Proc. IEEE Conf. Comput. Vis. Pattern Recognit. (CVPR)*, Jun. 2016, pp. 449–458.

[18] M. Borgerding, P. Schniter, and S. Rangan, "AMP-inspired deep networks for sparse linear inverse problems," *IEEE Trans. Signal Process.*, vol. 65, no. 16, pp. 4293–4308, Aug. 2017.

[19] D. L. Donoho, A. Maleki, and A. Montanari, "Message-passing algorithms for compressed sensing," *Proc. Nat. Acad. Sci. USA*, vol. 106, no. 45, pp. 18914–18919, Nov. 2009.

[20] K. Gregor and Y. LeCun, "Learning fast approximations of sparse coding," in *Proc. 27th Int. Conf. Int. Conf. Mach. Learn. (ICML)*, Haifa, Israel. Madison, WI, USA: Omnipress, 2010, pp. 399–406.

[21] A. Chambolle, R. A. De Vore, N.-Y. Lee, and B. J. Lucier, "Nonlinear wavelet image processing: Variational problems, compression, and noise removal through wavelet shrinkage," *IEEE Trans. Image Process.*, vol. 7, no. 3, pp. 319–335, Mar. 1998.

[22] A. S. Georghiades, P. N. Belhumeur, and D. J. Kriegman, "From few to many: Illumination cone models for face recognition under variable lighting and pose," *IEEE Trans. Pattern Anal. Mach. Intell.*, vol. 23, no. 6, pp. 643–660, Jun. 2001.

[23] Z. Liu, P. Luo, X. Wang, and X. Tang, "Deep learning face attributes in the wild," in *Proc. IEEE Int. Conf. Comput. Vis. (ICCV)*, Dec. 2015, pp. 3730–3738.

[24] L. Zhang, M. Yang, and X. Feng, "Sparse representation or collaborative representation: Which helps face recognition?" in *Proc. Int. Conf. Comput. Vis.*, Nov. 2011, pp. 471–478.

[25] M. Yamac, M. Ahishali, A. Degerli, S. Kiranyaz, M. E. H. Chowdhury, and M. Gabbouj, "Convolutional sparse support estimator based covid-19 recognition from X-ray images," 2020, *arXiv:2005.04014*. [Online]. Available: http://arxiv.org/abs/2005.04014

[26] O. D. Escoda, L. Granai, and P. Vandergheynst, "On the use of *a priori* information for sparse signal approximations," *IEEE Trans. Signal Process.*, vol. 54, no. 9, pp. 3468–3482, Sep. 2006.

[27] N. Vaswani and J. Zhan, "Recursive recovery of sparse signal sequences from compressive measurements: A review," *IEEE Trans. Signal Process.*, vol. 64, no. 13, pp. 3523–3549, Jul. 2016.

[28] D. L. Donoho and M. Elad, "Optimally sparse representation in general (nonorthogonal) dictionaries via ℓ_1 minimization," *Proc. Nat. Acad. Sci. USA*, vol. 100, no. 5, pp. 2197–2202, Mar. 2003.

[29] S. S. Chen, D. L. Donoho, and M. A. Saunders, "Atomic decomposition by basis pursuit," *SIAM Rev.*, vol. 43, no. 1, pp. 129–159, Jan. 2001.

[30] E. J. Candès, "The restricted isometry property and its implications for compressed sensing," *Comp. Rendus Mathematique*, vol. 346, nos. 9–10, pp. 589–592, May 2008.

[31] E. Candes and T. Tao, "The Dantzig selector: Statistical estimation when p is much larger than n," *Ann. Statist.*, vol. 35, no. 6, pp. 2313–2351, Dec. 2007.

[32] E. J. Candès, J. K. Romberg, and T. Tao, "Stable signal recovery from incomplete and inaccurate measurements," *Commun. Pure Appl. Math.*, vol. 59, no. 8, pp. 1207–1223, 2006.

[33] Y. C. Eldar and G. Kutyniok, *Compressed Sensing: Theory and Applications*. Cambridge, U.K.: Cambridge Univ. Press, 2012.

[34] M. S. Asif and J. Romberg, "On the lasso and dantzig selector equivalence," in *Proc. 44th Annu. Conf. Inf. Sci. Syst. (CISS)*, 2010, pp. 1–6.

[35] R. Tibshirani, "Regression shrinkage and selection via the lasso," *J. Roy. Stat. Soc. B, Methodol.*, vol. 58, no. 1, pp. 267–288, Jan. 1996.

[36] E. J. Candes and Y. Plan, "A probabilistic and RIPless theory of compressed sensing," *IEEE Trans. Inf. Theory*, vol. 57, no. 11, pp. 7235–7254, Nov. 2011.

[37] N. Durgin *et al.*, "Compressed anomaly detection with multiple mixed observations," in *Research in Data Science*. Cham, Switzerland: Springer, 2019, pp. 211–237.

[38] M. Yamacc, B. Sankur, and A. T. Cemgil, "Malicious users discrimination in organizec attacks using structured sparsity," in *Proc. 25th Eur. Signal Process. Conf. (EUSIPCO)*, Aug. 2017, pp. 266–270.

[39] B. Shim and B. Song, "Multiuser detection via compressive sensing," *IEEE Commun. Lett.*, vol. 16, no. 7, pp. 972–974, Jul. 2012.

[40] O. O. Oyerinde, "Multiuser detector for uplink grant free NOMA systems based on modified subspace pursuit algorithm," in *Proc. 12th Int. Conf. Signal Process. Commun. Syst. (ICSPCS)*, Dec. 2018, pp. 1–6.

[41] B. Wang, L. Dai, Y. Zhang, T. Mir, and J. Li, "Dynamic compressive sensing-based multi-user detection for uplink grant-free NOMA," *IEEE Commun. Lett.*, vol. 20, no. 11, pp. 2320–2323, Nov. 2016.

[42] M. Yamaç, M. Orhan, B. Sankur, A. S. Turk, and M. Gabbouj, "Through the wall target detection/monitoring from compressively sensed signals via structural sparsity," in *Proc. 5th Int. Workshop Compressed Sens. Appl. Radar, Multimodal Sensing, Imag.*, 2018, pp. 1–5.

[43] K. R. Rad, "Nearly sharp sufficient conditions on exact sparsity pattern recovery," *IEEE Trans. Inf. Theory*, vol. 57, no. 7, pp. 4672–4679, Jul. 2011.

[44] M. Wainwright, "Information-theoretic bounds on sparsity recovery in the high-dimensional and noisy setting," in *Proc. IEEE Int. Symp. Inf. Theory*, Jun. 2007, pp. 961–965.

[45] G. Reeves and M. C. Gastpar, "Approximate sparsity pattern recovery: Information-theoretic lower bounds," *IEEE Trans. Inf. Theory*, vol. 59, no. 6, pp. 3451–3465, Jun. 2013.

[46] E. J. Candès and Y. Plan, "Near-ideal model selection by ℓ_1 minimization," *Ann. Statist.*, vol. 37, no. 5A, pp. 2145–2177, Oct. 2009.

[47] T. T. Cai and L. Wang, "Orthogonal matching pursuit for sparse signal recovery with noise," *IEEE Trans. Inf. Theory*, vol. 57, no. 7, pp. 4680–4688, 2011.

[48] G. Reeves and M. Gastpar, "The sampling rate-distortion tradeoff for sparsity pattern recovery in compressed sensing," *IEEE Trans. Inf. Theory*, vol. 58, no. 5, pp. 3065–3092, May 2012.

[49] A. K. Fletcher, S. Rangan, and V. K. Goyal, "Necessary and sufficient conditions for sparsity pattern recovery," *IEEE Trans. Inf. Theory*, vol. 55, no. 12, pp. 5758–5772, Dec. 2009.

[50] T. Guha and R. K. Ward, "Learning sparse representations for human action recognition," *IEEE Trans. Pattern Anal. Mach. Intell.*, vol. 34, no. 8, pp. 1576–1588, Aug. 2012.

[51] W. Li and Q. Du, "A survey on representation-based classification and detection in hyperspectral remote sensing imagery," *Pattern Recognit. Lett.*, vol. 83, pp. 115–123, Nov. 2016.

[52] N. Vaswani and W. Lu, "Modified-CS: Modifying compressive sensing for problems with partially known support," *IEEE Trans. Signal Process.*, vol. 58, no. 9, pp. 4595–4607, Sep. 2010.

[53] E. Candès and J. Romberg, "Sparsity and incoherence in compressive sampling," *Inverse Problems*, vol. 23, no. 3, p. 969, 2007.

[54] D. Donoho and J. Tanner, "Observed universality of phase transitions in high-dimensional geometry, with implications for modern data analysis and signal processing," *Phil. Trans. Roy. Soc. A, Math., Phys. Eng. Sci.*, vol. 367, no. 1906, pp. 4273–4293, Nov. 2009.

[55] A. Y. Yang, Z. Zhou, A. G. Balasubramanian, S. S. Sastry, and Y. Ma, "Fast ℓ_1-minimization algorithms for robust face recognition," *IEEE Trans. Image Process.*, vol. 22, no. 8, pp. 3234–3246, May 2013.

[56] M. Abadi *et al.*, "TensorFlow: Large-scale machine learning on heterogeneous distributed systems," 2016, *arXiv:1603.04467*. [Online]. Available: http://arxiv.org/abs/1603.04467

[57] D. P. Kingma and J. Ba, "Adam: A method for stochastic optimization," 2014, *arXiv:1412.6980*. [Online]. Available: http://arxiv.org/abs/1412.6980

[58] D. E. King, "Dlib-ml: A machine learning toolkit," *J. Mach. Learn. Res.*, vol. 10, pp. 1755–1758, Jan. 2009.
[59] S. Boyd, "Distributed optimization and statistical learning via the alternating direction method of multipliers," *Found. Trends Mach. Learn.*, vol. 3, no. 1, pp. 1–122, 2010.
[60] D. M. Malioutov, M. Cetin, and A. S. Willsky, "Homotopy continuation for sparse signal representation," in *Proc. IEEE Int. Conf. Acoust., Speech, Signal Process. (ICASSP)*, vol. 5, Mar. 2005, pp. 5–733.
[61] M. A. T. Figueiredo, R. D. Nowak, and S. J. Wright, "Gradient projection for sparse reconstruction: Application to compressed sensing and other inverse problems," *IEEE J. Sel. Topics Signal Process.*, vol. 1, no. 4, pp. 586–597, Dec. 2007.
[62] K. Koh, S.-J. Kim, and S. Boyd, "An interior-point method for large-scale ℓ_1-regularized logistic regression," *J. Mach. Learn. Res.*, vol. 8, pp. 1519–1555, Jul. 2007.
[63] E. Candes and J. Romberg. (2005). *L1-Magic: Recovery of Sparse Signals via Convex Programming*. [Online]. Available: http://www.acm.caltech.edu/l1magic/downloads/l1magic.pdf
[64] P. Mooney. (2018). *Chest X-Ray Images (Pneumonia)*. Kaggle, Marzo. [Online]. Available: https://www.kaggle.com/paultimothymooney/chest-xray-pneumonia
[65] P. Rajpurkar *et al.*, "CheXNet: Radiologist-level pneumonia detection on chest X-rays with deep learning," 2017, *arXiv:1711.05225*. [Online]. Available: http://arxiv.org/abs/1711.05225
[66] C. Li, W. Yin, H. Jiang, and Y. Zhang, "An efficient augmented lagrangian method with applications to total variation minimization," *Comput. Optim. Appl.*, vol. 56, no. 3, pp. 507–530, Dec. 2013.
[67] E. Agustsson and R. Timofte, "NTIRE 2017 challenge on single image super-resolution: Dataset and study," in *Proc. IEEE Conf. Comput. Vis. Pattern Recognit. Workshops (CVPRW)*, Jul. 2017, pp. 126–135.
[68] M. Bevilacqua, A. Roumy, C. Guillemot, and M.-L. A. Morel, "Low-complexity single-image super-resolution based on nonnegative neighbor embedding," in *Proc. Brit. Mach. Vis. Conf.*, R. Bowden, J. Collomosse, and K. Mikolajczyk, Eds. BMVA Press, 2012, pp. 135.1–135.10, doi: 10.5244/C.26.135.
[69] G. Yu, G. Sapiro, and S. Mallat, "Solving inverse problems with piecewise linear estimators: From Gaussian mixture models to structured sparsity," *IEEE Trans. Image Process.*, vol. 21, no. 5, pp. 2481–2499, May 2012.
[70] R. G. Baraniuk, V. Cevher, M. F. Duarte, and C. Hegde, "Model-based compressive sensing," *IEEE Trans. Inf. Theory*, vol. 56, no. 4, pp. 1982–2001, Apr. 2010.
[71] D. Donoho and G. Kutyniok, "Microlocal analysis of the geometric separation problem," *Commun. Pure Appl. Math.*, vol. 66, no. 1, pp. 1–47, Jan. 2013.
[72] M. Kowalski and B. Torrésani, "Structured sparsity: From mixed norms to structured shrinkage," in *Proc. Signal Process. Adapt. Sparse Structured Represent. (SPARS)*, 2009, pp. 1–6.
[73] S. G. Mallat and Z. Zhang, "Matching pursuits with time-frequency dictionaries," *IEEE Trans. Signal Process.*, vol. 41, no. 12, pp. 3397–3415, Dec. 1993.
[74] S. Ji, Y. Xue, and L. Carin, "Bayesian compressive sensing," *IEEE Trans. Signal Process.*, vol. 56, no. 6, p. 2346, May 2008.
[75] A. Değerli, S. Aslan, M. Yamac, B. Sankur, and M. Gabbouj, "Compressively sensed image recognition," in *Proc. 7th Eur. Workshop Vis. Inf. Process. (EUVIP)*, Nov. 2018, pp. 1–6.
[76] S. Lohit, K. Kulkarni, and P. Turaga, "Direct inference on compressive measurements using convolutional neural networks," in *Proc. IEEE Int. Conf. Image Process. (ICIP)*, Sep. 2016, pp. 1913–1917.
[77] A. Mousavi and R. G. Baraniuk, "Learning to invert: Signal recovery via deep convolutional networks," in *Proc. IEEE Int. Conf. Acoust., Speech Signal Process. (ICASSP)*, Mar. 2017, pp. 2272–2276.

Mehmet Yamaç received the B.S. degree in electrical and electronics engineering from Anadolu University, Eskişehir, Turkey, in 2009, and the M.S. degree in electrical and electronics engineering from Boğaziçi University, Istanbul, Turkey, in 2014. He is currently pursuing the Ph.D. degree with the Department of Computing Sciences, Tampere University, Tampere, Finland.

He was a Research and Teaching Assistant with Boğaziçi University from 2012 to 2017 and a Researcher with Tampere University from 2017 to 2020. He is currently a Senior Researcher with Huawei Technologies Oy, Tampere. He has coauthored the papers nominated for the "Best Paper Award" or the "Student Best Paper Award" in European Workshop on Visual Information Processing (EUVIP) 2018 and European Signal Processing Conference (EUSIPCO) 2019. His research interests are computer and machine vision, machine learning, and compressive sensing.

Mete Ahishali received the B.Sc. degree (Hons.) in electrical and electronics engineering from the İzmir University of Economics, İzmir, Turkey, in 2017, and the M.Sc. degree (Hons.) in data engineering and machine learning from Tampere University, Tampere, Finland, in 2019, where he is currently pursuing the Ph.D. degree in computing and electrical engineering.

Since 2017, he has been a Researcher with the Signal Analysis and Machine Intelligence Research Group, Tampere University, under the supervision of Prof. Gabbouj. His research interests are pattern recognition, machine learning, and semantic segmentation with applications in computer vision, remote sensing, and biomedical images.

Serkan Kiranyaz (Senior Member, IEEE) is currently a Professor with Qatar University, Doha, Qatar. He has coauthored the papers that have nominated or received the "Best Paper Award" in IEEE International Conference on Image Processing (ICIP) 2013, International Conference on Pattern Recognition (ICPR) 2014, ICIP 2015, and IEEE TRANSACTIONS ON SIGNAL PROCESSING (TSP) 2018. He had the Most Popular Articles in the years 2010 and 2016 and the Most Cited Article in 2018 in IEEE TRANSACTIONS ON BIOMEDICAL ENGINEERING. From 2010 to 2015, he authored the fourth most-cited article of the *Neural Networks* journal. His theoretical contributions to advance the current state of the art in modeling and representation, targeting high long-term impact, while algorithmic, system-level design, and implementation issues target medium and long-term challenges for the next five to ten years. He, in particular, aims at investigating scientific questions and inventing cutting-edge solutions in "personalized biomedicine," which is in one of the most dynamic areas where science combines with technology to produce efficient signal and information processing systems. He published two books, five book chapters, more than 80 journal articles in high-impact journals, and 100 articles in international conferences. He made contributions to evolutionary optimization, machine learning, biosignal analysis, computer vision with applications to recognition, classification, and signal processing.

Dr. Kiranyaz's research team has won the second and first places in PhysioNet Grand Challenges 2016 and 2017, among 48 and 75 international teams, respectively. In 2019, he won the "Research Excellence Award" and the "Merit Award" of Qatar University.

Moncef Gabbouj (Fellow, IEEE) received the M.S. and Ph.D. degrees in electrical engineering from Purdue University, West Lafayette, IN, USA, in 1986 and 1989, respectively.

He was the Academy of Finland Professor from 2011 to 2015. He is currently a Professor of signal processing with the Department of Computing Sciences, Tampere University, Tampere, Finland. His research interests include big data analytics, multimedia content-based analysis, indexing and retrieval, artificial intelligence, machine learning, pattern recognition, nonlinear signal and image processing and analysis, voice conversion, and video processing and coding.

Dr. Gabbouj is also a member of the Academia Europaea and the Finnish Academy of Science and Letters. He has served as associate editor and a guest editor of many IEEE and international journals and the General Chair of two IEEE Signal Processing Society (SPS) and IEEE Circuits and Systems Society (CAS) Flagship conferences: IEEE International Conference on Image Processing (ICIP) and IEEE International Symposium on Circuits and Systems (ISCAS).

Convolutional Sparse Support Estimator Network (CSEN) *From energy efficient support estimation to learning-aided Compressive Sensing*: (supplemental document)

MEHMET YAMAÇ[1], METE AHISHALI[1], SERKAN KIRANYAZ[2], AND MONCEF GABBOUJ[1]

[1] *Tampere University, Faculty of Information Technology and Communication Sciences, Tampere, Finland*
[2] *Department of Electrical Engineering, Qatar University, Qatar*

This supplementary material presents additional information, tables and figures that may be useful for interested users.

1. INTRODUCTION

For convenience, we show the list of frequently used variables, and abbreviations in Table S2 and Table S1, respectively.

Table S1. Frequently used acronyms/abbreviations in the article.

SC	Sparse Representation or Sparse Coding
CS	Compressive Sensing
SR	Sparse Signal Recovery
SE	Sparse Support Estimation
SRC	Sparse Signal Recovery based Classification
CRC	Collaborative Representation based Classification
CSEN	Convolutional Support Estimator Network
LISTA	Learned Iterative Short Thresholding Algorithm
LAMP	Learned Approximate Message Passing Algorithm
CSEN-C	CSEN based Classification

2. RESULTS

This section includes the details and more experimental results for the Result section of the main article. For convenience, the organization scheme of the Experimental Section is given in Table S3.

A. End-to-end training of CSEN-C

Figure S1 shows the overall pipeline of the proposed end-to-end training of a convolutions support estimator-based classifier.

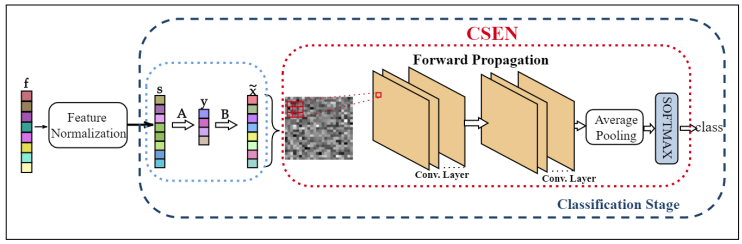

Fig. S1. End to end learning pipeline of CSEN based classifier (CSEN-C).

B. Equal size dictionary vs Equal Size Training Samples

Table S5 shows the recognition performance of CRC on the COVID-19 recognition task when the same dictionary that is used in CSEN-C. It may be the baseline for the proposed CSEN-C, as the classification is done using the same proxy. The computational complexity of this light CRC is reported in the main article. Similar experiments where both SRC and CRC use the same dictionary with CSEN-C were also conducted for the face recognition problems, and the performance vs. computational complexity graphs are reported in Figure S2 and Figure S3.

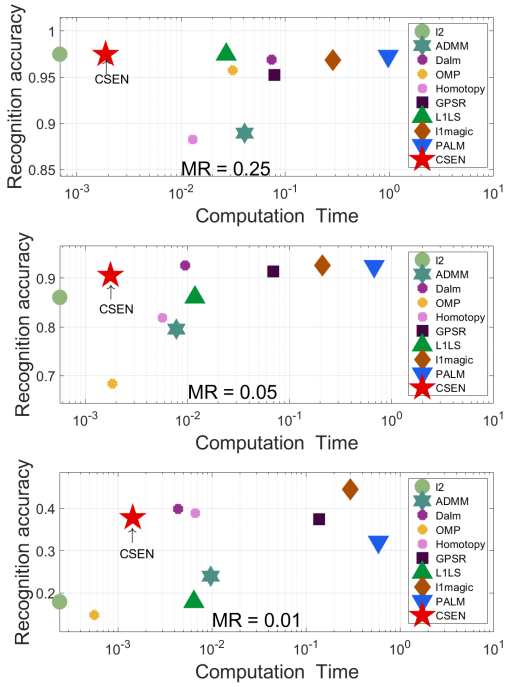

Fig. S2. Recognition accuracy vs. process time comparison of Algorithms using equal size dictionary with the training samples in Yale-B database.

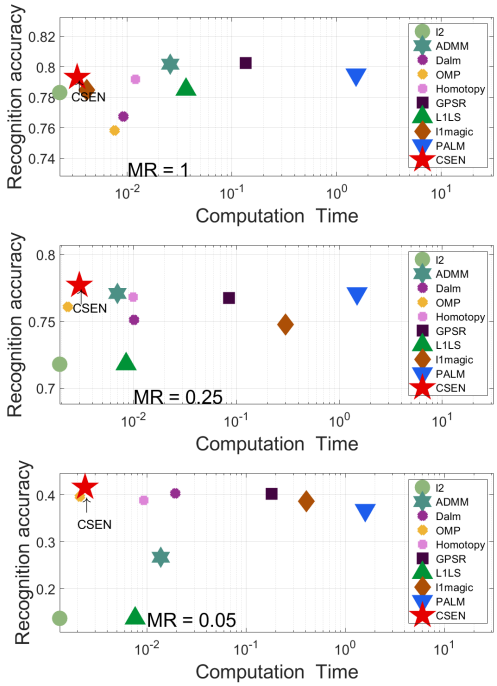

Fig. S3. Recognition accuracy vs. process time comparison of Algorithms using equal size dictionary with the training samples in CelebA database.

Table S2. Frequently used variables in the article.

Variable	Synonyms	Properties
$\mathbf{s} \in \mathbb{R}^d$	Signal	Sparse in $\mathbf{\Phi}$
$\mathbf{\Phi} \in \mathbb{R}^{d \times n}$	Sparsifying matrix (basis or dictionary)	
$\mathbf{x} \in \mathbb{R}^n$	Sparse coefficients of $\mathbf{s}$, the sparse code	i.e., $\|\mathbf{x}\|_0 \leq k$ for k-sparse signal
$\mathbf{A} \in \mathbb{R}^{m \times d}$	CS-measurement or compression matrix	$\mathbf{D} = \mathbf{A\Phi}$
Λ	Location index set of the non zero elements	$\Lambda \subset \{1, ..., n\}$
$\mathbf{y} \in \mathbb{R}^m$	Measurement vector	$\mathbf{y} = \mathbf{Dx} + \mathbf{z}$
$\mathbf{z} \in \mathbb{R}^m$	Possible additive noise	
$\mathcal{E}(.,.)$	A support Estimator	i.e., $\hat{\Lambda} = \mathcal{E}(\mathbf{y}, \mathbf{D})$
$\mathbf{B}$	Denoiser Matrix	e.g.,$\mathbf{B} = \left(\mathbf{D}^T\mathbf{D} + \lambda\mathbf{I}\right)^{-1}\mathbf{D}^T$ or$\mathbf{B} = \mathbf{D^T}$
$\tilde{\mathbf{x}}$	Proxy of the sparse coefficient vector	i.e., $\tilde{\mathbf{x}} = \mathbf{By}$
$\mathbf{X} \in \mathbb{R}^{n_1 \times n_2}$	Re-shaped (on 2-D plane) sparse code	i.e., $\mathbf{x} = vec(\mathbf{X}) \in \mathbb{R}^{n=n_1 \times n_2}$
$\mathbf{X} \in \mathbb{R}^{n_1 \times n_2}$	Re-shaped proxy	i.e., $\tilde{\mathbf{x}} = vec\left(\widetilde{\mathbf{X}}\right) \in \mathbb{R}^{n=n_1 \times n_2}$
$\mathbf{S} \in \mathbb{R}^{n_1 \times n_2}$	GT image (e.g. 2D signal)	
$\mathbf{X_h}$	The gradient of noisy free image on the horizontal axis	$\nabla_{\mathbf{h}}\mathbf{S} = \mathbf{X_h}$
$\mathbf{X_v}$	The gradient of noisy free image on the vertical axis	$\nabla_{\mathbf{v}}\mathbf{S} = \mathbf{X_v}$
$\widetilde{\mathbf{X_h}}$	The proximal of $\mathbf{X_h}$	
$\widetilde{\mathbf{X_v}}$	The proximal of $\mathbf{X_v}$	
$(\mathbf{p_h}, \mathbf{p_v})$	p-map, CSEN output when 2 channel input $\left(\widetilde{\mathbf{X_h}}, \widetilde{\mathbf{X_v}}\right)$ is given	i.e., $(\mathbf{p_h}, \mathbf{p_v}) = \mathcal{P}_\Theta\left(\widetilde{\mathbf{X_h}}, \widetilde{\mathbf{X_v}}\right)$

Table S3. The organization of the experiments: List of applications, experiments and used datasets in the article.

	Experiments			Datasets
Prof of the concept	Generic SE from CS measurements		Experiment I	MNIST
Application I	CSEN-C	Multiclass Classification	Dictionary consists of raw data (Experiment II-a)	Yale-B
			Dictionary consist of discriminative features (Experiment II-b)	Celeb-A
		Binary Classification	Dictionary consist of discriminative features (Experiment III)	QataCov-19
Application II	CSEN aided SR from CS measurements		Experiment IV: Signal is sparse in canonical domain, i.e., $\mathbf{\Phi} = \mathbf{I}$	MNIST
			Experiment V: Signal is sparse in a proper domain, e.g., $\mathbf{\Phi} = \nabla$	Set5, Barbara Cameraman

Table S4. Comparison of the number of trainable parameters in the networks.

Method	CSEN1	CSEN2	ReconNet	MLP
Parameters	11.089	16.297	22.914	672.706

Table S5. Performance of CRC algorithm when the dictionary is same with the one used in CSEN approach.

CRC (Light)								
Accuracy	TN	TP	FP	FN	Sensitivity	Specificity	F1-Score	F2-Score
0.9570	5578	438	246	24	0.9481	0.9578	0.7644	0.8649

PUBLICATION
II

Convolutional Sparse Support Estimator-Based COVID-19 Recognition From X-Ray Images

M. Yamaç, M. Ahishali, A. Degerli, S. Kiranyaz, M. E. H. Chowdhury, and M. Gabbouj

IEEE Transactions on Neural Networks and Learning Systems, vol. 32, no. 5, pp. 1810–1820
DOI: 10.1109/TNNLS.2021.3070467

Convolutional Sparse Support Estimator-Based COVID-19 Recognition From X-Ray Images

Mehmet Yamaç, Mete Ahishali, Aysen Degerli, Serkan Kiranyaz, *Senior Member, IEEE*, Muhammad E. H. Chowdhury, *Senior Member, IEEE*, and Moncef Gabbouj, *Fellow, IEEE*

***Abstract*— Coronavirus disease (COVID-19) has been the main agenda of the whole world ever since it came into sight. X-ray imaging is a common and easily accessible tool that has great potential for COVID-19 diagnosis and prognosis. Deep learning techniques can generally provide state-of-the-art performance in many classification tasks when trained properly over large data sets. However, data scarcity can be a crucial obstacle when using them for COVID-19 detection. Alternative approaches such as representation-based classification [collaborative or sparse representation (SR)] might provide satisfactory performance with limited size data sets, but they generally fall short in performance or speed compared to the neural network (NN)-based methods. To address this deficiency, convolution support estimation network (CSEN) has recently been proposed as a bridge between representation-based and NN approaches by providing a noniterative real-time mapping from query sample to ideally SR coefficient support, which is critical information for class decision in representation-based techniques. The main premises of this study can be summarized as follows: 1) A benchmark X-ray data set, namely QaTa-Cov19, containing over 6200 X-ray images is created. The data set covering 462 X-ray images from COVID-19 patients along with three other classes; bacterial pneumonia, viral pneumonia, and normal. 2) The proposed CSEN-based classification scheme equipped with feature extraction from state-of-the-art deep NN solution for X-ray images, CheXNet, achieves over 98% sensitivity and over 95% specificity for COVID-19 recognition directly from raw X-ray images when the average performance of 5-fold cross validation over QaTa-Cov19 data set is calculated. 3) Having such an elegant COVID-19 assistive diagnosis performance, this study further provides evidence that COVID-19 induces a unique pattern in X-rays that can be discriminated with high accuracy.**

***Index Terms*— Coronavirus disease (COVID-19) recognition, representation-based classification, severe acute respiratory syndrome coronavirus 2 (SARS-CoV-2) virus, transfer learning.**

I. Introduction

CORONAVIRUS disease 2019 (COVID-19) has been declared as a pandemic by the World Health Organization (WHO) a few months after its first appearance. It has infected more than 70 million people, caused a few million causalities, and has so far paralyzed mobility all around the world. The spreading rate of COVID-19 is so high that the number of cases is expected to be doubled every three days if the social distancing is not strictly observed to slow this accretion [1]. Roughly around half of the COVID-19 positive patients also exhibit a comorbidity [2], making it difficult to differentiate COVID-19 from other lung diseases. Automated and accurate COVID-19 diagnosis is critical for both saving lives and preventing its rapid spread in the community. Currently, reverse transcription-polymerase chain reaction (RT-PCR) and computed tomography (CT) are the common diagnostic techniques used today. RT-PCR results are ready at the earliest 24 h for critical cases and generally take several days to conclude a decision [3]. CT may be an alternative at initial presentation; however, it is expensive and not easily accessible [4]. The most common tool that medical experts use for both diagnostic and monitoring the course of the disease is X-ray imaging. Compared to RT-PCR or CT test, having an X-ray image is an extremely low cost and a fast process, usually taking only a few seconds. Recently, WHO reported that even RT-PCR may give false results in COVID-19 cases due to several reasons such as poor quality specimen from the patient, inappropriate processing of the specimen, taking the specimen at an early or late stage of the disease [5]. For this reason, X-ray imaging has a great potential to be an alternative technological tool to be used along with the other tests for an accurate diagnosis.

In this study, we aim to differentiate X-ray images of COVID-19 patients among other classes; bacterial pneumonia, viral pneumonia, and normal. For this work, a benchmark COVID-19 X-ray data set, Qata-Cov19 (**Qa**tar University and **Ta**mpere University **COVID-19** Data set) that contains 462 X-ray images from COVID-19 patients was collected. The images in the data set are different in quality, resolution, and SNR levels as shown in Fig. 1. QaTa-Cov19 also contains many X-ray images from the COVID-19 patients who are in the early stages; therefore, their X-ray images show mild or no-sign of COVID-19 infestation by the naked eye.[1] Some sample images are shown in Fig. 2(b). Another fact that makes the diagnosis far more challenging is that interclass similarity can be very high for many X-ray images as some samples are shown in Fig. 2(a). Against such high interclass similarities and intraclass variations, in this study, we aim for a high robustness level.

In numerous classification tasks, deep learning techniques have been shown to achieve state-of-the-art performance in

Manuscript received May 7, 2020; revised October 9, 2020 and December 21, 2020; accepted March 23, 2021. Date of publication April 19, 2021; date of current version May 3, 2021. *(Corresponding author: Mehmet Yamaç.)*

Mehmet Yamaç, Mete Ahishali, Aysen Degerli, and Moncef Gabbouj are with the Faculty of Information Technology and Communication Sciences, Tampere University, 33720 Tampere, Finland (e-mail: mehmet.yamac@tuni.fi).

Serkan Kiranyaz and Muhammad E. H. Chowdhury are with the Department of Electrical Engineering, Qatar University, Doha 2713, Qatar.

Color versions of one or more figures in this article are available at https://doi.org/10.1109/TNNLS.2021.3070467.

Digital Object Identifier 10.1109/TNNLS.2021.3070467

[1]The statements belong to the medical doctors whose names are listed in the Acknowledgment section.

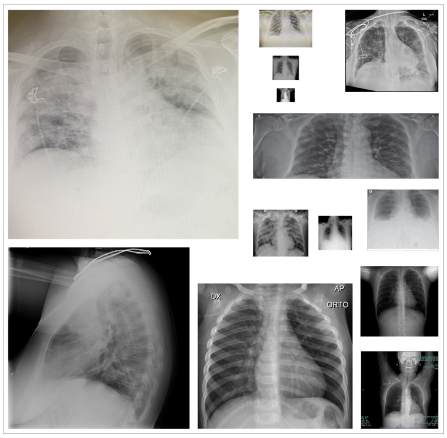

Fig. 1. Sample COVID-19 X-ray images from QaTa-Cov19.

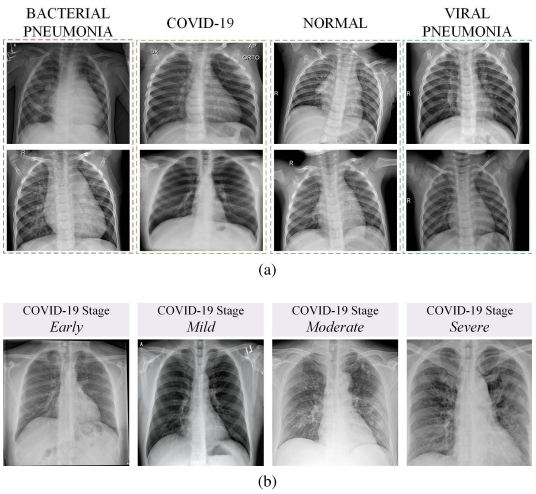

Fig. 2. Sample QaTa-Cov19 X-ray images. (a) X-ray images from different classes. (b) X-ray images from the COVID-19 patients who are in the different stages.

terms of both recognition accuracy and their parallelizable computing structures which play an important role, especially in real-time applications. Despite their advantages, in order to achieve the desired performance level in a deep model, proper training over a massive training data set is usually needed. Nevertheless, this is unfortunately unfeasible for this problem since the available data is still rather limited.

An alternative supervised approach, which requires a limited number of training samples to achieve satisfactory classification accuracy is representation-based classification [6]–[8]. In representation-based classification systems, a dictionary, the columns of which consist of the training samples that are stacked in such a way that a subset of them corresponding to a class, is predefined. A test sample is expected to be a linear combination of all points from the same class as the test sample. Therefore, given a predefined dictionary matrix, $\mathbf{D}$ and a test sample $\mathbf{y}$, we expect the solution $\hat{\mathbf{x}}$ from $\mathbf{y} = \mathbf{D}\mathbf{x}$, carry enough information about the class of $\mathbf{y}$. Overall, in this study, we draw a convolutional support estimation network (CSEN) [9]-based solution pipeline, which fuses the representation-based classification scheme into a neural network (NN) body.

The rest of this article is organized as follows. In Section II, notations and mathematical preliminaries are given with emphasis on sparse representation (SR) and sparse support estimation (SE). Then in Section III, a literature review on deep learning models over X-ray images and representation-based classification is presented. The proposed CSEN-based COVID-19 recognition system is introduced in Section IV along with two recent alternative approaches that are used as the competing methods. The data collection is also explained in this section. Experimental setup and the main results are provided in Section V. Finally, Section VII concludes this article and suggests topics for future research.

II. Preliminaries and Mathematical Notations

A. Notations

In this study, the ℓ_p-norm of a vector $\mathbf{x} \in \mathbb{R}^n$ is defined as $\|\mathbf{x}\|_{\ell_p^n} = \left(\sum_{i=1}^n |x_i|^p\right)^{1/p}$ for $p \geq 1$. On the other hand, the ℓ_0-norm of the vector $\mathbf{x} \in \mathbb{R}^n$ is defined as $\|\mathbf{x}\|_{\ell_0^n} = \lim_{p\to 0} \sum_{i=1}^n |x_i|^p = \#\{j : x_j \neq 0\}$ and the ℓ_∞-norm is defined as $\|\mathbf{x}\|_{\ell_\infty^n} = \max_{i=1,\ldots,n}(|x_i|)$. A signal $\mathbf{s}$ is called strictly k-sparse if $\|\mathbf{x}\|_0 \leq k$. Sparse support set or simply support set, $\Lambda \subset \{1, 2, 3, \ldots, n\}$ of sparse signal $\mathbf{x}$ can be defined as the set of nonzero coefficients' location, i.e., $\Lambda := \{i : x_i \neq 0\}$.

B. Sparse Signal Representation

SR of a signal $\mathbf{s} \in \mathbb{R}^d$ in a predefined set of waveforms, $\mathbf{\Phi} \in \mathbb{R}^{d\times n}$, can be defined as representing $\mathbf{s}$ as a linear combination of only a small subset of atoms in the dictionary $\mathbf{\Phi}$, i.e., $\mathbf{s} = \mathbf{\Phi}\mathbf{x}$. Defining these sets, which dates back to Fourier's pioneering work [10], has been excessively studied in the literature. In the early approaches, these sets of waveforms have been selected as a collection of linearly independent and generally orthogonal waveforms (which are called a complete dictionary or basis, i.e., $d = n$) such as Fourier transform, DCT, and wavelet transform, until the pioneering work of Mallat [11] on overcomplete dictionaries ($n \gg d$). In the last decade, interest in SR research increased tremendously. Their wide range of applications includes denoising [12], classification [13], anomaly detection [14], [15], deep learning [16], and compressive sensing (CS) [17], [18].

With a possible dimensional reduction that can be satisfied via a compression matrix $\mathbf{A} \in \mathbb{R}^{m\times d}$ ($m \ll d$), sample can be obtained from $\mathbf{s}$

$$\mathbf{y} = \mathbf{A}\mathbf{s} = \mathbf{A}\mathbf{\Phi}\mathbf{x} = \mathbf{D}\mathbf{x} \tag{1}$$

where $\mathbf{D} \in \mathbb{R}^{m\times n}$ can be called the equivalent dictionary. Because (1) describes an underdetermined system of linear equations, finding the representation coefficient vector $\mathbf{x}$ requires at least one more constraint to have a unique solution. Using the prior information about sparsity, the following

representation:

$$\min_{\mathbf{x}} \|\mathbf{x}\|_0 \text{ s.t. } \mathbf{D}\mathbf{x} = \mathbf{y} \tag{2}$$

which is also an SR of $\mathbf{x}$ has a unique solution provided that $\mathbf{x}$ is strictly sparse and $\mathbf{D}$ satisfies some required properties [19]. For instance, if $\|\mathbf{x}\|_0 = k$, the minimum number of linearly independent columns of $\mathbf{D}$, spark($\mathbf{D}$), should be greater than 2k, i.e., spark($\mathbf{D}$) $\geq$ 2k in order to not to have $\mathbf{D}\mathbf{x}' = \mathbf{D}\mathbf{x}''$ for distinct k-sparse signals, $\mathbf{x}'$ and $\mathbf{x}''$ [19]. However, the optimization problem in (2) is a NP-hard. Fortunately, the following relaxation:

$$\min_{\mathbf{x}} \|\mathbf{x}\|_1 \text{ s.t. } \mathbf{D}\mathbf{x} = \mathbf{y} \tag{3}$$

produces exactly the same solution as that of (2) provided that $\mathbf{D}$ obeys some criteria: the equivalence of ℓ_0–ℓ_1 minimization problems can be guaranteed when $\mathbf{D}$ satisfies a notation of null space property (NSP) [20], [21] not only for exact sparse signals but approximately sparse signals. Furthermore, the query sample $\mathbf{y}$ can be corrupted with an additive noise pattern. In this case, the equality constraint in (3) can be further relaxed such as in the basis pursuit denoising (BPDN) [22]: $\min_{\mathbf{x}}\|\mathbf{x}\|$ s.t. $\|\mathbf{y} - \mathbf{D}\mathbf{x}\| \leq \epsilon$, where ϵ is a small constant that depends on the noise level. In this case, a stronger property which is known as restricted isometry property (RIP) [23], [24] is frequently used which both cover conditions satisfying exact recovery of BP and stable recovery of BPDN, e.g., exact recovery of $\mathbf{x}$ from (3) is possible when $\mathbf{D}$ has RIP and $m > k(\log(n/k))$.

We may refer to the sparse SE problem as finding the indices a set, Λ, of nonzero elements of $\mathbf{x}$ [25], [26]. Indeed, in many applications, SE can be more important than finding the magnitude and sign of $\mathbf{x}$ as well as Λ, which refers to the sparse signal recovery (SSR) via a recovery technique, such as (3). For example, in a sparse representation-based classification (SRC) system, a query sample $\mathbf{y}$ can be represented with sparse coefficient vector, $\mathbf{x}$, in the dictionary, $\mathbf{D}$ in such a way that when we recover this representation coefficient from $\mathbf{y} = \mathbf{D}\mathbf{x}$, the solution vector $\hat{\mathbf{x}}$ is expected to have a significant number of nonzero coefficients coming from the particular locations corresponding to the class of $\mathbf{y}$.

Readers are referred to [9] for a more detailed literature review on SE and its applications. In the sequel, we briefly summarize the building blocks of the proposed approach.

III. Background and Prior Art

A. CheXNet

In the proposed approach, we first use the pretrained deep network, CheXNet, to extract discriminative features from raw X-ray images. CheXNet was developed for pneumonia detection from the chest X-ray images [27]. In [27], it was claimed that CheXNet can perform even better than expert radiologists in the pneumonia detection problem. This deep NN design is based on the previously proposed DenseNet [28] that consists of 121 layers. It is first pretrained over ImageNet data set [29] and performed transfer learning over 112120 frontal-view chest X-ray images in the ChestX-ray14 data set [30].

B. Representation-Based Classification

Consider we are given a test sample $\mathbf{y}$, which represents either the extracted features, $\mathbf{s}$, or their dimensionally reduced version, i.e., $\mathbf{y} = \mathbf{A}\mathbf{s}$. In developing the dictionary, training samples are stacked in the dictionary $\mathbf{D}$ with particular locations in such a way that the optimal support for a given query $\mathbf{y}$ should be the set of all points coming from the same class as $\mathbf{y}$. Therefore, a solution vector, $\hat{\mathbf{x}}$ of $\mathbf{y} = \mathbf{D}\mathbf{x}$ is supposed to have enough information, i.e., the sparse support should be the set of location indices of the training sample from the same class as $\mathbf{y}$. This strategy is generally known as representation-based classification. However, a typical solution $\hat{\mathbf{x}}$ of $\mathbf{y} = \mathbf{D}\mathbf{x}$ is not necessarily a sparse one especially when its size grows with more training samples, which results in a highly underdetermined system of linear equations. Fortunately, if one estimates the representation coefficient vector with a sparse recovery design such as ℓ_1-minimization as in (3), we can expect that the important nonzero entries of the solution, $\hat{\mathbf{x}}$, are grouped in the particular locations that correspond to the locations of the training samples from the same class as $\mathbf{y}$. This can be a typical example of scenarios where SE can be more valuable than the magnitudes and sign recovery as explained in Section II-B.

For instance, Wright *et al.* [8] proposed a systematic way of determining the identity of face images using ℓ_1-minimization. The authors develop a three-step classification technique that includes: (i) normalization of all the atoms in $\mathbf{D}$ and $\mathbf{y}$ to have unit ℓ_2-norm; (ii) estimating the representation coefficient vector via sparse recovery, i.e., $\hat{\mathbf{x}} = \arg\min_{\mathbf{x}}\|\mathbf{x}\|_1$ s.t.$\|\mathbf{y} - \mathbf{D}\mathbf{x}\|_2$; and (iii) finding the residuals corresponding to each class via $\mathbf{e_i} = \|\mathbf{y} - \mathbf{D_i}\hat{\mathbf{x}}_\mathbf{i}\|_2$, where $\hat{\mathbf{x}}_\mathbf{i}$ is the group of the estimated coefficients, $\hat{\mathbf{x}}$, that correspond to class i.

This technique, which is known as SRC, and its variants have been applied to a wide range of applications in the literature [31], [32], e.g., human action recognition [33], and hyperspectral image classification [34], to name a few. Despite the good recognition accuracy performance of SRC systems, their main drawbacks is the fact that their sparse recovery algorithms (e.g., ℓ_1-minimization) are iterative methods and computationally costly, rendering them infeasible in real-time applications. Later, the authors of [6] introduced collaborative representation-based classification (CRC), which is similar to SRC except for the use of traditional ℓ_2-minimization in the second step; $\hat{\mathbf{x}} = \arg\min_{\mathbf{x}}\{\|\mathbf{y} - \mathbf{D}\mathbf{x}\|_2^2 + \lambda\|\mathbf{x}\|_2^2\}$. Thus, CRC does not require an iterative solution to obtain representation coefficient thanks to that ℓ_2-minimization has a closed form solution, $\hat{\mathbf{x}} = \left(\mathbf{D}^{\mathrm{T}}\mathbf{D} + \lambda\mathbf{I}_{n\times n}\right)^{-1}\mathbf{D}^{\mathrm{T}}\mathbf{y}$. Although, the sparsity in $\hat{\mathbf{x}}$ cannot be guaranteed, it has often been reported to achieve a comparable classification performance, especially in small-size training data sets.

IV. Proposed Approach

For a computer-aided COVID-19 recognition system design, our primary objective is to achieve the highest sensitivity possible in the diagnosis of COVID-19 induced pneumonia with an acceptable false-alarm rate (e.g., specificity > 95%). In particular, the misdiagnosis of a COVID-19 X-ray image

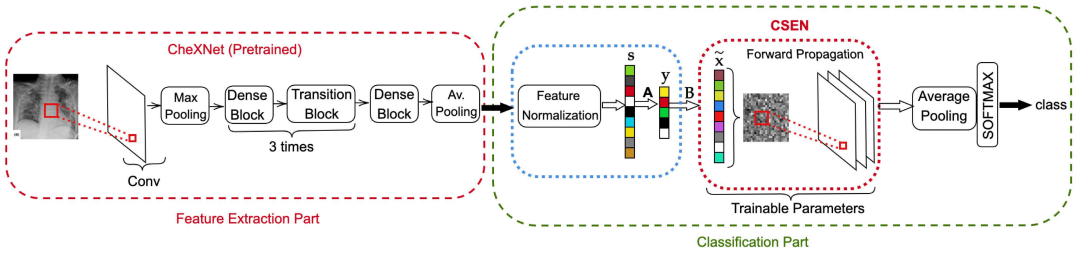

Fig. 3. Proposed approach for Covid recognition from X-ray images. The proposed convolution support estimator network (CSEN) which can be trained from a moderate size training set. The pipeline employs the pretrained deep NN for feature extraction. $\mathbf{A}$ is the dimensional reduction (PCA) matrix, the coarse estimation of representation coefficient (sparse in ideal case), $\hat{\mathbf{x}}$ is obtained via the denoiser matrix, $\mathbf{B} = \left(\mathbf{D}^T\mathbf{D} + \lambda\mathbf{I}\right)^{-1}\mathbf{D}^T$, where $\mathbf{D} = \mathbf{A}\Phi$ and Φ is the predefined dictionary matrix of training samples (before dimensional reduction).

as a normal case should be minimized whilst a small number of false negatives (FNs) is tolerable.

Our interest in representation-based classification is that they perform well in classification tasks even in the cases where training data is scarce. As mentioned, the two well-known representation-based classification methodologies are SRC [7] and CRC [6]. Among them, SRC provides slightly improved accuracy by solving an SR problem, i.e., producing a sparse solution $\hat{\mathbf{x}}$ from $\mathbf{y} = \mathbf{D}\mathbf{x}$. Then, the location of the nonzero elements of $\hat{\mathbf{x}}$, which is also known as support set, provides the class information of the query $\mathbf{y}$. Despite improved recognition accuracy, SRC solutions are iterative solutions and can be computationally demanding compared to CRC. In a recent work [9], a compact NN design that can be considered as a bridge between NN-based and representation-based methodologies was proposed. The so-called CSEN uses a predefined dictionary and learns a direct mapping using moderate/low size training set, which maps query samples, $\mathbf{y}$, directly to the support set of representation coefficients, $\mathbf{x}$ (as it should be purely sparse in the ideal case).

In this study, to address the data scarcity limitations in COVID-19 diagnosis from X-ray images we propose a CSEN-based approach. Since a relatively larger set of COVID-19 X-ray images ever compiled is used in this study, the proposed approach can be evaluated rigorously against a high level of diversity to obtain a reliable analysis. The general pipeline of the proposed CSEN-based recognition scheme is illustrated in Fig. 3. In order to obtain highly discriminative features, we use the recently proposed CheXNet [27], which is the fine-tuned version of 121 layer Dense Convolutional Network (DenseNet-121) [28] by using over 100 000 frontal view X-ray images form 14 classes. Having the pretrained CheXNet for feature extraction, we develop two different strategies to obtain the classes of query X-ray images: 1) using CRC with proper preprocessing; 2) a slightly modified version of our recently proposed convolution support estimator (CSEN) models. In the sequel, both techniques will be explained in detail as well as alternative solutions.

A. Benchmark Data Set: QaTa-Cov19

Accordingly, there are several recent works [35]–[38] that have been proposed for COVID-19 detection/classification from X-ray images. However, they use a rather small data set (the largest containing only a few hundreds of X-ray images), with only a few COVID-19 samples. This makes it difficult to generalize their results in practice. To address this deficiency and provide reliable results, in this study the researchers of **Qa**tar University and **Ta**mpere University have compiled a bechmark **Cov**id-**19** data set, called QaTa-Cov19. Compared to the earlier benchmark data set created in this domain, such as COVID Chestxray Data set [39] or COVID-19 DATA SET [40], QaTa-Cov19 has the following unique benchmarking properties. First, it is a larger data set, not only in terms of the number of images (more than 6200 images) but its versatility, i.e., QaTa-Cov19 contains additional major pneumonia categories, such as viral and bacterial, along with the control (normal) class. Moreover, this is a diverse data set encapsulating X-ray images from several countries (e.g., Italy, Spain, China, etc.) produced by different X-ray machines.

COVID-19 chest X-ray images were gathered from different publicly available but scattered image sources. However, the major sources of COVID-19 images are Italian Society of Medical and Interventional Radiology (SIRM) COVID-19 Database [40], Radiopaedia [41], Chest Imaging (Spain) at thread reader [42] and online articles and news portals [43]. The authors have carried out the task of collecting and indexing the X-ray images for COVID-19 positive cases reported in the published and preprint articles from China, South Korea, USA, Taiwan, Spain, and Italy, as well as online news-portals (up to 20th April 2020). Therefore, these X-ray images represent different age groups, gender, ethnicity, and country. Negative Covid19 cases were normal, viral, and bacterial pneumonia chest X-ray images and collected from the Kaggle chest X-ray database. Kaggle chest X-ray database contains 5863 chest X-ray images of normal, viral, and bacterial pneumonia with varying resolutions [44]. Out of these 5863 chest X-ray images, 1583 images are normal images and the remaining are bacterial and viral pneumonia images. Sample X-ray images from QaTa-Cov19 data set are shown in Fig. 4.

B. Feature Extraction

With their outstanding performance in image classification along with other inference tasks, deep NNs became a dominant paradigm. However, these techniques usually necessitate a large number of training samples (e.g., several

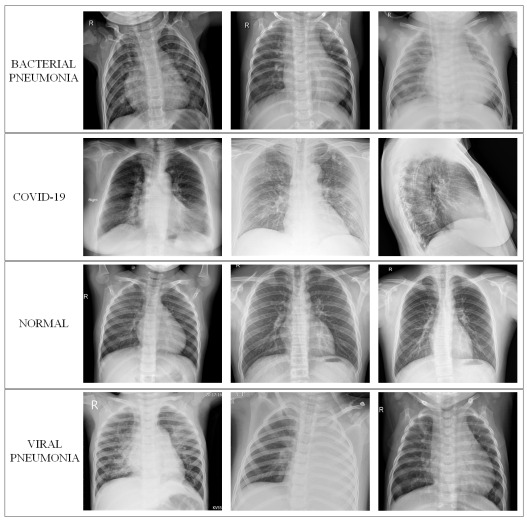

Fig. 4. Samples from the benchmark QU-Chest data set.

hundred-thousand to millions depending on the network size) to achieve an adequate generalization capability. Albeit, we can still leverage their power by finding properly pretrained models for similar problems. To this end, we use a state-of-the-art pneumonia detection network, CheXNet, whose details are summarized in Section III-A. With the pretrained model, we extract 1024-long vectors, right after the last average pooling layer. After data normalization (zero mean and unit variance), we obtain a feature vector $\mathbf{s} \in \mathbb{R}^{d=1024}$.

A dimensionality reduction PCA is applied to $\mathbf{s}$ in order to get the query sample, $\mathbf{y} = \mathbf{A}\mathbf{s} \in \mathbb{R}^m$, where $\mathbf{A} \in \mathbb{R}^{m \times d}$ is PCA matrix ($m < d$).

C. Proposed CSEN-Based Classification

Considering the limited number of training data in our COVID-19 data set, a representation-based classification can be applied hereafter to obtain the class of $\mathbf{y}$ using the dictionary $\mathbf{\Phi}$ (in the form of $\mathbf{D} = \mathbf{A}\Phi$), whose columns are stacked training samples with class-specific locations.

As discussed earlier, SRC is an SE problem which is expected to be an easier task than an SSR problem. On the other hand, even if the exact signal recovery is not possible in noisy cases or in cases where $\hat{\mathbf{x}}$ is not exactly but approximately sparse (which is the case almost all the time in dictionary-based classification problems), it is still possible to recover the support set exactly [25], [38], [45], [46] or partially [46]–[48]. However, many works in the literature dealing with SE problems tend to first apply a sparse recovery technique on $\mathbf{y}$ to first get $\hat{\mathbf{x}}$, then use simple thresholding over $\hat{\mathbf{x}}$ to obtain a sparse SE, $\hat{\Lambda}$. However, SSR techniques such as ℓ_1-minimization are rather slow and their performance varies from one SRR tool to another [9]. In our previous work [9], we proposed an alternative solution for this iterative sparse recovery approach which aims to learn a direct mapping from a test sample $\mathbf{y}$ to the corresponding support set $\hat{\Lambda}$. Along with

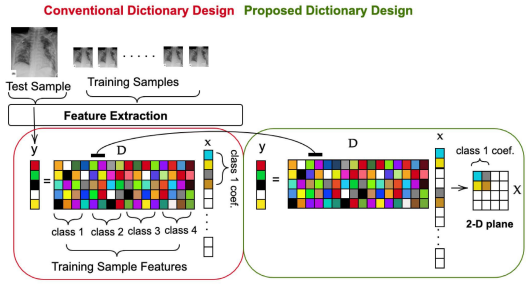

Fig. 5. Illustration of proposed dictionary design versus conventional design in representation-based classifiers.

the speed and stability compared to conventional SSR-based techniques and recent deep learning-based SSR solutions, CSEN has the crucial advantage of having a compact design that can achieve a good performance level even over scarce training data.

Mathematically speaking, an ideal CSEN is supposed to yield a binary mask $\mathbf{v} \in \{0, 1\}^n$

$$v_i = 1 \quad \text{if } i \in \Lambda \tag{4}$$

which indicates the true support, i.e., $\Lambda = \{i \in \{1, 2, \ldots, n\} : v_i = 1\}$. In order to approximate this ideal case, a CSEN network, $\mathcal{P}(\mathbf{y}, \mathbf{D})$ produces a probability vector $\mathbf{p}$ which returns a measure about the probability of each index being in Λ such that $p_i \in [0, 1]$. Having the estimated probability map, estimating the support can easily be done via $\hat{\Lambda} = \{i \in \{1, 2, \ldots, n\} : p_i > \tau\}$, by thresholding $\mathbf{p}$ with τ where τ is a fixed threshold.

A CSEN is composed of fully convolutional layers, and as input it takes a proxy, $\tilde{\mathbf{x}}$, of sparse coefficient vector, which is a coarse estimation of $\mathbf{x}$, i.e., $\left(\mathbf{D}^T\mathbf{D} + \lambda\mathbf{I}\right)^{-1}\mathbf{D}^T\mathbf{y}$ or simply $\tilde{\mathbf{x}} = \mathbf{D}^T\mathbf{y}$. Then, it yields the aforementioned probability like vector $\mathbf{p}$ via fully convolutional layers. Using such a proxy of $\mathbf{x}$, instead of making inference directly on $\mathbf{y}$ has also studied in a few more recent studies. For instance, in [49] and [50], the authors proposed reconstruction-free image classification from compressively sensed images. Alternatively, one may design a network to learn proxy $\tilde{\mathbf{x}}$ by fully connected dense layers [49]. However, it increases the computational complexity and may result in an even over-fitting problem with scarce training data [9].

The input vector $\tilde{\mathbf{x}}$ is reshaped to have a 2-D plane representation in order to use it with 2-D convolutional layers. This transformation is performed via reordering the indices of the atoms in such a way that the nonzero elements of the representation vector $\mathbf{x}$ for a specific class come together in the 2-D plane. A representative illustration of the proposed dictionary design compared to the traditional one is shown in Fig. 5.

Hereafter, the proxy $\tilde{\mathbf{x}}$ is convolved with the weight kernels, connecting the input with the next layer with N_l filters to yield the inputs of the next layer, with the biases $\mathbf{b_1}$ as follows:

$$\mathbf{f_1} = \left\{S_1\left(\mathrm{ReLu}\left(\mathbf{b_1^i} + \mathbf{w_1^i} * \tilde{\mathbf{x}}\right)\right)\right\}_{i=1}^{N_1} \tag{5}$$

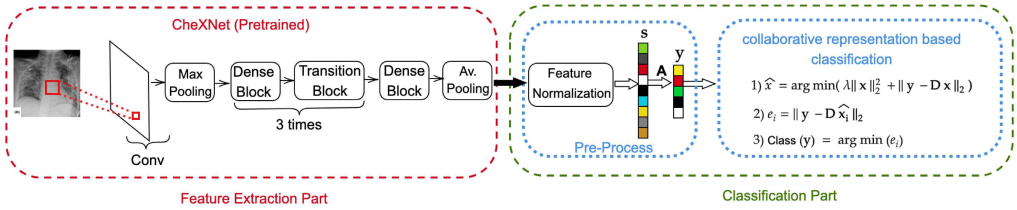

Fig. 6. Baseline Approach I: CRC is fed by deep learning-based extracted features that are preprocessed.

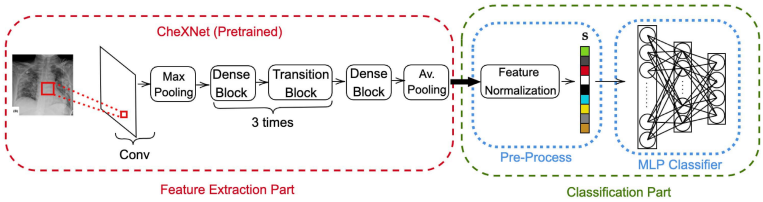

Fig. 7. Baseline Approach II: A 5-layer MLP layer is used over the features of CheXNet.

where $\mathbf{b_1}$ is the weight bias, $S_1(.)$ is either identity or sub-sampling operator predefined according to network structure and $\mathrm{ReLu}(x) = \max(0, x)$. For other layers, i.e., $l > 2$, the kth feature map of layer l is defined as

$$\mathbf{f_l^k} = S_l\left(\mathrm{ReLu}\left(\mathbf{b_l^k} + \sum_i^{N_{l-1}} \mathbf{w_l^{ik}} * \mathbf{f_{l-1}^i}\right)\right) \tag{6}$$

where $S_l(.)$ is either identity operator or one the operations from down- and up-sampling and N_l is the number of feature maps in lth layer. Therefore, the trainable parameters of CSEN will be: $\Theta_{\mathbf{CSEN}} = \left\{\{\mathbf{w}_1^i, \mathbf{b}_1^i\}_{i=1}^{N_1}, \{\mathbf{w}_2^i, \mathbf{b}_2^i\}_{i=1}^{N_2}, \ldots, \{\mathbf{w}_L^i, \mathbf{b}_L^i\}_{i=1}^{N_L}\right\}$ for an L layer CSEN design.

In developing the dictionary that is to be used in the SRC, the training samples are stacked-in by grouping them according to their classes. Thus, instead of using traditional ℓ_1-minimization formulation as in (3), the following group ℓ_1-minimization formulation may result in increased classification accuracy:

$$\min_{\mathbf{x}}\left\{\|\mathbf{Dx} - \mathbf{y}\|_2^2 + \lambda \sum_{i=1}^{c} \|\mathbf{x_{Gi}}\|_2\right\} \tag{7}$$

where $\mathbf{x_{Gi}}$ is the group of coefficients from the ith class. In this manner, one possible cost function for a SE network would be

$$E(\mathbf{x}) = \sum_p (\mathcal{P}_\Theta(\tilde{\mathbf{x}})_p - \upsilon_p)^2 + \lambda \sum_{i=1}^{c} \|\mathcal{P}_\Theta(\tilde{\mathbf{x}})_{Gi}\|_2 \tag{8}$$

where $\mathcal{P}_\Theta(\tilde{\mathbf{x}})_p$ is network output at location p and υ_p is the ground truth binary mask of the sparse code $\mathbf{x}$. Due to its high computational complexity, we approximate the cost function in (8) with a simpler average pooling layer after convolutional layer, which can produce directly the estimated class in our CSEN design. An illustration of proposed CSEN-based COVID-19 recognition is shown in Fig. 3.

D. Competing Methods

This section summarizes the competing methods that are selected among numerous alternatives due to their superior performance levels obtained in similar problems. For fair comparative evaluations, all classification methods have the same input feature vectors fed to the proposed CSENs.

1) Collaborative Representation-Based Classification: As a possible competing technique to the proposed CSEN-based technique which is a hybrid method, CRC [6] is a direct and representation-based classification method that can be applied to this problem as shown in Fig. 6. It is a noniterative SE technique, that satisfies faster and comparable classification performance with SRC while it is more stable compared to existing iterative sparse recovery tools as it is shown in [9]. In the first step of CRC, the tradeoff parameter of the regularized least-square solution is set as $\lambda = 2 * 10^{-12}$. In order to obtain the best possible λ, a grid search was made in the range $[10^{-15}, 10^{-1}]$ with a log scale.

2) Multilayer Perceptron (MLP) Classification: The proposed COVID-19 recognition pipeline can be modified by replacing CSEN or CRC part with another classifier. As one of the most-common classifiers, a 4-hidden layer multilayer perceptron (MLP) is used for this problem as shown in Fig. 7. For training, we used back-propagation (BP) with Adam optimization technique [51]. The network and training hyperparameters are as follows: learning rate, $\alpha = 10^{-4}$, and moment updates $\beta_1 = 0.9$, $\beta_2 = 0.999$, and 50 as the number of epochs. Fig. 8 illustrates the network configuration in detail. This network configuration has achieved the best performance among others (deeper and shallower) where deep configurations have suffered from *over-fitting* while the shallow ones exhibit an inferior learning performance.

3) Support Vector Machines (SVMs): For a multiclass problem, the first objective is to select the SVM topology for ensemble learning: one-versus-one or one-versus-all. In order to find the optimal topology and the hyperparameters (e.g., kernel type and its parameters) we first performed a grid-search with the following variations and setting: kernel function

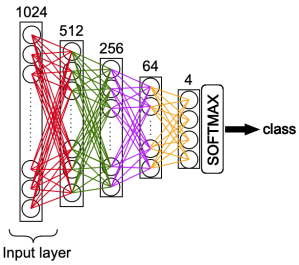

Fig. 8. MLP configuration.

TABLE I

CLASSIFICATION PERFORMANCES OF THE PROPOSED CSEN AND COMPETING METHODS. THE BEST COVID-19 RECOGNITION RATES ARE HIGHLIGHTED

		k-NN	SVM	MLP	CRC	ReconNet	CSEN1	CSEN2
Accuracy	**Bacterial**	0.777	0.780	0.763	0.820	0.765	0.793	0.794
	Viral	0.801	0.787	0.765	0.827	0.785	0.805	0.803
	Normal	0.903	0.934	0.933	0.928	0.918	0.926	0.927
	COVID-19	0.950	0.945	0.949	0.955	0.936	0.955	**0.959**
TN	**Bacterial**	3166	3219	3114	3063	3180	3177	3173
	Viral	4123	3965	3923	4385	4005	4109	4091
	Normal	4253	4444	4442	4380	4364	4388	4396
	COVID-19	5525	5489	5522	5554	5435	5548	**5572**
TP	**Bacterial**	1720	1687	1680	2091	1629	1810	1818
	Viral	909	979	884	816	928	954	959
	Normal	1420	1427	1421	1456	1407	1431	1428
	COVID-19	446	452	444	447	448	**455**	**455**
FP	**Bacterial**	360	307	412	463	346	349	353
	Viral	678	836	878	416	796	692	710
	Normal	454	263	265	327	343	319	311
	COVID-19	299	335	302	270	389	276	**252**
FN	**Bacterial**	1040	1073	1080	669	1131	950	942
	Viral	576	506	601	669	557	531	526
	Normal	159	152	158	123	172	148	151
	COVID-19	16	10	18	15	14	**7**	**7**
Sensitivity	**Bacterial**	0.623	0.611	0.609	0.758	0.590	0.656	0.659
	Viral	0.612	0.660	0.595	0.550	0.625	0.642	0.646
	Normal	0.899	0.904	0.900	0.922	0.891	0.906	0.904
	COVID-19	0.965	0.978	0.961	0.968	0.970	**0.985**	**0.985**
Specificity	**Bacterial**	0.898	0.913	0.883	0.869	0.902	0.901	0.900
	Viral	0.859	0.826	0.817	0.913	0.834	0.856	.852
	Normal	0.904	0.944	0.944	0.931	0.927	0.932	0.934
	COVID-19	0.949	0.943	0.948	0.954	0.933	0.953	**0.957**
F1-score	**Bacterial**	0.711	0.710	0.693	0.787	0.688	0.736	0.737
	Viral	0.592	0.593	0.545	0.601	0.578	0.609	0.608
	Normal	0.823	0.873	0.870	0.866	0.845	0.860	0.861
	COVID-19	0.740	0.724	0.735	0.758	0.690	0.763	**0.778**

{linear, radial basis function (RBF)}, box constraint (C parameter) in the range $[1, 10^3]$ with a log scale, and kernel scale (γ for the RBF kernel) in the range $[10^{-4}, 10^{-2}]$ with a log scale.

4) k-Nearest-Neighbor (k-NN): Finally, we use a traditional approach, k-nearest neighbor (k-NN) is used with PCA dimensionality reduction. In a similar fashion, the distance metric and the k-value are optimized by a prior grid-search. The following distance metrics are evaluated: City-block, Chebyshev, correlation, cosine, Euclidean, Hamming, Jaccard, Mahalanobis, Minkowski, standardized Euclidean, and Spearman metrics. The k-value is varied within the range of $[1, 4416]$ with a log scale.

V. EXPERIMENTAL RESULTS

A. Experimental Setup

We have performed our experiments over the QaTa-Cov19 data set, which consists of normal and three pneumonia classes: bacterial, viral, and COVID-19.

TABLE II

NUMBER OF IMAGES PER CLASS AND PER-FOLD BEFORE AND AFTER DATA AUGMENTATION

Class	# of Samples	Training Samples	Augmented Training Samples	Test Samples
Bacterial Pneumonia	2760	2208	2208	552
Viral Pneumonia	1485	1188	2208	297
Normal	1579	1263	2208	316
COVID-19	462	370	2208	92
Total	6286	5029	8832	1257

The proposed approach is evaluated using a stratified fivefold cross-validation (CV) scheme with a ratio of 80% for training and 20% for the test (unseen folds) splits, respectively.

Table II shows the number of X-ray images per class in the QaTa-Cov19 data set. Since the data set is unbalanced, we have applied data augmentation to the training set in order to balance the size of each class in the train set. Therefore, the X-ray images in viral and COVID-19 pneumonia and normal classes are augmented up to the same number as the bacterial pneumonia class in the train set. We use Image Data Generator by Keras to perform data augmentation by randomly rotating the X-ray images in a range of 10°, randomly shifting images both horizontally and vertically within the interval of $[-0.1, +0.1]$. In each CV fold, we use a total of 8832 and 1257 images in the train and test (unseen in the fold) sets, respectively.

The experimental evaluations of SVM, k-NN, and CRC are performed using MATLAB version 2019a, running on PC with Intel® i7-8650U CPU and 32 GB system memory. On the other hand, MLP and CSEN methods are implemented using Tensorflow library [52] with Python on NVidia® TITAN-X GPU card. For the CSEN training, ADAM optimizer [51] is used with the proposed default learning parameters: learning rate, $\alpha = 10^{-3}$, and moment updates $\beta_1 = 0.9$, $\beta_2 = 0.999$ with only 15 back-propagation epochs. Neither grid-search nor any other parameter or configuration optimization was performed for CSEN.

B. Experimental Results

The same network configurations are used for CSEN as in [9]. Accordingly, we use two compact CSEN designs: CSEN1 and CSEN2, respectively. The first CSEN network consists of only two hidden convolutional layers, the first layer has 48 neurons and the second has 24. ReLu activation function is used in the hidden layers and the filter size was 3×3. On the other hand, CSEN2 uses max-pooling and has one additional hidden layer with 24 neurons to perform transposed-convolution. CSEN1 and CSEN2 are compared against the 6 competing methods under the same experimental setup.

For the dictionary construction in $\mathbf{\Phi}$ each CSEN design, 625 images for each class (from the augmented training samples per fold) are stacked in such way that the representation coefficient in the 2-D plane, $\mathbf{X}$ has 50×50 size as shown in Fig. 5. The rest of the images in the training set are used to train each CSEN, i.e., 1583 samples from each class. We use PCA dimensional reduction matrix, $\mathbf{A}$ with the compression ratio, $\text{CR} = (m/d) = 0.5$. Therefore, we have 512×2500 equivalent

TABLE III
NUMBER OF NETWORK PARAMETERS OF EACH METHOD

	MLP	CSEN1	CSEN2	ReconNet
# of trainable parameters	672,836	11,089	16,297	22,914

dictionary, $\mathbf{D}$, and 2500×512 denoiser $\mathbf{B} = \left(\mathbf{D}^T\mathbf{D} + \lambda\mathbf{I}\right)^{-1}\mathbf{D}^T$ to obtain a coarse estimation of the representation (sparse in the ideal case) coefficients, $\tilde{\mathbf{x}} \in \mathbb{R}^{n=2500}$. Hereafter, the CSEN networks are trained to obtain the class information of $\mathbf{y}$ from input $\tilde{\mathbf{x}}$ as illustrated in Fig. 3.

Due to the lack of other learning-based SE studies in the literature, we chose a deeper network compared to CSEN designs to investigate the role of network depth in this problem. ReconNet [53] was proposed as a noniterative deep learning solution to CS problem, i.e., $\hat{\mathbf{s}} \leftarrow \mathcal{P}(\mathbf{y})$ and it is one of the state of the art in compressively sensed image recognition task. It consists of six fully convolutional layers and one dense layer in front of the convolutional ones, which act as the learned denoiser for the mapping from $\mathbf{y} \in \mathbb{R}^m$ to $\tilde{\mathbf{s}} \in \mathbb{R}^d$. Then, the convolutional layers are responsible for producing the reconstructed signal, $\hat{\mathbf{s}}$ from $\tilde{\mathbf{s}}$. Therefore, by replacing this dense layer with the denoiser matrix $\mathbf{B}$, this network can be used as a competing method.

Both CSEN and the modified ReconNet use $\tilde{\mathbf{x}}$ as an input, which is produced using an equivalent dictionary $\mathbf{D}$ and its pseudo-inverse matrix $\mathbf{B}$.

In designing the dictionary of the CRC system, all training samples are stacked in the dictionary, $\mathbf{\Phi}$, i.e., 2208 samples from each class. The same PCA matrix used in CSEN-based recognition, $\mathbf{A}$ is applied to features, $\mathbf{s} \in \mathbb{R}^{d=1024}$. Therefore, a dictionary $\mathbf{D}$ of size 512×8832 and the corresponding denoiser matrix $\mathbf{B}$ of size 8832×512 are used in the CRC framework.

Overall, the confusion matrix elements are formed as follows: true positive (TP): the number of correctly detected positive class members, true negative (TN): the number of correctly detected negative class samples, false positive (FP): the number of misclassified negative class members as positive, and FN: the number of misclassified positive class samples as negative (i.e., missed positive cases). Then, the standard performance evaluation metrics are defined as follows:

$$\text{Sensitivity} = \frac{\text{TP}}{\text{TP} + \text{FN}} \tag{9}$$

where sensitivity (or Recall) is the rate of correctly detected positive samples in the positive class

$$\text{Specificity} = \frac{\text{TN}}{\text{TN} + \text{FP}} \tag{10}$$

where specificity is the ratio of accurately detected negative class samples to all negative class

$$\text{Precision} = \frac{\text{TP}}{\text{TP} + \text{FP}} \tag{11}$$

where precision is the rate of correctly classified positive class samples among all the members classified as a positive sample

$$\text{Accuracy} = \frac{\text{TP} + \text{TN}}{\text{TN} + \text{TP} + \text{FP} + \text{FN}} \tag{12}$$

TABLE IV
COMPUTATION TIMES (SEC) OF EACH METHOD OVER 1257 TEST IMAGES

	CRC (light)	CRC	CSEN1	CSEN2	ReconNet	MLP
Computation Time (in sec.)	13.4176	40.7878	0.2196	0.2272	0.2993	0.2935

TABLE V
OVERALL (CUMULATIVE) CONFUSION MATRIX OF THE PROPOSED RECOGNITION SCHEME

CSEN2	**Predicted**				
		Bacterial	Viral	Normal	COVID-19
Real	Bacterial	1818	636	180	126
	Viral	338	959	127	61
	Normal	15	71	1428	65
	COVID-19	0	3	4	455

where accuracy is the ratio of correctly classified elements among all the data

$$F(\beta) = \left(1 + \beta^2\right)\frac{(\text{Precision} + \text{Sensitivity})}{\left(\beta^2 * \text{Precision}\right) + \text{Sensitivity}} \tag{13}$$

where F-score is defined by the weighting parameter β. The $F1$-score is calculated with $\beta = 1$, which is the harmonic average of precision and sensitivity.

The classification performance of the proposed CSEN-based approach and the competing methods is presented in Table I. As can be easily observed from Table I, the proposed approaches surpass all competing methods in COVID-19 recognition performance by achieving 98.5% sensitivity, and over 95% specificity. As shown in Table III, compared to MLP and ReconNet, the proposed CSEN designs are very compact and computationally efficient. This is evident in Table IV where the computational complexity (measured as total computation, time over the 1257 test images) is reported.

Finally, Table V presents the overall (cumulative) confusion matrix of the proposed CSEN-based COVID-19 recognition approach over the new QaTa-Cov19 data set. The most critical misclassifications are the false-positives, i.e., the misclassified COVID-19 X-ray images. The confusion matrix shows that the proposed approach has misclassified seven COVID-19 images (out of 462). The 3 out of 7 misclassifications are still in "viral pneumonia" category, which can be an expected confusion due to the viral nature of COVID-19. However, the other four cases are misclassified as "Normal" which is indeed a severe clinical misdiagnosis. A close look at these false-negatives in Fig. 9 reveals the fact that they are indeed very similar to normal images where typical COVID-19 patterns are hardly visible even by an expert's naked eye. It is possible that these images come from patients who were in the very early stages of COVID-19.

VI. DISCUSSION

A. CRC Versus CSEN

When compared against CRC in particular, CSEN-based classification has two advantages; computational efficiency and, a superior COVID-19 recognition performance. The computational efficiency comes from the fact that a larger size dictionary matrix (of the size of 512×8832) is used

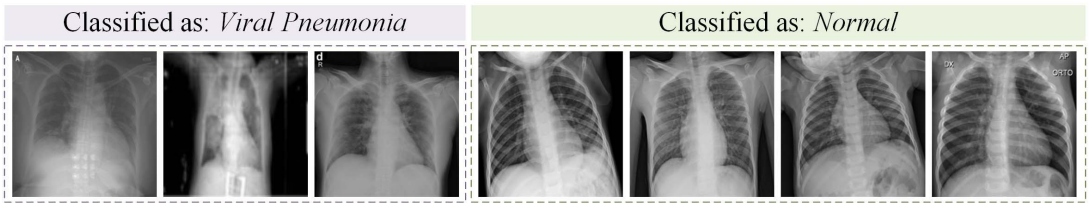

Fig. 9. FNs of the proposed COVID-19 recognition scheme.

TABLE VI

PERFORMANCE OF CRC ALGORITHM WHEN THE DICTIONARY (SIZE OF 625 PER CLASS) THAT IS USED IN CSEN IS USED

	CRC (Light)		
	Accuracy	**Sensitivity**	**Specificity**
Bacterial	0.8129	0.7464	0.8650
Viral	0.8163	0.5461	0.8998
Normal	0.9267	0.9170	0.9299
COVID-19	0.9564	0.9394	0.9578

in CRC and hence, this requires more computations in terms of matrix-vector multiplications. Furthermore, saving the trainable parameters (∼16k) and a light dictionary matrix coefficients (∼1280k) in the test device is more memory efficient compared to saving coefficients (∼4521k) of larger size dictionary used in CRC.

For further analysis, we also tested the CRC framework by using the light dictionary (of size 512×2500) used in CSEN-based recognition. We called it CRC (light), and as it can be seen in Table VI, the performance of CRC further reduced, and there was no significant improvement concerning the computational cost. When it comes to creating deeper convolutional layers instead of using CSEN designs, such as the modified ReconNet, the results presented in Table I shows us that compact CSEN structures are indeed preferable to achieve superior classification performances compared to deeper networks.

B. Compact Versus Deep CSENs

Representation-based classifications are known for providing satisfactory performance when it comes to limited size data sets. On the other hand, deep artificial NNs usually require a large training set to achieve a satisfactory generalization capability.

In a representation-based (dictionary) classification scheme when the dictionary size getting bigger (increase the number of training samples), the computational complexity of the method drastically increases. The proposed CSEN is an alternative approach to handle both moderate and scarce data sets via compact as possible NN structures for the dictionary-based classification.

Since there is no other learning-based SE method except CSEN in the literature, we chose ReconNet as a possible competing algorithm for this problem as explained in detail in Section V. ReconNet has six fully convolution layers. As an ablation study, we also add more hidden layers to proposed CSEN models to compare: CSEN3 and CSEN4 models were obtained by adding one and two hidden layers to CSEN2, respectively, after the transposed convolutional layer.

TABLE VII

PERFORMANCE OF ALTERNATIVE DEEPER DESIGNS COMPARED TO COMPACT CSENS

	Accuracy		Sensitivity		Specificity	
	CSEN3	CSEN4	CSEN3	CSEN4	CSEN3	CSEN4
Bacterial	0.793	0.792	0.651	0.653	0.904	0.900
Viral	0.808	0.805	0.642	0.638	0.859	0.856
Normal	0.922	0.921	0.907	0.899	0.927	0.928
Covid-19	0.954	0.954	0.990	0.987	0.951	0.952

TABLE VIII

NUMBER OF NETWORK PARAMETERS OF COMPETING SE NETWORKS

	CSEN1	CSEN2	CSEN3	ReconNet	CSEN 4
# of trainable parameters	11,089	16,297	21,505	22,914	26,713

Additional layers have 24 neurons, ReLu activation functions and filter size 3×3. As we can observe from Tables VII and VIII, the proposed compact designs, CSEN1 and CSEN2, both surpass deeper counterparts both in performance and the required number of parameters.

VII. CONCLUSION

The commonly used methods in COVID-19 diagnosis, namely RT-PCR and CT have certain limitations and drawbacks such as long processing times and unacceptably high misdiagnosis rates. These drawbacks are also shared by most of the recent works in the literature based on deep learning due to data scarcity from the COVID-19 cases. Although deep learning-based recognition techniques are dominant in computer vision where they achieved state-of-the-art performance, their performance degrades fast due to data scarcity, which is the reality in this problem at hand. This study aims to address such limitations by proposing a robust and highly accurate COVID-19 recognition approach directly from X-ray images. The proposed approach is based on the CSEN that can be seen as a bridge between deep learning models and representation-based methods. CSEN uses both a dictionary and a set of training samples to learn a direct mapping from the query samples to the sparse support set of representation coefficients. With this unique ability and having the advantage of a compact network, the proposed CSEN-based COVID-19 recognition systems surpass the competing methods and achieve over 98% sensitivity and over 95% specificity. Furthermore, they yield the most computationally efficient scheme in terms of speed and memory.

ACKNOWLEDGMENT

The authors would like to thank the following medical doctor team for their generous feedbacks and continuous

proof reading: Khalid Hameed is a MD in Reem Medical Center, Doha, Qatar. Tahir Hamid is consultant cardiologist in Hamad Medical Corporation Hospital and with Weill Cornell Medicine-Qatar, Doha. Rashid Mazhar is a MD in Hamad Medical Corporation Hospital, Doha, Qatar.

REFERENCES

[1] L. Pellis *et al.*, "Challenges in control of COVID-19: Short doubling time and long delay to effect of interventions," 2020, *arXiv:2004.00117*. [Online]. Available: http://arxiv.org/abs/2004.00117

[2] F. Zhou *et al.*, "Clinical course and risk factors for mortality of adult inpatients with COVID-19 in Wuhan, China: A retrospective cohort study," *Lancet*, vol. 395, no. 10229, pp. 1054–1062, Mar. 2020.

[3] Y. Fang *et al.*, "Sensitivity of chest CT for COVID-19: Comparison to RT-PCR," *Radiology*, vol. 296, no. 2, pp. E115–E117, Aug. 2020.

[4] K. A. Erickson, K. Mackenzie, and A. Marshall, "Advanced but expensive technology. Balancing affordability with access in rural areas," *Can. Family Physician Medecin de Famille Canadien*, vol. 39, pp. 28–30, Jan. 1993.

[5] World Health Organization, "Laboratory testing for coronavirus disease (COVID-19) in suspected human cases: Interim guidance," World Health Org., Tech. Rep. WHO/COVID-19/laboratory/2020.5, Mar. 2020.

[6] L. Zhang, M. Yang, and X. Feng, "Sparse representation or collaborative representation: Which helps face recognition?" in *Proc. Int. Conf. Comput. Vis.*, Nov. 2011, pp. 471–478.

[7] J. Wright, A. Y. Yang, A. Ganesh, S. S. Sastry, and Y. Ma, "Robust face recognition via sparse representation," *IEEE Trans. Pattern Anal. Mach. Intell.*, vol. 31, no. 2, pp. 210–227, Feb. 2009.

[8] J. Wright, Y. Ma, J. Mairal, G. Sapiro, T. S. Huang, and S. Yan, "Sparse representation for computer vision and pattern recognition," *Proc. IEEE*, vol. 98, no. 6, pp. 1031–1044, Jun. 2010.

[9] M. Yamac, M. Ahishali, S. Kiranyaz, and M. Gabbouj, "Convolutional sparse support estimator network (CSEN) from energy efficient support estimation to learning-aided compressive sensing," 2020, *arXiv:2003.00768*. [Online]. Available: http://arxiv.org/abs/2003.00768

[10] B. de Fourier and J. B. Joseph, *Théorie Analytique de la Chaleur*. Firmin Didot, 1822.

[11] S. G. Mallat and Z. Zhang, "Matching pursuits with time-frequency dictionaries," *IEEE Trans. Signal Process.*, vol. 41, no. 12, pp. 3397–3415, Dec. 1993.

[12] J.-L. Starck, E. J. Candes, and D. L. Donoho, "The curvelet transform for image denoising," *IEEE Trans. Image Process.*, vol. 11, no. 6, pp. 670–684, Jun. 2002.

[13] J. Yang, K. Yu, Y. Gong, and T. Huang, "Linear spatial pyramid matching using sparse coding for image classification," in *Proc. IEEE Conf. Comput. Vis. Pattern Recognit.*, Jun. 2009, pp. 1794–1801.

[14] A. Adler, M. Elad, Y. Hel-Or, and E. Rivlin, "Sparse coding with anomaly detection," *J. Signal Process. Syst.*, vol. 79, no. 2, pp. 179–188, May 2015.

[15] D. Carrera, G. Boracchi, A. Foi, and B. Wohlberg, "Detecting anomalous structures by convolutional sparse models," in *Proc. Int. Joint Conf. Neural Netw. (IJCNN)*, Jul. 2015, pp. 1–8.

[16] W. Wen, C. Wu, Y. Wang, Y. Chen, and H. Li, "Learning structured sparsity in deep neural networks," in *Adv. neural Inf. Process. Syst.*, 2016, pp. 2074–2082.

[17] D. L. Donoho, "Compressed sensing," *IEEE Trans. Inf. Theory*, vol. 52, no. 4, pp. 1289–1306, Apr. 2006.

[18] E. J. Candès, "Compressive sampling," in *Proc. Int. Congr. Math.*, vol. 3. Madrid, Spain, 2006, pp. 1433–1452.

[19] D. L. Donoho and M. Elad, "Optimally sparse representation in general (nonorthogonal) dictionaries via 1 minimization," *Proc. Nat. Acad. Sci. USA*, vol. 100, no. 5, pp. 2197–2202, Mar. 2003.

[20] A. Cohen, W. Dahmen, and R. DeVore, "Compressed sensing and best K-term approximation," *J. Amer. Math. Soc.*, vol. 22, no. 1, pp. 211–231, 2009.

[21] H. Rauhut, "Compressive sensing and structured random matrices," in *Theoretical Foundations and Numerical Methods for Sparse Recovery* (Radon Series on Computational and Applied Mathematics), vol. 9, M. Fornasier, Ed. deGruyter, 2010, pp. 1–92.

[22] S. S. Chen, D. L. Donoho, and M. A. Saunders, "Atomic decomposition by basis pursuit," *SIAM Rev.*, vol. 43, no. 1, pp. 129–159, Jan. 2001.

[23] E. J. Candès and T. Tao, "Decoding by linear programming," *IEEE Trans. Inf. Theory*, vol. 51, no. 12, pp. 4203–4215, Dec. 2005.

[24] E. J. Candès, "The restricted isometry property and its implications for compressed sensing," *Comp. Rendus Mathematique*, vol. 346, nos. 9–10, pp. 589–592, May 2008.

[25] W. Wang, M. J. Wainwright, and K. Ramchandran, "Information-theoretic limits on sparse support recovery: Dense versus sparse measurements," in *Proc. IEEE Int. Symp. Inf. Theory*, Jul. 2008, pp. 2197–2201.

[26] J. Haupt and R. Baraniuk, "Robust support recovery using sparse compressive sensing matrices," in *Proc. 45th Annu. Conf. Inf. Sci. Syst.*, Mar. 2011, pp. 1–6.

[27] P. Rajpurkar *et al.*, "CheXNet: Radiologist-level pneumonia detection on chest X-rays with deep learning," 2017, *arXiv:1711.05225*. [Online]. Available: http://arxiv.org/abs/1711.05225

[28] G. Huang, Z. Liu, L. Van Der Maaten, and K. Q. Weinberger, "Densely connected convolutional networks," in *Proc. IEEE Conf. Comput. Vis. Pattern Recognit. (CVPR)*, Jul. 2017, pp. 4700–4708.

[29] J. Deng, W. Dong, R. Socher, L.-J. Li, K. Li, and L. Fei-Fei, "ImageNet: A large-scale hierarchical image database," in *Proc. IEEE Conf. Comput. Vis. Pattern Recognit.*, Jun. 2009, pp. 248–255.

[30] X. Wang, Y. Peng, L. Lu, Z. Lu, M. Bagheri, and R. M. Summers, "ChestX-ray8: Hospital-scale chest X-ray database and benchmarks on weakly-supervised classification and localization of common thorax diseases," in *Proc. IEEE Conf. Comput. Vis. Pattern Recognit. (CVPR)*, Jul. 2017, pp. 2097–2106.

[31] S. Shekhar, V. M. Patel, N. M. Nasrabadi, and R. Chellappa, "Joint sparse representation for robust multimodal biometrics recognition," *IEEE Trans. Pattern Anal. Mach. Intell.*, vol. 36, no. 1, pp. 113–126, Jan. 2014.

[32] X. Mei and H. Ling, "Robust visual tracking and vehicle classification via sparse representation," *IEEE Trans. Pattern Anal. Mach. Intell.*, vol. 33, no. 11, pp. 2259–2272, Nov. 2011.

[33] T. Guha and R. K. Ward, "Learning sparse representations for human action recognition," *IEEE Trans. Pattern Anal. Mach. Intell.*, vol. 34, no. 8, pp. 1576–1588, Aug. 2012.

[34] W. Li and Q. Du, "A survey on representation-based classification and detection in hyperspectral remote sensing imagery," *Pattern Recognit. Lett.*, vol. 83, pp. 115–123, Nov. 2016.

[35] M. E. H. Chowdhury *et al.*, "Can AI help in screening viral and COVID-19 pneumonia?" 2020, *arXiv:2003.13145*. [Online]. Available: http://arxiv.org/abs/2003.13145

[36] I. D. Apostolopoulos and T. A. Mpesiana, "Covid-19: Automatic detection from X-ray images utilizing transfer learning with convolutional neural networks," *Phys. Eng. Sci. Med.*, vol. 43, no. 2, pp. 635–640, Jun. 2020.

[37] L. O. Hall, R. Paul, D. B. Goldgof, and G. M. Goldgof, "Finding covid-19 from chest X-rays using deep learning on a small dataset," 2020, *arXiv:2004.02060*. [Online]. Available: http://arxiv.org/abs/2004.02060

[38] M. Wainwright, "Information-theoretic bounds on sparsity recovery in the high-dimensional and noisy setting," in *Proc. IEEE Int. Symp. Inf. Theory*, Jun. 2007, pp. 961–965.

[39] J. P. Cohen, P. Morrison, and L. Dao, "COVID-19 image data collection," 2020, *arXiv:2003.11597*. [Online]. Available: http://arxiv.org/abs/2003.11597

[40] (2020). *COVID-19 database*. [Online]. Available: https: //www.sirm.org/category/senza-categoria/covid-19/

[41] (2020). [Online]. Available: https://radiopaedia.org/playlists/25975?

[42] (2020). [Online]. Available: https://threadreaderapp.com/thread/1243928581983670272.html

[43] J. C. Monteral. (2020). *COVID-Chestxray Database*, [Online]. Available: https://github.com/ieee8023/covid-chestxray-dataset

[44] P. Mooney. (2018). *Chest X-ray Images (Pneumonia)*. kaggle, Marzo. [Online]. Available: https://www.kaggle.com/paultimothymooney/chest-xray-pneumonia

[45] K. Rahnama Rad, "Nearly sharp sufficient conditions on exact sparsity pattern recovery," *IEEE Trans. Inf. Theory*, vol. 57, no. 7, pp. 4672–4679, Jul. 2011.

[46] J. Scarlett and V. Cevher, "Limits on support recovery with probabilistic models: An information-theoretic framework," *IEEE Trans. Inf. Theory*, vol. 63, no. 1, pp. 593–620, Jan. 2017.

[47] G. Reeves and M. Gastpar, "Sampling bounds for sparse support recovery in the presence of noise," in *Proc. IEEE Int. Symp. Inf. Theory*, Jul. 2008, pp. 2187–2191.

[48] G. Reeves and M. C. Gastpar, "Approximate sparsity pattern recovery: Information-theoretic lower bounds," *IEEE Trans. Inf. Theory*, vol. 59, no. 6, pp. 3451–3465, Jun. 2013.

[49] A. Degerli, S. Aslan, M. Yamac, B. Sankur, and M. Gabbouj, "Compressively sensed image recognition," in *Proc. 7th Eur. Workshop Vis. Inf. Process. (EUVIP)*, Nov. 2018, pp. 1–6.
[50] S. Lohit, K. Kulkarni, and P. Turaga, "Direct inference on compressive measurements using convolutional neural networks," in *Proc. IEEE Int. Conf. Image Process. (ICIP)*, Sep. 2016, pp. 1913–1917.
[51] D. P. Kingma and J. Ba, "Adam: A method for stochastic optimization," 2014, *arXiv:1412.6980*. [Online]. Available: http://arxiv.org/abs/1412.6980
[52] M. Abadi *et al.*, "TensorFlow: Large-scale machine learning on heterogeneous distributed systems," 2016, *arXiv:1603.04467*. [Online]. Available: http://arxiv.org/abs/1603.04467
[53] K. Kulkarni, S. Lohit, P. Turaga, R. Kerviche, and A. Ashok, "ReconNet: Non-iterative reconstruction of images from compressively sensed measurements," in *Proc. IEEE Conf. Comput. Vis. Pattern Recognit. (CVPR)*, Jun. 2016, pp. 449–458.

Mehmet Yamaç received the B.S. degree in electrical and electronics engineering from Anadolu University, Eskisehir, Turkey, in 2009, and the M.S. degree in electrical and electronics engineering from Bogazici University, Istanbul, Turkey, in 2014. He is currently pursuing the Ph.D. degree with the Department of Computing Sciences, Tampere University, Tampere, Finland.

He was a Research and Teaching Assistant with Bogazici University from 2012 to 2017 and a Researcher with Tampere University from 2017 to 2020. He is currently working as a Senior Researcher with Huawei Technologies Oy, Helsinki, Finland. He has coauthored the articles nominated for the "Best Paper Award" or the "Student Best Paper Award" in EUVIP 2018 and EUSIPCO 2019. His research interests are computer and machine vision, machine learning, and compressive sensing.

Mete Ahishali received the B.Sc. degree (Hons.) in electrical and electronics engineering from the Izmir University of Economics, Izmir, Turkey, in 2017, and the M.Sc. degree (Hons.) in data engineering and machine learning from Tampere University, Tampere, Finland, in 2019, where he is currently pursuing the Ph.D. degree in computing and electrical engineering.

Since 2017, he has been working as a Researcher with the Signal Analysis and Machine Intelligence Research Group under the supervision of Prof. Gabbouj. His research interests are pattern recognition, machine learning, and semantic segmentation with applications in computer vision, remote sensing, and biomedical images.

Aysen Degerli received the B.Sc. degree (Hons.) in electrical and electronics engineering from the Izmir University of Economics, Izmir, Turkey, in 2017, and the M.Sc. degree (Hons.) in data engineering and machine learning from Tampere University, Tampere, Finland, in 2019, where she is currently pursuing the Ph.D. degree in computing and electrical engineering with the Signal Analysis and Machine Intelligence Research Group led by Prof. M. Gabbouj.

Her research interests include machine learning, compressive sensing, and biomedical image processing.

Serkan Kiranyaz (Senior Member, IEEE) is a Professor with Qatar University, Doha, Qatar. He published two books, five book chapters, more than 80 journal articles in high impact journals, and 100 articles in international conferences. He made contributions on evolutionary optimization, machine learning, bio-signal analysis, computer vision with applications to recognition, classification, and signal processing. He has coauthored the articles which have nominated or received the "Best Paper Award" in ICIP 2013, ICPR 2014, ICIP 2015, and IEEE TRANSACTIONS ON SIGNAL PROCESSING (TSP) 2018. He had the most-popular articles in the years 2010 and 2016, and most-cited article in 2018 in IEEE TRANSACTIONS ON BIOMEDICAL ENGINEERING. From 2010 to 2015, he authored the 4th most-cited article of the *Neural Networks* journal. His research team has won the second and first places in PhysioNet Grand Challenges 2016 and 2017, among 48 and 75 international teams, respectively. His theoretical contributions to advance the current state of the art in modeling and representation, targeting high long-term impact, while algorithmic, system level design and implementation issues target medium and long-term challenges for the next five to ten years. He in particular aims at investigating scientific questions and inventing cutting edge solutions in "personalized biomedicine" which is in one of the most dynamic areas where science combines with technology to produce efficient signal and information processing systems.

Prof. Kiranyaz received the "Research Excellence Award" and the "Merit Award" of Qatar University in 2019.

Muhammad E. H. Chowdhury (Senior Member, IEEE) received the Ph.D. degree from the University of Nottingham, Nottingham, U.K., in 2014.

He worked as a Postdoctoral Research Fellow with the Sir Peter Mansfield Imaging Center, University of Nottingham. He is currently working as an Assistant Professor with the Department of Electrical Engineering, Qatar University, Doha, Qatar. He has two patents and published around 80 peer-reviewed journal articles, conference papers, and four book chapters. His current research interests include biomedical instrumentation, signal processing, wearable sensors, medical image analysis, machine learning, embedded system design, and simultaneous EEG/fMRI. He is also running several QNRF grants and internal grants from Qatar University along with academic and government projects along with different national and international projects. He has worked as a Consultant for the projects entitled, "Driver Distraction Management Using Sensor Data Cloud (2013–14)," Information Society Innovation Fund (ISIF) Asia).

Dr. Chowdhury received the ISIF Asia Community Choice Award 2013 for a project entitled, "Design and Development of Precision Agriculture Information System for Bangladesh." He has recently won the COVID-19 Data Set Award for his contribution to the fight against COVID-19. He is serving as an Associate Editor for IEEE ACCESS and a Topic Editor for *Frontiers in Neuroscience*.

Moncef Gabbouj (Fellow, IEEE) received the B.S. degree from Oklahoma State University, Stillwater, OK, USA, in 1985, and the M.S. and Ph.D. degrees from Purdue University, in 1986 and 1989, respectively, all in electrical engineering.

He is a Professor of signal processing with the Department of Computing Sciences, Tampere University, Tampere, Finland. He was an Academy of Finland Professor from 2011 to 2015. His research interests include big data analytics, multimedia content-based analysis, indexing and retrieval, artificial intelligence, machine learning, pattern recognition, nonlinear signal and image processing and analysis, voice conversion, and video processing and coding.

Dr. Gabbouj is a member of the Academia Europaea and the Finnish Academy of Science and Letters. He is the past Chairman of the IEEE CAS TC on DSP and the Committee Member of the IEEE Fourier Award for Signal Processing. He served as an Associate Editor and the Guest Editor of many IEEE, and international journals and a Distinguished Lecturer for the IEEE CASS. He is the Finland Site Director of the NSF IUCRC funded Center for Visual and Decision Informatics (CVDI) and leads the Artificial Intelligence Research Task Force of the Ministry of Economic Affairs and Employment funded Research Alliance on Autonomous Systems (RAAS).

PUBLICATION III

Through the Wall Target Detection/Monitoring from Compressively Sensed Signals via Structural sparsity

M. Yamaç, M. Orhan, B. Sankur, A. S. Turk, and M. Gabbouj

Through the wall Target Detection/Monitoring from Compressively Sensed Signals via Structural Sparsity

Mehmet Yamaç[1], Melek Orhan[2,3], Bulent Sankur[4], Ahmet Serdar Turk[5], and Moncef Gabbouj[1]

[1]Tampere University of Technology, Laboratory of Signal Processing, Tampere, Finland
[4]Boğaziçi University, Electrical and Electronics Engineering Department, Istanbul, Turkey
[2]Gebze Technical University, Institute of Defense Technologies, Kocaeli, Turkey
[3]Gebze Technical University, Electronics Engineering Department, Kocaeli, Turkey
[5]Yildiz Technical University, Electronics and Communications Engineering Department, Istanbul, Turkey

***Abstract*—We develop a through-the-wall radar imaging (TWRI) system using stepped-frequency radar for the detection of stationary objects at close distances. This system uses the random frequency sampling and a structural sparsity based reconstruction method. The proposed reconstruction algorithm employs the block sparse structure and smoothness characteristics of the illuminated scene. In experiments on real data, we show that the proposed sparsity-based reconstruction algorithm outperforms the conventional ℓ_1 minimization-based radar imaging results.**

***Index Terms*—Compressive Sensing, Radar Imaging, Structural Sparsity, Random Frequency Radar Imaging**

I. Introduction

A stepped-frequency system (SFS) [1] works based on transmission of short electromagnetic waveforms at sequenced frequency steps, and measurement of the magnitude of the reflected signal and its phase difference with reference to the transmitted signal. One can consider the SFS method as a sampling in the frequency domain over a wide bandwidth. Modulated short pulses at stepped frequencies achieve ultra-bandwidth illumination of the medium, which is a crucial requirement where both low and high frequencies need to be employed as in the case of ground penetrating radar (GPR) [2] or TWRI. Other advantages of SFS list as lower transmission power, higher SNR value since the receiver is exposed to less noise in the smaller bands at stepped discrete frequencies [3], and finally use of existing efficient hardware implementation. Despite these advantages, one shortcoming is that they suffer from high data acquisition time since the radar transmitter and receiver has to operate at only a-single-frequency at-a-time. There have been some studies [4] where multi-frequencies are transmitted concurrently. However, the state-of-the-art approach is to transmit a subset of stepped frequencies and reconstruct the signal using techniques from Compressive Sensing theory [5]. In this study, we adopt this approach and use measurements of random subsets of Fourier coefficients to reconstruct the A-scan data.

There has been a recent interest in the literature in random frequency radar imaging [5], [6], [9], [10]. These works assume either a point-like sparse scene where the number of targets is less than the number of grid points in a 2-D uniformly discretized space and that the target's body is small or the whole vectorized 2-D radar image is sparse in some domain, but the sparsity is not structured. In [5], random frequency GPR measurements are considered that compressively sense the A-scan of a sparse scene and the 1-D A-scan vectors are then estimated using CS reconstruction methods. In [6], the same methodology is applied for through-the-wall imaging, but sparse estimation of A-scan vectors are further improved by applying delay-and-sum beam-forming. In [7], [8], CS is also applied in TWRI, but the authors also assume point-like sparse scene. In a different vein, [9] assumes that the scene is not necessarily sparse in the canonical base, but sparse in a specific dictionary, e.g., GPR dictionary. A SAR version of these works takes place in [10], where the authors consider the sensed 2D scene image and reconstruct the SAR image by vectorizing it and assuming sparsity in a suitable 2-D sparsifying transform included canonical domain.

These schemes, however, are not convenient for scenarios where the illuminated scene exhibits structural sparsity pattern: a block-sparse model in x-position axis where each sparse A-Scan vector shares the same support or at least these successive scan vectors encounter smooth changes. While in [5], [6], [9] each A-scan 1-D vector is reconstructed as a sparse vector and then the B-Scan 2-D radar image is constructed by concatenating them, we use a different approach and estimate consecutive A-scan vectors in ensembles over sliding intervals. We assume that in TWRI scenarios, depth data does not contain step changes unless a new object starts being seen by the A-scan. We can thus assume that each A-scan vector to be sparse and that the locations of their non-zero amplitude coefficients remain practically the same during the viewing of an object. Our approach also enables to adaptively change the measurement matrix while compressively sensing A-scan signals in every successive position if we apply the reconstruction algorithm in an on-line manner during sensing. This is because we reconstruct the 2-D scene in sliding window

mode and we can detect the energy increase in measurement if a new object comes to picture. In addition to the random frequency-based CS radar imaging, a time-domain CS radar system is also possible [11], and our algorithm would still be applicable provided the structural sparsity assumption is satisfied. The time-domain scheme, however, requires more complex hardware design and is out of the scope of this work.

We organize the rest of this paper as follows. Section II provides the notation, the mathematical preliminaries and brief review of CS theory. Section III provides a brief review of stepped-frequency radar data acquisition method and explains the compressive stepped frequency data sampling. In Section IV, we propose our ADMM based radar image reconstruction approach. Finally, experimental setup and reconstructed radar images are given and the conclusion is drawn. In this work, we set up a UWB SF-GPR scenario in the laboratory and use Anritsu Network analyzer obtain real data through the wall.

II. Preliminaries

To introduce our notation, we define, the ℓ_p norm of a vector $x \in \mathbb{R}^N$ as $\|x\|_p = \left(\sum_{i=1}^N |x_i|^p\right)^{1/p}$ for $p \geq 1$. For compressive sensing (CS) [12], we have m of measurements $y \in \mathbb{R}^m$ of a signal vector $S \in \mathbb{R}^N$, i.e., $y = \Psi S$ where Ψ is the $m \times N$ measurement matrix. Assuming that this signal is k-sparse in a sparsifying basis Φ, then the general compressive sensing setup becomes $y = \Psi\Phi x = Ax$, where $A = \Psi\Phi$. The compressively sampled sparse signal can be reconstructed by solving the following ℓ_1 minimization problem;

$$\min_x \ \|x\|_1 \text{ subject to } Ax = y. \tag{1}$$

For the measurement matrix Φ one may use randomly selected m rows of an orthonormal basis, Θ, which are indexed with $\Omega \in \{1, 2, 3, ..., N\}$. With such a measurement matrix Φ, then the k-sparse signal can be exactly reconstructed as solution of (1) (see [13] for Mutual Coherence).

Finally, we define the proximal operator of a function f at a point $z \in \mathbb{R}^N$ with a parameter $\gamma > 0$ as

$$\text{prox}_{\gamma f}(z) = \arg\min_u \{f(u) + \frac{1}{2\gamma}\|u - z\|_2^2\}. \tag{2}$$

to be used in Eqs. (11) and (12).

III. Compressive GPR system

A. Stepped Frequency

Assume that the frequency of n^{th} pulse is given as,

$$f_n = f_0 + n\Delta f, \quad n = 0, ..., N-1 \tag{3}$$

where Δ_f is frequency interval. The reflected signal is defined as [14]

$$r(n,t) \approx \kappa.s(\frac{t - 2R/c}{T_d})e^{\left(-j\frac{4\pi(f_0+n\Delta f)R}{c}\right)} \tag{4}$$

where κ is a constant representing attenuation effect, c is the speed of light, $s(t)$ is the base modulated signal transmitted, R is the range and T_d is the pulse duration. Since the phase

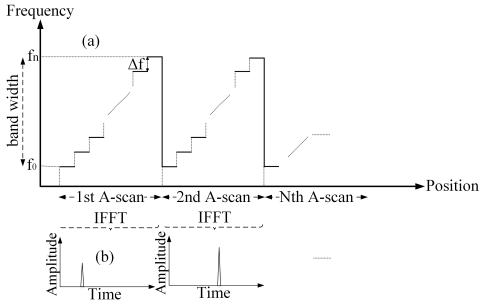

Fig. 1: Representation of stepped frequency waveform (a) transmitted signal (b) received signal after inverse Fourier transform.

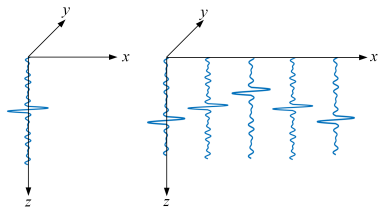

Fig. 2: Scan type of the GPR (a) A-scan (b) B-scan.

of the reflected signal is linearly related to n for a fixed R, we expect a pulse-like response in the dispersion-free case [10]. The location of this return pulse in time domain gives the depth information of the object as pictured in Figure 1.

For TWRI, we consider two scan types, the A-scan and the B-scan. The A-scan data gives the range profile corresponding to a single pulse of the radar. The radar signal sent by the transmitting antenna is reflected from the targets and the return signals are captured by the receiving antenna. The information about the target is obtained by interpreting the amplitude and phase value of the received signal.

Along the x-axis scan direction, the A-scan data is collected in constant spatial displacements to generate a 2-D matrix. This 2-D matrix allows us to create a 2-D image, called the B-scan, of the scene. This B-scan pictures the x-z reflectivity plane of the space behind the wall, where the range (z-axis) indicates the distance from the target, and the position (x-axis) defines the horizontal motion of the antenna. The method of obtaining A-Scan and B-Scan is pictured in Figure 2. It is possible to obtain a 3D image, called C-scan, including the vertical position (y-axis).

B. Incoherent Measurements

A natural selection of measurement matrix for the stepped frequency TWRI case consists in randomly choosing rows from Fourier basis F_Ω. This corresponds simply to measuring randomly m frequency responses at some location l,i.e.,

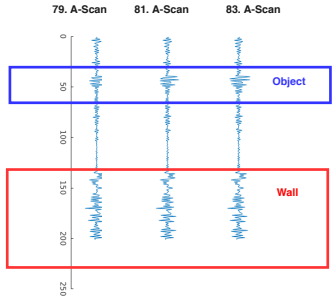

Fig. 3: A-Scan signals are obtained by taking IFFT of $N = 201$ uniformly sampled frequencies between 0.1 GHz-15 GHz at positions 79, 81 and 83.

$y_l = F_{\Omega_l} x_l$, $x \in \mathbb{R}^N$, $y \in \mathbb{R}^m$. For B-scan, one slides the TWRI device from position l to $l+1$ to take the next m measurements, $y_{l+1} = F_{\Omega_{l+1}} x_{l+1}$ and so on along the x trajectory. In this setup, each 1-D vector, x_l representing the depth information is considered to be sparse, hence amenable to CS-based reconstruction from (1).

In the ideal case where x_l is exactly k-sparse, we know that it can be exactly reconstructed if we have $m \geq O(k.logN)$ [13]. But in reality, we obtain noisy time domain A-Scans with spiky peaks in the range of object positions as illustrated in Figure 3. These signals are therefore not exactly sparse, but compressible in the sense that one may zero-out the small coefficients to make the object visible and obtain sparse range-profile.

IV. Proposed Reconstruction

Through-the-wall imaging is a well-established technique to detect and identify objects behind opaque structures. A case in point is an urgent rescue operation after an earthquake where bodies and limbs need to be identified or a terrorist attack where persons and possibly arms need to be detected behind concrete walls.

In these cases, radar imaging of a human body cannot be assumed as a point-like sparse signal. One then expects the entries in the x-z matrix of the B-scan to possess a block-sparse structure of some size D. In the B-scan matrix, l refer to each scan position of the radar as a column. Thus if there is a reflecting object behind the wall, then the B-scan non-zero coefficients will start emerging at some position l and continue the position $l+D$. Conversely, we do not expect a change vis-a-vis the background until a new object comes into picture at some location l for the duration of D A-scan steps. The non-zero coefficients from position x_l till the end of the reflecting body will continue without much variation both in (i) magnitude and (ii) indices of non-zero coefficients. Condition (i) can be satisfied by adding a total variation term to be minimized i.e., $\sum_{l=\tau}^{T+\tau-1} \|x_{l+1} - x_l\|_1$, where T is sliding window length and τ is the current position. Assumption (ii) can be satisfied if we allow the supports of non-zero coefficients in successive A-scans by minimizing the number of non-zero rows in the current window, i.e., $\sum_{i=1}^{N} \left\| x^i_{\tau:(\tau+T-1)} \right\|_2$. The necessity of this term enforcing row sparsity can be seen in Figure 3 since the non-sparse supports of successive A-Scans are expected to remain same during object. However, this row sparsifying may cause an undesirable noise effect in the solution of the system when $T >> D$. Because the non-sparse support in the solution continue to remain same for a while, i.e, between 1 to T new scan. Therefore, we may wish to divide this T A-Scan solutions into group of adjacent columns of length L with $L \leq T$. These groups can be formed in non-overlapping manner, i.e, $\underset{\sim}{x}^{i,k} = x^i_{\tau+(k-1)L:(\tau+kL-1)}$, or over-lapping manner, i.e., $\underset{\sim}{x}^{i,k} = x^i_{\tau+(k-1):(\tau+L+k-1)}$, where $\underset{\sim}{x}^{i,k}$ is the k.th group of i.th row. We can formulate a cost function that satisfies these assumptions as follows:

$$\hat{x}_{\tau:(\tau+T)} = \arg \min_{x_{\tau:(\tau+T)}} (\frac{\lambda_1}{2} \sum_{t=\tau}^{T+\tau} \|y_l - F_l x_l\|_2^2 + \lambda_2 \sum_{i=1}^{N} \sum_{k} \left\|\underset{\sim}{x}^{i,k}\right\|_2 + \lambda_3 \sum_{t=\tau}^{T+\tau-1} \|x_{t+1} - x_t\|_1) \quad (5)$$

where $\lambda_1, \lambda_2, \lambda_3$ are regularization parameters. The first term is simply the data fidelity term, the second is the block sparsity constraint and the third one constrains the reflection coefficients from the object to remain the same. If we represent the concatenation of desired signals from time τ to $T+\tau$ in matrix form, i.e., $x_{\tau:(\tau+T-1)} = X \in \mathbb{R}^{N \times T}$ then we can rewrite equation (5) as

$$\hat{X} = \arg\min_X (\frac{\lambda_1}{2} \sum_{d=1}^{T} \|y_d - F_d x_d\|_2^2 + \lambda_2 \|X\|_{2,1;L} + \lambda_3 \|X\|_{Tv,1}) \quad (6)$$

where $\|X\|_{2,1;L} = \sum_{i=1}^{N} \sum_k \left\|\underset{\sim}{x}^{i,k}\right\|_2$ parameter enforcing row base group sparsity with window length L , $X \in \mathbb{R}^{N \times T}$ is current sliding window matrix and x_d is d.th column of this matrix with corresponding measurement matrix F_d.

We will follow a ADMM based scheme to solve this problem. A consensus form of (5) can be written as

$$\left(\hat{X}, \hat{Z}_1, \hat{Z}_2\right) = \arg\min_X (\frac{\lambda_1}{2} \sum_{d=1}^{T} \|y_d - F_d x_d\|_2^2 + \lambda_2 \|Z_1\|_{2,1;L} + \lambda_3 \|Z_2\|_{Tv,1}) \quad \text{subject to} \quad Z_1 = X, Z_2 = X. \quad (7)$$

The augmented Lagrangian form of (7) can be cast as

$$L(\beta_1, \beta_2, X, Z_1, Z_2) = (\frac{\lambda_1}{2} \sum_{d=1}^{T} \|y_d - F_d x_d\|_2^2 + \lambda_2 \|Z_1\|_{2,1} + \lambda_3 \|Z_2\|_{Tv,1} + \langle \beta_1, (Z_1 - X) \rangle + \langle \beta_2, (Z_2 - X) \rangle + \frac{\mu_1}{2} \|X - Z_1\|_F^2 + \frac{\mu_2}{2} \|X - Z_2\|_F^2), \quad (8)$$

where the last two penalty terms with $\mu_1, \mu_2 > 0$ and $\beta_1 \in \mathbb{R}^{N \times T}, \beta_2 \in \mathbb{R}^{N \times T}$ are dual variables. In ADMM, primal and dual variables can be updated in alternating manner. Dual variable updates can be easily done by applying gradient

ascent steps [15] as given in Algorithm 1. Therefore, for the sake of convenience we will derive just primal updates. The updates of Z_1 can be done via

$$Z_1^{k+1} = \arg\min_{Z_1}\{\lambda_2 \|Z_1\|_{2,1} + \langle \beta_1, (Z_1 - X)\rangle + \frac{\mu_1}{2}\|X - Z_1\|_F^2\} \quad (9)$$

which is equivalent to

$$Z_1^{k+1} = \arg\min_{Z_1}\left\{\lambda_2 \|Z_1\|_{2,1;L} + \frac{\mu_1}{2}\left\|Z_1 - \left(X^{k+1} - \frac{\beta_1^k}{\mu_1}\right)\right\|_F^2\right\} \quad (10)$$

This is nothing but the proximal operator of windowed $\ell_{2,1}$-norm,

$$Z_1^{k+1} = prox_{(\frac{\lambda_2}{\mu_1})\|.\|_{2,1;L}}\left(X^{k+1} - \frac{\beta_1^k}{\mu_1}\right). \quad (11)$$

For non-overlapping groups, one can derive it as follows

$$(\underbrace{prox_{\gamma\|.\|_{2,1;L}}}(Z))^{i,k} = \begin{cases}\left(1 - \frac{\gamma}{\|\underbrace{Z}^{i,k}\|}\right)\underbrace{Z}^{i,k} & \text{if } \gamma < \|\underbrace{Z}^{i,k}\| \\ 0 & \text{else}\end{cases}$$

by using [16] section 6.5.4, where $\underbrace{M}^{i,k}$ is the k.th group of row i. For over-lapping case, it will be [17]

$$(prox_{\gamma\|.\|_{2,1}}(Z))(j,k) = \begin{cases}\left(1 - \frac{\gamma}{\|\underbrace{Z}^{i,k}\|}\right)Z(j,k) & \text{if } \gamma < \|\underbrace{Z}^{i,k}\| \\ 0 & \text{else}\end{cases}$$

where $M(j,k)$ is the k-th element of j-th row. Similarly, the update of Z_2 will be proximal operator of $\ell_{TV,1}$ as follows

$$Z_2^{k+1} = prox_{(\frac{\lambda_3}{\mu_2})\|.\|_{TV,1}}\left(X^{k+1} - \frac{\beta_2^k}{\mu_2}\right). \quad (12)$$

On can also find the X update equation by solving $\nabla_x L(.) = 0$, because the right hand side of the equation is differentiable. The overall algorithm is given in Algorithm 1, where we define M_d as d-th column of a matrix M.

Algorithm 1 ADMM for Problem

repeat

Primal Updates

$x_d^{k+1} \leftarrow (\lambda_1 F_d^T F_d + I\mu_1 + I\mu_2)^{-1}$
$(\lambda_1 F_d^T y_d + \mu_1 Z_{1_d} + \mu_2 Z_{2_d} + \beta_{1_d}^k + \beta_{2_d}^k)$

$Z_1^{k+1} \leftarrow prox_{(\frac{\lambda_2}{\mu_1})\|.\|_{2,1;L}}\left(X^{k+1} - \frac{\beta_1^k}{\mu_1}\right)$

$Z_2^{k+1} \leftarrow prox_{(\frac{\lambda_3}{\mu_2})\|.\|_{TV,1}}\left(X^{k+1} - \frac{\beta_2^k}{\mu_2}\right)$

Dual Updates:

$\beta_1^{k+1} \leftarrow \beta_1^k + \mu_1(Z_1^{k+1} - X^{k+1})$

$\beta_2^{k+1} \leftarrow \beta_2^k + \mu_2(Z_2^{k+1} - X^{k+1})$

until Convergence

return $\hat{X}$

V. Experiments

A. Experimental setup

In this study, the stepped frequency scanning was performed using the Anritsu vector network analyzer and two horn antennas in the spectral frequency band from 100 MHz to 15 GHz in 201 frequency steps. The receiver and transmitter antenna pairs were shifted 150 times to combine the B-scan data with 2 cm step length along a 3 m fixed x-axis. In the designed scenario, we aimed to detect a target concealed behind the wall. In accordance with this purpose, a metal body model was placed behind a wall of approximately 30 cm to perform the screening. The distance between the antenna pairs and the metal target is 85 cm. Dimensions of the metal body model detailed in the figure are in the rough 44x95 cm.

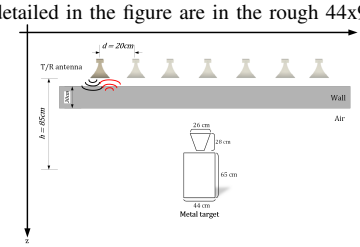

Fig. 8: Measurement scenario concerning with detection of the target behind the wall.

B. Experimental Results

In Figure 4 (a), we shows the B-Scan obtained using from IFFT of all $N = 201$ frequencies. A wall closed the reader and an object in the middle easily identifiable. Figure 4 (b) shows IFFT results of $m = 0.2 * N$ randomly chosen frequencies, we can call it ℓ_2 minimization result. Figure 5 (a) shows the when we randomly choose $m = 0.2 * N$ random frequencies and ℓ_1 minimization method where each A-Scan estimate is done independently. As it is shown in Figure 5 (a) and Figure 6 (a), in ℓ_1 results, object is not identifiable when $m = 0.2$ but when we increase it to $m = 0.4$ it becomes more visible. Both Figure 5-6 (b) shows us then proposed approach when successive A-Scan estimates support each other, object is visible even for $m = 0.2 * N$.

We also extend this experiment to the situation where we exactly know the wall location, despite an improvement in the result of ℓ_1 minimization method due to increase in sparsity level we achieve much more improvement in the result of the proposed method if we consider the location and shape estimate of the object. We use over-lapping groups in that experiment with $L = 10$. As shown in Figure 8, the object length $D = 22$ (22) cm in our experimental setup which is approximately estimated in all experiments.

VI. Conclusion

In this work, we define a random frequency through the all imaging system. Then, we have proposed a new CS reconstruction algorithm working on sliding window mode for this system. This reconstruction method enjoys the information that successive A-Scan signals have similar structures. The algorithm can also be applied in an on-line manner during the measurement process, therefore can help to adaptively

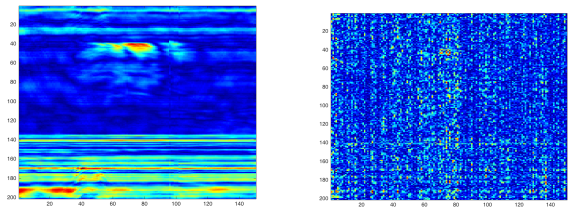

Fig. 4: Estimated B-Scan images. There is a wall through all A-scan and object to be detected in the middle. (a) Non-CS B-scan. IFFT is applied to get A-scan data to $N = 201$ uniformly sampled frequency in the signal band between 0.1 GHz-15GHz. (b) B-scan estimation when IFFT applied to $m = 0.2 * N$ randomly chosen subset of these frequencies.

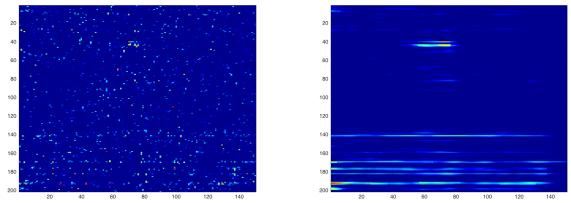

Fig. 5: (a) B-scan estimation when ℓ_1 minimization is applied to randomly chosen $m = 0.2 * N$ frequencies. (b) B-scan estimation of proposed Reconstruction.

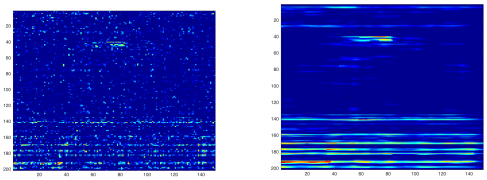

Fig. 6: (a) B-scan estimation when ℓ_1 minimization is applied to randomly chosen $m = 0.4 * N$ frequencies. (b) B-scan estimation of proposed Reconstruction.

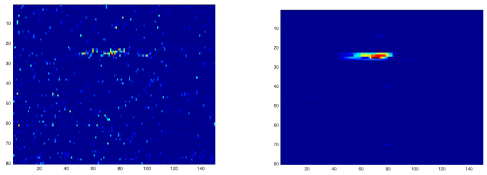

Fig. 7: Estimated B-Scan images when the wall location is known in advance. (a) B-scan estimation when ℓ_1 minimization is applied to randomly chosen $m = 0.2 * N$ frequencies. (b) B-scan estimation of proposed Reconstruction.

change the number of measurements taken in a fixed position. This study can also be extended to the randomized position choosing such as in SAR imaging or randomized B-Scan choosing in C-Scan case.

REFERENCES

[1] Noon, David Andrew. "Stepped-frequency radar design and signal processing enhances ground penetrating radar performance." (1996).

[2] Sugak, Vladimir G., and Alexander V. Sugak. "Phase spectrum of signals in ground-penetrating radar applications." IEEE Transactions on Geoscience and Remote Sensing 48.4 (2010): 1760-1767.

[3] Nguyen, Cam, and Joongsuk Park. Stepped-Frequency Radar Sensors: Theory, Analysis and Design. Springer International Publishing, 2016.

[4] van Genderen, Piet. "Multi-waveform SFCW radar." Microwave Conference, 2003 33rd European. IEEE, 2003.

[5] Suksmono, Andriyan Bayu, et al. "Compressive stepped-frequency continuous-wave ground-penetrating radar." IEEE geoscience and remote sensing letters 7.4 (2010): 665-669.

[6] Yoon, Yeo-Sun, and Moeness G. Amin. "Imaging of behind the wall targets using wideband beamforming with compressive sensing." Statistical Signal Processing, 2009. SSP'09. IEEE/SP 15th Workshop on. IEEE, 2009.

[7] Huang, Qiong, et al. "UWB through-wall imaging based on compressive sensing." IEEE Transactions on Geoscience and Remote Sensing 48.3 (2010): 1408-1415.

[8] Leigsnering, Michael, et al. "Compressive sensing based specular multipath exploitation for through-the-wall radar imaging." Acoustics, Speech and Signal Processing (ICASSP), 2013 IEEE International Conference on. IEEE, 2013.

[9] Gurbuz, Ali Cafer, James H. McClellan, and Waymond R. Scott. "A compressive sensing data acquisition and imaging method for stepped frequency GPRs." IEEE Transactions on Signal Processing 57.7 (2009): 2640-2650.

[10] Yang, Jungang, et al. "Random-frequency SAR imaging based on compressed sensing." IEEE Transactions on Geoscience and Remote Sensing 51.2 (2013): 983-994.

[11] Baraniuk, Richard, and Philippe Steeghs. "Compressive radar imaging." Radar Conference, 2007 IEEE. IEEE, 2007.

[12] Candes, Emmanuel J. "Compressive sampling." Proceedings of the international congress of mathematicians. Vol. 3. 2006.

[13] Candes, E. and J. Romberg, Sparsity and Incoherence in Compressive Sampling, Inverse Problems, Vol. 23, No. 3, p. 969, 2007

[14] Yang, Jungang, et al. "Random-frequency SAR imaging based on compressed sensing." IEEE Transactions on Geoscience and Remote Sensing 51.2 (2013): 983-994.

[15] Boyd, Stephen, et al. "Distributed optimization and statistical learning via the alternating direction method of multipliers." Foundations and Trends in Machine Learning 3.1 (2011): 1-122.

[16] Parikh, Neal, and Stephen P. Boyd. "Proximal Algorithms." Foundations and Trends in optimization 1.3

[17] Kowalski, Matthieu, Kai Siedenburg, and Monika Drfler. "Social sparsity! neighborhood systems enrich structured shrinkage operators." IEEE transactions on signal processing 61.10 (2013): 2498-2511.

PUBLICATION
IV

Multi-Level Reversible Data Anonymization via Compressive Sensing and Data Hiding

M. Yamaç, M. Ahishali, N. Passalis, J. Raitoharju, B. Sankur, and M. Gabbouj

IEEE Transactions on Information Forensics and Security, vol. 16, pp. 1014–1028
DOI: 10.1109/TIFS.2020.3026467

Multi-Level Reversible Data Anonymization via Compressive Sensing and Data Hiding

Mehmet Yamaç, Mete Ahishali, Nikolaos Passalis, Jenni Raitoharju, *Member, IEEE*, Bülent Sankur, *Life Senior Member, IEEE*, and Moncef Gabbouj, *Fellow, IEEE*

***Abstract*— Recent advances in intelligent surveillance systems have enabled a new era of smart monitoring in a wide range of applications from health monitoring to homeland security. However, this boom in data gathering, analyzing and sharing brings in also significant privacy concerns. We propose a Compressive Sensing (CS) based data encryption that is capable of both obfuscating selected sensitive parts of documents and compressively sampling, hence encrypting both sensitive and non-sensitive parts of the document. The scheme uses a data hiding technique on CS-encrypted signal to preserve the one-time use obfuscation matrix. The proposed privacy-preserving approach offers a low-cost multi-tier encryption system that provides different levels of reconstruction quality for different classes of users, e.g., semi-authorized, full-authorized. As a case study, we develop a secure video surveillance system and analyze its performance.**

***Index Terms*— Reversible privacy preservation, multi-level encryption, compressive sensing, video monitoring.**

I. Introduction

MANY emergent smart surveillance applications (i.e., buildings, infrastructure, stores, ambient-assisted living, public areas) necessitate time-continuous data gathering and processing. Upcoming 5G and IoT technologies will enable continuous data collection and processing for persistent monitoring [1]. For example, an intelligent building system equipped with monitoring sensors such as CO2 meters, thermometers, cameras or other types of IoT devices will be instrumental in effectively automating tasks of heating, ventilation, and conditioning (HVAC) systems, or in improving the fault and hazard detection performance [2]. Another case in point is an intelligent network of cameras for continuous site surveillance or a health monitoring system [3], which gathers users' bio-signals along with video/speech data to be processed remotely. These applications and their variants that collect data via sensors or edge devices bear the concern of the privacy of people and possibly of sites. In fact, the European General Data Protection Regulation (GDPR) legislation [4] has specifically addressed these privacy concerns in data collection and processing.

Currently, there exist a plethora of privacy-preserving technologies that vary in the data type and in the application scenario. Even the definition of privacy is up to change for different application areas and use cases, depending on whether it is signal processing, a database system, secure communication, etc., [5]. Under privacy concern, documents are considered to consist of private, i.e., sensitive parts, those parts that could potentially expose compromising information to unauthorized users, and of public, i.e., non-sensitive parts. Privacy-preserving data processing then aims to encrypt the private parts of a document without deteriorating its public parts. Recent comprehensive surveys provide useful guidelines in privacy-preserving data mining [6], [7], signal processing [8], [9], and privacy metrics [5].

In principle, a naive application of strong cryptography methods such as AES [10] or RSA [11] would provide a high degree of security, in addition to privacy. However first, these encryption methods are relatively costly; but more importantly, it is neither useful nor necessary to encrypt the whole signal in real-time multimedia applications such as in video [12], image, health [13] monitoring systems or other types of IoT applications. Only the selected parts of the multimedia document deemed to carry private information need to be protected; this then gives rise to a two-tier approach. More generally in a multi-tiered approach, different parts of the document can be privacy protected at differential levels, the most strongly protected parts accessible by the highest authorization level, and so forth. We can also state the three desiderata of privacy-protection algorithms: a) The technique should be able to secure the privacy of selected sensitive portions of the data; e.g., for face hiding, it should be stronger than any automatic face recognition algorithm; b) The method should not degrade the non-sensitive parts of the documents; c) It should be able to reverse the sensitive part encryption (for authorized users) in good quality. A concomitant desideratum is that the computation cost of the data encryption should be reasonably low.

Although Compressive Sensing (CS) [14] is an alternative data acquisition strategy to conventional Nyquist/Shannon based technique, it also provides encryption with a reasonable

Manuscript received March 16, 2020; revised June 22, 2020 and September 6, 2020; accepted September 7, 2020. Date of publication September 24, 2020; date of current version October 12, 2020. This work was supported in part by the NSF-Business Finland CVDI Project under Grant Amalia 3333/31/2018 and in part by the Business Finland Project VIRPA D through Tieto Oyj and other companies under Grant 7940/31/2017. The associate editor coordinating the review of this manuscript and approving it for publication was Dr. Patrick Bas. *(Corresponding author: Mehmet Yamaç.)*

Mehmet Yamaç, Mete Ahishali, Nikolaos Passalis, Jenni Raitoharju, and Moncef Gabbouj are with the Faculty of Information Technology and Communication Sciences, Tampere University, 33720 Tampere, Finland (e-mail: mehmet.yamac@tuni.fi).

Bülent Sankur is with the Electrical and Electronics Engineering Department, Boğaziçi University, 34342 Istanbul, Turkey.

Digital Object Identifier 10.1109/TIFS.2020.3026467

security level via its randomized sensing mechanism. In consequence, using CS setup alone or with another lightweight encryption shell applied on top of it has recently been a popular approach for multimedia applications [15].

In this work, we pursue the approach of compressive sensing to accomplish both compression and cryptographic security on the whole data, and data hiding technology [16], [17] to hide and then recover the masked-out private parts of the document. The novel method achieves privacy protection by obfuscating the sensitive parts of the document while the CS-encryption is applied to the whole document, i.e., the combined public and private parts. We assume that the document has been pre-processed and segmented into its sensitive and non-sensitive parts. We use terms *de-identification* and *anonymization* interchangeably, in the sense of rendering unintelligible the privacy bearing segments of a document. Although our method is applicable to any document type, images, video, audio, etc., with appropriate modifications, in the sequel we will consider images as an application case.

Our scheme provides a two-tiered privacy, in which the semi-authorized user, i.e., the entity with lower authorization level can decode and view only the non-sensitive parts of the image, while the fully-authorized user decodes and sees the entire image. The semi-authorized one with only key **A** (CS-Encryption matrix) is able to recover images whose sensitive parts remain obfuscated after decoding whereas the fully authorized person with keys **A** and **B** (the latter being watermark embedding matrix) is able to recover the whole image. In both cases, the image quality is stipulated to remain close to the original quality. The significant merits of our proposed method are first to enable a low-cost, two-level encryption and second to provide reversible anonymization for the selected authorized users. Although the experiments are run only on image data, our method is general enough to be applied to any data involving privacy concerns, such as to videos as detailed in Section VI, or to bio-signals. In this work, we select face de-identification problem [18], [19] as a case study, within the context of a privacy-preserving image/video monitoring system.

The privacy protection concern in image/video has been addressed in a plethora of papers in the last decades. In summary, the technical solutions can be discussed in three groups: a) automatic blurring of faces, context-dependent blurring, e.g., bystanders only; b) blacking out of faces with random patterns, and recently; c) anonymous face substitutions or iterative regeneration schemes. Our method is in line with the noise pattern overlay methods in the literature. However, we differ from these methods in two respects: i) while we are able to fully remove the obfuscating noise pattern, we provide multi-tier differential protection; ii) we use compressive sensing for data reduction and cryptographic security, and watermark the compressed signal with the data hiding pattern).

A privacy-preserving method to which our method has some resemblance was recently described in [20]. In the method of [20], the images are first processed through a parallel group of trained auto-encoders, each generating its own sufficiently diversified sparse code. They obfuscate the sparse code by adding random noise with statistics similar to sparse code statistics to coefficients to a group of coefficients outside the sparse code support set. The support set is predefined or shared via a secret channel to the trusted user. Only the trusted user possesses the key to recover the support set of the sparse code coefficients, and thus is able to decode the sensitive image (the face). Codes from multiple auto-encoders are used to successively refine the results, i.e., incrementally improve reconstructed image quality. In contrast, our method is not face specific, does not need to find sparse codes in the encoding part, does hence not require a separate secret channel to share the obfuscation key. In addition, data reduction via CS-compression is a byproduct of our scheme.

A preliminary version of this work was presented at [21]. This early version had briefly introduced the methodology and presented some test results on a token dataset (6 faces in a controlled laboratory environment). In this article, we provide a theoretical worst-case analysis on the watermark guarantee conditions (Lemma 1, Theorem 4). We have extended the paper by incorporating a discussion on the design of alternative obfuscating matrices [21] as well as on the alternative designs of the watermark embedding matrix (see Section IV-E). Simulation experiments are run on a realistic public dataset with a much bigger size (a subset of YouTube Faces Database [22]) containing 100 classes (videos of 100 identities). We have also briefly described two extensions of the proposed method: 1. Its adaptation to video signals, beyond the simple frame-by-frame privacy processing; 2. A three-tiered privacy protection in images. In the detailed performance evaluation, we illustrate the reconstruction accuracy of masked regions as a function of watermark embedding power and the choice of obfuscating masks, both being user-defined parameters. Recognition accuracies with original faces, with de-identified faces, and with faces reverse de-identified via recovered watermark are given. The result of a test against an adversary with a strong computational capability and with access to the full labeled training set is also reported.

The rest of the paper is organized as follows. The notation is provided in Section II. We give a brief overview of compressive sensing and its usage in encryption systems in Section III. We emphasize the compressive sensing properties that we have exploited in our proposed scheme. In Section IV, the proposed two-tier privacy-preserving system is presented in detail. Section V introduces a case study of the proposed method in video monitoring and gives the results of the extensive simulation studies. Finally, conclusions are drawn in Section VII.

II. Notations

In this work, the ℓ_p norm of a vector $\mathbf{x} \in \mathbb{R}^N$ is given as $\|\mathbf{x}\|_p = \left(\sum_{i=1}^N |x_i|^p\right)^{1/p}$ for $p \geq 1$. We also define the ℓ_0-norm of the vector $\mathbf{x} \in \mathbb{R}^N$ as $\|\mathbf{x}\|_0 = \lim_{p\to 0} \sum_{i=1}^N |x_i|^p = \#\{l : x_l \neq 0\}$. The exactly (or strictly) k-sparse signal in some appropriate domain is the signal, $\mathbf{x} \in \mathbb{R}^N$ with $\|\mathbf{x}\|_0 \leq k$. On the other hand, the approximately k-sparse signal (or compressible) is a signal $\mathbf{x}$ with $\|\mathbf{x} - \check{\mathbf{x}}\|_2 \leq \kappa$, where κ is a small constant and $\check{\mathbf{x}}$ is obtained via zero-outing the elements of $\mathbf{x}$ except the

TABLE I

FROM LEFT TO RIGHT: a) SYMBOLS OF THE FREQUENTLY USED VARIABLES IN THE ARTICLE. b) DENOTATIONS OF THESE SYMBOLS. c) THE CORRESPONDING CRYPTOGRAPHIC TERMINOLOGY, IF APPLICABLE. d) THE CONDITIONS THE VARIABLES MUST SATISFY FOR THE ENCRYPTION SCHEME TO WORK PROPERLY

Variable	Synonyms	In Crypt.	Properties
$\mathbf{s} \in \mathbb{R}^N$	Signal, document, data	Plain-text	Sparse in $\mathbf{\Phi}$
$\mathbf{\Phi} \in \mathbb{R}^{N \times N}$	Sparsifying matrix (basis)		
$\mathbf{x} \in \mathbb{R}^N$	Sparse coefficients of $\mathbf{s}$	Plain-text	$\|\mathbf{x}\| \leq k$
$\mathbf{A} \in \mathbb{R}^{m \times N}$	CS-measurement matrix	CS-encryption matrix (Key $\mathbf{A}$)	$\mathbf{H} = \mathbf{A\Phi}$ to have RIP
Λ_p	Location index set of the obfuscated sensitive part		$\Lambda_p \subset \{1, ..., N\}$
$\mathbf{s_s} \in \mathbb{R}^N$	Sensitive part of $\mathbf{s}$	$\mathbf{s_s} = \begin{cases} (\mathbf{s_s})_{\Lambda_p} = \mathbf{s}_{\Lambda_p} \\ (\mathbf{s_s})_{\Lambda_p^c} = \mathbf{0} \end{cases}$	
$\mathbf{s_n} \in \mathbb{R}^N$	Non-sensitive part of $\mathbf{s}$	$\mathbf{s_n} = \begin{cases} (\mathbf{s_n})_{\Lambda_p^c} = \mathbf{s}_{\Lambda_p^c} \\ (\mathbf{s_n})_{\Lambda_p} = \mathbf{0} \end{cases}$	
$\mathbf{s}_{\mathbf{\Lambda_p}} \in \mathbb{R}^{\lvert\Lambda_p\rvert}$	Masked out sensitive part		$\lvert\Lambda_p\rvert$: Size of the masked region
$\mathbf{\Delta}_{\mathbf{\Lambda_p}}$	Obfuscation matrix	Anonymization operator	$\lvert\Lambda_p\rvert \times \lvert\Lambda_p\rvert$ matrix
$\mathbf{M} \in \mathbb{R}^{m \times N}$	Masking matrix	Anonymization operator	
$\mathbf{y} \in \mathbb{R}^m$	CS-based encrypted signal	Cipher-text	$\mathbf{y} = \mathbf{As}$
$\mathbf{y_d} \in \mathbb{R}^m$	Jointly CS-based encrypted and anonymized signal	Cipher-text	$\mathbf{y_d} = (\mathbf{A} + \mathbf{M})\mathbf{s}$
$\mathbf{w}$	Ternary Watermark	Length, T, and watermark magnitude, a, are predefined: $w_i \in \{a, 0, -a\}$	
$\mathbf{B} \in \mathbb{R}^{m \times T}$	Watermark embedding matrix		$T < m$
$\mathbf{F} \in \mathbb{R}^{p \times m}$	Left annihilator matrix		$\mathbf{FB} = 0$, $p = m - T$
$\mathbf{y_w} \in \mathbb{R}^m$	Marked $\mathbf{y_d}$	Cipher-text (marked)	$\mathbf{y_w} = \mathbf{y_d} + \mathbf{Bw}$

ones with k-largest magnitude. For convenience, we show in Table I the list of frequently used symbols, the terminology used in paper and their synonymous definitions in the cryptography literature.

III. PRELIMINARIES AND PRIOR ART

Our interest in compressive sensing is twofold: to compress the signal if it is already sampled or to sample analog signals directly at rates below the Nyquist-Shannon bound and to exploit the inherent cryptographic capability of compressive sensing.

A. Compressive Sensing

Compressive sensing (CS) theory has significantly impacted the field of signal processing since its inception in 2005 [14]. According to the CS theory, a signal can be sampled using far fewer measurements than the traditional Nyquist-Shannon acquisition rate, provided it is sparse or compressible in some proper domain. CS-based MRI imaging [23], radar monitoring systems [24], [25], and ECG measurements in a health monitoring system [13] are some of its success stories. It is also seen as a potential solution for hardware/software design in the applications requiring very high sampling frequencies such as wideband spectrum sensing [26] and ultra-wideband communication schemes [27]. In fact, CS is expected to play an important role in the next-generation communications systems such as 5G [28].

Let us consider the linear mapping of a discrete signal $\mathbf{s} \in \mathbb{R}^N$ as

$$\mathbf{y} = \mathbf{As}, \tag{1}$$

where $\mathbf{A} \in \mathbb{R}^{m \times N}$ is known as the measurement matrix with $m < N$. The minimum-energy solution for the underdetermined linear system of equations (1) is given by

$$\min_{\mathbf{s}} \|\mathbf{s}\|_2^2 \text{ subject to } \mathbf{As} = \mathbf{y}. \tag{2}$$

The solution of (2) is unique and has a closed form solution, $\hat{\mathbf{s}} = \mathbf{A}^T \left(\mathbf{AA}^T\right)^{-1} \mathbf{y}$ provided that $\text{rank}(\mathbf{A}) = m \leq N$ which makes $\mathbf{AA}^T$ invertible. The minimum achievable reconstruction error is $\left\|\mathbf{s} - \hat{\mathbf{s}}\right\|_2 = \mathbf{s}^T \left(\mathbf{I} - \mathbf{A}^T \left(\mathbf{AA}^T\right)^{-1} \mathbf{A}\right) \mathbf{s}$, which shows that exact recovery is not possible since $\mathbf{I} \neq \mathbf{A}^T \left(\mathbf{AA}^T\right)^{-1} \mathbf{A}$ when $m < N$. The CS theory addresses signals that are sparse in a proper domain, $\Phi \in \mathbb{R}^{N \times N}$, i.e., $\mathbf{s} = \Phi\mathbf{x}$ with $\|\mathbf{x}\|_0 \leq k$. Therefore, (1) can be reformulated as follows,

$$\mathbf{y} = \mathbf{As} = \mathbf{A}\Phi\mathbf{x} = \mathbf{Hx}, \tag{3}$$

where $\mathbf{H} = \mathbf{A}\Phi$, and even if (3) has infinitely many solution we can look for the sparsest one,

$$\min_{\mathbf{x}} \|\mathbf{x}\|_0 \text{ subject to } \mathbf{Hx} = \mathbf{y}. \tag{4}$$

Eq. (4) is also known as sparse representation of $\mathbf{y}$ in $\mathbf{H}$ and it is unique, provided that the minimum number of linearly independent columns of $\mathbf{H}$, as defined in [29], is greater than $2k$. Thus for $spark(\mathbf{H}) \geq 2k$, any two distinct k-sparse signals $\mathbf{x}', \mathbf{x}''$ can be uniquely recovered from their undersampled measurements $\mathbf{y}'$, $\mathbf{y}''$ if $m \geq 2k$. Put differently, one has the surprising result that, while it is not possible to recover $\mathbf{s}$ exactly using minimum norm decoder as in (2), exact recovery of the signal is possible in the sparsifying domain.

The nonconvex problem (4) with ℓ_0-quasi-norm can be relaxed to its closest convex form, ℓ_1 as

$$\min_{\mathbf{x}} \|\mathbf{x}\|_1 \text{ subject to } \mathbf{x} \in \Upsilon(\mathbf{y}), \tag{5}$$

where $\Upsilon(\mathbf{y}) = \{\mathbf{x} : \mathbf{Hx} = \mathbf{y}\}$, an optimization problem that is also known as Basis Pursuit [30]. The equivalence of ℓ_0-ℓ_1 minimization problems is well investigated in the literature in terms of the properties of $\mathbf{H}$. For instance, the Null Space Property (NSP) [31] not only satisfies the ℓ_0-ℓ_1 equivalence but also comes very handy for the recovery performance analysis when $\mathbf{x}$ is not exactly k-sparse but only compressible. In the case we deal with approximately sparse signals or/and with a case where the measurements are contaminated by additive noise, the problem can be relaxed with $\Upsilon(\mathbf{y}) = \left\{\mathbf{x} : \|\mathbf{Hx} - \mathbf{y}\|_2 \leq \epsilon\right\}$, where ϵ is a small positive constant. Problem (5), with this new constraint, is known as Basis Pursuit Denoising (BPDN) [32]. The stability conditions of CS signal recovery techniques are also well understood: a stable solution, $\hat{\mathbf{x}}$, is expected to obey $\left\|\mathbf{x} - \hat{\mathbf{x}}\right\|_2 \leq \kappa \|\mathbf{z}\|$ with a small constant, κ for additive noise $\mathbf{z}$ perturbation in the measurements, $\mathbf{y} = \mathbf{Hx} + \mathbf{z}$.

When approximately sparse signals are measured under noise, a property stronger than NSP gives a stable

recovery guarantee. This property is called Restricted Isometry Property (RIP), which is defined as follows:

Definition 1 (Restricted Isometry Property): A matrix $\mathbf{H} \in \mathbb{R}^{m\times N}$ has RIP with order k, if there exist a smallest $\delta_k(\mathbf{H})$ that satisfies

$$(1-\delta_k(\mathbf{H}))\,\|\mathbf{x}\|_2^2 \le \|\mathbf{H}\mathbf{x}\|_2^2 \le (1+\delta_k(\mathbf{H}))\,\|\mathbf{x}\|_2^2 \qquad (6)$$

for all k-sparse signal, $\mathbf{x} \in \mathbb{R}^N$. The constant, $\delta_k(\mathbf{H})$ is called the Restricted Isometry Constant (RIC) of order k for matrix $\mathbf{H}$.

The stability and ℓ_0-ℓ_1 equivalence conditions w.r.t. RIC of a measurement matrix are thoroughly studied in the literature. The authors in [33] show that the ℓ_0-ℓ_1 equivalence is achieved when $\delta_{2k}(\mathbf{H}) \le \sqrt{2}-1$. Likewise, the stability of the ℓ_1 minimization problem is investigated in Basis Pursuit Denoising [34] and Dantzig Selector [35]. In [34], it is shown that for $\Upsilon(\mathbf{y}) = \left\{\mathbf{x} : \|\mathbf{H}\mathbf{x}-\mathbf{y}\|_2 \le \epsilon\right\}$ and $\|\mathbf{z}\|_2 \le \epsilon$, the solution of (5) satisfies

$$\left\|\mathbf{x}-\hat{\mathbf{x}}\right\|_2 \le C_0\epsilon, \qquad (7)$$

where C_0 depends on $\delta_{2k}(\mathbf{H}) < \sqrt{2}-1$ [33]. Notice that the recovery guarantee conditions of an arbitrary k-sparse signal enforce $2k$-order RIC, $\delta_{2k}(\mathbf{H})$ instead of $\delta_k(\mathbf{H})$. The intuition behind this is simply that for noise-free measurements, the null space analysis indicates that $spark(\mathbf{H}) \ge 2k$ in order for $\mathbf{H}$ not to map any two arbitrary but distinct $k-$sparse signals $\mathbf{x}'$ and $\mathbf{x}''$ to the same point, so that one always has $\mathbf{H}\mathbf{x}' \ne \mathbf{H}\mathbf{x}''$. In this sense, RIP gives us a stronger guarantee that after mapping with a $\mathbf{H}$, the distance between points $\mathbf{x}', \mathbf{x}''$ should be preserved at least as follows: $(1-\delta_{2k}(\mathbf{H}))\left\|\mathbf{x}'-\mathbf{x}''\right\|_2^2 \le \left\|\mathbf{H}\mathbf{x}'-\mathbf{H}\mathbf{x}''\right\|_2^2$.

The good measurement matrices $\mathbf{A}$ that preserve the information in the sparse domain Φ, or alternatively $\mathbf{A}\Phi = \mathbf{H}$ are the ones that satisfy the RIP property. Certain random measurement matrices are known to satisfy this property, one popular such case being the matrix whose elements $A_{i,j}$ are i.i.d. (independent identically distributed) and drawn from a Gaussian distribution, i.e.,

$$A_{i,j} \sim \mathcal{N}\left(0, \frac{1}{m}\right) \qquad (8)$$

and for $m > k(\log(N/k))$, and $\mathbf{H}$ inherits this property as well. We recall the following lemma that gives the stability condition of BPDN for measurements under additive white Gaussian noise (AWGN) contamination, since it will be handy in the sequel for the stability analysis of our encryption scheme.

Corollary 1 (Refined from Corrollary 1.1 of [35, p. 32]): Let $\mathbf{H} \in \mathbb{R}^{m\times N}$ satisfy the RIP of order $2k$ with $\delta_{2k}(\mathbf{H}) < \sqrt{2}-1$. Assume that measurements are corrupted by i.i.d. noise with elements z_i drawn from $\mathcal{N}\left(0, \frac{1}{\sigma^2}\right)$. Then, the error of the solution of (5) with $\Upsilon(\mathbf{y}) = \left\{\mathbf{x} : \|\mathbf{H}\mathbf{x}-\mathbf{y}\|_2 \le \epsilon\right\}$ is upper bounded by

$$\left\|\mathbf{x}-\hat{\mathbf{x}}\right\|_2 \le 4\frac{\sqrt{1+\delta_{2k}(\mathbf{H})}}{1-(1+\sqrt{2})\delta_{2k}(\mathbf{H})}(1+\gamma)\sqrt{m}\sigma \qquad (9)$$

with probability of at least $1-\exp(-\frac{3m}{4}\gamma^2)$ where $0 < \gamma < 1$ and $\epsilon = (1+\gamma)\sqrt{m}\sigma$.

B. Compressive Sensing Based Encryption

Since in the CS setup, a signal is linearly sampled using random or pseudo-random measurement matrices, there exists an inherent capability to provide privacy and cryptographic protection [36], [37]. One advantage of CS-based encryption is that the linearity and the dimensionality reduction of the CS scheme result in low-cost operations. This could be a crucial advantage for data encryption carried out on the edge devices before data transmission to a cloud or a fusion center. In fact, it has been reported in several works [38], [39] that CS-based encryption has a much lower cost as compared to well-established encryption standards such as AES [10] or RSA [11].

The idea of formally using CS theory in the encryption system was first introduced in [40]. These authors have considered a sparse signal $\mathbf{x}$ as a plain-text input signal and encrypted it in cipher-text $\mathbf{y}$. A Gaussian measurement matrix, as in (8), was used in the role of the CS-encryption matrix, i.e., $\mathbf{y} = \mathbf{H}\mathbf{x}$. They consider the Shannon perfect secrecy [41] definition as a metric of security. CS-based encryption can be viewed as a particular case of a multiplicative randomization technique, which is also a well-known privacy-preserving method. Using the definition of Shannon [41], CS-based encryption literature generally defines the perfect secrecy in the information-theoretical sense as follows:

Definition 2 (Perfect Encryption System): A perfect encryption system satisfies

$$\Pr(\mathbf{x}|\mathbf{y}) = \Pr(\mathbf{x}) \qquad (10)$$

for any plain-text $\mathbf{x}$ and cipher-text $\mathbf{y}$ pair.

The authors of [40] conclude that even if the Shannon perfect secrecy is not satisfied with the CS-based encryption scheme since the CS-measurements preserve the energy of plain-text as $\mathbf{H}$ must satisfy the condition, they argue that CS-based encryption guarantees computational secrecy, i.e., an attacker with bounded time. In a later work, it is shown that the CS-based encryption with the Gaussian compression matrix used only once and re-drawn for each coding instance reveals only the energy of $\mathbf{x}$ [42]. Therefore, a Gaussian CS-encryption can be said to satisfy perfect secrecy if the cipher-text, $\mathbf{y}$ is normalized to some constant energy [36, Theorem 4]. Efforts on giving privacy guarantee conditions for both normalized and unnormalized energy cipher-texts for different measurement matrix schemes continue [43], [44] (using different security metrics). Similarly, instead of Shannon perfect secrecy, Wyner-sense perfect secrecy, or their extended version have also been used in security analysis for CS-based encryption schemes [45]. In the meantime, the robustness of the CS-based encryption against attacks is investigated in [46], [47]. In [46], the authors consider a brute force and structural attack where an adversary tries a grid search to estimate the CS-encryption matrix, $\mathbf{A}$. This attack type can be considered as a known cipher-text attack under one-time usage (or one-time secret, OTS). They conclude that the computational complexity of such an attack makes this type of brute-force attack infeasible. The known plain-text type attack (KPA) under one time usage is addressed in [47], where the adversary captures the plaintext and ciphertext pair, $(\mathbf{x}, \mathbf{y})$. Furthermore, the systems that use

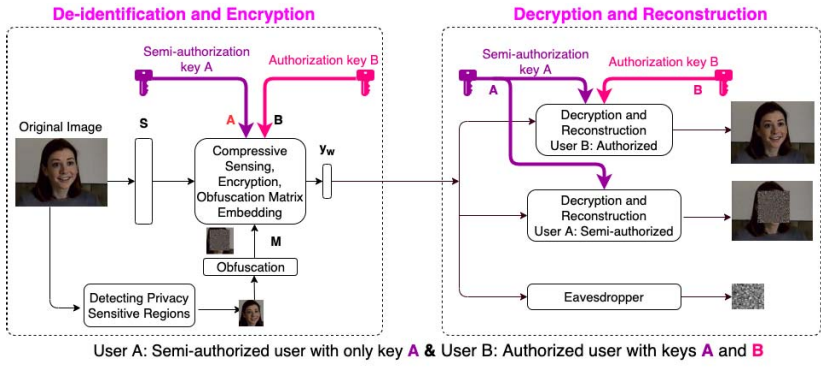

Fig. 1. Proposed Reversible Privacy-Preserving Video Monitoring.

the same CS-encryption matrix many times are well known to be unsecure against this type of attacks [40], [42].

Due to interest in application scenarios of CS-based encryption, recently hybrid models that use both CS and conventional cipher systems have become popular. For instance, [48] applies a homomorphic cryptography function on top of the CS-encryption in a wireless sensor network system. In that sense, even in multi-usage of $\mathbf{A}$, the system can be made resilient against KPA. In another vein, authors in [49] have proposed a multi-class encryption system where the CS-encryption matrix is partially corrupted differently for each user, i.e., $\mathbf{A} = \mathbf{A} + \Delta\mathbf{A}$, $\Delta\mathbf{A}$ being the partial perturbation matrix. Their scheme suggests a framework to partially corrupt the CS-encryption matrix in order to obfuscate the sensitive region of the signal. However, it is not obvious how one transmits $\Delta\mathbf{A}$ to the receiving party for reversible de-identification. One intuitive approach would be sending $\Delta\mathbf{A}$ in a secure channel, which could be problematic, especially when the obfuscation pattern changes from usage to usage. Another solution is to use steganographic methods [16], [17], [50] to embed $\Delta\mathbf{A}$ directly on CS measurements, that is, by encoding the obfuscation matrix directly on the cipher-text $\mathbf{y}$. This is the path we follow and its details are introduced in the following section.

It is worth mentioning some recent work in the vein of compression (via sparsification) and encryption strategy. These methods extract a sparse code, $\mathbf{x}$, of the private signal and then obfuscate it. In [51]–[53] a ternary representation of the signal is extracted from its sparse code. Then this code is ambiguated for the privacy-protected data-sharing applications, e.g., outsourced media search or person identification applications. In [54], the authors study the reconstruction capability of sparse ternary codes given the information loss during its encoding to a ternary code. A more recent work [20] ambiguates the sparse code directly by noise addition while enabling high-quality recovery with successive refinement user.

IV. Proposed Two-Tiered Encryption

The proposed method exploits techniques of compressive sampling, compressive encryption and data hiding [14], [16], [17], [36], [37], [55]–[57]. The advantage of the CS-based technique is, on one side, that exact recovery (in strictly sparse case) or stable recovery (in approximately sparse case) of the undersampled signal is possible, and on the other side, cryptographic security can be provided.

As shown in Fig. 1, one tier of the security consists of the generation of a random corruption mask (one-time usage) to obfuscate the sensitive parts of the image. This information is then embedded directly onto the CS-encrypted signal with a ternary watermark. This data hiding scheme provides reversibility and one-time usage of the random corruption mask, which is essential for secure de-identification. In the two-tiered protection scheme, the semi-authorized user will be able to recover only the non-sensitive part while a fully authorized user is allowed to recover the whole signal.

A. Problem Definition

In the following section, we first start by giving a formal definition of the two-tiered protection scheme in the spirit of Shannon secrecy. We will define the desiderata that the ideal triple consisting of two decoders (type A, B) and an encoder must satisfy. The problem becomes then formally the design of the three mappings that guarantee the recovery and secrecy properties. Following these definitions, we give our compressive sensing based solution to the problem with a discussion of the advantages of the proposed system.

The signals of interest, $\mathbf{s} \in \mathbb{R}^N$ is composed of a sensitive part and a non-sensitive part, denoted as an orthogonal sum

$$\mathbf{s} = \mathbf{s_n} + \mathbf{s_s}, \tag{11}$$

where $\mathbf{s_s}$ is the sensitive part of the signal that can be obtained by zero-outing the coefficients of $\mathbf{s}$ which are not indexed by the corresponding index set Λ_p, and $\mathbf{s_n}$ is the remaining non-sensitive part of the signal whose non-zero coefficients are indexed by Λ_p^c. In what follows, we state the information-theoretic desiderata of the encoder and of the two decoders.

Definition 3: Fully Secure and Stable Encoder-Decoders Triple: $\mathcal{E}^*(.)$, $\mathcal{D}_1^*(.)$, $\mathcal{D}_2^*(.)$

1) We define the data coding operator (CS-Encryption) as $\mathcal{E}^*(.)$ that encrypts both the sensitive and non-sensitive

parts,

$$\mathcal{E}^*(\mathbf{s}) = \mathbf{y}, \tag{12}$$

which is perfectly secure in that the coded signal, $\mathbf{y}$ does not reveal any information about $\mathbf{s}$, i.e., $\Pr(\mathbf{s}|\mathbf{y}) = \Pr(\mathbf{s})$.

2) The first-tier decoder, $\mathcal{D}_1^*(.)$ which stably recovers the non-sensitive part while not disclosing any information about the sensitive part is characterized as follows

$$\left\| \left(\mathcal{D}_1^*\left(\mathcal{E}^*(\mathbf{s}) + \mathbf{e}\right)\right)_{\Lambda_\mathbf{p}^c} - \mathbf{s}_{\Lambda_\mathbf{p}^c} \right\|_2 \leq \kappa \|\mathbf{e}\|_2 \tag{13}$$

and

$$\Pr\left(\mathbf{s}_{\Lambda_\mathbf{p}} | \left(\mathcal{D}_1^*\left(\mathcal{E}^*(\mathbf{s}) + \mathbf{e}\right)\right)_{\Lambda_\mathbf{p}}\right) \approx \Pr\left(\mathbf{s}_{\Lambda_\mathbf{p}}\right), \tag{14}$$

where $\mathbf{e}$ is a possible additive perturbation on $\mathbf{y}$, i.e., $\mathbf{y} = \mathcal{E}^*(\mathbf{s}) + \mathbf{e}$.

3) Finally, the second-tier decoder that stably recovers both sensitive and non-sensitive parts is defined as

$$\left\| \left(\mathcal{D}_2^*\left(\mathcal{E}^*(\mathbf{s}) + \mathbf{e}\right)\right) - \mathbf{s} \right\|_2 \leq \kappa \|\mathbf{e}\|_2. \tag{15}$$

The goal now is to find a practical coding operator, $\mathcal{E}(.)$ that jointly encrypts the sensitive and non-sensitive parts, which is as close as possible to the ideal operator $\mathcal{E}^*(.)$.

B. Embedding Operator, $\mathcal{E}(.)$

1) Obfuscation of the Sensitive Part Within CS-Encryption: The proposed embedding operator obfuscates the sensitive part $\mathbf{s}_{\Lambda_\mathbf{p}}$ of the signal with the masking pattern $\Delta_{\Lambda_\mathbf{p}}$, and then compressively samples the whole, consisting of the combination of the non-sensitive part $\mathbf{s}_\mathbf{n}$ and the masked sensitive part. The resulting intermediate code $\mathbf{y_d}$ is given by:

$$\mathbf{y_d} = \mathbf{A}_{\Lambda_\mathbf{p}^c}\mathbf{s}_{\Lambda_\mathbf{p}^c} + \mathbf{A}_{\Lambda_\mathbf{p}}\Delta_{\Lambda_\mathbf{p}}\mathbf{s}_{\Lambda_\mathbf{p}} = \mathbf{A}\mathbf{s}_\mathbf{n} + \mathbf{A}_{\Lambda_\mathbf{p}}\Delta_{\Lambda_\mathbf{p}}\mathbf{s}_{\Lambda_\mathbf{p}}, \tag{16}$$

where $\mathbf{s}_{\Lambda_\mathbf{p}}$ and $\mathbf{s}_{\Lambda_\mathbf{p}^c}$ are the extracted sensitive and non-sensitive parts of $\mathbf{s}$, respectively. Here $\Delta_{\Lambda_\mathbf{p}} \in \mathbb{R}^{|\Lambda_p| \times |\Lambda_p|}$ is the multiplicative obfuscation operator, i.e., a diagonal matrix consisting of random numbers and operates only on the (vectorized) sensitive part of the signal, $\mathbf{s_s}$. In other words, $\mathbf{A}_{\Lambda_\mathbf{p}} \in \mathbb{R}^{m \times |\Lambda_p|}$ and $\mathbf{A}_{\Lambda_\mathbf{p}^c} \in \mathbb{R}^{m \times (N - |\Lambda_p|)}$ are the matrices consisting of the subsets of columns of $\mathbf{A}$ that are indexed by index sets Λ_p and Λ_p^c, respectively. The encoding in $\mathbf{y_d}$ can also be formulated as an additive mask:

$$\mathbf{y_d} = (\mathbf{A} + \mathbf{M})\,\mathbf{s}, \tag{17}$$

where $\mathbf{M} \in \mathbb{R}^{m \times N}$ is the masking matrix with all zeros except the columns, $\mathbf{M}_{\Lambda_\mathbf{p}} \in \mathbb{R}^{m \times |\Lambda_p|}$. The non-zero columns of the masking matrix form can be easily calculated from Eq. (16), i.e., $\mathbf{M}_{\Lambda_\mathbf{p}} = \mathbf{A}_{\Lambda_\mathbf{p}}\Delta_{\Lambda_\mathbf{p}} - \mathbf{A}_{\Lambda_\mathbf{p}}$.

2) Data Hiding With Reversibility: The obfuscation matrix $\Delta_{\Lambda_\mathbf{p}}$ and its location information (if necessary) are converted to a binary code to be secretly embedded on top of the compressively sensed (encrypted) signal $\mathbf{y_d}$. The conversion of this information to a binary code is necessary to achieve reversibility. Indeed, the exact recovery of the watermark sequence is possible [16], even in noisy case (In our scheme, noise corresponds to the masking in the sensitive part) provided the signal, $\mathbf{s}$, is sparse. In a practical application, errors in a few bits on the recovered watermark is tolerable. We can define a procedure that spits out a watermark $\mathbf{w}'$ corresponding to the binary representation of $\beta\left(\Delta_{\Lambda_\mathbf{p}}\right)$,

$$\beta\left(\Delta_{\Lambda_\mathbf{p}}\right) \rightarrow \mathbf{w}' \in \{-a, +a\}^{T'}, \tag{18}$$

where $\beta\left(\Delta_{\Lambda_\mathbf{p}}\right)$ is sufficient information to re-produce $\Delta_{\Lambda_\mathbf{p}}$. An example of such an operator is given in Eqs. (35) - (36c). We also need an inverse operator of (18) in order to reproduce $\Delta_{\Lambda_\mathbf{p}}$ from watermark signal, i.e., $\mathbf{w}'$ as $\hat{\mathbf{w}} \overset{\beta^{-1}}{\rightarrow} \hat{\Delta}_{\Lambda_p}$. This operator is defined in Eqs. (25)- (28). Note that the length of the watermark, T', can change for each use case. To accommodate varying length watermarks one can fix a maximum watermark length, T, and extend the binary code $\mathbf{w}'$ to a ternary one by stuffing with zeros the remaining $T - T'$ bits, i.e.,

$$\beta\left(\Delta_{\Lambda_\mathbf{p}}\right) \rightarrow \mathbf{w} \in \{-a, +a, 0\}^T. \tag{19}$$

Data hiding limits [16], [17] determine the maximum steganographic capacity T one can expect to realize. Finally, a watermark embedding matrix (based on the second authorization key) $\mathbf{B} \in \mathbb{R}^{m \times T}$, $T < m$ is generated to linearly spread the watermark $\mathbf{w}$ directly onto the CS-encrypted signal, i.e., the cipher-text

$$\mathbf{y_w} = \mathbf{y_d} + \mathbf{B}\mathbf{w} = (\mathbf{A} + \mathbf{M})\mathbf{s} + \mathbf{B}\mathbf{w}. \tag{20}$$

An embedding power constraint $\|\mathbf{B}\mathbf{w}\| \leq P_E$ must be imposed in order to limit the degeneration of the recovered (non-sensitive) part of the image for semi-authorized users. The proposed embedding scheme, $\mathcal{E}(.)$ is given in Algorithm 1.

Algorithm 1 Proposed Embedding, $\mathcal{E}(.)$

Input: $\mathbf{s}$, $\mathbf{A}$, $\mathbf{B}$;
1. Determine the mask and the obfuscation matrix, $\Delta_{\Lambda_\mathbf{p}}$
2. Generate the watermark: $\beta\left(\Delta_{\Lambda_\mathbf{p}}\right) \rightarrow \mathbf{w} \in \{-a, +a, 0\}^T$
3. Joint CS-encryption and sensitive part obfuscation:
$\mathbf{y_d} = \mathbf{A}_{\Lambda_\mathbf{p}^c}\mathbf{s}_{\Lambda_\mathbf{p}^c} + \mathbf{A}_{\Lambda_\mathbf{p}}\Delta_{\Lambda_\mathbf{p}}\mathbf{s}_{\Lambda_\mathbf{p}}$
4. Watermark Embedding: $\mathbf{y_w} = \mathbf{y_d} + \mathbf{B}\mathbf{w}$
Return: $\mathbf{y_w}$

C. Design of the Two-Tiered Decoders, $\mathcal{D}_1(.)$, $\mathcal{D}_2(.)$

Users (type A or B) receive the watermarked and encrypted signal, $\mathbf{y_w}$ which can be re-cast as

$$\mathbf{y_w} = (\mathbf{A} + \mathbf{M})\mathbf{s} + \mathbf{B}\mathbf{w} = \mathbf{H}\mathbf{x} + \mathbf{B}\mathbf{w} + \mathbf{n}, \tag{21}$$

where $\mathbf{H}\mathbf{x} = \mathbf{A}\mathbf{\Phi}\mathbf{x} = \mathbf{A}\mathbf{s}$, and $\mathbf{x} \in \mathbb{R}^N$ is the sparse representation of $\mathbf{s}$ in Φ, and the masked part can be expressed as noise term, i.e., $\mathbf{n} = \mathbf{M}\mathbf{s} = \mathbf{M}_{\Lambda_\mathbf{p}}\mathbf{s}_{\Lambda_\mathbf{p}} = \left(\mathbf{A}_{\Lambda_\mathbf{p}}\Delta_{\Lambda_\mathbf{p}} - \mathbf{A}_{\Lambda_\mathbf{p}}\right)\mathbf{s}_{\Lambda_\mathbf{p}}$. For the receiver of Type-A (the semi-authorized user A) only the key $\mathbf{A}$ is available. Since this user does not have the watermark encrypting key, $\mathbf{B}$, (s)he will perceive the cyper-text as

$$\mathbf{y_w} = \mathbf{H}\mathbf{x} + \mathbf{z}, \tag{22}$$

where $\mathbf{z}$ behaves like an additive structural noise, i.e., $\mathbf{z} = \mathbf{B}\mathbf{w} + \mathbf{n}$. In the light of the discussion in Section 1, the ℓ_1-minimization scheme in (5) can be used to recover $\mathbf{x}$ with

$\Upsilon(\mathbf{y}) = \{\mathbf{x} : \|\mathbf{Hx} - \mathbf{y}\|_2 \leq \epsilon\}$. Afterwards, using the outcome of the ℓ_1 minimization technique, $\hat{\mathbf{x}}$, one can obtain an estimate of the signal $\mathbf{s}$ with mask, $\hat{\mathbf{s}}$, straightforwardly via $\hat{\mathbf{s}} = \mathbf{\Phi}\hat{\mathbf{x}}$. The decoding algorithm for semi-authorized users, $\mathcal{D}_1(.)$ is given in Algorithm 2.

Algorithm 2 Type a Decoding Algorithm, $\mathcal{D}_1(.)$

Input: $\mathbf{y_w}$, $\mathbf{A}$, $\mathbf{\Phi}$;
Hyper-parameters: ϵ
1. Estimate $\hat{\mathbf{x}}$: $\tilde{\mathbf{x}} = \arg\min_{\mathbf{x}} \|\mathbf{x}\|_1 \quad \text{s.t.} \quad \|\mathbf{y_w} - \mathbf{Hx}\|_2 \leq \epsilon$
2. $\hat{\mathbf{s}} = \mathbf{\Phi}\hat{\mathbf{x}}$.
Return: $\hat{\mathbf{s}}$

The receiver of Type-B, (the fully-authorized user B) will possess both CS-encryption key, $\mathbf{A}$, and watermark encryption key, $\mathbf{B}$. Type-B decoder must recover the whole signal $\mathbf{s_n} + \mathbf{s_s}$ with as low a reconstruction error as possible. A three-stage recovery scheme is proposed, which is adapted from the recovery method proposed in [16]: First, a raw estimate of the sparse signal is obtained by disregarding the watermark part $\mathbf{Bw}$ and using the ℓ_1-minimization (5). Second, after having a preliminary estimation of $\mathbf{x}$, the watermark can be recovered from the over-determined system of linear equations by subtracting the estimated $\mathbf{x}$ component from $\mathbf{y_w}$. In the final stage, the masking matrix, $\mathbf{M}$, can be produced via the recovered watermark, and an improved estimation is obtained using the $\mathbf{A} + \mathbf{M}$ as CS-encryption matrix and ℓ_1-minimization. The details of the proposed scheme are as follows:

First, we produce a left annihilator matrix $\mathbf{F} \in \mathbb{R}^{p \times m}$ of $\mathbf{B} \in \mathbb{R}^{m \times T}$ so that $\mathbf{FB} = 0$, where $p = m - T$. Left multiplying $\mathbf{y_w}$ with $\mathbf{F}$ we obtain,

$$\tilde{\mathbf{y}} = \mathbf{Fy_w} = \mathbf{F}(\mathbf{Hx} + \mathbf{Bw} + \mathbf{n}) = \mathbf{FHx} + \mathbf{n}', \tag{23}$$

where $\mathbf{n}' = \mathbf{Fn}$. Eq. (23) is also an underdetermined linear system of equations and can be solved via ℓ_1-minimization as discussed in Section 1:

$$\tilde{\mathbf{x}} = \arg\min \|\mathbf{x}\|_1 \ \text{ s.t. } \ \|\tilde{\mathbf{y}} - \mathbf{FHx}\|_2 \leq \epsilon. \tag{24}$$

After inserting the pre-estimation of $\mathbf{x}$ in $\mathbf{H}\tilde{\mathbf{x}}$ and subtracting it from the $\mathbf{y_w}$, we get an over-determined system of linear equations: $\mathbf{y_w} - \mathbf{H}\tilde{\mathbf{x}} = \mathbf{Bw}$. Therefore, a raw estimation of the watermark can be obtained via

$$\mathbf{w}'' = (\mathbf{B}^T\mathbf{B})^{-1}\mathbf{B}^T(\mathbf{y_w} - \mathbf{H}\tilde{\mathbf{x}}). \tag{25}$$

The 0's in the ternary watermark, $\mathbf{w}$ can be extracted using simple thresholding if the length of active bits T' is unknown to user B:

$$\tilde{\mathbf{w}} = \mathbf{w}'' \odot \mathbf{1}_{|w_i''| > \eta}, \tag{26}$$

where η is the threshold value

$$1_{|w_i''| > \eta, i} = \begin{cases} 1, & \text{if } |w_i''| > \eta, \quad (27a) \\ 0 & \text{else}, \quad (27b) \end{cases}$$

and $\odot$ denotes the element-wise multiplication operator between two vectors. In some practical applications such as person de-identification on video streams (details will be given in Section V), this step is simplified to $\tilde{\mathbf{w}} = \mathbf{w}'' \odot \mathbf{1}_{T'}$, where $\mathbf{1}_{T'}$ is T-length vector with the first T' elements 1's and the rest is all zeros. The locations of the non-zero elements of $\mathbf{1}_{T'}$ can be found using the information of Λ_p, inherent in the pre-estimated signal, $\mathbf{\Phi}\tilde{\mathbf{x}}$. Alternatively, a pre-allocated set from watermark, $\mathbf{w}$, can be dedicated to secretly carry information about T'. Hereafter, the finer estimation of $\mathbf{w}$ can be easily found via

$$\hat{w}_i = a \times \text{sgn}(\tilde{w}_i). \tag{28}$$

Meanwhile the decoder can obtain the masking matrix, $\mathbf{M}$, i.e., $\hat{\mathbf{M}} = \left(\mathbf{A}_{\Lambda_\mathbf{p}}\Delta_{\hat{\Lambda}_p} - \mathbf{A}_{\Lambda_\mathbf{p}}\right)$, where $\hat{\mathbf{w}} \overset{\beta^{-1}}{\rightarrow} \Delta_{\hat{\Lambda}_p}$. Finally, the sensitive and non-sensitive parts can be jointly recovered as:

$$\hat{\mathbf{x}} = \arg\min_{\mathbf{x}} \ \|\mathbf{x}\|_1 \ \text{ s.t. } \ \left\|(\mathbf{y} - \mathbf{B}\hat{\mathbf{w}}) - (\mathbf{A} + \hat{\mathbf{M}})\mathbf{\Phi x}\right\|_2 \leq \epsilon. \tag{29}$$

Algorithm 3 Type B Decoding Algorithm, $\mathcal{D}_2(.)$

Input: $\mathbf{y_w}$, $\mathbf{A}$, $\mathbf{B}$, $\mathbf{\Phi}$;
Hyper-parameters: ϵ, a, η
1. Apply $\mathbf{F}$ to $\mathbf{y_w}$: $\tilde{\mathbf{y}} = \mathbf{Fy_w}$
2. Estimate $\tilde{\mathbf{x}}$: $\tilde{\mathbf{x}} = \arg\min_{\mathbf{x}} \|\mathbf{x}\|_1 \ \text{ s.t. } \ \|\tilde{\mathbf{y}} - \mathbf{FHx}\|_2 \leq \epsilon$
3. Estimate $\mathbf{w}''$: $\mathbf{w}'' = (\mathbf{B}^\mathrm{T}\mathbf{B})^{-1}\mathbf{B}^\mathrm{T}(\mathbf{y_w} - \mathbf{H}\tilde{\mathbf{x}})$
4a. Thresholding $\mathbf{w}''$: $\tilde{\mathbf{w}} = \mathbf{w}'' \odot \mathbf{1}_{|w_i''| > \eta}$
4b. Forming $\hat{\mathbf{w}}$, where $\hat{w}_i = a * \text{sgn}(\tilde{w}_i)$
5. Obtain $\hat{\mathbf{M}}$ from $\hat{\mathbf{w}}$: i) $\hat{\mathbf{w}} \overset{\beta^{-1}}{\rightarrow} \Delta_{\hat{\Lambda}_p}$ ii) $\hat{\mathbf{M}} = \left(\mathbf{A}_{\Lambda_\mathbf{p}}\Delta_{\hat{\Lambda}_p} - \mathbf{A}_{\Lambda_\mathbf{p}}\right)$
6. $\hat{\mathbf{x}} = \arg\min_{\mathbf{x}} \ \|\mathbf{x}\|_1 \ \text{ s.t. } \ \left\|(\mathbf{y_w} - \mathbf{B}\hat{\mathbf{w}}) - (\mathbf{A} + \hat{\mathbf{M}})\Phi\mathbf{x}\right\|_2 \leq \epsilon$
7. $\hat{\mathbf{s}} = \Phi\hat{\mathbf{x}}$.
Return: $\hat{\mathbf{s}}$

D. Impact of Random Matrices on CS Encryption Performance

Generations of the CS-encryption matrix $\mathbf{A}$ and of the watermark embedding matrix $\mathbf{B}$ play an important role for the security and recovery robustness of the encryption scheme $\mathcal{E}(.), \mathcal{D}_1(.), \mathcal{D}_2(.)$. The choice of random Gaussian matrices as in (8) for $\mathbf{A}$ is convenient because they are known to be universally optimum in the sense that they satisfy both robustness and security conditions regardless of the sparsifying basis Φ. These matrices have been well investigated in the literature in terms of both recovery performance as in Corollary 1 and in terms of security metrics as discussed in Section III-B. In the sequel, we will consider $\mathbf{A}$ as in (8) and $\mathbf{B}$ consisting of orthonormal columns. For this scenario, we make a RIP based theoretical guarantee condition in watermark recovery for $\mathcal{D}_2(.)$. The following lemma will be useful for the stability analysis of the decoder type-B:

Lemma 1: Consider that the embedding, $\mathcal{E}(.)$, given by Algorithm 1 produces an encrypted signal $\mathbf{y_w}$ from $\mathbf{s}$ with keys $\mathbf{A}$ and $\mathbf{B}$, i.e., $\mathcal{E}(\mathbf{s}) = \mathbf{y_w} = \mathbf{Hx} + \mathbf{Bw} + \mathbf{n}$. Let $\mathbf{s_p} \in \mathbb{R}^{|\Lambda_p| \times 1}$ denote the perturbation on the sensitive part of the signal such that $\mathbf{s_p} = \Delta_{\Lambda_\mathbf{p}}\mathbf{s}_{\Lambda_\mathbf{p}} - \mathbf{s}_{\Lambda_\mathbf{p}}$. Let also $\mathbf{A}$ be an $m \times N$

CS-encryption matrix with elements $A_{i,j}$ drawn i.i.d. according to $\mathcal{N}(0, \frac{1}{m})$. Therefore the noise pattern $\mathbf{n}$ *in* (21) *is also a Gaussian random vector which has i.i.d. elements*

$$n_i \sim \mathcal{N}(0, \frac{\|\mathbf{s_p}\|_2^2}{m}). \tag{30}$$

Proof: Let A_{i,Λ_p} be the the i^{th} row of $\mathbf{A}_{\Lambda_\mathbf{p}}$. Then the elements of the vector, $\mathbf{A}_{\Lambda_\mathbf{p}}\mathbf{s_p} \in \mathbb{R}^{m\times 1}$ will be $\mathbf{n}_i = \langle A_{i,\Lambda_p}, \mathbf{s_p}\rangle$ independent Gaussian random variables with zero means, where $\langle \mathbf{v_1}, \mathbf{v_2}\rangle$ refers to inner product of vectors $\mathbf{v_1}, \mathbf{v_2}$. Therefore, it remains to prove that $\mathbb{E}(n_i^2) = \frac{\|\mathbf{s_p}\|_2^2}{m}$, which can be straightforwardly obtained (using i.i.d. property)

$$\mathbb{E}\left(n_i^2\right) = \mathbb{E}\left(\langle A_{i,\Lambda_p}, \mathbf{s_p}\rangle^2\right) = \mathbb{E}\left(\sum_{j\in\Lambda_p} A_{i,j}^2\ s_{p_j}^2\right)$$
$$= \sum_{j\in\Lambda_p} s_{p_j}^2\, \mathbb{E}\left(A_{i,j}^2\right) = \frac{1}{m}\sum_{j\in\Lambda_p} s_{p_j}^2 = \frac{\|\mathbf{s_p}\|_2^2}{m}. \tag{31}$$

■

Having Lemma (1), and using Corollary 1 from the literature, we are ready to state the following theorem for watermark recovery probability of $\mathcal{D}_2(.)$:

Theorem 4: Consider the Gaussian CS-encryption matrix defined in Eq. (8)*. Let the watermark-encoding matrix* $\mathbf{B}$ *have orthonormal columns. $\delta_{2k}(\mathbf{H}) < \sqrt{2}-1$ and $\delta_{2k}(\mathbf{FH}) < \sqrt{2}-1$ are given. Let also the annihilator matrix* $\mathbf{F}$ *have orthogonal rows such that $\|F_{i,:}\|_2 = \frac{m}{p}$, where $F_{i,:}$ denotes the i^th row of* $\mathbf{F}$*. For a marked ciphertext,* $\mathbf{y_w}$*, for a particular setting of $\epsilon = (1+\gamma)\sqrt{m}\sigma_n$, Eq.* (28) *to be used in Algorithm 3 can recover w_i, the watermark bits, correctly* $\Pr(w_i = \hat{w_i})$ *with probability at least*

$$\left(1 - 2\exp\left(\frac{-a'^2\ m}{8\left\{C^2(1+\gamma)^2\right\}\|\mathbf{s_p}\|^2}\right)\right)$$
$$\times\left(1 - \exp\left(-\frac{3p}{4}\gamma^2\right)\right), \tag{32}$$

where $C = 4\frac{\sqrt{1+\delta_{2k}(\mathbf{FH})}}{1-(1+\sqrt{2})\delta_{2k}(\mathbf{FH})}$ and $a' = a - \eta$, where a, ϵ and η are hyper-parameters used in Algorithm 3.

The proof of the theorem is given in Appendix VII. Theorem 4 establishes a bound on the watermark recovery probability as a function of the energy of perturbation on the sensitive part, RIC of the matrix $\mathbf{FH}$ and watermark embedding strength a. This type of analysis based on RIP for the CS reconstruction algorithm as in Corollary 1 is known as theoretical guarantee conditions in worst-case scenario [58]. In general, for most of the practical applications, the algorithms perform much better than the performance bounds given by this kind of RIP based analysis. Nevertheless, it gives us an indication on how to design the related matrices for the encoder (such as $\mathbf{A}$, $\mathbf{B}$, $\mathbf{H}$) and how to choose hyperparameters for the decoders. For example, choosing both $\mathbf{F}$ and $\mathbf{H}$ as Gaussian matrices may not be the right decision since the product of two random Gaussian matrices is a random matrix with coefficients drawn from a heavy-tailed distribution [59], which yields a $\delta_{2k}(\mathbf{FH})$ bigger than the Gaussian case.

E. Choice of the Encryption Matrix

Although random measurement matrices are optimal in the universal sense, they become computationally unwieldy for realistic signal and measurement dimensions, N and m, respectively. Recall that the iterative signal reconstruction algorithms require transposition and multiplication of the measurement matrix several times. To ease this computational burden, one can choose the rows of the measurement (CS-encryption) matrix randomly as a subset of an orthonormal and fast implementable transform base such as Fourier, DCT, or Hadamard. In other words, one can choose m rows randomly out of the N the rows of an orthonormal transform, Θ. These rows are indexed by $\Omega \in \{1, 2, 3, \ldots, N\}$, i.e., with cardinality $|\Omega| = m$. Thanks to these types of structural CS matrices, the computational cost of $\mathbf{As}$ can be reduced significantly, i.e., down to $O(N \log N)$ flops from $O(m \times N)$ flops for general random CS matrices. For a good choice of the measurement matrix, $\mathbf{A} = \Theta_\Omega$ in terms of a sparsifying basis Φ the rows of $\mathbf{H}$ must be as flat (dense with nonzero elements) as possible. This can be satisfied when the rows of the measurement matrix $\mathbf{A}$ are not sparse in the sparsifying basis Φ. This requirement can be quantified via the "mutual coherence" functional, i.e, $\mu(\mathbf{H}) = \max_{i,j}|H_{i,j}|$. The performance limits of the ℓ_1-decoding schemes such as (BPDN) case are given in terms of the functional $\mu(\mathbf{H})$. If one chooses randomly m rows of an orthonormal basis, Θ, indexed by $\Omega \in \{1, 2, 3, \ldots, N\}$ to build a measurement matrix $\mathbf{A}$, then a k-sparse signal can be exactly reconstructed as a solution of the ℓ_1-decoding (BP) in (5), satisfying $m \geq O(\mu^2(\Theta)\times k \times \log N)$, with an overwhelming probability [60].

We have chosen the Noiselet basis and the 2-D Wavelet basis to create a CS-encryption matrix and a sparsifying matrix, respectively. First, since these two transforms are known to be maximally incoherent with each other, and second because they have fast implementations. The indices of the chosen rows are randomly drawn and then permuted to increase the security level.

F. Design of the Annihilator Matrix $\mathbf{F}$ *and Its Corresponding Watermark Embedding Matrix* $\mathbf{B}$

The watermark embedding matrix $\mathbf{B}$, which must be the right null space matrix of $\mathbf{F}$, can also be chosen from a fast transform. For example, one can constitute the columns of $\mathbf{B}$ by choosing randomly a subset of the rows of DCT basis matrix, then, the rows of $\mathbf{F}$ can be made up of the remaining rows of this DCT matrix.

Theorem 4 implies that the choice of matrices $\mathbf{F}$ and $\mathbf{H}$ influences the performance of the Algorithm 3. To investigate the impact of the choice of $\mathbf{F}$ on $\mathbf{FH}$, we compare the performance of the ℓ_1 minimization on the recovery of sparse signal $\mathbf{x}$ from $\mathbf{y} = \mathbf{FHx}$, for three different settings: (i) First, with the random Gaussian measurement matrix $\mathbf{FH}$ as in Lemma 1, Theorem 4. (ii) Second, for the case where $\mathbf{F}$ is made up of a subset of the rows of DCT, $\mathbf{A}$ is similarly made of a subset of Noiselet basis, sparsifying matrix Φ is chosen as Haar basis. Figure 2a shows the average mutual coherence values of $\mathbf{FH}$ under different setups. Figure 2b shows the exact recovery probabilities at

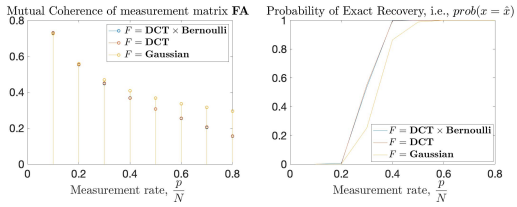

Fig. 2. Average mutual coherence of the matrix $\mathbf{FH} = \mathbf{FA}\Phi$ for different realizations of $\mathbf{A}$ and calculated probability of exact recovery over 250 trials. An exactly sparse signal is synthetically produced for $N = 256$ and $k = 30$.

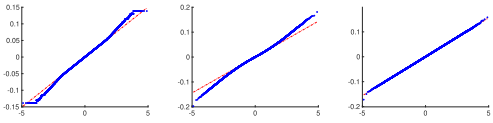

Fig. 3. Q-Q plots of the elements of the measurement matrices in reduced dimension, **FH**. Vertical: sample data quantiles; horizontal: standard normal quantiles. a) $\mathbf{FH} = \mathbf{Noiselet} \times \mathbf{Wavelet}$ b) $\mathbf{FH} = \mathbf{DCT} \times \mathbf{Noiselet} \times \mathbf{Wavelet}$ c) $\mathbf{FH} = \mathbf{DCT} \times \mathbf{Bernoulli} \times \mathbf{Noiselet} \times \mathbf{Wavelet}$.

different measurement rates for the three different choices of $\mathbf{F}$. These results prove that even if the random measurement matrix is universally optimum in the sense that it guarantees the exact recovery for any sparsifying basis in the worst case scenario, in practice structured matrices obtained from orthonormal transforms can perform even better. We make use of the mutual coherence functional; the formula below is slightly different from that given in the previous subsection, though related to it: $\mu(\mathbf{H}) = \max_{1\le i\le j\le N}\left(\frac{|<\mathbf{h_i},\mathbf{h_j}>|}{\|\mathbf{h_i}\|\|\mathbf{h_j}\|}\right)$ where $\mathbf{h_i}$ is the i^{th} column of matrix $\mathbf{H}$.

(iii) Alternatively, based on the arguments in [61], a randomization matrix can be applied to $\mathbf{F}$, i.e., $\mathbf{F}' = \mathbf{FR}$, where $\mathbf{R}$ is $m \times m$ matrix of all zeros, except the diagonal terms that are drawn from the Bernoulli distribution. In [61], it is proven that the matrix **FRH** with any orthonormal basis pair, $\mathbf{F}$, $\mathbf{H}$ and randomization matrix $\mathbf{R}$ with diagonal Bernoulli elements, approaches a Gaussian matrix. This is, in fact, illustrated in Figure 3 as quantile-quantile plots. Although, this does not result in any performance increase vis-à-vis mutual coherence and recovery performance as shown in Figure 2, this scheme will enhance the security level with only negligible additional computation in the recovery part. In Figure 3, the vertical axis denotes the level at which the empirical distribution falls below a Q level (e.g., 50%), while the horizontal axis indicates the quantiles for the standard Gaussian distribution. In all cases, the similarity between the distribution of the **FH** sensing matrices and that of a Gaussian sensing matrix is obvious. Distribution of sensing matrices approaching that of a Gaussian is a desirable characteristic both for data hiding and CS-encryption purposes.

G. Design of the Obfuscation Matrix

The region of interest (e.g., a face) to be obfuscated is delineated by Λ_p. Obfuscation matrix is constituted with all zero entries except for the diagonal elements that are drawn from a Bernoulli distribution with probability p_1, i.e.,

$$\Pr\left(\left(\Delta_{\Lambda_\mathbf{p}}\right)_{i,i} = \pm 1\right) = p_1 \tag{33}$$

The corresponding masking matrix $\mathbf{M}$ will be

$$M_{i,j} = \begin{cases} 0, & \text{if } j \in \Lambda_p \text{ and } \left(\Delta_{\Lambda_\mathbf{p}}\right)_{i,i} = 1 \quad (34a) \\ -2 * A_{i,j}, & \text{if } j \in \Lambda_p \text{ and } \left(\Delta_{\Lambda_\mathbf{p}}\right)_{i,i} = -1 \quad (34b) \\ 0, & j \notin \Lambda_p. \quad (34c) \end{cases}$$

Thus, the watermark generating procedure, will be

$$\beta\left(\Delta_{\Lambda_\mathbf{p}}\right) \rightarrow \left[\mathbf{w}'\ \mathbf{w}''\right], \tag{35}$$

where T'' bits $\mathbf{w}'$ are allocated for the location information of the sensitive part, i.e., the starting and ending points of rectangular region of interest including faces in the image and

$$w_i'' = \begin{cases} a, & \text{if } i \le \left|\Lambda_p\right| \text{ and } \left(\Delta_{\Lambda_\mathbf{p}}\right)_{i,i} = 1 \quad (36a) \\ -a, & \text{if } i \le \left|\Lambda_p\right| \text{ and } \left(\Delta_{\Lambda_\mathbf{p}}\right)_{i,i} = -1 \quad (36b) \\ 0 & i > \left|\Lambda_p\right|. \quad (36c) \end{cases}$$

Alternatively, having the intermediate estimation of image $\tilde{\mathbf{s}} = \Phi\tilde{\mathbf{x}}$, the obfuscated region can be easily deduced and extracted, without the need of data hiding the location information in $\mathbf{w}'$.

H. More Secure Obfuscation With a Key for a Gaussian Vector

A semi-authorized user with only key-A may try to make a brute-force attack, by trying out all possible binary combinations of $\left(\Delta_{\Lambda_\mathbf{p}}\right)_{i,i}$'s to un-hide the obfuscated region. Even though the computational complexity of this attack is impractically high, i.e., $2^{|\Lambda_p|}$, to make the privacy protection stronger one can make use a third key, g. This can be realized using a predefined vector $\mathbf{g} \in \mathbb{R}^N$, that is known only to fully-authorized user (type B), which is used to generate another obfuscation matrix as

$$\left(\Delta_{\Lambda_\mathbf{p}}\right)_{i,i} = \begin{cases} \left(g_{\Lambda_p}\right)_i \text{ with probability } p_1, & (37a) \\ -\left(g_{\Lambda_p}\right)_i \text{ with probability } 1-p_1, & (37b) \end{cases}$$

where $g_j \sim \mathcal{N}\left(\mu_g, \sigma_g^2\right)$.

V. A Case Study: Reversible Privacy-Preserving Video Monitoring

As a use case of the proposed two-tier image encryption algorithm, we investigate a video surveillance application where sensitive segments are to be concealed from semi-authorized users and revealed only to fully-authorized users. The sensitive parts of the image are the faces of people in the scene.

For face de-identification performance, we use two criteria: i) the Structural SIMilarity (SSIM) index [62] to measure the quality of the decoded and reconstructed image parts [63]; ii) face recognition accuracy via a machine learning algorithm

Fig. 4. Sample recovered frames for the semi-authorized (User A) and authorized (User B) (measurement rates 0.6, 0.7).

as an indicator of privacy protection [64], [65]. For the semi-authorized user (with only key **A**), we aim to have both minimum classification accuracy in the concealed parts and also minimum degradation in the reconstructed non-sensitive parts. For the fully-authorized user, we want to achieve the highest classification accuracy and highest reconstruction accuracy when both **A** and **B** keys are used for decoding.

We also test an attack scenario where the malicious user (e.g., a semi-authorized one or an attacker who has stolen the CS-encryption key, **A**) has access to the labels of face images in the training set, so that (s)he can train a classifier to make inferences from de-identified images. The experimental results (Section V-C and Table VI) show that our one-time usage of random obfuscation matrix prevents an adversarial from making an inference (identify the faces) even if the labels of the training set are captured.

A. Experimental Setup

The experimental evaluation is conducted on the YouTube Faces Database [22] to demonstrate the viability of the proposed method in such applications as video surveillance, intelligent access control, and in general, analytics for intelligent buildings. Accordingly, we have randomly chosen 5000 frames from YouTube Faces Database corresponding to 100 identities (50 frames per identity). Recovery performances are reported using 3000 frames while non-overlapping 2000 frames are collected to build the training set for privacy preservation performance evaluations. The Matlab implementation of the experiments and additional demos can be downloaded from https://github.com/mehmetyamac/CS-Privacy-Protection. We use a randomly chosen subset of the rows of noiselet basis as the measurement matrix. The implementation of the real-valued "dragon" noiselet is borrowed from [66]. As the sparsifying matrix, we choose wavelet "Coiflet 2" and use WaveLab850 [67] wavelet toolbox.[1] The columns of the encoding matrix **B** were chosen from the random subset of the columns of $m \times m$ DCT basis, and then were shuffled. Therefore, the rows of the annihilator matrix, **F** has been picked from the remaining columns and shuffled (i.e., $\mathbf{H} = \textbf{Noiselet} \times \textbf{Wavelet}$ and $\mathbf{F} = \textbf{DCT}$). Moreover, Gradient Projection for Sparse Reconstruction (GPSR) [68] was used for ℓ_1-minimization.

[1]The original packet requires the input images to be square with dyadic sides, the Matlab modification in http://gtwavelet.bme.gatech.edu/ can be used to perform wavelet transformation with rectangular images with dyadic sides.

TABLE II
LIST OF THE USER DEFINED PARAMETERS

Variable	Name	Chosen Value	Mentioned Section
T	Watermark capacity	30000	Section IV-B2
T''	Number of bits allocated to encode segment location	$T'' = 0$ (Assuming that Λ_p is correctly found from $\tilde{\mathbf{s}}$)	Eq. (35)
$\frac{\|\mathbf{Bw}\|}{\|\mathbf{y_d}\|}$	Watermark embedding power	Tuned from the training set	Section V-B
μ_g	Mean of Gaussian key, g	0.9	Eq. (37a)-(37b)
σ_g^2	Variance of Gaussian key, g	0.1	Eq. (37a)-(37b)
p_1	Parameter p of Bernoulli dist. to sample obfuscation matrix.	0.5	Eq. (33)

The various parameters taking place in the experiments are listed in Table II. For different watermark embedding power-to-signal ratio, $\frac{\|\mathbf{Bw}\|}{\|\mathbf{y_d}\|}$, and compression (measurement) rates, the performance of the decoders is reported in Section V-B.

B. Recovery Performance of $\mathcal{D}_1^*(.)$ and $\mathcal{D}_2^*(.)$

Choice of the watermark amplitude, a or alternatively the watermark embedding power is the determining factor in the watermark recovery performance (recall Theorem 4). In other words, the embedding power-to-signal ratio, $\frac{\|\mathbf{Bw}\|}{\|\mathbf{y_d}\|}$, forms the trade-off between the type A non-sensitive image recovery quality and type B sensitive image recovery quality. On the one hand, a should not be too small since the erroneous estimation of the watermark bits affects the recovery of w and $\Delta_{\hat{\Lambda}_p}$, hence the quality of the reconstructed sensitive part. On the other hand, increasing a could impede the decompression performance compromising the overall,$\mathbf{s_s} + \mathbf{s_{ns}}$ signal recovery, because the embedded watermark **Bw** acts as an additive noise in the decoder (Eq. (22)). This trade-off, recovery quality of sensitive regions (type B) and non-sensitive region for type A user, is observed in Figure 5. We have found empirically that good values of a are in the [0.085, 0.15] range, based on peak signal-to-noise ratios (PSNRs) and quality of recovered images.

In Table III, we show the recovery performance of type A and type B decoders for the concealed region, for the non-concealed region, and for the whole frame. Recovery qualities are reported for different compression rates (CS measurement rates: MR = m/N) and for two chosen values of $\frac{\|\mathbf{Bw}\|}{\|\mathbf{y_d}\|}$, namely, 0.15 and 0.085. Based on the visual assessment of the sample frames in Figure 4 and on the reported PSNR values in Table III, we can say that User A's reconstructed faces are unrecognizable, whereas their outside regions have adequate quality, albeit around 5 dB lower in PSNRs as compared to those of User B, especially at low MRs. For User B,

TABLE III

PSNR VALUES OVER SENSITIVE AND NON-SENSITIVE REGIONS OF THE FRAMES FOR DIFFERENT MEASUREMENT RATES (MR) WITH A BINARY MASK AND A BINARY MASKED GAUSSIAN FOR MASKING, AND FOR EMBEDDING STRENGTH $\frac{\|\mathbf{Bw}\|}{\|\mathbf{y_d}\|} = 0.085$ (TABLES a AND b); $\frac{\|\mathbf{Bw}\|}{\|\mathbf{y_d}\|} = 0.15$ (TABLES c AND d), RESPECTIVELY

(a)

	Sensitive Region		Non-sensitive Region		Whole Frame	
MR	**User A**	**User B**	**User A**	**User B**	**User A**	**User B**
0.3	11.90	16.61	26.37	27.31	21.67	24.24
0.4	11.65	20.23	28.61	30.91	22.20	27.36
0.5	11.48	24.63	30.51	34.59	22.50	30.92
0.6	11.36	29.79	32.06	38.17	22.66	34.92
0.7	11.28	35.0	33.29	41.30	22.75	38.83
0.8	11.22	39.37	34.25	43.69	22.80	42.02

(b)

	Sensitive Region		Non-sensitive Region		Whole Frame	
MR	**User A**	**User B**	**User A**	**User B**	**User A**	**User B**
0.3	12.06	16.82	26.56	27.34	21.81	24.37
0.4	11.84	20.31	28.78	30.93	22.35	27.49
0.5	11.68	24.49	30.64	34.62	22.67	31.02
0.6	11.57	29.34	32.18	38.22	22.84	34.96
0.7	11.49	34.18	33.40	41.33	22.94	38.79
0.8	11.43	38.17	34.36	43.71	22.99	41.90

(c)

	Sensitive Region		Non-sensitive Region		Whole Frame	
MR	**User A**	**User B**	**User A**	**User B**	**User A**	**User B**
0.3	11.93	20.08	24.94	27.57	21.11	25.58
0.4	11.70	24.54	26.46	31.46	21.57	29.38
0.5	11.53	29.46	27.64	35.37	21.83	33.46
0.6	11.40	34.33	28.54	38.83	21.98	37.31
0.7	11.30	38.14	29.22	41.65	22.06	40.47
0.8	11.22	40.72	29.73	43.85	22.11	42.79

(d)

	Sensitive Region		Non-sensitive Region		Whole Frame	
MR	**User A**	**User B**	**User A**	**User B**	**User A**	**User B**
0.3	12.09	20.21	25.11	27.68	21.24	25.74
0.4	11.88	24.45	26.61	31.57	21.71	29.52
0.5	11.72	29.10	27.77	35.48	21.98	33.56
0.6	11.60	33.61	28.66	38.90	22.13	37.32
0.7	11.50	37.07	29.32	41.69	22.22	40.39
0.8	11.43	39.42	29.83	43.88	22.27	42.67

TABLE IV

STRUCTURAL SIMILARITY INDEX (SSIM) OVER ANONYMIZED REGIONS FOR DIFFERENT MEASUREMENT RATES (MR) USING BINARY MASK AND BINARY MASKED GAUSSIAN FOR MASKING FOR EMBEDDING STRENGTH $\frac{\|\mathbf{Bw}\|}{\|\mathbf{y_d}\|} = 0.085$ IN (a) AND 0.15 IN (b)

(a)

	Binary		Gaussian	
MR	**User A**	**User B**	**User A**	**User B**
0.3	0.207	0.509	0.210	0.520
0.4	0.198	0.635	0.204	0.643
0.5	0.191	0.751	0.197	0.756
0.6	0.187	0.848	0.192	0.851
0.7	0.183	0.914	0.189	0.915
0.8	0.180	0.948	0.186	0.948

(b)

	Binary		Gaussian	
MR	**User A**	**User B**	**User A**	**User B**
0.3	0.205	0.646	0.211	0.656
0.4	0.196	0.768	0.202	0.775
0.5	0.190	0.864	0.195	0.867
0.6	0.185	0.921	0.190	0.921
0.7	0.181	0.951	0.186	0.951
0.8	0.177	0.966	0.183	0.965

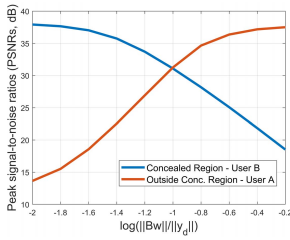

Fig. 5. Peak signal-to-noise ratios (PSNRs, dB) over recovered non-sensitive part (red curve), and sensitive part (blue curve) with the keys, respectively, of User A and User B. Measurement rate is fixed at 0.6.

the reconstruction quality of both the concealed regions and the whole frame are satisfactory; there is only small detail losses in the privacy-sensitive parts.

In Table IV, SSIM values for the concealed region of reconstructed images are reported. It can be seen that faces in recovered images with using only Key **A** result in very low SSIM scores, making the unrecognizable, while their SSIM scores are very high for user type B, especially at MRs above 0.5.

C. Performance in Privacy Preservation

Privacy-preserving performance of the proposed method is evaluated by demonstrating its robustness against the state-of-art face recognition attacks. To this end, we employed a pre-trained Convolutional Neural Network (CNN) provided by the dlib library [69] to extract the facial features. Then, face recognition is performed as follows: We extract 128-dimensional embedded (CNN) face recognition features and build a database consisting of labeled faces for the query; then, perform a nearest-neighbor search and select the first nearest identity as the classification output. The experimental results are evaluated for two types of attacks.

1) Attack Type I: Known Plain-Text (Original Faces), Known Labels: In this scenario, a malicious user with the stolen Key **A** (or a malevolent type A user) may capture the training set with its labels to train a classifier to decipher the anonymized faces. The experiment designed to test the de-identification robustness against this type of attack is as follows: We construct a query database consisting of 2000 original clear frames (20 frames per identity). Then, we perform face recognition in the face regions that have

TABLE V

FACE RECOGNITION RATES OF USER A AND USER B, THE SEMI-AUTHORIZED AND AUTHORIZED USERS, RESPECTIVELY, FOR DIFFERENT MEASUREMENT RATES (MR) USING A BINARY MASK AND A BINARY MASKED GAUSSIAN FOR MASKING, AT $\frac{\|\mathbf{Bw}\|}{\|\mathbf{y_d}\|} = 0.085$ (TABLES A AND B), AND AT $\frac{\|\mathbf{Bw}\|}{\|\mathbf{y_d}\|} = 0.15$ (TABLES C AND D), RESPECTIVELY. THE RECOGNITION ACCURACY ON ORIGINAL FRAMES IS 77.37%

(a)

MR	0.3	0.4	0.5	0.6	0.7	0.8
User A	0.0167	0.0183	0.0197	0.019	0.0187	0.0183
User B	0.0813	0.2353	0.4347	0.6107	0.7037	0.7353

(b)

MR	0.3	0.4	0.5	0.6	0.7	0.8
User A	0.017	0.0183	0.022	0.018	0.0207	0.019
User B	0.0797	0.2213	0.419	0.6073	0.707	0.7347

(c)

MR	0.3	0.4	0.5	0.6	0.7	0.8
User A	0.0147	0.021	0.0187	0.0173	0.0167	0.017
User B	0.199	0.4207	0.6323	0.705	0.7457	0.7553

(d)

MR	0.3	0.4	0.5	0.6	0.7	0.8
User A	0.0173	0.019	0.0183	0.0193	0.0173	0.0177
User B	0.1887	0.415	0.6193	0.6977	0.7417	0.7527

TABLE VI

FACE RECOGNITION RATES OF THE SEMI-AUTHORIZED USER WHEN THE CORRUPTED IMAGES FROM USER A ARE ADDED INTO SEARCH SPACE FOR NEAREST-NEIGHBOR. THE ACCURACIES ARE REPORTED FOR DIFFERENT MEASUREMENT RATES (MR) WITH $\frac{\|\mathbf{Bw}\|}{\|\mathbf{y_d}\|} = 0.085$, AND 0.15 USING A BINARY MASK AND A BINARY MASKED GAUSSIAN FOR THE MASKING

	Binary		Gaussian	
MR	0.085	0.15	0.085	0.15
0.3	0.017	0.0147	0.017	0.0173
0.4	0.0187	0.021	0.0183	0.019
0.5	0.0197	0.0187	0.022	0.0183
0.6	0.019	0.0173	0.018	0.0193
0.7	0.0187	0.0167	0.021	0.0177
0.8	0.0187	0.0177	0.019	0.0177

been reconstructed with User A Key $\mathbf{A}$ and with the two User B keys. The recognition accuracies are reported in Table V. The performance of User A is about 1%, which is like a random guessing score while accuracies for User B are very satisfactory, i.e., around 75% for high MRs. This is comparable to the recognition rate achieved when the same face recognition software is tested on the original images.

2) Attack Type II: Known Plain-Text (Original Faces), Known Anonymized and Their Labels: The ability of the proposed method to withstand a more challenging case, the parrot attack [70], where the user with Key $\mathbf{A}$ has captured both labeled clear images and their anonymized counterparts in the training set, is tested in the following experiment: The aforementioned query with NN-search is constructed in a way that each identity has 20 clean and 10 anonymized images with true labels. Face recognition algorithm is run over face regions in recovered images of type A. The results in Table VI reveal that the reconstructed faces for User A do not leak any useful information that can be exploited in a parrot attack since a different randomized corruption matrix was employed for each frame, i.e., the occurrence of the face with the same identity.

VI. DISCUSSION

A. Privacy Protection in Video

We have so far tacitly assumed that privacy protection in video were to be realized in a frame-by-frame privacy processing mode. Thus, the sensitive part in each frame, e.g., face region was to be separately obfuscated and each such frame CS-encrypted via the $\mathbf{B}$, i.e., $\mathbf{y_w} = (\mathbf{A} + \mathbf{M})\mathbf{s} + \mathbf{Bw}$ formulation. A simple extension to a multi-frame video case would be to vectorize groups of frames, and straightforwardly adapt the above methodology, where now $\mathbf{s}_{\Lambda_\mathbf{p}}$ and $\Delta_{\Lambda_\mathbf{p}}$ denote the sensitive parts and masking patterns striding over the frames in the group. A more principled way to extend the scheme to multi-frame video must leverage a tensor based CS-encryption scheme [71]. The video is considered as a 3-D signal, $\mathcal{S} \in \mathbb{R}^{n_1 \times n_2 \times n_3}$, which is a sequence of n_3 consecutive $n_1 \times n_2$ images. Then, the CS-encryption matrices, $\mathbf{A_1} \in \mathbb{R}^{m_1 \times n_1}$, $\mathbf{A_2} \in \mathbb{R}^{m_2 \times n_2}$, $\mathbf{A_3} \in \mathbb{R}^{m_3 \times n_3}$, can be applied over to $\mathcal{S}$ in order to obtain an encrypted and compressed tensor, i.e., $\mathcal{Y} = \mathcal{S} \times_1 \mathbf{A_1} \times_2 \mathbf{A_2} \times_3 \mathbf{A_3}$, where $\mathcal{S} \times_i \mathbf{A_i}$ is the i-mode product of tensor $\mathcal{S}$ and matrix $\mathbf{A_i}$. Let $\mathcal{S}_\mathbf{s}$ be the sensitive part of the video that is obtained by zero-outing the coefficients of $\mathcal{S}$ and $\mathcal{S}_\mathbf{n}$ is non-sensitive part of it. Similar to our matrix-vector notation, jointly CS-encrypted and anonymized tensor can be obtained via $\mathcal{Y}_\mathbf{d} = (\mathcal{S}_\mathbf{n} + \mathcal{P} \circ \mathcal{S}_\mathbf{s}) \times_1 \mathbf{A_1} \times_2 \mathbf{A_2} \times_3 \mathbf{A_3}$ where $\mathcal{P}$ is the degradation tensor and $\circ$ is element-wise (Hadamard) product of two tensors. Then, the marked vector, $\mathbf{y_w}$ can be easily obtained i.e., $\mathbf{y_w} = \mathrm{vec}(\mathcal{Y}_\mathbf{d}) + \mathbf{Bw}$. In the decoder part, a recovery algorithm with $\mathcal{D}_1(.)$ and $\mathcal{D}_2(.)$ similar to those in Algorithm 2 and Algorithm 3 can be used with replacing ℓ_1 based sparse vector recovery to a sparse tensor estimation method.

B. Multi-Tier Privacy Protection

It is possible to extend the proposed scheme to more than two-tiers by replicating the scheme outlined in Subsection IV-C and Figure 1. Recall that the obfuscation mask encoded as $\mathbf{w}$ and embedded via an appropriate watermarking matrix $\mathbf{B}$ resulted in the expression $\mathbf{y_w} = (\mathbf{A} + \mathbf{M})\mathbf{s} + \mathbf{Bw}$. Consider, for example, a three-tier scenario, where $\mathbf{s}_{\mathbf{s_1}}$ and $\mathbf{s}_{\mathbf{s_2}}$ are identified as sensitive parts, the higher indexed components having, for example, a higher privacy concern. The respective obfuscation matrices, $\mathbf{M_1}$ and $\mathbf{M_2}$ are encoded by their corresponding watermarks $\mathbf{w_1}$ and $\mathbf{w_2}$. These watermark signals can be spread over $\mathbf{y_d}$, for example, as $\mathbf{y_w} = (\mathbf{A} + \mathbf{M_1} + \mathbf{M_2})\mathbf{s} + \mathbf{B_1 w_1} + \mathbf{B_2 w_2}$ or $\mathbf{y_w} = (\mathbf{A} + \mathbf{M_1} + \mathbf{M_2})\mathbf{s} + [\mathbf{B_1}\ \mathbf{B_2}]\,[\mathbf{w_1}; \mathbf{w_2}]$. If desired, the resulting signal $\mathbf{y_w}$ can be

finally subjected to another layer of light-weight encryption. The decoding of the three-tier scheme follows steps similar to Section IV-C and Algorithm 3.

In this work, we have considered privacy protection in images and video as an application case. However, the proposed signal acquisition, privacy-protection and encryption scheme can be applied to any multimedia data that can be differentiated into sensitive (private) and non-sensitive (public) parts. A case in point could be the monitoring data of a wireless sensor network [72]. In such a distributed sensing mechanism, one may want to hide data in the sensor readings that would lead to traffic analysis and flow tracing. Another example would be a CS-based telehealth system [13] where health personnel with different authorization would have differential access to parts of medical data and biosignals.

Furthermore, using CS-encryption together with other light-weight encryption techniques is a common practice in the literature. For instance, in [72], the authors used Pailier cryptosystem over $\mathbf{y} = \mathbf{As}$, to strengthen the security. Similar approaches can be applied over $\mathbf{y_w}$ provided that invertibility of the applied encryption method.

VII. Conclusion

We have presented a two-tiered (potentially, multi-tiered) privacy-preserving scheme based on compressive sensing theory. The scheme accommodates two levels of users: A public user A (with only Key **A**), who can recover only the non-sensitive portions of the document, and private B, i.e., the fully-authorized user who (with keys A and B) who can recover the whole document. This prioritization is enabled via a data hiding technique such that the full user in possession of (Key **B**) can undo the obfuscation from within the CS-enciphered signal.

The watermark capacity of the system allows one-time usage of the obfuscation matrix, which in turn provides a higher level of security against any attacker, e.g., a curious semi-authorized user. In conclusion, the proposed approach satisfies all the criteria of privacy-protecting encoding, as itemized in the introduction section. Security can be corroborated by extra randomization as in Eq. (37a)-(37b). Extensive tests on a face anonymization use case revealed that the system is robust against cipher breaking attacks (i.e., face recognition) and that the image recovery quality is adequate for measurement rates m/N above 0.5. The experiments yielded guidelines for the selection of system parameters like compression rate and watermark embedding strength.

The proposed scheme with its experimentally proven merits of reversible anonymization provides a promising alternative of privacy-protecting encryption. An application scenario would be a video surveillance system where the collected real-time data must be transmitted and uploaded in a security monitoring center.

Appendix
Proof of Theorem 4

Using Equation 9 in Lemma 1 of [16] and the fact that $\mathbf{n'}_i \sim \mathcal{N}(0, \frac{m}{p}\sigma_n^2)$, where $\mathbf{n'} = \mathbf{Fn}$ we get

$$\Pr(\|\mathbf{Fn}\|_2 \geq (1+\gamma)\frac{\sqrt{m}}{\sqrt{p}}\sqrt{p}\sigma_n) \leq e^{-\frac{3p}{4}\gamma^2}. \tag{A.1}$$

Therefore, when we set $\epsilon = (1+\gamma)\sqrt{m}\sigma_n$ in Algorithm 3 and use the inequality that $\tilde{\mathbf{x}}$ in (24) satisfies

$$\|\mathbf{x} - \tilde{\mathbf{x}}\|_2 \leq C\epsilon \tag{A.2}$$

with probability at least $1 - \exp(-\frac{3p}{4}\gamma^2)$, where

$$C = 4\frac{\sqrt{1+\delta_{2k}(\mathbf{FH})}}{1-(1+\sqrt{2})\delta_{2k}(\mathbf{FH})} \tag{A.3}$$

Now, we define the error causing uncertainty, $\mathbf{z}$ on over-determined system, $\mathbf{y_w} - \mathbf{H}\tilde{\mathbf{x}} = \mathbf{Bw} + \mathbf{z}$. When we insert the $\tilde{\mathbf{x}}$ in Equation (21), we get

$$\mathbf{y_w} = \mathbf{Bw} + \mathbf{H}(\mathbf{x} - \tilde{\mathbf{x}}) + \mathbf{H}\tilde{\mathbf{x}} + \mathbf{n}, \tag{A.4}$$

which can be re-cast as

$$\mathbf{y_w} - \mathbf{H}\tilde{\mathbf{x}} = \mathbf{Bw} + \mathbf{H}(\mathbf{x} - \tilde{\mathbf{x}}) + \mathbf{n} = \mathbf{Bw} + \mathbf{z'}, \tag{A.5}$$

where $\mathbf{z'} = \mathbf{H}(\mathbf{x} - \tilde{\mathbf{x}}) + \mathbf{n}$. Given $\|\mathbf{x} - \tilde{\mathbf{x}}\|_2 \leq C\epsilon$ and $\mathbf{H}_{i,j} \sim \mathcal{N}(0, \frac{1}{m})$. Via a similar mathematical derivation given in Lemma 1, we can claim that $\mathbf{H}(\mathbf{x} - \tilde{\mathbf{x}})$ is a Gaussian random vector where each element has a variance $\sigma^2 \leq \frac{C^2\epsilon^2}{m} = \frac{C^2(1+\gamma)^2\ m\sigma_n^2}{m} = C^2(1+\gamma)^2\sigma_n^2$. Therefore, elements of $\mathbf{z'}$ is also a Gaussian vector with elements having variance $\sigma_{z'}^2 \leq 4\left\{C^2(1+\gamma)^2\right\}\sigma_n^2$. Knowing that the matrix $\mathbf{B}$ has orthonormal vectors, the pre-estimation $\mathbf{w''}$ from (25) satisfies

$$\mathbf{w} - \mathbf{w''} = \mathbf{B}^T\mathbf{z'} = \mathbf{z''}, \tag{A.6}$$

with $z_i{}'' \sim \mathcal{N}\left(0, \sigma_{z'}^2\right)$. Finally, using Equation 2.17 in [73, Chapter 2], the probability of making an error in watermark bits can be easily found as

$$\begin{aligned}&\Pr(w_i \neq \hat{w}_i | \{\|\mathbf{x} - \tilde{\mathbf{x}}\|_2 \leq C\epsilon\}) = \Pr\left(\left|(z_i{}'\right| \geq a'\right)\\ &\leq 2\exp\left(\frac{-a'^2}{2\sigma_{z'}^2}\right) = 2\exp\left(\frac{-a'^2\ m}{8\left\{C^2(1+\gamma)^2\right\}\left\|\mathbf{s}_p\right\|^2}\right),\end{aligned} \tag{A.7}$$

where $a' = a - \eta$ with a and η are user defined parameters to be used in Algorithm 3.

References

[1] M. R. Palattella *et al.*, "Internet of Things in the 5G era: Enablers, architecture, and business models," *IEEE J. Sel. Areas Commun.*, vol. 34, no. 3, pp. 510–527, Mar. 2016.

[2] T. A. Nguyen and M. Aiello, "Energy intelligent buildings based on user activity: A survey," *Energy Buildings*, vol. 56, pp. 244–257, Jan. 2013.

[3] S. M. R. Islam, D. Kwak, M. H. Kabir, M. Hossain, and K.-S. Kwak, "The Internet of Things for health care: A comprehensive survey," *IEEE Access*, vol. 3, pp. 678–708, 2015.

[4] P. Voigt and A. Von dem Bussche, *The EU General Data Protection Regulation (GDPR): A Practical Guide*, 1st ed. Cham, Switzerland: Springer, 2017.

[5] I. Wagner and D. Eckhoff, "Technical privacy metrics: A systematic survey," *ACM Comput. Surv.*, vol. 51, no. 3, pp. 57:1–57:38, Jun. 2018.

[6] C. C. Aggarwal and S. Y. Philip, "A general survey of privacy-preserving data mining models and algorithms," in *Privacy-Preserving Data Mining*. Boston, MA, USA: Springer, 2008, pp. 11–52.

[7] R. Mendes and J. P. Vilela, "Privacy-preserving data mining: Methods, metrics, and applications," *IEEE Access*, vol. 5, pp. 10562–10582, 2017.

[8] J. R. Padilla-López, A. A. Chaaraoui, and F. Flórez-Revuelta, "Visual privacy protection methods: A survey," *Expert Syst. Appl.*, vol. 42, no. 9, pp. 4177–4195, Jun. 2015.

[9] J. R. Troncoso-pastoriza and F. Perez-Gonzalez, "Secure signal processing in the cloud: Enabling technologies for privacy-preserving multimedia cloud processing," *IEEE Signal Process. Mag.*, vol. 30, no. 2, pp. 29–41, Mar. 2013.

[10] S. Heron, "Advanced encryption standard (AES)," *Netw. Secur.*, vol. 2009, no. 12, pp. 8–12, 2009. [Online]. Available: http://www.sciencedirect.com/science/article/pii/S1353485810700064

[11] R. L. Rivest, A. Shamir, and L. Adleman, "A method for obtaining digital signatures and public-key cryptosystems," *Commun. ACM*, vol. 21, no. 2, pp. 120–126, Feb. 1978.

[12] F. Nilsson *et al.*, *Intelligent Network Video: Understanding Modern Video Surveillance Systems*. Boca Raton, FL, USA: CRC Press, 2016.

[13] H. Mamaghanian, N. Khaled, D. Atienza, and P. Vandergheynst, "Compressed sensing for real-time energy-efficient ECG compression on wireless body sensor nodes," *IEEE Trans. Biomed. Eng.*, vol. 58, no. 9, pp. 2456–2466, Sep. 2011.

[14] E. J. Candès, "Compressive sampling," in *Proc. Int. Congr. Math.*, vol. 3, 2006, pp. 1433–1452.

[15] Y. Zhang, Y. Xiang, and L. Y. Zhang, *Secure Compressive Sensing in Multimedia Data, Cloud Computing and IoT*. Singapore: Springer, 2018.

[16] M. Yamaç, Ç. Dikici, and B. Sankur, "Hiding data in compressive sensed measurements: A conditionally reversible data hiding scheme for compressively sensed measurements," *Digit. Signal Process.*, vol. 48, pp. 188–200, Jan. 2016.

[17] M. Yamac, B. Sankur, and M. Gabbouj, "Robust data hiding scheme for compressively sensed signals," in *Proc. 26th Eur. Signal Process. Conf. (EUSIPCO)*, Sep. 2018, pp. 1760–1764.

[18] L. Du, M. Yi, E. Blasch, and H. Ling, "GARP-face: Balancing privacy protection and utility preservation in face de-identification," in *Proc. IEEE Int. Joint Conf. Biometrics*, Sep. 2014, pp. 1–8.

[19] P. Agrawal and P. J. Narayanan, "Person de-identification in videos," *IEEE Trans. Circuits Syst. Video Technol.*, vol. 21, no. 3, pp. 299–310, Mar. 2011.

[20] S. Ferdowsi, B. Razeghi, T. Holotyak, F. P. Calmon, and S. Voloshynovskiy, "Privacy-preserving image sharing via sparsifying layers on convolutional groups," in *Proc. ICASSP-IEEE Int. Conf. Acoust., Speech Signal Process. (ICASSP)*, May 2020, pp. 2797–2801.

[21] M. Yamac, M. Ahishali, N. Passalis, J. Raitoharju, B. Sankur, and M. Gabbouj, "Reversible privacy preservation using multi-level encryption and compressive sensing," in *Proc. 27th Eur. Signal Process. Conf. (EUSIPCO)*, Sep. 2019, pp. 1–5.

[22] L. Wolf, T. Hassner, and I. Maoz, "Face recognition in unconstrained videos with matched background similarity," in *Proc. CVPR*, Jun. 2011, pp. 529–534.

[23] M. Lustig, D. Donoho, and J. M. Pauly, "Sparse MRI: The application of compressed sensing for rapid MR imaging," *Magn. Reson. Medicine, Off. J. Int. Soc. Magn. Reson. Med.*, vol. 58, no. 6, pp. 1182–1195, 2007.

[24] A. C. Gurbuz, J. H. McClellan, and W. R. Scott, "A compressive sensing data acquisition and imaging method for stepped frequency GPRs," *IEEE Trans. Signal Process.*, vol. 57, no. 7, pp. 2640–2650, Jul. 2009.

[25] M. Yamaç, M. Orhan, B. Sankur, A. S. Turk, and M. Gabbouj, "Through the wall target detection/monitoring from compressively sensed signals via structural sparsity," in *Proc. 5th Int. Workshop Compressed Sens. Appl. Radar, Multimodal Sens., Imag.*, 2018, pp. 1–5.

[26] B. Hamdaoui, B. Khalfi, and M. Guizani, "Compressed wideband spectrum sensing: Concept, challenges, and enablers," *IEEE Commun. Mag.*, vol. 56, no. 4, pp. 136–141, Apr. 2018.

[27] S. Gishkori, V. Lottici, and G. Leus, "Compressive sampling-based multiple symbol differential detection for UWB communications," *IEEE Trans. Wireless Commun.*, vol. 13, no. 7, pp. 3778–3790, Jul. 2014.

[28] Z. Gao, L. Dai, S. Han, C.-L. I, Z. Wang, and L. Hanzo, "Compressive sensing techniques for next-generation wireless communications," *IEEE Wireless Commun.*, vol. 25, no. 3, pp. 144–153, Jun. 2018.

[29] D. L. Donoho and M. Elad, "Optimally sparse representation in general (nonorthogonal) dictionaries via ℓ_1 minimization," *Proc. Nat. Acad. Sci. USA*, vol. 100, no. 5, pp. 2197–2202, 2003.

[30] S. Chen and D. Donoho, "Basis pursuit," in *Proc. 28th Asilomar Conf. Signals, Syst. Comput.*, vol. 1, Oct./Nov. 1994, pp. 41–44.

[31] A. Cohen, W. Dahmen, and R. DeVore, "Compressed sensing and best k-term approximation," *J. Amer. Math. Soc.*, vol. 22, no. 1, pp. 211–231, Jul. 2008.

[32] S. S. Chen, D. L. Donoho, and M. A. Saunders, "Atomic decomposition by basis pursuit," *SIAM Rev.*, vol. 43, no. 1, pp. 129–159, Jan. 2001.

[33] E. J. Candès, "The restricted isometry property and its implications for compressed sensing," *Comp. Rendus Mathematique*, vol. 346, nos. 9–10, pp. 589–592, May 2008. [Online]. Available: http://www.sciencedirect.com/science/article/pii/S1631073X08000964

[34] E. J. Candès, J. K. Romberg, and T. Tao, "Stable signal recovery from incomplete and inaccurate measurements," *Commun. Pure Appl. Math.*, vol. 59, no. 8, pp. 1207–1223, 2006.

[35] Y. C. Eldar and G. Kutyniok, *Compressed Sensing: Theory and Applications*. Cambridge, U.K.: Cambridge Univ. Press, 2012.

[36] Y. Zhang, Y. Xiang, L. Y. Zhang, Y. Rong, and S. Guo, "Secure wireless communications based on compressive sensing: A survey," *IEEE Commun. Surveys Tuts.*, vol. 21, no. 2, pp. 1093–1111, 2nd Quart., 2019.

[37] Y. Zhang, L. Y. Zhang, J. Zhou, L. Liu, F. Chen, and X. He, "A review of compressive sensing in information security field," *IEEE Access*, vol. 4, pp. 2507–2519, 2016.

[38] R. Dautov and G. R. Tsouri, "Establishing secure measurement matrix for compressed sensing using wireless physical layer security," in *Proc. Int. Conf. Comput., Netw. Commun. (ICNC)*, Jan. 2013, pp. 354–358.

[39] R. Huang, K. H. Rhee, and S. Uchida, "A parallel image encryption method based on compressive sensing," *Multimedia Tools Appl.*, vol. 72, no. 1, pp. 71–93, Sep. 2014.

[40] Y. Rachlin and D. Baron, "The secrecy of compressed sensing measurements," in *Proc. 46th Annu. Allerton Conf. Commun., Control, Comput.*, Sep. 2008, pp. 813–817.

[41] C. E. Shannon, "Communication theory of secrecy systems," *Bell Syst. Tech. J.*, vol. 28, no. 4, pp. 656–715, Oct. 1949.

[42] T. Bianchi, V. Bioglio, and E. Magli, "Analysis of one-time random projections for privacy preserving compressed sensing," *IEEE Trans. Inf. Forensics Security*, vol. 11, no. 2, pp. 313–327, Feb. 2016.

[43] M. Testa, D. Valsesia, T. Bianchi, and E. Magli, "Compressed sensing as a cryptosystem," in *Compressed Sensing for Privacy-Preserving Data Processing*. Singapore: Springer, 2019, pp. 25–71.

[44] N. Y. Yu, "Indistinguishability and energy sensitivity of Gaussian and Bernoulli compressed encryption," *IEEE Trans. Inf. Forensics Security*, vol. 13, no. 7, pp. 1722–1735, Jul. 2018.

[45] Z. Yang, W. Yan, and Y. Xiang, "On the security of compressed sensing-based signal cryptosystem," *IEEE Trans. Emerg. Topics Comput.*, vol. 3, no. 3, pp. 363–371, Sep. 2015.

[46] A. Orsdemir, H. O. Altun, G. Sharma, and M. F. Bocko, "On the security and robustness of encryption via compressed sensing," in *Proc. MILCOM-IEEE Mil. Commun. Conf.*, Nov. 2008, pp. 1–7.

[47] V. Cambareri, M. Mangia, F. Pareschi, R. Rovatti, and G. Setti, "On known-plaintext attacks to a compressed sensing-based encryption: A quantitative analysis," *IEEE Trans. Inf. Forensics Security*, vol. 10, no. 10, pp. 2182–2195, Oct. 2015.

[48] P. Zhang, S. Wang, K. Guo, and J. Wang, "A secure data collection scheme based on compressive sensing in wireless sensor networks," *Ad Hoc Netw.*, vol. 70, pp. 73–84, Mar. 2018.

[49] V. Cambareri, M. Mangia, F. Pareschi, R. Rovatti, and G. Setti, "Low-complexity multiclass encryption by compressed sensing," *IEEE Trans. Signal Process.*, vol. 63, no. 9, pp. 2183–2195, May 2015.

[50] M. Yamaç, C. C. Dikici, and B. Sankur, "Robust watermarking of compressive sensed measurements under impulsive and Gaussian attacks," in *Proc. Eur. Signal Process. Conf.*, Sep. 2013, pp. 1–5.

[51] B. Razeghi, S. Voloshynovskiy, S. Ferdowsi, and D. Kostadinov, "Privacy-preserving identification via layered sparse code design: Distributed servers and multiple access authorization," in *Proc. 26th Eur. Signal Process. Conf. (EUSIPCO)*, Sep. 2018, pp. 2578–2582.

[52] B. Razeghi, S. Voloshynovskiy, D. Kostadinov, and O. Taran, "Privacy preserving identification using sparse approximation with ambiguization," in *Proc. IEEE Workshop Inf. Forensics Secur. (WIFS)*, Dec. 2017, pp. 1–6.

[53] B. Razeghi and S. Voloshynovskiy, "Privacy-preserving outsourced media search using secure sparse ternary codes," in *Proc. IEEE Int. Conf. Acoust., Speech Signal Process. (ICASSP)*, Apr. 2018, pp. 1992–1996.

[54] S. Rezaeifar, B. Razeghi, O. Taran, T. Holotyak, and S. Voloshynovskiy, "Reconstruction of privacy-sensitive data from protected templates," in *Proc. IEEE Int. Conf. Image Process. (ICIP)*, Sep. 2019, pp. 1163–1167.

[55] D. L. Donoho, "Compressed sensing," *IEEE Trans. Inf. Theory*, vol. 52, no. 4, pp. 1289–1306, Apr. 2006.

[56] K. Liu, H. Kargupta, and J. Ryan, "Random projection-based multiplicative data perturbation for privacy preserving distributed data mining," *IEEE Trans. Knowl. Data Eng.*, vol. 18, no. 1, pp. 92–106, Jan. 2006.

[57] H. Kargupta, S. Datta, Q. Wang, and K. Sivakumar, "Random-data perturbation techniques and privacy-preserving data mining," *Knowl. Inf. Syst.*, vol. 7, no. 4, pp. 387–414, May 2005.

[58] K. Schnass and P. Vandergheynst, "Average performance analysis for thresholding," *IEEE Signal Process. Lett.*, vol. 14, no. 11, pp. 828–831, Nov. 2007.

[59] B. G. Ivanoff and N. C. Weber, "Tail probabilities for weighted sums of products of normal random variables," *Bull. Austral. Math. Soc.*, vol. 58, no. 2, pp. 239–244, Oct. 1998.

[60] E. Candès and J. Romberg, "Sparsity and incoherence in compressive sampling," *Inverse Problems*, vol. 23, no. 3, p. 969, 2007.
[61] T. T. Do, L. Gan, N. H. Nguyen, and T. D. Tran, "Fast and efficient compressive sensing using structurally random matrices," *IEEE Trans. Signal Process.*, vol. 60, no. 1, pp. 139–154, Jan. 2012.
[62] Z. Wang, A. C. Bovik, H. R. Sheikh, and E. P. Simoncelli, "Image quality assessment: From error visibility to structural similarity," *IEEE Trans. Image Process.*, vol. 13, no. 4, pp. 600–612, Apr. 2004.
[63] F. Dufaux, "Video scrambling for privacy protection in video surveillance: Recent results and validation framework," *Proc. SPIE*, vol. 8063, May 2011, Art. no. 806302, doi: 10.1117/12.883948.
[64] P. Korshunov, A. Melle, J.-L. Dugelay, and T. Ebrahimi, "Framework for objective evaluation of privacy filters," *Proc. SPIE*, vol. 8856, Sep. 2013, Art. no. 88560T, doi: 10.1117/12.2027040.
[65] F. Dufaux and T. Ebrahimi, "A framework for the validation of privacy protection solutions in video surveillance," in *Proc. IEEE Int. Conf. Multimedia Expo*, Jul. 2010, pp. 66–71.
[66] J. Romberg, "Imaging via compressive sampling," *IEEE Signal Process. Mag.*, vol. 25, no. 2, pp. 14–20, Mar. 2008.
[67] D. Donoho, A. Maleki, and M. Shahram, "Wavelab 850," *Softw. Toolkit Time-Freq. Anal.*, 2006. [Online]. Available: http://statweb.stanford.edu/~wavelab/Wavelab_850/members.html
[68] M. A. T. Figueiredo, R. D. Nowak, and S. J. Wright, "Gradient projection for sparse reconstruction: Application to compressed sensing and other inverse problems," *IEEE J. Sel. Topics Signal Process.*, vol. 1, no. 4, pp. 586–597, Dec. 2007.
[69] D. E. King, "DLIB-ML: A machine learning toolkit," *J. Mach. Learn. Res.*, vol. 10, pp. 1755–1758, Jan. 2009.
[70] E. M. Newton, L. Sweeney, and B. Malin, "Preserving privacy by de-identifying face images," *IEEE Trans. Knowl. Data Eng.*, vol. 17, no. 2, pp. 232–243, Feb. 2005.
[71] Q. Wang, M. Wei, X. Chen, and Z. Miao, "Joint encryption and compression of 3D images based on tensor compressive sensing with non-autonomous 3D chaotic system," *Multimedia Tools Appl.*, vol. 77, no. 2, pp. 1715–1734, Jan. 2018.
[72] K. Xie *et al.*, "An efficient privacy-preserving compressive data gathering scheme in WSNs," *Inf. Sci.*, vol. 390, pp. 82–94, Jun. 2017.
[73] M. J. Wainwright, *High-Dimensional Statistics: A Non-Asymptotic Viewpoint*. Cambridge, U.K.: Cambridge Univ. Press, 2019, vol. 48.

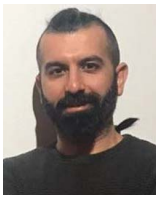

Mehmet Yamaç received the B.S. degree in electrical and electronics engineering from Anadolu University, Eskisehir, Turkey, in 2009, and the M.S. degree in electrical and electronics engineering from Boğaziçi University, Istanbul, Turkey, in 2014. He is currently pursuing the Ph.D. degree with the Department of Computing Sciences, Tampere University, Tampere, Finland. He was a Researcher and a Teaching Assistant with Boğaziçi University from 2012 to 2017. His research interests include computer and machine vision, machine learning, and compressive sensing.

Mete Ahishali received the B.Sc. degree (Hons.) in electrical and electronics engineering from the Izmir University of Economics, Izmir, Turkey, in 2017, and the M.Sc. degree (Hons.) in data engineering and machine learning from Tampere University, Tampere, Finland, in 2019, where he is currently pursuing the Ph.D. degree in computing and electrical engineering. Since 2017, he has been working as a Researcher with the Signal Analysis and Machine Intelligence Research Group under the supervision of Prof. Gabbouj. His research interests include pattern recognition, machine learning, and semantic segmentation with applications in computer vision, remote sensing, and biomedical images.

Nikolaos Passalis received the B.Sc. degree in informatics, the M.Sc. degree in information systems, and the Ph.D. degree in informatics from the Aristotle University of Thessaloniki, Thessaloniki, Greece, in 2013, 2015, and 2018, respectively. From 2018 to 2019, he also conducted Post-Doctoral Research with the Faculty of Information Sciences, Tampere University, Finland. Since 2019, he has been a Post-Doctoral Researcher with the Aristotle University of Thessaloniki. He has (co)authored more than 30 journal articles and 45 conference papers. His research interests include deep learning, information retrieval, time-series analysis, and computational intelligence.

Jenni Raitoharju (Member, IEEE) received the Ph.D. degree from the Tampere University of Technology, Finland, in 2017. Since then, she has been working as a Post-Doctoral Research Fellow with the Faculty of Information Technology and Communication Sciences, Tampere University, Finland. In 2019, she started working as a Senior Research Scientist with The Finnish Environment Institute, Jyväskylä, Finland, after receiving the Academy of Finland Post-Doctoral Researcher funding for the period of 2019–2022. She has coauthored 19 journal articles and 29 papers in international conferences. Her research interests include machine learning and pattern recognition methods along with applications in biomonitoring and autonomous systems. She has been the Chair of Young Academy Finland since 2019.

Bülent Sankur (Life Senior Member, IEEE) is currently with the Department of Electrical-Electronic Engineering, Boğaziçi University. His research interests include in the areas of digital signal processing, security and biometry, cognition, and multimedia systems. He has served as a Consultant in several industrial and government projects and has been involved in various European framework and/or bilateral projects. He has held visiting positions at the University of Ottawa, the Technical University of Delft, Ecole Nationale Supérieure des Télécommunications, Paris, and Istanbul Technical University. He was the Chairman of EUSIPCO'05: The European Conference on Signal Processing, in ICT'96: Inter. Conference on Telecommunications, as well as the technical chairman of ICASSP'00. He is also an Associate Editor of JOURNAL OF IMAGE AND VIDEO PROCESSING, and *Journal of Image and Vision Computing*. He is a member of the Academy of Sciences in Turkey.

Moncef Gabbouj (Fellow, IEEE) received the B.S. degree from Oklahoma State University in 1985, and the M.S. and Ph.D. degrees from Purdue University, in 1986 and 1989, respectively, all in electrical engineering. He was Academy of Finland Professor from 2011 to 2015. He is currently a Professor of Signal Processing with the Department of Computing Sciences, Tampere University, Tampere, Finland. His research interests include big data analytics, multimedia content-based analysis, indexing and retrieval, artificial intelligence, machine learning, pattern recognition, nonlinear signal and image processing and analysis, voice conversion, and video processing and coding. He is a member of the Academia Europaea and the Finnish Academy of Science and Letters. He is the past Chairman of the IEEE CAS TC on DSP and a Committee Member of the IEEE Fourier Award for Signal Processing. He served as Associate Editor and a Guest Editor of many IEEE, and international journals, and Distinguished Lecturer for the IEEE Circuits and Systems Society (CASS). He is the Finland Site Director of the NSF IUCRC funded Center for Visual and Decision Informatics (CVDI) and leads the Artificial Intelligence Research Task Force of the Ministry of Economic Affairs and Employment funded Research Alliance on Autonomous Systems (RAAS).

PUBLICATION
V

Robust Data Hiding Scheme for Compressively Sensed Signals

M. Yamaç, B. Sankur, and M. Gabbouj

DOI: 10.23919/EUSIPCO.2018.8553522

2018 26th European Signal Processing Conference (EUSIPCO)

Robust Data Hiding Scheme for Compressively Sensed Signals

Mehmet YAMAÇ
Laboratory of Signal Processing
Tampere University of Technology
Tampere, Finland
Email: mehmet.yamac@tut.fi

Bülent Sankur
Electrical and Electronics Engineering
Boğaziçi University
Bebek 34342, Istanbul, Turkey
Email: bulent.sankur@boun.edu.tr

Moncef Gabbouj
Laboratory of Signal Processing
Tampere University of Technology
Tampere, Finland
Email:moncef.gabbouj@tut.fi

***Abstract*—We consider the problem of linear data hiding or watermark embedding directly onto compressively sensed measurements (CSMs). In our encoding and decoding scheme, we seek exact recovery of concealed data and a small reconstruction error for a sparse signal under the additive noise model. We propose an efficient Alternating Direction of Methods of Multiplier (ADMM) based decoding algorithm and we show through experimental results that proposed decoding scheme is more robust against additive noise compared to competing algorithms in the literature.**

***Index Terms*—Compressive Sensing, Data Hiding, Watermarking, Image Encryption, Privacy Preserving**

I. Introduction

Compressive sensing [1] (CS) theory has emerged as a remedy for applications where data acquisition is costly, e.g., expensive sensor are required or when the resulting sampled data volume is impractically large. CS theory states a signal can be represented with far fewer samples compared to the Nyquist rate if in a proper domain it is sparse or at least compressible. There are already success stories of CS such in MRI imaging [2] where as a consequence the signal acquisition time has been significantly reduced, or in a health monitoring system where compressive sampling of streaming ECG signals increases the battery life span [3]. In addition, single-pixel cameras have been developed [4] using compressive image sensing for mobile phones [5].

Data hiding and watermarking technologies have witnessed tremendous developments in the last two decades, becoming thus a mainstream technology. A good illustrative case is a health monitoring system where patient biomedical data is transmitted to a health center. In this case, data hiding and watermarking enable [6] embedding of meta-data such as Electronic Health Records or patient's identity for identification and authentication purposes. The overwhelming majority of these attempts, however, use embedding medium signals sampled according to the Nyquist-Shannon theorem and can not be applied to CS acquisition systems such as [2], [3], [4], [5].

Although CS is conceived as a data acquisition method, a CS framework is also capable of inherently providing confidentiality with a reasonable level of security. Furthermore, this capability comes at practically no additional cost and data encryption [7] can be added right into the sampling process. Compressive sensing enables encryption via random or pseudo-random sampling matrices.

There have been few attempts in the literature [8] to embed metadata directly onto a compressively sensed signal. The benefits of data hiding in compressively sampled signals are as follows: First, the compressive samples can be used as a carrier for subliminal information, and such a scheme can perform data hiding at a low cost by implementing linear encoding and spreading the hidden message directly during sensing. Second, encryption is enabled for the sensed samples and the additional embedding makes it harder for malicious user to hack the signals. In this case, the hacker must obtain both the encryption matrix (i.e., sensing matrix), and the data hiding or encoding matrix.

In this work, we propose a new decoding strategy for the data embedding in which the meta data is spread directly onto CSMs (compressively sensed measurements). This new method builds upon our previous method for data hiding in CSMs [8]. The novelty of the work is that it addresses the extraction of the watermark/hidden data and recovery of the carrier message as a sparse signal reconstruction problem. To this effect, we use proximal calculus and ADMM: Alternating Direction Method of Multipliers based decoding method. We show that this novel signal recovery and hidden data extraction method is more robust to additive noise, Gaussian or non-Gaussian, compared to the scheme in [8].

The rest of the paper is organized as follows. Section II provides the notation and the mathematical preliminaries. In Section III, we briefly review the CS framework. Then, in Section IV, we explain the proposed scheme and give the details of the ADMM-based decoding algorithm. Finally, the performance of the proposed algorithm is analyzed and conclusions are drawn.

ISBN 978-90-827970-1-5 © EURASIP 2018

II. Preliminaries

We define the ℓ_p norm of any vector $x \in \mathbb{R}^N$ as $\|x\|_{\ell_p^N} = \left(\sum_{i=1}^N |x_i|^p\right)^{1/p}$ for $p \geq 1$. The ℓ_0-norm of the vector $x \in \mathbb{R}^N$ is given as $\|x\|_{\ell_0^N} = \lim_{p\to 0} \sum_{i=1}^N |x_i|^p = \#\{j : x_j \neq 0\}$. The indicator function, $i_c : \mathbb{R}^N \to \{0, \infty\}$, of a convex set C is also defined as

$$i_C(x) = \begin{cases} 0 & \text{if } x \in C \\ \infty & \text{if } x \notin C. \end{cases}$$

A signal S is said to be strictly k-sparse if the number of non-zero coefficients is less than a constant k when we represent this signal in a proper basis (or dictionary), Φ, i.e.,

$$\|x\|_{\ell_0^N} \leq k, \tag{1}$$

where $S = \Phi x \in \mathbb{R}^N$. Indeed, most signals we encounter in real-world applications exhibit a power law decay in some apropriate Φ. Consider the coefficients of x sorted in descending order in magnitude, i.e., $\left|x^1\right| \geq \left|x^2\right| \geq ... \geq \left|x^{N-1}\right| \geq \left|x^N\right|$, where x^i is the i.th largest coefficient of x (in magnitude). Let $\wedge^{(k)}$ be the set of indices corresponding to the k largest coefficients. Then, the signal of interest S is said to be approximately k-sparse if

$$\|S - \Phi x_{\wedge^{(k)}}\|_{\ell_2}^N \leq \kappa, \tag{2}$$

where κ is a small constant.

The Restricted Isometry Constant (RIC) of order k of a $m \times N$ matrix A is defined as the smallest constant, $\delta_k(A) \in (0, 1)$ satisfying

$$(1 - \delta_k(A)) \|x\|_{\ell_2^N} \leq \|Ax\|_{\ell_2^m} \leq (1 + \delta_k(A)) \|x\|_{\ell_2^N} \tag{3}$$

for all k-sparse $x \in \mathbb{R}^N$.

Since we use in this work an ADMM-based decoding scheme, a brief reminder on proximal method is in order. ADMM [9] is a special type of a proximal algorithm [10]. Proximal operator or proximal mapping [11] of a function f at a point z with a parameter $\gamma > 0$ is defined as

$$\text{prox}_{\gamma f}(z) = \arg\min_u \{f(u) + \frac{1}{2\gamma} \|u - z\|_{\ell_2^N}^2\}. \tag{4}$$

A proximal operator can be considered as a gradient descent step for the smooth approximation of f. This method proves to be very useful in optimization problems involving non-differentiable functions. It can be interpreted as a generalization of the projection operator [12]. For instance, when f is the indicator function, i_C, the proximal operator will simply be the projection operation onto C, i.e.,

$$\Pi_c(z) = \arg\min_{x \in C} \|x - z\|_{\ell_2^N}.$$

III. Compressive Sensing Review

In compressive sensing we have m measurements of an N-dimensional signal $S \in \mathbb{R}^{\mathbb{N}}$, i.e.,

$$y = \Psi S, \tag{5}$$

where Ψ is the $m \times N$ (typically, $m << N$) linear measurement matrix. Assuming that this signal is compressible (approximately k-sparse) in a proper sparsifying basis Φ, we can re-arrange the equation as

$$y = \Psi S = \Psi\Phi x_{\wedge^{(k)}} + \Psi\Phi x_{\Lambda^c} = A x_{\wedge^{(k)}} + n^0, \tag{6}$$

where $\Psi\Phi$ and the complement of set $\wedge^{(k)}$, defined as $\Lambda^c = \{1, 2, 3, ..., N\} \setminus \wedge^{(k)}$, represents the indices of the non-compressible small magnitude part of x, and n^0 is the corresponding additive distortion due to the discarded measurements (it vanishes in strictly sparse case). In addition CSMs can be corrupted by channel errors during transmission, also modeled as additive noise, or by quantization errors. Then, the reconstruction algorithm must handle

$$y = Ax + n, \tag{7}$$

where n is a general additive noise and x is a sparse signal (hereafter, we use the notation of x instead of $x_{\wedge^{(k)}}$ for convenience). Even in the noise-free case when n vanishes, Equation (7) is an underdetermined system of linear equations and has infinitely many solutions. In this case, one may find the sparsest solution from infinitely many by solving

$$\hat{x} = \arg\min_x \ \|x\|_{\ell_0^N} + i_{\{Ax=y\}}(x). \tag{8}$$

The problem formulated in (8) is not convex, and hence one can relax and convexify it so that, e.g., the well-known Basis Pursuit problem can be applied:

$$\hat{x} = \arg\min_x \ \|x\|_{\ell_1^N} + i_{\{Ax=y\}}(x). \tag{9}$$

It is proven that the solution of (9) is unique given that A has certain properties (e.g., null space property) [13].

In the noisy case, (9) can be expressed in terms of the following Basis Pursuit Denoising problem [14],

$$\hat{x} = \arg\min_x \|x\|_{\ell_0^N} \quad \text{s.t} \quad \|y - Ax\|_{\ell_2^m} \leq \epsilon \tag{10}$$

The stability of the solution of (10) is well studied in the literature. For instance, given that $\|n\|_{\ell_2} \leq \epsilon$, if matrix A possesses RIC with $\delta_{2k} < \sqrt{2} - 1$, equation (10) approximates x with

$$\|x - \hat{x}\|_{\ell_2^N} \leq C_0 \epsilon, \tag{11}$$

where C_0 depends on $\delta_{2k}(A)$ [15]. As an example of the measurement matrix, A with i.i.d. elements $A_{i,j}$ drawn according to $\mathcal{N}\left(0, \frac{1}{m}\right)$, $m > k(\log(N/k))$ guarantees with high probability exact signal reconstruction when the noise n vanishes [15].

ISBN 978-90-827970-1-5

IV. DATA HIDING

Let $x \in \mathbb{R}^N$ be a k-sparse signal and $w \in \{a, -a\}^M$ be an M-length binary hidden message (e.g., watermark) that we wish to linearly embed into CSMs of S. Recall that compressive sensing algorithms relocate the computational burden from the sampling side (e.g., transmitting end) to the reconstruction side (receiving end) by performing linear sampling and non-linear reconstruction. On the other hand, the M-long binary hidden message can be linearly spread directly onto CSMs via the encoding matrix $B \in \mathbb{R}^{m\times M}, M < m$, resulting in the marked signal $y = Ax+Bw$, where $A \in \mathbb{R}^{m\times N}$ is the measurement matrix.

Finally, the marked signal carrying the hidden data can be modified by an additive noise or as a consequence of some attack, yielding:

$$y = Ax + Bw + n. \tag{12}$$

A. Previous Decoding Scheme

In [8], the authors proposed a joint reconstruction and recovery algorithm as in Algorithm 1. Here $F \in \mathbb{R}^{p\times m}$ is the left annihilator matrix of B, i.e., $FB = 0$ with $p = m-M$. Briefly in this iterative method, we first try to remove the watermark via the annihilator matrix F, reconstruct the original signal x sparsely, deflate accordingly the received signal y, and then proceed to extract the binary watermark w via thresholding.

Algorithm 1 Algorithm 1 in [8]

Input: y, A, B;
Determine: ϵ
1. Apply F to $y : \tilde{y} = Fy$
2. Estimate $\tilde{x} : \tilde{x} = \arg\min_x \|x\|_{\ell_1^N}$ s.t. $\|\tilde{y} - FAx\|_{\ell_2^p} \leq \epsilon$
3. Estimate $\tilde{w} : \tilde{w} = (B^{\mathrm{T}}B)^{-1}B^{\mathrm{T}}(y - A\tilde{x})$
4. Threshold $\tilde{w} : \hat{w}_i = a * \mathrm{sgn}(\tilde{w}_i)$
5. $\hat{x} = \arg\min_x \|x\|_{\ell_1^N}$ s.t. $\|(y - B\hat{w}) - Ax\|_{\ell_2^m} \leq \epsilon$
Return: $\hat{x}$, $\hat{w}$

It is stated in [8] that the data embedding capacity depends on the restricted isometry constant of FA and the signal to noise ratio (SNR).

B. Proposed Robust Decoding Scheme

1) Problem Formulation: In this work, we formulate the joint estimation of embedded data and sparse signal recovery as an optimization problem:

$$(x^*, w^*) = \arg\min_{(x,w)} \{\frac{\lambda_1}{2}\|y - (Ax + Bw)\|_{\ell_2^m}^2 + \lambda_3\|x\|_{\ell_1^N} + \frac{\lambda_2}{2}\|Fy - FAx\|_{\ell_2^p}^2 + i_{\{-a,+a\}^M}(w)\}. \tag{13}$$

In (13), a second fidelity term, $\|Fy - FAx\|_{\ell_2^p}^2$ is added to increase the solution stability, as it was done in Algorithm 1 along with the first term $\|y - (Ax + Bw)\|_{\ell_2^m}^2$. While the second term increases the stability, the first term is instrumental for the ADMM formulation, and this can be seen as a feed-back mechanism. Finally, the last term represents the projection on a non-convex set and corresponds to the thresholding operation to extract the hidden binary message. The optimization problem (13) becomes a non-convex one due to last term, since w_i is an integer. We can solve this problem using the following ADMM strategy. In the following subsection, we first explain the primal-dual conversion of (13) and then proceed with the ADMM solution for (13).

2) From dual ascent to ADMM: The equivalent consensus form can be written as

$$(x^*, w^*, z_1^*, z_2^*) = \arg\min_{(x,w,z_1,z_2)} \{\frac{\lambda_1}{2}\|y - (Ax + Bw)\|_{\ell_2^m}^2 + \lambda_3\|z_2\|_{\ell_1^N} + \frac{\lambda_2}{2}\|Fy - FAx\|_{\ell_2^p}^2 + i_{\{-a,+a\}^M}(z_1)\} \quad \text{subject to} \quad w = z_1, x = z_2. \tag{14}$$

The Augmented Lagrangian form for this problem in (14) can be cast as

$$L_{(\mu_1,\mu_2)}(\beta_1, \beta_2, x, w, z_1, z_2) = \frac{\lambda_1}{2}\|y - (Ax + Bw)\|_{\ell_2^m}^2 + \lambda_3\|z_2\|_{\ell_1^N} + \frac{\lambda_2}{2}\|Fy - FAx\|_{\ell_2^p}^2 + i_{\{-a,+a\}^M}(z_1) + \langle\beta_1, (z_1 - w)\rangle + \langle\beta_2, (z_2 - x)\rangle + \frac{\mu_1}{2}\|w - z_1\|_{\ell_2^M}^2 + \frac{\mu_2}{2}\|x - z_2\|_{\ell_2^N}^2, \tag{15}$$

where $\beta_1 \in \mathbb{R}^M, \beta_2 \in \mathbb{R}^N$ are called Lagrange multipliers or dual variables, and the last two terms are penalty terms with parameters, $\mu_1, \mu_2 > 0$, respectively. The corresponding dual function can be written as

$$g_{(\mu_1,\mu_2)}(\beta_1, \beta_2) = \inf_{(x,w,z_1,z_2)} L_{(\mu_1,\mu_2)}(\beta_1, \beta_2, x, w, z_1, z_2). \tag{16}$$

Instead of the primal problem in (13), we can approximate the optima of the primal function (with some duality gap due to the non-convex term) by maximizing the dual function which is

$$(\beta_1^*, \beta_2^*) = \arg\max_{\beta_1,\beta_2} \left\{g_{(\mu_1,\mu_2)}(\beta_1, \beta_2)\right\}. \tag{17}$$

Then, we can approximate the primal optimal points by solving following problem:

$$(x^*, w^*, z_1^*, z_2^*) = \arg\min_{(x,w,z_1,z_2)} L_{(\mu_1,\mu_2)}(\beta_1^*, \beta_2^*, x, w, z_1, z_2). \tag{18}$$

In maximizing Problem (17), the primal values are updated jointly. This is called augmented Lagrangian method or method of multipliers [16], which has the following iterative form for our problem,

$$(x, w, z_1, z_2)^{k+1} \leftarrow \arg\min_{(x,w,z_1,z_2)} L_{(\mu_1,\mu_2)}(\beta_1^k, \beta_2^k, .., z_1, z_2)$$
$$\beta_1^{k+1} \leftarrow \beta_1^k + \mu_1(z_1^{k+1} - w^{k+1})$$
$$\beta_2^{k+1} \leftarrow \beta_2^k + \mu_2(z_2^{k+1} - x^{k+1}),$$

where the last two terms come from the gradient ascent step for the dual function and the specific choice of the ascent step

ISBN 978-90-827970-1-5 © EURASIP 2018

μ_1, μ_2 (these dual variable updates can be done independently since $\nabla_{(\beta_1,\beta_2)} g_{(\mu_1,\mu_2)}(\beta_1,\beta_2)$ are separable in β_1 and β_2).

The joint optimization stated in Eq. (18) can be solved conveniently for the x, w, z_1, z_2 variables using ADMM [17] (see the recent review [9] for details.) We can derive an algorithm in which the primal and dual variables are updated independently in an alternating manner. The general structure of ADMM algorithm for Problem (13) is given in Algorithm 2.

3) Primal Variable Updates: Let us start from the update of z_2,

$$z_2^{k+1} = \arg\min_{z_2} \{\lambda_2 \|z_2\|_{\ell_1^N} + \langle \beta_2^k, (z_2 - x^{k+1}) \rangle + \frac{\mu_2}{2} \|x^{k+1} - z_2\|_{\ell_2^N}^2\} \quad (19)$$

which is actually equivalent to

$$z_2^{k+1} = \arg\min_{z_2} \left\{ \lambda_2 \|z_2\|_{\ell_1^N} + \frac{\mu_2}{2} \left\| z_2 - \left(x^{k+1} - \frac{\beta_2^k}{\mu_2} \right) \right\|_{\ell_2^N}^2 \right\}. \quad (20)$$

By the definition in (4), one can easily see that it is nothing but the the proximity operator of $f(x) = \|x\|_{\ell_1^N}$ with the parameter $(\frac{\lambda_2}{\mu_2})$

$$z_2^{k+1} = prox_{(\frac{\lambda_2}{\mu_2})\ell_1^N} \left(x^{k+1} - \frac{\beta_2^k}{\mu_2} \right). \quad (21)$$

Using the separable sum property for proximal maps [11], one can obtain the proximal operator of $f(x) = \|x\|_{\ell_1^N}$ with parameter γ at vector z as follows,

$$prox_{\gamma f}(z_i) = \begin{cases} z_i + \gamma & \text{if } z_i \leq -\gamma \\ 0 & \text{if } -\gamma \leq z_i \leq +\gamma \\ z_i - \gamma & \text{if } z_i \geq \gamma \end{cases}$$

where z_i is the i-th element of the vector z. This operation is actually the well-known soft thresholding. Similarly, the z_1 update can be performed by solving

$$z_1^{k+1} = \arg\min_{z_1} \left\{ i_C(z_1) + \frac{\mu_1}{2} \left\| z_1 - \left(w^{k+1} - \frac{\beta_1^k}{\mu_1} \right) \right\|_{\ell_2^M}^2 \right\} \quad (22)$$

Algorithm 2 ADMM for Problem

repeat

Primal Updates

$x^{k+1} \leftarrow \arg\min_x L_{(\mu_1,\mu_2)}(\beta_1^k, \beta_2^k, x, w^k, z_1^k, z_2^k)$

$w^{k+1} \leftarrow \arg\min_x L_{(\mu_1,\mu_2)}(\beta_1^k, \beta_2^k, x^{k+1}, w, z_1^k, z_2^k)$

$z_1^{k+1} \leftarrow \arg\min_x L_{(\mu_1,\mu_2)}(\beta_1^k, \beta_2^k, x^{k+1}, w^{k+1}, z_1, z_2^k)$

$z_2^{k+1} \leftarrow \arg\min_x L_{(\mu_1,\mu_2)}(\beta_1^k, \beta_2^k, x^{k+1}, w^{k+1}, z_1^{k+1}, z_2)$

Dual Updates:

$\beta_1^{k+1} \leftarrow \beta_1^k + \mu_1(z_1^{k+1} - w^{k+1})$

$\beta_2^{k+1} \leftarrow \beta_2^k + \mu_2(z_2^{k+1} - x^{k+1})$

until Convergence

return $\hat{x}, \hat{w}$

and we can easily see that it is the following operator

$$z_1^{k+1} = proj_{\{\{-a,+a\}^M\}} \left(w^{k+1} - \frac{\beta_1^k}{\mu_1} \right) \quad (23)$$

where we can approximate the projection onto the set $C = \{-a, +a\}^M$ as the simple thresholding operator

$$proj_{\{\{-a,+a\}^M\}}(z_i) \approx a * \text{sgn}(z_i) \quad (24)$$

for the i-th element of a vector z. We can see that the operation is a relax-and-round heuristic for integer valued non-convex optimization problem (22) by relaxing the set $\{-a, +a\}$ to $(-a, +a)$, solving the corresponding convex problem and rounding the solution to the nearest integer $-a$ or a [18].

Update of the primal variable x can be done by solving

$$x^{k+1} = \arg\min_x \{\frac{\lambda_1}{2} \|y - (Ax + Bw^k)\|_{\ell_2^m}^2 + \langle \beta_2, (x - z_2^k) \rangle + \frac{\lambda_2}{2} \|Fy - FAx\|_{\ell_2^p}^2 + \frac{\mu_2}{2} \|x - z_2^k\|_{\ell_2^N}^2\}. \quad (25)$$

Since the right hand side is differentiable, the update equation can be cast as solving the linear equation $\nabla_x L(.) = 0$, which reduces to

$$x^{k+1} = (\lambda_1 A^T A + \lambda_2 A^T F^T F A + I\mu_2)^{-1} (\lambda_1 A^T (y - Bw^k) + \lambda_2 (A^T F^T F y) + \beta_2^k + \mu_2 z_2^k) \quad (26)$$

Similarly, the update of primal variable w can be achieved by solving

$$w^{k+1} = (\arg\min_w \frac{\lambda_1}{2} \|y - (Ax^{k+1} + Bw)\|_{\ell_2^m}^2 + \langle \beta_1^k, (z_1^k - w) \rangle + \frac{\mu_1}{2} \|w - z_1^k\|_{\ell_2^M}^2) \quad (27)$$

which yields

$$w^{k+1} = (\lambda_1 B^T B + \mu_1 I)^{-1} \left[\lambda_1 B^T (y - Ax^{k+1}) + \beta_1^k + \mu_1 z_1^k \right] \quad (28)$$

by solving $\nabla_w L(.) = 0$. In addition to these variables, robustness parameters (μ_1, μ_2) can also be updated,

$$(\mu_1^{k+1}, \mu_2^{k+1}) \leftarrow \left(\rho_1 \mu_1^k, \rho_2 \mu_2^k \right). \quad (29)$$

V. Simulation Results

We generate a $k = \frac{m}{5}$-sparse $N = 512$ length synthetic signal. A and F are chosen as explained in Section IV. The M-long watermark, w, is generated with $\|w\|_{\ell_2^M} = \frac{\|Ax\|_{\ell_2^m}}{4}$ so that the embedded-data-to document ratio is -6 dB and the marked measurements are contaminated with AWGN with different signal-to-noise ratios (SNR). We define the SNR as $20 \log_{10} \left(\frac{\|Ax + Bw\|_{\ell_2^m}}{\|n\|_{\ell_2^m}} \right)$. Each experiment is conducted 250 times and the average performance results are reported. Similar experiments are also conducted with different sparsity level and SNR, but for the sake of brevity we report only the cases for 32 dB and 24 dB in Figure 1 and Figure 2, respectively.

ISBN 978-90-827970-1-5 © EURASIP 2018

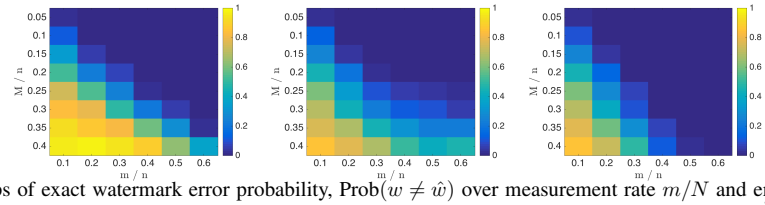

Fig. 1: Heat-maps of exact watermark error probability, Prob$(w \neq \hat{w})$ over measurement rate m/N and embedding rate M/m under AWGN at 32 db SNR. (a) Algorithm 1. (b) The proposed method without the term $\|Fy - FAx\|_{\ell_2^p}^2$. (c) The proposed method.

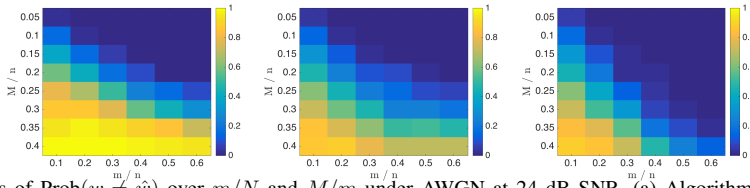

Fig. 2: Heat-maps of Prob$(w \neq \hat{w})$ over m/N and M/m under AWGN at 24 dB SNR. (a) Algorithm 1. (b) The proposed method without the term $\|Fy - FAx\|_{\ell_2^p}^2$. (c) The proposed method.

Similar performance was observed in the experiments not reported here. We compare the performance results of Algorithm 1, the proposed Algorithm with and without the data fidelity term $\|Fy - FAx\|_{\ell_2^p}^2$ for different embedding rates, $\frac{M}{m}$ and the different measurement rates $\frac{m}{N}$. From Figure 1-(b), (c) and Figure 2-(b), (c), it can be clearly seen that modeling the problem as joint optimization problem in (13) which includes an extra data fidelity term $\|Fy - FAx\|_{\ell_2^p}^2$, which is in dimensionality reduced measurement domain clearly surpasses the performance of modeling without it. It is also apparent from the Figure 1-(a), (c) and Figure 2-(a), (c) that the performance of final ADMM based solution to (13) exceeds the previous state of art [8].

In our experiments we set $\lambda_1 = \lambda_2 = 1$, $\lambda_3 = 1 \times 10^{-2}$, $\mu_1 = 3.3 \times 10^{-6}$, $\mu_2 = 8 \times 10^{-3}$, $\rho_1 = 1$, $\rho_2 = 1.035$.

ℓ_1-magic [19] solver (it was observed that different solvers, such as CVX, resulted in a similar performance) is used to conduct Algorithm Algorithm 1 with $\epsilon \approx \sqrt{m\sigma_n^2}$.

VI. Conclusion

In this work we have proposed a new iterative decoding strategy for joint watermark extraction and signal recovery in compressively sampled signals. The new approach boosts the watermark capacity of the compressively sampled signals and improves also its noise robustness. We plan to extend this framework to embed meta-data onto CSMs to structurally sparse signals such as group sparse ones.

References

[1] Candes, Emmanuel J. "Compressive sampling." Proceedings of the international congress of mathematicians. Vol. 3. 2006.

[2] Lustig, Michael, David Donoho, and John M. Pauly. "Sparse MRI: The application of compressed sensing for rapid MR imaging." Magnetic resonance in medicine 58.6 (2007): 1182-1195.

[3] Mamaghanian, Hossein, et al. "Compressed sensing for real-time energy-efficient ECG compression on wireless body sensor nodes." IEEE Transactions on Biomedical Engineering 58.9 (2011): 2456-2466.

[4] Takhar, Dharmpal, et al. "A new compressive imaging camera architecture using optical-domain compression." Computational Imaging IV. Vol. 6065. International Society for Optics and Photonics, 2006.

[5] Oike, Yusuke, and Abbas El Gamal. "CMOS image sensor with per-column ADC and programmable compressed sensing." IEEE Journal of Solid-State Circuits 48.1 (2013): 318-328.

[6] Kozat, Suleyman S., et al. "Embedding and retrieving private metadata in electrocardiograms." Journal of medical systems 33.4 (2009): 241-259.

[7] Orsdemir, Adem, et al. "On the security and robustness of encryption via compressed sensing." Military Communications Conference, 2008. MILCOM 2008. IEEE. IEEE, 2008.

[8] Yamaç Mehmet, Çağatay Dikici, and Bülent Sankur. "Hiding data in compressive sensed measurements: A conditionally reversible data hiding scheme for compressively sensed measurements." Digital Signal Processing 48 (2016): 188-200.

[9] Boyd, Stephen, et al. "Distributed optimization and statistical learning via the alternating direction method of multipliers." Foundations and Trends in Machine Learning 3.1 (2011): 1-122.

[10] Combettes, Patrick L., and Jean-Christophe Pesquet. "Proximal splitting methods in signal processing." Fixed-point algorithms for inverse problems in science and engineering. Springer New York, 2011. 185-212.

[11] Parikh, Neal, and Stephen P. Boyd. "Proximal Algorithms." Foundations and Trends in optimization 1.3 (2014): 127-239.

[12] Moreau, Jean-Jacques. "Proximité et dualité dans un espace hilbertien." Bull. Soc. Math. France 93.2 (1965): 273-299.

[13] Cohen, Albert, Wolfgang Dahmen, and Ronald DeVore. "Compressed sensing and best -term approximation." Journal of the American mathematical society 22.1 (2009): 211-231.

[14] Chen, Scott Shaobing, David L. Donoho, and Michael A. Saunders. "Atomic decomposition by basis pursuit." SIAM review 43.1 (2001): 129-159.

[15] Candes, Emmanuel J. "The restricted isometry property and its implications for compressed sensing." Comptes rendus mathematique 346.9-10 (2008): 589-592.

[16] Hestenes, Magnus R. "Multiplier and gradient methods." Journal of optimization theory and applications 4.5 (1969): 303-320.

[17] Gabay, Daniel, and Bertrand Mercier. "A dual algorithm for the solution of nonlinear variational problems via finite element approximation." Computers & Mathematics with Applications 2.1 (1976): 17-40.

[18] Wu, Baoyuan, and Bernard Ghanem. "ℓ_p-Box ADMM: A Versatile Framework for Integer Programming." arXiv preprint arXiv:1604.07666 (2016).

[19] Candes, Emmanuel, and Justin Romberg. "l1-magic: Recovery of sparse signals via convex programming." URL: www. acm. caltech. edu/l1magic/downloads/l1magic. pdf 4 (2005): 14.

ISBN 978-90-827970-1-5 © EURASIP 2018

PUBLICATION
VI

Compressively Sensed Image Recognition

A. Değerli, S. Aslan, M. Yamac, B. Sankur, and M. Gabbouj

DOI: 10.1109/EUVIP.2018.8611657

Compressively Sensed Image Recognition

Ayşen Değerli[1], Sinem Aslan[2,3], Mehmet Yamaç[1], Bülent Sankur[4], and Moncef Gabbouj[1]

[1]Tampere University of Technology, Laboratory of Signal Processing, Tampere, Finland
[2]Ca' Foscari University of Venice, European Centre for Living Technology, Venice, Italy
[3]Ege University, International Computer Institute, İzmir, Turkey
[4]Boğaziçi University, Electrical and Electronics Engineering Department, İstanbul, Turkey

***Abstract*—Compressive Sensing (CS) theory asserts that sparse signal reconstruction is possible from a small number of linear measurements. Although CS enables low-cost linear sampling, it requires non-linear and costly reconstruction. Recent literature works show that compressive image classification is possible in CS domain without reconstruction of the signal. In this work, we introduce a DCT base method that extracts binary discriminative features directly from CS measurements. These CS measurements can be obtained by using (i) a random or a pseudo-random measurement matrix, or (ii) a measurement matrix whose elements are learned from the training data to optimize the given classification task. We further introduce feature fusion by concatenating Bag of Words (BoW) representation of our binary features with one of the two state-of-the-art CNN-based feature vectors. We show that our fused feature outperforms the state-of-the-art in both cases.**

***Index Terms*—Compressive Sensing, Compressive Learning, Inference on Measurement Domain, Learned Measurement Matrix, Compressive Classification, DCT-based Binary Descriptor.**

I. Introduction

The first step in any signal processing task is the acquisition of signals. The classical pathway for band-limited signals is to instantaneously sample the signal at the Nyquist-Shannon rate, then compress the signal to remove redundancies and/or irrelevancies, typically using a transform-based compression technique for efficient storage and transmission. The compressed signal must be decompressed before executing any further signal processing operation such as classification, detection, inference. etc.

The new sampling paradigm, *Compressive Sensing* (*CS*) [1] bypasses this laborious Nyquist-Shannon data acquisition scheme in that signals are being compressed while being sampled with random patterns. Thus the sampling and compression steps are combined into one action. However, the reconstruction of the signal from *compressively sensed measurements* (*CSMs*) becomes non-linear and considerably costlier in the computational effort. This costly signal reconstruction operation would be counterproductive were it not for the emerging signal processing algorithms in the compressed domain. A newly emerging idea [2]–[4] is using CSMs directly in inference problems without executing any reconstruction. This promising approach can potentially be advantageous in real-time applications and/or when dealing with big data.

In a pioneering work, Davenport et al. [4] have addressed the problem of inference directly on compressively sensed measurements. In [5], it is theoretically shown that the accuracy of the soft margin SVM classifier is preserved when data is collected with sparse random projections. The authors in [6] have introduced the idea of smashed filter and, based on the Johnson-Lindenstrauss Lemma [7] have shown that the inner product of two signals is relatively preserved for compressively sampled signals when the sampling matrix consists of random values, chosen from some specific probability distributions. Different versions of the smashed filter are used in various applications [8], [9]. For instance in [9], a compressive smashed filter technique is proposed by first producing a set of correlation filters from uncompressed images in the training set, and then at the testing stage by correlating CSMs of test images and with the CSMs of learned filters. A linear feature extraction method in CS domain is developed in [10] for direct classification of compressively sensed EEG data. In [11] fed an SVM classifier with a fusion of CSMs (projected data) and dynamic features and they reported performance beyond the state-of-the-art for 1-D ECG data classification.

Other works, e.g., [12], [13], have provided theoretical guarantees for achievable accuracy in different CSM setups for both sparse and non-sparse cases.

All the above works try to use compressed samples directly to solve the inference problem. A second approach is to boost the size of CSMs to the original image size by a simple linear projection, but avoiding the costly nonlinear reconstruction procedure. This simple back-projection yields a pseudo-image and one then proceeds with the inference task on this imperfectly reconstructed image. This image, restituted to its original dimension and also known as *proxy image*, is usually a heavily degraded version of the original image. One way to obtain the proxy image is by premultiplying the compressed image by the transpose of the sampling matrix. In [14], the authors apply a CNN-based feature extraction method on such a proxy image. Their measurement matrix consists of random Gaussian distributed numbers. Another work [15] uses a deeper network structure (as compared to [14]) by adding two fully connected layers at the beginning of the network. Thus this network can learn as well the linear dimension reduction (so-called measurement matrix) and linear back projection to the image domain (i.e., the transpose of the measurement matrix).

In this work, following the vein of the second approach we propose a DCT-based discriminative feature scheme, computed

directly from the proxy image. This feature vector (called MB-DCT) is binary, hence simple and low cost. A preliminary version of this feature was presented in EUSIPCO [16]. In this work, we applied MB-DCT on non-compressively sampled images. In [16] we had shown that this simple scheme of selected binarized DCT coefficients, computed in increasing scales of local windows was remarkably robust against linear and nonlinear image degradations, such as additive white Gaussian noise, contrast and brightness changes, blurring, and strong JPEG compression. We use MB-DCT scheme in [16] for feature extraction from image proxies. Our experimental results show that using this simple binary feature method surpasses the performance of Smashed Filters [9]. We further introduce feature fusion by concatenating Bag of Words (BoW) representation of our binary features with one of the two state-of-the-art CNN-based feature vectors, i.e., in [14] and [15]. In the method [14], elements of measurement matrices were drawn from a random distribution as typical in conventional CS theory, whereas in the method [15] sampling matrices were learned from a deep network; the latter method proved to be superior for smaller measurement rates. However, random sensing scheme may still be needed for some applications where one needs to pre-classify the data directly using CSMs, then reconstruct the signal for further analysis. For instance in a remote health monitoring system, we may wish to detect anomalies directly from CSMs of ECG signal on the sensor side. Then based on the sensor side classification, CSMs of selected cases can be transmitted for a more detailed analysis by a medical doctor. Therefore, we consider the random sensing approach and learned sensing approach as two different set-ups. In this paper, we show that our fused features outperforms the aforementioned works for both of the schemes and gives the state-of-the-art performance.

We briefly introduce the notation used and some preliminary information. We define the ℓ_0-norm of the vector $x \in \mathbb{R}^N$ as $\|x\|_{\ell_0^N} = \lim_{p\to 0} \sum_{i=1}^{N} |x_i|^p = \#\{j : x_j \neq 0\}$. The compressive sensing (CS) scheme extracts m number of measurements from the N-dimensional input signal $S \in \mathbb{R}^N$, i.e.,

$$y = \Psi S, \tag{1}$$

where Ψ is the $m \times N$ measurement matrix and typically $m << N$. Consider this signal to be k-sparse in a sparsifying basis Φ such that $S = \Phi x$ with $\|x\|_{\ell_0^N} \leq k$. Then, the general compressive sensing setup is

$$y = \Psi\Phi x = Ax, \tag{2}$$

where $A = \Psi\Phi$ is sometimes called as holographic matrix. It has been demonstrated that the sparse representation in (3) is unique if $m \geq 2k$ [17].

$$\min_x \ \|x\|_{\ell_0^N} \ \text{subject to} \ Ax = y \tag{3}$$

The organization of the rest of the paper is as follows. In Section II, we provide the notation, mathematical foundations and a brief review of CS theory. The difference between the two measurement approaches, namely, based random weights or learned weights in the acquisition of CMSs and reconstruction of proxies are explained in Section III. Then in Section IV, we introduce the proposed feature extraction method from the two proxy varieties. Finally, performance evaluations of the proposed method are given and a conclusion is drawn.

II. Related Works

The signal reconstruction expounded in (3) is an NP-hard problem. Among the plethora of methods to overcome the computational impasse one can list convex relaxation, various greedy algorithms, Bayesian framework, non-convex optimization, iterative thresholding methods etc. [18]. However, these algorithms still suffer from computational complexity and must be restricted mostly to non-real time applications. For an application where a fast and real-time data inference is required, one possible solution could be designing a non-iterative solution such as a simple forward pass re-constructor [19], [20] based on neural networks. These types of solutions, nevertheless, remain still wasteful of resources since we have to return to the high-dimensional ambient domain from the compressed domain in order to execute tasks such as feature extraction, classification etc. Furthermore the exact recovery probability, that is the phase diagram of the recovery algorithms, depends critically on the sparsity level k and the number of measurements, m [21]. When the proportion of measurements is very low, typically for $\frac{m}{N} \leq 0.1$ most reconstruction algorithms fail. Approaches to tackle the reconstruction bottleneck have been to bypass the reconstruction step altogether, and make inferences directly on the CSMs signal y [9], or on some proxy of the signal, $\tilde{S} = \Psi^T y$ without solving the inverse problem for sparse reconstruction $\hat{x}$ as in Eq. (3), therefore $\hat{S} = \Phi\hat{x}$, where $\hat{S}$ full recovery of the vectorized image. We can express the linear degradation on the proxy as

$$\tilde{S} = \Psi^T y = \Psi^T \Psi S = HS, \tag{4}$$

where $H = \Psi^T\Psi$ is a non-invertible matrix that represents the non-linear degradation on original signal S.

A. Feature extraction from compressively sensed signals with random measurement matrices

In order to guarantee the exact recovery of the k-sparse signal x from y, the measurement matrix Ψ should satisfy certain properties. For example, the measurement matrix, Ψ with i.i.d. elements $\Psi_{i,j}$ drawn according to $\mathcal{N}\left(0, \frac{1}{m}\right)$, and $m > k(\log(N/k))$ guarantees with high probability the exact signal reconstruction when we relax the ℓ_0 to ℓ_1 in (3) [22]. Random measurement matrices are known to be universally optimum in the sense that they are data independent of characteristics of the data, and they satisfy minimum reconstruction error with minimum m when we do not have another prior information about k-sparse signal. The acquisition of the proxy signal is obviously done as, $\tilde{S} = \Psi^T y$, where $\Psi^T \in \mathbb{R}^{N\times m}$ is the transpose of the measurement matrix Ψ. An example proxy image is shown in Figure 1.

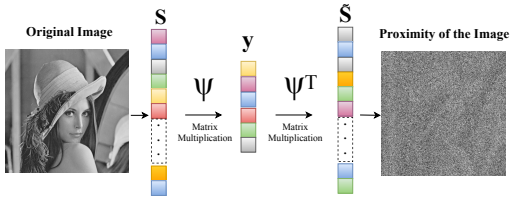

Fig. 1: The image of Lena and its proxy $\Psi^T y$ obtained from CSMs, where y results from projecting the original image on a Gaussian random measurement matrix.

B. Feature extraction from compressively sensed signals based on measurement matrices with learned coefficients

Design of optimal measurement matrices for CS reconstruction and/or for inference tasks is an active research area. An approach to learn a projection operator from image to measurement domain and its backprojection operator from compressed domain to image domain is presented in [14]. The authors have used two fully-connected layers that are followed by convolution layers. The first layer takes the original image S and projects it to the measurement domain, y. The learned weights of this layer represent the elements of measurement matrix for compressively sensing images. The second layer represents the back projection to the image domain to produce a proxy of the image, i.e., $\tilde{S} = \tilde{\Psi}^T y$. In this expression $\tilde{\Psi}^T$ is the learned transpose of the measurement matrix, which is used instead of the transpose of the true measurement matrix, Ψ^T. The output of this layer, the proxy image, is given as input to convolutional layers to realize some non-linear inference task, e.g., classification. Thus the measurement matrix, the pseudo-transpose of the measurement matrix and convolutional network are all jointly learned from the training data. Figure 2 illustrates the first two fully-connected layers of this network.

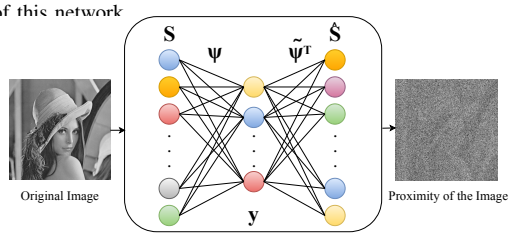

Fig. 2: An original image and its proxy $\Psi^T y$ where y that is obtained using the learned measurement matrix.

III. Proposed Approach

In this work, we have employed MB-DCT features extracted from proxy images (see Eq. 4) for classification tasks. Specifically, we applied the MB-DCT of [16] as follows: i) we use 4 window scales (instead of 6 as in [16]) and the size of the largest window is now 24 pixels instead of 128 pixels [16]) to fit smaller sized MNIST images (28×28 pixels); ii) we apply a different scheme of coefficient elimination in that we keep the best performing of the three sets (based on AC energy preservation) of DCT coefficients in the sense of classification accuracy. An MB-DCT descriptor consists of mean quantization of 2D-DCT transform coefficients as computed from multiscale blocks around (densely or sparsely chosen) image points [16].

We employ the mentioned scheme of MB-DCT features in two main modes: 1) The conventional BoW framework as in [16]; 2) A fusion scheme where MB-DCT features are complemented with deep learning features.

A. MB-DCT

We review briefly the MB-DCT features:

(1) DCT computation: 2D-DCT coefficients are computed in multiple nested blocks around selected image points, each incrementally changing in size. Similar to [16], we employ various sized windows in this work, in order to capture contextual information in different sized neighbourhoods around every image point. We compute 2D-DCT in four scales corresponding to block sizes $\{8,\ 12,\ 16,\ 24\}$, which seemed adequate for 28×28 pixel-sized MNIST images. For larger images, larger block sizes can be investigated for performance-computational cost tradeoff.

(2) Eliminating irrelevant coefficients: A subset of zig-zag ordered DCT coefficients are kept for each block as features and the remaining coefficients are eliminated as irrelevant. The DC term was discarded in all scales as in [16], which also desensitizes the feature vectors to illumination level. We experimented for different sized subsets of the zig-zag ordered coefficients in each scale. Specifically, to determine the quantity of DCT coefficients kept, we start with a random subset of training images. Then, we find three sets of zig-zag ordered DCT coefficients for every pixel location preserving, respectively, 90% and 95% of the AC energy. We repeat this experiment for each scale and for each window size. Finally, we fix the number of coefficients for each energy level (and for each scale) to the average, over all training images, number of coefficients that have met energy preservation percentages. For 100% of the energy preservation we keep all the AC coefficients. For the window sizes of $\{8, 12, 16, 24\}$, we found that the average number of AC coefficients corresponding to 90% and 95% energy are $\{15, 26, 37, 73\}$ and $\{21, 40, 63, 130\}$, respectively. Using these sets of coefficients specific to the window size, we measured the classification error rate on MNIST proxy images at different sensing rates. The resulting error rates are given in Table 1, where one can see that the performances do not differ significantly. Notice that one needs to use quite larger set of coefficients as compared to when original images were used [16]. Due to the imperfect reconstruction of proxy images, the structural information in the image is not as compact as in the original one.

(3) Binarization of the coefficients: Since binary features are memory and computation efficient, we binarized the selected coefficients of each block by mean quantization similar to [16]. We also tried median quantization and also trimming, but the

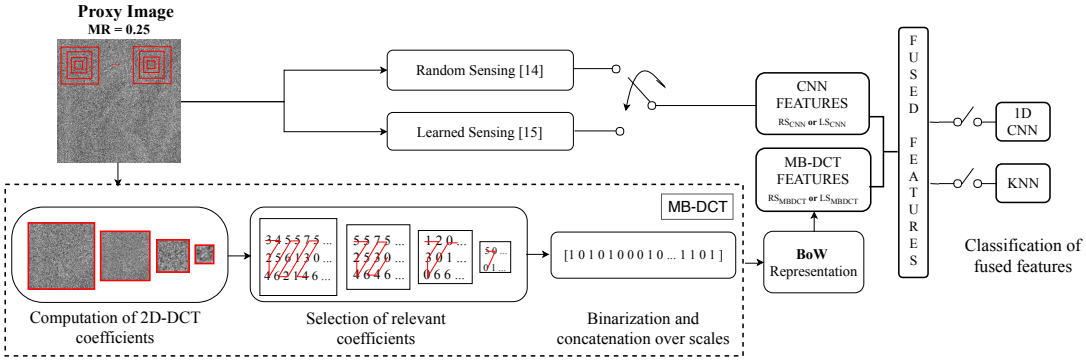

Fig. 3: Computational pipeline for the proposed approach.

mean quantization provide slightly better results (around 0.5% improvement).

(4) Concatenation of different scales: The final binary descriptor for a given keypoint is obtained by concatenation of binarized DCT coefficient sets at each scale.

The computational pipeline of the MB-DCT scheme is illustrated in Figure 3.

B. Performance of MB-DCT features for classification of CS proxies

We first compute MB-DCT features densely on the CS proxies of input images as in Eq. 4. Then, we extract image descriptors from these features according to the two schemes explained in the sequel.

1) MB-DCT in the BoW framework: In this scheme, we follow the conventional BoW procedure to compute descriptors of CS proxies. We learn a visual dictionary by K-Means clustering of dense MB-DCT features using hamming distance and computed on a training image set. The MB-DCT feature of each image point is assigned the nearest binary descriptor from the dictionary with hard voting. Finally, we apply average pooling to compute a single image signature to obtain the BoW representation of each image.

2) Fusion of MB-DCT with Deep Learning features: Deep learning approaches have been shown to provide superior performance in the solution of inference problems provided sufficient amount of training data is available. Nevertheless, recent studies have demonstrated that the joint use of learned features and hand-crafted features (e.g., MB-DCT) can result in improved performance [23], [24].

For this purpose, we have jointly used the BoW descriptors obtained from MB-DCT features with CNN features computed as in the two recent works, i.e. [14] and [15]. In both cases, proxy images are recovered by pre-multiplying the CSM vector with the transpose of the sensing matrix. In [14], the sensing matrix consists of random Gaussian numbers while in *Compressive Learning* (*CL*) the sensing matrix is obtained using a deep learning architecture. In both approaches, CNN features are computed on the proxy images. This procedure of MB-DCT and CNN features is shown in the two upper branches of the block diagram in Figure 3. We have named the CNN-derived feature scheme in [14] as *Random Sensing + CNN* (shortly RS_{CNN}) and that in [15] as *Learned Sensing + CNN* (shortly LS_{CNN}), respectively.

Some examples of proxy images recovered with the transpose of the random Gaussian matrix using Eq. 4 are shown in Figure 4 for four sampling rates. Starting from such a proxy image, we compute CNN features (coefficients of the fully connected last layer) using the Lenet5 model [14]. We also compute in parallel BoW descriptors from MB-DCT features, and we refer to this method as RS_{MB-DCT}. Finally, after L_2 normalization, separately of each descriptor, we concatenate them to obtain the joint descriptor. We denote the fused descriptor as $RS_{(CNN|MB-DCT)}$.

TABLE I: Effect of the quantity of DCT coefficients, as a function of energy preserved, on classification performance of MNIST proxy images at different measurement rates.

Measurement Rate	90% Energy	95% Energy	100% Energy
0.25	8.75	8.67	7.26
0.10	10.81	10.57	9.49
0.05	16.04	15.21	14.28
0.01	41.99	41.1	41.33

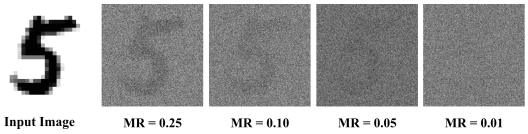

Fig. 4: Proxy images recovered when random sensing is used at different sensing rate

For the LS_{CNN} algorithm [15], we learned the sampling matrix for the MNIST dataset, i.e. we get the Ψ and Ψ^T matrices in Eq. 4 from the first and second fully connected

TABLE II: Test error rates on MNIST dataset. MR: Measurement Rate; RS: Random Sensing; LS: Learned Sensing, [†] denotes our re-implementation of [14] and [15]; [*] denotes our proposed features. Presented results are obtained with the KNN classifier.

MR	Smashed Filter [9]	RS_{CNN} [14]	$RS^{\dagger}_{CNN}$	RS^{*}_{MBDCT}	$RS^{*}_{(CNN\|MBDCT)}$	LS_{CNN} [15]	$LS^{\dagger}_{CNN}$	LS^{*}_{MBDCT}	$LS^{*}_{(CNN\|MBDCT)}$
0.25	27.42%	**1.63%**	1.73%	7.26%	2.17%	**1.56%**	1.95%	5.84%	1.58%
0.10	43.55%	**2.99%**	2.98%	9.46%	3.02%	1.91%	1.88%	5.90%	**1.58%**
0.05	53.21%	5.18%	4.78%	14.28%	**4.44%**	2.86%	2.12%	5.80%	**1.59%**
0.01	63.03%	41.06%	45.8%	41.33%	**24.78%**	6.46%	5.52%	19.88%	**3.87%**

TABLE III: Test error rates of the proposed features on MNIST dataset obtained with different classifiers

Measurement Rate	RS_{MBDCT}		$RS_{(CNN\|MBDCT)}$		LS_{MBDCT}		$LS_{(CNN\|MBDCT)}$	
	KNN	1D-CNN	KNN	1D-CNN	KNN	1D-CNN	KNN	1D-CNN
0.25	7.26%	8.37%	2.17%	1.69%	5.84%	5.88%	1.58%	1.58%
0.10	9.46%	10.01%	3.02%	2.87%	5.90%	6.19%	**1.58%**	1.75%
0.05	14.28%	14.16%	**4.44%**	4.66%	5.80%	5.64%	**1.59%**	1.63%
0.01	41.33%	48.42%	**24.78%**	28.11%	19.88%	21.09%	**3.87%**	4.57%

layers of the trained network. We compute BoW representation of MB-DCT features on these proxies referred to as LS_{MB-DCT}. Similarly, we get the CNN features from the last fully connected layer of the network. Finally, applying L_2 normalization to each, we concatenate them to obtain the joint features that we name as $LS_{(CNN|MB-DCT)}$.

IV. Performance Evaluation

A. Experimental setup

We have experimented on the MNIST dataset that contains hand-written digit images and we followed the same experimental setup in [14] as 50K and following 10K images are used in training and testing, respectively.

a) Computation of the features: To compute MB-DCT features, we learned a visual dictionary by K-means clustering based on hamming distance and using training set consisting of 100 randomly selected proxy images. We worked with K=512 clusters as in [16]. The following procedures are as mentioned in Section IV.B.1.

In order to compute RS_{CNN} and LS_{CNN} features we have re-implemented the corresponding architectures in [14] and [15] using the Keras library. For the RS_{CNN} case, we have trained the network in [14] using stochastic gradient descent with the parameters: learning rate 0.01, momentum 0.9, weight decay 0.0005, and we applied 15K epochs following [14]. For the implementation of LS_{CNN} we have trained the network in [15] with Adam optimizer, using learning rate 0.00025 and 500 epochs. Training took around 60 (due to high number of epochs) and 2 hours for the techniques of RS_{CNN} and LS_{CNN}, respectively, with the GPU of GTX 1080 Ti.

b) Choice of the classifier: We ran experiments with two different classifiers, namely, KNN and 1D-CNN. For KNN, we used the chi-square distance to compare histograms. We decided for the best value of 'k' by 5-fold cross-validation on the training set and then measured the performance on the test set.

We further wanted to examine the classification performance with a multilayer neural network. However, since the length of the features were quite high, i.e., 1012 for RS_{CNN} and 596 for LS_{CNN} (recall that these are also to be augmented with the 512 dimensional MB-DCT features in the fusion scheme), we decided not to follow this path to avoid excessive computational overhead. Instead we opted to train a 1D-CNN network, adopting Lenet-5 model, with the computed features of the training images. We used Adam optimizer with a learning rate of 0.00025 and 500 epochs in training which took around 2 hours for all the techniques.

B. Performance results

The performance results that are obtained with the aforementioned techniques in terms of test error are presented at Table II. We also present three published performance results in the literature, namely, Smashed Filter [9], RS_{CNN} [14] and LS_{CNN} [15].

We observe that with our re-implementation of RS_{CNN} and LS_{CNN}, we get performances quite close to the reported ones in [14] and [15]. For the degraded proxy image with random sampling, our binary descriptor (RS_{MB-DCT}) outperforms Smashed Filters [9] significantly. RS_{MB-DCT} also gives competitive results with respect to RS_{CNN} [14] for the lowest measurement rate (0.01). We outperform RS_{CNN} [14] at the lowest measurement rate significantly when we use the fused feature (41.06% vs 24.78%).

The significant performance gain is achieved when degradation is created by the learned matrices. In that case, although LS_{MB-DCT} was behind the reported LS_{CNN} results in [15], our re-implementation of LS_{CNN} was slightly better than theirs. More significantly, lowest classification error rates which can be accepted as the new state-of-the-art are obtained when we use joint features in $LS_{(CNN|MB-DCT)}$ implementation (3.87% test error for 0.01 measurement rate).

The performance results presented in Table II are obtained with the KNN classifier. We also present the performance results obtained with 1D-CNN at Table III. As it can be seen in Table III, although they were competitive for higher sampling rates, KNN always gives better result, more significantly at lowest measurement rate. However, execution time of KNN

classifier was much higher than the 1D-CNN execution time on GPU.

V. Conclusion

In this work, we proposed a DCT-based discriminative feature scheme, computed directly from the proxy image which is usually a heavily degraded version of the original image. This feature vector (called MB-DCT) is binary, hence simple and low cost. We further introduced feature fusion by concatenating Bag of Words (BoW) representation of our binary features with one of the two state-of-the-art CNN-based feature vectors. Our experimental results show that proposed scheme gives the state-of-the-art performance for compressively sensed image classification even at the lowest measurement rate.

References

[1] E. J. Candès *et al.*, "Compressive sampling," in *Proceedings of the international congress of mathematicians*, vol. 3, pp. 1433–1452, Madrid, Spain, 2006.

[2] T. Wimalajeewa, H. Chen, and P. K. Varshney, "Performance limits of compressive sensing-based signal classification," *IEEE Transactions on Signal Processing*, vol. 60, no. 6, pp. 2758–2770, 2012.

[3] J. Haupt, R. Castro, R. Nowak, G. Fudge, and A. Yeh, "Compressive sampling for signal classification," in *Signals, Systems and Computers, 2006. ACSSC'06. Fortieth Asilomar Conference on*, pp. 1430–1434, IEEE, 2006.

[4] M. A. Davenport, P. T. Boufounos, M. B. Wakin, and R. G. Baraniuk, "Signal processing with compressive measurements," *IEEE Journal of Selected Topics in Signal Processing*, vol. 4, no. 2, pp. 445–460, 2010.

[5] R. Calderbank, S. Jafarpour, and R. Schapire, "Compressed learning: Universal sparse dimensionality reduction and learning in the measurement domain," *preprint*, 2009.

[6] M. A. Davenport, M. F. Duarte, M. B. Wakin, J. N. Laska, D. Takhar, K. F. Kelly, and R. G. Baraniuk, "The smashed filter for compressive classification and target recognition," in *Computational Imaging V*, vol. 6498, p. 64980H, International Society for Optics and Photonics, 2007.

[7] W. B. Johnson and J. Lindenstrauss, "Extensions of lipschitz mappings into a hilbert space," *Contemporary mathematics*, vol. 26, no. 189-206, p. 1, 1984.

[8] K. Kulkarni and P. Turaga, "Reconstruction-free action inference from compressive imagers," *IEEE transactions on pattern analysis and machine intelligence*, vol. 38, no. 4, pp. 772–784, 2016.

[9] S. Lohit, K. Kulkarni, P. Turaga, J. Wang, and A. C. Sankaranarayanan, "Reconstruction-free inference on compressive measurements," in *Proceedings of the IEEE Conference on Computer Vision and Pattern Recognition Workshops*, pp. 16–24, 2015.

[10] M. Shoaib, N. K. Jha, and N. Verma, "Signal processing with direct computations on compressively sensed data," *IEEE Transactions on Very Large Scale Integration (VLSI) Systems*, vol. 23, no. 1, pp. 30–43, 2015.

[11] S. Chen, W. Hua, Z. Li, J. Li, and X. Gao, "Heartbeat classification using projected and dynamic features of ecg signal," *Biomedical Signal Processing and Control*, vol. 31, pp. 165–173, 2017.

[12] A. Kabán, "New bounds on compressive linear least squares regression," in *Artificial Intelligence and Statistics*, pp. 448–456, 2014.

[13] R. J. Durrant and A. Kabán, "Compressed fisher linear discriminant analysis: Classification of randomly projected data," in *Proceedings of the 16th ACM SIGKDD international conference on Knowledge discovery and data mining*, pp. 1119–1128, ACM, 2010.

[14] S. Lohit, K. Kulkarni, and P. Turaga, "Direct inference on compressive measurements using convolutional neural networks," in *Image Processing (ICIP), 2016 IEEE International Conference on*, pp. 1913–1917, IEEE, 2016.

[15] A. Adler, M. Elad, and M. Zibulevsky, "Compressed learning: A deep neural network approach," *arXiv preprint arXiv:1610.09615*, 2016.

[16] S. Aslan, M. Yamaç, and B. Sankur, "A dct-based multiscale binary descriptor robust to complex brightness changes," in *Signal Processing Conference (EUSIPCO), 2016 24th European*, pp. 1573–1577, IEEE, 2016.

[17] D. L. Donoho and M. Elad, "Optimally sparse representation in general (nonorthogonal) dictionaries via l minimization," *Proceedings of the National Academy of Sciences*, vol. 100, no. 5, pp. 2197–2202, 2003.

[18] J. A. Tropp, "Just relax: Convex programming methods for identifying sparse signals in noise," *IEEE transactions on information theory*, vol. 52, no. 3, pp. 1030–1051, 2006.

[19] A. Mousavi and R. G. Baraniuk, "Learning to invert: Signal recovery via deep convolutional networks," in *Acoustics, Speech and Signal Processing (ICASSP), 2017 IEEE International Conference on*, pp. 2272–2276, IEEE, 2017.

[20] S. Lohit, K. Kulkarni, R. Kerviche, P. Turaga, and A. Ashok, "Convolutional neural networks for non-iterative reconstruction of compressively sensed images," *arXiv preprint arXiv:1708.04669*, 2017.

[21] C. A. Metzler, A. Maleki, and R. G. Baraniuk, "From denoising to compressed sensing," *IEEE Transactions on Information Theory*, vol. 62, no. 9, pp. 5117–5144, 2016.

[22] E. J. Candes, "The restricted isometry property and its implications for compressed sensing," *Comptes rendus mathematique*, vol. 346, no. 9-10, pp. 589–592, 2008.

[23] E. G. Danaci and N. Ikizler-Cinbis, "Low-level features for visual attribute recognition: An evaluation," *Pattern Recognition Letters*, vol. 84, pp. 185–191, 2016.

[24] S. Aslan, C. B. Akgül, B. Sankur, and E. T. Tunalı, "Exploring visual dictionaries: a model driven perspective," *Journal of Visual Communication and Image Representation*, vol. 49, pp. 315–331, 2017.

PUBLICATION VII

Multilinear Compressive Learning

D. T. Tran, M. Yamaç, A. Degerli, M. Gabbouj, and A. Iosifidis

IEEE Transactions on Neural Networks and Learning Systems, vol. 32, no. 4, pp. 1512–1524
DOI: 10.1109/TNNLS.2020.2984831

Multilinear Compressive Learning

Dat Thanh Tran*, Mehmet Yamaç*, Aysen Degerli*, Moncef Gabbouj*, Alexandros Iosifidis†
*Department of Computing Sciences, Tampere University, Tampere, Finland
†Department of Engineering, Aarhus University, Aarhus, Denmark
Email:{thanh.tran,mehmet.yamac, aysen.degerli, moncef.gabbouj}@tuni.fi, alexandros.iosifidis@eng.au.dk

***Abstract*—Compressive Learning is an emerging topic that combines signal acquisition via Compressive Sensing and Machine Learning to perform inference tasks directly on a small number of measurements. Many data modalities naturally have a multi-dimensional or tensorial format, with each dimension or tensor mode representing different features such as the spatial and temporal information in video sequences or the spatial and spectral information in hyperspectral images. However, in existing Compressive Learning frameworks, the Compressive Sensing component utilizes either random or learned linear projection on the vectorized signal to perform signal acquisition, thus discarding the multi-dimensional structure of the signals. In this paper, we propose Multilinear Compressive Learning, a framework that takes into account the tensorial nature of multi-dimensional signals in the acquisition step and builds the subsequent inference model on the structurally sensed measurements. Our theoretical complexity analysis shows that the proposed framework is more efficient compared to its vector-based counterpart in both memory and computation requirement. With extensive experiments, we also empirically show that our Multilinear Compressive Learning framework outperforms the vector-based framework in object classification and face recognition tasks, and scales favorably when the dimensionalities of the original signals increase, making it highly efficient for high-dimensional multi-dimensional signals.**

I. Introduction

The classical sample-based signal acquisition and manipulation approach usually involve separate steps of signal sensing, compression, storing or transmitting, then the reconstruction. This approach requires the signal to be sampled above the Nyquist rate in order to ensure high-fidelity reconstruction. Since the existence of spatial-multiplexing cameras, over the past decade, Compressive Sensing (CS) [1] has become an efficient and a prominent approach for signal acquisition at sub-Nyquist rates, combining the sensing and compression step at the hardware level. This is due to the assumption that the signal often possesses specific structures that exhibit sparse or compressible representation in some basis, thus, can be sensed at a lower rate than the Nyquist rate but still allows almost perfect reconstruction [2], [3]. In fact, many data modalities that we operate on are often sparse or compressible. For example, smooth signals are compressible in the Fourier domain or subsequent frames in a video are piecewise smooth, thus compressible in a wavelet domain. With the efficient realization at the hardware level such as the popular Single Pixel Camera, CS becomes an efficient signal acquisition framework, however, making the signal manipulation an intimidating task. Indeed, over the past decade, since reversing the signal to its original domain is often considered the necessary step for signal manipulation, a significant amount of works have been dedicated to signal reconstruction, giving certain insights and theoretical guarantees for the successful recovery of the signal from compressively sensed measurements [2], [1], [3].

While signal recovery plays a major role in some sensing applications such as image acquisition for visual purposes, there are many scenarios in which the primary objective is the detection of certain patterns or inferring some properties in the acquired signal. For example, in many radar applications, one is often interested in anomaly patterns in the measurements, rather than signal recovery. Moreover, in certain applications [4], [5], signal reconstruction is undesirable since the step can potentially disclose private information, leading to the infringement of data protection legislation. These scenarios naturally led to the emergence of Compressive Learning (CL) concept [6], [7], [8], [9] in which the inference system is built on top of the compressively sensed measurements without the explicit reconstruction step. While the amount of literature in CL is rather insignificant compared to signal reconstruction in CS, different attempts have been made to modify the sensing component in accordance with the learning task [10], [11], to extract discriminative features [7], [12] from the randomly sensed measurements or to jointly optimize the sensing matrix [13], [14] and the subsequent inference system. Improvements to different components of CL pipeline have been proposed, however, existing frameworks utilize the same compressive acquisition step that performs a linear projection of the vectorized data, thereby operating on the vector-based measurements and thus losing the tensorial structure in the measurements of multi-dimensional data.

In fact, many data modalities naturally possess the tensorial format such as color images, videos or multivariate time-series. The multi-dimensional representation naturally reflects the semantic differences inherent in different dimensions or tensor modes. For example, the spatial and temporal dimensions in a video or the spatial and the spectral dimensions in hyperspectral images represent two different concepts, having different properties. Thus by exploiting this natural form of the signals and considering the semantic differences between different dimensions, many tensor-based signal processing, and learning algorithms have shown its superiority over the vector-based

approach, which simply operates on the vectorized data [15], [16], [17], [18], [19], [20], [21]. Indeed, tensor representation and its associated mathematical operations and properties have found various applications in the Machine Learning community. For example, in multivariate time-series analysis, the multilinear projection was utilized in [18], [22] to model the dependencies between data points along the feature and temporal dimension separately. Several multilinear regression [23], [24] or discriminant models [25], [26] have been developed to replace their linear counterparts, with improved performance. In neural network literature, multilinear techniques have been employed to compress pre-trained networks [27], [28], [29], or to construct novel neural network architectures [19], [30], [22].

It is worth noting that CS plays an important role in many applications that involves high-dimensional tensor signals because the standard point-based signal acquisition is both memory and computationally intensive. Representative examples include Hyperspectral Compressive Imaging (HCI), Synthetic Aperture Radar (SAR) imaging, Magnetic Resonance Imaging (MRI) or Computer Tomography (CT). Therefore, the tensor-based approach has also found its place in CS, also known as Multi-dimensional Compressive Sensing (MCS) [31], which replaces the linear sensing and reconstruction model with multilinear one. Similar to vector-based CS, thereupon simply referred to as CS, the majority of efforts in MCS are dedicated to constructing multilinear models that induce sparse representation along each tensor mode with respect to a set of bases. For example, the adoption of sparse Tucker representation and the Kronecker sensing scheme in MRI allows computationally efficient signal recovery with very low Peak Signal to Noise Ratio (PSNR) [31], [32]. In addition, the availability of optical implementations of separable sensing operators such as [33] naturally enables MCS, significantly reducing the amount of data collection and reconstruction cost.

While multilinear models have been successfully applied in Compressive Sensing and Machine Learning, to the best of our knowledge, we have not seen their utilization in Compressive Learning, which is the joint framework combining CS and ML. In this paper, in order to leverage the multi-dimensional structure in many data modalities, we propose Multilinear Compressive Learning framework, which adopts a multilinear sensing operator and a neural network classifier that is designed to utilize the multi-dimensional structure-preserving compressed measurements. The contribution of this paper is as follows:

- We propose Multilinear Compressive Learning (MCL), a novel CL framework that consists of a multilinear sensing module, a multilinear feature synthesis component, both taking into account the multi-dimensional property of the signals, and a task-specific neural network. The multilinear sensing module compressively senses along each separate mode of the original tensor signal, producing structurally encoded measurements. Similarly, the feature synthesis component performs the feature learning steps separately along each mode of the compressed measurements, producing inputs to the subsequent task-specific neural network which has the structure depending on the inference problem.
- We show both theoretically and empirically that the proposed MCL framework is highly cost-effective in terms of memory and computational complexity. In addition, theoretical analysis and experimental results also indicate that our framework scales well when the dimensionalities of the original signal increases, making it highly efficient for high-dimensional tensor signals.
- We conduct extensive experiments in object classification and face recognition tasks to validate the performance of our framework in comparison with its vector-based counterpart. Besides, the effect of different components and hyperparameters in the proposed framework were also empirically analyzed.
- We publicly provide our implementation of the experiments reported in this paper to facilitate future research. By following our detailed instructions on how to set up the software environment, all experiment results can be reproduced in just one line of code. [1]

The remainder of the paper is organized as follows: in Section 2, we review the background information in Compressive Sensing, Multi-dimensional Compressive Sensing and Compressive Learning. In Section 3, the detailed description of the proposed Multilinear Compressive Learning framework is given. Complexity analysis and comparison with the vector-based framework are also given in Section 3. In Section 4, we provide details of our experiment protocols and quantitative analysis of different experiment configurations. Section 5 concludes our work with possible future research directions.

II. Related Work

A. Notation

In this paper, we denote scalar values by either lower-case or upper-case characters $(x, y, X, Y \dots)$, vectors by lower-case bold-face characters $(\mathbf{x}, \mathbf{y}, \dots)$, matrices by upper-case or Greek bold-face characters $(\mathbf{A}, \mathbf{B}, \mathbf{\Phi}, \dots)$ and tensor as calligraphic capitals $(\mathcal{X}, \mathcal{Y}, \dots)$. A tensor with K modes and dimension I_k in the mode-k is represented as $\mathcal{X} \in \mathbb{R}^{I_1 \times I_2 \times \cdots \times I_K}$. The entry in the i_kth index in mode-k for $k = 1, \dots, K$ is denoted as $\mathcal{X}_{i_1, i_2, \dots, i_K}$. In addition, $vec(\mathcal{X})$ denotes the vectorization operation that rearranges elements in $\mathcal{X}$ to the vector representation.

Definition 1 (The Kronecker Product): The Kronecker product between two matrices $\mathbf{A} \in \mathbb{R}^{M \times N}$ and $\mathbf{B} \in \mathbb{R}^{P \times Q}$ is denoted as $\mathbf{A} \otimes \mathbf{B}$ having dimension $MP \times NQ$, is defined by:

$$\mathbf{A} \otimes \mathbf{B} = \begin{bmatrix} \mathbf{A}_{11}\mathbf{B} & \dots & \mathbf{A}_{1N}\mathbf{B} \\ \vdots & \ddots & \vdots \\ \mathbf{A}_{M1}\mathbf{B} & \dots & \mathbf{A}_{MN}\mathbf{B} \end{bmatrix} \tag{1}$$

Definition 2 (Mode-k Product): The mode-k product between a tensor $\mathcal{X} = [x_{i_1}, \dots, x_{i_K}] \in \mathbb{R}^{I_1 \times \dots I_K}$ and a

[1] https://github.com/viebboy/MultilinearCompressiveLearningFramework

matrix $\mathbf{W} \in \mathbb{R}^{J_k \times I_k}$ is another tensor of size $I_1 \times \cdots \times J_k \times \cdots \times I_K$ and denoted by $\mathcal{X} \times_k \mathbf{W}$. The element of $\mathcal{X} \times_k \mathbf{W}$ is defined as $[\mathcal{X} \times_k \mathbf{W}]_{i_1,\ldots,i_{k-1},j_k,i_{k+1},\ldots,i_K} = \sum_{i_k=1}^{I_K} [\mathcal{X}]_{i_1,\ldots,i_{k-1},i_k,\ldots,i_K} [\mathbf{W}]_{j_k,i_k}$.

The following relationship between the Kronecker product and k-mode product is the cornerstone in MCS:

$$\mathcal{Y} = \mathcal{X} \times_1 \mathbf{W}_1 \times \cdots \times_N \mathbf{W}_N \tag{2}$$

can be written as

$$\mathbf{y} = (\mathbf{W}_1 \otimes \cdots \otimes \mathbf{W}_N)\mathbf{x} \tag{3}$$

where $\mathbf{y} = vec(\mathcal{Y})$ and $\mathbf{x} = vec(\mathcal{X})$

B. Compressive Sensing

Compressive Sensing (CS) [1] is a signal acquisition and manipulation paradigm that performs simultaneous sensing and compression on the hardware level, leading to large reduction in computation cost and the number of measurements. The signal $\mathbf{y}$ working under CS is assumed to have a sparse or compressible representation $\mathbf{x}$ in some basis or dictionary $\mathbf{\Psi} \in \mathbb{R}^{I \times I}$, that is:

$$\mathbf{y} = \mathbf{\Psi}\mathbf{x} \quad \text{with} \quad \|\mathbf{x}\|_0 \leq K \quad \text{and} \quad K \ll I \tag{4}$$

where $\|\mathbf{x}\|_0$ denotes the number of non-zero entries in $\mathbf{x}$. While the dictionary presented in Eq. (4) is complete, i.e., the number of columns in $\mathbf{\Psi}$ is equal to the signal dimension I, we should note that signal models with over-complete dictionaries can also work, i.e., $\mathbf{\Psi} \in \mathbb{R}^{J \times I}$ with some modifications [34].

With the assumption on the sparsity, CS performs the linear sensing step using the sensing operator $\mathbf{\Phi} \in \mathbb{R}^{M \times I}$, acquiring a small number of measurements $\mathbf{z} \in \mathbb{R}^M$ with $M < I$, from analog signal $\mathbf{y}$:

$$\mathbf{z} = \mathbf{\Phi}\mathbf{y} \tag{5}$$

Eq. (5) represents both the sensing and compression step that can be efficiently implemented at the sensor level. Thus, what we obtain from CS sensors is a limited number of measurements $\mathbf{z}$ that is used for other processing steps. By combining Eq. (4, and 5), the CS model is usually expressed as:

$$\mathbf{z} = \mathbf{\Phi}\mathbf{\Psi}\mathbf{x} \quad \text{with} \quad \|\mathbf{x}\|_0 \leq K \quad \text{and} \quad K \ll I \tag{6}$$

In some applications, we are interested in recovering the signal $\mathbf{y}$ from $\mathbf{z}$. This involves developing theoretical properties and algorithms to determine the sensing operator $\mathbf{\Phi}$, the dictionary or basis $\mathbf{\Psi}$, and the number of nonzero coefficients K in order to ensure that the reconstruction is unique, and of high-fidelity [2], [35], [3]. The reconstruction of $\mathbf{y}$ is often posed as finding the sparsest solution of the under-determined linear system [36], particularly:

$$\arg\min_{\mathbf{x}} \|\mathbf{x}\|_0 \quad \text{s.t} \quad \|\mathbf{z} - \mathbf{\Phi}\mathbf{\Psi}\mathbf{x}\|_2 \leq \epsilon \tag{7}$$

where ϵ is a small constant specifying the amount of residual error allowed in the approximation. A large body of research has been dedicated to solve the problem in Eq. (7) and its variants with two main approaches: *basis pursuit* (BP) which transforms Eq. (7) to a convex one to be solved by linear programming [37] or second-order cones programs [2], and *matching pursuit* (MP), a class of greedy algorithms, which iteratively refines the solution to the sparsest ones [38], [39]. Both BP and MP algorithms are computationally intensive when the number of elements in $\mathbf{y}$ is big, especially in the case of multi-dimensional signals.

C. Multi-dimensional Compressive Sensing

Given a multi-dimensional signal $\mathcal{Y} \in \mathbb{R}^{I_1 \times \cdots \times I_N}$, a direct application of the sparse representation in Eq. (4) requires vectorizing $\mathbf{y} = vec(\mathcal{Y})$ and the calculations on $\mathbf{\Phi}\mathbf{\Psi} \in \mathbb{R}^{M \times (I_1 \ldots I_N)}$, which is a very big matrix with the number of elements scales exponentially with N. Instead of assuming $vec(\mathcal{Y})$ is sparse in some basis or dictionary, MCS adopts a sparse Tucker model [40] as follows:

$$\mathcal{Y} = \mathcal{X} \times_1 \mathbf{\Psi}_1 \times \cdots \times_N \mathbf{\Psi}_N \tag{8}$$

which assumes that the signal $\mathcal{Y}$ is sparse with respect to a set of bases or dictionaries $\mathbf{\Psi}_n, n = 1, \ldots, N$. Since in some cases, the sensing step can be taken in a multilinear way, i.e., by using a set of linear operators along each mode separately, also known as separable sensing operators:

$$\mathcal{Z} = \mathcal{Y} \times_1 \mathbf{\Phi}_1 \times \cdots \times_N \mathbf{\Phi}_N \tag{9}$$

that allows us to obtain the measurements $\mathcal{Z}$ with retained multi-dimensional structure. From Eq. (2, 3, 8 and 9), the MCS model is often expressed as:

$$\mathbf{z} = (\mathbf{B}_1 \otimes \cdots \otimes \mathbf{B}_N)\mathbf{x} \quad \text{with} \quad \|\mathbf{x}\|_0 \leq K \tag{10}$$

where $\mathbf{z} = vec(\mathcal{Z})$, and $\mathbf{B}_n = \mathbf{\Phi}_n \mathbf{\Psi}_n$ $(n = 1, \ldots, N)$. The formulation in Eq. (10) is also known as Kronecker CS [41].

Since MCS can be expressed in the vector form, the existing algorithms and theoretical bounds for vector-based CS have also been extended for MCS. Representative examples include Kronecker OMP and its tensor block-sparsity extension [42] that improves the computation significantly. It is worth noting that by adopting a multilinear structure, MCS operates with a set of smaller sensing and dictionaries, therefore, requires much lower memory and computation compared to the vectorization approach [31]. For detailed formulation, motivation as well as extensions of MCS, we refer interested readers to the comprehensive review paper on this topic [31].

D. Compressive Learning

The idea of learning directly from the compressed measurements dates back to the early work of [7] in which the authors proposed a framework termed *compressive classification* which introduces the concept of *smashed filters* and operates directly on the compressive measurements without reconstruction as the first proxy step. The result in [7] was subsequently

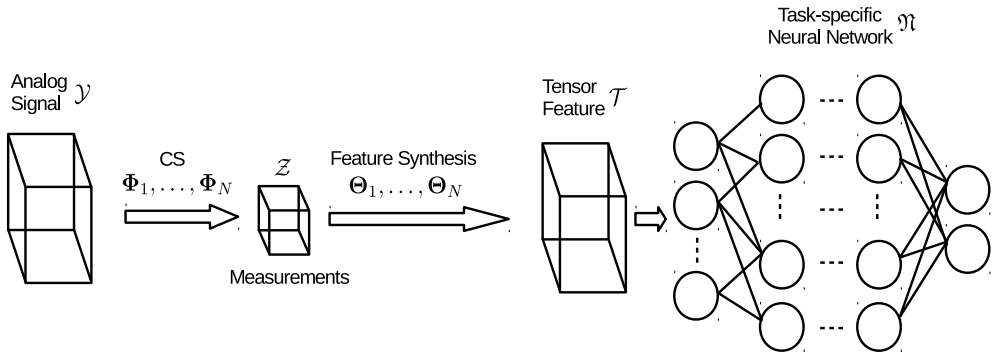

Fig. 1. Illustration of the proposed Multilinear Compressive Learning framework

strengthened in [43] showing that when sufficiently large random sensing matrix is used, it can capture the structure of the data manifold. Later, further extensions that extract discriminative features from compressive measurements for activity recognition [44], [45] or face recognition [12] have also been proposed.

The concept of CL was introduced in [6], which provides theoretical analysis illustrating that learning machines can be built directly in the compressed domain. Particularly, given certain conditions of the sensing matrix $\mathbf{\Phi}$, the performance of a linear Support Vector Machine (SVM) trained on compressed measurements is as good as the best linear threshold classifier trained on the original signal $\mathbf{y}$. Later, for compressive learning of signals described by a Gaussian Mixture Model, asymptotic behavior of the upper-bound [9] and its extension [11] to learn the sensing matrix were also derived.

In applications where input signal acquisition, signal labeling, and system optimization can be done separately such as distributed sensor networks or vision-based multi-agent control systems, jointly optimizing the sensing matrix with the classifier is feasible and thus, is widely adopted in recent literature. For example, in [10], the authors proposed an adaptive version of *feature-specific imaging* system to learn an optimal sensing matrix based on past measurements. With the advances in computing hardware and stochastic optimization techniques, end-to-end CL system was proposed in [13], and several follow-up extensions and applications [46], [47], [48], indicating superior performances when simultaneously optimizing the sensing component and the classifier via task-specific data. Our work is closely related to the end-to-end CL system in [13] in that we also optimize the CL system via stochastic optimization in an end-to-end manner. Different from [13], our proposed framework efficiently utilizes the tensor structure inherent in many types of signals, thus outperforming the approach in [13] in both inference performance and computational efficiency.

III. Multilinear Compressive Learning Framework

In this Section, we first give our description of the proposed Multilinear Compressive Learning (MCL) framework that operates directly on the tensor representation of the signals. Then, the initialization scheme and optimization procedures of the proposed framework is discussed. Lastly, theoretical analysis of the framework's complexity in comparison with its vector-based counterpart is provided.

A. Motivation

In order to model the multi-dimensional structure in the signal of interest, we assume that the discriminative structure in $\mathcal{Y} \in \mathbb{R}^{I_1 \times \cdots \times I_N}$ can be captured in a lower-dimensional multilinear subspace $\mathfrak{F} \subset \mathbb{R}^{J_1 \times \cdots \times J_N}$ of $\mathbb{R}^{I_1 \times \cdots \times I_N}$ with $(J_n < I_n, \forall n = 1, \ldots, N)$:

$$\mathcal{Y} = \bar{\mathcal{X}} \times_1 \bar{\mathbf{\Psi}}_1 \times \cdots \times_N \bar{\mathbf{\Psi}}_N \tag{11}$$

where $\bar{\mathbf{\Psi}}_n \in \mathbb{R}^{I_n \times J_n}, \forall n = 1, \ldots, N$ denotes the factor matrices and $\bar{\mathcal{X}} \in \mathbb{R}^{J_1 \times \cdots \times J_N}$ is the signal representation in this multilinear subspace.

Here we should note that although Eq. (11) in our framework and Eq. (8) in MCS look similar in its mathematical form, the assumption and motivation are different. The objective in MCS is to reconstruct the signal $\mathcal{Y}$ by assuming the existence of the set of sparsifying dictionaries or bases $\mathbf{\Psi}_n$ and optimizing $\mathbf{\Psi}_n$ to induce the sparsest $\mathcal{X}$. Since our objective is to learn a classification or regression model, we make no assumption or constraint on the sparsity of $\bar{\mathcal{X}}$ but assume that the factorization in Eq. (11) can lead to a tensor subspace $\mathfrak{F}$ in which the representation $\bar{\mathcal{X}}$ is discriminative or meaningful for the learning problem.

As mentioned in the previous Section, in some applications, the measurements can be taken in a multilinear fashion, with different linear sensing operators operating along different

tensor modes, i.e., separable sensing operators, we obtain the measurements $\mathcal{Z}$ from the following sensing equation:

$$\mathcal{Z} = \mathcal{Y} \times_1 \mathbf{\Phi}_1 \times \cdots \times_N \mathbf{\Phi}_N \tag{12}$$

where $\mathbf{\Phi}_n \in \mathbb{R}^{M_n \times I_n}$ $(n = 1, \ldots, N)$ represent the sensing matrices of those linear operators.

Here we should note that the proposed framework is not only applicable for multilinear sensing hardwares but also linear sensing hardwares. That is, the usefulness of the proposed framework is independent of the hardware implementation. In cases where the sensor is only capable of vector-based sensing, i.e., its sensing mechanism is described by the following equation:

$$\mathbf{z} = \mathbf{\Phi}\, vec(\mathcal{Y}) \tag{13}$$

with a single sensing operator $\mathbf{\Phi} \in \mathbb{R}^{M \times I_1 * \cdots * I_N}$, we can still enforce a structure-preserving sensing operation similar to the multilinear sensing scheme in Eq. (12) by setting:

$$\mathbf{\Phi} = \mathbf{\Phi}_1 \otimes \cdots \otimes \mathbf{\Phi}_N \tag{14}$$

to obtain $\mathcal{Z}$ in Eq. (12) from $\mathbf{z}$ in Eq. (13).

Combining Eq. (11 and 12), we can express our measurements $\mathcal{Z}$ as:

$$\mathcal{Z} = \bar{\mathcal{X}} \times_1 (\mathbf{\Phi}_1 \bar{\mathbf{\Psi}}_1) \times \cdots \times_N (\mathbf{\Phi}_N \bar{\mathbf{\Psi}}_N) \tag{15}$$

By setting the sensing matrices $\mathbf{\Phi}_n$ to be pseudo-inverse of $\bar{\mathbf{\Psi}}_n$ for all $n = 1, \ldots, N$, we obtain the measurements $\mathcal{Z}$ that lie in the discriminative-induced tensor subspace $\mathfrak{F}$ mentioned previously.

B. Design

Figure 1 illustrates our proposed MCL framework which consists of the following components:

- CS component: the data acquisition step of the multi-dimensional signals is done via separable linear sensing operators $\mathbf{\Phi}_n, n = 1, \ldots, N$. As mentioned previously, in cases where the actual hardware implementation only allows vector-based sensing scheme, Eq. (14) allows the simulation of this multilinear sensing step. This component produces measurements $\mathcal{Z}$ with encoded tensor structure, having the same number of tensor modes (N) as the original signal.
- Feature Synthesis (FS) component: from $\mathcal{Z}$, this step performs feature extraction along N modes of the measurements $\mathcal{Z}$ with the set of learnable matrices $\mathbf{\Theta}_n$. Since the measurements typically have many fewer elements compared to the original signal $\mathcal{Y}$, the FS component expands the dimensions of $\mathcal{Z}$, allowing better separability between the sensed signals from different classes in a higher multi-dimensional space that is found through optimization. While the sensing step performs linear interpolations for computational efficiency, the FS component can be either multilinear or nonlinear transformations. A typical nonlinear transformation step is to perform zero-thresholding, i.e., ReLU, on $\mathcal{Z}$ before multiplying with $\mathbf{\Theta}_n, n = 1 \ldots, N$, i.e., $\mathrm{ReLU}(\mathcal{Z}) \times_1 \mathbf{\Theta}_1 \times \cdots \times_N \mathbf{\Theta}_N$. In applications which require the transmission of $\mathcal{Z}$ to be analyzed, this simple thresholding step can, before transmission, increase the compression rate by sparsifying the encoded signal and discarding the sign bits. While nonlinearity is often considered beneficial for neural networks, adding the thresholding step as described above further restricts the information retained in a limited number of measurements $\mathcal{Z}$, thus, adversely affects the inference system. In the Experiments Section, we provide empirical analysis on the effect of nonlinearity towards the inference tasks at different measurement rates. Here we should note that while our FS component resembles the reprojection step in the vector-based framework [13], our FS and CS components have different weights ($\mathbf{\Theta}_n$ and $\mathbf{\Phi}_n$, $n = 1, \ldots, N$) and the dimensionality of the tensor feature $\mathcal{T}$ produced by FS component is task-dependent, and is not constrained to that of the original signal.
- Task-specific Neural Network $\mathfrak{N}$: from the tensor representation $\mathcal{T}$ produced by FS step, a neural network with task-dependent architecture is built on top to generate the regression or classification outputs. For example, when analyzing visual data, the $\mathfrak{N}$ can be a Convolutional Neural Network (CNN) in case of static images or a Convolutional Recurrent Neural Network in case of videos. In CS applications that involve distributed arrays of sensors that continuously collect data, specific architectures for time-series analysis such as Long-Short Term Memory Network should be considered for $\mathfrak{N}$. Here we should note that the size of $\mathcal{T}$ is also task-dependent and should match with the neural network component. For example, in object detection and localization task, it is desirable to keep the spatial aspect ratio of $\mathcal{T}$ similar to $\mathcal{Y}$ to allow precise localization.

C. Optimization

In our proposed MCL framework, we aim to optimize all three components, i.e., $\mathbf{\Phi}_n$, $\mathbf{\Theta}_n$ and $\mathfrak{N}$, with respect to the inference task. A simple and straightforward approach is to consider all components in this framework as a single computation graph, then randomly initialize the weights according to some popular initialization scheme [49], [50] and perform stochastic gradient descend on this graph with respect to the loss function defined by the learning task. However, this approach does not take into account any existing domain knowledge of each component that we have.

As mentioned in Section III.A, with the assumption of the existence of a tensor subspace $\mathfrak{F}$ and the factorization in Eq. (11), the sensing matrix $\mathbf{\Phi}_n$ in the CS component can be initialized equal to the pseudo-inverse of $\bar{\mathbf{\Psi}}_n$ for all $n = 1, \ldots, N$ to obtain initial $\mathcal{Z}$ that are discriminative or meaningful. There have been several algorithms proposed to learn the factorization in Eq. (11) with respect to different

TABLE I
COMPLEXITY OF THE PROPOSED MCL FRAMEWORK AND VECTOR-BASED FRAMEWORK [13]

	Our	Vector [13]
Memory	$O(2\sum_{n=1}^{N} I_n * M_n)$	$O(\prod_{n=1}^{N} I_n * M_n)$
Computation	$O\big(\sum_{n=1}^{N}\big(\prod_{p=1}^{n} M_p * \prod_{k=n}^{N} I_k\big) + \sum_{n=1}^{N}\big(\prod_{p=1}^{n} I_p * \prod_{k=n}^{N} M_k\big)\big)$	$O(2\prod_{n=1}^{N} I_n * M_n)$

criteria such as the multi-class discriminant [25], class-specific discriminant [26], max-margin [51] or Tucker Decomposition with non-negative constraint [52].

In a general setting, we propose to apply Higher Order Singular Value Decomposition (HOSVD) [40] and initialize $\mathbf{\Phi}_n$ with the left singular vectors that correspond to the largest singular values in mode n. The sensing matrices are then adjusted together with other components during the stochastic optimization process. This initialization scheme resembles the one proposed for vector-based CL framework which utilizes Principal Component Analysis (PCA). In a general case where one has no prior knowledge on the structure of $\mathfrak{F}$, a transformation that retains the most energy in the signal such as PCA or HOSVD is a popular choice when reducing dimensionalities of the signal. While for higher-order data, HOSVD only provides a quasi-optimal condition for data reconstruction in the least-square sense [53], since our objective is to make inferences, this initialization scheme works well as indicated in our Experiments Section.

With the aforementioned initialization scheme of CS component for a general setting, it is natural to also initialize $\mathbf{\Theta}_n$ in FS component with the right singular vectors corresponding to the largest singular values in mode n of the training data. With this initialization of $\mathbf{\Theta}_n$, during the initial forward steps in stochastic gradient descent, the FS component produces an approximate version of $\mathcal{Y}$, and in cases where a classifier $\mathfrak{C}$ pre-trained on $\mathcal{Y}$ or its approximated version $\hat{\mathcal{Y}}$ exists, the weights of neural network $\mathfrak{N}$ can be initialized with that of $\mathfrak{C}$. It is worth noting that the reprojection step in the vector-based framework in [13] shares the weights with the sensing matrices, performing inexplicit signal reconstruction while we have different sensing $\mathbf{\Phi}_n, n = 1, \ldots, N$ and feature extraction $\mathbf{\Theta}_n, n = 1, \ldots, N$ weights. Since the vector-based framework involves large sensing and reprojection matrices, from the optimization point of view, enforcing shared weights might be essential in their framework to reduce overfitting as indicated by their empirical results.

After performing the aforementioned initialization steps, all three components in our MCL framework are jointly optimized using Stochastic Gradient Descent method, i.e., end-to-end training after the initialization. It is worth noting that above initialization scheme for CS and FS component is proposed in a generic setting, which can serve as a good starting point. In cases where certain properties of the tensor subspace $\mathfrak{F}$ or the tensor feature $\mathcal{T}$ are known to improve the learning task, one might adopt a different initialization strategy for CS and FS components to induce such properties.

D. Complexity Analysis

Since the complexity of the neural network component $\mathfrak{N}$ varies with the choice of the architecture, we will estimate the theoretical complexity for the CS and FS component and make comparison with the vector-based framework [13]. Let $\mathbb{R}^{I_1 \times \cdots \times I_N}$ and $\mathbb{R}^{M_1 \times \cdots \times M_N}$ denote the dimensionality of the original signal $\mathcal{Y}$ and its measurements $\mathcal{Z}$, respectively. In addition, to compare with the vector-based framework, we also assume that the dimensionality of the feature $\mathcal{T}$ is also $\mathbb{R}^{I_1 \times \cdots \times I_N}$. Thus, $\mathbf{\Phi}_n$ belongs to $\mathbb{R}^{M_n \times I_n}$ and $\mathbf{\Theta}_n$ belongs to $\mathbb{R}^{I_n \times M_n}$ for $n = 1, \ldots, N$ in our CS and FS component, while in [13], the sensing matrix $\mathbf{\Phi}$ and the reconstruction matrix $\mathbf{\Phi}^T$ belong to $\mathbb{R}^{(I_1 * \cdots * I_N) \times (M_1 * \cdots * M_N)}$ and $\mathbb{R}^{(M_1 * \cdots * M_N) \times (I_1 * \cdots * I_N)}$, respectively.

It is clear that the memory complexity of CS and FS component in our MCL framework is $O(2\sum_{n=1}^{N} I_n * M_n)$, and that of the vector-based framework is $O(\prod_{n=1}^{N} I_n * M_n)$. To see the huge difference between the two frameworks, let us consider 3D MRI image of size $I_1 \times I_2 \times I_3 = 256 \times 256 \times 64$ with the sampling ratio 70%, i.e., $M_1 \times M_2 \times M3 = 214 \times 214 \times 64$, the memory complexity in our framework is $O(256 * 214 + 256 * 214 + 64 * 64) \approx O(10^5)$ while that of the vector-based framework is $O(256 * 214 * 256 * 214 * 64 * 64) = O(10^{13})$

Regarding computational complexity of our framework, the CS component performs $\mathcal{Z} = \mathcal{Y} \times_1 \mathbf{\Phi}_1 \times \cdots \times_N \mathbf{\Phi}_N$ having complexity of $O\big(\sum_{n=1}^{N}\big(\prod_{p=1}^{n} M_p * \prod_{k=n}^{N} I_k\big)\big)$, and the FS component performs $\mathcal{T} = \mathcal{Z} \times_1 \mathbf{\Theta}_1 \times \cdots \times_N \mathbf{\Theta}_N$ having complexity of $O\big(\sum_{n=1}^{N}\big(\prod_{p=1}^{n} I_p * \prod_{k=n}^{N} M_k\big)\big)$. For the vector-based framework, the sensing step computes $\mathbf{z} = \mathbf{\Phi} vec(\mathcal{Y})$ and reprojection step computes $\mathbf{\Phi}^T \mathbf{z}$, resulting in total complexity of $O(2\prod_{n=1}^{N} I_n * M_n)$. With the same 3D MRI example as in the previous paragraph, the total computational complexity of our framework is $O(10^9)$ while that of the vector-based framework is $O(10^{13})$.

Table I summarizes the complexity of the two frameworks. It is worth noting that by taking into account the multi-dimensional structure of the signal, the proposed framework has both memory and computational complexity several orders of magnitudes lower than its vector-based counterpart.

IV. EXPERIMENTS

In this section, we provide a detailed description of our empirical analysis of the proposed MCL framework. We start by describing the datasets and the experiments' protocols that have been used. In the standard set of experiments, we analyze the performance of MCL in comparison with the vector-based framework proposed in [13], [54]. We further investigate

the effect of different components in our framework in the Ablation Study Subsection.

A. Datasets and Experiment Protocol

We have conducted experiments on the object classification and face recognition tasks on the following datasets:

- CIFAR-10 and CIFAR-100: CIFAR dataset [55] is a color (RGB) image dataset for evaluating object recognition task. The dataset consists of 50K images for training and 10K images for testing with resolution 32×32 pixels. CIFAR-10 refers to the 10-class objection recognition task in which each individual image has a single class label coming from 10 different categories. Likewise, CIFAR-100 refers to a more fine-grained classification task with each image having a label coming from 100 different categories. In our experiment, from the training set of CIFAR-10 and CIFAR-100, we randomly selected 5K images for validation purpose and only trained the algorithms on 45K images.
- CelebA: CelebA [56] is a large-scale face attributes dataset with more than 200K images at different resolutions from more than 10K identities. In our experiment, we used a subset of 100 identities in this dataset which corresponds to 7063, 2373, and 2400 samples for training, validation, and testing, respectively. In order to evaluate the scalability of our proposed framework, we resized the original images to different set of resolutions, including: 32×32, 48×48, 64×64, and 80×80 pixels, which are subsequently denoted as CelebA-32, CelebA-48, CelebA-64, and CelebA-80, respectively.

In our experiments, two types of network architecture have been employed for the neural network component $\mathfrak{N}$: the AllCNN architecture [57] and the ResNet architecture [58]. AllCNN is a simple 9-layer feed-forward architecture which has no max-pooling (pooling is done via convolution with stride more than 1) and no fully-connected layer. ResNet is a 110-layer CNN with residual connections. The exact topologies of AllCNN and ResNet in our experiment can be found in our publicly available implementation[2].

Since all of the datasets contain RGB images, we followed the implementation proposed in [54] for the vector-based framework, which is an extension of [13], which has 3 different sensing matrices for each of the color channel, and the corresponding reprojection matrices are enforced to share weights with the sensing matrices. The sensing matrices in MCL were initialized with the HOSVD decomposition on the training sets while the sensing matrices in the vector-based framework were initialized with PCA decomposition on the training set. Likewise, the bases obtained from HOSVD and PCA were also used to initialize the FS component in our framework and the reprojection matrices in the vector-based framework. In addition, we also trained the neural network component $\mathfrak{N}$ on uncompressed data with respect to the learning tasks and initialized the classifier in each framework with these pre-trained networks' weights. After the initialization step, both frameworks were trained in an end-to-end manner.

[2]https://github.com/viebboy/MultilinearCompressiveLearningFramework

TABLE II
DIFFERENT CONFIGURATIONS OF MEASUREMENTS BETWEEN VECTOR-BASED FRAMEWORK AND OUR FRAMEWORK. * *Measurement Rate* IS CALCULATED WITH RESPECT TO THE ORIGINAL SIGNAL OF SIZE $32 \times 32 \times 3$

Type	Configuration	#measurements	Measurement Rate
vector [54]	256×3	768	0.250
MCL (our)	$20 \times 19 \times 2$	760	0.247
MCL (our)	$28 \times 27 \times 1$	756	0.246
vector [54]	102×3	306	0.100
MCL (our)	$14 \times 11 \times 2$	308	0.100
MCL (our)	$18 \times 17 \times 1$	306	0.100
vector [54]	18×3	54	0.018
MCL (our)	$9 \times 6 \times 1$	54	0.018
MCL (our)	$6 \times 9 \times 1$	54	0.018

All algorithms were trained with ADAM optimizer [59] with the following learning rate the schedule $\{10^{-3}, 10^{-4}, 10^{-5}\}$, changing at epoch 80 and 120. Each algorithm was trained for 160 epochs in total. Weight decay coefficient was set to 0.0001 to regularize all the trainable weights in all experiments. We performed no data preprocessing step, except scaling all the pixel values to $[0, 1]$. In addition, data augmentation was employed by random flipping on the horizontal axis and image shifting within 10% of the spatial dimensions. In all experiments, the final model weights which are used to measure the performance on the test sets, are obtained from the epoch which has the highest validation accuracy.

For each experiment configuration, we performed 3 runs and the mean and standard deviation of test accuracy are reported.

B. Comparison with the vector-based framework

In order to compare with the vector-based framework in [13], [54], we performed experiments on 3 datasets: CIFAR-10, CIFAR-100, and CelebA-32. To compare the performances at different measurement rates, we employed three different measurement values Z for the vector-based framework: $256 \times 3 = 768$, $102 \times 3 = 306$, and $18 \times 3 = 54$. Here $\times 3$ indicates that the vector-based framework has 3 different sensing matrices for each color channel. Since we cannot always select the size of the measurements $\mathcal{Z}$ in MCL to match the number of measurements in the vector-based framework, we try to find the configurations of $\mathcal{Z}$ that closely match with the vector-based ones. In addition, with a target number of measurements, there can be more than one configuration of $\mathcal{Z}$ that yields a similar number of measurements. For each measurement value $(768, 102, 54)$ in the vector-based framework, we evaluated two different values of $\mathcal{Z}$, particularly, the following sizes of $\mathcal{Z}$ were used: $20 \times 19 \times 2 = 760$, $28 \times 27 \times 1 = 756$, $14 \times 11 \times 2 = 308$, $18 \times 17 \times 1 = 306$, $6 \times 9 \times 1 = 54$ and $9 \times 6 \times 1 = 54$. The measurement configurations are summarized in Table II.

In order to effectively compare the CS and FS component in MCL with those in [54], two different neural network architectures with different capacities have been used. Table III and IV show the accuracy on the test set with AllCNN and ResNet architecture, respectively. The second row of each table shows the performance of the base classifier on the uncompressed data, which we term as *Oracle*.

It is clear that our proposed framework outperforms the vector-based framework in all compression rates and datasets with both AllCNN and ResNet architecture, except for CIFAR-100 dataset at the lowest measurement rate (0.018). The performance gaps between the proposed MCL framework and the vector-based one are huge, with more than 10% differences for the CIFAR datasets at measurement rates 0.25 and 0.10. In case of CelebA-32 dataset and at measurement rate 0.246 (configuration $28 \times 27 \times 1$), the inference systems learned by our proposed framework even slightly outperform the Oracle setting for both AllCNN and ResNet architecture. One possible explanation for the inferior performance of MCL model for CIFAR-100 dataset at the lowest measurement rate might come from regularization hyper-parameter. Since the number of parameters of MCL at this configuration is significantly smaller than the vector-based model, the effect of weight decay regularization at coefficient 0.0001 might be too aggressive for the MCL model but moderate for the vector-based counterpart.

Although the capacities of AllCNN and ResNet architecture are different, their performances on the uncompressed data are roughly similar. Regarding the effect of two different base classifiers in the two Compressive Learning pipelines, it is clear that the optimal configurations of our framework at each measurement rate are consistent between the two classifiers, i.e., the bold patterns from both Table III and IV are similar. When switching from AllCNN to ResNet, the vector-based framework observes performance drop at the highest measurement rate (0.25), but increases in lower rates (0.1 and 0.018). For our framework when switching from AllCNN to ResNet, the test accuracies stay approximately similar or improve.

Table V shows the empirical complexity of both frameworks with respect to different measurement configurations, excluding the base classifiers. Since all three datasets employed in this experiment have the same input size and the size of the feature tensor $\mathcal{T}$ in MCL was set similar to the original input size, the complexities of CS and FS components in all three datasets are similar. It is clear that our proposed MCL framework has much lower memory and computational complexity compared to the vector-based counterpart. *In our proposed framework, even operating at the highest measurement rate* 0.247*, the CS and FS components require only* 2.5K *parameters and* 5K *FLOPs, which are approximately* 20 *times fewer than that of the vector-based framework operating at the lowest measurement rate* 0.018. Interestingly, the optimal configuration at each measurement rate obtained in our framework also has lower or similar complexity than the other configuration.

In Figure 2, we visualize the features obtained from the reprojection step and the FS component in the proposed framework, respectively. It is worth noting that the sensing matrices and the reprojection matrices (in case of the vector-based framework) or $\mathbf{\Theta}_n$ (in FS component of MCL framework) were initialized with PCA and HOSVD. In addition, the base network classifiers were also initialized with the ones trained on the original data. Thus, it is intuitive to expect the features obtained from both frameworks to be visually interpretable for human, despite no explicit reconstruction objective was incorporated during the training phase. Indeed, from Figure 2, we can see that with the highest number of measurements, the feature images obtained from both frameworks look very similar to the original images. Particularly, the ones synthesized by the vector-based framework look visually closer to the original images than those obtained from our MCL framework. This is due to the fact that [54] enforces the weight sharing between the projection step (CS matrices) and the re-projection step, i.e., the input to the classifier in [54] is $\mathbf{\Phi}^T\mathbf{\Phi}\, vec(\mathcal{Y})$, with $\mathcal{Y}$ is the signal and $\mathbf{\Phi}$ and $\mathbf{\Phi}^T$ are the sensing and reprojection matrices, respectively. In addition, $\mathbf{\Phi}$ is initialized with PCA, thus the whole system is more constrained to reconstruct the signals.

When the number of measurements drops to approximately 10% of the original signal, the reverse scenario happens: the feature images (in configuration $14 \times 11 \times 2$, $28 \times 27 \times 1$) obtained from our framework retain more facial features compared to those from the vector-based framework (102×3), especially in the $28 \times 27 \times 1$ configuration. This is due to the fact that most of the facial information in particular, and natural images in general, lie on the spatial dimensions, i.e., height and width. Besides, when the dimension of the third mode of the measurement $\mathcal{Z}$ is set to 1 (as in configuration $28 \times 27 \times 1$, $18 \times 17 \times 1$), after the optimization procedure, our proposed framework effectively discards the color information which is less relevant to the facial recognition task, and retains more lightness details, thus, performs better than the configurations with the 3-mode dimension set to 2 (in configuration $20 \times 19 \times 2$, $14 \times 11 \times 2$).

With the above observations from the empirical analysis, it is clear that structure-preserving Compressive Sensing and Feature Synthesis components in our proposed MCL framework can better capture essential information inherent in the multi-dimensional signal for the learning tasks, compared with the vector-based framework.

C. Ablation Study

In this subsection, we provide the empirical analysis on the effect of different components in MCL framework. These factors include the effect of the popular nonlinear thresholding step discussed in Section III.B; the choice of having shared or separate weights in CS and FS component; the initialization step discussed in Section III.C; the scalability of the proposed framework when the original dimensionalities of the signal increase. Since the total number of experiment settings when combining all of the aforementioned factors is huge, and the

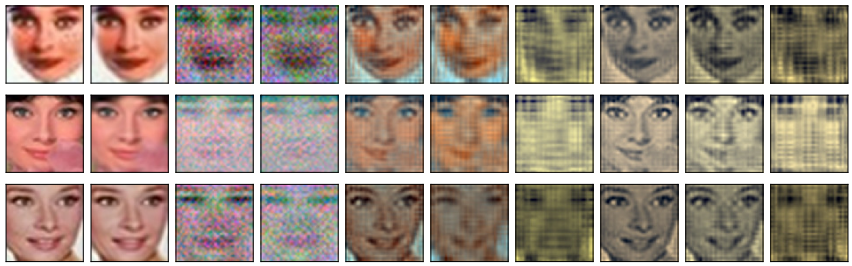

Fig. 2. Illustration of the feature images (inputs to ResNet) synthesized by the proposed framework and the vector-based counterpart. The original images come from the test set of CelebA-32.

TABLE III
TEST ACCURACY WITH ALLCNN ARCHITECTURE AS THE BASE CLASSIFIER

Configuration	CIFAR-10	CIFAR-100	CelebA-32
Oracle	92.33	72.25	92.58
256×3 [54]	81.36 ± 00.00	55.32 ± 00.00	89.25 ± 00.00
$20 \times 19 \times 2$ (our)	$\mathbf{89.35} \pm 00.26$	$\mathbf{65.97} \pm 00.19$	92.36 ± 00.07
$28 \times 27 \times 1$ (our)	88.56 ± 00.14	62.82 ± 00.09	$\mathbf{92.74} \pm 00.31$
102×3 [54]	65.14 ± 02.37	44.03 ± 03.60	67.04 ± 02.36
$14 \times 11 \times 2$ (our)	$\mathbf{84.15} \pm 00.55$	$\mathbf{59.77} \pm 00.12$	87.01 ± 00.99
$18 \times 17 \times 1$ (our)	83.17 ± 00.32	54.96 ± 00.17	$\mathbf{91.26} \pm 00.13$
18×3 [54]	61.38 ± 00.05	$\mathbf{37.78} \pm 00.08$	63.76 ± 00.22
$9 \times 6 \times 1$ (our)	$\mathbf{64.45} \pm 00.39$	34.74 ± 00.29	$\mathbf{68.49} \pm 00.28$
$6 \times 9 \times 1$ (our)	64.28 ± 00.35	35.16 ± 00.16	65.92 ± 00.77

TABLE IV
TEST ACCURACY WITH RESNET ARCHITECTURE AS THE BASE CLASSIFIER

Configuration	CIFAR-10	CIFAR-100	CelebA-32
Oracle	92.47	72.38	93.08
256×3 [54]	78.56 ± 00.00	53.03 ± 00.00	87.29 ± 00.00
$20 \times 19 \times 2$ (our)	$\mathbf{89.22} \pm 00.27$	$\mathbf{67.21} \pm 00.18$	92.00 ± 00.48
$28 \times 27 \times 1$ (our)	88.24 ± 00.15	63.37 ± 00.44	$\mathbf{93.54} \pm 00.32$
102×3 [54]	67.65 ± 02.99	47.90 ± 01.22	76.32 ± 02.35
$14 \times 11 \times 2$ (our)	$\mathbf{84.74} \pm 00.16$	$\mathbf{60.30} \pm 00.21$	88.50 ± 00.26
$18 \times 17 \times 1$ (our)	83.31 ± 00.21	55.51 ± 00.08	$\mathbf{90.82} \pm 00.14$
18×3 [54]	61.96 ± 00.17	$\mathbf{41.03} \pm 00.22$	67.29 ± 00.44
$9 \times 6 \times 1$ (our)	$\mathbf{64.14} \pm 00.24$	33.67 ± 00.17	$\mathbf{69.90} \pm 00.41$
$6 \times 9 \times 1$ (our)	64.07 ± 00.16	32.40 ± 01.62	67.39 ± 00.34

TABLE V
COMPLEXITY OF THE PROPOSED FRAMEWORK AND THE VECTOR-BASED COUNTERPART, EXCLUDING THE BASE CLASSIFIER COMPONENT

Configuration	#Parameters	#FLOPs
256×3 [54]	786K	1573K
$20 \times 19 \times 2$ (our)	**2.5**K	**5**K
$28 \times 27 \times 1$ (our)	3.5K	7K
102×3 [54]	313K	627K
$14 \times 11 \times 2$ (our)	**1.6**K	**3.2**K
$18 \times 17 \times 1$ (our)	2.2K	4.5K
18×3 [54]	55K	111K
$9 \times 6 \times 1$ (our)	**1.0**K	**1.9**K
$6 \times 9 \times 1$ (our)	**1.0**K	**1.9**K

results involved multiple factors are difficult to interpret, we analyze these factors in a progressive manner.

1) Linearity versus Nonlinearity and Shared versus Separate Weights: Firstly, the choice of linearity or nonlinearity and the choice of shared or separate weights in CS and FS component are analyzed together since the two factors are closely related. In this setting, the CS and FS components are initialized by HOSVD decomposition as described in Section III.C. The neural network classifier $\mathfrak{N}$ has the AllCNN architecture with the weights initialized from the corresponding pre-trained network on the original data. Table VI shows the test accuracies on CIFAR-10, CIFAR-100 and CelebA-32 at different measurements. It is clear that most of the highest test accuracies are obtained without the thresholding step and with separate weights in CS and FS component, i.e., most bold-face numbers appear in the lower quarter on the left side of Table VI. Comparing between linearity and nonlinearity option, it is obvious that the nonlinearity effect of ReLU adversely affect the performances, especially when the number of measurements decreases. The reason might be that applying ReLU to the compressed measurements restricts the information to be represented in the positive subspace only, thus further losing the representation power in the compressed measurements when only a limited number of measurements allowed.

In the linearity setting, while the performance differences between shared and separate weights in some configurations are small, here we should note that allowing non-shared weights can be beneficial in cases where we know that certain features should be synthesized in the FS component in order

to make inferences.

2) Effect of The Initialization Step: From the observation obtained from the above analysis on the effect of linearity and separate weights, we investigated the effect of the initialization step discussed in Section III.C. All setups were trained with a multilinear FS component having separate weights from CS component. From Table VII, we can easily observe that by initializing the CS and FS components with HOSVD, the performances of the learning systems increase significantly. When CS and FS components are initialized with HOSVD, utilizing a pre-trained network further improves the inference performance of the systems, especially in the low measurement rate regime. Thus, the initialization strategy proposed in Section III.C is beneficial in a general setting for the learning tasks.

3) Scalability: Finally, the scalability of the proposed framework is validated in different resolutions of the CelebA dataset. All of the previous experiments were demonstrated with CelebA-32 dataset, which we assume that there are only 3072 elements in the original signal. To investigate the scalability, we pose the following question: *What if the original dimensions of the signal are higher than* $32 \times 32 \times 3$*, with the same numbers of measurements presented in Table II, can we still learn to recognize facial images with feasible costs?*. To answer this question, we trained our framework on CelebA-32, CelebA-48, CelebA-64 and CelebA-80 and recorded the test accuracies, the number of parameters and the number of FLOPs at different number of measurements, which are shown in Table VIII. It is clear that at each measurement configuration, when the original signal resolution increases, the measurement rate drops at a similar rate, however, without any adverse effect on the inference performance. Particularly, if we look into the last column of Table VIII, with a sampling rate of only 4%, the proposed framework achieves 93% accuracy, which is only 2% lower compared to that of the base classifier trained on the original data. Here we should note that most of the images in CelebA dataset have higher resolution than $80 \times 80 \times 3$ pixel, therefore, 4 different versions of CelebA ($32 \times 32 \times 3$, $48 \times 48 \times 3$, $64 \times 64 \times 3$, $80 \times 80 \times 3$) in our experiments indeed contain increasing levels of data fidelity. From the performance statistics, we can observe that the performance of our framework is characterized by the number of measurements, rather than the measurement rates or compression rates.

Due to the memory limitation when training the vector-based framework at higher resolutions, we could not perform the same set of experiments for the vector-based framework. However, to compare the scalability in terms of computation and memory between the two frameworks, we measured the number of FLOPs and parameters in the vector-based framework, excluding the base classifier and visualize the results on Figure 3. It is worth noting that on the y-axis is the log scale and as the dimensions of the original signal increase, the complexity of the vector-based framework increases by an order of magnitude while our proposed MCL framework scales favorably in both memory and computation.

V. Conclusions

In this paper, we proposed Multilinear Compressive Learning, an efficient framework to tackle the Compressive Learning task that operates on multi-dimensional signals. The proposed framework takes into account the tensorial nature of the multi-dimensional signals and performs the compressive sensing as well as the feature extraction step along different modes of the original data, thus being able to retain and synthesize essential information on a multilinear subspace for the learning task. We show theoretically and empirically that the proposed framework outperforms its vector-based counterpart in both inference performance and computational efficiency. Extensive ablation study has been conducted to investigate the effect of different components in the proposed framework, giving insights into the importance of different design choices.

References

[1] E. J. Candès and M. B. Wakin, "An introduction to compressive sampling [a sensing/sampling paradigm that goes against the common knowledge in data acquisition]," *IEEE signal processing magazine*, vol. 25, no. 2, pp. 21–30, 2008.

[2] E. J. Candes, J. K. Romberg, and T. Tao, "Stable signal recovery from incomplete and inaccurate measurements," *Communications on Pure and Applied Mathematics: A Journal Issued by the Courant Institute of Mathematical Sciences*, vol. 59, no. 8, pp. 1207–1223, 2006.

[3] D. L. Donoho *et al.*, "Compressed sensing," *IEEE Transactions on information theory*, vol. 52, no. 4, pp. 1289–1306, 2006.

[4] P. Mohassel and Y. Zhang, "Secureml: A system for scalable privacy-preserving machine learning," in *2017 IEEE Symposium on Security and Privacy (SP)*, pp. 19–38, IEEE, 2017.

[5] E. Hesamifard, H. Takabi, and M. Ghasemi, "Cryptodl: Deep neural networks over encrypted data," *arXiv preprint arXiv:1711.05189*, 2017.

[6] R. Calderbank and S. Jafarpour, "Finding needles in compressed haystacks," in *2012 IEEE International Conference on Acoustics, Speech and Signal Processing (ICASSP)*, pp. 3441–3444, IEEE, 2012.

[7] M. A. Davenport, M. F. Duarte, M. B. Wakin, J. N. Laska, D. Takhar, K. F. Kelly, and R. G. Baraniuk, "The smashed filter for compressive classification and target recognition," in *Computational Imaging V*, vol. 6498, p. 64980H, International Society for Optics and Photonics, 2007.

[8] M. A. Davenport, P. Boufounos, M. B. Wakin, R. G. Baraniuk, *et al.*, "Signal processing with compressive measurements.," *J. Sel. Topics Signal Processing*, vol. 4, no. 2, pp. 445–460, 2010.

[9] H. Reboredo, F. Renna, R. Calderbank, and M. R. Rodrigues, "Compressive classification," in *2013 IEEE International Symposium on Information Theory*, pp. 674–678, IEEE, 2013.

[10] P. K. Baheti and M. A. Neifeld, "Adaptive feature-specific imaging: a face recognition example," *Applied optics*, vol. 47, no. 10, pp. B21–B31, 2008.

[11] H. Reboredo, F. Renna, R. Calderbank, and M. R. Rodrigues, "Projections designs for compressive classification," in *2013 IEEE Global Conference on Signal and Information Processing*, pp. 1029–1032, IEEE, 2013.

[12] S. Lohit, K. Kulkarni, P. Turaga, J. Wang, and A. C. Sankaranarayanan, "Reconstruction-free inference on compressive measurements," in *Proceedings of the IEEE Conference on Computer Vision and Pattern Recognition Workshops*, pp. 16–24, 2015.

[13] A. Adler, M. Elad, and M. Zibulevsky, "Compressed learning: A deep neural network approach," *arXiv preprint arXiv:1610.09615*, 2016.

[14] S. Lohit, K. Kulkarni, and P. Turaga, "Direct inference on compressive measurements using convolutional neural networks," in *2016 IEEE International Conference on Image Processing (ICIP)*, pp. 1913–1917, IEEE, 2016.

[15] D. Nion and N. D. Sidiropoulos, "Tensor algebra and multidimensional harmonic retrieval in signal processing for mimo radar," *IEEE Transactions on Signal Processing*, vol. 58, no. 11, pp. 5693–5705, 2010.

TABLE VI

TEST ACCURACY WITH RESPECT TO THE CHOICE OF LINEARITY OR NONLINEARITY IN CONJUNCTION WITH THE CHOICE OF SHARED OR SEPARATE WEIGHTS IN CS AND FS COMPONENT. THE **BOLD** NUMBERS DENOTE THE BEST TEST ACCURACY (AMONG 4 COMBINATIONS OF *LINEARITY* VERSUS *NONLINEARITY* AND *SHARED* VERSUS *SEPARATE*) IN THE SAME DATASET WITH THE SAME CONFIGURATION

	Configuration	LINEARITY			NONLINEARITY		
		CIFAR-10	CIFAR-100	CelebA-32	CIFAR-10	CIFAR-100	CelebA-32
SHARED	$20 \times 19 \times 2$	89.25 ± 00.39	66.00 ± 00.26	92.24 ± 00.21	89.16 ± 00.14	$\mathbf{66.11} \pm 00.10$	91.69 ± 00.46
	$28 \times 27 \times 1$	88.44 ± 00.04	62.62 ± 00.30	92.42 ± 00.64	88.32 ± 00.20	61.99 ± 01.24	92.61 ± 00.61
	$14 \times 11 \times 2$	$\mathbf{84.37} \pm 00.35$	59.75 ± 00.23	$\mathbf{88.00} \pm 00.38$	83.84 ± 00.21	58.01 ± 00.80	84.75 ± 01.37
	$18 \times 17 \times 1$	$\mathbf{83.73} \pm 00.10$	54.88 ± 00.23	91.22 ± 00.43	83.57 ± 00.30	54.47 ± 00.39	90.85 ± 00.60
	$6 \times 9 \times 1$	64.27 ± 00.28	33.17 ± 00.20	64.47 ± 00.61	62.18 ± 01.37	33.04 ± 00.08	49.46 ± 00.95
	$9 \times 6 \times 1$	64.43 ± 00.25	32.82 ± 00.39	68.25 ± 00.09	62.34 ± 00.16	33.08 ± 00.16	59.29 ± 01.83
SEPARATE	$20 \times 19 \times 2$	$\mathbf{89.35} \pm 00.26$	65.97 ± 00.19	92.36 ± 00.07	88.19 ± 01.00	64.28 ± 02.29	91.79 ± 00.21
	$28 \times 27 \times 1$	$\mathbf{88.56} \pm 00.14$	$\mathbf{62.82} \pm 00.09$	$\mathbf{92.74} \pm 00.31$	88.14 ± 00.34	62.15 ± 00.04	92.49 ± 00.43
	$14 \times 11 \times 2$	84.15 ± 00.55	$\mathbf{59.77} \pm 00.12$	87.01 ± 00.99	82.16 ± 02.61	59.15 ± 00.16	84.64 ± 00.57
	$18 \times 17 \times 1$	83.17 ± 00.32	$\mathbf{54.96} \pm 00.17$	$\mathbf{91.26} \pm 00.14$	82.90 ± 00.19	53.90 ± 00.41	90.10 ± 00.69
	$6 \times 9 \times 1$	$\mathbf{64.28} \pm 00.35$	$\mathbf{35.16} \pm 00.16$	$\mathbf{65.92} \pm 00.77$	61.09 ± 00.20	32.15 ± 00.49	50.68 ± 01.00
	$9 \times 6 \times 1$	$\mathbf{64.45} \pm 00.39$	34.74 ± 00.29	68.49 ± 00.28	62.18 ± 00.25	32.68 ± 00.81	61.54 ± 01.40

TABLE VII

TEST ACCURACY WITH RESPECT TO THE INITIALIZATION OF CS & FS COMPONENT AND THE BASE CLASSIFIER (ALLCNN). THE **BOLD** NUMBERS DENOTE THE BEST TEST ACCURACY (AMONG 4 COMBINATIONS OF *PRECOMPUTE CLASSIFIER* VERSUS *RANDOM CLASSIFIER* AND *PRECOMPUTE CS & FS* VERSUS *RANDOM CS & FS*) IN THE SAME DATASET WITH THE SAME CONFIGURATION

	Configuration	PRECOMPUTE CS & FS			RANDOM CS & FS		
		CIFAR-10	CIFAR-100	CelebA-32	CIFAR-10	CIFAR-100	CelebA-32
PRECOMPUTE CLASSIFIER	$28 \times 27 \times 1$	88.56 ± 00.14	$\mathbf{62.82} \pm 00.09$	$\mathbf{92.74} \pm 00.31$	71.47 ± 00.62	38.59 ± 02.60	68.65 ± 01.56
	$18 \times 17 \times 1$	83.17 ± 00.32	$\mathbf{54.96} \pm 00.17$	$\mathbf{91.26} \pm 00.14$	69.46 ± 01.16	38.65 ± 00.28	65.65 ± 00.70
	$9 \times 6 \times 1$	$\mathbf{64.45} \pm 00.39$	$\mathbf{34.74} \pm 00.29$	$\mathbf{68.49} \pm 00.28$	59.88 ± 00.17	29.03 ± 01.69	60.43 ± 02.29
RANDOM CLASSIFIER	$28 \times 27 \times 1$	$\mathbf{88.71} \pm 00.05$	60.36 ± 00.62	85.56 ± 00.84	71.37 ± 01.24	38.98 ± 01.40	67.18 ± 00.32
	$18 \times 17 \times 1$	$\mathbf{83.82} \pm 00.28$	49.41 ± 04.07	84.71 ± 01.39	68.93 ± 01.16	37.84 ± 03.06	64.12 ± 02.06
	$9 \times 6 \times 1$	63.99 ± 00.11	33.66 ± 00.66	65.62 ± 02.71	59.85 ± 00.67	30.90 ± 00.17	56.61 ± 02.27

TABLE VIII

TEST PERFORMANCE & COMPLEXITY OF THE PROPOSED FRAMEWORK AT DIFFERENT RESOLUTIONS OF THE ORIGINAL CELEBA DATASET, WITH ALLCNN AS THE BASE CLASSIFIER

Configuration	ACCURACY				MEASUREMENT RATE			
	CelebA-32	CelebA-48	CelebA-64	CelebA-80	CelebA-32	CelebA-48	CelebA-64	CelebA-80
Oracle	92.58	93.37	94.75	95.04	1.0	1.0	1.0	1.0
$20 \times 19 \times 2$	92.36 ± 00.07	91.24 ± 00.23	92.62 ± 00.36	93.01 ± 00.32	0.247	0.110	0.062	0.040
$28 \times 27 \times 1$	92.74 ± 00.31	92.43 ± 00.19	93.39 ± 00.52	93.42 ± 00.37	0.246	0.109	0.062	0.039
$14 \times 11 \times 2$	87.01 ± 00.99	87.00 ± 00.87	87.75 ± 00.27	88.67 ± 00.26	0.100	0.045	0.025	0.016
$18 \times 17 \times 1$	91.26 ± 00.14	90.17 ± 00.30	91.36 ± 00.43	91.89 ± 00.46	0.1	0.044	0.025	0.016
$6 \times 9 \times 1$	65.92 ± 00.77	66.56 ± 00.05	66.69 ± 00.46	66.03 ± 00.37	0.018	0.008	0.004	0.003
$9 \times 6 \times 1$	68.49 ± 00.28	68.69 ± 00.96	67.75 ± 01.62	67.31 ± 00.49	0.018	0.008	0.004	0.003
Configuration	#FLOP				#PARAMETER			
	CelebA-32	CelebA-48	CelebA-64	CelebA-80	CelebA-32	CelebA-48	CelebA-64	CelebA-80
$20 \times 19 \times 2$	5.0K	7.5K	10.0K	12.5K	2.5K	3.8K	5.0K	6.3K
$28 \times 27 \times 1$	7.0K	10.6K	14.1K	17.6K	3.5K	5.3K	7.0K	8.8K
$14 \times 11 \times 2$	3.2K	4.8K	6.4K	8.0K	1.6K	2.4K	3.2K	4.0K
$18 \times 17 \times 1$	4.5K	6.7K	9.0K	11.2K	2.2K	3.4K	4.9K	5.6K
$6 \times 9 \times 1$	1.9K	2.9K	3.9K	4.8K	1.0K	1.4K	1.9K	2.4K
$9 \times 6 \times 1$	1.9K	2.9K	3.9K	4.8K	1.0K	1.4K	1.9K	2.4K

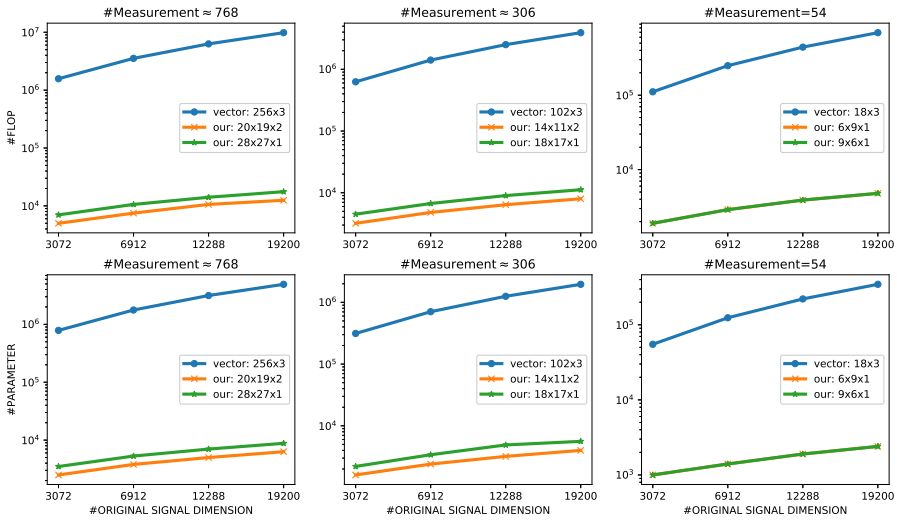

Fig. 3. #FLOP and #PARAMETER versus the original dimensionalities of the signal, measured in the proposed framework and the vector-based framework, excluding the base classifier. The x-axis represents the original dimension of the input signal. The y-axis on the first row represents the number of FLOPs in log scale while the y-axis on the second row represents the number of parameters

[16] F. Miwakeichi, E. Martınez-Montes, P. A. Valdés-Sosa, N. Nishiyama, H. Mizuhara, and Y. Yamaguchi, "Decomposing eeg data into space–time–frequency components using parallel factor analysis," *NeuroImage*, vol. 22, no. 3, pp. 1035–1045, 2004.

[17] D. M. Dunlavy, T. G. Kolda, and W. P. Kegelmeyer, "Multilinear algebra for analyzing data with multiple linkages," in *Graph algorithms in the language of linear algebra*, pp. 85–114, SIAM, 2011.

[18] D. T. Tran, M. Magris, J. Kanniainen, M. Gabbouj, and A. Iosifidis, "Tensor representation in high-frequency financial data for price change prediction," in *2017 IEEE Symposium Series on Computational Intelligence (SSCI)*, pp. 1–7, IEEE, 2017.

[19] D. T. Tran, A. Iosifidis, and M. Gabbouj, "Improving efficiency in convolutional neural networks with multilinear filters," *Neural Networks*, vol. 105, pp. 328–339, 2018.

[20] A. Cichocki, D. Mandic, L. De Lathauwer, G. Zhou, Q. Zhao, C. Caiafa, and H. A. Phan, "Tensor decompositions for signal processing applications: From two-way to multiway component analysis," *IEEE Signal Processing Magazine*, vol. 32, no. 2, pp. 145–163, 2015.

[21] F. Malgouyres and J. Landsberg, "Multilinear compressive sensing and an application to convolutional linear networks," 2018.

[22] D. T. Tran, A. Iosifidis, J. Kanniainen, and M. Gabbouj, "Temporal attention-augmented bilinear network for financial time-series data analysis," *IEEE transactions on neural networks and learning systems*, 2018.

[23] T. L. Youd, C. M. Hansen, and S. F. Bartlett, "Revised multilinear regression equations for prediction of lateral spread displacement," *Journal of Geotechnical and Geoenvironmental Engineering*, vol. 128, no. 12, pp. 1007–1017, 2002.

[24] Q. Zhao, C. F. Caiafa, D. P. Mandic, Z. C. Chao, Y. Nagasaka, N. Fujii, L. Zhang, and A. Cichocki, "Higher order partial least squares (hopls): a generalized multilinear regression method," *IEEE transactions on pattern analysis and machine intelligence*, vol. 35, no. 7, pp. 1660–1673, 2013.

[25] Q. Li and D. Schonfeld, "Multilinear discriminant analysis for higher-order tensor data classification," *IEEE transactions on pattern analysis and machine intelligence*, vol. 36, no. 12, pp. 2524–2537, 2014.

[26] D. T. Tran, M. Gabbouj, and A. Iosifidis, "Multilinear class-specific discriminant analysis," *Pattern Recognition Letters*, vol. 100, pp. 131–136, 2017.

[27] E. L. Denton, W. Zaremba, J. Bruna, Y. LeCun, and R. Fergus, "Exploiting linear structure within convolutional networks for efficient evaluation," in *Advances in neural information processing systems*, pp. 1269–1277, 2014.

[28] M. Jaderberg, A. Vedaldi, and A. Zisserman, "Speeding up convolutional neural networks with low rank expansions," *arXiv preprint arXiv:1405.3866*, 2014.

[29] V. Lebedev, Y. Ganin, M. Rakhuba, I. Oseledets, and V. Lempitsky, "Speeding-up convolutional neural networks using fine-tuned cp-decomposition," *arXiv preprint arXiv:1412.6553*, 2014.

[30] Y. Yang, D. Krompass, and V. Tresp, "Tensor-train recurrent neural networks for video classification," in *Proceedings of the 34th International Conference on Machine Learning-Volume 70*, pp. 3891–3900, JMLR. org, 2017.

[31] C. F. Caiafa and A. Cichocki, "Multidimensional compressed sensing and their applications," *Wiley Interdisciplinary Reviews: Data Mining and Knowledge Discovery*, vol. 3, no. 6, pp. 355–380, 2013.

[32] Y. Yu, J. Jin, F. Liu, and S. Crozier, "Multidimensional compressed sensing mri using tensor decomposition-based sparsifying transform," *PloS one*, vol. 9, no. 6, p. e98441, 2014.

[33] R. Robucci, L. K. Chiu, J. Gray, J. Romberg, P. Hasler, and D. Anderson, "Compressive sensing on a cmos separable transform image sensor," in *2008 IEEE International Conference on Acoustics, Speech and Signal Processing*, pp. 5125–5128, IEEE, 2008.

[34] M. Aharon, M. Elad, A. Bruckstein, *et al.*, "K-svd: An algorithm for designing overcomplete dictionaries for sparse representation," *IEEE Transactions on signal processing*, vol. 54, no. 11, p. 4311, 2006.

[35] D. L. Donoho and M. Elad, "Optimally sparse representation in general (nonorthogonal) dictionaries via 1 minimization," *Proceedings of the National Academy of Sciences*, vol. 100, no. 5, pp. 2197–2202, 2003.

[36] J. A. Tropp and S. J. Wright, "Computational methods for sparse solution of linear inverse problems," *Proceedings of the IEEE*, vol. 98, no. 6, pp. 948–958, 2010.

[37] S. S. Chen, D. L. Donoho, and M. A. Saunders, "Atomic decomposition by basis pursuit," *SIAM review*, vol. 43, no. 1, pp. 129–159, 2001.

[38] J. A. Tropp, "Greed is good: Algorithmic results for sparse approximation," *IEEE Transactions on Information theory*, vol. 50, no. 10, pp. 2231–2242, 2004.

[39] J. A. Tropp and A. C. Gilbert, "Signal recovery from random measurements via orthogonal matching pursuit," *IEEE Transactions on information theory*, vol. 53, no. 12, pp. 4655–4666, 2007.

[40] L. De Lathauwer, B. De Moor, and J. Vandewalle, "A multilinear singular value decomposition," *SIAM journal on Matrix Analysis and Applications*, vol. 21, no. 4, pp. 1253–1278, 2000.

[41] M. F. Duarte and R. G. Baraniuk, "Kronecker compressive sensing," *IEEE Transactions on Image Processing*, vol. 21, no. 2, pp. 494–504, 2012.

[42] C. F. Caiafa and A. Cichocki, "Computing sparse representations of multidimensional signals using kronecker bases," *Neural computation*, vol. 25, no. 1, pp. 186–220, 2013.

[43] R. G. Baraniuk and M. B. Wakin, "Random projections of smooth manifolds," *Foundations of computational mathematics*, vol. 9, no. 1, pp. 51–77, 2009.

[44] K. Kulkarni and P. Turaga, "Recurrence textures for human activity recognition from compressive cameras," in *2012 19th IEEE International Conference on Image Processing*, pp. 1417–1420, IEEE, 2012.

[45] K. Kulkarni and P. Turaga, "Reconstruction-free action inference from compressive imagers," *IEEE transactions on pattern analysis and machine intelligence*, vol. 38, no. 4, pp. 772–784, 2016.

[46] B. Hollis, S. Patterson, and J. Trinkle, "Compressed learning for tactile object recognition," *IEEE Robotics and Automation Letters*, vol. 3, no. 3, pp. 1616–1623, 2018.

[47] A. Değerli, S. Aslan, M. Yamac, B. Sankur, and M. Gabbouj, "Compressively sensed image recognition," in *2018 7th European Workshop on Visual Information Processing (EUVIP)*, pp. 1–6, IEEE, 2018.

[48] Y. Xu and K. F. Kelly, "Compressed domain image classification using a multi-rate neural network," *arXiv preprint arXiv:1901.09983*, 2019.

[49] X. Glorot and Y. Bengio, "Understanding the difficulty of training deep feedforward neural networks," in *Proceedings of the thirteenth international conference on artificial intelligence and statistics*, pp. 249–256, 2010.

[50] K. He, X. Zhang, S. Ren, and J. Sun, "Identity mappings in deep residual networks," in *European conference on computer vision*, pp. 630–645, Springer, 2016.

[51] F. Wu, X. Tan, Y. Yang, D. Tao, S. Tang, and Y. Zhuang, "Supervised nonnegative tensor factorization with maximum-margin constraint," in *Twenty-Seventh AAAI Conference on Artificial Intelligence*, 2013.

[52] Y.-D. Kim and S. Choi, "Nonnegative tucker decomposition," in *2007 IEEE Conference on Computer Vision and Pattern Recognition*, pp. 1–8, IEEE, 2007.

[53] L. Grasedyck, D. Kressner, and C. Tobler, "A literature survey of low-rank tensor approximation techniques," *GAMM-Mitteilungen*, vol. 36, no. 1, pp. 53–78, 2013.

[54] E. Zisselman, A. Adler, and M. Elad, "Compressed learning for image classification: A deep neural network approach," *Processing, Analyzing and Learning of Images, Shapes, and Forms*, vol. 19, p. 1, 2018.

[55] A. Krizhevsky and G. Hinton, "Learning multiple layers of features from tiny images," tech. rep., Citeseer, 2009.

[56] Z. Liu, P. Luo, X. Wang, and X. Tang, "Deep learning face attributes in the wild," in *Proceedings of International Conference on Computer Vision (ICCV)*, 2015.

[57] J. T. Springenberg, A. Dosovitskiy, T. Brox, and M. Riedmiller, "Striving for simplicity: The all convolutional net," *arXiv preprint arXiv:1412.6806*, 2014.

[58] K. He, X. Zhang, S. Ren, and J. Sun, "Delving deep into rectifiers: Surpassing human-level performance on imagenet classification," in *Proceedings of the IEEE international conference on computer vision*, pp. 1026–1034, 2015.

[59] D. P. Kingma and J. Ba, "Adam: A method for stochastic optimization," *arXiv preprint arXiv:1412.6980*, 2014.

PUBLICATION VIII

Generalized Tensor Summation Compressive Sensing Network (GTSNET): An Easy to Learn Compressive Sensing Operation

M. Yamaç, U. Akpinar, E. Sahin, S. Kiranyaz, and M. Gabbouj

IEEE Transactions on Image Processing, vol. 32, pp. 5637–5651
DOI: 10.1109/TIP.2023.3318946

Generalized Tensor Summation Compressive Sensing Network (GTSNET): An Easy to Learn Compressive Sensing Operation

Mehmet Yamaç, Ugur Akpinar, Erdem Sahin, *Member, IEEE*, Serkan Kiranyaz, *Senior Member, IEEE*, and Moncef Gabbouj, *Fellow, IEEE*

***Abstract*— The efforts in compressive sensing (CS) literature can be divided into two groups: finding a measurement matrix that preserves the compressed information at its maximum level, and finding a robust reconstruction algorithm. In the traditional CS setup, the measurement matrices are selected as random matrices, and optimization-based iterative solutions are used to recover the signals. Using random matrices when handling large or multi-dimensional signals is cumbersome especially when it comes to iterative optimizations. Recent deep learning-based solutions increase reconstruction accuracy while speeding up recovery, but jointly learning the whole measurement matrix remains challenging. For this reason, state-of-the-art deep learning CS solutions such as convolutional compressive sensing network (CSNET) use block-wise CS schemes to facilitate learning. In this work, we introduce a separable multi-linear learning of the CS matrix by representing the measurement signal as the summation of the arbitrary number of tensors. As compared to block-wise CS, tensorial learning eases blocking artifacts and improves performance, especially at low measurement rates (MRs), such as MRs < 0.1. The software implementation of the proposed network is publicly shared at https://github.com/mehmetyamac/GTSNET.**

***Index Terms*— Compressive sensing, deep reconstruction, tensorial compressive learning, separable compressive learning.**

I. Introduction

COMPRESSIVE sensing (CS) theory has attracted a lot of attention since its first appearance in 2005 [1]. CS theory claims that a signal can be sampled with far fewer measurements than the conventional Nyquist/Shannon-based sampling methods use. It has been applied in many fields such as CS-based MRI imaging [2], radar monitoring systems [3], [4], and ECG measurements in a health monitoring system [5]. Along with sampling, the technology has been adopted in many other fields. For instance, in a conventional CS system, random or pseudo-random measurement matrices are used, enabling a CS-based encryption mechanism [6], [7].

Manuscript received 2 October 2021; revised 6 October 2022; accepted 24 August 2023. Date of publication 29 September 2023; date of current version 17 October 2023. This work was supported in part by the EU H2020 OpenDR, in part by the Academy of Finland AWcHA, and in part by Business Finland AMALIA. The associate editor coordinating the review of this manuscript and approving it for publication was Prof. Xiaolin Wu. *(Corresponding author: Mehmet Yamaç.)*

Mehmet Yamaç, Ugur Akpinar, Erdem Sahin, and Moncef Gabbouj are with the Faculty of Information Technology and Communication Sciences, Tampere University, 33720 Tampere, Finland (e-mail: mehmet.yamac@tuni.fi).

Serkan Kiranyaz is with the Department of Electrical Engineering, Qatar University, Doha, Qatar.

This article has supplementary downloadable material available at https://doi.org/10.1109/TIP.2023.3318946, provided by the authors.

Digital Object Identifier 10.1109/TIP.2023.3318946

In Nyquist/Shannon based data acquisition systems, the reconstruction process is performed by sinc interpolation, which is a linear process and does not require expensive computations. The traditional CS-based data acquisition systems require advanced optimization-based iterative algorithms such as ℓ_1-minimization techniques [8], [9], [10]. Even if convex relaxation can bring a guarantee of sparse recovery with polynomial time, most solvers work in an iterative manner, and it makes them infeasible for real-time applications especially for large-scale signals, such as vectorized images. Moreover, ℓ_1 type estimators may lead to an unbiased estimation of the sparse signal [11]. There have been significant efforts spent to have faster recovery algorithms such as [12], [13], and [14] which are more feasible for a CS imaging system or similar multi-dimensional signals. However, the optimization-based recovery in a sparse domain can completely fail under some measurement rates, which are determined by the phase transition of the algorithms [15]. Moreover, the signal of interest in real applications rarely becomes strictly sparse in any sparsifying domain.

The first category of the deep learning-based CS approaches includes the works that use neural networks only for the reconstruction part [16], [17], [18]. They generally use conventional random matrices as the CS operators. To handle the images (2D signal), they apply the CS matrices to the vectorized smaller blocks of the image of interest. The well-known state-of-the art examples of this category of work can be listed as stacked denoising autoencoder (SDA) [16], non-iterative reconstruction of the compressively sensed images using CNN (ReconNet) [17], and learned version of iterative shrinkage thresholding algorithm for CS imaging (ISTA-Net) [18]. Among them, SDA uses the fully connected layers while the others adopt convolutional layers in their network. As a reconstruction part, ReconNet introduces fully convolutional layers, and this is why it is a non-iterative recovery framework that significantly reduces the computational time. ISTA-Net is based on iterative soft thresholding algorithms, and can be put into the category of deep unrolling techniques.

The second category of deep learning attempts can be enlisted as the ones that jointly learn CS matrices and reconstruction part instead of using conventional CS matrices. The recent state-of-the-art networks in this category are convolutional compressive sensing network (CSNET) [19] and scalable convolutional compressive sensing network (SCSNET) [20]. These works also handle CS of both

gray-scale and RGB images in a block-by-block manner. However, they learn these CS matrices using convolutional kernels having the same size as the image blocks. In the reconstruction part they use convolutional layers to recover the full image as a whole. In this way, they can significantly improve the blocking artifacts.

In this study, we propose a novel network, Generalized Tensor Summation Networks (GTSNETs), that can *jointly* learn both CS matrix and reconstruction algorithm. With the proposed learned CS operator, conventional CS setup, matrix-vector multiplication, is approximated as T-number of measurement tensors' summation, where each measurement tensor is determined by the mode product of tensor and matrices (i.e. smaller sizes than full-sized CS matrices). As a result, GTSNETs can factorize and approximate unfactorized full-size CS matrices (i.e., matrices that can be applied to a vectorized image or multidimensional signal in the traditional CS setting) using Kronecker products [21] of smaller-size matrices. In contrast to previous attempts, a GTSNET is capable of replacing a wide range of compressive sensing systems, such as sub-Gaussian [22], separable [23], and structural CS matrices (e.g., sparsifying basis as a part of the CS matrix [6], [24], [25]). Some CS systems, however, in which hardware limitations impose special requirements over CS matrices (e.g., CS MRI [26], [27], CS Radar [3], [4] etc.), are outside the scope of this study.

In a GTSNET, CS operation can be performed directly over the spatial domain or in any other separable transformation basis like CS in the frequency domain using DCT. This is why GTSNET can generalize many CS systems, and thus we use the term Generalized Tensor Summation (GTS). When it comes to the performance comparison with a traditional deep learning approach, especially for lower measurement rates, the proposed system exhibits a superior performance in terms of PSNR and SSIM with a particular improvement over the fine details. At the same time, GTSNET performs signal reconstruction from compressively sensed measurements in a feed-forward manner and this significantly reduces the computational complexity compared to the iterative approaches.

The rest of the paper is organized as follows. In Section II, we shall make a brief introduction to compressive sensing, separable and multidimensional. Then, the proposed learnable compressive sensing operations will be presented in Section III. In Section IV extensive experimental results will be presented for the CS in both gray-scale and RGB images. We shall then present comparative evaluations in spatial and frequency domains. In addition, we shall investigate which information is more preserved when T is increased. Finally, the conclusions are drawn in Section VI.

II. Preliminaries and Prior Art

A. Compressive Sensing

CS [1], [28] theory has shown that a sparse signal can be recovered from far fewer measurements than traditional Shannon-Nyquist-based data acquisition methods use. Mathematically speaking, let a CS scheme linearly extracts m number of measurements of the signal, $\mathbf{s} \in \mathbb{R}^N$, i.e.,

$$\mathbf{y} = \Psi \mathbf{s}, \tag{1}$$

where the measurement matrix, $\Psi \in \mathbb{R}^{m \times N}$ represents the linear data acquisition with $m \ll N$. In the CS literature, the efforts of designing such a linear measurement system can be categorized into two groups: (i) Finding a measurement matrix, Ψ which maximally preserves the information of $\mathbf{s}$ while transforming it in a lower-dimensional subspace as in (1). (ii) Finding a robust reconstruction algorithm, which is able to recover $\mathbf{s}$ from $\mathbf{y}$ in a reasonable time with a tolerable reconstruction error.

From elementary linear algebra, one can easily say that (1) is an underdetermined linear system of equations where for a given Ψ and $\mathbf{y}$ pair, $\mathbf{s}$ has infinitely many solutions. Therefore, at least one more assumption is needed to have unique solution. For instance, if we know that the signal of interest, $\mathbf{s}$, is sparse in a proper sparsifying domain Φ, then (1) can be expressed as

$$\mathbf{y} = \Psi \Phi \mathbf{x} = \mathbf{A}\mathbf{x}, \tag{2}$$

where $\mathbf{x} \in \mathbb{R}^N$ is sparse or compressible coefficient vector (e.g., if it is k-sparse $\|\mathbf{x}\|_{\ell_0^N} \leq k$) and $\mathbf{A} = \Psi\Phi$, which can be named as equivalent dictionary [29]. Under the assumption that the coefficient vector is k-sparse, then the following sparse representation,

$$\min_{\mathbf{x}} \ \|\mathbf{x}\|_0 \ \text{ subject to } \mathbf{A}\mathbf{x} = \mathbf{y} \tag{3}$$

is unique if $m \geq 2k$ and the minimum number of linearly dependent columns of $\mathbf{A}$ (see the definition of spark of a matrix [30]) is greater than $2k$ [30]. However, the problem in (3) is non-convex and known to be NP-hard. Fortunately, the most common approach will be the relaxation of it to an ℓ_1 minimization problem,

$$\arg\min_{\mathbf{x}} \|\mathbf{x}\|_1 \ \ s.t. \ \mathbf{x} \in \mho(\mathbf{y}) \tag{4}$$

where $\mho(\mathbf{y}) = \{\mathbf{x} : \mathbf{A}\mathbf{x} = \mathbf{y}\}$ in noisy-free case, which is known as Basis Pursuit (BP) [8]. To guarantee the equivalence of the solutions of (3) and (4), some properties of $\mathbf{A}$ are needed such as Null Space Property (NSP) [31], [32]. NSP can also be used to deal with approximately sparse signals. Moreover, if one should deal with approximately sparse signals in a noisy environment, a stronger property known as Restricted Isometry Property (RIP) [33], [34] can be borrowed from the CS literature. In this noisy case, the constraint in the optimization problem can be relaxed by setting $\mho(\mathbf{y}) = \left\{\mathbf{x} : \|\mathbf{A}\mathbf{x} - \mathbf{y}\|_2 \leq \epsilon\right\}$ which is known as Basis Pursuit Denoising (BPDN) [9] or Dantzig Selector [35] if we set $\mho(\mathbf{y}) = \left\{\mathbf{x} : \left\|\mathbf{A}'(\mathbf{y} - \mathbf{A}\mathbf{x})\right\|_\infty \leq \lambda\right\}$. Although RIP can be used for both stability and uniqueness analysis, the calculation of Restricted Isometric Constant (RIC) of $\mathbf{A}$ (defined with RIP of $\mathbf{A}$) generally requires a combinatorial search. Therefore, instead of RIC of a matrix, another important measure of a measurement matrix is defined in the literature. This is a functional $\mu(\mathbf{A}) = \max_{i,j} |A_{i,j}|$, which is known as coherence. In CS literature, choosing the best measurement matrix Ψ according to sparsifying matrix Φ is well studied in terms of $\mu(\mathbf{A})$. The system in (2) is nothing but a linear dimensional reduction system. To be able to preserve enough information while transforming $\mathbf{x}$ to $\mathbf{y}$, we generally wish each row of matrix $\mathbf{A}$ to get enough information from each element of $\mathbf{x}$.

In other words, the flatness of the rows of $\mathbf{A}$ is desired. This can be satisfied when the rows of the measurement matrix Ψ is not sparse in Φ. To describe this concept, the functional called "mutual coherence" is defined,

$$\mu(\Psi, \Phi) := \max_{1\leq k\leq m, 1\leq j\leq N} \left|\langle \psi_k, \phi_j \rangle\right| \tag{5}$$

which measures the coherence between Ψ and Φ, where ψ_k is the k'th row of Ψ and ϕ_j is the j'th column of Φ. It is clear that $\mu(\Psi, \Phi) \in \left[\frac{1}{\sqrt{N}}, 1\right]$ when Ψ has normalized rows and Φ has normalized columns. A theoretical lower bound to guarantee exact recovery for BP on the number of measurement in terms of defined mutual coherence can be found in [36] and [37] as,

$$m \geq \kappa . N . \mu^2(\Psi, \Phi) . k . \log N, \tag{6}$$

where κ is a positive constant. In plain terms, the minimum number of required measurements is dictated by the mutual coherence, and one wishes to keep it a minimum in a CS system. For instance, the measurement matrices, which have random waveforms with *i.i.d* elements such as Gaussian, are well known to be incoherent with any fixed basis, i.e., $\mu(\Psi, \Phi) \approx \frac{\sqrt{2\log(N)}}{\sqrt{N}}$ [38].

B. Multi-Dimensional and Separable Compressive Sensing

As reviewed above, the mathematical foundation of the conventional CS scheme is well established. However, this traditional scheme, where dimensional reduction is performed via vector-matrix multiplication and recovery is represented via ℓ_1-minimization, may not be convenient in most multi-dimensional signal acquisition schemes such as compressive sensing of imaging systems. For instance, assume that the signal of interest is a 512×512 gray-scale image, $\mathbf{S}$. Assume that we wish to build a sub-Gaussian CS system with a measurement rate of $\frac{m}{N} = 0.36$. In that CS scheme that samples the vectorized image, $\mathbf{s} \in \mathbb{R}^N$ with $N = 512^2$, the measurement matrix size will be $m \times N = 94372 \times 262144$. The conventional CS recovery algorithms such as ℓ_1-minimization techniques are iterative algorithms and in each iteration, they perform matrix-vector multiplications using CS matrix and the transpose of it. However, even saving alone such massive size matrices requires more than 80GB of storage. Therefore, the computational complexity of the iterative recovery algorithms becomes cumbersome. As a remedy, block-base CS and separable CS imaging [23] have become the most frequently used approaches. Among them, separable CS (also known as Kronecker CS) has the advantage of introducing fewer blocking artifacts. In a separable CS imaging introduced in [23], the CS sampling operator is separable over horizontal and vertical axes, i.e., $\mathbf{Y} = \Psi_1 \mathbf{S} \Psi_2'$, where $\mathbf{S} \in \mathbb{R}^{\sqrt{N}\times\sqrt{N}}$ is the input image, $\mathbf{s} \in \mathbb{R}^N$, in its original matrix form, and $\Psi_1 \in \mathbb{R}^{\sqrt{m}\times\sqrt{N}}$ and $\Psi_2 \in \mathbb{R}^{\sqrt{m}\times\sqrt{N}}$ are the measurement matrices. In that way, the computational cost of the matrix multiplications is reduced from $2 \times m \times N$ flops to $4 \times \sqrt{m} \times N$ flops compared to conventional CS setup. Moreover, this separable CS setup can be easily formulated in a traditional CS setup, which makes the analysis and algorithms of CS theory still valid. For instance, consider that the sparsifying basis is also separable as in 2D DCT matrices, then CS in matrix-vector form is nothing but $vec(\mathbf{Y}) = \Psi_1 \otimes \Psi_2 \; vec(\mathbf{S}) = \mathbf{A}_1 \otimes \mathbf{A}_2 \; vec(\mathbf{X})$, where $\mathbf{A}_i = \Psi_i \Phi_i$, $\mathbf{X} \in \mathbb{R}^{\sqrt{N}\times\sqrt{N}}$ is a sparse coefficient matrix and $\otimes$ is the Kronecker product. Let us assume the separable measurement matrices are Gaussian projection matrices, then mutual coherence between $\Psi_1 \otimes \Psi_2$ and $\Phi_1 \otimes \Phi_2$ can be easily calculated, i.e., $\mu(\Phi_1 \otimes \Phi_2, \Psi_1 \otimes \Psi_2) \approx \frac{log(N)}{\sqrt{N}}$. Hence, the mutual coherence increases $\sqrt{\frac{1}{2}log(N)}$ times and the number of the necessary measurement increases by the square of it compared to a conventional setup where CS matrix is unfactorized Gaussian projection matrix. *That is to say, in a separable CS setup, although computational complexity decreases, the minimum number of required measurements increases as a trade-off compared to conventional unfactorized CS scheme.* On the other hand, based on RIP or mutual coherence properties, these types of analysis for the CS reconstruction algorithm have been referred to by the term theoretical guarantee conditions in the worst-case scenario [39]. It is generally found, however, that algorithms perform much better than the performance bounds given by these types of worst-case scenario analyses, especially for recovering structurally sparse signals [27], [40].

In general multi dimensional and separable CS setup, the J-dimensional signal, $\mathcal{S} \in \mathbb{R}^{n_1\times n_2 \ldots \times n_J}$ with $N = \prod_{j=1}^{J} n_j$, can be acquired by separable sensing operator:

$$\mathcal{Y} = \mathcal{S} \times_1 \Psi_1 \times_2 \Psi_2 \ldots \Psi_{J-1} \times_J \Psi_J, \tag{7}$$

where $\mathcal{S} \times_i \Psi_i$ is the i-mode product of tensor $\mathcal{S}$ and matrix $\Psi_i \in \mathbb{R}^{m_i \times n_i}$ and $\mathcal{Y} \in \mathbb{R}^{m_1\times m_2 \ldots \times m_J}$ is CS tensor, with $m = \prod_{j=1}^{J} m_j$. Assuming that the sparsifying basis is also separable, then (7) can be re-cast as,

$$\mathcal{Y} = \mathcal{X} \times_1 \mathbf{A}_1 \times_2 \mathbf{A}_2 \ldots \mathbf{A}_{J-1} \times_J \mathbf{A}_J \tag{8}$$

where $\mathbf{A}_i = \Psi_i \Phi_i$ and $\mathcal{X} \in \mathbb{R}^{n_1\times n_2 \ldots \times n_J}$ is the sparse representation tensor. (8) can be cast as a vector-matrix multiplication,

$$\mathbf{y} = (\mathbf{A}_1 \otimes \mathbf{A}_2 \otimes \ldots \otimes \mathbf{A}_J)\, \mathbf{x}, \tag{9}$$

where $\mathbf{y} = vec(\mathcal{Y})$ and $\mathbf{x} = vec(\mathcal{X})$. Therefore, the conventional CS recovery techniques defined in (4) can be used and this setup is also known as tensor compressive sensing or Kronecker compressive sensing [21].

III. Generalized Structural Tensor Sum Compressive Sensing

A. Tensor Sum as a Computationally Efficient Approximation of Non-Separable CS Matrix

Earlier, we discussed in detail the trade-off for computational complexity versus the minimum number of measurements when we move from conventional non-separable CS scheme to separable CS setup. In the sequel, to our knowledge for the first time in literature, we will demonstrate that non-separable or unfactorized CS matrix can be approximated with the summation of tensorial sum operation. By doing this, while preserving the "goodness" of the CS matrix (i.e., the

probability of exact sparse signal recovery) as possible as close to unfactorized CS case, we can reduce the number of parameters to represent the CS matrix. This will enable us to have a feasible number of learnable parameters when we will attempt to jointly learn CS operation and recovery system using a neural network architecture. Mathematically speaking, let us sum T number of different separable CS tensor obtained from $\mathcal{S}$:

$$\mathcal{Y} = \sum_{t=1}^{T} \mathcal{S} \times_1 \Psi_1^{(t)} \times_2 \Psi_2^{(t)} \ldots \Psi_{J-1}^{(t)} \times_J \Psi_J^{(t)}, \tag{10}$$

where $\Psi_i^{(t)}$ is the i^{th} dimension CS matrix of t^{th} operation. (10) can be re-formulated in a non-separable CS setup via

$$\mathbf{y} = \sum_{t=1}^{T} \left(\Psi_1^{(t)} \otimes \Psi_2^{(t)} \otimes \ldots \otimes \Psi_J^{(t)}\right) \mathbf{s} = \sum_{t=1}^{T} \mathbf{P}^{(t)} \mathbf{s} = \mathbf{P}\mathbf{s}, \tag{11}$$

where $\mathbf{P}^{(t)} = \left(\Psi_1^{(t)} \otimes \Psi_2^{(t)} \otimes \ldots \otimes \Psi_J^{(t)}\right)$ and $\mathbf{P} = \sum_{t=1}^{T} \mathbf{P}^{(t)}$. Note that (11) is nothing but conventional non-separable CS operation with measurement matrix $\mathbf{P}$. For special case where $T = 1$, (10) reduces to a separable CS scheme as in (7). Compared to the conventional CS, $\mathbf{y} = \Psi\mathbf{s}$ with unfactorized CS matrix Ψ, the number of parameters to represent the CS matrix is reduced from $mN = \prod_{j=1}^{J} m_j n_j$ to $T \sum_{j=1}^{J} m_j n_j$. We design an experiment to show how the goodness of the new CS matrix $\mathbf{P}$ is increased with T. For the goodness metric, we selected the probability of exact recovery of the k-sparse signal in our experimental results. As the CS matrices, we selected Gaussian random projection matrices; in the case of Ψ which is unfactorized, $\prod_{j=1}^{J} m_j \times \prod_{j=1}^{J} n_j$ size Gaussian matrix is produced with each element of it is randomly drawn from the Gaussian distribution. For the new case, CS matrix $\mathbf{P}$ is generated with the summation of Kronecker products of the separable random Gaussian matrices as shown in (11). Figure 1 shows us that when T increases the probability of exact recovery from $\mathbf{y} = \mathbf{P}\mathbf{x}$ also increases. The sparse signal length is set to 1024 and orthogonal matching pursuit algorithm [41] was used as the CS recovery algorithm. For $T = 5$, $\mathbf{P}$ can achieve similar performance in recovery when $k = 80$. The exact recovery probability is estimated over 250 trials.

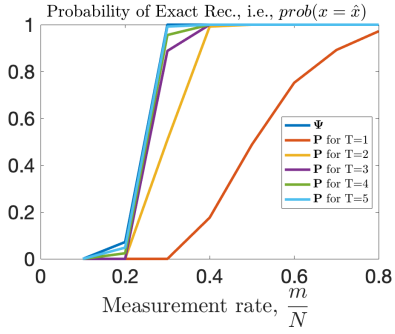

Fig. 1. Estimated probability of exact recovery over 250 trials for different realizations of CS matrix. An exactly sparse signal is synthetically produced for $N = 1024$ and $k = 80$.

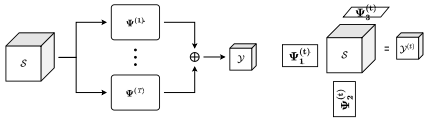

Fig. 2. CS Matrix configuration. Left: The CS operation modeled as the summation of tensor sums. Right: An individual tensor sum for the case of 3D tensors.

B. Structural Tensor Sum or Transformation Basis as a Part of the CS Matrix

In the literature, adjusting the measurement matrix as the multiplication of two or more matrices is a common practice. For instance, in [42], structural compressive sensing matrices are constructed as the multiplication of random permutation, an orthonormal basis, and sub-sampling matrices. Thanks to such pseudo-random matrices, faster recovery can be possible compared to the CS system with full random matrices. Moreover, in [24] and [25], CS matrix is in the form of multiplication of a sparsifying basis and a random matrix (i.e., an ordinary CS sensing matrix such as Gaussian projection matrix) i.e., $\Psi = \Psi^*\Omega'$, where Ω' is transformation domain basis, and Ψ^* is ordinary random CS matrix. Even though this CS system was originally proposed for CS-based encryption in the frequency domain, in Section V we will discuss that the learned CS systems in the frequency domain may slightly carry more high-frequency details compared to the learned CS system in the spatial domain. If the transformation basis is also separable like DCT, such a system can also be injected in the proposed tensorial and sum of tensorial CS scheme, i.e., $\Psi_i^{(t)} = \Psi_i^{(t)*}\Omega_i^{(t)'}$, where $\Omega_i^{(t)'}$ is i^{th}-coordinate matrix of the separable transformation basis.

C. Generalized Tensor Summation Compressive Sensing Network (GTSNET)

In this section, we propose a neural network architecture that jointly learns the CS sensing mechanism (CS matrix), and the reconstruction of the signal. The proposed network is composed of three parts: i) A CS operation, ii) Adjoint of the CS operation (or coarse estimation of the signal), and iii) a refinement module.

1) Separable and Multi-Linear Learning of CS Operation (i.e., Learnable CS matrix): Our learnable CS matrix $\mathbf{P}$ is factorized as

$$\mathbf{P} = \sum_{t=1}^{T} \left(\Psi_1^{(t)} \otimes \Psi_2^{(t)} \otimes \ldots \otimes \Psi_J^{(t)}\right), \tag{12}$$

where $\Psi_i^{(t)} = \Psi_i^{(t)*}\Omega_i^{(t)'}$, $\Omega_i^{(t)'}$ is i^{th}-coordinate matrix of the t^{th} separable transformation matrix such as the one that represents 8×8 size block-wise 2D DCT on the horizontal axis and $\Psi_i^{(t)*}$ learnable i^{th}-coordinate matrix of the t^{th} term in the summation. The CS operation can be factorized using a

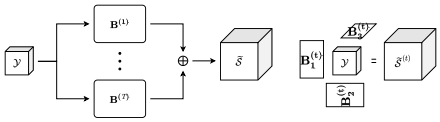

Fig. 3. Course estimation module. Left: The adjoint operation modeled as the summation of tensor sums. Right: An individual tensor sum with an input tensor in 3D.

reasonable number of training parameters thanks to the mode-j product:

$$\mathcal{Y} = \sum_{t=1}^{T} \mathcal{S} \times_1 \left(\Psi_1^{(t)^*} \Omega_1^{(t)'}\right) \times_2 \ldots \times_J \left(\Psi_J^{(t)^*} \Omega_J^{(t)'}\right). \quad (13)$$

A schematic explanation of (13) is given in Figure 2.

- For special case, $\Omega_J^{(t)'} = \mathbf{I}$, the CS system reduces to an un-structural tensor sum system, which is the learned version of the CS system defined in (10).
- For $T = 1$, the unfactorized system reduces to a separable CS system (e.g., the learned version of the separable CS imaging [23]).
- The system is valid for compressively sensing of any signal, $\mathcal{S}$.
- Thanks to the formulation in (13), the number of trainable parameters for unfactorized CS matrix is reduced from $\prod_{j=1}^{J} m_j n_j$ to $T \sum_{j=1}^{J} m_j n_j$, compared to conventional matrix-vector multiplication formula. Therefore, it makes the learning unfactorized CS sensing possible for large-scale and multi-dimensional signals.

Considering these properties, we call our learnable CS operation Generalized Tensor Summation Compressive Sensing.

2) A Coarse Estimation of the Signal: Separable Learning of Adjoint of CS Operation: In traditional iterative CS reconstruction algorithms, the transposition or the pseudo-inverse of the CS matrix is used in each iteration. On the other hand, in reconstruction-free inference tasks over CS signals [43], [44] or non-iterative deep learning-based recovery algorithms [17], a coarse estimation of the signal, also known as the proxy of the signal is first obtained, i.e., $\widetilde{\mathbf{s}} = \Psi' \mathbf{y}$. Although, it is also possible to obtain such a proxy using the regularized pseudo inverse of CS matrix, i.e., $\widetilde{\mathbf{s}} = \left(\Psi'\Psi + \lambda \mathbf{I}\right)^{-1} \Psi' \mathbf{y}$ [45], we follow the notation with the transpose or adjoint operator in general for simplicity. Eventually, the adjoint operator will be a learnable linear transformation. The adjoint of the $\mathbf{P}$ that is defined with the factorization in (12) can simply be expressed as,

$$\begin{aligned} \mathbf{P}' &= \sum_{t=1}^{T} \left(\Psi_1^{(t)} \otimes \Psi_2^{(t)} \otimes \ldots \otimes \Psi_J^{(t)}\right)' \\ &= \sum_{t=1}^{T} \left(\Psi_J^{(t)'} \otimes \Psi_{J-1}^{(t)'} \otimes \ldots \otimes \Psi_1^{(t)'}\right). \end{aligned} \quad (14)$$

where $\Psi_i^{(t)'} = \Omega_i^{(t)} \left(\Psi_i^{(t)^*}\right)'$, $\Omega_i^{(t)}$ is i^{th}-coordinate matrix of the inverse of the t^{th} separable transformation matrix such as the one that represents the inverse operation of the 8×8 size block-wise 2D DCT transformation on the horizontal axis and $\left(\Psi_i^{(t)^*}\right)'$ is the transpose of $\left(\Psi_i^{(t)^*}\right)$. As stated above we introduce to learn the adjoint CS matrix from the training set. Mathematically speaking, we wish to have the proxy signal, $\widetilde{\mathbf{s}} = \mathbf{B}\mathbf{y}$ where the operation $\mathbf{B}$ is learned by a neural network instead of directly applying $\mathbf{P}'$. In practice, there is no need to formulate it in vector-matrix multiplication formulation since the adjoint can be applied directly on the tensorized measurement. As shown in Figure 3, it can be expressed as,

$$\widetilde{\mathcal{S}} = \sum_{t=1}^{T} \mathcal{Y} \times_1 \left(\Omega_J^{(t)'} \mathbf{B}_1^{(t)^*}\right) \times_2 \ldots \times_J \left(\Omega_J^{(t)} \mathbf{B}_J^{(t)^*}\right), \quad (15)$$

where $\mathbf{B}_i^{(t)^*}$ is the i^{th}- coordinate learnable adjoint operation matrix for the t^{th} term and $\Omega_i^{(t)}$ is the corresponding fix (non-trainable) inverse transformation operation. As it was in the case of CS operation, the tensorial factorization in (15) makes the adjoint operation trainable instead of attempting directly to learn the elements of the unfactorized matrix $\mathbf{B}$.

3) Reconstruction Free Recovery With Deep Neural Network: Having the proxy signal, $\widetilde{\mathcal{S}}$, we train a conventional CNN, $C(.)$, which takes the proxy signal, $\widetilde{\mathcal{S}}$ as input and produce a finer estimation of the signal, i.e., $\widehat{\mathcal{S}} = C(\widetilde{\mathcal{S}})$. In that way, a non-iterative reconstruction network and CS operation can jointly be optimized (learned). The final network is called Generalized Tensor Summation Compressive Sensing Network (GTSNET-T) which includes T tensor summation in its formula. Our solution introduces a generalized but flexible learning paradigm, it encapsulated many special cases which are set as the adjustable parameter of the network. For instance, one can set $T = 1$ to have a separable optimal CS operation and its reconstruction. Or alternatively, the transformation $\Omega_i^{(t)}$ can be set to the identity operator to sense in the spatial domain.

For the refinement module, $C(.)$, we incorporate a modified version of the Residual Dense Network (RDN) [46]. Such network takes advantage of the so-called residual dense blocks (RDBs), within which all the layer outputs are fully utilized via local feature fusion. The outputs of each RDB are further connected via a global feature fusion, where the information from each block is effectively preserved. The performance of the network is improved by both local and global residual learning. We modify the original RDN configuration by omitting the upscale layer as it was proposed for image super-resolution [46]. Furthermore, we adapt the overall RDN structure as a residual network, i.e., the output of the modified RDN is added to the input proxy signal, $\widetilde{\mathcal{S}}$, to obtain $\widehat{\mathcal{S}}$.

The overall GTSNET-T structure is illustrated in Figure 4, including the learnable CS matrix and the adjoint operation, as well as the final refinement module. The adjoint operation matrices $\Omega_j^{(t)} \mathbf{B}_j^{(t)^*}$ are denoted altogether as $\mathbf{B}_j^{(t)} = \Omega_j^{(t)} \mathbf{B}_j^{(t)^*}$ for simplicity. Each branch t in the CS matrix (pink blocks in Figure 4) performs a single tensor product with the input tensor $\mathcal{S}$, while the final CS operation is the summation over the products as dictated by (10) and (11). Similarly, the adjoint operation is the summation over the individual tensor products with the compressed signal $\mathcal{Y}$ (green blocks in Figure 4), as given by (15). The refinement module composes of D RDBs, each of which having C convolution layers with

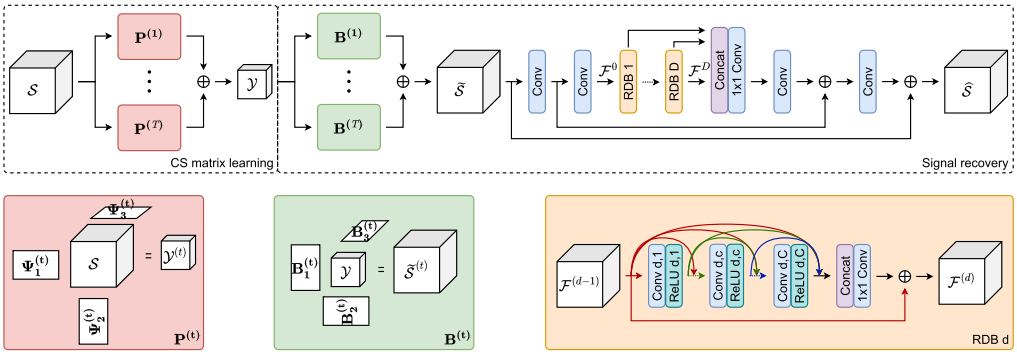

Fig. 4. Overall block diagram of the proposed end-to-end system.

rectified linear units (ReLUs) [47] as activation functions. The input feature map to each RDN, $\mathcal{F}^{(d-1)}$ has G_0 channels, while each convolution layer inside has G filters with a 3×3 filter size. The concatenated feature maps at the end of the RDB are processed through one 1×1 convolution layer to map the output channel size back to G_0. In our implementation, we set $D = 4$, $C = 3$, $G_0 = 30$, and $G = 12$.

We train the network with an overall loss function $L(\widetilde{\mathcal{S}}, \widehat{\mathcal{S}}, \mathcal{S})$, which is the combination of two loss functions defined over the proxy signal, $\widetilde{\mathcal{S}}$, and the final output, $\widehat{\mathcal{S}}$, respectively. The loss over the proxy signal, $\widetilde{L}(\widetilde{\mathcal{S}}, \mathcal{S})$, is set to be a simple L_1-loss, as it was previously demonstrated to achieve better performance compared to the L_2-loss in various image processing problems [48]. Assuming each training batch contains K input tensors $\{\mathcal{S}_1, \mathcal{S}_2, \ldots, \mathcal{S}_K\}$,

$$\widetilde{L}(\widetilde{\mathcal{S}}, \mathcal{S}) = \frac{1}{K} \sum_{k=1}^{K} \|\widetilde{\mathbf{s}}_k - \mathbf{s}_k\|_1 . \tag{16}$$

The loss over the final output, $\widehat{L}(\widehat{\mathcal{S}}, \mathcal{S})$, is also an L_1-loss with an additional regularization term, $\widehat{R}(\widehat{\mathcal{S}}, \mathcal{S})$,

$$\widehat{L}(\widehat{\mathcal{S}}, \mathcal{S}) = \frac{1}{K} \sum_{k=1}^{K} \left(\|\widehat{\mathbf{s}}_k - \mathbf{s}_k\|_1 + \alpha \widehat{R}(\widehat{\mathcal{S}}_k, \mathcal{S}_k) \right), \tag{17}$$

where α is a hyperparameter. Our regularization term is a modified sparse gradient prior [49] applied on the spatial domain, which has been proposed for image debluring as it provides sharper details compared to, e.g., Gaussian prior. The mathematical description of the regularization is expressed as follows:

$$\begin{aligned} \widehat{R}(\widehat{\mathcal{S}}, \mathcal{S}) = & \sum_{n_1, \ldots, n_J} \exp\left(-\beta |\nabla_{n_1} \mathcal{S}|^{\gamma}\right) |\nabla_{n_1} \widehat{\mathcal{S}}|^{\gamma} \\ & + \sum_{n_1, \ldots, n_J} \exp\left(-\beta |\nabla_{n_2} \mathcal{S}|^{\gamma}\right) |\nabla_{n_2} \widehat{\mathcal{S}}|^{\gamma}, \end{aligned} \tag{18}$$

where ∇_{n_1} and ∇_{n_2} are the discrete differential operators over the first and second dimensions, respectively. The exponential weights $\exp(-\beta |\nabla_{n_1} \mathcal{S}|^{\gamma})$ and $\exp(-\beta |\nabla_{n_2} \mathcal{S}|^{\gamma})$ are introduced to decrease the prior term over the edges of the original tensor $\mathcal{S}$, as proposed in [49]. We empirically set, $\alpha = 0.005$, $\beta = 10$, and $\gamma = 0.9$. Finally, the overall loss function is $L(\widetilde{\mathcal{S}}, \widehat{\mathcal{S}}, \mathcal{S}) = \widetilde{L}(\widetilde{\mathcal{S}}, \mathcal{S}) + \widehat{L}(\widehat{\mathcal{S}}, \mathcal{S})$.

IV. Experimental Setup and Results

A. Training Setup

We prepare the training dataset in the following manner: Div2K image dataset was used and 256×256 image patches were selected with stride 512 and they were cropped. Data augmentation was applied during the data generation with rotations in four different degrees; 0, 90, 180, and 270, flipping and downsampling with scale factors; 1, 0.8, and 0.6. Hence, by using the training set of DIV2K total of 89272 image patches were obtained to be used as the training set. Similarly, as the validation set, we obtained 1512 images from the validation set of DIV2K. All the images are normalized to range $[0, 1]$. The batch size was selected as 16 and the networks were trained with 100 epochs. During training, the learning rates are scheduled to be 10^{-3} for the first 50 epoch, 10^{-4} for the later 30 epoch, and 10^{-5} for the last 20 epoch. The network of the 100. epoch was chosen as final. The implementation of the GTSNET was done using MatConvNet package [50].

B. Comparative Evaluations

As traditional CS reconstruction methods, which are well-known state-of-the-art sparse recovery methods, comparative evaluations are performed against the following three methods; Gradient Projection for Sparse Reconstruction (GPSR) [14], TV Minimization by Augmented Lagrangian and Alternating Direction Algorithms (TVAL3) [12] and Denoising-based AMP (D-AMP) [13]. GPSR is a sparse recovery algorithm that was specifically proposed as computationally more efficient and feasible to apply for any image CS framework. As the CS matrix, a randomly selected subset of the rows of noiselet basis [51] was used. As the sparsifying transform, wavelet "Coiflet 2" was used with the toolbox WaveLab850 [52]. TVAL3 is one of the state-of-the-art TV minimization solvers. Walsh Hadamard Transform whose fast implementation available in the TVAL3 toolbox was used as the CS matrix. The parameters on TVAL3 toolbox were set as follows: $\mu = 2^{13}$,

TABLE I

PERFORMANCE METRICS (PSNR AND SSIM) OBTAINED BY THE COMPETING AND PROPOSED METHODS OVER THREE BENCHMARK DATASETS

Measurement Rates (MRs)	Datasets	GPSR		TVAL3		DAMP		CSNET+		SCSNET		GTSNET-1		GTSNET-3	
		PSNR	SSIM	PSNR	SSIM	PSNR	SSIM	PSNR	SSIM	PSNR	SSIM	PSNR	SSIM	PSNR	SSIM
MR = 0.01	SET5	16.25	0.378	17.08	0.552	8.30	0.066	24.18	0.669	24.21	0.669	24.61	0.696	**24.66**	**0.697**
	SET14	16.61	0.349	16.46	0.474	7.69	0.041	22.93	0.588	22.97	0.588	**23.08**	**0.600**	**23.08**	**0.600**
	SET11	14.07	0.289	13.94	0.441	5.61	0.024	21.02	0.589	21.04	0.589	**21.39**	**0.609**	21.38	**0.609**
	Avg.	15.64	0.339	15.83	0.489	7.20	0.044	22.71	0.615	22.74	0.615	23.03	**0.635**	**23.04**	**0.635**
MR = 0.05	SET5	20.58	0.413	23.44	0.661	26.56	0.766	29.75	0.848	29.74	0.847	**30.25**	**0.861**	30.24	**0.861**
	SET14	20.17	0.361	19.95	0.555	24.70	0.658	27.04	0.739	27.04	0.739	**27.16**	**0.747**	27.15	**0.747**
	SET11	17.69	0.307	17.27	0.576	21.77	0.684	25.86	0.788	25.86	0.787	**26.27**	**0.806**	26.25	**0.806**
	Avg.	19.48	0.360	20.22	0.597	24.34	0.703	27.55	0.792	27.55	0.791	**27.89**	**0.805**	27.88	**0.805**
MR = 0.1	SET5	23.18	0.505	26.00	0.743	31.42	0.872	32.60	0.906	32.78	0.908	33.03	0.912	**33.11**	**0.913**
	SET14	22.31	0.438	20.76	0.620	28.77	0.769	29.24	0.820	**29.32**	**0.821**	29.17	**0.821**	29.24	**0.821**
	SET11	20.05	0.396	18.59	0.670	26.17	0.852	28.34	0.859	28.52	0.862	28.79	0.871	**28.83**	**0.872**
	Avg.	21.85	0.446	21.78	0.678	28.79	0.831	30.06	0.862	30.21	0.864	30.33	0.868	**30.39**	**0.869**
MR = 0.2	SET5	26.76	0.659	27.92	0.823	35.26	0.926	36.07	0.949	36.17	0.949	**36.29**	**0.950**	36.27	**0.950**
	SET14	25.23	0.578	23.04	0.717	32.05	0.851	32.26	0.896	**32.30**	**0.897**	31.88	0.893	31.94	0.894
	SET11	23.49	0.561	20.85	0.789	27.89	0.913	31.67	0.921	31.83	0.922	31.81	**0.924**	**31.86**	0.923
	Avg.	25.16	0.599	23.94	0.776	31.73	0.897	33.33	0.922	**33.43**	**0.923**	33.33	0.922	33.36	0.922
MR = 0.3	SET5	29.55	0.763	26.27	0.843	36.86	0.946	38.29	0.965	**38.49**	**0.966**	37.95	0.964	38.00	0.964
	SET14	27.61	0.690	23.70	0.745	33.33	0.894	34.46	0.931	**34.64**	**0.933**	33.64	0.926	33.74	0.927
	SET11	26.48	0.692	23.21	0.854	27.11	0.943	34.32	0.950	**34.66**	**0.952**	34.09	0.951	33.98	0.950
	Avg.	27.88	0.715	24.39	0.814	32.43	0.928	35.69	0.949	**35.93**	**0.950**	35.23	0.947	35.24	0.947

$\beta = 2^6$, $\mu_0 = 2^2$, $\beta_0 = 2^{-2}$, $tol = 10^{-6}$, $maxit = 300$. D-AMP was proposed to improve the performance of CS recovery for the natural signals by employing off-the-shelf denoising algorithms. We test the algorithm with default settings, where the elements of the CS matrix are picked from *i.i.d.* Gaussian distribution and BM3D [53] is used as the denoiser. The number of iterations and the image block size are empirically set as 30 and 128×128, respectively.

As the akin state-of-the-art deep learning methods, we selected CSNET [19] and SCSNET [20]. The algorithms and the trained models were taken from the competing algorithms' web pages. Both methods jointly learn the CS matrix and reconstruction of the image from the measurement as proposed in this study. However, these methods learn the block-wise CS matrix using convolution operation in a non-overlapping manner. In that sense, when the kernel size is increased to full image size, the method turns out to be the classical unfactorized CS setup with an infeasible increase in the number of parameters to train.

We trained two GTSNET versions; GTSNET-1 and GTSNET-3. Among them GTSNET-1 learns tensorial representation of CS matrix, therefore suitable for both separable and unfactorized CS schemes. For this network, separable transformation matrices Ω_1' and Ω_2' were chosen as 8×8 DCT transformation matrices in the horizontal and vertical directions, respectively. GTSNET-3 includes the three-tensor summation as the CS operation and represents an unfactorized CS setup. As the sparsifying matrices, $\Omega_i^{(t)'}$, we selected 8×8, 16×16 and 32×32 2D DCT transformations for $t = 1, t = 2, t = 3$, respectively. All the competing algorithms were tested on three commonly-used datasets: Set14 [54], Set5 [55], and Set11 [17]. The results on five different measurement rates (MRs) are presented in Table I. Against the competing traditional methods, GPRS, TVAL3 and DAMP, a significant gap on the average performance is observed. In particular, we achieve 7.21 dB, 4.55 dB, 1.6 dB, 1.63 dB, and 2.81 dB improvements in PSNRs compared to the closest performance, for MRs of 0.01, 0.05, 0.1, 0.2 and 0.3, respectively. When we compare against the deep learning-based competing methods, CSNET+ and SCSNET, GTSNET-T shows superiority for the lower MRs (< 0.2), i.e., 0.3 dB, 0.3 dB, 0.18 dB PSNR improvement over the best competing method, for the MRs of 0.01, 0.05 and 0.1, respectively. Figure 1 presents visual comparisons over the state-of-the-art CS methods. Although there is no significant gap between the PSNR and SSIM of GTSNET-1 and GTSNET-3 results, one can observe GTSNET-3 outputs preserve high frequency details better, e.g., see Parrot and Flinstone images in Figure 5 and Figure 6. The performance gap in both PSNR and SSIM measures becomes significant in RGB images while the visual quality of the GTSNET-3 outputs especially at the fine details noticeably improves.

C. Comparative Evaluations Against Deep Learning-Based CS Methods

As the competing deep learning-based solutions,

(i) the stacked denoising autoencoder (SDA) [16], which is the pioneer method,
(ii) non-iterative reconstruction of the compressively sensed images using CNN (ReconNet) [17]
(iii) the learned version of iterative shrinkage thresholding algorithm for CS imaging (ISTA-Net),
(iv) akin state of the art techniques convolutional compressive sensing network (CSNET) [19]
(v) scalable convolutional compressive sensing network (SCSNET) [20],
(vi) memory augmented cascading Network (MAC-Net) [56],
(vii) dual-path attention network for compressed sensing (DPA-Net) [57], and the most recent deep unrolling techniques,
(viii) OPINE-NET [58],
(ix) AMP-Net+ [59], and

(x) COAST [60]

are selected as the most recent techniques. This article was updated to include a few more deep learning-based solutions [61], [62] while it was being prepared. Through self-attention mechanisms, these algorithms enhance the performance of recovery refinement parts of end-to-end CS networks based on vision transformers [63], which have recently become an active research area. While learning compressively sensing operator part, however, they use a strided convolution (block-by-block sensing) based module similar (or identical) to the ones used by CSNET, SCSNET, OPINE-NET, and AMP-Net.

For ISTA-Net, CSNET, and AMPNet we choose their improved versions ISTA-Net+, CSNET+, and AMP-Net+, respectively. The comparative evaluations are conducted on the benchmark SET11 dataset. The results for different measurement rates are presented in Table II. All the algorithms and the trained models were downloaded from authors' web pages and run over SET11 except SDA and DPA-Net, whose source codes are not available online. The results of SDA were taken from [17] and the results of DPA-Net were taken from [57]. The average PSNR values show the superiority of the proposed network over all competing methods especially for the case of lower sampling rates, e.g., for MR < 0.1. Figure 6 shows samples for the qualitative performance comparison where it is clear that the outputs of SDA, ReconNet, and ISTA-Net+ may exhibit strong blocking artifacts. The reason is that they use block-by-block sampling strategy to compressively sense the signal, and then apply block-by-block recovery strategy. On the other hand, CSNET, MAC-Net, and SCSNet algorithms have block-by-block compressive sensing setup, but their reconstruction step recovers the image as a whole by using convolutional layers. Therefore, their outputs show fewer blocking artifacts. On the other hand, GTSNET-1 CS module is convenient for both separable and unfactorized (conventional vector-matrix CS system) CS setup. When it comes to reconstruction, it uses a CNN similar to CSNET and SCSNET and recovers the image as a whole. For the use case, where one wants to use a traditional sampling setup with a better approximation of unfactorized CS matrices, the GTSNET-T ($T > 1$) can be used. The sampling strategies of deep learning methods are summarized in Table I. Although there is no significant gap in PSNR and SSIM values on average, GTSNET-3 can recover more high-frequency details as seen in the Parrot image in Figure 6. In Section V, we will discuss the effects of the tensor sum in the frequency domain.

D. Comparative Evaluations Over RGB Images

Unfortunately, most aforementioned competing methods except CSNET were designed only for gray-scale images. Therefore, we compare GTSNET with CSNET. An extensive set of comparative evaluations was conducted on the following benchmark RGB image datasets: Set5, Set11, Manga109 [64], and Urban100 [65]. The results are reported in Table III. For GTSNET-5, as the sparsifying matrices, we selected, 8×8, 16×16, 32×32, 64×64 and 128×128 2D DCT transformations for $\Omega^{(1)'}$, $\Omega^{(2)'}$, $\Omega^{(3)'}$, $\Omega^{(4)'}$ and $\Omega^{(5)'}$, respectively. As clearly observable from the table that the performance gap between GTSNET-1 and GTSNET-T ($T > 1$) widens in terms of PSNR and SSIM. Compared to CSNET+, a comparable performance with the separable CS setup (GTSNET-1) is achieved. For the unfactorized CS matrix setup ($T > 1$), the performance gap between CSNET+ and the best operating GTSNET configuration becomes significant, i.e., 1.15 dB, 0.92 dB and 2.91 dB for sampling rates of 0.05, 0.1 and 0.2, respectively. Moreover, some samples for visual comparison of the recovered images are shown in Figure 5. The outputs of CSNET+ exhibit certain level of blocking artifacts that are entirely absent in any of the outputs of the proposed GTSNET-T networks.

TABLE II

SAMPLING AND RECOVERY STRATEGIES OF THE DEEP LEARNING-BASED ALGORITHMS. GTSNET-T CAN BE USED FOR BOTH CLASSICAL (UNFACTORIZED) CS AND SEPARABLE CS SYSTEMS

Algorithm	Sampling Strategy	Reconstruction Strategy
SDA	Block-by-block CS	Block-by-block Auto-encoder
ReconNet	Block-by-block CS	Block-by-block CNN
ISTA-Net+	Block-by-block CS	Block-by-block CNN
MAC-Net	Block-by-block CS	CNN
CSNET+	Block-by-block CS	CNN
SCSNET	Block-by-block CS	CNN
GTSNET-1	Unfactorized or separable CS	CNN
GTSNET-T ($T > 1$)	Unfactorized CS	CNN

TABLE III

PSNR LEVELS OBTAINED BY THE COMPETING AND PROPOSED METHODS OVER SET11 DATASET

Algorithm	Measurement Rate			
	0.25	0.1	0.04	0.01
SDA	25.34	22.65	20.12	17.29
ReconNet	25.60	24.28	20.63	17.27
ISTA-Net+	32.44	26.49	21.56	17.45
DPA-Net	31.74	26.99	23.50	18.05
MAC-Net	32.91	27.68	24.22	18.26
CSNET+	-	28.34	-	21.02
SCSNET	-	28.52	-	21.04
OPINE-NET	**34.44**	29.33	25.04	19.87
AMP-Net+	-	29.40	25.26	20.20
COAST	-	**30.03**	-	-
GTSNET-1	32.47	28.79	25.44	**21.39**
GTSNET-3	32.36	28.83	**25.45**	21.38

V. DISCUSSION

A. Tensor Vs Tensor Sum for CS Matrix Learning

In this section, we perform an ablation study concerning the effects of the number of tensor sums, T, over the final reconstruction quality. As a starting point, we plot the PSNR values of each image in Set5, sensed and reconstructed via three different setups, for $T = 1, T = 3$, and $T = 5$. We perform analysis on both gray-scale and RGB images,

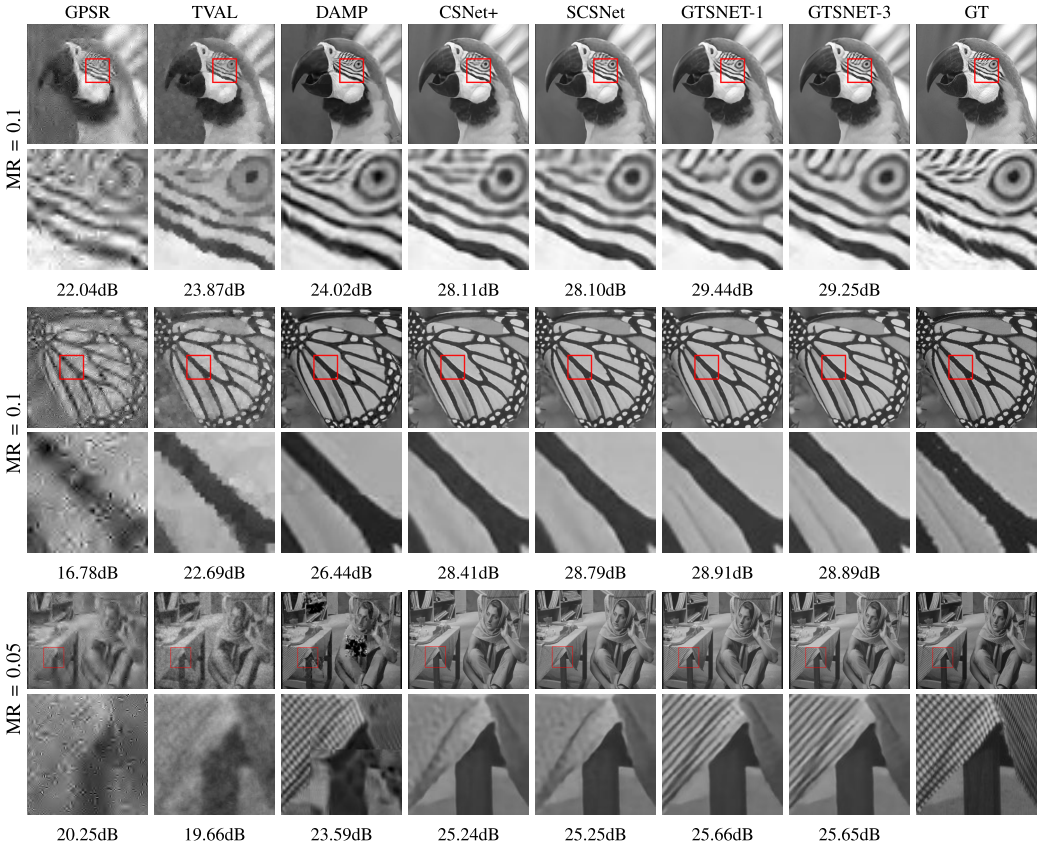

Fig. 5. Visual comparison with the state-of-the-art on grayscale images with varying measurement rates.

TABLE IV

PERFORMANCE METRICS (PSNR AND SSIM) OBTAINED BY THE COMPETING AND PROPOSED METHODS OVER FOUR BENCHMARK RGB IMAGE DATASETS

Ratio	MR = 0.01								MR = 0.05							
Method / *Dataset*	CSNET+		GTSNET-1		GTSNET-3		GTSNET-5		CSNET+		GTSNET-1		GTSNET-3		GTSNET-5	
	PSNR	SSIM	PSNR	SSIM	PSNR	SSIM	PSNR	SSIM	PSNR	SSIM	PSNR	SSIM	PSNR	SSIM	PSNR	SSIM
SET5	**24.35**	0.858	23.17	0.843	24.23	**0.865**	24.16	**0.865**	29.18	0.940	28.53	0.935	29.82	0.948	**30.48**	**0.955**
SET14	**22.83**	0.734	21.55	0.707	22.62	**0.736**	22.49	0.732	26.71	0.869	25.43	0.818	26.41	0.849	**27.15**	**0.872**
Manga109	21.18	0.821	20.43	0.825	**21.38**	0.842	21.35	**0.843**	25.41	0.914	26.04	0.929	27.48	0.946	**28.36**	**0.953**
Urban100	**20.93**	**0.697**	19.51	0.649	20.61	0.692	20.31	0.686	**25.05**	0.857	23.01	0.794	24.40	0.843	24.97	**0.858**
Avg.	**22.32**	0.778	21.17	0.756	22.21	**0.784**	22.08	0.782	26.59	0.895	25.75	0.869	27.03	0.897	**27.74**	**0.910**
	MR = 0.1								MR=0.2							
SET5	32.07	0.966	31.16	0.959	**32.97**	**0.971**	32.45	0.968	35.15	0.979	34.13	0.975	35.33	0.981	**37.28**	**0.986**
SET14	29.31	**0.926**	27.30	0.870	**29.35**	0.922	28.53	0.898	32.26	0.960	29.79	0.922	31.35	0.944	**34.15**	**0.972**
Manga109	28.82	0.957	29.49	0.961	**31.63**	**0.976**	31.04	0.973	30.96	0.969	33.62	0.983	34.67	0.987	**36.11**	**0.990**
Urban100	**27.78**	**0.918**	25.13	0.861	27.74	**0.918**	26.88	0.903	30.64	0.955	27.94	0.920	29.94	0.949	**33.11**	**0.972**
Avg.	29.50	0.942	28.27	0.913	**30.42**	**0.947**	29.73	0.936	32.25	0.966	31.37	0.950	32.82	0.965	**35.16**	**0.980**

where the measurement rate is set as 0.1. The gray-scale images are constructed via taking the luminance channel of each image in YCbCr color space. The results are shown in Figure 6. While the performance gap is negligible difference on the gray-scale images, we observe a significant performance improvement in reconstructing the RGB images as T increases from 1 to 3, e.g., up to 2.74 dB PSNR improvement on the "woman" image. An interesting observation worth mentioning is that GTSNET-T with $T = 3$ outperforms the one with $T = 5$, both for each individual image in Set5, and for the average of each dataset presented in Table III. This might seem at first contradictory to our derivations within the theoretical discussions, where we demonstrate in Section III-A and Figure 1 that the mutual coherence decreases as T increases.

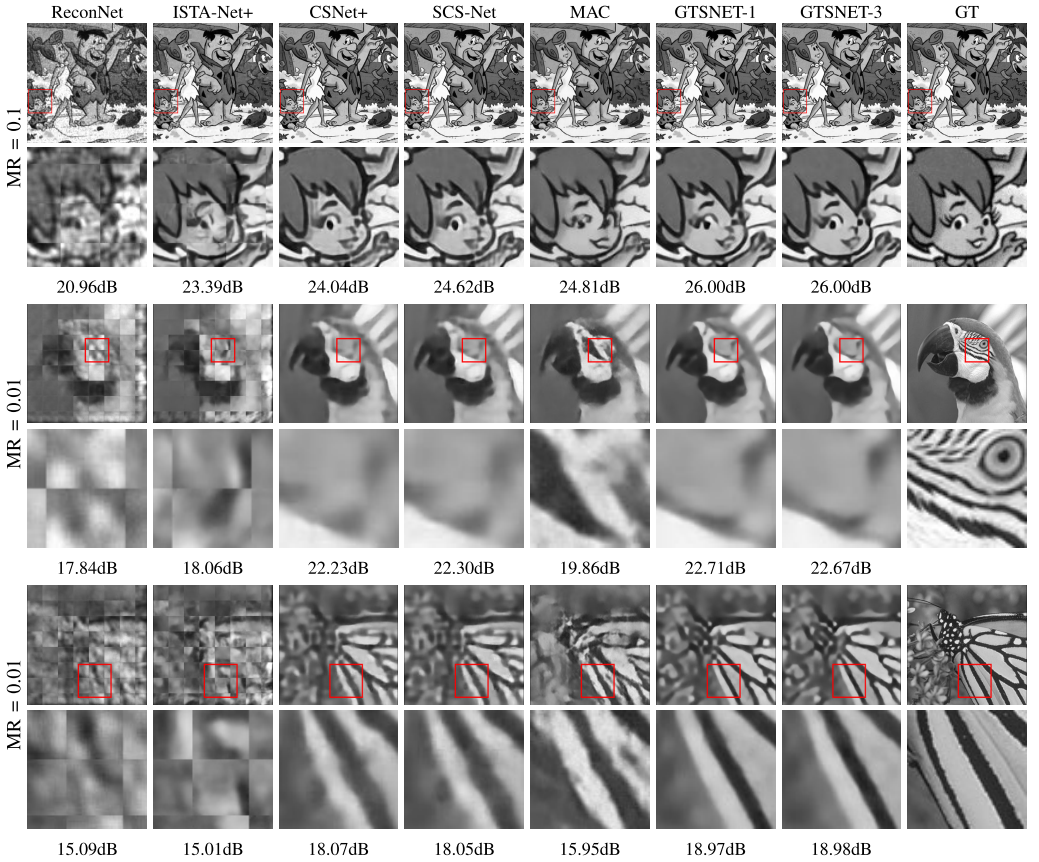

Fig. 6. The recovered images of the competing and proposed methods with the GT image on the left.

However, within such analysis each tensor is chosen to be composed of Gaussian random matrices. As in practice we further learn the CS matrices to improve performance over the random matrices, an inherent trade-off occurs, where the number of learned parameters increases linearly with increasing T. The experimental analysis shows that $T = 3$ provides best of both worlds with a consistently superior image quality for MR $= 0.1$.

To enrich the discussion above, we visually compare the three methods over a rather tricky color image: "zebra" from Set14. In particular, we examine the frequency responses of both the proxy signals, $\widetilde{\mathcal{S}}$, as the immediate reconstruction, and the final outputs, $\widehat{\mathcal{S}}$. The results are shown in Figure 9. The differences between each method are clearly visible over the frequency responses of the proxy signals (middle row), where the cut-off frequency of GTSNET-3 is higher compared to that of GTSNET-1 and GTSNET-5. Subsequently, the final output of GTSNET-3 can preserve the higher frequency information while providing better quantitative result in terms of PSNR value.

Having shown the improvement in image quality with $T > 1$, we now provide the information flowing from each branch of the adjoint operator. Figure 10 illustrate the tentative reconstruction results, where one of the branches ($\mathbf{B}^{(3)}$) performs the majority of the reconstruction over the lower frequency region and the residual high-frequency details are recovered through branches $\mathbf{B}^{(1)}$ and $\mathbf{B}^{(2)}$. In addition, the first and second branches carry information regarding the different regions of the spectrum; the support of $\mathbf{B}^{(2)}$ is more concentrated towards the low-frequency region, whereas the frequency response of the first branch contains higher frequencies. The proximal signal, $\widetilde{\mathcal{S}}$ (Figure 10, fourth column), is the summation of each output, having a wider response than each individual branch.

B. Tensor Sum vs Structural Tensor for CS Matrix Learning

In Section III-C1, we discuss that the proposed method is suitable for designs of both structured and unstructured tensor summations, whereas we mainly demonstrate our results via the learned structured matrices. In this subsection, we compare a network trained for unstructured tensor sums, i.e., $\Omega_J^{(t)'} = \mathbf{I}$, with the previously discussed structured tensors. We train both setups for GTSNET-3, where the measurement rate is set as

TABLE V

PERFORMANCE COMPARISON OF TIED VS. UNTIED LEARNING OF CS MATRICES

Algorithm	GTSNET-T										ℓ_1-minimization
Measurement M. / Adjoint	A, B are learned with constraint $B = A^T$ (Tied Learning)					A, B are learned without constraint					A is Gaussian matrix, $B = A^T$
Measurement Rates (MRs)	T=1	T=2	T=3	T=4	T=5	T=1	T=2	T=3	T=4	T=5	Unfactorized
MR=0.01	16.81	17.28	17.15	17.40	17.54	17.33	17.44	17.50	17.50	**17.80**	9.85
MR=0.04	23.62	23.70	23.86	23.84	23.81	23.95	23.86	23.98	**24.42**	24.35	9.96
MR=0.05	25.30	25.30	25.29	25.55	25.51	25.62	25.46	25.68	25.66	**25.71**	10.00
MR=0.1	28.11	28.12	28.24	28.28	28.08	28.55	28.39	28.24	28.50	**28.56**	10.25

Fig. 7. The recovered images of the competing and proposed methods with the GT image on the left.

0.1. A test image is picked from the Urban100 dataset for the experiment, carrying high-frequency components with fixed patterns. Figure 11 shows the results. While the differences are not prominent through visual inspection on the spatial domain at first, the proxy output of the structured tensor summation is observed to contain a wider frequency response. We also notice a decrease in the high-frequency region of the final output with the unstructured tensor sum, visible as a box in the middle of the frequency response (Figure 11, bottom left), and a decrease of 0.43 dB in PSNR. For such

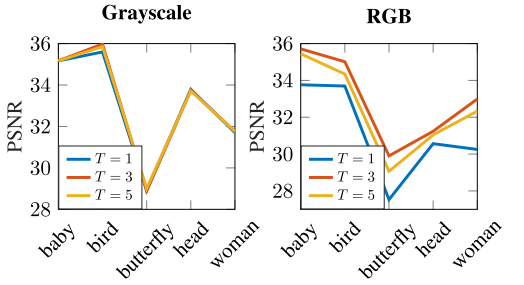

Fig. 8. Quantitative reconstruction results of Set5 dataset, with varying number of tensor sums T. Left: Gray-scale (luminance) images. Right: Original color (RGB) images. The measurement rate is set to be 0.1 in both scenarios.

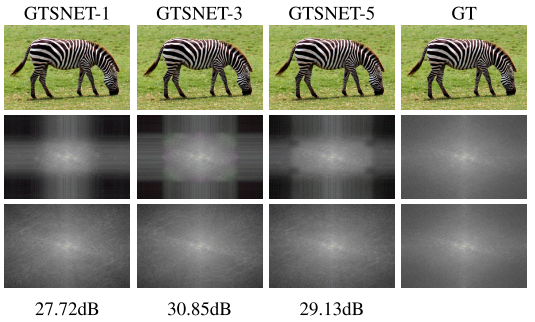

Fig. 9. Frequency analysis with varying number of tensor sums. Top: Final outputs $\widehat{S}$ in spatial domain. Middle: Proxy signals $\widehat{S}$ in frequency domain. Bottom: Final outputs $\widehat{S}$ in frequency domain. Measurement rate is set as 0.1.

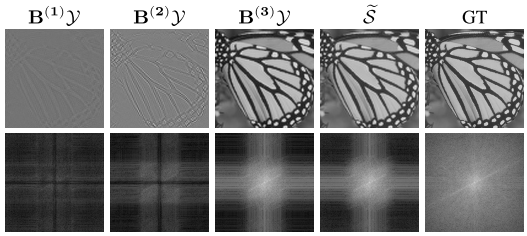

Fig. 10. Tentative reconstruction result of each individual adjoint operation in GTSNET-3, as well as the proxy signal $\widehat{S}$ as the summation of each branch.

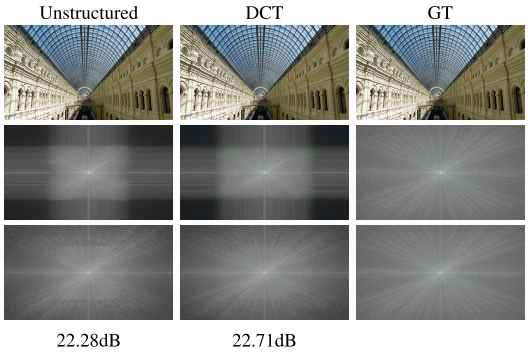

Fig. 11. Visual comparison between the unstructured and structured (DCT) Tensor sums. Top: Final outputs $\widehat{S}$ in the spatial domain. Middle: Proxy signals $\widehat{S}$ in the frequency domain. Bottom: Final outputs $\widehat{S}$ in the frequency domain. The results are shown for GTSNET-3 with MR $= 0.1$.

purposes, we proceed with the structured matrices. Nevertheless, it is important to demonstrate that the proposed method has flexibility generalizing various types of CS matrix designs.

C. Performance on Sparse Signals

The proposed GTSNET-T scheme is able to sense the images in sparsifying domain e.g., DCT basis directly. The adjoint operator consists of two parts; one is a learned adjoint matrix and the other is the fixed inverse transform basis of the sparsifying transform. Therefore, the coarse estimation of the image is also done in sparsifying, firstly. However, the natural images do not exhibit exact sparsity but approximate sparsity in any sparsifying domain. This is why in the sequel, we will investigate the the performance of the GTSNET-T in the recovery of exact sparse signals.

In this section, we use the MNIST dataset for our experiments. Images in this dataset have resolutions of 28×28 pixels, and intensities ranging from 0 to 1. The background of each image covers a larger area than the foreground, making it a sparse signal in the canonical basis. Non-zero coefficients to vectorized signal dimension ratios (i.e., $\frac{k}{N}$) range from 0.05 to 0.4 [45]. Therefore it is actually a challenging sparse signal dataset for the traditional CS setup since it includes a large number of less sparse samples. The dataset includes 70000 samples, among them 50000 were used to train the networks, and 20000 were used for the test.

1) Tied Learning ($\mathbf{B} = \mathbf{A}'$) vs Untied Learning $\mathbf{B} \neq \mathbf{A}'$: In conventional solutions for linear inverse problems, the adjoint operator is taken as the transpose of the linear degradation matrix $\mathbf{A}$, i.e., $\mathbf{B} = \mathbf{A}^T$. However, the adjoint $\mathbf{B}$ is also learned without any constraint depending on $\mathbf{A}$. In this section, we will investigate the advantages/disadvantages of such a learning scheme instead of tied learning where $\mathbf{A}$ and $\mathbf{B}$ are learned with a constraint $\mathbf{B} = \mathbf{A}^T$. For the MNIST dataset, we assume that the i^{th} vectorized sparse signal $\mathbf{x}_i \in \mathbb{R}^{N=784}$ is compressively sensed, $\mathbf{y_i} = \mathbf{A}\mathbf{x_i}$, where $\mathbf{A} \in \mathbb{R}^{m\times N}$ for different m values. The measurement matrix $\mathbf{A}$ is selected in three different ways: a) Unfactorized full-size Gaussian matrix. b) Learned CS matrix with GTSNET-T with constraint $\mathbf{B} = \mathbf{A}^T$. c) Learned CS matrix with GTSNET-T without such constraint.

As an example let us consider that one wants to take $m = 81$ measurements. In this setup, the number of parameters to represent the unfactorized conventional Gaussian matrix can be calculated as $81 \times 728 = 58968$. On the contrary for the learning matrix with $T = 3$-tensor sum scheme will be $2 \times T \times 9 \times 28 = 1512$ since each Kronecker product is represented by left and right matrix multiplications with the matrices of size 9×28. If there is no constraint in the adjoint operator then the number of parameters to represent the abjoint B will be the same. In the meanwhile, when there is a such constraint then, there is no additional parameter in order to represent the adjoint matrix.

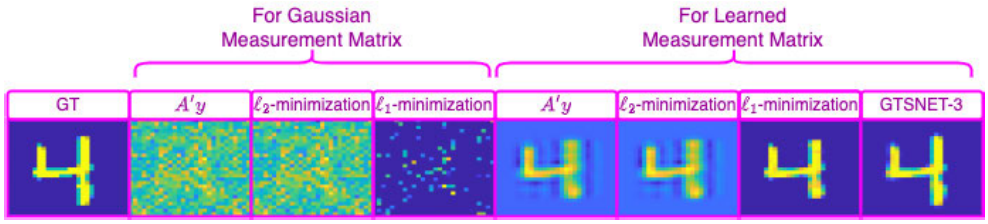

Fig. 12. Comparison of Gaussian measurement matrix and learned measurement matrix: Proxy, minimum norm solution, ℓ_1-minimization results from the measurement vector **As** when **A** is Gaussian matrix (on the left) and when **A** is learned with proposed tensorial sum approach (on the right).

Table V shows the comparison of the reconstruction performance of these three setups with different measurement rates and with different T values. For the conventional CS setup, we used ℓ_1-minimization to solve the recovery problem: $\hat{\mathbf{x}} = \arg\min_{\mathbf{x}} \|\mathbf{x}\|_1 \text{ s.t } \|\mathbf{y} - \mathbf{A}\mathbf{x}\|_2^2$. There is a clear pattern that shows that untied learning can achieve superior performance with increasing margin, especially when MR gets smaller. On the other hand, conventional CS setup performs very poorly due to the fact that the data sparsity ratio makes the sparse recovery very challenging.

2) Learned Measurement Matrix Within ℓ_1-Minimization Based Sparse Recovery: In order to compare the goodness of the learned measurement matrices to conventional sub-Gaussian matrices, the following experimental setup is designed: Learned measurement matrices are obtained via $\mathbf{A} = \sum_{t=1}^{T} \mathbf{A}_1^{(t)} \otimes \mathbf{A}_2^{(t)}$, where $\mathbf{A}_1^{(t)}$ and $\mathbf{A}_2^{(t)}$ are left and right multiplication matrices for t^{th} Kronecker product. Then, compressive sensing of vectorized sparse signal, $\mathbf{x}$, is done, i.e., $\mathbf{y} = \mathbf{A}\mathbf{x}$. In order to recover recover sparse signal, ℓ_1-minimization is used: $\hat{\mathbf{x}} = \arg\min_{\mathbf{x}} \|\mathbf{x}\|_1 \text{ s.t } \|\mathbf{y} - \mathbf{A}\mathbf{x}\|_2^2$. ADMM [66] is used to solve this optimization problem. Figure 7 shows an example visual comparison of the recovered outputs in this vector CS setup for conventional Gaussian CS matrix vs. learned CS matrix. Even coarse estimations of $\mathbf{x}$ via minimum norm solution and simple matrix vector multiplication with adjoint matrix (tied learning is used in this experiment, i.e., $\mathbf{B} = \mathbf{A}^{\mathbf{T}}$) are significantly improved compared to the ones from conventional Gaussian projection CS setup.

VI. Conclusion and Future Work

We propose generalized tensor summation networks for fast and high-quality CS. Our framework incorporates end-to-end learning where the parameters of both the CS matrix and the signal recovery are jointly optimized. On the sensing part, the CS matrices are modeled as the summation of T tensors, which has certain critical advantages. On one hand, the complexity and the number of parameters are greatly reduced thanks to the separability of tensors. By keeping $T = 1$, for instance, we can reduce the system to a Kronecker CS. On the other hand, unfactorized CS matrices can be approximated well enough by increasing T. In addition, we can design structured matrices by incorporating any separable basis into our framework, such as DCT.

The reconstruction step of the proposed algorithm takes advantage of an adjoint operator learned similarly in tensorial sum representation to perform a tentative reconstruction. In this proof of concept work, a non-iterative, CNN-based deep learning architecture is used as the refinement module. To further increase the performance, one can use the most advance deep backbone structures such as transformers or optimization-inspired deep neural networks in future works. We further note that increasing T improves the recovery until it reaches a maximum value at a certain T value (generally at $T = 3$ or 4). However, contrary to the expectation of staying in saturation, after this point, the performance metric starts decreasing with a further increase in T. Future works can be devoted to analyzing the reason for such behavior which may lead to better training strategies and increased performance.

References

[1] D. L. Donoho, "Compressed sensing," *IEEE Trans. Inf. Theory*, vol. 52, no. 4, pp. 1289–1306, Sep. 2004.

[2] M. Lustig, D. Donoho, and J. M. Pauly, "Sparse MRI: The application of compressed sensing for rapid MR imaging," *Magn. Reson. Med.*, vol. 58, no. 6, pp. 1182–1195, 2007.

[3] A. C. Gurbuz, J. H. McClellan, and W. R. Scott, "A compressive sensing data acquisition and imaging method for stepped frequency GPRs," *IEEE Trans. Signal Process.*, vol. 57, no. 7, pp. 2640–2650, Jul. 2009.

[4] M. Yamaç, M. Orhan, B. Sankur, A. S. Turk, and M. Gabbouj, "Through the wall target detection/monitoring from compressively sensed signals via structural sparsity," in *Proc. 5th Int. Workshop Compressed Sens. Appl. Radar, Multimodal Sens., Imag.*, 2018. [Online]. Available: https://new.eurasip.org/Proceedings/Ext/CoSeRa2018/papers/p-yamac.pdf

[5] H. Mamaghanian, N. Khaled, D. Atienza, and P. Vandergheynst, "Compressed sensing for real-time energy-efficient ECG compression on wireless body sensor nodes," *IEEE Trans. Biomed. Eng.*, vol. 58, no. 9, pp. 2456–2466, Sep. 2011.

[6] Y. Zhang, Y. Xiang, L. Y. Zhang, Y. Rong, and S. Guo, "Secure wireless communications based on compressive sensing: A survey," *IEEE Commun. Surveys Tuts.*, vol. 21, no. 2, pp. 1093–1111, 2nd Quart., 2019.

[7] M. Yamaç, M. Ahishali, N. Passalis, J. Raitoharju, B. Sankur, and M. Gabbouj, "Multi-level reversible data anonymization via compressive sensing and data hiding," *IEEE Trans. Inf. Forensics Security*, vol. 16, pp. 1014–1028, 2021.

[8] S. Chen and D. Donoho, "Basis pursuit," in *Proc. 28th Asilomar Conf. Signals, Syst. Comput.*, 1994, pp. 41–44.

[9] S. S. Chen, D. L. Donoho, and M. A. Saunders, "Atomic decomposition by basis pursuit," *SIAM Rev.*, vol. 43, no. 1, pp. 129–159, Jan. 2001.

[10] M. S. Asif and J. Romberg, "On the LASSO and Dantzig selector equivalence," in *Proc. 44th Annu. Conf. Inf. Sci. Syst. (CISS)*, Mar. 2010, pp. 1–6.

[11] C. Olsson, M. Carlsson, and D. Gerosa, "Bias reduction in compressed sensing," 2018, *arXiv:1812.11329*.

[12] C. Li, W. Yin, H. Jiang, and Y. Zhang, "An efficient augmented Lagrangian method with applications to total variation minimization," *Comput. Optim. Appl.*, vol. 56, no. 3, pp. 507–530, Dec. 2013.

[13] C. A. Metzler, A. Maleki, and R. G. Baraniuk, "From denoising to compressed sensing," *IEEE Trans. Inf. Theory*, vol. 62, no. 9, pp. 5117–5144, Sep. 2016.

[14] M. A. T. Figueiredo, R. D. Nowak, and S. J. Wright, "Gradient projection for sparse reconstruction: Application to compressed sensing and other inverse problems," *IEEE J. Sel. Topics Signal Process.*, vol. 1, no. 4, pp. 586–597, Dec. 2007.

[15] D. Donoho and J. Tanner, "Observed universality of phase transitions in high-dimensional geometry, with implications for modern data analysis and signal processing," *Phil. Trans. Roy. Soc. A, Math., Phys. Eng. Sci.*, vol. 367, no. 1906, pp. 4273–4293, Nov. 2009.

[16] A. Mousavi, A. B. Patel, and R. G. Baraniuk, "A deep learning approach to structured signal recovery," in *Proc. 53rd Annu. Allerton Conf. Commun., Control, Comput. (Allerton)*, Sep. 2015, pp. 1336–1343.

[17] K. Kulkarni, S. Lohit, P. Turaga, R. Kerviche, and A. Ashok, "ReconNet: Non-iterative reconstruction of images from compressively sensed measurements," in *Proc. IEEE Conf. Comput. Vis. Pattern Recognit. (CVPR)*, Jun. 2016, pp. 449–458.

[18] J. Zhang and B. Ghanem, "ISTA-Net: Interpretable optimization-inspired deep network for image compressive sensing," in *Proc. IEEE/CVF Conf. Comput. Vis. Pattern Recognit.*, Jun. 2018, pp. 1828–1837.

[19] W. Shi, F. Jiang, S. Liu, and D. Zhao, "Image compressed sensing using convolutional neural network," *IEEE Trans. Image Process.*, vol. 29, pp. 375–388, 2020.

[20] W. Shi, F. Jiang, S. Liu, and D. Zhao, "Scalable convolutional neural network for image compressed sensing," in *Proc. IEEE/CVF Conf. Comput. Vis. Pattern Recognit. (CVPR)*, Jun. 2019, pp. 12282–12291.

[21] M. F. Duarte and R. G. Baraniuk, "Kronecker compressive sensing," *IEEE Trans. Image Process.*, vol. 21, no. 2, pp. 494–504, Feb. 2012.

[22] Y. C. Eldar and G. Kutyniok, *Compressed Sensing: Theory and Applications*. Cambridge, U.K.: Cambridge Univ. Press, 2012.

[23] Y. Rivenson and A. Stern, "Compressed imaging with a separable sensing operator," *IEEE Signal Process. Lett.*, vol. 16, no. 6, pp. 449–452, Jun. 2009.

[24] M. Impiö, M. Yamaç, and J. Raitoharju, "Multi-level reversible encryption for ECG signals using compressive sensing," in *Proc. IEEE Int. Conf. Acoust., Speech Signal Process. (ICASSP)*, Jun. 2021, pp. 1005–1009.

[25] L. Y. Zhang, K.-W. Wong, Y. Zhang, and J. Zhou, "Bi-level protected compressive sampling," *IEEE Trans. Multimedia*, vol. 18, no. 9, pp. 1720–1732, Sep. 2016.

[26] M. Lustig, L. D. Donoho, M. Juan Santos, and M. J. Pauly, "Compressed sensing MRI," *IEEE Signal Process. Mag.*, vol. 25, no. 2, pp. 72–82, Mar. 2007.

[27] B. Adcock, A. C. Hansen, C. Poon, and B. Roman, "Breaking the coherence barrier: A new theory for compressed sensing," in *Forum of Mathematics, Sigma*, vol. 5. Cambridge, U.K.: Cambridge Univ. Press, 2017.

[28] E. J. Candès, "Compressive sampling," in *Proc. Int. Congr. Math.*, vol. 3, Aug. 2006, pp. 1433–1452.

[29] G. Li, Z. Zhu, D. Yang, L. Chang, and H. Bai, "On projection matrix optimization for compressive sensing systems," *IEEE Trans. Signal Process.*, vol. 61, no. 11, pp. 2887–2898, Jun. 2013.

[30] D. L. Donoho and M. Elad, "Optimally sparse representation in general (nonorthogonal) dictionaries via ℓ_1 minimization," *Proc. Nat. Acad. Sci. USA*, vol. 100, no. 5, pp. 2197–2202, Mar. 2003.

[31] A. Cohen, W. Dahmen, and R. DeVore, "Compressed sensing and best k-term approximation," *J. Amer. Math. Soc.*, vol. 22, no. 1, pp. 211–231, Jan. 2009.

[32] H. Rauhut, "Compressive sensing and structured random matrices," in *Theoretical Foundations and Numerical Methods for Sparse Recovery*, vol. 9. Berlin, Germany: de Gruyter, 2010, pp. 1–92.

[33] E. J. Candès and T. Tao, "Decoding by linear programming," *IEEE Trans. Inf. Theory*, vol. 51, no. 12, pp. 4203–4215, Dec. 2005.

[34] E. J. Candès, "The restricted isometry property and its implications for compressed sensing," *Comp. Rendus Mathematique*, vol. 346, nos. 9–10, pp. 589–592, May 2008.

[35] E. Candes and T. Tao, "The Dantzig selector: Statistical estimation when p is much larger than n," *Ann. Statist.*, vol. 35, no. 6, pp. 2313–2351, Dec. 2007.

[36] E. Candès and J. Romberg, "Sparsity and incoherence in compressive sampling," *Inverse Problems*, vol. 23, no. 3, pp. 969–985, Jun. 2007.

[37] J. M. Duarte-Carvajalino and G. Sapiro, "Learning to sense sparse signals: Simultaneous sensing matrix and sparsifying dictionary optimization," *IEEE Trans. Image Process.*, vol. 18, no. 7, pp. 1395–1408, Jul. 2009.

[38] D. L. Donoho and X. Huo, "Uncertainty principles and ideal atomic decomposition," *IEEE Trans. Inf. Theory*, vol. 47, no. 7, pp. 2845–2862, Nov. 2001.

[39] K. Schnass and P. Vandergheynst, "Average performance analysis for thresholding," *IEEE Signal Process. Lett.*, vol. 14, no. 11, pp. 828–831, Nov. 2007.

[40] I. Y. Chun and B. Adcock, "Compressed sensing and parallel acquisition," *IEEE Trans. Inf. Theory*, vol. 63, no. 8, pp. 4860–4882, Aug. 2017.

[41] S. K. Sahoo and A. Makur, "Signal recovery from random measurements via extended orthogonal matching pursuit," *IEEE Trans. Signal Process.*, vol. 63, no. 10, pp. 2572–2581, May 2015.

[42] T. T. Do, L. Gan, N. H. Nguyen, and T. D. Tran, "Fast and efficient compressive sensing using structurally random matrices," *IEEE Trans. Signal Process.*, vol. 60, no. 1, pp. 139–154, Jan. 2012.

[43] A. Degerli, S. Aslan, M. Yamac, B. Sankur, and M. Gabbouj, "Compressively sensed image recognition," in *Proc. 7th Eur. Workshop Vis. Inf. Process. (EUVIP)*, Nov. 2018, pp. 1–6.

[44] S. Lohit, K. Kulkarni, and P. Turaga, "Direct inference on compressive measurements using convolutional neural networks," in *Proc. IEEE Int. Conf. Image Process. (ICIP)*, Sep. 2016, pp. 1913–1917.

[45] M. Yamac, M. Ahishali, S. Kiranyaz, and M. Gabbouj, "Convolutional sparse support estimator network (CSEN) from energy efficient support estimation to learning-aided compressive sensing," 2020, *arXiv:2003.00768*.

[46] Y. Zhang, Y. Tian, Y. Kong, B. Zhong, and Y. Fu, "Residual dense network for image super-resolution," in *Proc. IEEE/CVF Conf. Comput. Vis. Pattern Recognit.*, Jun. 2018, pp. 2472–2481.

[47] X. Glorot, A. Bordes, and Y. Bengio, "Deep sparse rectifier neural networks," in *Proc. 14th Int. Conf. Artif. Intell. Statist.*, 2011, pp. 315–323.

[48] H. Zhao, O. Gallo, I. Frosio, and J. Kautz, "Loss functions for image restoration with neural networks," *IEEE Trans. Comput. Imag.*, vol. 3, no. 1, pp. 47–57, Mar. 2017.

[49] H. Son and S. Lee, "Fast non-blind deconvolution via regularized residual networks with long/short skip-connections," in *Proc. IEEE Int. Conf. Comput. Photography (ICCP)*, May 2017, pp. 1–10.

[50] A. Vedaldi and K. Lenc, "MatConvNet: Convolutional neural networks for MATLAB," in *Proc. 23rd ACM Int. Conf. Multimedia*, Oct. 2015, pp. 689–692.

[51] J. Romberg, "Imaging via compressive sampling," *IEEE Signal Process. Mag.*, vol. 25, no. 2, pp. 14–20, Mar. 2008.

[52] D. Donoho, A. Maleki, and M. Shahram, "WaveLab 850," in *Software Toolkit for Time-Frequency Analysis*. Stanford, CA, USA: Stanford Univ. Press, 2006.

[53] K. Dabov, A. Foi, V. Katkovnik, and K. Egiazarian, "Image denoising by sparse 3-D transform-domain collaborative filtering," *IEEE Trans. Image Process.*, vol. 16, no. 8, pp. 2080–2095, Aug. 2007.

[54] R. Zeyde, M. Elad, and M. Protter, "On single image scale-up using sparse-representations," in *Proc. Int. Conf. Curves Surf.* Cham, Switzerland: Springer, 2010, pp. 711–730.

[55] M. Bevilacqua, A. Roumy, C. Guillemot, and M. L. Alberi-Morel, "Low-complexity single-image super-resolution based on nonnegative neighbor embedding," in *Proc. 23rd Brit. Mach. Vis. Conf. (BMVC)*. BMVA Press, 2012, pp. 135.1–135.10.

[56] J. Chen, Y. Sun, Q. Liu, and R. Huang, "Learning memory augmented cascading network for compressed sensing of images," in *Proc. ECCV*, 2020, pp. 513–529.

[57] Y. Sun, J. Chen, Q. Liu, B. Liu, and G. Guo, "Dual-path attention network for compressed sensing image reconstruction," *IEEE Trans. Image Process.*, vol. 29, pp. 9482–9495, 2020.

[58] J. Zhang, C. Zhao, and W. Gao, "Optimization-inspired compact deep compressive sensing," *IEEE J. Sel. Topics Signal Process.*, vol. 14, no. 4, pp. 765–774, May 2020.

[59] Z. Zhang, Y. Liu, J. Liu, F. Wen, and C. Zhu, "AMP-Net: Denoising-based deep unfolding for compressive image sensing," *IEEE Trans. Image Process.*, vol. 30, pp. 1487–1500, 2021.

[60] D. You, J. Zhang, J. Xie, B. Chen, and S. Ma, "COAST: Controllable arbitrary-sampling network for compressive sensing," *IEEE Trans. Image Process.*, vol. 30, pp. 6066–6080, 2021.

[61] W. Cui, S. Liu, F. Jiang, and D. Zhao, "Image compressed sensing using non-local neural network," *IEEE Trans. Multimedia*, vol. 25, pp. 816–830, 2023.

[62] D. Ye, Z. Ni, H. Wang, J. Zhang, S. Wang, and S. Kwong, "CSformer: Bridging convolution and transformer for compressive sensing," 2021, *arXiv:2112.15299*.

[63] A. Dosovitskiy et al., "An image is worth 16×16 words: Transformers for image recognition at scale," in *Proc. Int. Conf. Learn. Represent.*, 2021. [Online]. Available: https://openreview.net/forum?id=YicbFdNTTy
[64] A. Fujimoto, T. Ogawa, K. Yamamoto, Y. Matsui, T. Yamasaki, and K. Aizawa, "Manga109 dataset and creation of metadata," in *Proc. 1st Int. Workshop coMics Anal., Process. Understand.*, Dec. 2016, pp. 1–5.
[65] J.-B. Huang, A. Singh, and N. Ahuja, "Single image super-resolution from transformed self-exemplars," in *Proc. IEEE Conf. Comput. Vis. Pattern Recognit. (CVPR)*, Jun. 2015, pp. 5197–5206.
[66] S. Boyd, "Distributed optimization and statistical learning via the alternating direction method of multipliers," *Found. Trends® Mach. Learn.*, vol. 3, no. 1, pp. 1–122, 2010.

Mehmet Yamaç received the B.S. degree in electrical and electronics engineering from Anadolu University, Eskisehir, Turkey, in 2009, and the M.S. degree in electrical and electronics engineering from Bogaziçi University, Istanbul, Turkey, in 2014. He is currently pursuing the Ph.D. degree with the Department of Computing Sciences, Tampere University, Tampere, Finland. He was a Research and Teaching Assistant with Bogazici University from 2012 to 2017 and a Researcher with Tampere University from 2017 to 2020. He has been a Senior Researcher with Huawei Technologies Oy, Tampere, from 2020 to 2023. He has coauthored more than 35 papers, two of them nominated for the "Best (or Student Best) Paper Award" in EUVIP 2018 and EUSIPCO 2019. His research interests are computer and machine vision, machine learning, and compressive sensing.

Ugur Akpinar received the B.Sc. degree in electrical and electronics engineering from Middle East Technical University in 2015 and the M.Sc. degree in information technology from the Tampere University of Technology in 2017. He is currently pursuing the Ph.D. degree with the Faculty of Information Technology and Communication Sciences, Tampere University. His research interests include multidimensional signal processing, optics, 3D imaging, and display technologies.

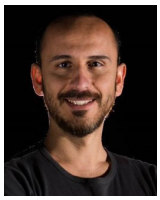

Erdem Sahin (Member, IEEE) received the Ph.D. degree from the Electrical and Electronics Engineering Department, Bilkent University, in 2013. In 2014, he joined the 3D Media Group, Faculty of Information Technology and Communication Sciences, Tampere University, as a Marie Curie Experienced Researcher, where he has been a Senior Research Fellow since 2019. His current research interests include development of computational light field and holographic imaging systems and algorithms.

Serkan Kiranyaz (Senior Member, IEEE) was born in Turkey in 1972. He received the B.S. and M.S. degrees from the Electrical and Electronics Department, Bilkent University, Ankara, Turkey, in 1994 and 1996, respectively, and the Ph.D. and Docency degrees from the Institute of Signal Processing, Tampere University of Technology, in 2005 and 2007, respectively.

He was a Professor with the Signal Processing Department, Tampere University of Technology, from 2009 to 2015. He is currently a Professor with Qatar University, Doha, Qatar. He has noteworthy expertise and background in various signal processing domains. He has published two books, seven book chapters, ten patents/applications, more than 100 journal articles in several IEEE TRANSACTIONS and other high impact journals, and more than 120 papers in international conferences. He served as a PI and a LPI in several national and international projects. His principal research field is machine learning and signal processing. He is rigorously aiming for reinventing the ways in novel signal processing paradigms, enriching it with new approaches especially in machine intelligence and revolutionizing the means of "learn-to-process" signals. He made significant contributions on bio-signal analysis, particularly EEG and ECG analysis and processing, classification and segmentation, computer vision with applications to recognition, classification, multimedia retrieval, evolving systems and evolutionary machine learning, swarm intelligence, and evolutionary optimization.

Moncef Gabbouj (Fellow, IEEE) is currently a Professor in information technology with the Department of Computing Sciences, Tampere University, Finland. He was an Academy of Finland Professor. His research interests include big data analytics, multimedia analysis, artificial intelligence, machine learning, pattern recognition, nonlinear signal processing, video processing, and coding. He is a fellow of the Asia–Pacific Artificial Intelligence Association. He is a member of the Academia Europaea, the Finnish Academy of Science and Letters, and the Finnish Academy of Engineering Sciences. He is also the Finland Site Director of the NSF IUCRC funded Center for Big Learning.

Generalized Tensor Summation Compressive Sensing Network (GTSNET): An Easy to Learn Compressive Sensing Operation

MEHMET YAMAÇ[1], UGUR AKPINAR[1], ERDEM SAHIN[1], SERKAN KIRANYAZ[2], AND MONCEF GABBOUJ[1]

[1] *Tampere University, Faculty of Information Technology and Communication Sciences, Tampere, Finland*
[2] *Department of Electrical Engineering, Qatar University, Qatar*

This supplementary material presents additional information, tables and figures that may be useful for interested users.

1. DERIVATIVE OF GENERALIZED TENSOR SUM OPERATIONS FOR BACK PROPAGATION

Eq. (10) and Eq. (11) of the main article provide a mathematical description of the proposed CS module. In practice, we implement a single custom Tensor layer $P^{(t)}(.)$ to perform a tensor product with the input signal, as in the pink blocks in Figure S1,

$$P^{(t)}(\mathcal{S}) = \mathcal{S} \times_1 \mathbf{\Psi_1^{(t)}} \times_2 \mathbf{\Psi_2^{(t)}} ... \mathbf{\Psi_{J-1}^{(t)}} \times_J \mathbf{\Psi_J^{(t)}}. \tag{S1}$$

Here, with respect to the error, we derive the input derivatives of such layer, which are to be calculated during the backward pass. Let us first denote a $j-$ dimensional tensor multiplication,

$$\mathcal{Y}_j^{(t)} = \mathcal{S} \times_1 \mathbf{\Psi_1^{(t)}} \times_2 \mathbf{\Psi_2^{(t)}} ... \times_j \mathbf{\Psi_j^{(t)}}, \tag{S2}$$

where we can immediately see

$$\mathcal{Y}_j^{(t)} = \mathcal{Y}_{j-1}^{(t)} \times_j \mathbf{\Psi_j^{(t)}}, \tag{S3}$$

with $\mathcal{Y}_0^{(t)} = \mathcal{S}$ and $P^{(t)}(\mathcal{S}) = \mathcal{Y}_J^{(t)}$. In the backward pass, we assume that the partial derivative of the error with respect to the output, $\partial L / \partial \mathcal{Y}_J^{(t)}$, is known. From Eq. Eq. (S3) and the basics of linear algebra,

$$\frac{\partial L}{\partial \mathcal{Y}_{J-1}^{(t)}} = \frac{\partial L}{\partial \mathcal{Y}_J^{(t)}} \times_J \mathbf{\Psi_J^{(t)}}', \tag{S4}$$

form which we iteratively go back to conclude

$$\frac{\partial L}{\partial \mathcal{S}} = \frac{\partial L}{\partial \mathcal{Y}_J^{(t)}} \times_J \mathbf{\Psi_J^{(t)}}' \times_{J-1} \mathbf{\Psi_{J-1}^{(t)}}' ... \times_2 \mathbf{\Psi_2^{(t)}}' \times_1 \mathbf{\Psi_1^{(t)}}', \tag{S5}$$

which is nothing but the multiplication with the transposed tensor.

To calculate the partial derivatives with respect to the individual matrices of the CS tensor, $\mathbf{\Psi_j^{(t)}}$, we can start by rearranging Eq. Eq. (S3) in discrete form as

$$\mathcal{Y}_j^{(t)}[n_1, ..., n_j, ...n_J] = \sum_{\tilde{n}_j} \mathbf{\Psi}_j^{(t)}[n_j, \tilde{n}_j] \mathcal{Y}_{j-1}^{(t)}[n_1, ..., \tilde{n}_j, ...n_J]. \tag{S6}$$

Eq. Eq. (S6) can be converted to a simpler form as follows: Suppose an operator $mat_j(.)$ takes a $J-$dimensional input $\mathcal{Y}$ and convert it to a matrix $\mathbf{Y_j}$, by first permuting its dimensions so that the jth dimension of $\mathcal{Y}$ become the rows of $\mathbf{Y_j}$, and then rescaling so that all the other dimensions become the columns. Then

$$\mathcal{Y}_j^{(t)} = mat_j^{-1}(\mathbf{\Psi_j^{(t)}} mat_j(\mathcal{Y}_{j-1}^{(t)})), \tag{S7}$$

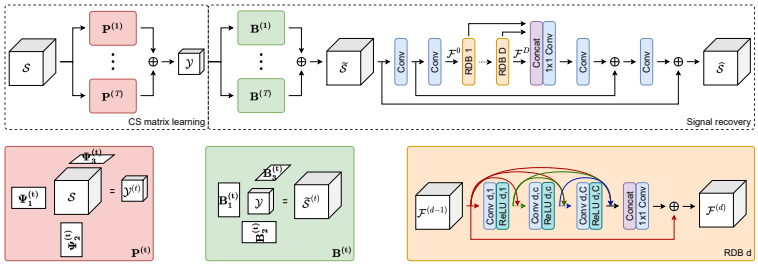

Fig. S1. Overall block diagram of the proposed end-to-end system.

where mat_j^{-1} is the inverse of the above-mentioned $mat_j(.)$ operator. It is then straightforward to see that

$$\frac{\partial L}{\partial \mathbf{\Psi_j^{(t)}}} = mat_j\left(\frac{\partial L}{\partial \mathcal{Y}_j^{(t)}}\right) mat_j(\mathcal{Y}_{j-1}^{(t)}))', \tag{S8}$$

Unfortunately, Eq. Eq. (S8) requires a forward propagation of $\mathcal{Y}_{j-1}^{(t)}$ all the way up to $\mathcal{Y}_{J-1}^{(t)}$, which practically indicates another forward propagation before starting the backward pass. However, as these matrix multiplications at each dimension are relatively fast, such requirement does not add any noticeable overhead to the computational complexity.

2. DERIVATIVE OF LOSS FUNCTION FOR BACK PROPAGATION

Here we aim to provide the partial derivatives of error with respect to the final estimation $\widehat{\mathcal{S}}$, $\partial L/\partial \widehat{\mathcal{S}}$. As we discussed previously, our loss function is a combination of an L_1-loss over proxy, $\widetilde{L}(\widetilde{\mathcal{S}}, \mathcal{S})$, and a regularized L_1-loss over the final output, $\widehat{L}(\widehat{\mathcal{S}}, \mathcal{S})$. As the derivatives of L_1-losses are well-known, the derivation of the partial derivative of the regularization function with respect to $\widehat{\mathcal{S}}$, $\partial R/\partial \widehat{\mathcal{S}}$ will be sufficient. Furthermore, considering Eq. (18) of the main article is separable into first and second dimensions, we can derive the derivative in 1D for simplicity, from which the extension to 2D is straightforward. If we then reformulate Eq. (18) of the main article in 1D

$$\widehat{R}_{n_1}(\widehat{\mathcal{S}}, \mathcal{S}) = \sum_{n_1,\dots,n_J} \exp\left(-\beta|\nabla_{n_1}\mathcal{S}|^\gamma\right)|\nabla_{n_1}\widehat{\mathcal{S}}|^\gamma, \tag{S9}$$

where $\nabla_{n_1}\widehat{\mathcal{S}} = \widehat{\mathcal{S}}[n_1+1, n_2, ..., n_J] - \widehat{\mathcal{S}}[n_1, n_2, ..., n_J]$ in discrete form. Let us first denote

$$\widehat{\mathcal{G}}_{n_1} = \nabla_{n_1}\widehat{\mathcal{S}}, \quad \mathcal{G}_{n_1} = |\widehat{\mathcal{G}}_{n_1}|, \quad \mathcal{W}_{n_1} = \exp\left(-\beta|\nabla_{n_1}\mathcal{S}|^\gamma\right). \tag{S10}$$

From now on we can treat $\mathcal{W}_{n_1}$ as a constant, element-wise weighting factor, as it only depends on the label $\mathcal{S}$. Then, using Eq. Eq. (S9), the first partial derivative is

$$\frac{\partial R_{n_1}}{\partial \mathcal{G}_{n_1}} = \gamma \mathcal{W}_{n_1} \mathcal{G}_{n_1}^{(\gamma-1)}. \tag{S11}$$

Assuming the derivative of $|.|$ is $sgn(.)$, i.e., the sign function,

$$\frac{\partial R_{n_1}}{\partial \widehat{\mathcal{G}}_{n_1}} = \gamma \mathcal{W}_{n_1} \mathcal{G}_{n_1}^{(\gamma-1)} sgn(\widehat{\mathcal{G}}_{n_1}). \tag{S12}$$

The partial derivative $\partial \widehat{G}/\partial \widehat{\mathcal{S}}$ is defined as follows

$$\frac{\partial \widehat{\mathcal{G}}_{n_1}[n_1, ..., n_J]}{\partial \widehat{\mathcal{S}}[\tilde{n}_1, ..., \tilde{n}_J]} = \begin{cases} 1, & \text{if } \tilde{n}_1 = n_1 - 1 \ \ \& \ \ \tilde{n}_2, ..., \tilde{n}_J = n_2, ..., n_J \\ -1, & \text{if } \tilde{n}_1 = n_1 \ \ \& \ \ \tilde{n}_2, ..., \tilde{n}_J = n_2, ..., n_J \\ 0, & \text{otherwise} \end{cases} \tag{S13}$$

Using Eq. Eq. (S12) and Eq. Eq. (S13), and the chain rule, one can find in 1D

$$\frac{\partial R_{n_1}}{\partial \widehat{S}} = \frac{\partial R_{n_1}}{\partial \widehat{\mathcal{G}}_{n_1}}[n_1 - 1, n_2, ..., n_J] - \frac{\partial R_{n_1}}{\partial \widehat{\mathcal{G}}_{n_1}}[n_1, n_2, ..., n_J]. \tag{S14}$$

By changing dimension from n_1 to n_2 and extending to 2D, we can conclude that

$$\frac{\partial R}{\partial \widehat{S}} = \frac{\partial R_{n_1}}{\partial \widehat{S}} + \frac{\partial R_{n_2}}{\partial \widehat{S}}. \tag{S15}$$

PUBLICATION IX

A Personalized Zero-shot Ecg Arrhythmia Monitoring System: From Sparse Representation Based Domain Adaption to Energy Efficient Abnormal Beat Detection for Practical Ecg Surveillance

M. Yamaç, M. Duman, İ. Adalıoğlu, S. Kiranyaz, and M. Gabbouj

IEEE Transactions on Neural Networks and Learning Systems, Under review. Pre-print version available on arXiv. ArXiv ID: 2207.07089v1.